

# Application of Coda Wave Interferometry with embedded Smart Aggregate in a prestressed cast-in-situ concrete continuous slab bridge

---

**Danny Fu**

1/17/2022





# Application of Coda Wave Interferometry with embedded Smart Aggregate in a prestressed cast-in-situ concrete continuous slab bridge

By

Danny Fu

in partial fulfilment of the requirements for the degree of

**Master of Science**

in Civil Engineering, Structural Engineering

at the Delft University of Technology,

to be defended publicly on Wednesday January 26, 2022 at 3:30 PM.

Supervisor:	Dr. ir. Y. Yang,	TU Delft
Thesis committee:	Dr. ir. W. H. M. van der Ham,	TU Delft, Boskalis
	Dr. ir. D. Draganov,	TU Delft

# Acknowledgements

Foremost, my utmost respect and gratitude go out to the members of my thesis committee at TU Delft, Dr. ir. Yuguang Yang, Dr. ir. Herbert van der Ham and Dr. ir. Deyan Draganov, for guiding me through my research and sharing their insight with me.

Additional gratitude goes to Yuguang Yang for suggesting this amazing thesis topic to me and for setting me on this journey.

I have great appreciation for Jorn Leijen from Boskalis, who contributed immensely to this study. Without him and Herbert van der Ham this thesis would not have been possible, as they not only provided access to the monitored structure but they have also played part in designing it.

Special credit goes out to ing. Kees van Beek at TU Delft. Even though I have not had the pleasure to meet him, his contribution to this thesis is invaluable. The MUX-system he constructed was crucial for this study.

I thank PhD candidates Fengqiao Zhang and Hao Cheng at TU Delft for helping me familiarize with the Coda Wave Interferometry mapping algorithm and guiding me through the learning process.

Additional thanks go to Hao Cheng, Shizhe Zhang and Jakub Pawlowicz for their help with setting up the laboratory tests and the assistance during execution of the tests.

All of the individuals mentioned were essential for the completion of my MSc thesis and I will forever be grateful for their contribution.

# Abstract

In recent years, the area of structural engineering has found new interesting prospects in the theory of waves. The acoustoelastic properties of materials are utilized in a new promising structural health monitoring (SHM) technique. The propagation of ultrasonic waves through stressed elements gives the ability to find invaluable information on the stress-state of the concerned element. This information is then analyzed with the use of Coda Wave Interferometry (CWI). This technique explores the late arrivals of the wave field, which is referred to as the coda. Due to scattering of the waves through heterogeneous elements, this part of the wave field holds additional information compared to the early arrivals, which makes it very suitable for application on concrete elements.

The use of ultrasonic waves with CWI in concrete elements has been studied enthusiastically by engineers due to its promising prospects. Nevertheless, this technique is still developing both in theory and in practice. The majority of previous similar studies have been conducted in laboratory settings, and thus conditions are very controlled. In this study, the monitoring technique is applied in conjunction with Smart Aggregate (SA) to a concrete structure for practical use. The SA sensors are positioned in groups at key location in the first concrete cast of a cast-in-situ prestressed concrete bridge, which entails two bridge spans of approximately 30 meters length. Measurements are done at different phases during the construction of the bridge, when the stress-state at the positions shifts due to change in loading and boundary conditions. The resulting data is analyzed with CWI and subsequently evaluated whether it coincides with expectations. Deviations from these expectations are rationalized or an attempt thereof is made.

The results show significant differences between field measurement results and expectations based on laboratory tests. These differences are explained by the presence of a greater amount of parameters, which influence the data gathered from field measurements. With the appropriate measures, the various factors acting on the structure are isolated and subsequently validated with laboratory data. The most prominent factors affecting the acoustoelastic properties of the structure are established to be time related. These factors involve concrete shrinkage, creep deformation and the concrete hydration process. With laboratory testing the effect of these factors on the wave propagation velocity are determined. By taking into account the additional factors, a strong correlation between changes in the stress-state and changes in the wave propagation velocity is observed when the data is read in an adjusted manner.

With a proper protocol, the use of smart aggregates in combination with CWI could be very valuable in accessing concrete structures on-site in both its construction stage and service stage. As it stands, prerequisite knowledge of the monitored structure is necessary to make use of the full potential of the SHM involving CWI and SA. The demand for prerequisite knowledge of the structure increases as the monitored structure becomes more complex, because it increases the amount of additional endeavors required to properly assess the acquired data. As such, the discussed monitoring technique in its current stage of development generally has low accessibility for practical use. But with further research and more understanding of monitoring method, the discussed SHM technique might be applicable for general use in the near future.

# Contents

Acknowledgements .....	III
Abstract .....	IV
1 Introduction .....	1
1.1 Context .....	1
1.2 Research question and sub-questions .....	2
1.3 Approach .....	2
1.4 Reading guide.....	3
2 Theory of Coda Wave Interferometry .....	4
2.1 Coda Wave Interferometry (CWI).....	4
2.2 Acoustoelastic effect .....	4
2.3 Time of flight.....	5
2.4 Coda waves.....	5
2.5 Fast Fourier Transform.....	6
2.6 Wave types .....	6
2.7 Wavelength.....	7
2.8 Stretching technique .....	7
2.9 Wave-velocity change ( $dv/v$ ).....	8
2.10 Cross-correlation coefficient ( $CC$ ) .....	8
2.11 Cycle skipping.....	9
2.12 Sensitivity kernel.....	10
3 Methodology for field measurements and laboratory testing .....	12
3.1 Field measurements location details.....	12
3.1.1 Field application .....	13
3.2 Measurement equipment .....	14
3.3 Smart Aggregate (SA) .....	15
3.4 Software and post-processing method.....	16
3.5 Sensor configuration setup in concrete bridge .....	17
3.6 Compression stress test setup .....	18
3.7 Concrete hydration test setup .....	19
3.8 Creep test setup .....	19
4 Coda Wave Interferometry results of field measurements .....	21
4.1 Field measurement specifics.....	21
4.1.1 Cycle skipping.....	22

4.2	Results of Measurement 1-5 of the concrete structure .....	24
4.3	Results of Measurement 6-7 of the concrete structure .....	34
4.4	Results of Measurement 8 of the concrete structure.....	36
5	Coda Wave Interferometry results of laboratory tests.....	38
5.1	Concrete hydration .....	38
5.2	Concrete compression .....	41
5.3	Geopolymer creep .....	43
5.3.1	Effects of temperature .....	46
6	Analysis of results .....	47
6.1	Structural analysis of the concrete structure.....	47
6.1.1	Calculation of cross-sectional stresses .....	47
6.1.2	Calculation of time dependent deformations.....	54
6.2	Visualization of $dv/v$ -distribution of the sensor groups within the concrete structure from measured data.....	56
6.3	Simulated stress distribution from field measurement data.....	62
6.4	Comparison between expected and measured cross-sectional stress distributions within the concrete structure .....	65
6.5	Comparison between expected and measured effect of time-dependent factors on the concrete structure .....	71
7	Discussion .....	75
7.1	Cycle skipping prevention.....	75
7.2	CWI data processing .....	75
7.3	Structural analysis .....	76
7.4	Recommendations for future studies .....	76
8	Conclusions .....	77
	References .....	79
A.	MATLAB-script for data reading and CWI computation .....	81
B.	FFT analysis .....	87
C.	Cycle skipping correction.....	90
D.	CWI results of field measurements .....	100
E.	CWI results of concrete hydration tests.....	206
F.	CWI results of cylinder compression tests .....	247
G.	CWI results of geopolymer creep test .....	276

# 1 Introduction

## 1.1 Context

In the last few decades, the knowledge and understanding for structural design of concrete structures has improved significantly across Europe. With the establishment of the Eurocode, structural design rules have been harmonized over multiple countries. This was made possible by international collaboration wherein knowledge and expertise are exchanged. The Eurocode has in most cases completely replaced the previously applied national Dutch design codes. These new codes allow for more certainty in designing larger and more complex structures.

Although the Eurocode has opened the way for more possibilities in the present and future, it has also brought some concerning problems to light. Existing structures which were designed with old codes are no longer sufficient when evaluated by the new Eurocode and their new standards. To prevent the same problem from occurring in the future, the application of a system which monitors the structure will be most valuable. Rather than evaluating structures based on codes, the actual state of the structure can be determined with such a monitoring system. Therefore, implementing a system able to measure the stress-state of the structure can prove to be very beneficial.

The process of monitoring the condition of a structure in real time with sensors and associated algorithms is called Structural Health Monitoring (SHM). The practice of monitoring a structure does not only tell about the structural integrity, but it can also give more insight on how the structure behaves during its life cycle. Implementing a monitoring system during the construction of new structures can prevent the predicament many old structures in the Netherlands face today. As a large quantity of concrete bridges are nearing the end of their intended lifespan, the coming years will be crucial for the longevity of the structures that are to replace them. Having the ability to directly monitor how the structure behaves, removes the uncertainty of whether the structure still has sufficient functionality in changing circumstances. A structure can thus be serviceable well beyond its intended lifespan.

The concerned monitoring system used in this study consists of data collection using embedded Smart Aggregate and data post-processing with Coda Wave Interferometry. The Smart Aggregate has the ability to send and receive ultrasonic wave signals through a medium of interest. The received wave signals are logged and eventually analyzed. Post-processing with Coda Wave Interferometry is realized by analyzing the coda part of the wave signal. The coda wave refers to the slowly decaying waves, which have scattered through the medium by heterogeneities or element boundaries. Due to the scattering, the coda wave is able to detect small changes within the medium. By cross-correlating the wave signals of two instances, the changes in properties of the medium and even changes in stress-state can be determined.

The aim of this research is to validate the obtained data from Smart Aggregates in a prestressed concrete cast-in-situ bridge during its construction phase by analyzing the wave signals from the Smart Aggregate with Coda Wave Interferometry. The concrete bridge in question is constructed by contractor Boskalis, connecting the N69 in the province Noord-Brabant in the Netherlands. As the large majority of bridges in the Netherlands are constructed with prefabricated elements, the construction of this cast-in-situ bridge opens up the unique opportunity for the application of Smart Aggregate within the concrete cast of the structure. In collaboration with Boskalis' structural engineer John Leijen, the monitoring system is implemented in the concrete bridge and data is collected afterwards with periodic field measurements.

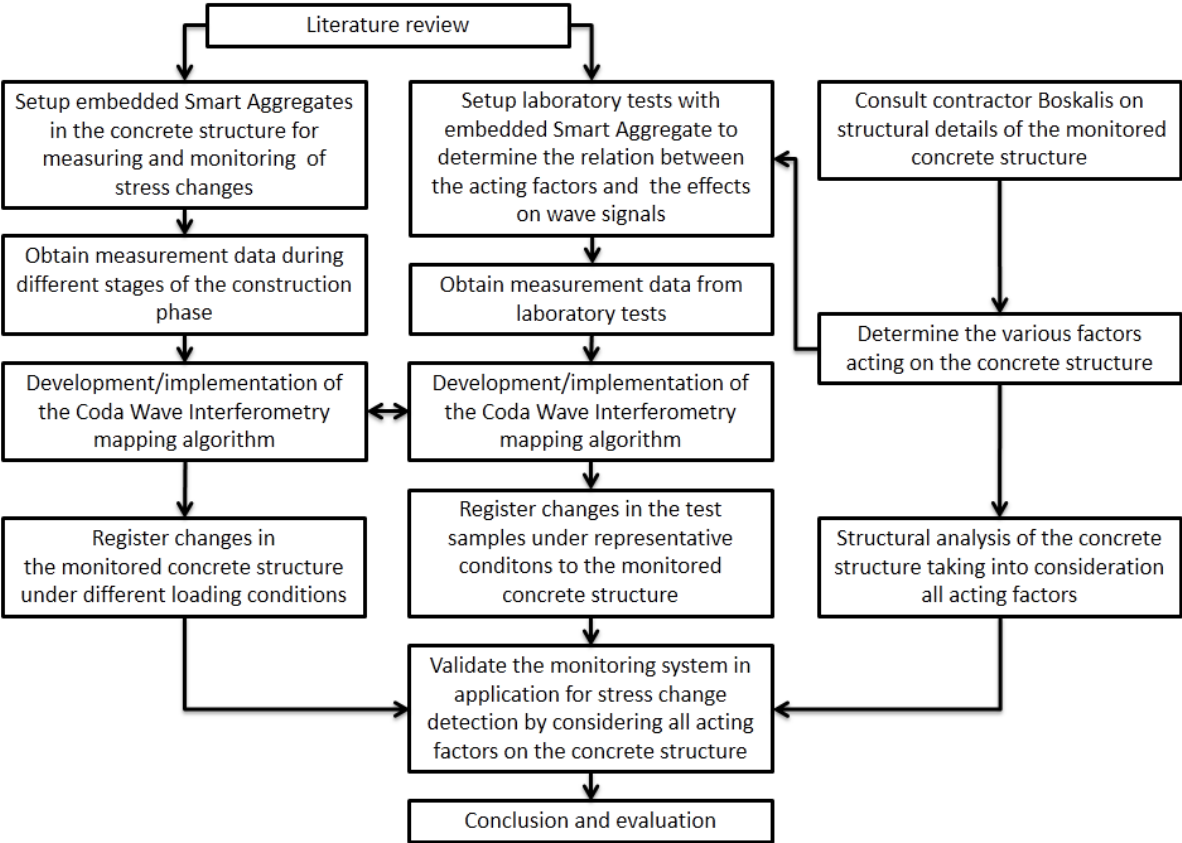
The measurements on the bridge to obtain the wave signals from the Smart Aggregate take place during different phases of the construction, where the stress distribution changes due to differences in loading conditions (e.g. prestressing, removal of supports). With reliable feedback from the bridge on its stress-state, one has the ability to determine the forces acting on the structure and appraise the structure’s structural integrity. Thus, monitoring the behavior of the structure during this phase can prove to be very advantageous.

**1.2 Research question and sub-questions**

How can the structural behavior of a cast-in-situ concrete structure be monitored with Coda Wave Interferometry and embedded Smart Aggregate during its construction phase?

- How can Coda Wave Interferometry be used to monitor stress changes in concrete structures with embedded Smart Aggregate?
- Which acting factors affect the acoustoelastic properties of the concrete structure during the construction phase and how can the factors acting on the structure be assessed with Coda Wave Interferometry and embedded Smart Aggregate?
- How do the results from the experimental Coda Wave Interferometry translate and compare to a structural analysis of the concrete structure?

**1.3 Approach**



The above diagram illustrates the multilateral manner in which this study is approached. The research process diverges in three divisions: field measurements, laboratory tests and structural analysis, and ultimately converges at the end of the study to draw the main conclusions.

The proceedings regarding the field measurement and the laboratory testing follow the same general progression, namely setup, data acquisition and data processing. A preliminary literature review provides the necessary knowledge to correctly set up the methodology of the field measurements and laboratory tests. Additionally, structural engineer Jorn Leijen of construction company Boskalis is consulted on the structural specifics of the monitored cast-in-situ concrete bridge. This information is then used in conjunction with the literature review to determine which factors affect the acoustoelastic properties of the structure and how laboratory testing is to be used to demonstrate these effects.

The specifics of the laboratory tests are decided based on the most prominent factors acting on the monitored concrete structure. After setup, measurements are conducted periodically on the monitored structure and the laboratory tests according to a predetermined schedule. The intervals between measurements are established on the basis of what the measurements are to represent, be it load related or time related. Subsequently, the post-processing of the acquired data is done by cross-correlation of various data sets with Coda Wave Interferometry. The original mapping algorithm is provided by PhD candidate Fengqiao Zhang at TU Delft, which is then modified to fit the needs of this study and to obtain the appropriate results for analysis.

Simultaneously, a structural analysis is run on the monitored structure based on the structural details given by contractor Boskalis. The analytical calculations act in juxtaposition to the experimental derivations of the field measurements and laboratory tests. The outcomes of the three divisions are appropriated and collated to conclude whether the monitoring system and the described approach are suitable.

## **1.4 Reading guide**

The research report is divided into sections and the sections discuss the following aspects of the report:

- Section 2 explains the background theory of CWI and additional theory relevant for this study.
- Section 3 explains the methodology of the research and includes details of the equipment used. The various procedures regarding field measurements and laboratory testing are devised and the significance thereof is explained.
- Section 4 shows the CWI results of the field measurements, including what each measurement entails.
- Section 5 shows the CWI results of the various laboratory tests and the purpose of the tests in regards to the field measurements is described.
- Section 6 includes a structural analysis and further derivation of the CWI results. In this section, comparisons are made between analytical results from the structural analysis and experimental results from the field measurements.
- Section 7 discusses the scope of the research and the difficulties encountered, with prospects for future research.
- Section 8 shows the main conclusions of the research and provides answers to the research questions.

## 2 Theory of Coda Wave Interferometry

### 2.1 Coda Wave Interferometry (CWI)

To fully understand the workings of CWI, one must delve into the history of the technique. CWI finds the majority of its past usage in seismology. Similarly, to its application in structural engineering, CWI cross-correlates observed waves which have propagated through a medium. For CWI in the field of seismology, the medium in question refers to (part of) the subsurface.

In recent years, the same CWI technique has been applied to monitor structural behavior of concrete [1] [2] [3] [4] [5]. This jump from geoscience to concrete-structure analysis is quite logical when one considers the intended propagation medium. The approach of the method to the heterogeneities in the subsurface is applied similarly to the heterogeneities in concrete.

### 2.2 Acoustoelastic effect

In Murnaghan's work [6], the relation between wave propagation velocity and stress is extrapolated and expressed in the "acoustoelastic effect" of the medium. The wave equation is found by substituting the nominal stress tensor into Cauchy's first law of motion:

$$\frac{\partial^2 u}{\partial t^2} - c_{xx}^2 \frac{\partial^2 u}{\partial x^2} = 0, \quad 2.1$$

where  $u$  is the displacement differentiated over time  $t$  and space  $x$ .  $c_{xx}$  is the wave velocity of longitudinal waves propagating in the  $x$ -direction and is defined as

$$c_{xx} = \sqrt{\frac{\lambda + 2\mu + (2l + \lambda)\theta + (4\lambda + 4m + 10\mu)\alpha_1}{\rho_a}}, \quad 2.2$$

where  $\rho_a$  is the initial mass density.  $\lambda$  and  $\mu$  are the first and second Lamé parameter, respectively, and can be expressed in terms of the Young's modulus ( $E$ ) and Poisson's ratio ( $\nu$ ):

$$\lambda = \frac{E\nu}{(1 + \nu)(1 - 2\nu)}; \mu = \frac{E}{2(1 + \nu)}. \quad 2.3$$

$l$  and  $m$  are Murnaghan constants, which are all material-dependent quantities.  $\alpha_1$  is the uniaxial strain and  $\theta$  is the summation of the uniaxial strains in three dimensions:

$$\theta = \alpha_1 + \alpha_2 + \alpha_3 = \alpha_1(1 - 2\nu) = \alpha_1 \frac{\mu}{\lambda + \mu}. \quad 2.4$$

The general notation of Hooke's law for linear elasticity,

$$\begin{bmatrix} \sigma_{xx} \\ \sigma_{yy} \\ \sigma_{zz} \end{bmatrix} = \frac{E}{(1 + \nu)(1 - 2\nu)} \begin{bmatrix} 1 - \nu & \nu & \nu \\ \nu & 1 - \nu & \nu \\ \nu & \nu & 1 - \nu \end{bmatrix} \begin{bmatrix} \varepsilon_{xx} \\ \varepsilon_{yy} \\ \varepsilon_{zz} \end{bmatrix}, \quad 2.5$$

can be rewritten with the first and second Lamé parameter into

$$\begin{bmatrix} \sigma_{xx} \\ \sigma_{yy} \\ \sigma_{zz} \end{bmatrix} = \begin{bmatrix} 2\mu + \lambda & \lambda & \lambda \\ \lambda & 2\mu + \lambda & \lambda \\ \lambda & \lambda & 2\mu + \lambda \end{bmatrix} \begin{bmatrix} \alpha_1 \\ \alpha_2 \\ \alpha_3 \end{bmatrix} \quad 2.6$$

and further simplified into

$$\sigma_{ii} = (3\lambda + 2\mu)\theta = 3K_0\theta, \quad 2.7$$

where  $K_0$  is termed the bulk modulus.

Subsequently, Equation 2.4 and Equation 2.7 can be substituted into Equation 2.2 to find the relation between wave velocity and stresses parallel to the wave propagation direction:

$$c_{xx}^{\sigma_{xx}} = \sqrt{\frac{\lambda + 2\mu \pm \frac{\sigma_{xx}}{3K_0} [2l + \lambda + \frac{\lambda + \mu}{\mu} (4\lambda + 4m + 10\mu)]}{\rho_a}}. \quad 2.8$$

### 2.3 Time of flight

To better understand the theory behind CWI, an older monitoring method can act as a starting point. The ‘‘Time of Flight’’ technique [7] is established on the simple relation between velocity, distance and time. A wave propagates through the medium, and the time interval for the wave to travel the distance from source to receiver is taken as data output. Due to the simplicity of the technique, it is entirely possible to perform this technique analytically. However, this technique has limitations and these limitations make the technique unsuitable for this study. The technique assumes that a straight path between the source and receiver is present. In other words, it requires a travel path with homogeneous properties. The technique is also limited by the information the output data holds as only the material along the straight path is taken into consideration.

### 2.4 Coda waves

CWI is able to overcome the limitations of the more simplistic Time of Flight technique, because it has a more complex and extensive approach. As the waves pass through the medium they undergo scattering from the heterogeneities of the medium. As a result, the signal will have a distinct shape when it arrives at the receiver (Figure 1). The signal consists of early arrivals and the coda waves with each part holding different information about the medium. The early arrivals travel a more direct path from source to receiver with minimal scattering. On the other hand, the later part of the coda waves contains information on a wider area around the source and receiver. The heterogeneities cause the signal to scatter in a controlled chaotic manner. As a result, the signal travels a diverted path through the medium, and arrives at the receiver at a later point in time.

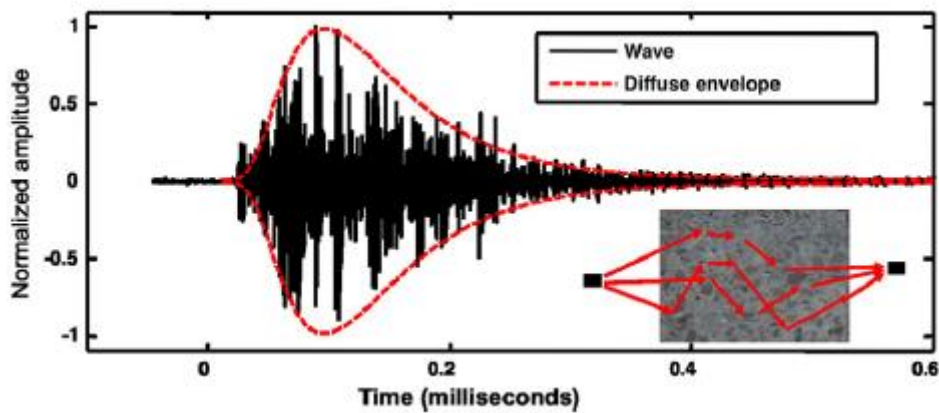


Figure 1: A typical waveform in the time domain (black) with the medium characteristic diffuse envelope (red) encapsulating the waveform (main illustration), due to scattering (red arrows) throughout the concrete medium (bottom right illustration) [3]

The degree of scattering of the waves is affected by the frequency of the signal and the presence of heterogeneities in the material and their scale. Generally, a higher frequency increases the sensitivity to heterogeneities as it results in shorter wavelengths. The size of the wavelength indicates the size of the heterogeneities that will cause scattering of the signal. Planes and Larose [3] categorized the scattering of the signal in four regimes based on the frequency (Figure 2): Modal analysis, simple scattering, multiple scattering and strong absorption. One must find a balance between the wider range of effect from the scattering and the decrease of signal strength due to absorption. Relatively higher frequencies should be avoided to maintain a good distinction between signal and noise in the waveform. According to the International Organization for Standardization [8], the general range of the frequencies for testing concrete with good balance is between 20 kHz and 150 kHz.

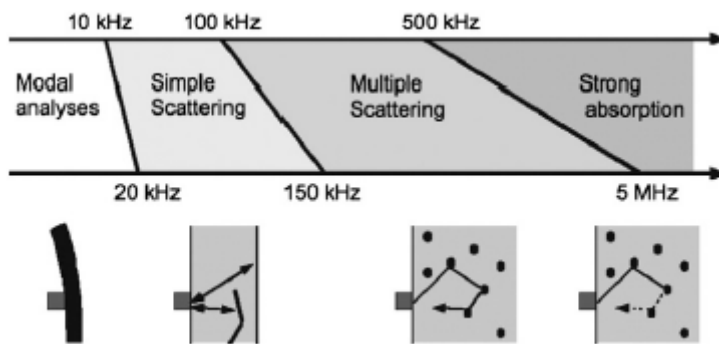


Figure 2: Categorized regimes of signal scattering by frequency with dynamic boundaries reliant on concrete mix (top) and the illustrated travel path through the medium for each category (bottom) [3]

## 2.5 Fast Fourier Transform

For this study, the dominant frequency of the recorded wave field is determined with the use of the Fast Fourier Transform (FFT), which is an efficient method for calculating the Discrete Fourier Transform (DFT) based on the complex transform with an imaginary part in the time domain [9]. In short, the complex DFT transforms the signals in the time domain, which hold the amplitudes of the waves in cosine and sine, into frequency-domain signals. FFT is relatively simple to code even though the algorithm is very complicated, making it very efficient for computational DFT application. Results of the FFT analysis can be found in Appendix A.

## 2.6 Wave types

Waves propagating through a medium can be categorized in body waves and surface waves, as commonly used in seismology to describe the emitted seismic energy of earthquakes. As their names suggest, the difference lies in how the waves propagate through the medium. Surface waves travel along the medium surface, while body waves travel within the medium. In this study, the test setups are as such that the sensors are embedded within the medium. Therefore, only body waves will be considered for the sake of simplicity.

Body waves propagating through a medium can be further categorized in either longitudinal/compressional waves (P-waves) or transverse/shear waves (S-waves) [4] [10]. The distinction between these two types is the direction of particle vibration in relation to the direction of wave propagation. For P-waves, particles in the medium vibrate parallel to the direction of the wave propagation. For S-waves, particles in the medium vibrate orthogonal to the direction of the wave propagation. In uniaxial loading conditions with sensors orientated to send and receive signals parallel to the loading direction, P-waves are associated with normal/compressional stresses and S-waves are associated with shear stresses. When the waves pass heterogeneities, the dissimilarities in the medium

causes the waves to refract, reflect and diffract. When a P-waves travel through an elastic solid and hit an interface at an angle, mode conversion can occur, where particle movement in the transverse direction can result in the generation of S-waves (Figure 3). These phenomena enable scattering paths to form between source and receiver. To limit the computational costs and the complexity of this study, all media are considered visco-acoustic, which are defined as media without cross propagation but exhibiting attenuation in the amplitude of the longitudinal wave [11].

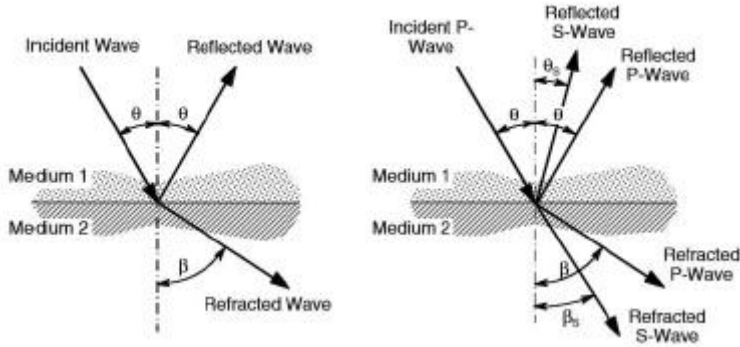


Figure 3: The behavior of incident P-waves and S-waves as they strike the boundary between two media with different acoustic properties without mode conversion (left) and with mode conversion (right) [10]

## 2.7 Wavelength

For ordinary concrete, the ultrasonic wave velocity has an average value of 3700 m/s for longitudinal waves (P-waves) and 2500 m/s for shear waves (S-waves), according to the Proceq pulser manual [12]. ASTM D2845 [13] recommends a minimum lateral dimension of 5 times the wavelength between sensors and recommends a wavelength of at least 3 times the average aggregate size. As the main purpose of this research is the detection of compressional/normal stress changes, the mean propagation velocity is considered equal to the longitudinal wave velocity.

The measured wave velocity of the concrete mix with the Proceq pulser has an average value of 4200 m/s, which is simply calculated by equating the straight-line path between source and receiver with the first arrival time of the recording. With the simple relation between wave propagation velocity and wave frequency,

$$Wavelength = \frac{propagation\ velocity}{frequency}, \quad 2.9$$

and an average propagation velocity of 4200 m/s, the corresponding wavelength is 47 to 84 mm, for frequencies of 88 kHz to 50 kHz, respectively. The significance of the wavelength translates to a minimum lateral distance of 235 mm and the average size of heterogeneities in the medium should not exceed 16 mm to limit the degree of scattering of the signal.

## 2.8 Stretching technique

The premise that the stress changes in a medium can be detected using recorded waves that have propagated through the medium, has its fundamentals in the acoustoelastic properties of elastic solids as described by Murnaghan [6]. As the deformations in the medium are assumed small, concrete can be considered an elastic solid and linear elasticity theory can be utilized with Hooke's Law (Equation 2.5). The acoustoelastic properties of the medium make it possible to equate changes in wave velocity to changes in stress-state [4] [14]. With CWI, changes in wave velocity are calculated by cross-correlating

perturbed signals and unperturbed signals with the aim of determining the wave-velocity change. For small velocity changes, a linear relation can be assumed between travel time and wave velocity:

$$t' = t + dt = t \left( 1 + \frac{dt}{t} \right), \quad 2.10$$

$$v' = v - dv = v \left( 1 - \frac{dv}{v} \right), \quad 2.11$$

$$\text{Change in wave velocity} = \frac{dv}{v} = -\frac{dt}{t}. \quad 2.12$$

With the Stretching technique or the doublet technique, as described by Snieder [15], one attempts to stretch the perturbed signal in the time domain to fit its corresponding unperturbed signal. This shift of the time axis between the modified and reference signal is then considered to be equal to the change in wave velocity [16], where the relation can be summed up as an increase in travel time being directly related to a decrease in velocity.

The Stretching technique is applied with the use of a stretching window, where the modified signal and reference signal within a time window of certain length are compared. The appropriate length of this stretching window depends on the wave frequencies as a sufficient number of signal periods needs to be present within the stretching window for accurate assessment. A window too short will return unreliable results since the stretching window will not hold sufficient information to make a proper analysis. A window too long will suffer from the limitations of the Stretching technique, as the Stretching technique assumes a constant time shift within the stretching window, which is not necessarily the case for long coda wave recordings, and the results will stray further from this assumption with longer time windows. With longer time windows, one also has to consider a larger number of deviations in the wave signals, which makes it more difficult for cross-correlation [17]. For this study, an approximate stretching window size of 50  $\mu\text{s}$  is used, as it has shown to return the best results between consistent wave-velocity change ( $dv/v$ ) and high cross-correlation coefficient ( $CC$ ).

In theory, the perturbed signal and its unperturbed counterpart are identical save for the change in arrival time. In practice, this statement is inaccurate to varying degrees when applied to materials with non-linear properties such as concrete. One will find that the perturbed wave signal will have somewhat mutated in shape in comparison to the unperturbed wave signal. There is a multitude of possibilities for causes of these mutations with the general consensus being alterations in the microstructure of concrete (e.g., cracks) [18] [19].

## 2.9 Wave-velocity change ( $dv/v$ )

The main output from the CWI is the wave propagation velocity or rather changes in the wave velocity (Equation 2.12). The change in wave velocity is annotated by  $dv/v$ , and is represented as a percentage change by means of the time shift of the modified signal within the stretching window, as explained in Section 2.8. Earlier studies have shown that there is a correlation between changes in the wave velocity and changes in stress-state [4] [14].

## 2.10 Cross-correlation coefficient ( $CC$ )

The cross-correlation coefficient can be considered a quality factor of a particular stretching window. The  $CC$  represents the degree to which the modified signal and reference signal match after stretching, where a  $CC$  of 1.0 equates to a perfect match. This parameter gives an indication on how reliable the results of the particular stretching window are and is determined as such:

$$CC = \frac{\int_0^T h'(t')h(t)dt}{\sqrt{\int_0^T h'^2(t')dt \int_0^T h^2(t)dt}}, \quad 2.13$$

where  $h'$  is the modified signal after stretching in time domain  $t'$ ,  $h$  is the reference signal in time domain  $t$ , and  $T$  is the stretching-window length with starting point 0.

### 2.11 Cycle skipping

A significant hurdle to applying CWI to the field data is the occurrence of cycle skipping. Cycle skipping is increasingly prevalent when there are alterations in the signal's waveform. An illustration of the issue is shown Figure 4 and Figure 5. In essence, the CWI process cross-correlates the wave signal with the wrong segments of the reference wave signal. This issue arises because of the way the process determines the  $dv/v$  in respect to the  $CC$  in a given stretching window. Figure 4 shows the plotted relation between  $dv/v$  and  $CC$  of the stretching window in Figure 5. The process determines the  $dv/v$  with certain criteria and how these criteria are weighed. Accounts of  $dv/v$  with a low absolute value and high  $CC$  are favorable. Complications occur when these criteria are not significant enough and do not coincide with the same result.

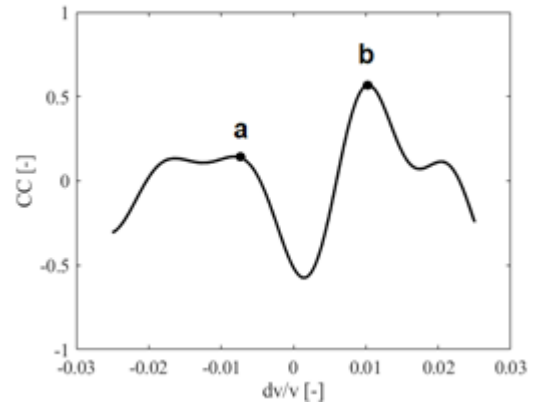


Figure 4: Plotted  $dv/v$ - $CC$  relation within a given stretching window with contending time shifts marked as (a) and (b)

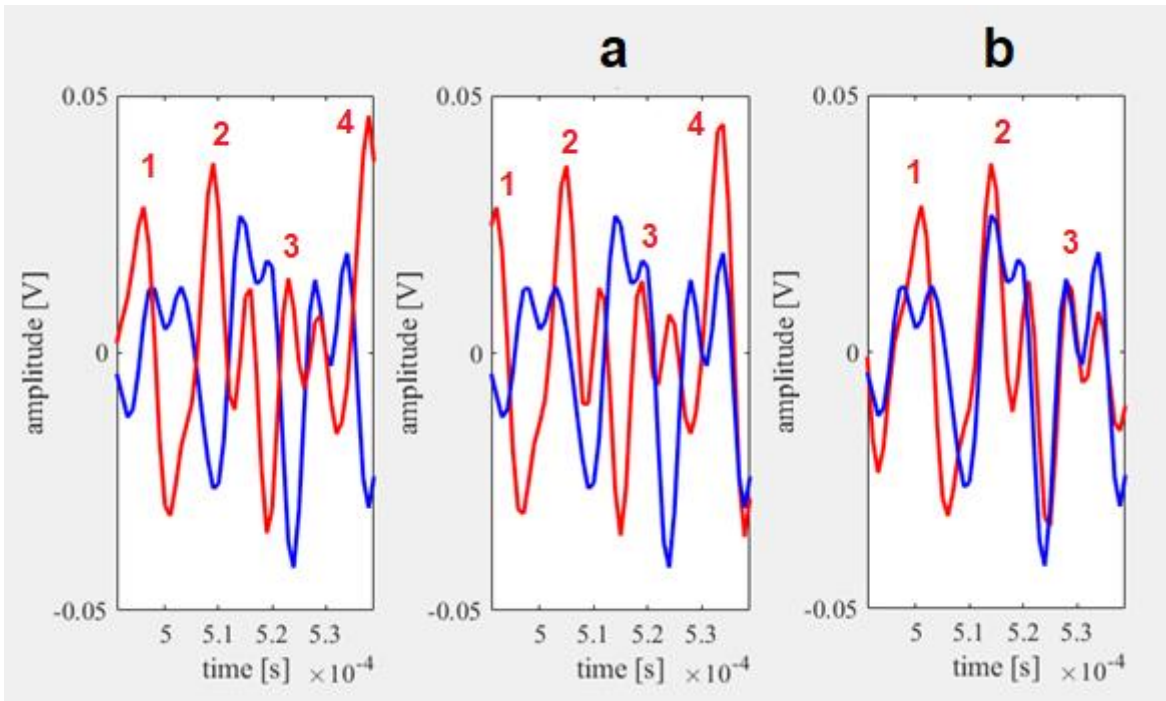


Figure 5: Illustration of the cycle skipping phenomenon: unmodified signal and reference signal (left), stretching result without cycle skipping prevention with faulty time shift (middle), stretching result with cycle skipping prevention with correct time shift (right)

## 2.12 Sensitivity kernel

As discussed earlier in Section 2.4, the later arrivals in the coda hold more information on the medium compared to the early arrivals due to the extended travel path. The precise path a wave has travelled due to scattering is near impossible to determine, but it can be estimated. To fully utilize the late coda-wave arrivals and the information they hold, a probability approximation is required, which comes in the form of the sensitivity function introduced by Pacheco & Snieder [20]. The Sensitivity Kernel is the statistical probability the wave passes through a specific point in the medium within a specific time interval, where the time interval is the total travel time from source to receiver. The goal of this description is to determine which part of the coda waves holds information on which part of the medium. Naturally, the probability a wave signal passes through a specific point increases as that point is positioned closer to the source and/or receiver. Similarly, a larger time interval will accommodate longer travel paths due to the signal scattering more distance away from the direct path between source and receiver. From a probability point of view, the sensitivity kernel is considered reliable in an ellipsoidal area around the source and receiver for a medium with a homogeneous background velocity and containing small perturbations from the background.

Pacheco and Snieder have derived the sensitivity function  $K(x, t)$  that relates the mean travel time change at time  $t$  with a localized slowness perturbation at position  $x$  for a given source and receiver configuration for single scattered waves. This prediction does not require any knowledge of the scattering properties of the medium and is entirely dependent on the wave propagation velocity and the sensor placement configuration:

$$K(x, t) = \frac{1}{2\pi h \sqrt{\left(\frac{v_0 t}{2h}\right)^2 - 1}} \left( \frac{r_s}{s} + \frac{r_g}{g} \right), \quad 2.14$$

where  $2h$  is the length of the direct path between source and receiver and  $v_0$  is the mean wave propagation velocity. The parameters  $s$  and  $g$ ,

$$s = \sqrt{(x+h)^2 + y^2 + z^2}; \quad g = \sqrt{(x-h)^2 + y^2 + z^2}, \quad 2.15$$

represent the position of the source and receiver, respectively, expressed in x,y,z-coordinates with the source and the receiver positioned on the x-axis and the origin positioned precisely halfway between them at distance  $h$  from the source/receiver.

All the possible travel paths of the signal due to scattering from source to receiver are covered in an ellipsoidal area (Figure 6). The dimensions of the ellipse are determined by the sensors' relative position and the wave propagation velocity:

$$r_s = h \frac{\left(\frac{v_0 t}{2h}\right)^2 - 1}{\frac{v_0 t}{2h} - \frac{x+h}{s}}; \quad r_g = h \frac{\left(\frac{v_0 t}{2h}\right)^2 - 1}{\frac{v_0 t}{2h} - \frac{-x+h}{g}}. \quad 2.16$$

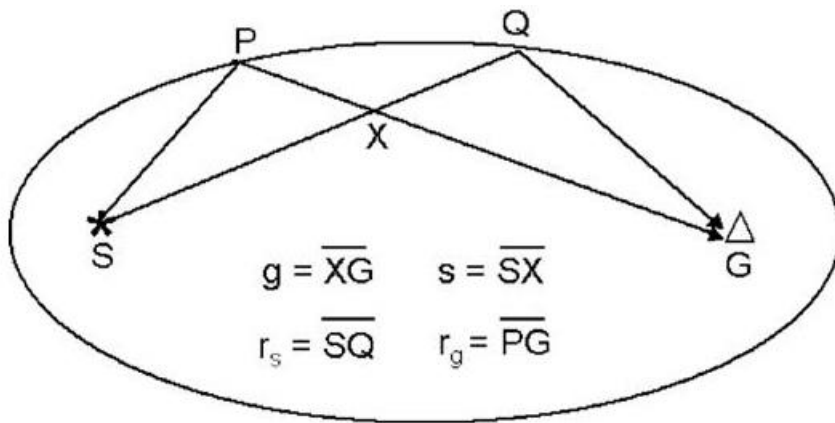


Figure 6: Ellipsoidal area of effect for a scattered travel path of the wave signal propagating from source (S) to receiver (G) through point X [20]

# 3 Methodology for field measurements and laboratory testing

## 3.1 Field measurements location details

The analyzed concrete structure in question for this study is located near Dommelen, Valkenswaard in the Netherlands. The construction of the prestressed cast-in-situ concrete bridge is realized by Dutch construction company Boskalis. The concrete bridge connects the provincial road N69 across a nature reserve and is intended for motor traffic. The structure is casted on site with post-tensioning. The cast-in-situ bridge has a total length of approximately 300 meters with ten spans of 30 meters each. The sensors are positioned in groups at key location along two adjacent spans (Figure 7). The sensors are glued to reinforcement bars (Figure 8) and placed within the reinforcement cage with fixed orientations (Figure 9). The concrete is then poured into the formwork, encasing the sensors in the concrete. Measurements are done at different phases during the construction phase, when the stress-state at the positions shifts due to changes in loading and boundary conditions.



Figure 7: Panoramic side view of the concrete bridge from the construction site and the four illustrated positions of the four sensor groups within the measured spans of the concrete bridge

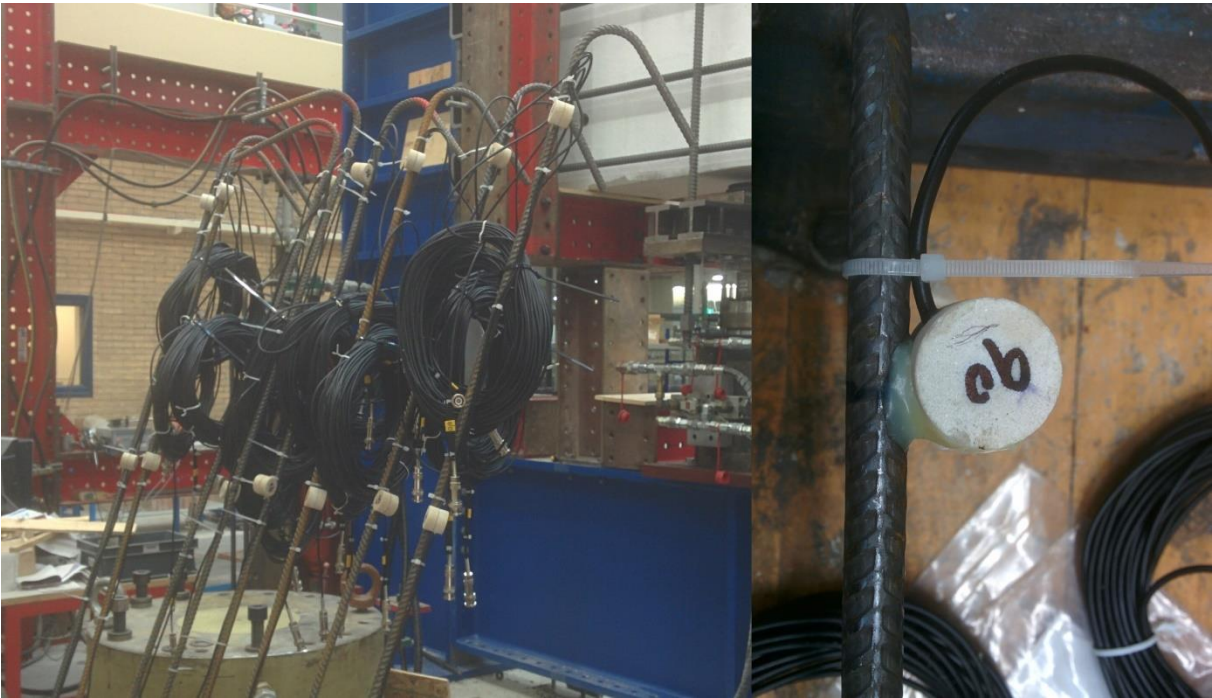


Figure 8: Cane-shaped reinforcement bars with glued on Smart Aggregate with fixed orientation



**Figure 9: Cane-shaped reinforcement bars with Smart Aggregate placed within the reinforcement cage of the bridge deck and glued in fixed position before concrete cast**

### **3.1.1 Field application**

When Code Wave Interferometry in conjunction with embedded Smart Aggregate is planned to be applied to in-field structures, one must determine towards what purpose the monitoring system is to be used. Before any sensor is placed, the user must have a clear vision on what the resulting data will represent. This particular method of monitoring concrete structures is relatively uncommon and thus there is no standardized procedure on how the Smart Aggregate should be applied. One will have to rely on personal judgment and any past experiences for successful execution.

The first point to consider is the physical placement of the sensors within the structure. The functioning of the sensors is dependent on their orientation and their position in respect of each other. When determining the placement of the sensors, the user must have a clear picture on what parts of the structure are of interest. The clearer the picture, the more relevant the acquired data will be and fewer resources will be required. This means the user must have the necessary pre-knowledge of the structure for effective application of the sensors. The sensors are required to be placed as such that the signal will be able to reach the points of interest and the sensors are able to receive the signal when propagating through the medium.

Another point to consider comes after the sensors have been placed within the structure, namely how the measured data will be acquired and how the data will be retrieved. Within the question of how the data will be acquired also lies the issue of when the data will be acquired. For monitoring systems set up for the purpose of detecting stress-states, the change in stresses is naturally tied to the course of time. In this study, which covers the usage of Smart Aggregate during the construction phase of a concrete bridge, the stress-state of the structure will evolve over the various stages of its construction. Ideally, measurements are done before, during and after loading conditions of the structure goes through significant changes as Coda Wave Interferometry requires modified and unperturbed data. But depending on the situation at the construction site and the method of data acquisition, it may not be possible for measurements to be conducted at these key points in time.

Retrieval of the measured data is a point that needs to be considered before the sensors are placed within the structure. Accessibility to the sensors is particularly important in case physical contact, such as a wired connection, is required for data acquisition and retrieval. A wireless connection between computing device and sensors is more favorable in that aspect. An automated process for data storage can also prove more ideal as it lowers the degree of necessary human involvement.

### 3.2 Measurement equipment



**Figure 10: Measuring setup on site (left) with the MUX system contained in a plastic box (right) with the voltage divider (purple), power supply unit (yellow), connector (blue) and MUX channels (red)**

The system used for conducting the field measurements on the bridge is referred to as the multiplexer system, or MUX system for short. It consists of a regular desktop PC, a pulser and two MUX boxes with sixteen available channels (Figure 10). The MUX is a multiple-input, single-output switch capable of connecting several input signals in a single device. During measurements each channel is connected to a passive sensor while the active sensor is disconnected from the MUX system (Figure 11). The active sensor is connected to the Proceq pulser [12], which allows the active sensor to send a signal for the passive sensors to receive. The MUX systematically switches between the sixteen input channels and forwards the selected input channel to the output. This allows the received signal from each passive sensor to be read in order. Additionally, the pulser is also connected to the connector through a voltage divider, which protects the connector from the high voltage signal of the pulser. The connector identifies the signal sent from the pulser as indication for the start of the measurement and subsequently processes the received signals before they are logged on the PC for analysis. The corresponding PSU powers the connector and the MUX channel boxes.

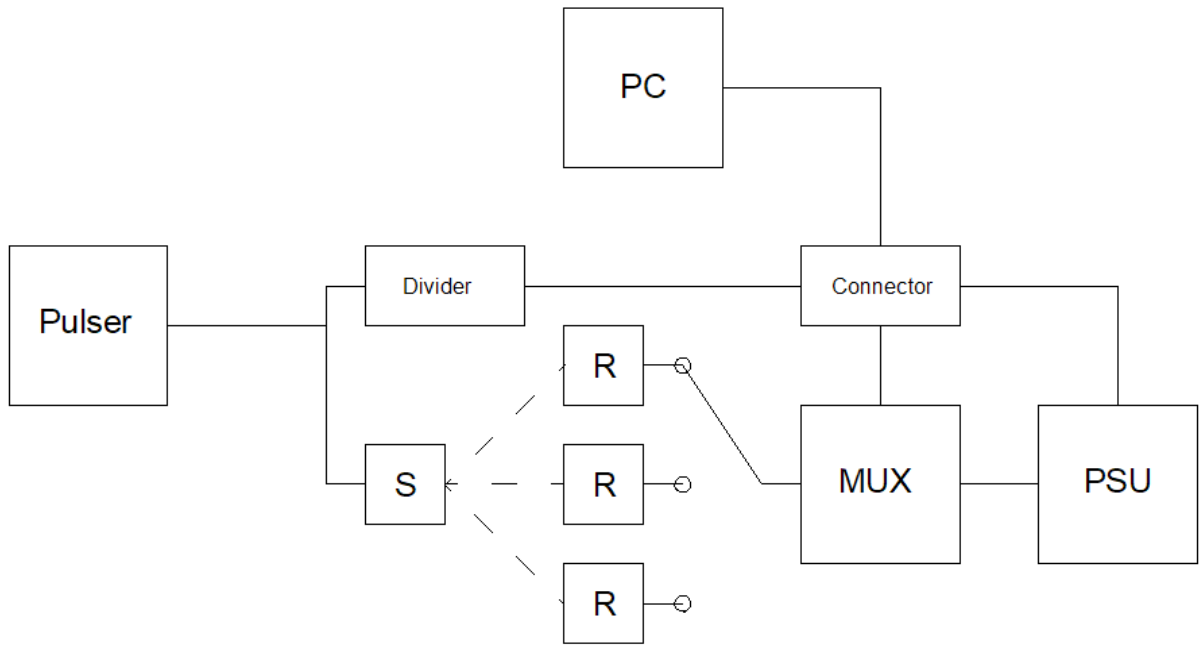


Figure 11: Simplified illustration of the interaction between the measuring system components and with the source sensor (S) and receiver sensors (R), solid lines indicate wired connection and dashed lines indicate connection through wave signals

### 3.3 Smart Aggregate (SA)

The SA sensors used in this study are constructed out of a lead zirconate titanate (PZT) patch encased by two marble blocks for protection and held together by an epoxy resin layer (Figure 12). The piezoelectric effect of the PZT patch gives the ability to generate ultrasonic waves when exposed to an electric voltage. It can both transmit and receive wave signals, meaning every sensor is capable of acting as source and receiver. The diameter of the SA is roughly similar to that of a coin (25 mm) with a thickness of 20 mm. The attached electric wire with connector enables the user to connect the SA to a pulser, which sends voltage to the SA. It also allows the user to log the wave signals the SA receives.

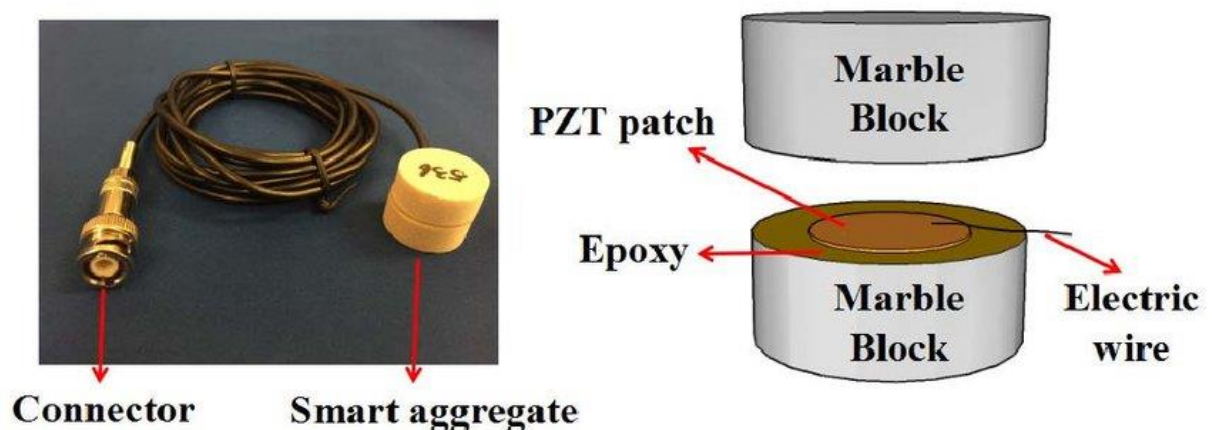


Figure 12: Smart Aggregate with wire and connector (left) and Smart Aggregate components layout (right) [21]

### 3.4 Software and post-processing method

The retrieved measurement data from the bridge is analyzed with the use of a post-processing MATLAB-script [22]. The full MATLAB-script used for data reading and post-processing is found in Appendix A. This script reads the data and categorizes it by measurement day, location and sensor. Subsequently, the script attempts to apply CWI by aligning the wave peaks of a modified signal to the reference signal. This method is called stretching, as explained in Section 2.8, where the concerned wave signal is shifted to fit the reference signal, illustrated in Figure 5. This is done in windows with predetermined length, which have an overlap of 50% with adjacent stretching windows. The magnitude of the shift is expressed as a variable change in velocity ( $dv/v$ ), described in Section 2.9, and the measure on how closely the concerned wave signal corresponds with the reference signal is expressed as a cross-correlation coefficient ( $CC$ ), described in Section 2.10. CWI outputs are acquired with the use of the “rolling reference” principle [23], where dynamic references are used in favor of a static reference (Figure 13). This method is preferred as the use of a static reference coheres with greater deviations, which can be detrimental for CWI accuracy.

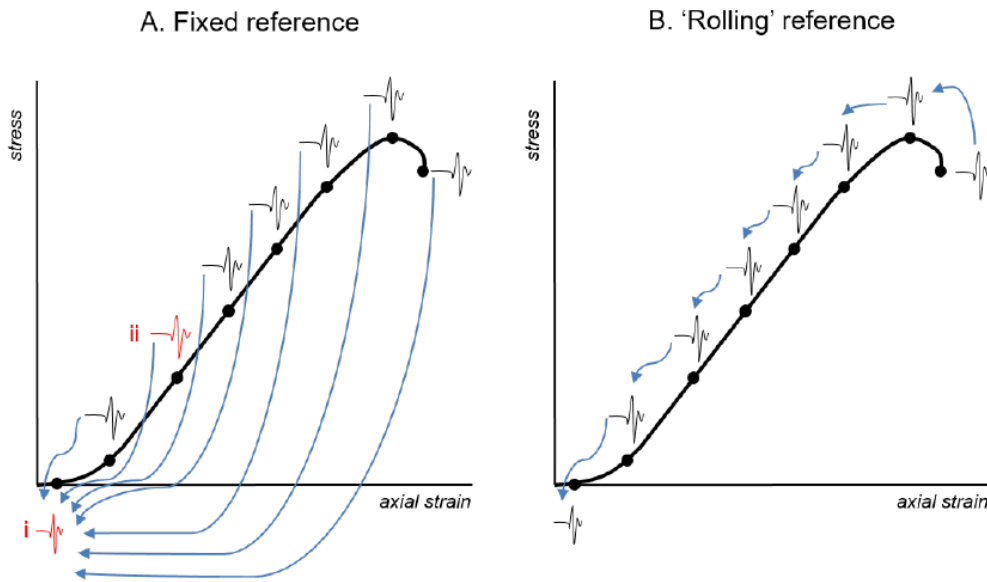


Figure 13: Difference in reference point in CWI between a static reference point (A) and dynamic reference points (B) [23]

Customarily, a single stretching window is selected for cross-correlation and results from the CWI are derived from that stretching window alone. The analysis of a single stretching window suffices for laboratory tests where the wave signal only perturbs slightly. However, for field measurements with multiple days of continued exposure in between measurements, the perturbations are much larger. As such, the use of a single stretching window in CWI is very prone to error as the medium deviates substantially in comparative wave signals. The use of multiple stretching windows is opted for instead with set criteria for inclusion to mitigate errors in cross-correlation.

For assertion of change of stress-state in a medium the first stretching window after the first arrival is theoretically accurately representative as this early part of the wave signal has undergone minimal scattering and therefore predominantly holds information on the medium directly in between the source and receiver. In the case of stresses due to bending moments, this attribute is of greater significance as stresses vary throughout the medium’s cross-section. Therefore, a scattered wave signal is likely to detect stress changes that are not applicable to the medium between the sensor pair. In the same sense, the later parts of the coda arguably have scattered too much and thus hold additional information not inherent to parts of the medium directly in between the sensor pair. However, by consulting the

Sensitivity Kernel in Section 2.12 and the interaction between source and receiver, validation for the use of later stretching windows can be found in the fact that the signal for every sensor pair must constitutionally pass the area around the source and receiver and thus the signal holds information around their position within the medium. Therefore, the use of multiple stretching windows for an averaged output value is acceptable, if the data is not of sufficient quality for the use of a single stretching window.

As mentioned in Section 2.11, cycle skipping is a common issue when data is less than ideal for CWI and this condition is easily met with field measurements. Thus, adjustments to the MATLAB-script are required. Additional criteria are set in the MATLAB-script to prevent cycle skipping from affecting the CWI results negatively. A cause of cycle skipping is the homogeneous waveform of the later coda wave and the lack of a singular significantly high valued  $CC$  within a stretching window. In contrast, the early arrivals of the wave signal generally have a distinct waveform and thus cross-correlation errors are less common. Therefore, the derived  $dv/v$  from the early stretching windows is used to set boundaries for the  $dv/v$ -values of the later parts of the coda wave, preventing those  $dv/v$ -values from deviating too much from their early arrival counterparts.

The first arrival of the wave signal is selected within the MATLAB-script, as shown in Appendix A, by means of Akaike Information Criterion (AIC), which is based on iterative statistical analysis [24] and is defined as:

$$AIC(k_w) = k_w \log\left(\text{var}(R_w(1, k_w))\right) + (n_w - k_w - 1) \log\left(\text{var}(R_w(1 + k_w, n_w))\right) \quad 3.1$$

where  $R_w$  represents the wave signal in the given time window,  $k_w$  is the index ranging from 1 to  $n_w$  and  $n_w$  is the last index of the time window series and should coincide with a time window after the first arrival. The time window with the minimum value in the AIC function specifies the first arrival of the wave signal. The term  $\text{var}(R_w(1, k_w))$  represents the variance in the wave signal from 1 to  $k_w$  and the term  $\text{var}(R_w(1 + k_w, n_w))$  represents the variance in the wave signal for all considered indices.

### 3.5 Sensor configuration setup in concrete bridge

The sensors are positioned in groups of 8, 12 and 14 at four locations within the concrete bridge over two spans (Figure 7, Figure 14). These groups are strategically placed at key locations, such as mid-span and near the support columns, as the largest variance in stresses are expected at these locations. The sensor group configuration is such as that it will allow measurements of change of stress-state due to axial loading and bending moments along the bridge span. The sensors are orientated in the longitudinal axial direction of the span to measure the axial stress-state and are positioned in a grid-like manner over the cross-section height of the bridge, so the stress gradient induced by bending moments can be gauged. As the bridge deck varies in height over the span, the amount of sensors placed in the vertical direction differs per sensor group position. The increased height at the bridge supports allow for an additional row of sensors in the vertical height of the bridge deck, for sensors should be placed at certain distance from one another, as discussed in Section 2.7. The sensor groups near the bridge supports consist of three rows of sensors over the bridge deck height instead of two rows for the sensor groups in the span of the bridge. Sensors are also placed in the lateral direction of the bridge deck, as it effectively increases the sample size of the measurements and thus increases the reliability of the data. This is only valid if stress differences in the lateral direction are expected to be insignificantly small, which is assumed for this study.

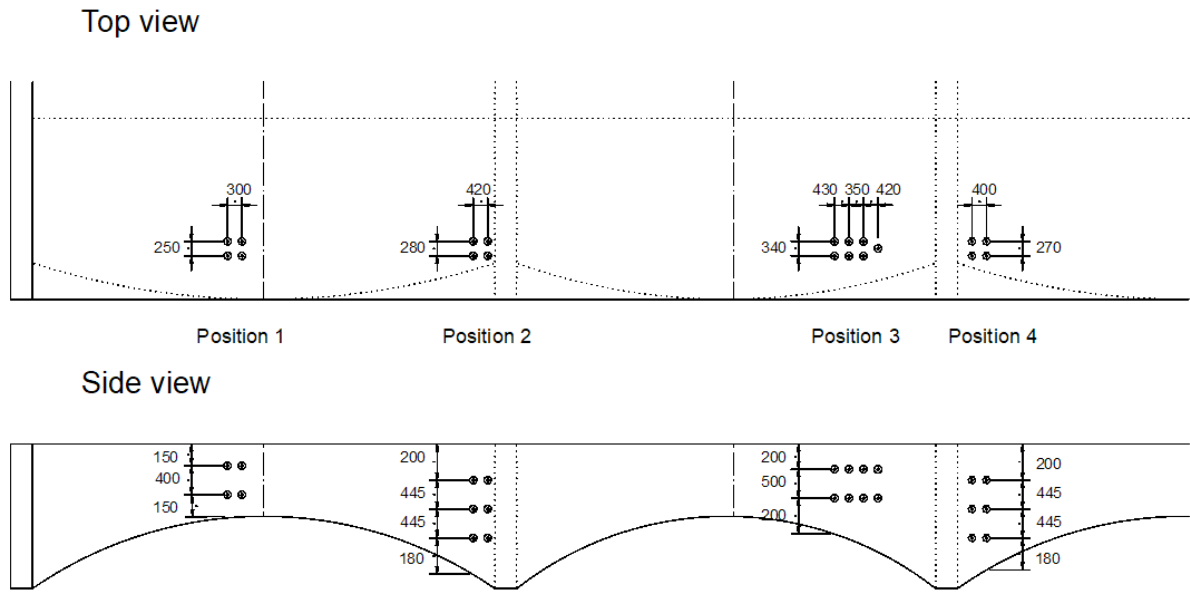


Figure 14: Stylized top view (top) and side view (bottom) drawings of the four sensor group positions within the concrete bridge with respective dimensions in millimeters and the land head located at the far left (drawing dimensions are not to scale)

### 3.6 Compression stress test setup

The effects of uniaxial force on the wave velocity are tested in the laboratory by means of cylinder compression tests. During casting of the bridge, three concrete cubes and two concrete cylinders are made from the same mixing batch. This detail in used material is of importance, because concrete is a heterogeneous material and the acoustoelastic properties differ between different concrete mixes.

The three concrete cubes are tested in a compression stress test, where the cubes are loaded to failure to determine the concrete compression strength. The 600x300 mm cylinders with embedded SA are tested in a stress-strain test setup (Figure 15). Two sensors facing each other are embedded over the height of the cylinder to measure the uniaxial stresses within the cylinder during loading. Displacement sensors are attached to the sides of the cylinder test sample and record the axial deformation while the sample is loaded in compression. Loading is done in two cycles. The cylinders are loaded to a maximum compressive load, which corresponds with the prestressed concrete compressive limit. Measurements of the wave signal between sensors are done in specific intervals in between load steps. The relation between applied load and wave propagation velocity is established with the rolling *CC* method (Figure 13).

The maximum applied load during the cylinder compression test is determined by means of concrete cube compression strength tests. Three 150x150x150 mm concrete cubes are loaded to failure in uniaxial compression. The results are shown in (Table 1). It should be noted that the experimental concrete strength is of a higher class than originally taken into account as a concrete strength class of C50/60 was ordered from the supplier. According to Eurocode [25] the initial prestressing force is limited to  $0.6 f_{ck}$ , where  $f_{ck}$  represents the cylinder compressive strength which equates to about 0.8 times the cube compressive strength. The maximum applied stress to the concrete due to the prestressing force is then shown in

$$\sigma_c = 0.6 * f_{ck} = 0.6 * 0.8 * f_{ck,cube} \quad 3.2$$

Following these equations the cylinders are loaded to a maximum of 2800 kN, which corresponds with the prestressed concrete compressive limit, in steps of 300 kN at a rate of 4 kN/s (Table 21). The wave signal between the sensors is measured at the end of each load step. The results of the concrete compression stress tests are shown in Section 5.2.

Cube #	Load speed (kN/s)	Load (kN)	Pressure (MPa)
1	13.5	2016.2	89.61
2	13.5	2010.1	89.34
3	13.5	2027.2	90.10

Table 1: Concrete strength test specifics with failure load/pressure of all three cube samples

### 3.7 Concrete hydration test setup

The concrete hydration process and its effects on the wave propagation velocity is measured through maturing 600x300 mm concrete cylinders with embedded SA. A total of two sensors, one source and one receiver, are positioned radially centered within the cylinder over the axial direction. The sensors are orientated as such that the signal is emitted towards one and the other, mimicking the sample setup used in the compression test, specified in Section 3.6. The concrete cylinders are stored in a controlled environment after casting and measurements are conducted in one-to-three-day time intervals. The concrete cylindrical samples used for measurements of this concrete hardening process have a different concrete mix design from the mix design used in the concrete bridge. As such, data between the two cases do not have a direct interrelationship with one another and one should show restraint when drawing comparisons. Therefore, the tests are instead utilized to establish a general trend between concrete hydration and wave signal behavior within the medium. The results of the concrete hydration tests are shown in Section 5.1.

### 3.8 Creep test setup

Unlike standard laboratory testing involving CWI, the SA within the concrete bridge is subjected to prestressing force, which is characteristically associated with concrete creep. The theory for stress change detection within the medium with the use of CWI assumes the material to be fully linear elastic, which equates an increase in stress to an increase in strain. For creep however, this linear relation is not applicable as it describes an increase of deformation over time under constant force [26].

The effects of creep on the wave propagation velocity are studied in a creep test, where two 400x100x100 mm rectangular samples are kept in a controlled environment under constant compressive load, as seen in Figure 16. Two embedded SA are casted centered within the samples with an orientation facing each other over the longitudinal length. Data is read from the SA every weekday. Unfortunately, there were not enough resources to facilitate concrete creep tests specifically for this study. As compromise, geopolymer samples with embedded SA of PhD candidate Shizhe Zhang at TU Delft are used instead of concrete samples. Geopolymer concrete is a material quite similar to ordinary concrete in its properties, but with a different binder than cement in its mix design. Thus, the creep tests of geopolymer are used as indicator for the effect of creep and shrinkage deformation on the acoustoelastic properties of a concrete-like medium. The developing mechanical properties of the geopolymer samples over time are shown in Table 2. In comparison, C50/60 concrete at 28 days has a compressive strength of 50 MPa and an elasticity modulus of 37 GPa [27]. The possible dissimilarities caused by the difference in material and the results of the geopolymer creep tests are discussed in Section 5.3.

Time [days]	1	7	28	56	90
Compressive strength [MPa]	33.05	49.86	57.70	61.28	66.32
Elasticity modulus [GPa]	21.18	29.10	30.58	30.35	30.65

Table 2: Geopolymer mechanical properties development over time



Figure 15: Compression stress test setup of a concrete cylinder with embedded SA



Figure 16: Creep test setup of two geopolymer samples with embedded SA loaded in tandem

# 4 Coda Wave Interferometry results of field measurements

## 4.1 Field measurement specifics

The data from the field measurements conducted on the concrete bridge are obtained during specific predetermined points in time. These measurement dates are established to showcase the effects of various loading conditions on the wave signal behavior. In total, there are eight instances when measurements are carried out. Measurement data is collected at all sensor group locations during each specified measurement with the exception of Position 4 during the 3<sup>rd</sup> measurement, as operations are made impossible due to weather conditions. The dates and significance of these measurements are shown in Table 3.

#	Date	Concrete age	Time	Attributes
1	2020/09/15	1 day	20:40 – 02:31	Day after concrete casting of measured spans
2	2020/09/21	7 days	11:54 – 16:39	Applied 20% post-tensioning to measured spans
3	2020/09/25	11 days	20:17 – 22:17	Applied 100% post-tensioning to measured spans
4	2020/10/30	46 days	12:21 – 14:08	Formwork removed from measured spans
5	2020/12/17	94 days	13:32 – 15:42	Formwork removed from adjacent spans
6	2021/08/31	351 days	12:08 – 16:33	All bridge spans cast and self-supporting
7	2021/09/02	353 days	11:44 – 15:45	Asphalt layer applied to all spans
8	2021/10/16	397 days	12:05 – 19:30	Bridge fully completed and ready for public use

**Table 3: Field measurement dates, age of the encasing concrete, start and end time of the measurement and attributes around the conditions of the measured concrete structure**

Casting of the concrete bridge deck is done in intervals of two bridge spans per sequence. The sensor groups are positioned within the first cast of the concrete bridge deck. Measurement 1 is conducted approximately 24 hours after the start of the concrete casting procedure. Measurement 2 and Measurement 3 are conducted shortly after 20% and 100% of the total post-tensioning force are applied to the measured bridge spans, respectively. Measurement 4 takes place after the supporting formwork of the measured spans is removed and before the second concrete casting sequence is started. Measurement 5 is done after the adjacent bridge spans have been cast and the corresponding formwork is removed. Measurement 6 and onwards are conducted after the concrete casting of the entire bridge deck has been finalized. Measurement 6 is done shortly before and Measurement 7 is done shortly after the asphalt layer is applied to the concrete deck. Measurement 8 is done a few days before the bridge opens up for public traffic and signifies slight additions to the structure, such as instalment of traffic guardrails.

CWI is applied between the measurement data of interest and the data of the preceding measurement with a rolling reference (Figure 13). CWI where the reference is not the first previous set of data is obviated. The primary reason for this decision is the detrimental effect it has on the cross-correlation accuracy. If for example the very first measurement is used as reference for the very last measurement in CWI, the various factors acting on the medium in between measurement dates have a significant effect on the signal’s waveform and that makes cross-correlation between the two wave signals increasingly difficult. As only the stress-state changes due to axial forces and bending moments are of interest for this study, the sensor group configuration is as such that certain sensor pairs acquire the majority of the relevant information. The relevant sensor pairs consist of sensors directly adjacent to one another with the sensors orientated to face each other.

### 4.1.1 Cycle skipping

As mentioned in Section 3.4, adjustments to the post-processing MATLAB-script (Appendix A) are made to actively counteract the occurrence of cycle skipping during CWI. Within the written code the resulting  $dv/v$ -value of the first stretching window directly after the first arrival is used as reference to set boundaries for  $dv/v$ -values of later arrivals. The boundaries are set as such that the  $dv/v$ -values within a range of 0.005 of the reference stretching window are prioritized.

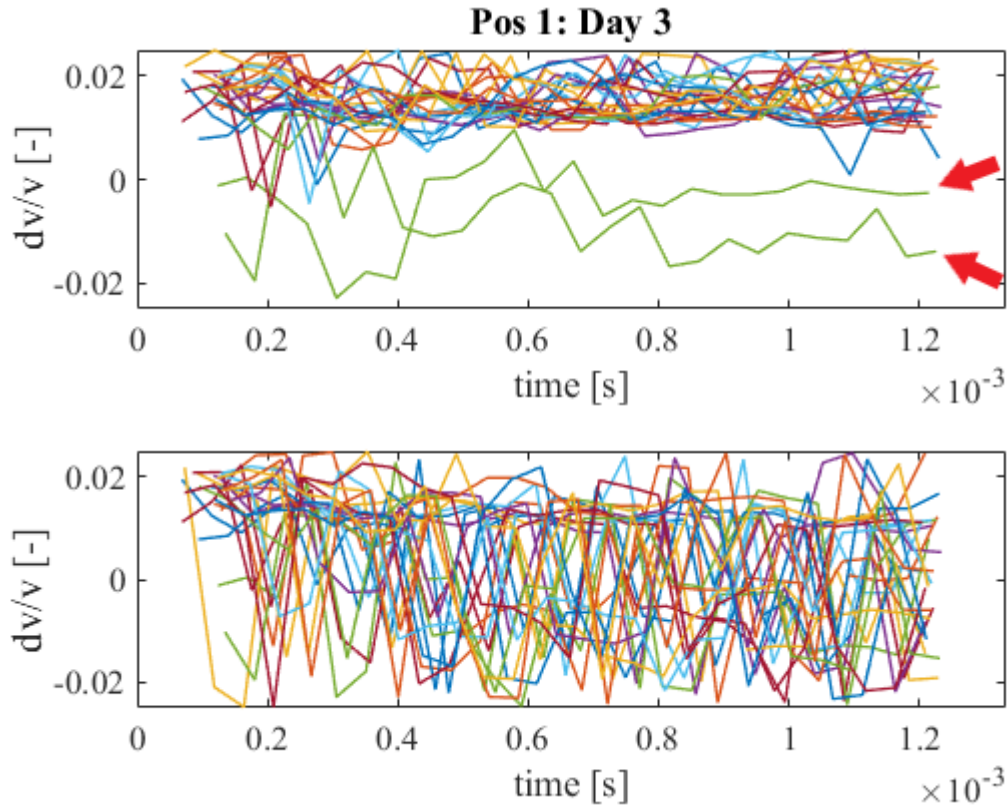


**Figure 17: Comparison of  $dv/v$  over time of CWI between Measurement 2 and Measurement 3 at Position 1 between modified script with cycle skipping prevention and two marked outliers from faulty first arrival selection (top) and original script without cycling prevention (bottom)**

To illustrate the effects of the adjustments to the script, the wave-velocity change  $dv/v$  is plotted over the travel time for all sensor pairs within a certain sensor group at a given location. Figure 17 shows comparisons between the original script and the adjusted script with cycle skipping prevention for all sensor pairs at Position 1 for cross-correlation between Measurement 2 and Measurement 3. Each line represents the cross-correlation results of a sensor pair. The effects of the adjustments to the post-processing script are very noticeable as the  $dv/v$ -values are more consistent over the arrival times. Variations in the wave velocity are to be expected, but turbulent results alike those from the original script are highly unlikely, if the medium is considered linear elastic. Similar comparisons for the other positions are found in Appendix C. It should be noted that the CWI results of later measurements are significantly more consistent compared to early measurements. The adjusted MATLAB-script is thus less impactful and necessary in those later measurements.

While the adjusted script has shown success in counteracting cycle skipping, there are instances where the adjusted script gives faulty results. In Figure 17, one can observe two outliers which do not conform to the other results. When an outlier at Position 2 is further investigated (Figure 18), one finds an issue with the first arrival selection. The first arrival selection is faulty and the third stretching window after

the faulty selection is identified as the correct first arrival time. The third stretching window is then correctly set as reference instead. The first arrival is determined with the use of AIC pick (Equation 3.1), which is an iterative method of determining the first arrival of the wave signal, as explained in Section 3.4. Crosstalk between sensors and background noise can interfere with the AIC method, causing a point before the signal has arrived from source to receiver to be selected as first arrival. In these outlier-cases, manual input is required to correct the first arrival pick. The post-processing script is corrected to set a later stretching window as reference for subsequent  $dv/v$ -values. This new reference stretching window is identified as the actual first arrival of the signal.

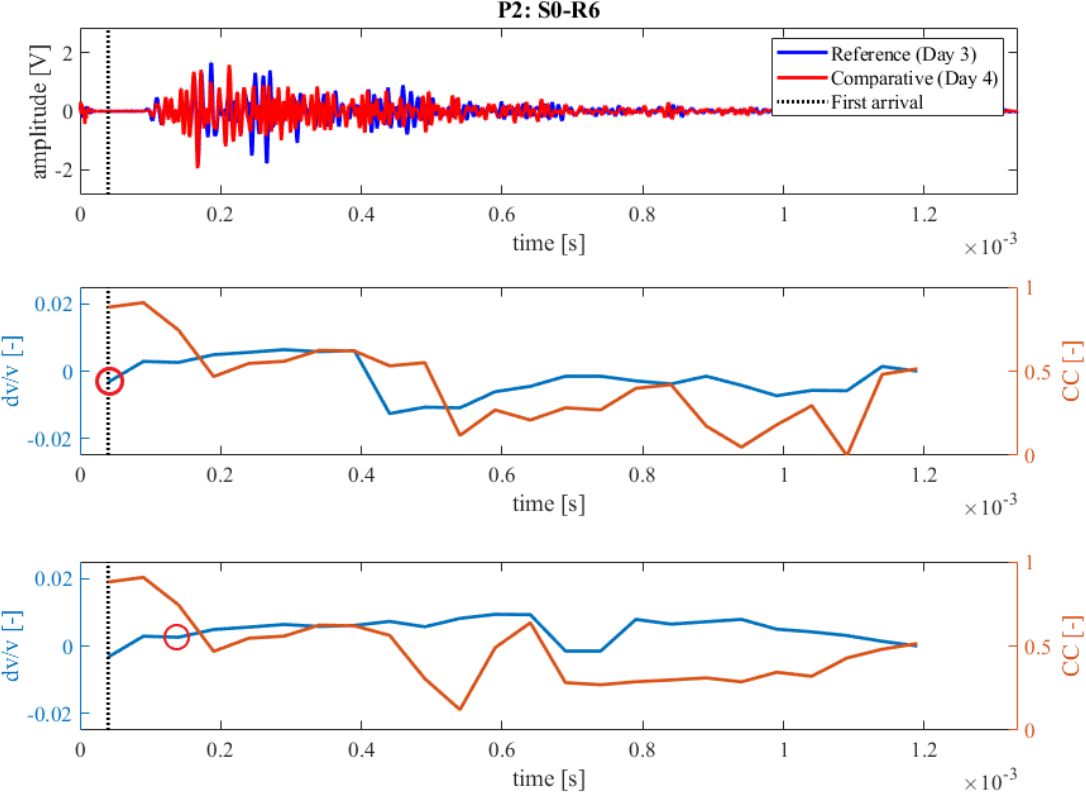


**Figure 18: Wave signals of Measurement 3 (blue) and Measurement 4 (red) between Source S0 and Receiver S6 at Position 2 (top) with faulty first arrival selection,  $dv/v$  and  $CC$  results from CWI with faulty reference window (middle),  $dv/v$  and  $CC$  results from CWI with corrected reference window (bottom)**

Figure 19 illustrates the corrections made to the adjusted MATLAB-script (Appendix A) with cycle skipping prevention for all measured data at Position 1 for cross-correlation between Measurement 2 and Measurement 3. With the corrections the two outliers conform to the results of the other corresponding sets of data. Results for the other positions on the concrete bridge can be found in Appendix D. Each outlier in the plotted  $dv/v$ -values from the adjusted MATLAB-script is manually investigated. Faulty reference stretching windows are identified and corrected.

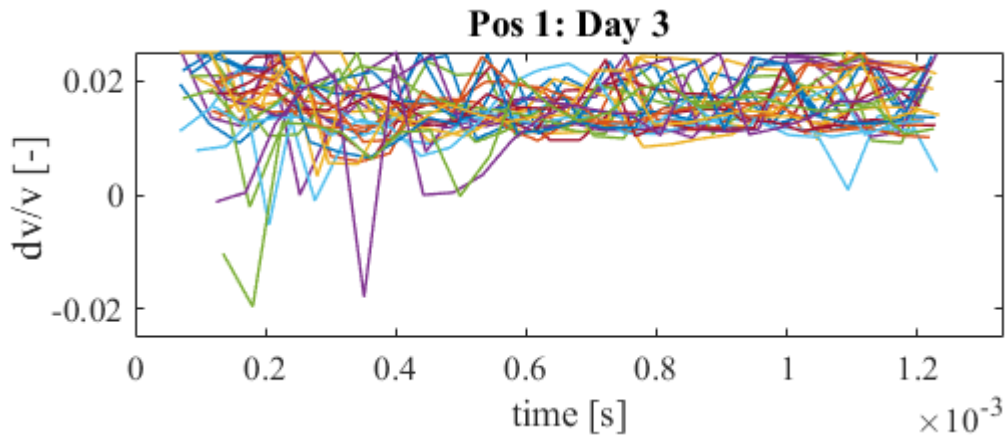


Figure 19: Corrected  $dv/v$  over time of CWI between Measurement 2 and Measurement 3 at Position 1 with cycle skipping prevention and outlier correction

## 4.2 Results of Measurement 1-5 of the concrete structure

The main outputs of the field measurements are the wave-velocity change ( $dv/v$ ), as explained in Section 2.9, and the cross-correlation coefficient ( $CC$ ), as explained in Section 2.10. The outputs are obtained by CWI of the measurement of interest with the preceding measurement as reference and are displayed in Appendix D. The significance of each measurement is displayed in Table 3. The data from Measurement 1 is not included for CWI. The concerned data is taken during a time when the concrete has not fully set and this causes compatibility issues with the corresponding measured wave signals of later measurements.

The sensor placement for the four positions within the structure are visualized in Figure 14. During the field measurements each sensor acts as both source and receiver. This signifies that each sensor pair holds two sets of data for cross-correlation with each sensor acting as source in one instance and acting as receiver in the other instance. While the signal from the source is received by all sensors in the sensor group, only certain sensor pairs are taken into account and only a select few sensor pairs are further analyzed in regards to stress change derivation. Only the principal sensor pairs directly adjacent to one another with the orientation of the sensors facing the other are considered in the results.

There are issues with the quality of the data of the first five field measurements for reasons unclear, which have detrimental effects on the reliability of the CWI results. Conventionally, the wave-velocity change is determined within a specific single stretching window and that  $dv/v$ -value is taken as the final result. However, the wide variation in  $CC$  between stretching windows during cross-correlation makes the results of a singular stretching window unreliable. Multiple stretching windows along the entire coda wave are therefore considered instead with the mean of the considered  $dv/v$  and  $CC$  as the final results.

The results of CWI of the concerned sensor pairs for the first five measurements are shown in the following tables. The stretching window threshold for inclusion is a  $CC$  above 0.5 and results with an average  $CC$  above 0.7 across all included stretching windows is considered to have good reliability, indicated with green. The data tied to the CWI results with high reliability are distinguished for later derivation of visualized  $dv/v$ -distributions in Section 6.3. Missing data, indicated with an “x” and red, follow from the lack of cross-correlation stretching windows that meet the  $CC$  criteria threshold and thus the corresponding data is deemed unreliable. The  $dv/v$  from CWI results of principal sensor pairs for further analysis in Section 6.2 are accentuated with double borders within the tables.

Position 1 is situated in the middle of the first span of the bridge with one end connected to the abutment. Table 4 shows the change in wave propagation velocity and the corresponding cross-correlation coefficient from cross-correlation between Measurement 2 and Measurement 3 at Position 1. Similarly, Table 5 and Table 6 show the change in wave propagation velocity and the corresponding cross-correlation coefficient at Position 1 from cross-correlation between Measurement 3 and Measurement 4, and between Measurement 4 and Measurement 5, respectively. The configuration of the sensors within the sensor group at Position 1 is displayed in Figure 20.

Position 1: Measurement 2 – Measurement 3								
Wave-velocity change ( $dv/v$ ) [‰]				Cross-correlation coefficient (CC) [%]				
	S4	S5	S6	S7	S4	S5	S6	S7
R0	<b>12.4</b>	15.7	15.1	14.3	<b>57</b>	59	66	59
R1	14.5	x	x	10.7	65	x	x	55
R2	17.3	14.3	<b>18.4</b>	17.8	57	60	<b>64</b>	60
R3	15.0	17.4	13.5	<b>16.4</b>	59	56	61	<b>59</b>
	S0	S1	S2	S3	S0	S1	S2	S3
R4	<b>14.1</b>	10.9	12.1	15.9	<b>56</b>	55	62	63
R5	14.4	<b>13.6</b>	16.6	12.8	60	<b>56</b>	61	56
R6	14.8	16.8	<b>16.5</b>	15.8	66	55	<b>72</b>	58
R7	13.7	16.5	14.8	<b>14.1</b>	69	56	66	<b>62</b>

Table 4: Resulting  $dv/v$  and CC from CWI between Measurement 2 and Measurement 3 of the concrete bridge at Position 1 of all relevant sensor pairs between source (S) and receiver (R), red marking and “x” indicate unreliable data and green marking indicates good cross-correlation match, principal sensor pairs are indicated with doubled borders

Position 1: Measurement 3 – Measurement 4								
Wave-velocity change ( $dv/v$ ) [‰]				Cross-correlation coefficient (CC) [%]				
	S4	S5	S6	S7	S4	S5	S6	S7
R0	<b>17.0</b>	12.1	15.7	9.3	<b>72</b>	69	65	69
R1	12.1	<b>7.4</b>	7.7	3.3	61	<b>60</b>	67	68
R2	17.1	12.4	<b>17.0</b>	11.3	65	<b>76</b>	<b>72</b>	<b>75</b>
R3	10.8	9.0	10.6	<b>4.2</b>	<b>74</b>	67	<b>74</b>	<b>66</b>
	S0	S1	S2	S3	S0	S1	S2	S3
R4	<b>17.7</b>	7.2	15.2	11.8	<b>67</b>	61	<b>71</b>	<b>70</b>
R5	11.4	<b>6.0</b>	9.6	5.8	<b>70</b>	<b>60</b>	<b>71</b>	<b>71</b>
R6	16.8	7.0	<b>16.7</b>	10.3	68	60	<b>77</b>	67
R7	12.1	5.6	11.5	<b>6.6</b>	<b>72</b>	62	<b>78</b>	<b>64</b>

Table 5: Resulting  $dv/v$  and CC from CWI between Measurement 3 and Measurement 4 of the concrete bridge at Position 1 of all relevant sensor pairs between source (S) and receiver (R), red marking and “x” indicate unreliable data and green marking indicates good cross-correlation match, principal sensor pairs are indicated with doubled borders

Position 1: Measurement 4 – Measurement 5								
	Wave-velocity change ( $dv/v$ ) [%]				Cross-correlation coefficient (CC) [%]			
	S4	S5	S6	S7	S4	S5	S6	S7
R0	6.5	5.8	6.6	5.4	82	75	81	78
R1	4.3	2.1	3.3	4.0	69	64	73	70
R2	6.1	4.9	6.3	4.8	84	71	82	82
R3	5.3	4.1	4.6	3.5	85	67	81	78
	S0	S1	S2	S3	S0	S1	S2	S3
R4	6.8	4.5	5.6	5.2	79	75	86	84
R5	5.5	1.9	4.7	3.6	71	64	72	82
R6	6.3	3.7	5.7	5.0	87	72	85	87
R7	6.0	3.7	5.1	4.4	83	73	84	84

Table 6: Resulting  $dv/v$  and CC from CWI between Measurement 4 and Measurement 5 of the concrete bridge at Position 1 of all relevant sensor pairs between source (S) and receiver (R), red marking and “x” indicate unreliable data and green marking indicates good cross-correlation match, principal sensor pairs are indicated with doubled borders

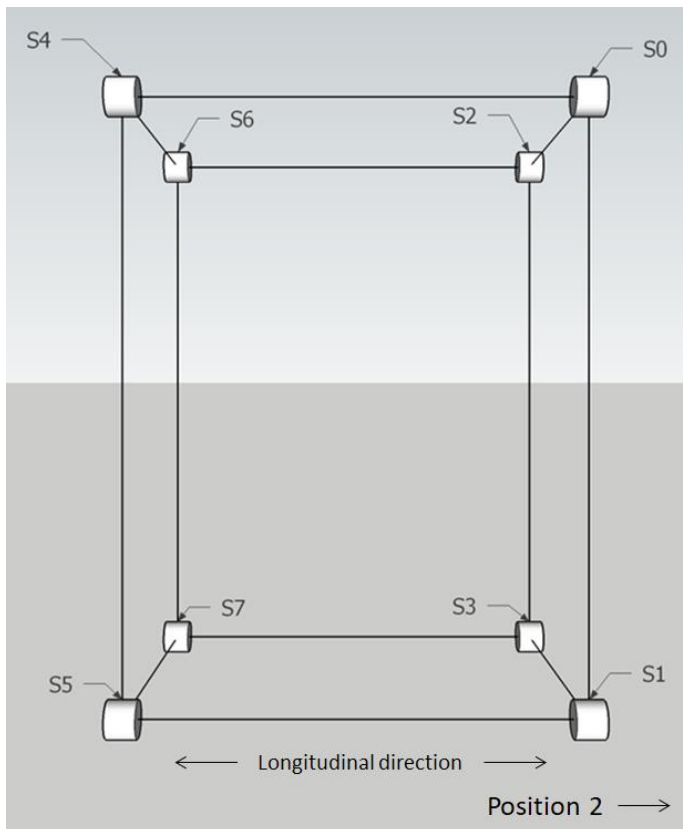


Figure 20: 3D side view of the sensor group configuration cast within the concrete bridge at Position 1 with the sensor numbering and indicator for the direction of the other sensor group positions (bottom corners)

Position 2 is located directly above the support between the first and second span of the bridge with both spans boasting the same length. Table 7 shows the change in wave propagation velocity and the corresponding cross-correlation coefficient from cross-correlation between Measurement 2 and Measurement 3 at Position 2. Similarly, Table 8 and Table 9 show the change in wave propagation velocity and the corresponding cross-correlation coefficient at Position 2 from cross-correlation between Measurement 2 and Measurement 3 and Measurement 4, and between Measurement 4 and Measurement 5, respectively. The configuration of the sensors within the sensor group at Position 2 is displayed in Figure 21.

Position 2: Measurement 2 – Measurement 3												
	Wave-velocity change ( $dv/v$ ) [%]						Cross-correlation coefficient (CC) [%]					
	S6	S7	S8	S9	S10	S11	S6	S7	S8	S9	S10	S11
R0	<b>11.3</b>	11.7	-	10.6	10.0	-	<b>63</b>	62	-	62	63	-
R1	17.2	<b>10.3</b>	9.2	11.3	10.8	9.0	58	<b>59</b>	60	58	58	61
R2	-	9.0	<b>8.4</b>	-	9.3	6.0	-	68	<b>60</b>	-	65	<b>71</b>
R3	18.0	9.2	-	<b>9.5</b>	9.8	-	61	64	-	<b>70</b>	64	-
R4	12.8	10.0	8.4	9.3	<b>8.4</b>	6.4	66	<b>72</b>	69	65	<b>66</b>	<b>77</b>
R5	-	8.6	8.3	-	8.3	<b>6.6</b>	-	<b>77</b>	69	-	66	<b>78</b>
	S0	S1	S2	S3	S4	S5	S0	S1	S2	S3	S4	S5
R6	<b>11.6</b>	10.8	-	11.5	10.8	-	<b>59</b>	65	-	<b>72</b>	65	-
R7	9.5	<b>9.5</b>	7.4	8.3	8.1	8.7	66	<b>69</b>	69	69	<b>81</b>	<b>71</b>
R8	-	9.2	<b>7.3</b>	-	8.3	7.6	-	65	<b>65</b>	-	<b>79</b>	<b>73</b>
R9	13.2	12.4	-	<b>12.1</b>	8.4	-	61	58	-	<b>59</b>	62	-
R10	11.1	x	9.2	11.9	<b>12.2</b>	10.3	60	<b>x</b>	55	54	<b>58</b>	66
R11	-	9.0	7.3	-	8.7	<b>9.2</b>	-	66	67	-	66	<b>67</b>

Table 7: Resulting  $dv/v$  and CC from CWI between Measurement 2 and Measurement 3 of the concrete bridge at Position 2 of all relevant sensor pairs between source (S) and receiver (R), red marking and "x" indicate unreliable data and green marking indicates good cross-correlation match, principal sensor pairs are indicated with doubled borders

Position 2: Measurement 3 – Measurement 4												
	Wave-velocity change ( $dv/v$ ) [%]						Cross-correlation coefficient (CC) [%]					
	S6	S7	S8	S9	S10	S11	S6	S7	S8	S9	S10	S11
R0	<b>4.8</b>	5.1	-	2.3	6.8	-	<b>63</b>	58	-	60	<b>75</b>	-
R1	5.2	<b>6.9</b>	9.5	4.4	5.4	8.8	64	<b>66</b>	65	69	62	61
R2	-	11.6	<b>x</b>	-	10.0	6.5	-	57	<b>x</b>	-	66	57
R3	1.6	5.7	-	<b>4.1</b>	5.6	-	67	<b>70</b>	-	<b>62</b>	63	-
R4	3.3	6.6	6.8	4.3	<b>4.5</b>	10.6	69	<b>74</b>	63	64	<b>68</b>	58
R5	-	13.4	14.3	-	9.8	<b>13.0</b>	-	68	63	-	65	<b>56</b>
	S0	S1	S2	S3	S4	S5	S0	S1	S2	S3	S4	S5
R6	<b>5.1</b>	6.1	-	5.2	5.3	-	<b>64</b>	65	-	66	<b>73</b>	-
R7	6.4	<b>7.0</b>	12.7	6.9	7.6	12.0	60	<b>71</b>	59	64	68	63
R8	-	9.7	<b>13.7</b>	-	10.7	12.2	-	65	<b>60</b>	-	65	64
R9	3.5	3.1	-	<b>2.3</b>	7.7	-	60	<b>70</b>	-	<b>63</b>	61	-
R10	8.9	7.0	12.5	6.5	<b>7.9</b>	15.6	68	69	59	59	<b>62</b>	65
R11	-	8.0	13.0	-	8.0	<b>14.9</b>	-	52	52	-	63	<b>58</b>

Table 8: Resulting  $dv/v$  and CC from CWI between Measurement 3 and Measurement 4 of the concrete bridge at Position 2 of all relevant sensor pairs between source (S) and receiver (R), red marking and "x" indicate unreliable data and green marking indicates good cross-correlation match, principal sensor pairs are indicated with doubled borders

Position 2: Measurement 4 – Measurement 5												
Wave-velocity change ( $dv/v$ ) [‰]						Cross-correlation coefficient (CC) [%]						
	S6	S7	S8	S9	S10	S11	S6	S7	S8	S9	S10	S11
R0	<b>6.4</b>	5.5	-	5.7	6.0	-	<b>64</b>	69	-	72	76	-
R1	4.0	<b>3.5</b>	3.2	4.1	3.4	3.2	<b>84</b>	<b>86</b>	89	84	87	89
R2	-	3.8	<b>3.5</b>	-	3.3	3.5	-	91	<b>91</b>	-	92	89
R3	4.0	3.9	-	<b>4.2</b>	3.4	-	<b>78</b>	82	-	<b>76</b>	80	-
R4	5.2	5.1	4.3	4.9	<b>4.0</b>	4.4	<b>78</b>	80	83	79	<b>79</b>	82
R5	-	3.8	3.7	-	3.4	<b>3.4</b>	-	92	93	-	92	<b>88</b>
	S0	S1	S2	S3	S4	S5	S0	S1	S2	S3	S4	S5
R6	<b>5.1</b>	3.7	-	4.8	4.9	-	<b>75</b>	78	-	75	76	-
R7	4.2	<b>3.4</b>	3.0	3.8	4.2	3.2	<b>80</b>	<b>88</b>	87	87	86	93
R8	-	3.1	<b>2.9</b>	-	3.9	2.8	-	85	<b>85</b>	-	83	87
R9	4.3	3.1	-	<b>x</b>	4.2	-	80	74	-	<b>x</b>	78	-
R10	3.9	2.6	2.8	3.4	<b>3.8</b>	2.9	<b>77</b>	82	88	83	<b>82</b>	91
R11	-	2.5	2.8	-	3.2	<b>2.5</b>	-	79	79	-	77	<b>78</b>

Table 9: Resulting  $dv/v$  and CC from CWI between Measurement 4 and Measurement 5 of the concrete bridge at Position 2 of all relevant sensor pairs between source (S) and receiver (R), red marking and "x" indicate unreliable data and green marking indicates good cross-correlation match, principal sensor pairs are indicated with doubled borders

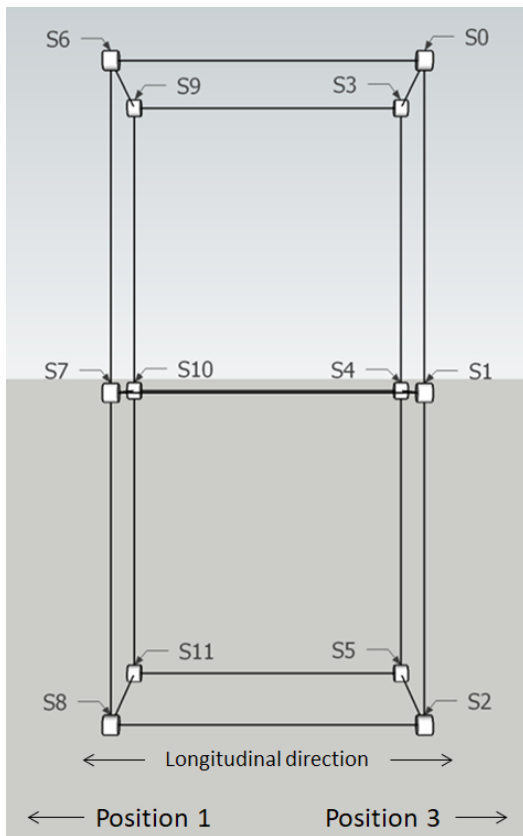


Figure 21: 3D side view of the sensor group configuration cast within the concrete bridge at Position 2 with the sensor numbering and indicator for the direction of the other sensor group positions (bottom corners)

Position 3 is located along the second span of the bridge halfway between mid-span and the support between the second and third bridge span. Table 10 shows the change in wave propagation velocity and the corresponding cross-correlation coefficient from cross-correlation between Measurement 2 and Measurement 3 at Position 3. Similarly, Table 11 and Table 12 show the change in wave propagation velocity and the corresponding cross-correlation coefficient at Position 3 from cross-correlation between Measurement 3 and Measurement 4, and between Measurement 4 and Measurement 5, respectively. The configuration of the sensors within the sensor group at Position 3 is displayed in Figure 22.

Position 3: Measurement 2 – Measurement 3								
Wave-velocity change ( $dv/v$ ) [%]								
	S4	S5	S6	S7	S8	S9	S10	S11
R0	14.2	13.2	14.1	14.7	16.8	11.9	17.9	11.5
R1	10.3	11.7	13.5	16.2	4.0	13.9	15.7	10.1
R2	14.4	14.9	14.8	18.3	13.0	12.7	19.0	15.5
R3	12.1	10.2	12.8	13.5	14.1	19.3	19.8	21.9
	S0	S1	S2	S3	S12	S13		
R4	13.9	16.6	14.0	12.7	-	-		
R5	13.7	20.2	12.1	14.0	-	-		
R6	13.2	14.5	13.8	11.7	-	-		
R7	13.4	15.2	14.5	16.2	-	-		
R8	14.0	14.2	13.8	13.0	13.7	14.4		
R9	11.7	14.6	13.8	11.2	14.8	12.5		
R10	17.5	10.6	15.4	13.0	14.6	15.0		
R11	12.6	16.8	13.0	16.6	11.4	13.4		
	S8	S9	S10	S11				
R12	13.9	13.9	17.9	14.2				
R13	16.2	10.7	14.6	13.2				
Cross-correlation coefficient (CC) [%]								
	S4	S5	S6	S7	S8	S9	S10	S11
R0	66	67	72	66	64	62	62	67
R1	66	66	67	60	61	65	67	61
R2	70	71	70	65	65	65	64	55
R3	60	57	57	55	63	56	64	56
	S0	S1	S2	S3	S12	S13		
R4	62	63	73	64	-	-		
R5	65	63	66	58	-	-		
R6	71	68	79	64	-	-		
R7	67	66	67	64	-	-		
R8	71	69	72	66	75	71		
R9	68	56	64	57	70	66		
R10	71	62	67	65	72	61		
R11	68	66	64	55	71	59		
	S8	S9	S10	S11				
R12	66	70	64	59				
R13	74	70	69	62				

Table 10: Resulting  $dv/v$  and CC from CWI between Measurement 2 and Measurement 3 of the concrete bridge at Position 3 of all relevant sensor pairs between source (S) and receiver (R), red marking and “x” indicate unreliable data and green marking indicates good cross-correlation match, principal sensor pairs are indicated with doubled borders

Position 3: Measurement 3 – Measurement 4								
Wave-velocity change ( $dv/v$ ) [%]								
	S4	S5	S6	S7	S8	S9	S10	S11
R0	<b>17.8</b>	12.3	17.2	11.6	<b>16.3</b>	10.8	17.5	10.1
R1	11.7	<b>2.1</b>	8.5	4.1	3.9	<b>-0.6</b>	8.0	1.3
R2	15.8	10.2	<b>16.4</b>	7.4	15.3	9.6	<b>19.4</b>	10.0
R3	9.3	5.1	10.0	x	2.3	2.9	3.3	<b>-13.1</b>
	S0	S1	S2	S3	S12	S13		
R4	<b>17.3</b>	6.8	15.4	8.1	-	-		
R5	9.8	<b>-4.2</b>	10.9	-0.4	-	-		
R6	14.3	8.2	<b>16.2</b>	9.6	-	-		
R7	9.3	0.6	10.5	<b>1.4</b>	-	-		
R8	<b>16.0</b>	7.6	15.6	9.2	<b>15.6</b>	10.7		
R9	3.5	<b>-7.6</b>	10.5	3.1	10.2	<b>6.9</b>		
R10	19.3	9.0	<b>15.8</b>	9.2	<b>12.9</b>	11.5		
R11	10.5	-3.7	11.1	<b>-4.9</b>	10.4	<b>4.0</b>		
	S8	S9	S10	S11				
R12	<b>11.7</b>	7.2	<b>12.9</b>	5.9				
R13	10.8	<b>5.1</b>	11.1	<b>2.6</b>				
Cross-correlation coefficient (CC) [%]								
	S4	S5	S6	S7	S8	S9	S10	S11
R0	<b>77</b>	76	<b>74</b>	64	<b>69</b>	69	67	62
R1	75	<b>65</b>	68	65	63	<b>60</b>	<b>70</b>	66
R2	69	<b>72</b>	<b>71</b>	63	<b>77</b>	63	<b>69</b>	67
R3	65	62	57	x	59	58	55	<b>60</b>
	S0	S1	S2	S3	S12	S13		
R4	<b>63</b>	<b>71</b>	<b>76</b>	56	-	-		
R5	62	<b>63</b>	69	62	-	-		
R6	<b>85</b>	<b>73</b>	<b>77</b>	61	-	-		
R7	<b>73</b>	64	<b>70</b>	<b>61</b>	-	-		
R8	<b>76</b>	67	<b>75</b>	68	<b>76</b>	<b>76</b>		
R9	66	<b>53</b>	69	59	<b>71</b>	<b>60</b>		
R10	67	67	<b>70</b>	61	<b>73</b>	66		
R11	<b>76</b>	<b>70</b>	67	<b>72</b>	<b>70</b>	<b>68</b>		
	S8	S9	S10	S11				
R12	<b>66</b>	<b>70</b>	<b>68</b>	67				
R13	<b>83</b>	<b>71</b>	<b>74</b>	<b>70</b>				

Table 11: Resulting  $dv/v$  and CC from CWI between Measurement 3 and Measurement 4 of the concrete bridge at Position 3 of all relevant sensor pairs between source (S) and receiver (R), red marking and “x” indicate unreliable data and green marking indicates good cross-correlation match, principal sensor pairs are indicated with doubled borders

Position 3: Measurement 4 – Measurement 5								
Wave-velocity change ( $dv/v$ ) [%]								
	S4	S5	S6	S7	S8	S9	S10	S11
R0	<b>3.2</b>	4.6	4.6	4.9	<b>1.5</b>	5.5	3.4	4.5
R1	5.6	<b>6.8</b>	6.4	6.8	5.9	<b>7.0</b>	8.6	7.5
R2	3.4	4.8	<b>4.8</b>	4.6	0.8	4.7	<b>2.4</b>	5.0
R3	5.5	6.7	6.0	<b>7.4</b>	5.6	7.5	5.9	<b>7.7</b>
	S0	S1	S2	S3	S12	S13		
R4	<b>3.3</b>	4.9	3.3	4.9	-	-		
R5	5.2	<b>7.5</b>	5.3	6.7	-	-		
R6	5.1	6.9	<b>4.2</b>	5.7	-	-		
R7	5.8	7.3	5.4	<b>6.6</b>	-	-		
R8	<b>3.8</b>	5.4	2.5	5.0	<b>3.0</b>	3.8		
R9	5.9	<b>9.5</b>	5.7	7.2	4.8	<b>5.7</b>		
R10	3.7	5.2	<b>4.2</b>	5.3	<b>4.5</b>	4.9		
R11	5.3	7.5	5.0	<b>7.1</b>	5.0	<b>6.3</b>		
	S8	S9	S10	S11				
R12	<b>2.6</b>	5.4	<b>1.7</b>	4.2				
R13	2.2	<b>6.0</b>	4.5	<b>6.3</b>				
Cross-correlation coefficient (CC) [%]								
	S4	S5	S6	S7	S8	S9	S10	S11
R0	<b>78</b>	79	73	78	<b>71</b>	67	<b>72</b>	73
R1	79	<b>82</b>	79	86	<b>85</b>	<b>68</b>	<b>80</b>	82
R2	69	70	<b>69</b>	69	60	67	<b>64</b>	72
R3	<b>81</b>	84	72	<b>74</b>	78	72	73	<b>79</b>
	S0	S1	S2	S3	S12	S13		
R4	<b>71</b>	69	81	70	-	-		
R5	82	<b>77</b>	83	79	-	-		
R6	70	79	<b>74</b>	70	-	-		
R7	86	85	87	<b>83</b>	-	-		
R8	<b>77</b>	77	80	80	<b>83</b>	85		
R9	66	<b>70</b>	71	70	74	<b>63</b>		
R10	84	83	<b>78</b>	76	<b>79</b>	81		
R11	87	82	87	<b>73</b>	85	<b>81</b>		
	S8	S9	S10	S11				
R12	<b>72</b>	74	<b>64</b>	76				
R13	80	<b>74</b>	83	<b>86</b>				

Table 12: Resulting  $dv/v$  and CC from CWI between Measurement 4 and Measurement 5 of the concrete bridge at Position 3 of all relevant sensor pairs between source (S) and receiver (R), red marking and “x” indicate unreliable data and green marking indicates good cross-correlation match, principal sensor pairs are indicated with doubled borders

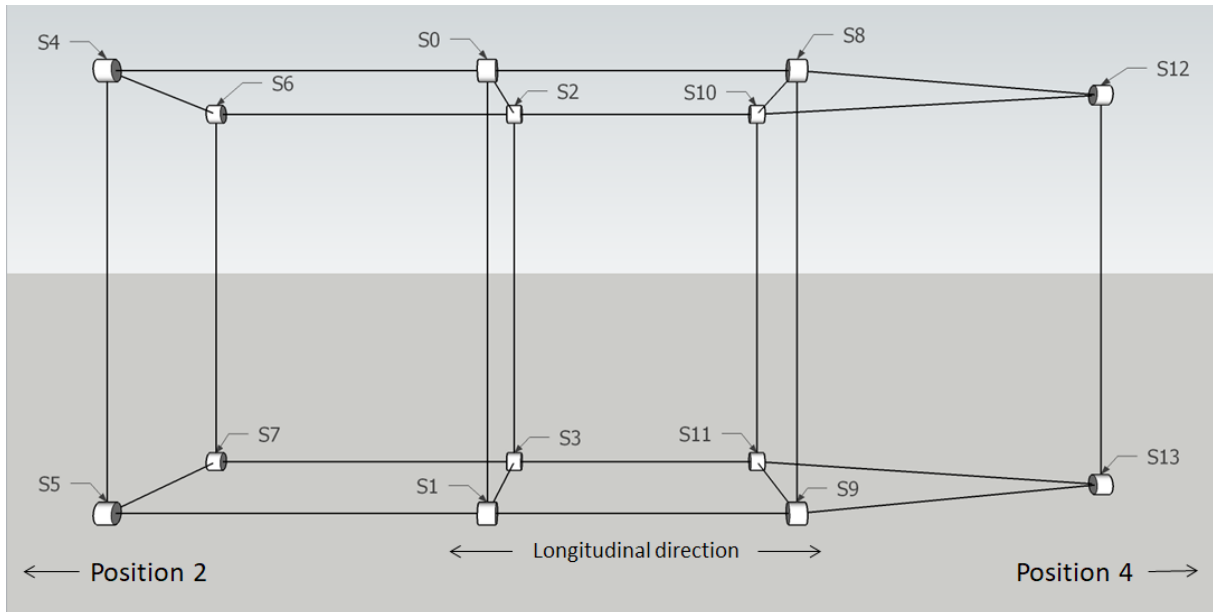


Figure 22: 3D side view of the sensor group configuration cast within the concrete bridge at Position 3 with the sensor numbering and indicator for the direction of the other sensor group positions (bottom corners)

During the first concrete cast of the bridge, part of the third span is included as a cantilever end. The sensor group at Position 4 is located along the cantilever close to the support. Table 13 and Table 14 show the change in wave propagation velocity and the corresponding cross-correlation coefficient at Position 4 from cross-correlation between Measurement 2 and Measurement 4, and between Measurement 4 and Measurement 5, respectively. The configuration of the sensors within the sensor group at Position 4 is displayed in Figure 23.

		Position 4: Measurement 2 – Measurement 4											
		Wave-velocity change ( $dv/v$ ) [%]						Cross-correlation coefficient (CC) [%]					
		S6	S7	S8	S9	S10	S11	S6	S7	S8	S9	S10	S11
R0	S6	23.2	x	-	21.5	12.7	-	54	x	-	56	52	-
R1	S7	x	23.3	16.7	18.0	23.0	11.2	x	59	63	62	61	62
R2	S8	-	16.4	14.0	-	14.1	11.7	-	65	74	-	57	70
R3	S9	17.3	16.0	-	24.6	21.8	-	57	56	-	56	57	-
R4	S10	15.1	12.9	12.2	16.2	13.7	12.3	54	70	67	67	58	65
R5	S11	-	17.6	14.7	-	14.6	13.5	-	69	70	-	56	66
		S0	S1	S2	S3	S4	S5	S0	S1	S2	S3	S4	S5
R6	S0	24.3	x	-	18.1	14.2	-	58	x	-	60	57	-
R7	S1	18.8	24.3	17.2	18.4	14.8	13.2	58	53	64	58	63	61
R8	S2	-	16.6	13.1	-	13.6	12.8	-	60	62	-	65	66
R9	S3	23.3	19.2	-	20.2	16.7	-	64	62	-	60	76	-
R10	S4	20.4	14.6	12.8	11.6	14.1	11.7	58	56	66	56	62	56
R11	S5	-	16.0	11.7	-	13.0	11.6	-	57	76	-	71	70

Table 13: Resulting  $dv/v$  and CC from CWI between Measurement 2 and Measurement 4 of the concrete bridge at Position 4 of all relevant sensor pairs between source (S) and receiver (R), red marking and "x" indicate unreliable data and green marking indicates good cross-correlation match, principal sensor pairs are indicated with doubled borders

Position 4: Measurement 4 – Measurement 5												
Wave-velocity change ( $dv/v$ ) [‰]						Cross-correlation coefficient (CC) [%]						
	S6	S7	S8	S9	S10	S11	S6	S7	S8	S9	S10	S11
R0	2.9	2.8	-	3.9	3.5	-	68	79	-	74	80	-
R1	2.7	3.0	3.9	3.8	3.4	4.0	75	86	87	85	90	91
R2	-	3.9	4.8	-	3.8	4.9	-	78	78	-	84	82
R3	3.2	3.1	-	3.8	3.3	-	77	82	-	77	88	-
R4	3.3	4.7	5.1	4.5	4.3	5.2	64	68	74	68	74	73
R5	-	4.8	5.3	-	4.8	5.4	-	83	81	-	78	77
	S0	S1	S2	S3	S4	S5	S0	S1	S2	S3	S4	S5
R6	2.1	3.1	-	2.9	3.8	-	64	76	-	77	75	-
R7	2.8	3.3	3.8	3.2	3.7	4.0	75	82	91	81	79	87
R8	-	3.9	4.5	-	4.4	4.6	-	90	85	-	87	85
R9	2.9	4.0	-	3.8	4.6	-	76	81	-	75	75	-
R10	3.1	3.4	3.6	2.9	3.6	3.8	69	78	83	86	80	82
R11	-	4.4	5.0	-	5.2	4.9	-	89	89	-	82	83

Table 14: Resulting  $dv/v$  and CC from CWI between Measurement 4 and Measurement 5 of the concrete bridge at Position 4 of all relevant sensor pairs between source (S) and receiver (R), red marking and "x" indicate unreliable data and green marking indicates good cross-correlation match, principal sensor pairs are indicated with doubled borders

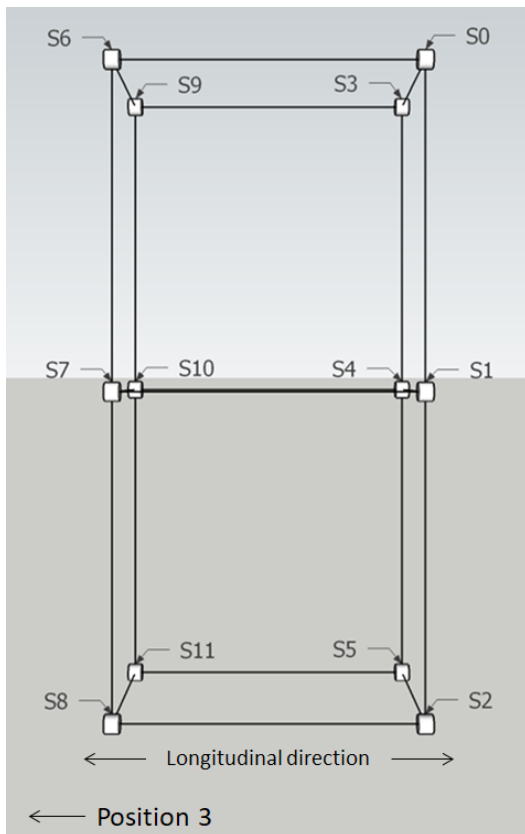


Figure 23: 3D side view of the sensor group configuration cast within the concrete bridge at Position 4 with the sensor numbering and indicator for the direction of the other sensor group positions (bottom corners)

### 4.3 Results of Measurement 6-7 of the concrete structure

During data collection of Measurement 6 and Measurement 7 the hardware setting of the measuring system deviated from those of the other measurements. The gain on the MUX channels was not correctly calibrated. This has resulted in significantly weaker signals to be received and consequently makes cross-correlation with the other measurements impossible. But due to the fact that the hardware settings are consistent during Measurement 6 and Measurement 7, cross-correlation between these two measurements is possible. As such, data from the two aforementioned measurements acts as standalone data.

Position 1: Measurement 6 – Measurement 7								
Wave-velocity change ( $dv/v$ ) [‰]					Cross-correlation coefficient (CC) [%]			
	S4	S5	S6	S7	S4	S5	S6	S7
R0	<b>0.4</b>	-0.3	1.1	-1.1	96	99	98	95
R1	-0.4	<b>0.1</b>	-0.1	-3.2	99	<b>97</b>	96	95
R2	1.5	x	<b>2.9</b>	x	99	x	<b>95</b>	x
R3	0.4	-0.5	1.0	<b>-1.6</b>	95	98	95	<b>97</b>
	S0	S1	S2	S3	S0	S1	S2	S3
R4	<b>-2.1</b>	-1.6	-1.6	-2.0	<b>97</b>	97	98	99
R5	-0.9	<b>-1.1</b>	-0.9	-3.3	93	<b>89</b>	87	92
R6	1.7	x	<b>2.3</b>	0.8	97	x	<b>93</b>	96
R7	-2.3	-2.3	-0.5	<b>-2.6</b>	75	84	91	<b>87</b>

Table 15: Resulting  $dv/v$  and CC from CWI between Measurement 6 and Measurement 7 of the concrete bridge at Position 1 of all relevant sensor pairs between source (S) and receiver (R), red marking and “x” indicate faulty/missing data and green marking indicates good cross-correlation match, principal sensor pairs are indicated with doubled borders

Position 2: Measurement 6 – Measurement 7												
Wave-velocity change ( $dv/v$ ) [‰]						Cross-correlation coefficient (CC) [%]						
	S6	S7	S8	S9	S10	S11	S6	S7	S8	S9	S10	S11
R0	<b>2.9</b>	0.7	-	0.9	1.2	-	<b>59</b>	98	-	92	97	-
R1	2.2	<b>0.9</b>	0.5	0.3	0.2	0.1	<b>89</b>	<b>98</b>	99	95	98	99
R2	-	0.3	<b>1.0</b>	-	x	0.8	-	97	<b>97</b>	-	x	97
R3	2.8	0.4	-	<b>1.8</b>	0.4	-	<b>77</b>	96	-	<b>96</b>	97	-
R4	2.4	0.8	0.4	0.3	<b>0.4</b>	1.3	<b>82</b>	97	99	97	<b>96</b>	98
R5	-	x	x	-	x	<b>x</b>	-	x	x	-	x	<b>x</b>
	S0	S1	S2	S3	S4	S5	S0	S1	S2	S3	S4	S5
R6	<b>x</b>	1.6	-	x	x	-	<b>x</b>	92	-	x	x	-
R7	2.4	<b>2.6</b>	1.0	1.6	1.9	x	<b>89</b>	<b>90</b>	90	90	89	x
R8	-	2.4	<b>2.0</b>	-	2.0	x	-	89	<b>78</b>	-	91	x
R9	1.8	-0.2	-	<b>0.2</b>	0.3	-	<b>88</b>	83	-	<b>78</b>	74	-
R10	1.9	0.7	0.7	1.5	<b>2.5</b>	x	<b>77</b>	81	83	83	<b>88</b>	x
R11	-	0.7	2.2	-	2.5	<b>x</b>	-	90	74	-	91	<b>x</b>

Table 16: Resulting  $dv/v$  and CC from CWI between Measurement 6 and Measurement 7 of the concrete bridge at Position 2 of all relevant sensor pairs between source (S) and receiver (R), red marking and “x” indicate faulty/missing data and green marking indicates good cross-correlation match, principal sensor pairs are indicated with doubled borders

Position 3: Measurement 6 – Measurement 7								
Wave-velocity change ( $dv/v$ ) [%]								
	S4	S5	S6	S7	S8	S9	S10	S11
R0	-1.6	-0.8	-0.8	0.2	0.5	-0.3	3.4	-0.3
R1	-2.3	-2.9	-3.1	-3.0	-0.8	-4.2	-0.3	-3.1
R2	-0.9	x	0.8	-1.5	-2.0	-0.9	1.0	-2.0
R3	-4.5	-3.8	-2.0	-4.0	-1.8	-3.5	-1.1	-4.1
	S0	S1	S2	S3	S12	S13		
R4	-1.5	-2.1	-0.6	-1.9	-	-		
R5	-1.3	-3.9	-2.2	-2.4	-	-		
R6	-1.0	-0.7	-3.2	x	-	-		
R7	0.7	-2.7	-3.6	-2.2	-	-		
R8	-0.1	-4.2	-1.5	-2.1	-2.4	-1.7		
R9	-0.8	-4.2	-2.7	-2.6	-2.3	-4.5		
R10	0.8	0	-0.9	0.8	-3.2	-3.6		
R11	x	x	x	x	x	x		
	S8	S9	S10	S11				
R12	-3.9	-1.4	-1.6	-1.6				
R13	-1.7	-2.5	-1.0	-3.4				
Cross-correlation coefficient (CC) [%]								
	S4	S5	S6	S7	S8	S9	S10	S11
R0	82	88	83	85	76	79	83	82
R1	90	91	84	80	87	90	96	96
R2	83	x	79	85	82	87	91	91
R3	93	87	93	86	82	82	98	88
	S0	S1	S2	S3	S12	S13		
R4	90	93	83	92	-	-		
R5	88	92	93	85	-	-		
R6	93	97	93	x	-	-		
R7	89	90	93	88	-	-		
R8	93	95	98	92	95	93		
R9	94	96	97	87	98	95		
R10	86	93	86	85	90	93		
R11	x	x	x	x	x	x		
	S8	S9	S10	S11				
R12	70	93	92	85				
R13	92	87	91	89				

Table 17: Resulting  $dv/v$  and CC from CWI between Measurement 6 and Measurement 7 of the concrete bridge at Position 3 of all relevant sensor pairs between source (S) and receiver (R), red marking and “x” indicate faulty/missing data and green marking indicates good cross-correlation match, principal sensor pairs are indicated with doubled borders

Position 4: Measurement 6 – Measurement 7												
Wave-velocity change ( $dv/v$ ) [‰]						Cross-correlation coefficient (CC) [%]						
	S6	S7	S8	S9	S10	S11	S6	S7	S8	S9	S10	S11
R0	x	x	-	x	x	-	x	x	-	x	x	-
R1	0.1	<b>-0.1</b>	0	-0.1	x	-0.1	100	100	100	99	x	100
R2	-	0	<b>0.1</b>	-	x	0	-	100	100	-	x	100
R3	0.6	1.7	-	<b>0.5</b>	x	-	97	94	-	91	x	-
R4	0.2	0.2	0.3	0.2	<b>x</b>	0	100	99	100	99	x	100
R5	-	-0.4	-0.3	-	x	<b>-0.1</b>	-	99	99	-	x	99
	S0	S1	S2	S3	S4	S5	S0	S1	S2	S3	S4	S5
R6	<b>3.4</b>	-0.2	-	0.9	-0.2	-	95	98	-	97	99	-
R7	1.9	<b>-0.5</b>	0.3	0.6	-0.9	0.1	94	96	99	98	95	97
R8	-	-2.0	<b>-1.5</b>	-	0.2	-0.1	-	83	91	-	80	91
R9	2.4	0	-	<b>-1.0</b>	0	-	91	98	-	93	98	-
R10	x	x	x	x	<b>x</b>	x	x	x	x	x	x	x
R11	-	-1.3	-1.0	-	-1.3	<b>-1.5</b>	-	89	95	-	91	97

Table 18: Resulting  $dv/v$  and CC from CWI between Measurement 6 and Measurement 7 of the concrete bridge at Position 4 of all relevant sensor pairs between source (S) and receiver (R), red marking and “x” indicate faulty/missing data and green marking indicates good cross-correlation match, principal sensor pairs are indicated with doubled borders

For Measurement 6 and Measurement 7, the method of determining the  $dv/v$  has changed. Measurements 6 and Measurement 7 are conducted in relatively close time proximity of one another when the concrete material has fully matured. Hence, time-dependent factors that are acting on the perceived wave velocity of the signal are far less significant. Another aspect to consider is the addition of the asphalt layer applied on top the concrete bridge deck. The additional material may alter the scattering path of the signal through the medium and cause differences in the signal’s waveform. Following the theory of the Sensitivity Kernel, as explained in Section 2.12, these alterations are primarily observed in the late coda-wave arrivals as the medium in the direct path between source and receiver remains unchanged. Therefore, for assessment of the CWI between Measurement 6 and Measurement 7 only the first stretching window directly after the first arrival is considered for determining the wave-velocity change and results are shown in Table 15, Table 16, Table 17 and Table 18 for Position 1, Position 2, Position 3 and Position 4, respectively.

After construction of the concrete road shoulder on the bridge deck, the connectors of the sensors are made accessible through sealed storage pits. The conditions around this storage method have proved to not be ideal and as a consequence, some connectors and wires of the sensors are found damaged from wear and exposure to rainwater. This issue arises in Measurement 6 and later measurements, where a comprehensible wave signal between certain sensor pairs is not able to be recorded. The missing data is marked with an “x” and red.

#### 4.4 Results of Measurement 8 of the concrete structure

The hardware settings for Measurement 8 have been adjusted accordingly to match the signal strength of the first five measurements. However, cross-correlation between Measurement 5 and Measurement 8 proves to be very difficult still as the CC rarely meets the 0.5 threshold. The most probable explanation is the large amount of elapsed time of ten months between the two measurements. During this time, the concrete structure is continuously exposed to environmental factors and loading from construction proceedings. These factors have an effect on the wave signal and change the signal’s waveform so considerably that the modified signal deviates too much from the reference signal for reliable cross-correlation.

During Measurement 8, some sensor pairs have been appraised multiple times in succession. At the time of both Measurement 6 and Measurement 8, a large amount of construction traffic was present at the measured bridge spans. This causes dynamic changes in the loading conditions as multiple heavy vehicles move across the bridge. During one sequence of Measurement 8 at Position 1, a lorry is stationed on the bridge span lateral from the location of the sensor group and thus equates to a static load on the bridge span. Another set of measured data is obtained at Position 1 without the stationary lorry and acts as the reference data for cross-correlation. Following this, the data from Measurement 8 is utilized similarly to the data from Measurement 6 and Measurement 7, i.e. as standalone data, for assessment of the influence of loading on the bridge with regards to the signal’s wave velocity. The resulting data is shown in Table 19.

Position 1: Measurement 8 without – with load								
Wave-velocity change ( $dv/v$ ) [%]					Cross-correlation coefficient (CC) [%]			
	S4	S5	S6	S7	S4	S5	S6	S7
R0	<b>0.6</b>	0.2	x	0.1	<b>100</b>	100	x	100
R1	0.2	<b>0</b>	x	-0.4	96	<b>100</b>	x	98
R2	0.3	-0.1	<b>x</b>	0.2	100	100	x	99
R3	-0.2	-0.2	x	<b>-0.3</b>	100	100	x	<b>100</b>
	S0	S1	S2	S3	S0	S1	S2	S3
R4	<b>-0.6</b>	0.1	0.7	0.2	<b>98</b>	98	99	99
R5	2.6	<b>2.1</b>	4.1	3.5	90	<b>86</b>	81	79
R6	1.8	2.0	<b>2.1</b>	0.1	96	95	<b>97</b>	97
R7	2.3	1.9	0.6	<b>1.3</b>	72	91	95	<b>89</b>

Table 19: Resulting  $dv/v$  and CC from CWI between Measurement 8 without and with load of the concrete bridge at Position 1 of all relevant sensor pairs between source (S) and receiver (R), red marking and “x” indicate faulty/missing data and green marking indicates good cross-correlation match, principal sensor pairs are indicated with doubled borders

# 5 Coda Wave Interferometry results of laboratory tests

## 5.1 Concrete hydration

Index	Day	Step size
1	1	-
2	4	3
3	5	1
4	6	1
5	7	1
6	12	5
7	13	1
8	14	1
9	15	1
10	18	3
11	19	1
12	20	1
13	21	1
14	22	1
15	25	3
16	26	1
17	27	1
18	28	1
19	29	1
20	32	3
21	34	2
22	35	1
23	36	1
24	39	3
25	40	1
26	42	2
27	43	1
28	46	3

Table 20: Concrete hydration test age specifics and measurement intervals

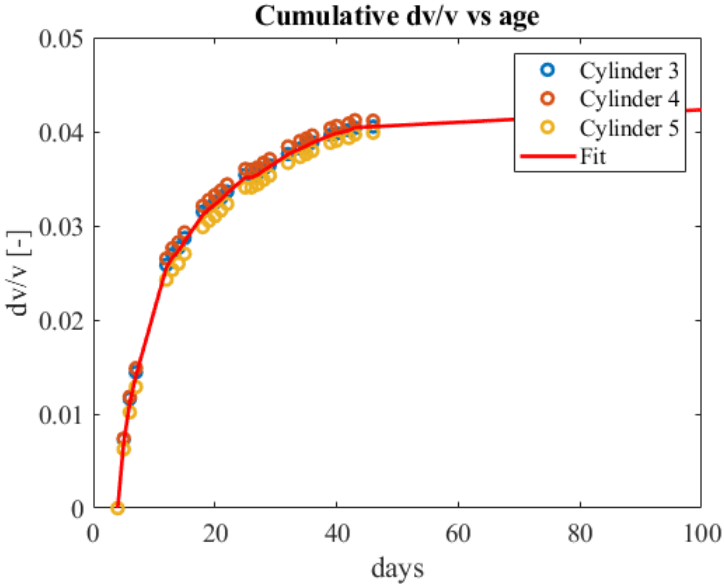


Figure 24: Accumulated wave-velocity change over concrete age in days for all three concrete hydration test cylinders with averaged fitted plot

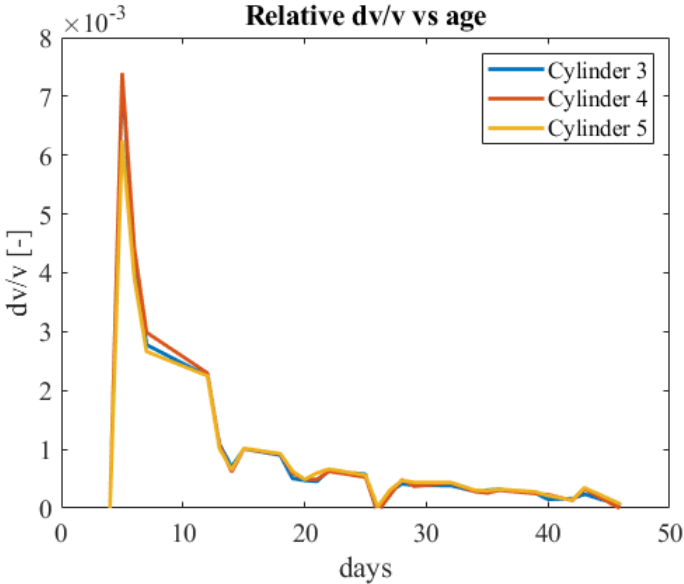


Figure 25: Wave-velocity change per concrete aging day measurement in comparison to previous measurement for all three concrete hydration test cylinders

Past studies [18] have shown that the maturity of not fully developed concrete has an effect on the acoustoelastic properties of the material. As young concrete is paired with a still developing Young’s modulus, the hydration of concrete will influence the wave propagation velocity in accordance with Section 2.2. The effects of concrete curing on the wave propagation velocity are examined with concrete

hydration tests of three concrete cylinders. Each wave signal measured every one to three days is cross-correlated through CWI with the preceding measured wave signal. It should be noted that the concrete mix design for the concrete hydration test samples is not identical to the concrete mix that envelop the SA in the concrete bridge for field measurements. As such the results of the cases are not directly interchangeable.

In Table 20, the scheduled measurement intervals are described, and from that, plots are produced from the acquired SA-data to demonstrate the relation between concrete age and wave propagation velocity. Figure 24 shows the total wave velocity increase over several days with four-days-old concrete as starting point and Figure 25 shows the estimated wave-velocity change per day. The graphs reveal that there is a significant increase in wave velocity during the early age of the concrete and that increase diminishes gradually over time.

In Figure 26, Figure 27 and Figure 28, all CWI resulting  $dv/v$ -plots over signal travel time are shown. From the graphs, one can swiftly conclude that the  $dv/v$ -values from CWI are consistent along the entire wave signal with the exception of a single plot in each cylinder. This outlier plot is affiliated with the cross-correlation of the first two measurements of the cylinder, i.e. when the concrete is at its youngest. Due to the rapidly developing properties of young concrete, changes in the signal’s waveform make CWI difficult. This is further showcased by the significantly lower  $CC$  from CWI of early measurements in contrast to the consistent high  $CC$  of later measurements. CWI results of the first measurements are therefore deemed unreliable and are not considered in further analysis. CWI results for every measurement of each cylinder are found in Appendix E.

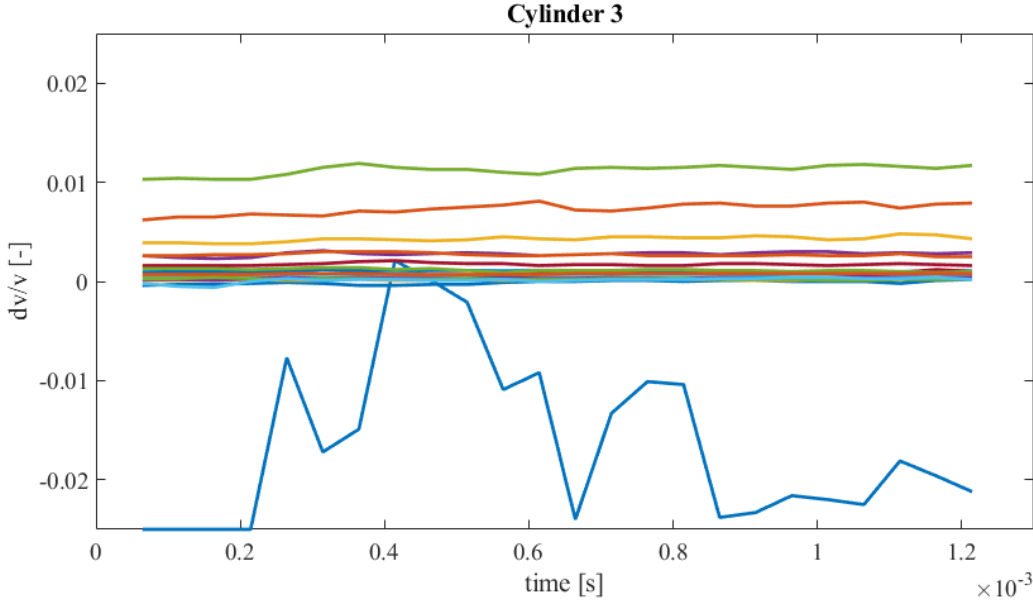


Figure 26: Plotted  $dv/v$  over wave travel time from CWI for all concrete aging measurements of Cylinder 3

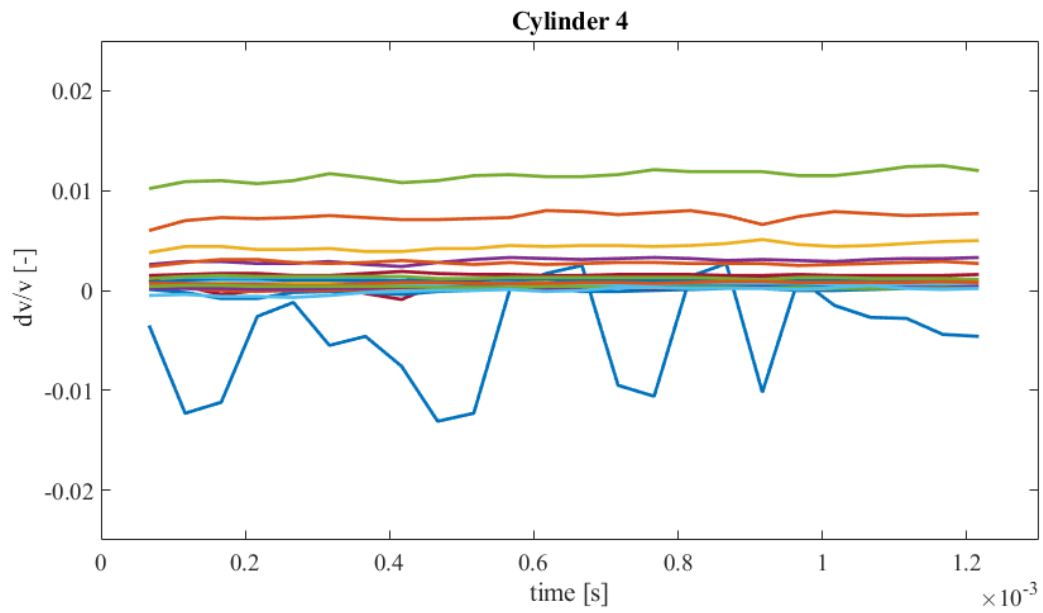


Figure 27: Plotted  $dv/v$  over wave travel time from CWI for all concrete aging measurements of Cylinder 4

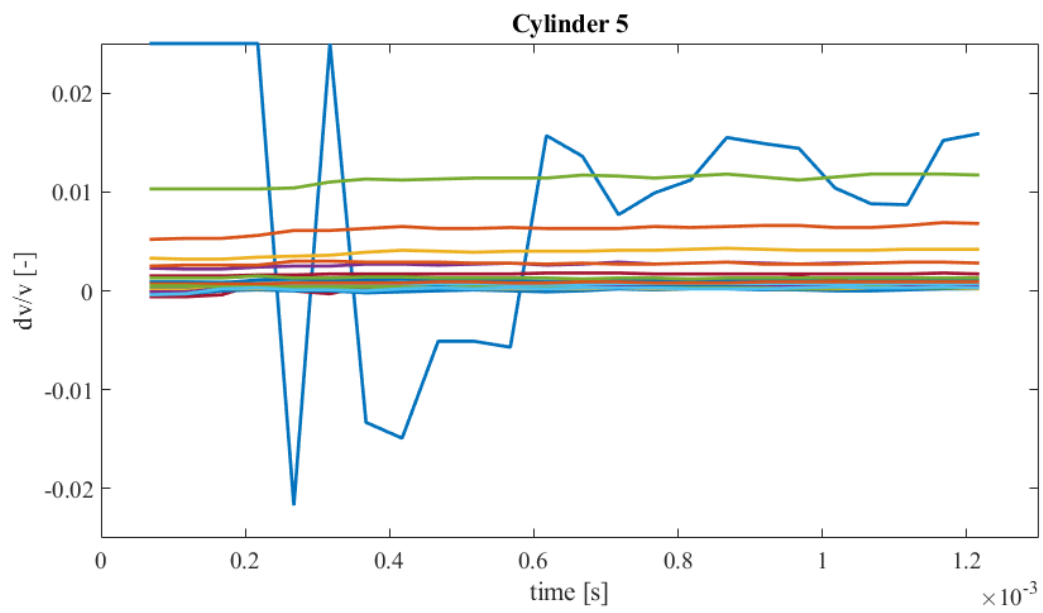


Figure 28: Plotted  $dv/v$  over wave travel time from CWI for all concrete aging measurements of Cylinder 5

## 5.2 Concrete compression

As explained in Section 2.2, the material characteristics of the medium dictate the relation between wave propagation velocity and the stress-state of the medium through the acoustoelastic effect. For proper assessment of the effects of the stress-state on the wave propagation velocity, compression stress tests are conducted. The two cylindrical test samples consist of the same concrete mix batch used for casting of the cast-in-situ bridge. The distinctive relation between wave velocity and stress is determined for the concerned concrete medium.

Load step	Force (kN)	Pressure (MPa)
1	700	9.90
2	1000	14.15
3	1300	18.39
4	1600	22.64
5	1900	26.88
6	2200	31.12
7	2500	35.37
8	2800	39.61
9	2500	35.37
10	2200	31.12
11	1900	26.88
12	1600	22.64
13	1300	18.39
14	1000	14.15
15	700	9.90
16	1000	14.15
17	1300	18.39
18	1600	22.64
19	1900	26.88
20	2200	31.12
21	2500	35.37
22	2800	39.61
23	2500	35.37
24	2200	31.12
25	1900	26.88
26	1600	22.64
27	1300	18.39
28	1000	14.15
29	700	9.90

Table 21: Concrete compression test loading force per measured load step

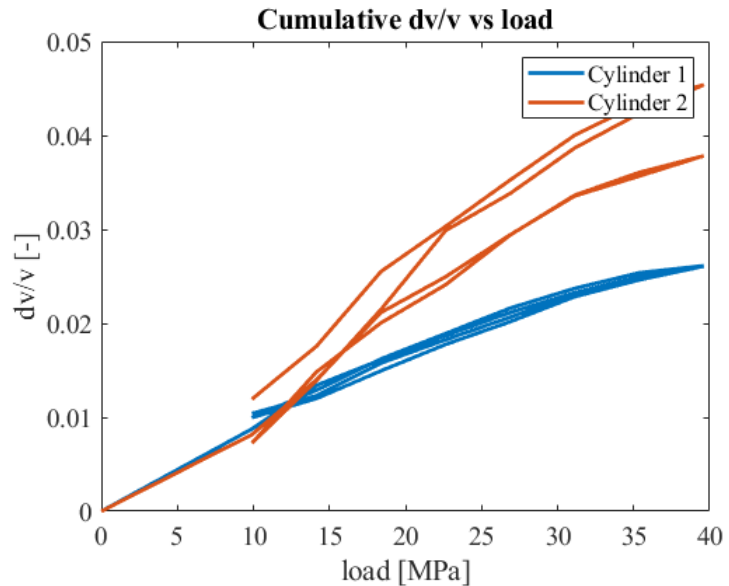


Figure 29: Total wave-velocity change over total applied load for compressive concrete loading test Cylinder 1 and Cylinder 2

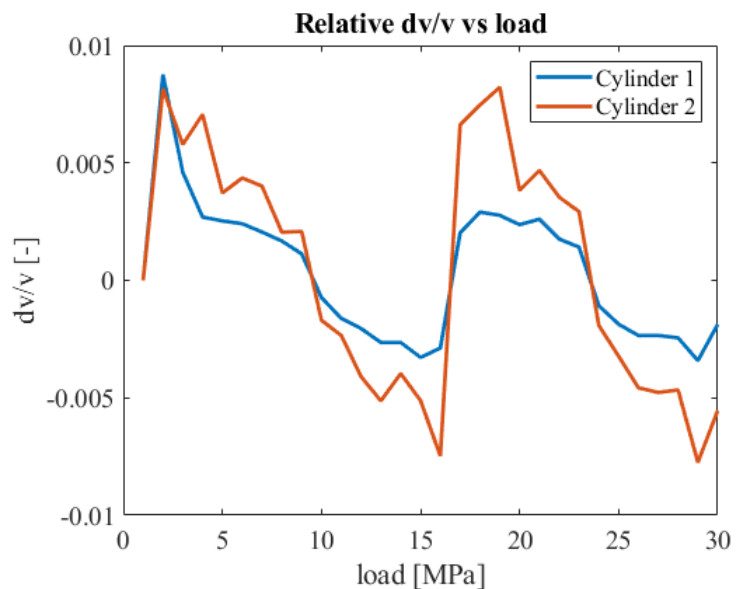


Figure 30: Wave-velocity change per load step for compressive concrete loading test Cylinder 1 and Cylinder 2

The cylinder loading test is done in cycles and the loading steps are according to Section 3.6 and are illustrated in Table 21. CWI results are acquired with the rolling reference principle (Figure 13). In Figure 29 the relation between the total applied load and the total increase in wave velocity is plotted with respect to an unloaded concrete sample. In Figure 30 the wave velocity increase for each individual

load step is plotted. One observes a nonlinear relation with a linear differential, where the increase in wave velocity diminishes as the load increases.

The subsequent wave-velocity change  $dv/v$  over wave travel time for each load step for each tested cylinder is shown in Figure 31 and Figure 32. CWI for each load step are found in Appendix F. The first interesting point is that the results from Cylinder 1 are more consistent in comparison to the results of Cylinder 2. The cause of this discrepancy is unclear. The second point is the low  $CC$  when the specimen is initially loaded and nearly fully unloaded. This phenomenon is likely caused by the formation and opening of microcracks from the damaged microstructure of the concrete due to the loading. The effect of cracks on the waveform and subsequently the  $CC$  has been established in a past study by Du and Yang [28]. This shows that initial loading and unloading are causes for complications when cross-correlating wave signals with the intention of detecting stress changes.

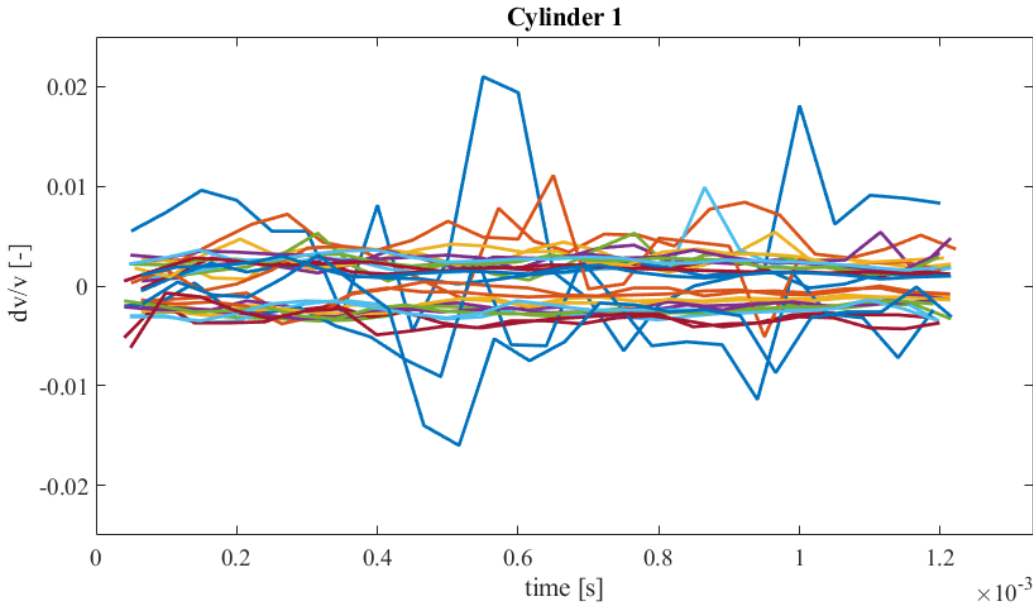


Figure 31: Plotted  $dv/v$  over wave travel time from CWI for all loading test measurements of Cylinder 1

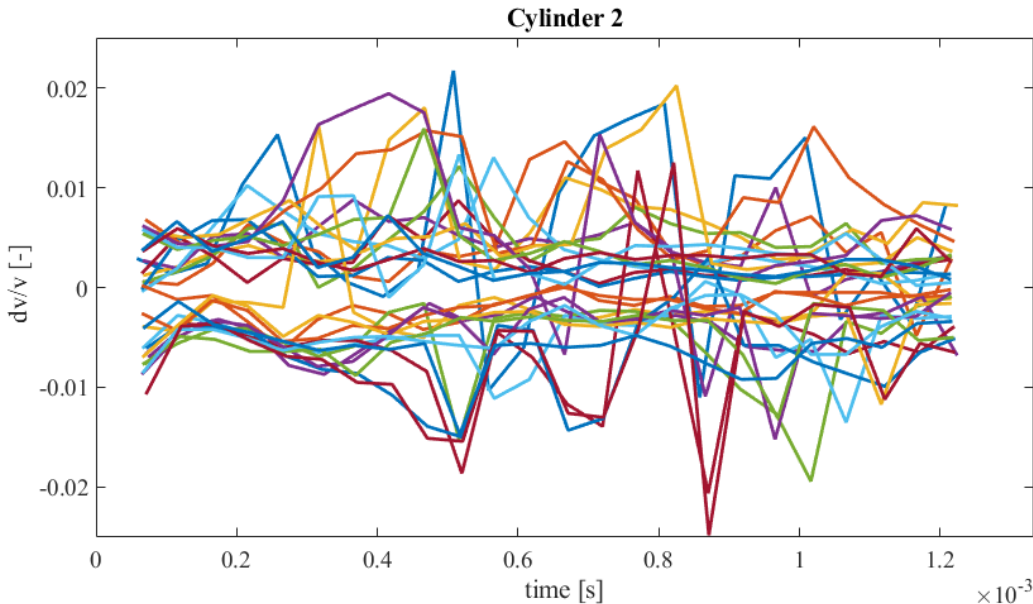


Figure 32: Plotted  $dv/v$  over wave travel time from CWI for all loading test measurements of Cylinder 2

### 5.3 Geopolymer creep

The examined concrete structure is loaded in post-tensioning and any form of prestressed concrete coincides with the presence of creep. The constant axial loading from the prestressing force causes the structure to deform over time. In Section 2.2, it has been established that deformations have an influence on the wave propagation velocity through the acoustoelastic effect of the medium. Generally, in CWI the medium is considered linear elastic and thus stress and deformation are linearly related. This relation is however not valid with regard to creep, as it is defined as continued deformation under constant load. Therefore, a creep test is conducted to establish the relation between time-dependent deformation and wave-velocity change  $dv/v$ .

Measurement	Elapsed time	Temperature (°C)	Deformation 1 ( $10^{-3}$ )	Deformation 2 ( $10^{-3}$ )	Cumulative $dv/v$ ( $10^{-3}$ )
0	Start	19.4	0	0	0
1	2.5 hours	19.4	0.417	0.457	6.8
2	1 day	19.4	0.563	0.568	19.8
3	4 days	19.4	0.600	0.590	38.9
4	5 days	19.4	0.673	0.644	39.5
5	6 days	19.4	0.687	0.665	38.9
6	7 days	19.4	0.742	0.721	38.0
7	8 days	19.4	0.793	0.772	37.2
8	11 days	19.4	0.919	0.897	36.6
9	12 days	19.4	0.954	0.931	36.1
10	13 days	19.4	0.988	0.964	35.3
11	14 days	19.4	1.016	0.995	35.1
12	15 days	19.4	1.045	1.023	34.7
13	18 days	19.4	1.131	1.097	33.8
14	19 days	19.4	1.154	1.120	33.5
15	20 days	19.4	1.176	1.144	33.2
16	21 days	19.4	1.197	1.164	32.9
17	22 days	19.4	1.219	1.183	32.6
18	25 days	20.5	1.290	1.247	29.2
19	26 days	26.8	1.281	1.251	27.5
20	27 days	28.8	1.314	1.290	27.0
21	28 days	29.4	1.357	1.331	26.6
22	29 days	30.0	1.397	1.371	26.1
23	32 days	31.1	1.531	1.490	24.1
24	33 days	25.3	1.574	1.520	23.1
25	35 days	22.4	1.594	1.534	18.8
26	36 days	22.4	1.614	1.553	19.2
27	39 days	19.5	1.647	1.583	19.5
28	40 days	19.5	1.656	1.590	19.3
29	41 days	19.5	1.664	1.597	19.3
30	57 days	19.3	1.789	1.711	17.1
31	60 days	19.4	1.809	1.730	16.7
32	61 days	19.4	1.816	1.736	16.6
33	64 days	19.4	1.837	1.754	16.2
34	67 days	19.4	1.855	1.772	15.9

Table 22: Geopolymer creep test results with measurement index, total creep test duration at time of measurement, ambient temperature and total deformation of creep test Sample 1 and Sample 2

The geopolymer test samples are stressed for an indefinite time, during which the samples are constantly loaded with a compressive pressure of 17 MPa. If the compressive stress within the test sample exceeds 45% of the characteristic compressive strength of the material, creep non-linearity is to be considered [25]. As that degree of loading on the monitored structure is not expected to be present during the field measurements, the compressive stress on the creep samples is kept below 45% of the compressive strength.

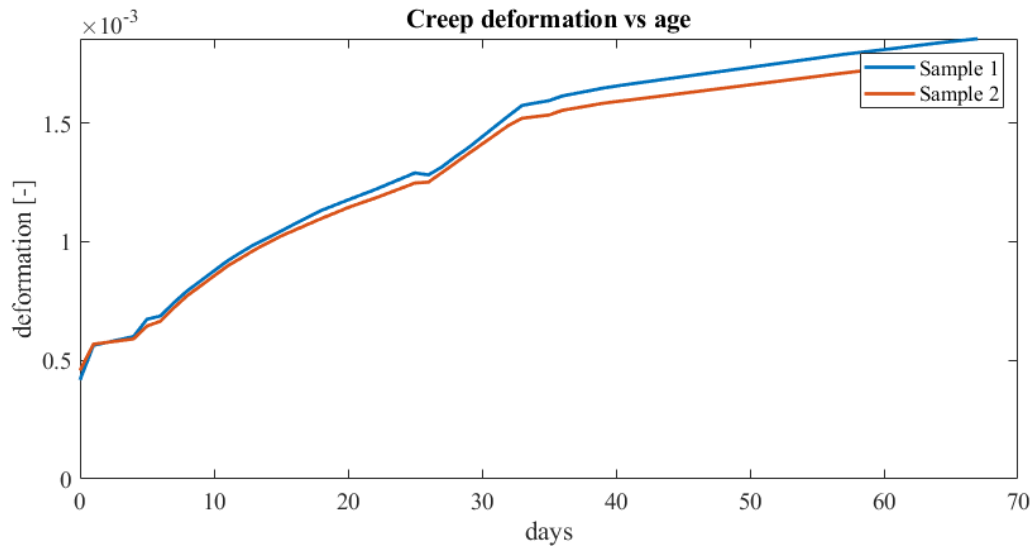


**Figure 33: Creep deformation of the geopolymer samples over the creep test duration for Sample 1 and Sample 2**

For this study, data is periodically collected from the test samples over 67 days. The deformation of the test samples in regard to their initial dimensions over this time period is noted in Table 22 and plotted in Figure 33. The environmental conditions are intended to be constant to eliminate unpredicted factors and the test was therefore conducted within a controlled climate room. Sadly, the air conditioning in the climate room in question malfunctioned, which caused the temperature in the room to rise considerably for a portion of the test's duration, as can be seen in Table 22. Past studies [1] have determined that the temperature of the concrete has an effect on the wave propagation velocity. So, the fluctuations in temperature during the test have somewhat skewed the results of the test as changes in  $dv/v$  are no longer exclusively from controlled creep and shrinkage deformation. The CWI data for each measurement can be found in Appendix G.

One can observe a steep wave velocity increase at the start of the creep test, as seen in Figure 34, which is likely caused by the loading of the test sample. It is notable that the relatively high positive  $dv/v$  persists for several days, even though there is no increase in load after the initial loading, which should only correspond with the CWI results of the first two measurements. The cause of this phenomenon is unclear, but the low  $CC$  in the late coda-wave arrivals (Appendix G) suggests alterations in the medium. So a logical deduction would lead to the cause being related to the formation of microcracks due to the loading on the samples, which is also observed during the concrete cylinder compression test (Appendix F).

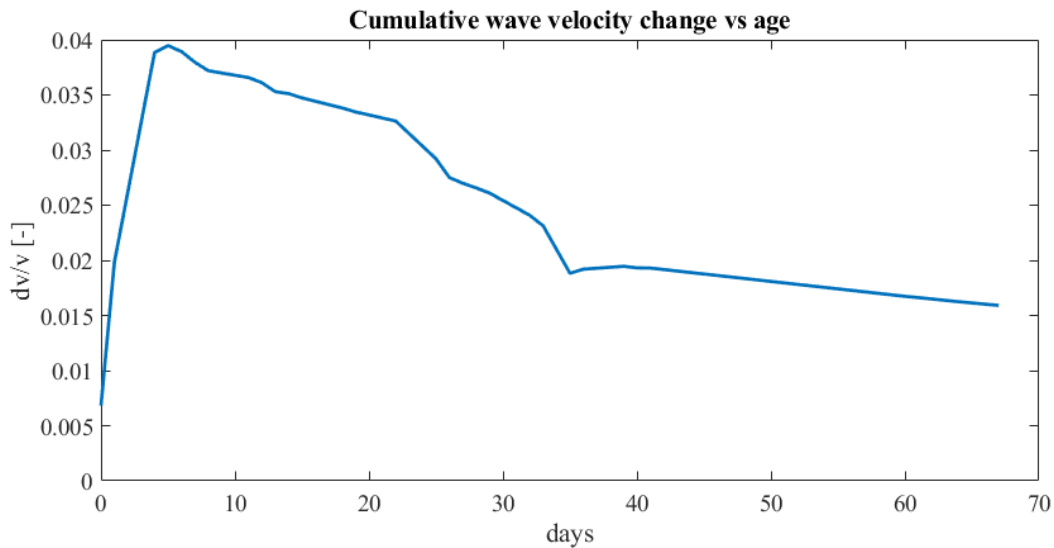


**Figure 34: Accumulated wave-velocity change over geopolymer creep test days**

After the first five days, the wave velocity decreases somewhat consistently with a linear relation to the creep deformation. Figure 35 shows a consistent decline in  $dv/v$  in both geopolymer samples for the increasing deformation due to creep after the initial loading has settled in. The trend of the wave-velocity change is displayed cumulatively in regards to the wave velocity in the samples before testing. The linear relation between deformation and  $dv/v$  results in a constant decrease in wave velocity as the geopolymer samples continues to decrease in size longitudinally. This trend is surprising as one would initially expect compressive strains to give similar results to compressive stresses, which would equate to an increase in  $dv/v$  rather than a decrease.

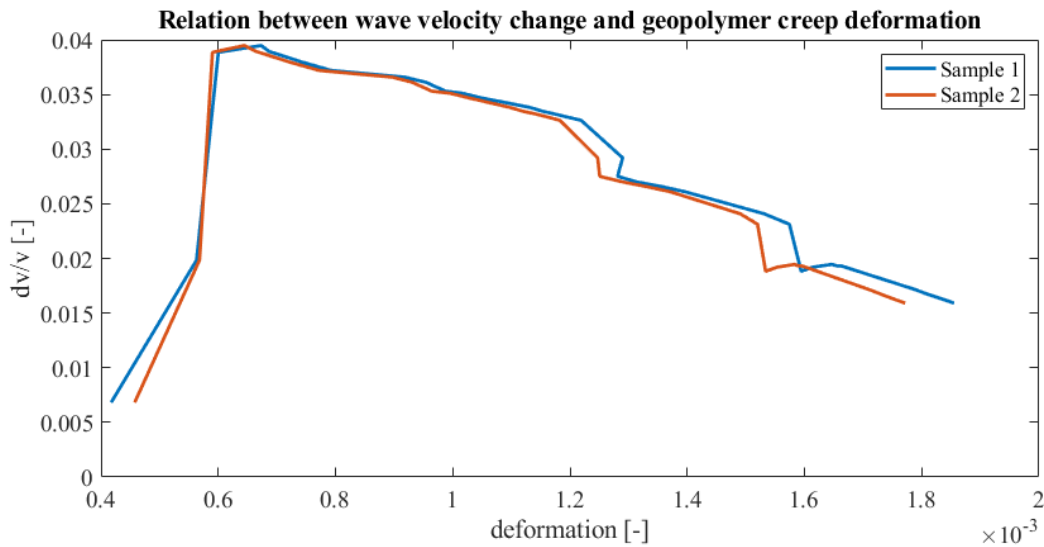


**Figure 35: Total wave-velocity change over creep deformation for geopolymer creep test Sample 1 and Sample 2**

A factor to consider is that geopolymer concrete has been found to decrease in stiffness over time. The documented stiffness development of this particular geopolymer mix design, as seen in Table 2, does show a slight decrease in elasticity modulus after 56 days, but the decrease is very small. Also, as the stiffness development is determined on a sample in a mold, an exposed geopolymer sample as with the creep test might develop differently. Nevertheless, the acquired data is taken as is for further analysis in this study.

### 5.3.1 Effects of temperature

The very notable influence of temperature on the wave velocity can be observed in the above graphs for  $dv/v$ -creep relation. As seen in Figure 34, the  $dv/v$ -values become inconsistent around the 25<sup>th</sup> day, which coincides with the moment the climate control in the test room breaks and the temperature in the room starts to rise. Another inconsistency is observed around the 35<sup>th</sup> day and coincides with the date the climate controlled room is fixed and the temperature is lowered again.

These same outliers in  $dv/v$ -values are observed in Figure 35 at deformation values tied to the aforementioned days. The  $dv/v$  seems to remain somewhat consistent during the period the temperature in the test room was uncontrolled, as the temperature was constant, albeit higher. The  $CC$  between measurements in varying temperature also has noticeable lower values in the late coda-wave compared to the measurement in controlled climate conditions. These observations suggest that environmental temperature change has a significant effect on the wave velocity and the signal's waveform.

The temperature has also shown to have an effect on the deformation, as seen in Figure 33, as the samples deform at an increased rate in higher temperatures. This is identified by the accompanied ambient temperature per measurement date in Table 22. A probable cause for the increased deformation is the increase in shrinkage due to moisture evaporation within the geopolymer samples from the higher ambient temperature.

## 6 Analysis of results

### 6.1 Structural analysis of the concrete structure

The end objective of this study is to validate the experimental CWI results through analytical calculations. Thus a structural analysis is done on the measured concrete structure in question.

#### 6.1.1 Calculation of cross-sectional stresses

The concrete structure of interest is a cast-in-situ post-tensioned concrete bridge. As the structure is tensioned during concrete hardening, the interaction between prestress eccentricity and self-weight loading is peculiar. Since the formwork is still in place during post-tensioning, the shoring provides support for the self-weight of the bridge. During casting of the concrete, the formwork and shoring carry the full weight of the structure. When post-tensioning is applied with draped tendons during concrete hardening, a portion of the load on the shores is balanced by the eccentric loading. This causes a certain amount of the self-weight load to be compensated by the eccentric force of the post-tensioning and another amount to still be carried by the formwork and shores.

Structural analysis on the structure is done with a simplified mechanical model. The parameters for the loading on the simplified model are displayed in Table 23. In the design calculation of the prestressing force in the concrete bridge, a distinction is made between the prestressing force in the span of the bridge ( $P_{span}$ ) and the prestressing force at the supports ( $P_{support}$ ). The same distinction is kept for this structural analysis. The load due to the self-weight of the structure and the load of the asphalt layer are modelled as uniformly distributed loads  $q_{sw}$  and  $q_{asphalt}$ , respectively.

Load Size	$P_{span}$	$P_{support}$	$q_{sw}$	$q_{asphalt}$
	5500 kN/m	6000 kN/m	$25 \cdot h_i$ kN/m <sup>2</sup>	2.5 kN/m <sup>2</sup>

Table 23: Loading parameters of the mechanical model of the concrete bridge structure

Structural analysis on the structure is done with a simulation in Maple [29], a computing program able to solve differential equations with the use of boundary conditions. The bridge structure is modelled as a statically indeterminate Euler-Bernoulli beam, which considers bending moments and no shear forces. The effect of prestressing on the bending moment distribution is modelled as distributed loads derived from the prestressing force and the curve radius of the prestressing tendons. The Euler-Bernoulli beam models are illustrated in Figure 36.

The transition of tendon curvature is determined by computing the equilibrium of longitudinal length for equal tendon rotation at the location of the transition, such that the transition between concave curvature and convex curvature is smooth. This entails that the global rotation of the prestressing tendons are identical at the point of transition. The drape of the tendons are assumed to follow the distinct parabolic shape of a bending moment distribution line associated with a uniformly distributed load and the rotation of the prestressing tendon is found with the derivative. The resulting dimensions of the tendon with respect to the curvature is as such:

$$q_{prestress} = \begin{cases} P_{span}/R_1 & x > 0.845m \text{ and } x < 30.405m \\ P_{support}/R_2 & x > 30.405m \text{ and } x < 32.095m \\ P_{span}/R_1 & \text{for } x > 32.095m \text{ and } x < 61.655m \\ P_{support}/R_2 & x > 61.655m \text{ and } x < 63.345m \\ P_{span}/R_1 & x > 63.345m \text{ and } x < 70.625m \end{cases} \quad 6.1$$

where  $q_{prestress}$  represents the uniformly distributed load due to the prestressing tendon curvature,  $P_{span}$  and  $P_{support}$  represent the prestressing force of the tendon, and  $R_1$  and  $R_2$  represents the prestressing tendon curvature radius. The  $x$ -axis represents the longitudinal distance along the bridge with the abutment acting as origin.

The variable cross-sectional height of the concrete bridge deck is simulated with a piecewise function. As the cross-sectional height of the concrete bridge structure is not constant, the beam model consists of multiple beam segments. The Euler-Bernoulli beam model consists of the following piecewise segments:

$$h = \begin{cases} h_1 = 1300 \text{ mm} & x > 0 \text{ and } x < 1.625m \\ h_2 = 1100 \text{ mm} & x > 1.625m \text{ and } x < 5.625m \\ h_3 = 800 \text{ mm} & x > 5.625m \text{ and } x < 11.625m \\ h_4 = 600 \text{ mm} & x > 11.625m \text{ and } x < 19.625m \\ h_3 = 800 \text{ mm} & x > 19.625m \text{ and } x < 25.625m \\ h_2 = 1100 \text{ mm} & x > 25.625m \text{ and } x < 29.625m \\ h_1 = 1300 \text{ mm} & x > 29.625m \text{ and } x < 32.875m \\ h_2 = 1100 \text{ mm} & \text{for } x > 32.875m \text{ and } x < 36.875m \\ h_3 = 800 \text{ mm} & x > 36.875m \text{ and } x < 42.875m \\ h_4 = 600 \text{ mm} & x > 42.875m \text{ and } x < 50.875m \\ h_3 = 800 \text{ mm} & x > 50.875m \text{ and } x < 56.875m \\ h_2 = 1100 \text{ mm} & x > 56.875m \text{ and } x < 60.875m \\ h_1 = 1300 \text{ mm} & x > 60.875m \text{ and } x < 64.125m \\ h_2 = 1100 \text{ mm} & x > 64.125m \text{ and } x < 68.125m \\ h_3 = 800 \text{ mm} & x > 68.125m \text{ and } x < 70.625m \end{cases} \quad 6.2$$

where  $h$  is the cross-sectional height of the bridge deck. The variation in cross-sectional height of the bridge deck is simulated with four variables:  $h_1$ ,  $h_2$ ,  $h_3$  and  $h_4$ . With the largest height located at the supports and the smallest located at mid-span. The significance of the inconstant cross-sectional height is the varying bending stiffness along the beam model and non-uniform distributed self-weight loading.

The boundary conditions of the beam are considered constant during the post-tensioning process and only change after the corresponding formwork is removed from the measured and adjacent spans, i.e., the spans become self-supporting. Afterwards, the boundary conditions are assumed to again remain constant during further construction of the bridge.

During the post-tensioning, the contribution of the structure self-weight on the bending moment distribution is derived by a simulation of the displacement field. The active portion of the self-weight loading is estimated as such that displacement due to induced bending moments from prestressing is minimal. As for the magnitude of the self-weight loading, the piecewise cross-sectional height of the bridge deck is used with the volumetric weight of concrete.

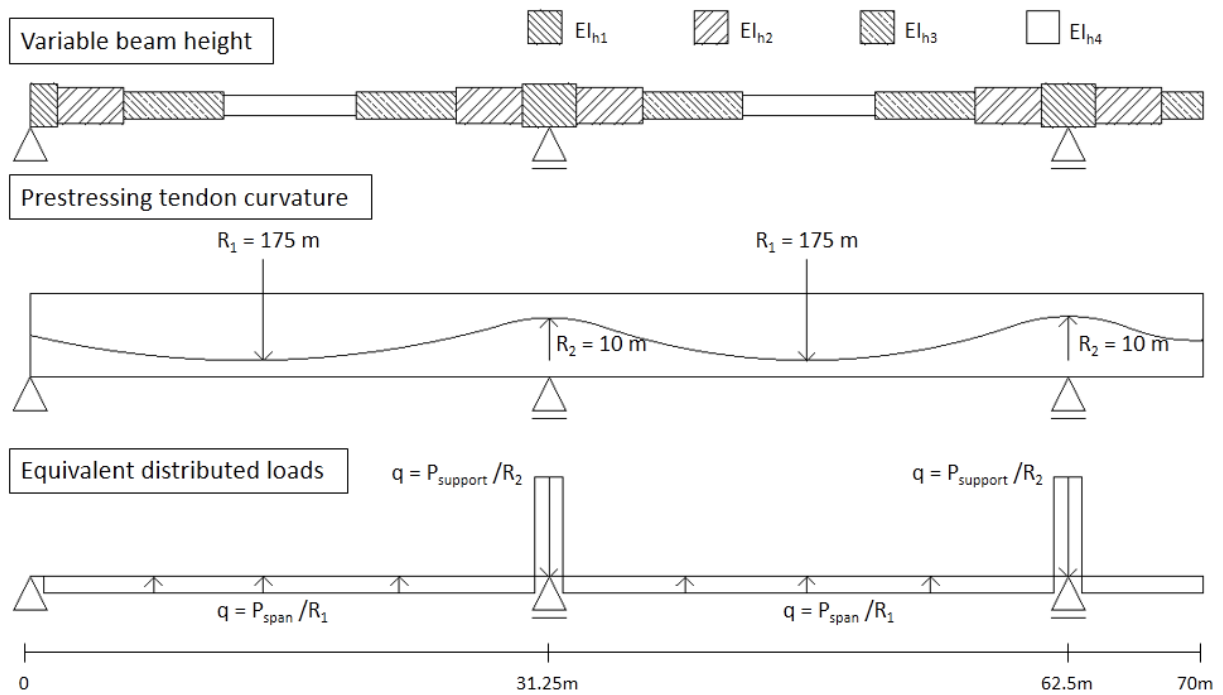
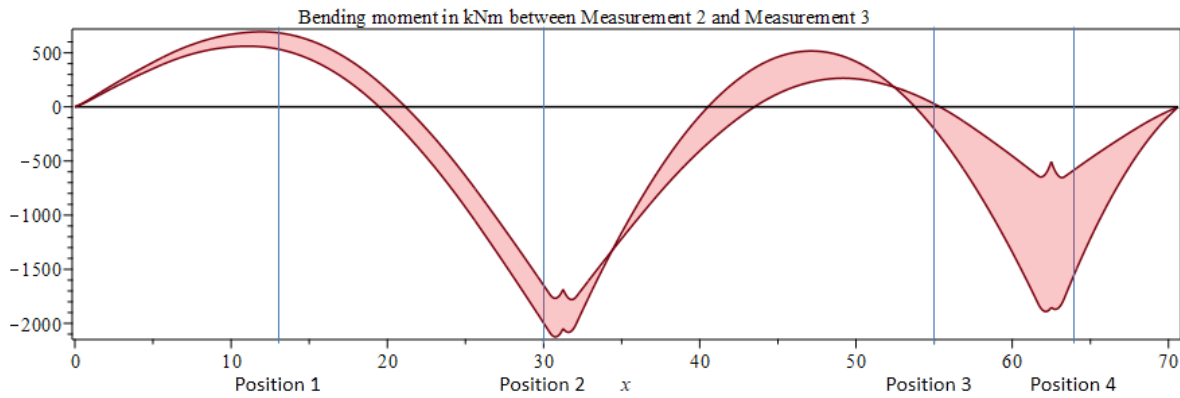


Figure 36: Euler-Bernoulli beam model of the prestressed bridge structure with variable bending stiffness (top), the prestressing tendon curvature with radius  $R$  (middle) and the subsequently derived distributed load  $q$  from the prestressing force  $P$  and tendon curvature  $R$  (bottom)

The following figures show the bending moment distribution along the bridge spans derived from the Euler-Bernoulli beam model, as shown in Figure 36, during each of the field measurements. During Measurement 2, during which 20% of the total prestressing force is applied, no bending moments are assumed to be generated by the post-tensioning. An equivalent portion of the self-weight loading of the structure is assumed to completely negate the bending moments from prestressing tendon curvature and the remaining portion of the self-weight is supported by the present formwork.

Figure 37 shows the bending moment distribution over the measured spans due to application of 100% of the total prestressing force, which naturally represents the change in bending moments between Measurement 2 and Measurement 3 as no residual bending moments are assumed to be present within the bridge deck during Measurement 2. The positions of the sensor groups are illustrated along the modelled beam. The simulated bending moment distribution during Measurement 3 is presented as a range with an upper limit and lower limit. This form of visualization is used because the precise percentage of the self-weight contributing to counteract the bending moment from the post-tensioning is unclear. The actual bending moment distribution is expected to reside within the limits.



**Figure 37: Estimated bending moment distribution in kNm (red) derived from the Euler-Bernoulli beam model over the bridge length  $x$  in meters after application of 100% of the total prestressing force with indicated positions of the sensor groups (blue)**

In Figure 37, the limits are derived from the active percentage of the self-weight loading. The upper limit is derived from loading of the entire self-weight of the structure. The lower limit is derived from the displacement field. Percentages of the self-weight is applied to the model to minimize the deflection of the beam model, as in actuality, the self-weight of the structure counteracts the precamber induced by the post-tensioning. However, downwards displacement is not possible due to the presence of the formwork. Therefore, the actual interaction between prestressing force and self-weight loading results in the slightest displacement with minor precamber. The displacement shown in Figure 38 is the result of applied self-weight loading in the following manner: 100% self-weight load in the first span ( $0 < x < 31.25m$ ) and 50% self-weight load in the second span ( $31.25m < x < 62.5m$ ). After multiple simulations, the aforementioned self-weight loading configuration returns the smallest displacement field with a maximum upwards deflection of 30 mm. However, as the simulation still results in upwards displacement, the actual contribution of the self-weight loading is possibly higher than simulated.

The largest variance in bending moment is expected at Position 4, as the precamber due to prestressing is largest at the first span ( $0 < x < 31.25m$ ) and the full self-weight is needed to counteract the upwards displacement of the beam. Therefore, the conditions between the upper and lower limit are the same for the first span. The second span ( $31.25m < x < 62.5m$ ) experiences less precamber due to the continuous nature of the beam model and is able to be negated with less than the full self-weight. The variance at Position 4 is due to the difference in the considered percentage of the self-weight loading on the second span.

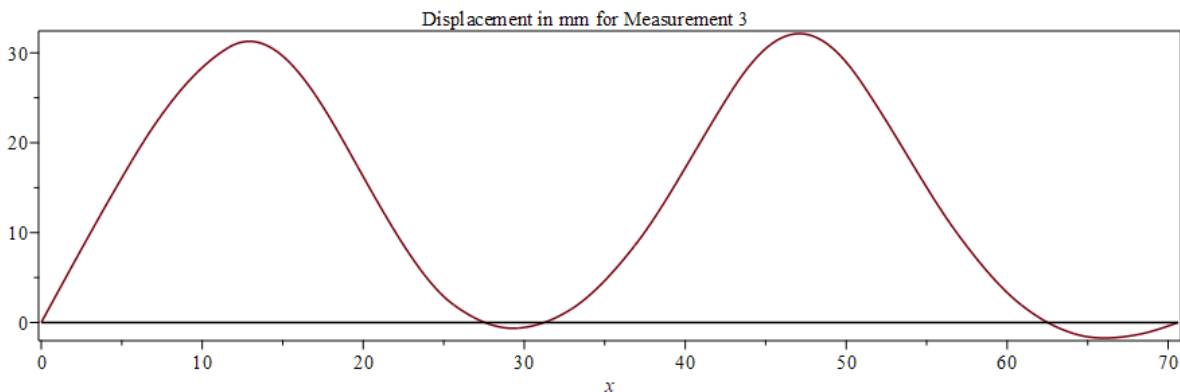


**Figure 38: Displacement field in mm derived from the Euler-Bernoulli beam model over the bridge length  $x$  in meters after application of 100% of the total prestressing force and estimated contribution of the self-weight loading**

In Figure 39, the bending moment distribution is shown of the fully prestressed structure after the formwork is removed from the measured spans, i.e., the structure is self-supporting and the self-weight of the structure is no longer carried by the formwork. The effect of the addition of the remaining self-weight load is illustrated in Figure 40 as the differential in bending moment distribution between Figure 37 and Figure 39. The largest increases in bending moment are expected at sensor group Position 3 and Position 4, as the free end at  $x > 62.5$  is no longer supported by the formwork and thus acts like a cantilever. Figure 40 is comparative to cross-correlation results between Measurement 3 and Measurement 4.

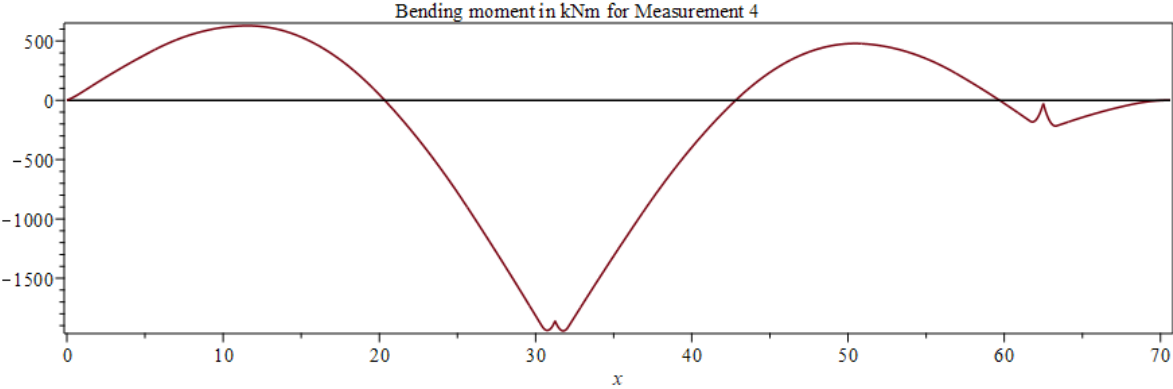


**Figure 39: Bending moment distribution in kNm derived from the Euler-Bernoulli beam model over the bridge length  $x$  in meters after removal of formwork from the measured spans**

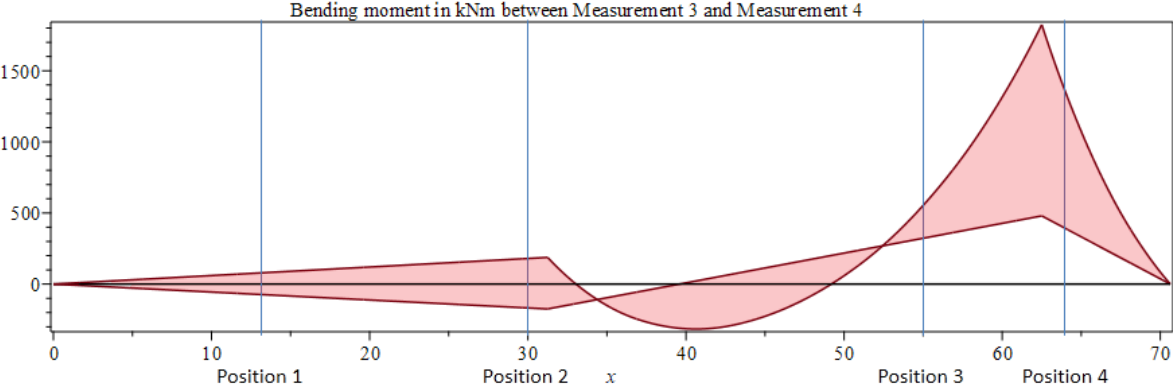


**Figure 40: Bending moment differential in kNm (red) over the bridge length  $x$  in meters between bending moment distributions at application of 100% of the total prestressing force and after removal of formwork from the measured spans with indicated positions of the sensor groups (blue)**

The bending moment differential between Measurement 3 and Measurement 4 is presented as a range with upper and lower limits with the actual bending moment distribution expected to be situated in between the limits. The variance in the bending moment distribution is due to the unclear interaction between self-weight loading and the loading due to the prestressing tendon curvature while the structure is still supported by the formwork and shoring. As Figure 40 is a differential and is derived from the bending moment distribution in the aforementioned conditions, as shown in Figure 37, the resulting distribution is naturally of a similar nature.

After the formwork is removed from the second concrete cast, which entails the cast of spans adjacent to the measured spans, the boundary conditions of the modelled structure change. Whereas the end of the beam is previously modelled as a free end, it is now connected to a continuous beam. The resulting bending moment distribution after the change in boundary conditions is shown in Figure 41 and the effect on the bending moment distribution due to this change is shown in Figure 42 as a differential in bending moments between Figure 39 and Figure 41. The effect of the change is subtle and is mainly noticeable around the second support at  $x = 62.5\text{ m}$  due to change in boundary conditions to simulate continuation of the beam model. The differential values in Figure 42 are comparative to cross-correlation results between Measurement 4 and Measurement 5.

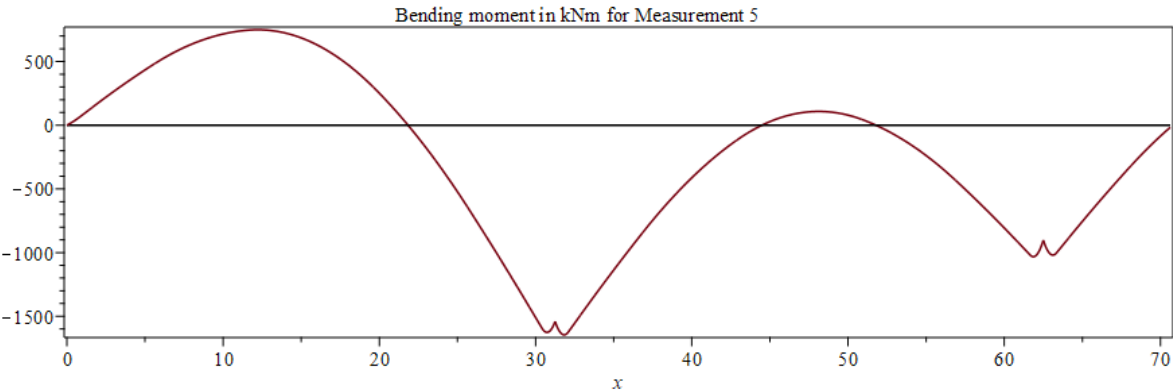


**Figure 41: Bending moment distribution in kNm derived from the Euler-Bernoulli beam model over the bridge length  $x$  in meters after removal of formwork from the adjacent spans**

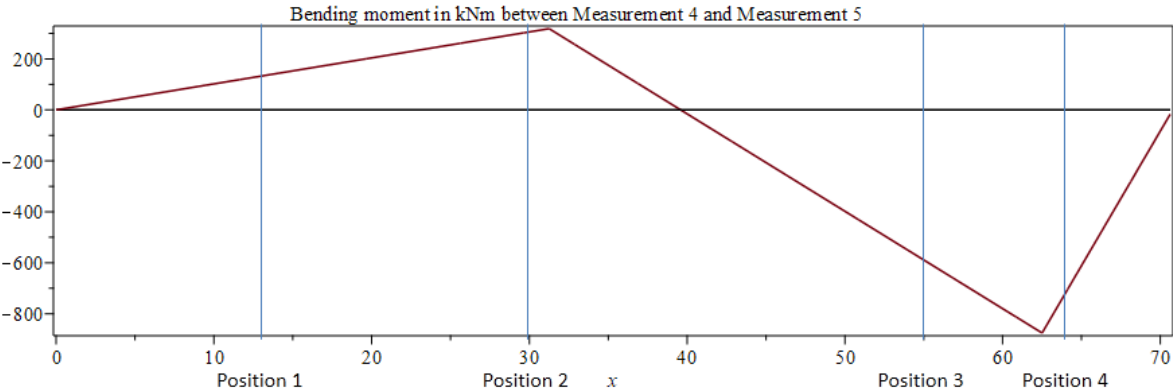


**Figure 42: Bending moment differential in kNm (red) over the bridge length  $x$  in meters between bending moment distributions after removal of formwork from the measured spans and the adjacent spans with indicated positions of the sensor groups (blue)**

The application of the asphalt layer on top of the concrete bridge deck translates to an additional uniformly distributed load on the structure. The bending moment distribution after the application of the asphalt layer is displayed in Figure 43 and the computed change in bending moment from the additional load is shown in Figure 44. As seen, the bending moment differential is limited as the load from the asphalt layer is small relative to the load from the prestressing and the self-weight of the concrete structure. The differential values in Figure 44 are comparative to cross-correlation results between Measurement 6 and Measurement 7, as loading conditions and boundary condition generally remain the same between Measurement 5 and Measurement 6.

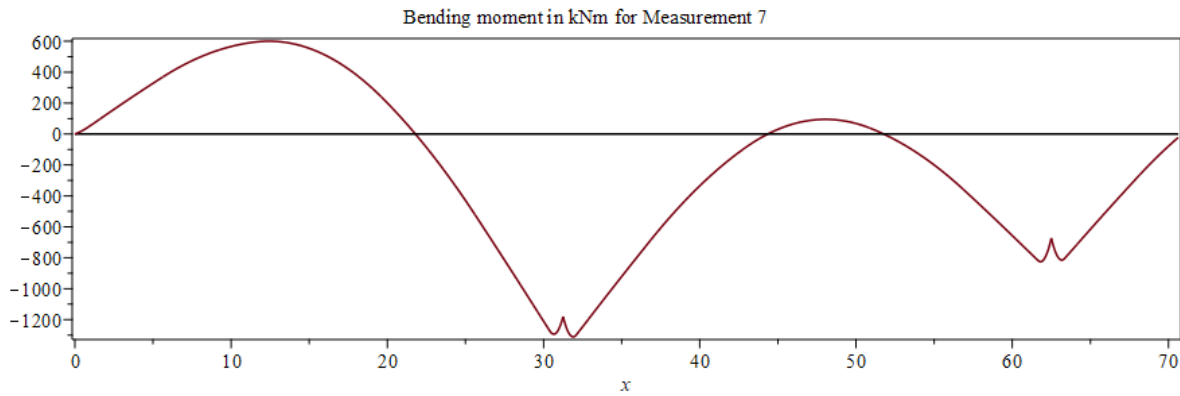


Figure 43: Bending moment distribution in kNm derived from the Euler-Bernoulli beam model over the bridge length  $x$  in meters after application of the asphalt layer on the bridge deck

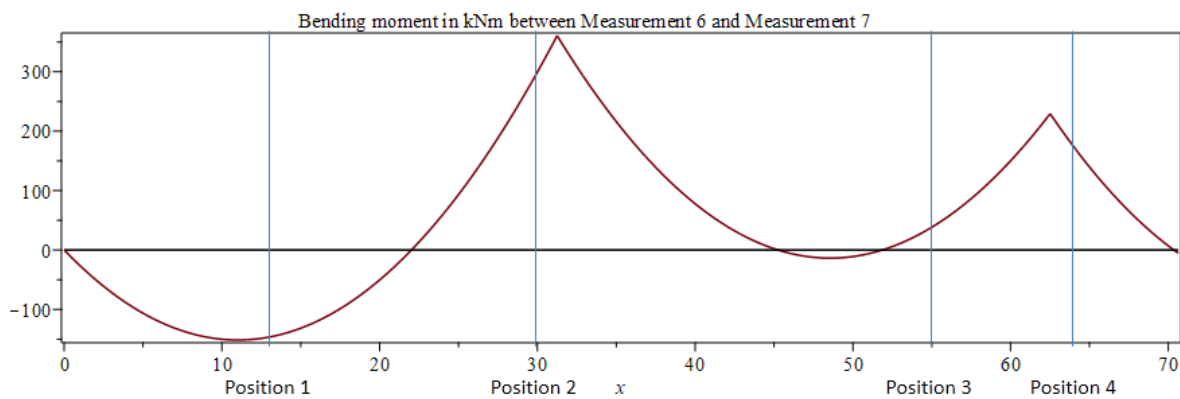


Figure 44: Bending moment differential in kNm (red) over the bridge length  $x$  in meters between bending moment distributions after removal of formwork from the adjacent spans and after application of the asphalt layer with indicated positions of the sensor groups (blue)

The parameters for cross-sectional calculations are determined by approximation of the sensor group locations and blueprints of the structure from the contracting company Boskalis. Geometrical specifics at the four sensor group locations are shown in Table 24. Within the table,  $x$  indicates the distance from the abutment over the span length,  $h$  represents the height of the cross-section. For the remaining parameters, the values are presented per meter width:  $A$  represents the cross-sectional area,  $W$  is the section modulus of the cross-section and  $P$  represents the prestressing force.

Cross-section parameters					
Position	$x$ [m]	$h$ [mm]	$A$ [mm <sup>2</sup> /m]	$W$ [mm <sup>3</sup> /m]	$P$ [kN/m]
1	13	700	700000	81666667	5500
2	30	1270	1270000	268816667	6000
3	55	900	900000	135000000	5500
4	64	1270	1270000	268816667	6000

Table 24: Geometrical parameters of the structure at the four sensor group positions

As the CWI results from the field measurements are expected to show changes in bending moments rather than the actual bending moment distribution, the differential in the structure's bending moment distribution between two measurements is of more interest than the exact bending moment distribution of the structure at the time of the measurement. Stress distributions are therefore computed from the bending moment differentials at the sensor group positions for comparison with CWI results. The cross-sectional stress distribution is found with parameters from Table 24 for the corresponding sensor group position and by calculating the outer fiber stresses as expressed in

$$\sigma_{t,i} = -\frac{0.8 * P_{i=1}}{A} + \frac{M_i}{W}; \sigma_{b,i} = -\frac{0.8 * P_{i=1}}{A} - \frac{M_i}{W}, \quad 6.3$$

where  $\sigma_{t,i}$  is the stress in the top fiber,  $\sigma_{b,i}$  is the stress in the bottom fiber and  $M_i$  is the bending moment differential derived from the Euler-Bernoulli beam model.  $i$  acts as the index for the differentials between corresponding simulations with varying boundary/loading conditions, e.g.,  $i = 1$  represents the differential caused by the increase of prestressing force from 20% to 100%. Following this, the bending moment distribution shown in Figure 37 equates to  $M_1$ , Figure 40 equates to  $M_2$ , Figure 42 equates to  $M_3$  and Figure 44 equates to  $M_4$ .  $P_i$  is the prestressing force, which is only applicable for  $i = 1$  as the prestressing force is increased by 80% and remains at full force afterwards. The resulting outer fiber stresses are shown in Table 25 with the corresponding bending moment differentials at the four sensor group positions. The cross-sectional stress distribution differential between the outer fibers is considered linear.

<b>Bending moment and stress differentials between Measurement 2 and Measurement 3</b>			
<b>Position</b>	<b><math>M_1</math> [kNm]</b>	<b><math>\sigma_{t,1}</math> [MPa]</b>	<b><math>\sigma_{b,1}</math> [MPa]</b>
1	-685 – -534	0.25 – 2.10	-14.67 – -12.82
2	1648 – 1996	-11.20 – -9.91	2.35 – 3.64
3	-28 – 202	-6.39 – -4.68	-5.10 – -3.39
4	578 – 1537	-9.50 – -5.93	-1.63 – 1.94
<b>Bending moment and stress differentials between Measurement 3 and Measurement 4</b>			
<b>Position</b>	<b><math>M_2</math> [kNm]</b>	<b><math>\sigma_{t,2}</math> [MPa]</b>	<b><math>\sigma_{b,2}</math> [MPa]</b>
1	-78 – 73	-0.89 – 0.96	-0.96 – 0.89
2	-180 – 168	-0.62 – 0.67	-0.67 – 0.62
3	-553 – -323	2.39 – 4.10	-4.10 – -2.39
4	-1350 – -391	1.46 – 5.02	-5.02 – -1.46
<b>Bending moment and stress differentials between Measurement 4 and Measurement 5</b>			
<b>Position</b>	<b><math>M_3</math> [kNm]</b>	<b><math>\sigma_{t,3}</math> [MPa]</b>	<b><math>\sigma_{b,3}</math> [MPa]</b>
1	-133	1.62	-1.62
2	-306	1.14	-1.14
3	589	-4.36	4.36
4	717	-2.67	2.67
<b>Bending moment and stress differentials between Measurement 6 and Measurement 7</b>			
<b>Position</b>	<b><math>M_4</math> [kNm]</b>	<b><math>\sigma_{t,4}</math> [MPa]</b>	<b><math>\sigma_{b,4}</math> [MPa]</b>
1	147	-1.79	1.79
2	-299	1.11	-1.11
3	-38	0.28	-0.28
4	-173	0.65	-0.65

Table 25: Bending moment differential values at the four sensor group locations derived from the Euler-Bernoulli beam model and the subsequently derived outer fiber stresses at the four sensor group locations

### 6.1.2 Calculation of time dependent deformations

As the analyzed structure is a prestressed cast-in-situ concrete structure, the presence of creep and shrinkage has to be considered [26]. A prestressed concrete structure is subjected to a constant compressive load, which causes the structure to deform over time, i.e., creep deformation. Also, a cast-in-situ concrete structure experiences shrinkage as the concrete hardens, which causes the concrete to decrease in volume. The total shrinkage consists of drying shrinkage and autogenous shrinkage. The distinction between the two types of shrinkage is that drying shrinkage is caused by the loss of water and autogenous shrinkage is the result of chemical reactions between cement and water. Both of these processes are dependent on time.

The development of creep deformation of concrete  $\varepsilon_{cc}(t, t_0)$  over time  $t$  for a constant compressive stress  $\sigma_c$  applied at concrete age  $t_0$  is given by the following equation:

$$\varepsilon_{cc}(t, t_0) = \varphi(t, t_0) \frac{\sigma_c}{E_c}, \quad 6.4$$

where  $E_c$  is the elasticity modulus of concrete and  $\varphi(t, t_0)$  is the linear creep coefficient over time  $t$ . As the compressive stress on the concrete due to prestress loading is not expected to exceed 45% of the concrete strength, the creep can be taken as linear, as stated by Eurocode 2 [25].

$$\varphi(t, t_0) = \varphi_0 * \beta_c(t, t_0), \quad 6.5$$

where  $\varphi_0$  is the notional creep coefficient and  $\beta_c(t, t_0)$  is a coefficient to described the development of creep with time after loading, expressed as

$$\beta_c(t, t_0) = \left[ \frac{t - t_0}{\beta_H + t - t_0} \right]^{0.3}, \quad 6.6$$

where  $\beta_H$  is a coefficient depending on the relative humidity and the notional member size  $h_0$ .

The total shrinkage strain  $\varepsilon_{cs}(t, t_s)$  is calculated as summation of the drying shrinkage strain  $\varepsilon_{cd}(t)$  and the autogenous shrinkage strain  $\varepsilon_{ca}(t)$  [25]:

$$\varepsilon_{cs}(t, t_s) = \varepsilon_{cd}(t, t_s) + \varepsilon_{ca}(t), \quad 6.7$$

The time-development curve of the drying shrinkage and the autogenous shrinkage over time  $t$  are expressed by

$$\varepsilon_{cd}(t, t_s) = \frac{t - t_s}{(t - t_s) + 0.04h_0^{1.5}} * k_h * \varepsilon_{cd,0} \quad 6.8$$

and

$$\varepsilon_{ca}(t) = (1 - \exp(-0.2t^{0.5})) * \varepsilon_{ca,\infty}, \quad 6.9$$

respectively, where  $h_0$  is the notional size of the cross-section and  $k_h$  is a coefficient depending on the notional size and equals 0.7 for  $h_0 \geq 500 \text{ mm}$ .  $\varepsilon_{cd,0}$  is the basic drying shrinkage and  $\varepsilon_{ca,\infty}$  is the autogenous shrinkage at infinite time.

With the parameters, shown in Table 26, the relevant parameters are calculated with an online Eurocode calculator [30]. In the table, the remaining unknown symbols represent the variable as such:  $f_{ck}$  represents the characteristic compressive strength of the concrete, derived from the cube compression test Table 1,  $A_c$  represents the cross-sectional area of the concrete structure,  $u$  represents the exposed perimeter of the cross-section,  $t_{0,20\%}$  and  $t_{0,100\%}$  represent the concrete age at which 20% and 100% of the total prestressing force are applied, respectively.  $T$  represents the average ambient temperature,  $RH$  represents the average relative humidity of the ambient environment and  $t_s$  represents the age of concrete at the end of curing.

Input								
Parameter	$f_{ck}$ [MPa]	$A_c$ [m <sup>2</sup> /m]	$u$ [m]	$t_{0,20\%}$ [days]	$t_{0,100\%}$ [days]	$T$ [°C]	$RH$ [%]	$t_s$ [days]
Size	72	0.7	2	7	11	20	70	7
Output								
Coefficient	$h_0$ [mm]	$\beta_H$ [-]	$\varphi_{0,20\%}$ [-]	$\varphi_{0,100\%}$ [-]	$\varepsilon_{cd,0}$ [10 <sup>-5</sup> ]	$\varepsilon_{ca,\infty}$ [10 <sup>-5</sup> ]		
Size	700	992	1.202	1.104	21.87	15.5		

Table 26: Input parameters of the concrete structure for derivation of the time dependent deformations (top) and derived output coefficients for calculation of the concrete shrinkage and creep deformation (bottom)

The calculated coefficients are utilized to plot the time dependent curve for the combined deformation of creep and shrinkage, illustrated in Figure 45. The clear points of interest are found at  $t = 7$  days and  $t = 11$  days concrete age. The 7-days mark equates to the end of the concrete curing and thus, the onset of drying shrinkage. Additionally, 20% of the prestressing force is applied to the 7-days-aged concrete and entails the introduction of creep deformations. At the 11-days mark, 100% of the total prestressing force is applied to the structure and results in an increase in creep deformation. The plotted concrete deformation curve over time is to be loosely compared to the geopolymer deformation curve shown in Figure 33, which is further explored in Section 6.4.

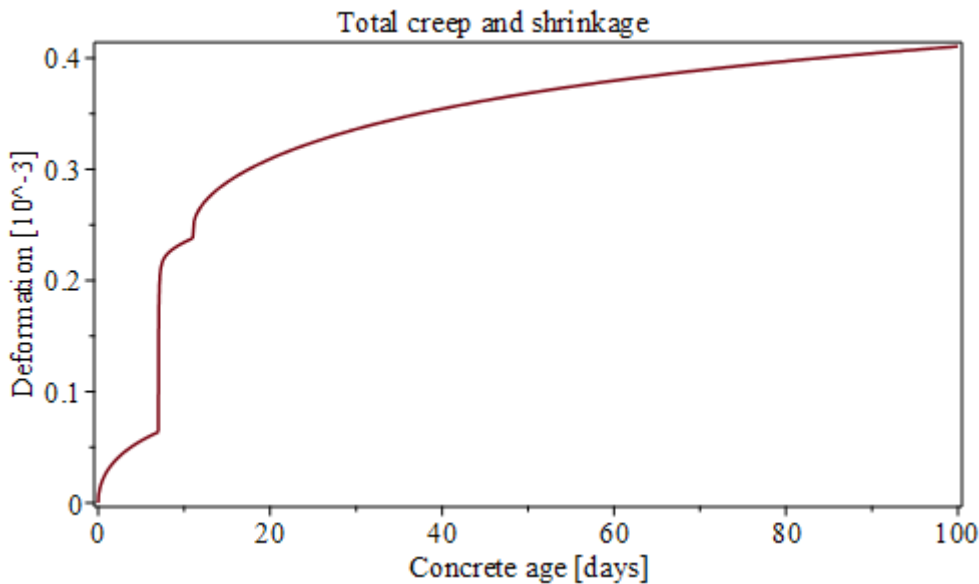


Figure 45: Total calculated creep and shrinkage deformation of the prestressed cast-in-situ concrete bridge structure over concrete age

## 6.2 Visualization of $dv/v$ -distribution of the sensor groups within the concrete structure from measured data

Table 4 to Table 19 contain the numerical results of CWI of the data from scheduled measurements on the concrete structure, as according to Table 3. From the available data, certain sensor pairs are of particular interest. The corresponding principal sensor pairs consist of sensors directly adjacent from one another in the longitudinal direction of the bridge span. These sensor pairs are positioned as such, that they are able to detect changes in stress along the longitudinal axis of the structure. For derivation of the stress distribution, the CWI resulting wave velocity change from Table 4 to Table 19 are visualized for further exposition.

In combination with the sensor group configuration at Position 1, as shown in Figure 20, the wave-velocity change within the sensor group from Measurement 2 to Measurement 5 is visualized in Figure 46. Within the figure, the arrows indicates the propagation direction of the wave signal from source to receiver, where it to travel in a straight path originating from the source to the receiver. The associated value with the arrow indicates the velocity change  $dv/v$  from cross-correlation between the corresponding measurements. A '+' in front of the value is paired with a red arrow and specifies a positive  $dv/v$  and an increase in wave velocity. The opposite applies for '-' paired with a blue arrow, which indicate a negative  $dv/v$  and a decrease in wave velocity. The same principle is followed for visualization of  $dv/v$  at the other three sensor group positions within the concrete bridge, Figure 47, Figure 48, Figure 49 for Position 2, Position 3 and Position 4, respectively. Not-accentuated arrows without attached values result from missing or faulty data.

The following figures show the  $dv/v$  resulting from CWI, but do not include the corresponding  $CC$ . Therefore, when viewing the visualized figures of the  $dv/v$  within the sensor group the complete data, as shown in Table 4 to Table 19, has to be considered, as the  $CC$  indicates the reliability of the data. With a quick glance through the aforementioned tables one can conclude that the results of cross-correlation between Measurement 2 and Measurement 3 and to a lesser extent between Measurement 3 and Measurement 4 have poor reliability, denoted by the low  $CC$ . With this in mind, discrepancies are likely to be found during analysis of the results and derivation of the stress distribution.

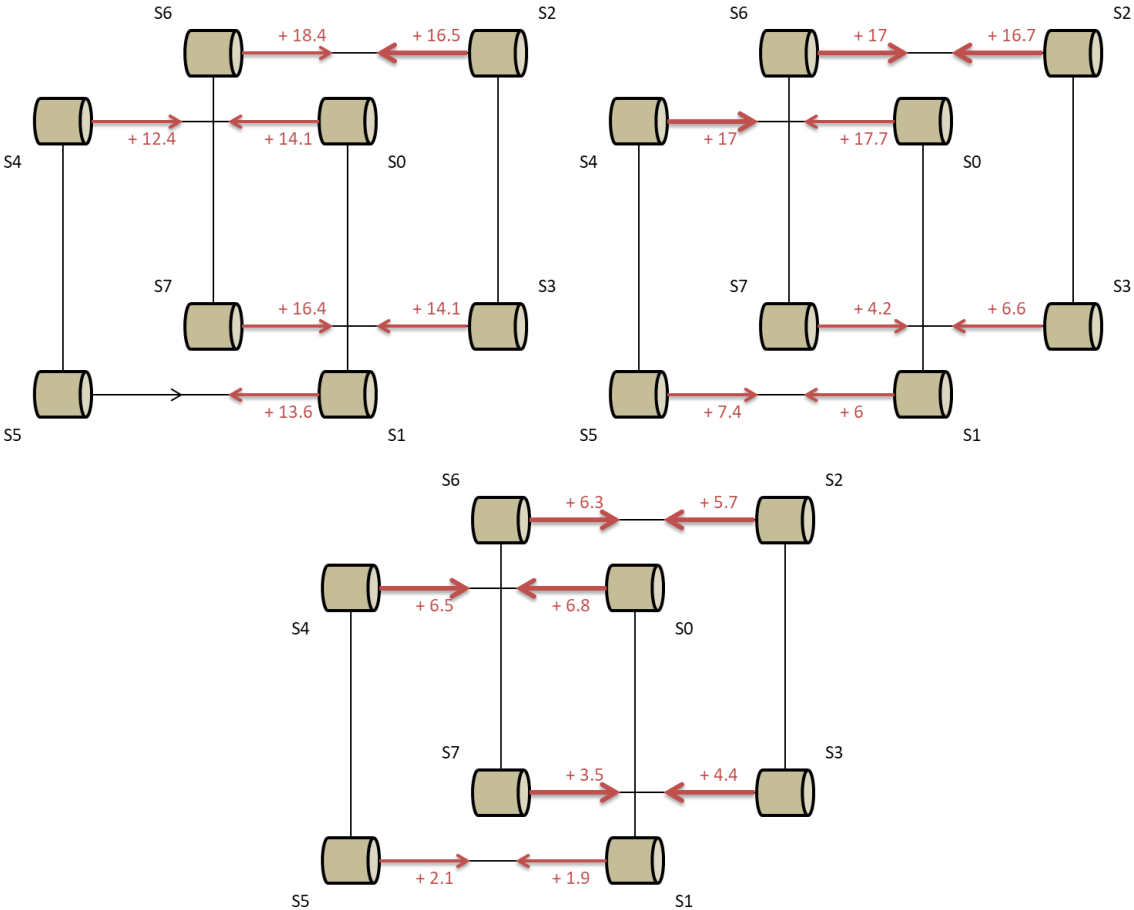


**Figure 46: Illustration of the  $dv/v$  [%] between principal sensor pairs at Position 1 between Measurement 2 and Measurement 3 (top left), between Measurement 3 and Measurement 4 (top right) and between Measurement 4 and Measurement 5 (bottom) with the arrow (red for positive  $dv/v$  and blue for negative  $dv/v$ ) originating from the source sensor**

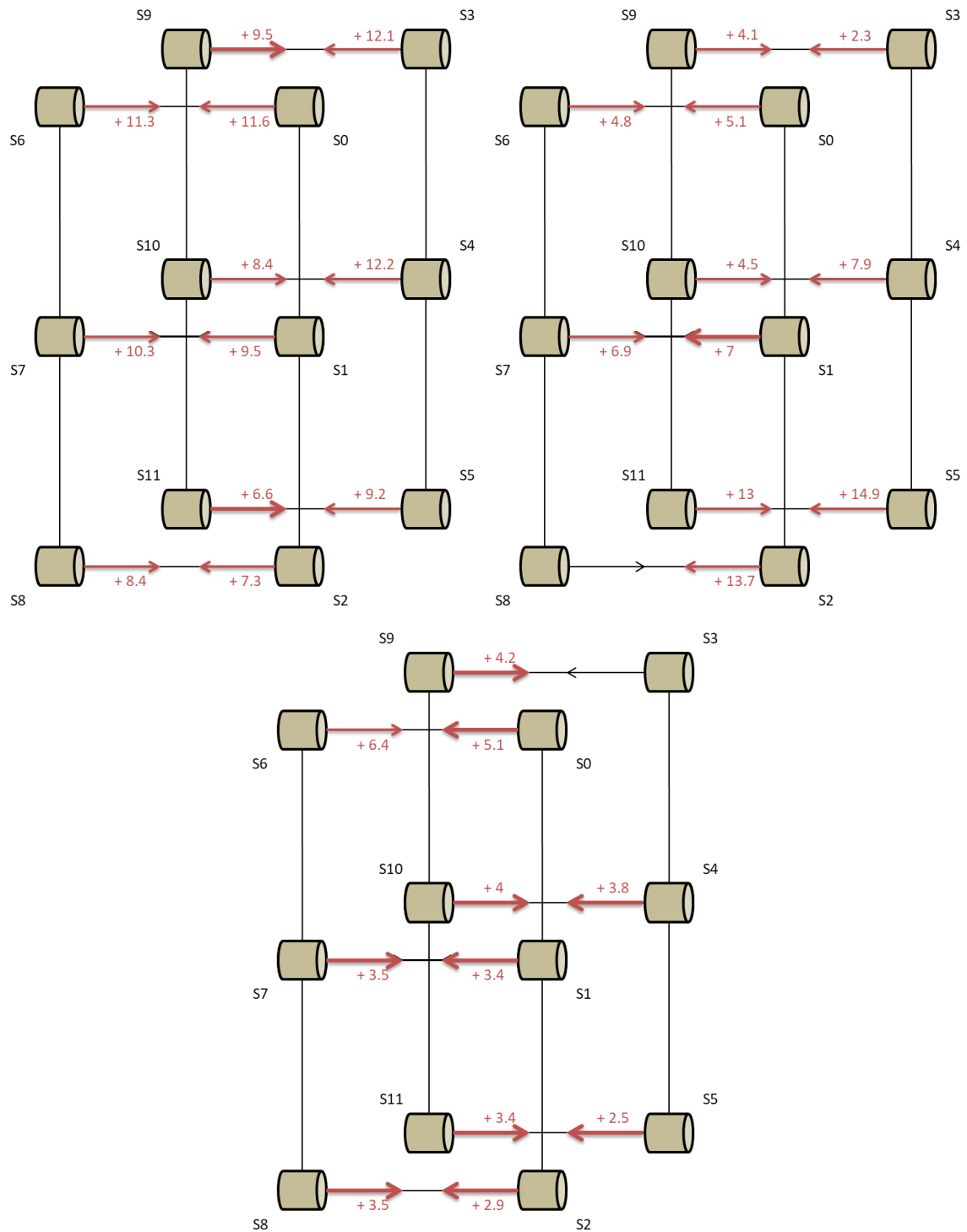


Figure 47: Illustration of the  $dv/v$  [%] between principal sensor pairs at Position 2 between Measurement 2 and Measurement 3 (top left), between Measurement 3 and Measurement 4 (top right) and between Measurement 4 and Measurement 5 (bottom) with the arrow (red for positive  $dv/v$  and blue for negative  $dv/v$ ) originating from the source sensor

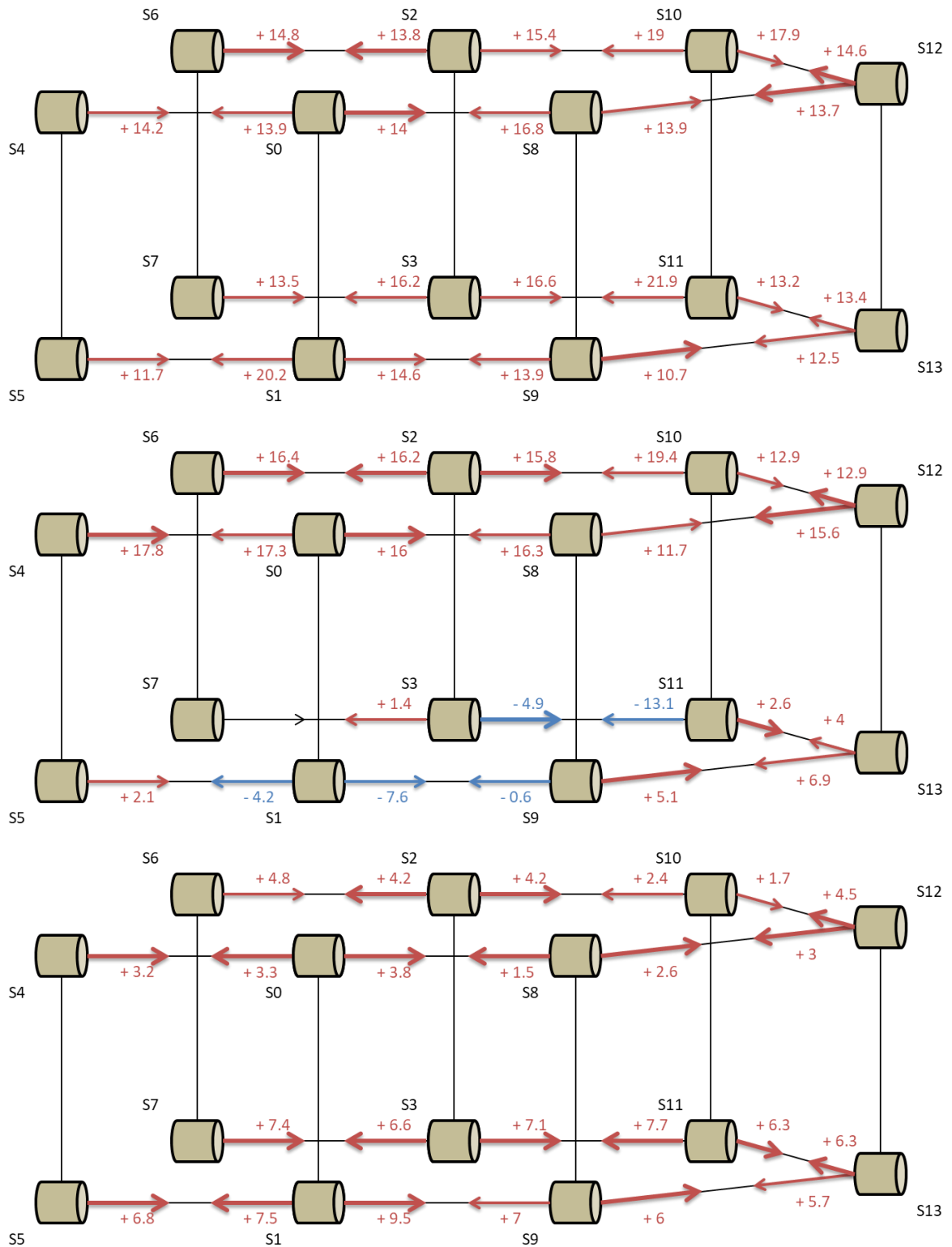
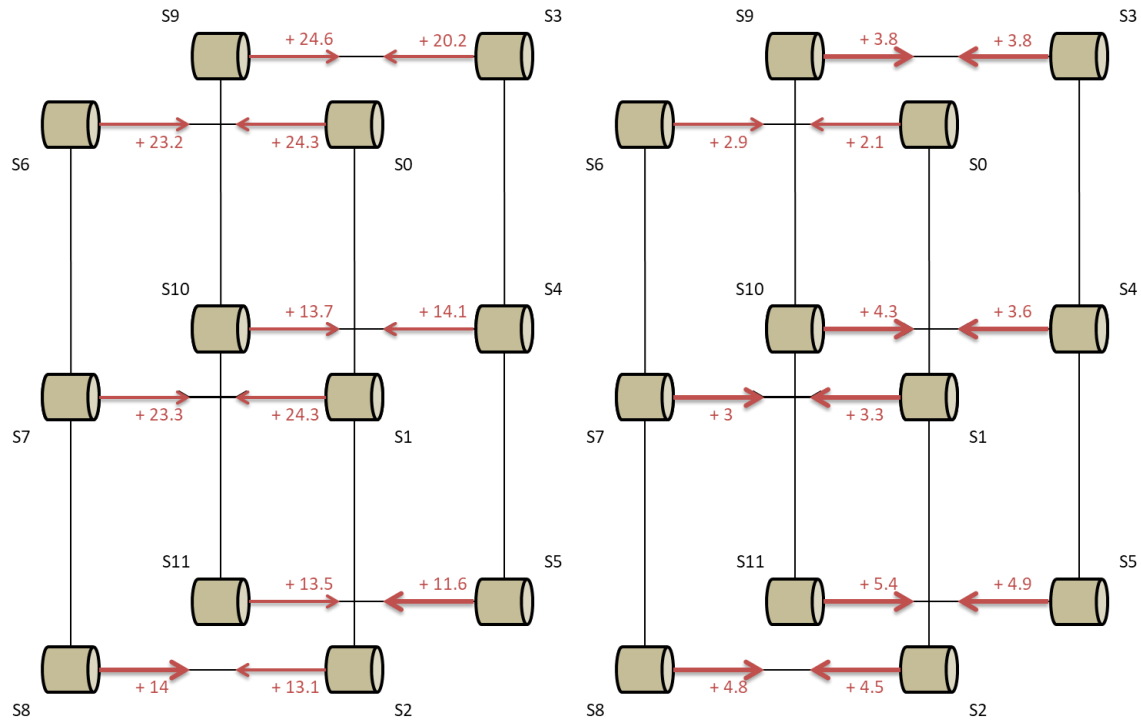


Figure 48: Illustration of the  $dv/v$  [%] between principal sensor pairs at Position 3 between Measurement 2 and Measurement 3 (top), between Measurement 3 and Measurement 4 (middle) and between Measurement 4 and Measurement 5 (bottom) with the arrow (red for positive  $dv/v$  and blue for negative  $dv/v$ ) originating from the source sensor



**Figure 49: Illustration of the  $dv/v$  [%] between principal sensor pairs at Position 4 between Measurement 2 and Measurement 4 (left) and between Measurement 4 and Measurement 5 (right) with the arrow (red for positive  $dv/v$  and blue for negative  $dv/v$ ) originating from the source sensor**

The cross-correlation results between Measurement 6 and Measurement 7 is shown in Figure 50 (left), Figure 51 and Figure 52 for Position 1, Position 3 and Position 2 and 4, respectively. The occasional missing data set is the consequence of faulty measurements or damaged sensors. As the two concerning measurements are conducted in fairly close time proximity and the concrete has fully set, the time-dependent factors affecting the signal's wave velocity should be minimal. Any major differentials in  $dv/v$  can therefore in theory be attributed to a change in stresses.

The  $CC$  from  $CWI$  of the principal sensor pairs is fairly consistent and above the 0.7 threshold (Table 15, Table 16, Table 17, Table 18), which indicates adequate reliable results. Even though the  $CWI$  results show the data to be of good quality, the illustrated  $dv/v$ -values in Figure 50 (left), Figure 51 and Figure 52 show contradicting results in some instances.  $CWI$  results between the same sensor pairs should be interchangeable regardless of which sensor in the pair acts as the source. However, one can observe a wave velocity increase in one instance and a wave velocity decrease in another instance. This discrepancy is explained by the presence of construction vehicle traveling along the bridge during Measurement 6, which causes dynamic loading conditions during the measuring procedure. The load on the structure is therefore different for measurements within the same sensor group. A sketched image with the measured data for the change in stress distribution solely due to the addition of the asphalt layer is therefore not accurate.

Figure 50 (right) illustrates the  $dv/v$  from  $CWI$  of data from Measurement 8 at Position 1. Two measuring sequences are conducted in succession. A set of data with a stationary lorry load present near the sensor group location acts as the modified signal and the data without the lorry load acts as the reference signal. Similarly to the  $CWI$  results between Measurement 6 and Measurement 7, shown in Figure 50 (left), there are certain discrepancies in the results for the same sensor pairs. The cause can again be led back to the heavy construction traffic on the bridge at the time of the measurements, where loading conditions change during the measuring procedure. The continuous variation in loading along the bridge deck

overshadows the arranged stationary lorry load and no longer can a case be made for an isolated cross-correlation between a measurement without a specified load and a measurement with a specified load.

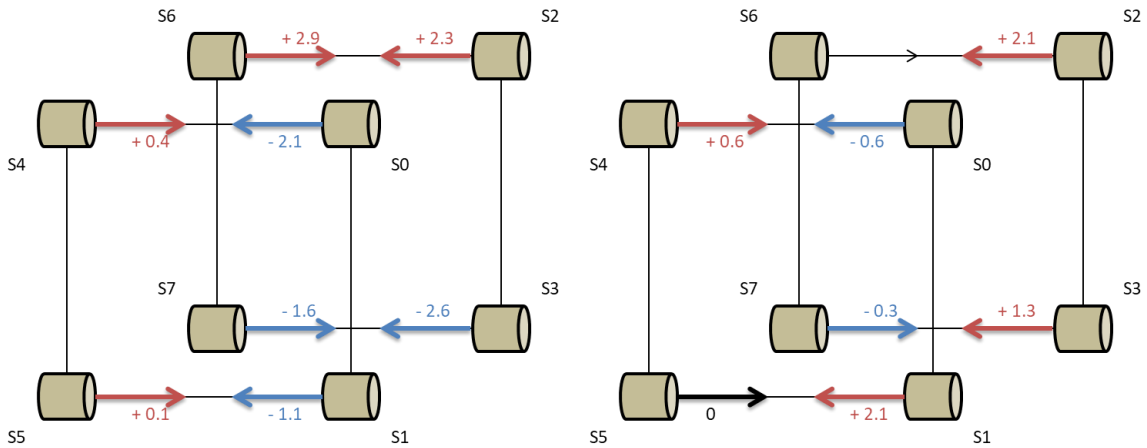


Figure 50: Illustration of the  $dv/v$  [%] between principal sensor pairs at Position 1 between Measurement 6 and Measurement 7 (left) and between Measurement 8 without and with stationary lorry load (right) with the arrow (red for positive  $dv/v$  and blue for negative  $dv/v$ ) originating from the source sensor

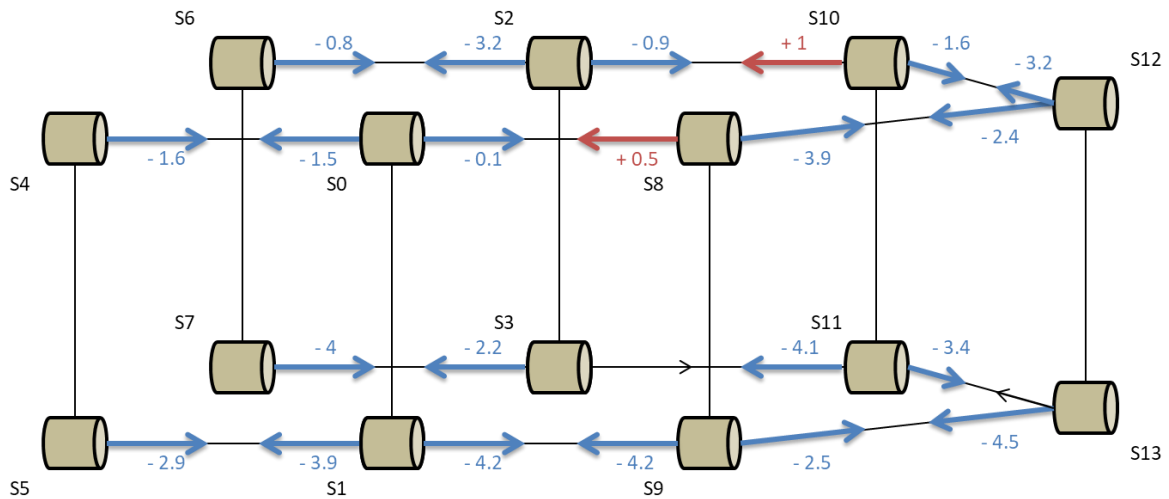


Figure 51: Illustration of the  $dv/v$  [%] between principal sensor pairs at Position 3 between Measurement 6 and Measurement 7 with the arrow (red for positive  $dv/v$  and blue for negative  $dv/v$ ) originating from the source sensor

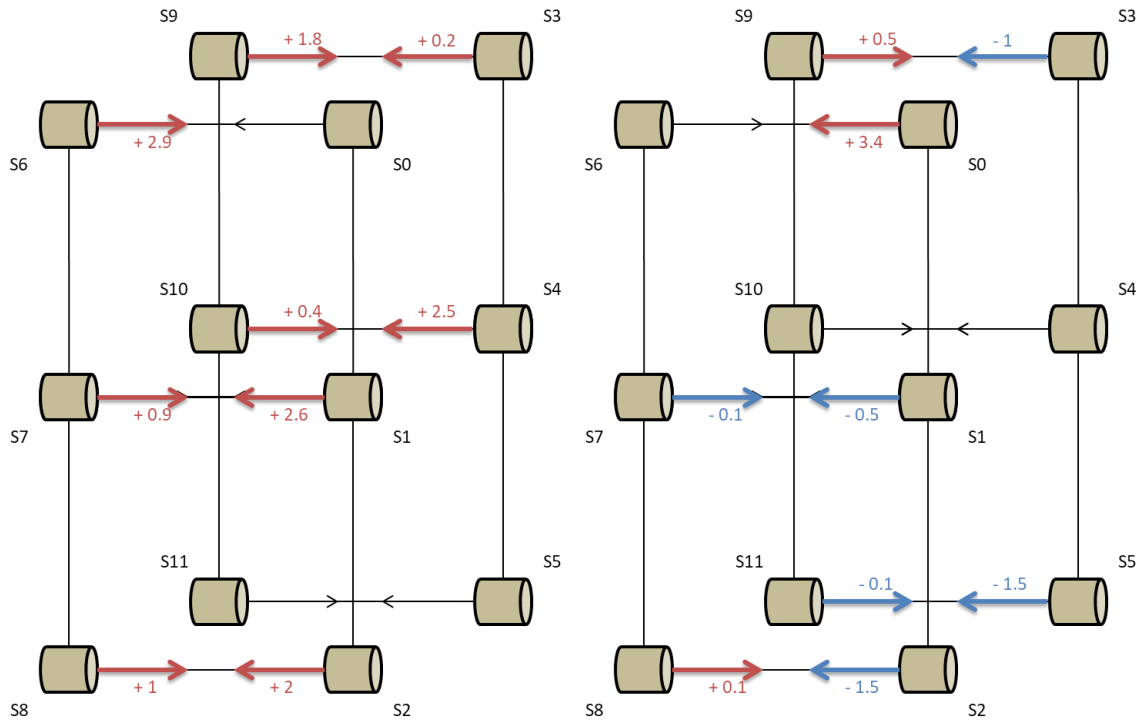


Figure 52: Illustration of the  $dv/v$  [%] between principal sensor pairs at Position 2 (left) and at Position 4 (right) between Measurement 6 and Measurement 7 with the arrow (red for positive  $dv/v$  and blue for negative  $dv/v$ ) originating from the source sensor

### 6.3 Simulated stress distribution from field measurement data

For conversion of CWI data to a simulation of the stress distribution, the data from laboratory tests are used as link between the effects of loading and wave-velocity change  $dv/v$  in concrete. For the relation between compressive stresses and  $dv/v$ , a fitted plot is made from the development curve of the  $dv/v$  against the increase and decrease of compressive stresses.

In Section 5.2, the results are shown from concrete cylinders in a uniaxial compression test. During the test the change in wave velocity is measured as the compressive loading is increased and decreased. The obtained data is used to determine the relation between compressive stress and  $dv/v$  in concrete. The approximation of this relation is found in Figure 53 as a fitted plot and gives the relation:

$$dv/v = 0.0008865 * \sigma , \quad 6.10$$

where  $dv/v$  represents the wave velocity change and  $\sigma$  represents the uniaxial compressive stress in MPa.

In Section 5.2, it has been established that the relation between  $dv/v$  and compressive stress is non-linear. However, this non-linearity is only really prevalent at high loads and as the conversion from  $dv/v$  to stress is but an approximation, the relation is assumed linear for simplicity. Furthermore, the changes in stresses in between cross-correlated field measured is not expected to reach the level of loading used in the compression tests.

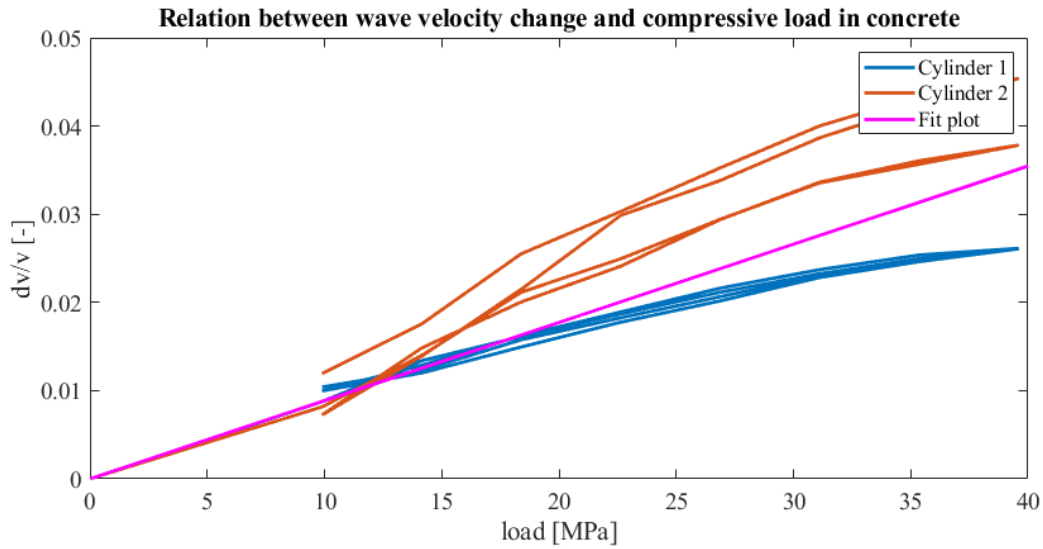


Figure 53: Total wave-velocity change over total applied load for the compressive concrete loading test with linear fitted curve

For consistency with the mechanical model used in the structural analysis in Section 6.1, the 3D environment of the field data is translated to 2D by equating the results of the sensor pairs in transverse direction with one another. To lower the detrimental effects of faulty data some rules are formulated in how the data is processed. For the field measured data, the *CC* will act as factor for weighted calculation of the  $dv/v$ . The weighted average  $dv/v$  from conversion from 3D to 2D is determined as such:

$$\overline{dv/v}_{2D} = \frac{\sum_{i=1}^n dv/v_{3D,i} w_i}{\sum_{i=1}^n w_i} \quad \text{with } \begin{cases} w_i = 1 \text{ for } CC < 0.7 \\ w_i = 2 \text{ for } CC \geq 0.7 \end{cases} \quad 6.11$$

where  $\overline{dv/v}_{2D}$  is the weighted average wave velocity change in a 2D configuration,  $dv/v_{3D,i}$  are the  $dv/v$ -values of the considered principal sensor pairs and  $w_i$  is the weight factor depending on the *CC*. Averaged *CC* of above 0.7 is considered well reliable and thus values tied to the high *CC* value are weighed double to those of lesser reliability, i.e. lower *CC*. An example is given in Figure 54 for the  $dv/v$ -values of the sensor group at Position 1 between Measurement 2 and Measurement 3, where the averaged wave velocity  $dv/v$  is stated for the sensor pairs in the transverse direction of the structure.

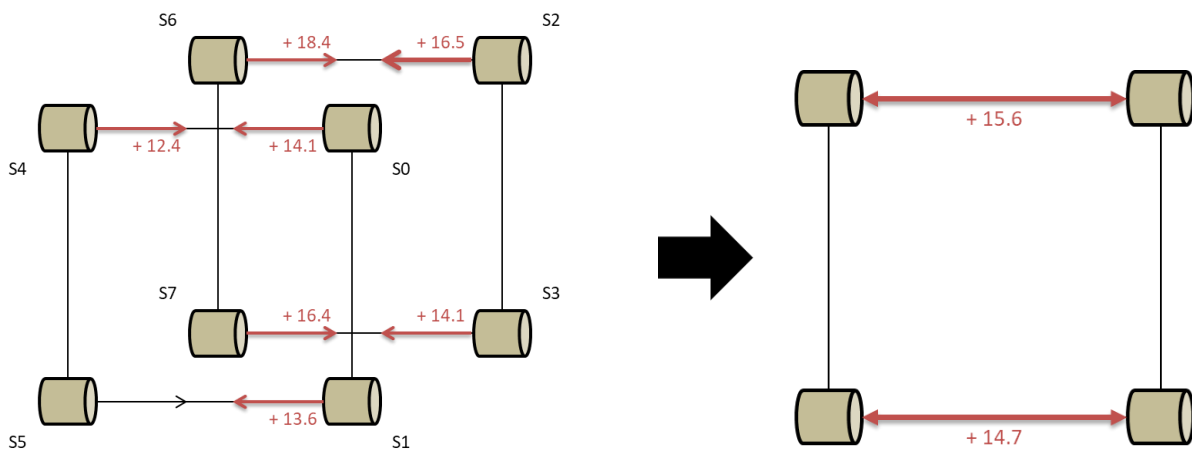


Figure 54: Transition from a 3D sensor group configuration to a 2D sensor group configuration with averaged  $dv/v$  [%] of sensor pairs in the transverse direction

With the information acquired from the CWI results of the field measurement data, a distribution is simulated for the stress changes at the four sensor group locations between Measurement 2, Measurement 3, Measurement 4 and Measurement 5. For conversion from wave-velocity change ( $dv/v$ ) to stress ( $\sigma$ ), the experimental test results of the cylinder compression test (Figure 53) are used as link between the two units with a relation as shown in Equation 6.10.

An attempt is made to split the  $dv/v$  distribution in approximated values for time-dependent factors (e.g. concrete maturity and creep/shrinkage deformation) and stresses. The  $dv/v$  due to change in stress-state is derived from the compressive loading test results, where an increase in compressive load is equated to an increase in wave velocity. The remaining wave velocity increase is associated with time-dependent factors. The stress change at Position 1 between Measurement 2 and Measurement 3 consist of two components, namely a uniform distribution from the increase in axial prestressing force and a linear distribution from the increase in prestressing force in the tendon curvature. As the exact increase in axial stress is easily determined with Table 24, the increase in  $dv/v$  due to axial stress is estimated with Equation 6.10 to obtain a uniformly distributed  $dv/v$ -component, as such:

$$dv/v = 0.0008865 * \frac{P}{A} = 0.0008865 * \frac{5500}{700} = 7.0e^{-3} \tag{6.12}$$

where  $P$  represents the prestressing force in kN and  $A$  represents the cross-sectional area in  $mm^2$ . The obtained uniformly distributed  $dv/v$ -component is subtracted from the total  $dv/v$ -distribution obtained from the field measurements. This process is illustrated in Figure 55.

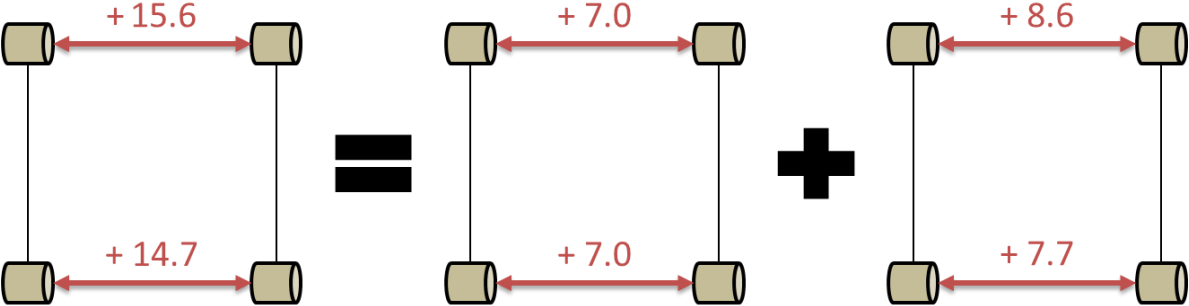


Figure 55: Separation of the  $dv/v$ -component attributed to axial stress change from the total computed 2D distribution of  $dv/v$  [‰]

Subsequently, the remaining component is further divided into a component corresponding with induced bending moments due to the prestressing tendon curvature and a component corresponding with the time-dependent factors, illustrated in Figure 56. It is assumed that the time-dependent factors act uniformly along the cross-section of the bridge. Therefore, the component from these time-dependent factors is assumed uniformly distributed. The resulting division consists of a uniform distribution corresponding with the time-dependent factors and a linear distribution due to bending moments.

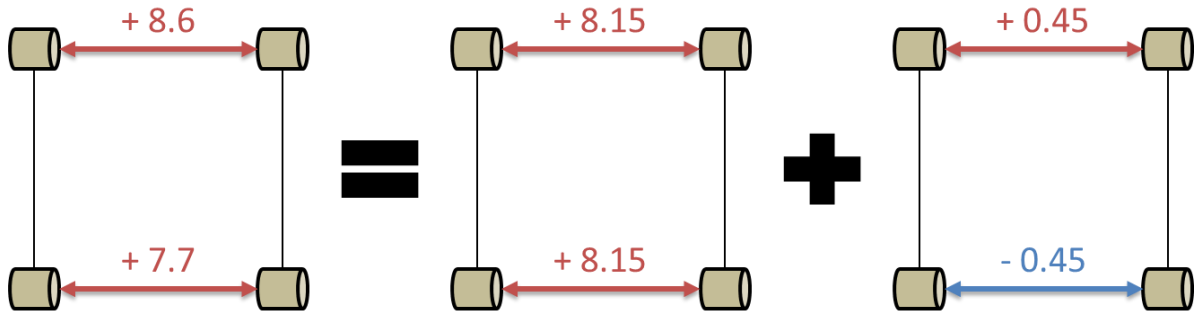


Figure 56: Separation of the  $dv/v$ -component attributed to time-dependent factors from the residual computed 2D distribution of  $dv/v$  [%]

After Measurement 3, stress changes within the structure are primarily induced by bending moments as the post-tensioning force has been fully applied and no increase of longitudinal axial forces to the bridge deck are expected. In this analysis, the medium is considered linear elastic and so, the  $dv/v$  over the cross-sectional height can be divided in a constant mean, associated with time-dependent factors, and a linear gradient, associated with stress change due to bending moments.

	Position 1		Position 2		Position 3		Position 4	
	$\sigma_t$ [MPa]	$\sigma_b$ [MPa]	$\sigma_t$ [MPa]	$\sigma_b$ [MPa]	$\sigma_t$ [MPa]	$\sigma_b$ [MPa]	$\sigma_t$ [MPa]	$\sigma_b$ [MPa]
M2-M3	-8.79	-7.01	-6.55	-1.46	-6.50	-5.69	-12.28	3.94
M3-M4	-10.76	10.76	5.94	-9.71	-16.35	16.35		
M4-M5	-2.97	2.97	-1.90	1.17	3.55	-3.55	0.78	-1.61
M6-M7	-2.18	2.18	0	0.16	-2.13	2.13	-1.78	1.13

Table 27: Outer fiber stresses derived from CWI results of field measurements

Ultimately, the  $dv/v$ -components corresponding with changes in stress in between field measurements, both from axial forces or bending moments, are added and converted to stress values with the use of Equation 6.10. The derived stress distributions are shown in Table 27. Within the table,  $\sigma_t$  indicates the stress in the top fiber and  $\sigma_b$  indicates the stress in the bottom fiber at the corresponding position within the concrete bridge structure. The rows in the table categorize the cross-correlation between the relevant measurements. For example, M2-M3 represents the cross-correlation between Measurement 2 and Measurement 3. As there is no Measurement 3 at Position 4, the derived stresses from cross-correlation between Measurement 2 and Measurement 4 are stated instead.

#### 6.4 Comparison between expected and measured cross-sectional stress distributions within the concrete structure

With the stress distribution from structural analysis, shown in Table 25, and the stress distribution from derivation of CWI of the field measurements, shown in Table 27, a comparison is drawn between expected analytical results and measured experimental results. Table 28 lists the analytically obtained stress distribution, as  $\sigma_{t,a}$  for the top fiber stress and  $\sigma_{b,a}$  for the bottom fiber stress, and the experimentally obtained stress distribution, as  $\sigma_{t,e}$  for the top fiber stress and  $\sigma_{b,e}$  for the bottom fiber stress, for comparison at each of the sensor group positions. The rows in the table indicate which measurements are considered for evaluation. The discrepancy in results is shown as a simple ratio between the two compared results expressed as the measured experimental result divided by the expected analytical result, noted as  $e/a$ . The closer this ratio is to 1.0, the better the compared results match. A negative ratio indicates incompatibility with regards to increase or decrease of compressive stresses.

The comparison in Table 28 is visualized by comparative illustrations of derived stress distributions in Figure 57 for the stated measurements. For the analytically obtained results (*a*), the outer fiber stresses are taken and a linear distribution is drawn. For the experimentally obtained results (*e*), the positions of the sensors are taken and the converted  $d\nu/\nu$  into stress according to Section 6.3 is used to draw linear gradients along the cross-sectional height. The sensor group configuration at Position 2 and Position 4 produce a non-linear stress distribution as three sensors are placed over the cross-section height and the simulated gradient is not constant between the sensors. This non-linearity is considered an acceptable inconsistency.

Position 1						
	$\sigma_{t,a}$ [MPa]	$\sigma_{t,e}$ [MPa]	$e/a$	$\sigma_{b,a}$ [MPa]	$\sigma_{b,e}$ [MPa]	$e/a$
<b>M2-M3</b>	0.25 – 2.10	-8.79	-7.48	-14.67 – -12.82	-7.01	0.51
<b>M3-M4</b>	-0.89 – 0.96	-10.76	-307.43	-0.96 – 0.89	10.76	-307.43
<b>M4-M5</b>	1.62	-2.97	-1.83	-1.62	2.97	-1.83
Position 2						
	$\sigma_{t,a}$ [MPa]	$\sigma_{t,e}$ [MPa]	$e/a$	$\sigma_{b,a}$ [MPa]	$\sigma_{b,e}$ [MPa]	$e/a$
<b>M2-M3</b>	-11.20 – -9.91	-6.55	0.62	2.35 – 3.64	-1.46	-0.49
<b>M3-M4</b>	-0.62 – 0.67	5.94	237.60	-0.67 – 0.62	-9.71	388.40
<b>M4-M5</b>	1.14	-1.90	-1.67	-1.14	1.17	-1.03
Position 3						
	$\sigma_{t,a}$ [MPa]	$\sigma_{t,e}$ [MPa]	$e/a$	$\sigma_{b,a}$ [MPa]	$\sigma_{b,e}$ [MPa]	$e/a$
<b>M2-M3</b>	-6.39 – -4.68	-6.50	1.17	-5.10 – -3.39	-5.69	1.34
<b>M3-M4</b>	2.39 – 4.10	-16.35	-5.04	-4.10 – -2.39	16.35	-5.04
<b>M4-M5</b>	-4.36	3.55	-0.81	4.36	-3.55	-0.81
Position 4						
	$\sigma_{t,a}$ [MPa]	$\sigma_{t,e}$ [MPa]	$e/a$	$\sigma_{b,a}$ [MPa]	$\sigma_{b,e}$ [MPa]	$e/a$
<b>M2-M3</b>	-9.50 – -5.93	-12.28	2.74	-1.63 – 1.94	3.94	-1.28
<b>M3-M4</b>	1.46 – 5.02	-12.28	2.74	-5.02 – -1.46	3.94	-1.28
<b>M4-M5</b>	-2.67	0.78	-0.29	2.67	-1.61	-0.60

**Table 28: Comparison of derived outer fiber stresses from expected analytical results (a) and measured experimental results (e) between stated measurements from Measurement 2 to Measurement 5 for all four sensor group positions**

The difference in results show significant discrepancies between analytical and experimental results. However, the disparity in results does not necessarily lead to a final verdict on the suitability of this particular method of measuring stresses within the structure. The possible causes for these discrepancies are numerous. A number of consequential assumptions have been made in the analysis and when these assumptions are taken into consideration, the disparities in results can be rationalized. A point to consider are the highly variable conditions surrounding the field measurements. The uncontrolled environment in which the monitored concrete structure is stationed, causes alterations the measurement results. The relevant assumptions made during the analysis are discussed for each instance of cross-correlation between field measurements.

For cross-correlation between Measurement 2, Measurement 3 and Measurement 4, the comparative analytically obtained linear stress distribution is presented as an estimation with upper and lower limits. This manner of presentation is the consequence of the unclear interaction between prestressing tendon curvature and structure self-weight loading while the structure is still supported by the formwork. The interactivity between these counteracting forces is explored superficially in this study and therefore, the exact stress-state of the structure during this construction phase is not included in the analysis. Consequently, exact comparisons are not possible and the matching ratio  $e/a$  is derived by taking the mean of the range of the analytical results.

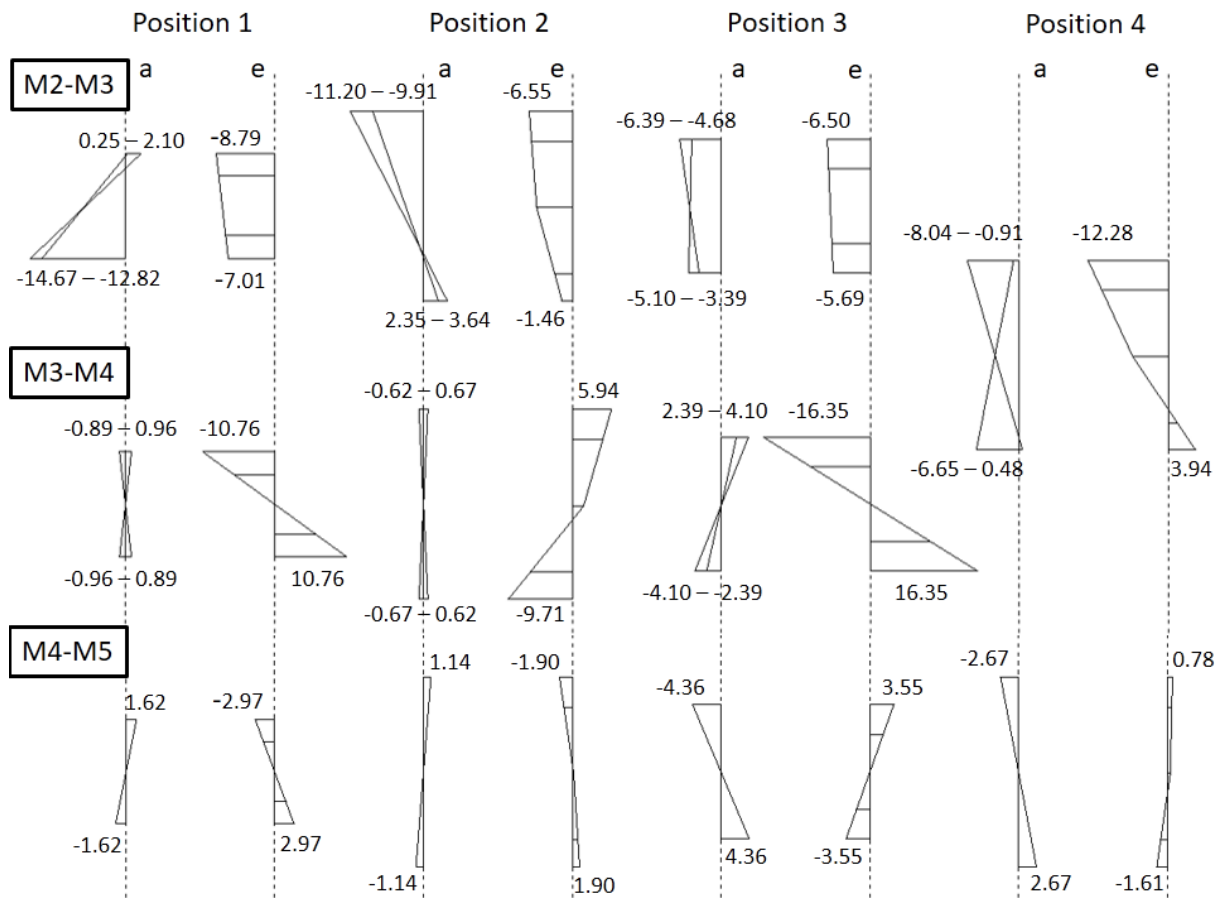


**Figure 57: Comparison between expected analytical results (a) and measured experimental results (e) as projected stress distributions in MPa over the vertical axis between stated measurements from Measurement 2 to Measurement 5 for all four sensor group positions**

From cross-correlation between Measurement 2 and Measurement 3, the  $dv/v$ -component associated with bending moments is less prevalent in comparison to the analytically calculated linear gradient due to bending moments from the prestressing tendon curvature, as seen in the top row of Figure 57. Thus, the stresses derived from the field measurement results show a linear distribution with a lesser gradient in comparison to the stresses calculated in the structural analysis. This occurrence is potentially the result of the incomplete structural analysis in Section 6.1.1, which does not compute the exact partial inclusion of self-weight loading during the post-tensioning of the structure. It is expected that during the post-tensioning, a portion of the bending moments due to tendon curvature is counteracted by the self-weight of the structure. This interaction decreases the residual stresses within the structure due to post-tensioning. It is possible that a certain configuration of forces results in a stress distribution with a smaller gradient, which is more in agreement with the experimentally obtained stress distribution.

The experimentally obtained stress gradients introduced between Measurement 3 and Measurement 4, and Measurement 4 and Measurement 5 are not in agreement with the analytically obtained bending moments induced by the removal of formwork of the measured span and adjacent span, as shown in Figure 57. Rather, the results show opposite stress-states in comparison to their counterpart and indicate a severe incompatibility issue. But interestingly enough, further analysis show that under certain loading configurations the comparative results do match.

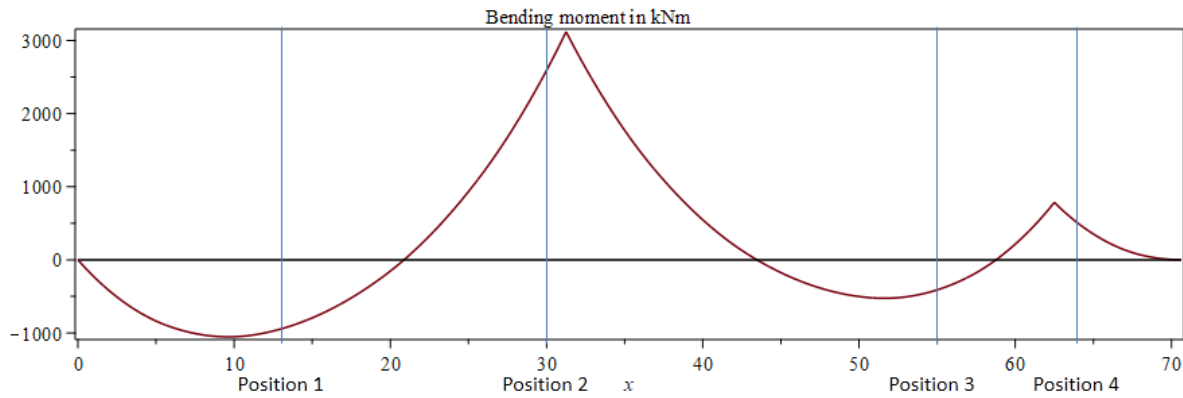


**Figure 58: Bending moment differential in kNm (red) over the bridge length  $x$  in meters due to the full self-weight loading of the measured bridge spans with indicated positions of the sensor groups (blue)**

Figure 58 shows the full effect of the self-weight of the structure on the bending moment distribution. If the formwork were to carry the full self-weight loading during post-tensioning, the structure would be loaded by the full self-weight when the formwork is removed and the shown distribution would accurately display the bending moment differential between Measurement 3 and Measurement 4. This would mean that the prestressing force carries none of the self-weight of the structure during the post-tensioning. Computing the outer fiber stresses, according to Equation 6.3, at the sensor group positions for the given bending moment distribution gives results that are significantly more compatible with the experimentally obtained results from the field measurements, as shown in Table 29.

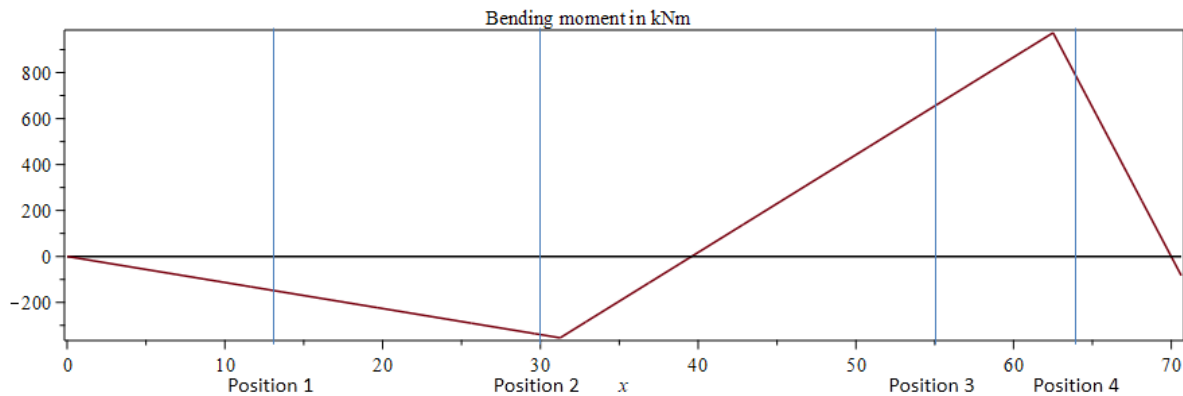


**Figure 59: Bending moment differential in kNm (red) over the bridge length  $x$  in meters due to the full self-weight loading of the adjacent spans with indicated positions of the sensor groups (blue)**

Similarly, with an alternative interpretation of the effect of the removal of formwork of the adjacent spans a more compatible bending moment differential between Measurement 4 and Measurement 5 is found. In Figure 59 the bending moment differential is shown due to the adjacent spans becoming self-supporting. In this interpretation the self-weight of the adjacent bridge spans is considered to be fully supported during post-tensioning and after removal of the formwork the full self-weight loading is applied to the structure. The outer fiber stresses and the comparison with experimentally obtained results are found in Table 29. The comparison is shown in a similar manner as in Table 28 and visualized in Figure 60.

		Position 1					
		$\sigma_{t,a}$ [MPa]	$\sigma_{t,e}$ [MPa]	$e/a$	$\sigma_{b,a}$ [MPa]	$\sigma_{b,e}$ [MPa]	$e/a$
M3-M4		-11.57	-10.76	0.93	11.57	10.76	0.93
M4-M5		-1.80	-2.97	1.65	1.80	2.97	1.65
		Position 2					
		$\sigma_{t,a}$ [MPa]	$\sigma_{t,e}$ [MPa]	$e/a$	$\sigma_{b,a}$ [MPa]	$\sigma_{b,e}$ [MPa]	$e/a$
M3-M4		9.64	5.94	0.62	-9.64	-9.71	1.01
M4-M5		-1.26	-1.90	1.51	1.26	1.17	0.93
		Position 3					
		$\sigma_{t,a}$ [MPa]	$\sigma_{t,e}$ [MPa]	$e/a$	$\sigma_{b,a}$ [MPa]	$\sigma_{b,e}$ [MPa]	$e/a$
M3-M4		-3.04	-16.35	5.38	3.04	16.35	5.38
M4-M5		4.85	3.55	0.73	-4.85	-3.55	0.73
		Position 4					
		$\sigma_{t,a}$ [MPa]	$\sigma_{t,e}$ [MPa]	$e/a$	$\sigma_{b,a}$ [MPa]	$\sigma_{b,e}$ [MPa]	$e/a$
M2-M3		-9.50 – -5.93	-12.28	2.10	-1.63 – 1.94	3.94	-2.30
M3-M4		1.87			-1.87		
M4-M5		2.90	0.78	0.27	-2.90	-1.61	0.56

Table 29: Comparison of alternative derived outer fiber stresses from expected analytical results (a) and measured experimental results (e) between stated measurements from Measurement 2 to Measurement 5 for all four sensor group positions

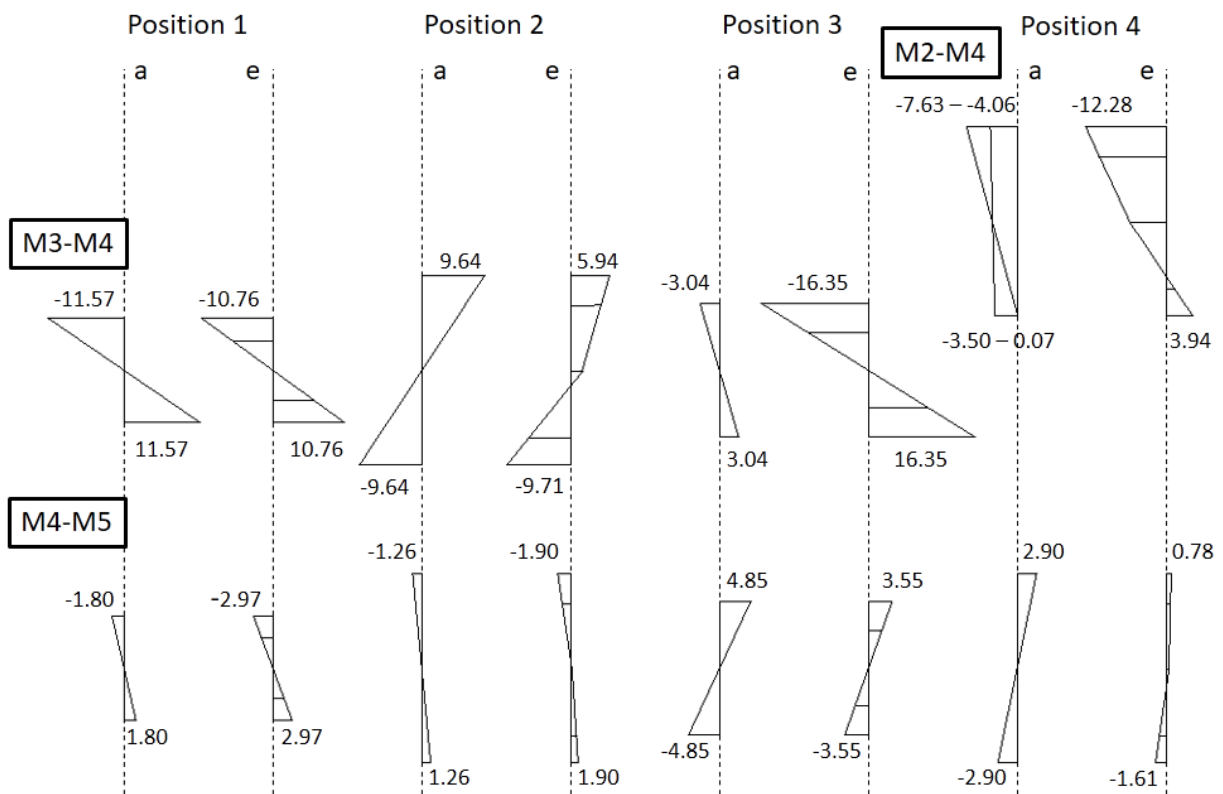


Figure 60: Comparison between alternative expected analytical results (a) and measured experimental results (e) as projected stress distributions in MPa over the vertical axis between stated measurements from Measurement 2 to Measurement 5 for all four sensor group positions

The exact values in Table 29 are not fully compatible as is, but deviations in result values are to be expected as the computation of the experimental results is quite rough and simplistic. The most noteworthy of the aforementioned comparisons is how in the majority of the instance an increase or decrease in compressive stresses is correctly represented. Even though the comparative results are more

in agreement, the manner in which the interaction between self-weight and prestressing force is handled is highly contested. As the structure experiences precamber from the post-tensioning, the gravitational force of the structure self-weight tends to naturally counteract this mechanism. Thus in reality, the self-weight of the structure is not excluded from the equation during post-tensioning, unless the formwork and shoring are in some way able to accommodate and adapt to the occurring precamber, which is not considered in this analysis. Nevertheless, the increased compatibility between results shown in Table 29 in comparison to Table 28 suggests a different interaction between loading forces than originally expected.

Position 1						
	$\sigma_{t,a}$ [MPa]	$\sigma_{t,e}$ [MPa]	$e/a$	$\sigma_{b,a}$ [MPa]	$\sigma_{b,e}$ [MPa]	$e/a$
M6-M7	-1.79	-2.18	1.22	1.79	2.18	1.22
Position 2						
	$\sigma_{t,a}$ [MPa]	$\sigma_{t,e}$ [MPa]	$e/a$	$\sigma_{b,a}$ [MPa]	$\sigma_{b,e}$ [MPa]	$e/a$
M6-M7	1.11	0	0	-1.11	0.16	-0.14
Position 3						
	$\sigma_{t,a}$ [MPa]	$\sigma_{t,e}$ [MPa]	$e/a$	$\sigma_{b,a}$ [MPa]	$\sigma_{b,e}$ [MPa]	$e/a$
M6-M7	0.28	-2.13	-7.61	-0.28	2.13	-7.61
Position 4						
	$\sigma_{t,a}$ [MPa]	$\sigma_{t,e}$ [MPa]	$e/a$	$\sigma_{b,a}$ [MPa]	$\sigma_{b,e}$ [MPa]	$e/a$
M6-M7	0.65	-1.78	-2.74	-0.65	1.13	-1.74

Table 30: Comparison of derived outer fiber stresses from expected analytical results (a) and measured experimental results (e) between Measurement 6 and Measurement 7 for all four sensor group positions

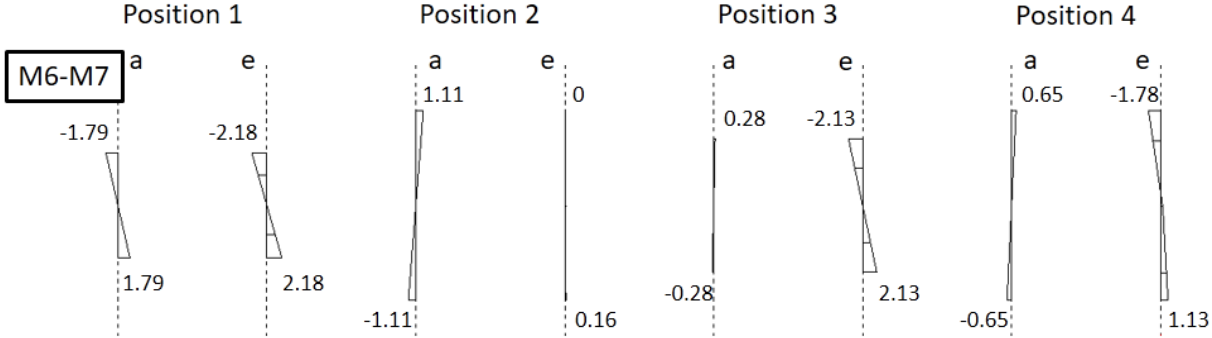


Figure 61: Comparison between expected analytical results (a) and measured experimental results (e) as projected stress distributions in MPa over the vertical axis between Measurement 6 and Measurement 7 for all four sensor group positions

For comparison of results between Measurement 6 and Measurement 7, the expectation is set to have a rather simple change in stress-state as the bending moment differential due to application of the asphalt top layer is accurately modelled with an additional uniformly distributed load. However, during Measurement 6 additional uncontrolled loading is present on the structure. It is therefore inaccurate to state that the experimental results from CWI only show the effects of the application of the asphalt layer to the stress-state of the structure. In actuality, the precise loading on the bridge deck is uncertain due to the alternating presence of heavy construction vehicles. The same holds true for the loading conditions on the structure during Measurement 8. Hence, appraisal of these later measurements with comparisons with analytically obtained values has overall low reliability, as the exact loading condition are not known and therefore a fair comparison cannot be drawn.

It should be noted that cross-correlation between the Measurement 6 and Measurement 7 offer significantly higher *CC* in comparison to cross-correlation between Measurement 2 and Measurement 3, despite the cross-correlated measurements having the same amount of time elapsed in between. This

further supports the claim of the negative effects of maturing young concrete on the CWI results. And the fact that the cross-correlation between Measurement 5 and Measurement 8 does not give satisfactory results shows that even when the concrete has fully matured and no active substantial changes are applied to the structure, the properties of the structure as an acoustoelastic medium still change considerably.

### 6.5 Comparison between expected and measured effect of time-dependent factors on the concrete structure

For comparison between expected and measured results for the time-dependent factors, the data from laboratory tests are used as link between creep and shrinkage behavior and wave velocity change  $dv/v$ . For the relation between creep and shrinkage deformation and  $dv/v$ , a fitted plot is made from the development curve of the  $dv/v$  against the strain in the geopolymer creep tests.

For determining the relation between creep and shrinkage deformation and  $dv/v$ , the same procedure is followed with the geopolymer creep tests as with the concrete compression tests. As specified in Section 5.3, the creep test results do not show data from exclusively creep and shrinkage. The data is skewed due to shifts in temperature during the tests. For determining the relation between creep and shrinkage deformation, only the data measured during constant ambient temperature is considered. The result is a fitted plot as seen in Figure 62 with the following relation:

$$dv/v = -11.84 * \varepsilon , \tag{6.13}$$

where  $dv/v$  represents the wave velocity change and  $\varepsilon$  represents the relative deformation in the loading direction.

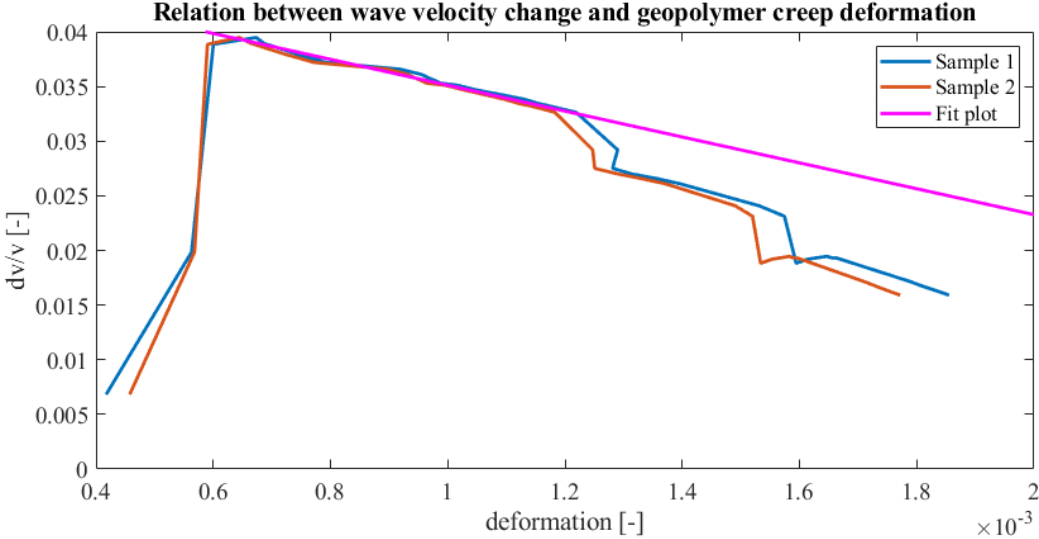
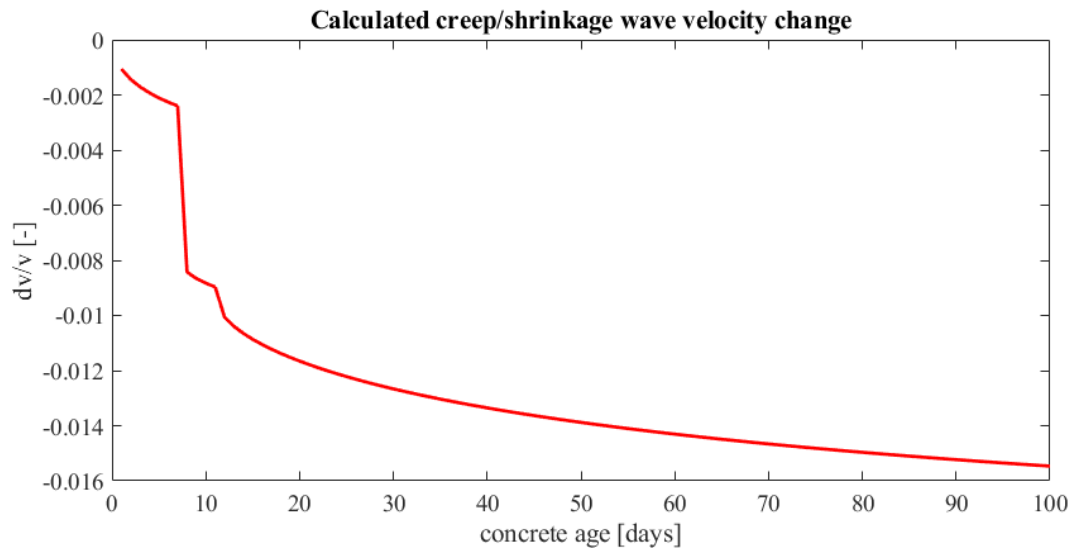


Figure 62: Total wave-velocity change over total deformation of the geopolymer creep test with linear fitted curve

With the determined relation between  $dv/v$  and creep and shrinkage deformation, the effects of the time-dependent factors on the wave velocity is calculated. The development of creep and shrinkage deformation according to Eurocode 2 [25], as shown in Figure 45, is converted to the development of  $dv/v$  over time due to the time-dependent deformations with Equation 6.13. The resulting relation between  $dv/v$  and concrete age is illustrated in Figure 63.



**Figure 63: Converted wave-velocity change over concrete age derived from the analytically calculated creep and shrinkage deformation**

For a complete illustration of the time-dependent factors and their effects on the wave velocity, the hydration process of the concrete is considered in conjunction with the time-dependent deformations. In Section 5.1, the  $dv/v$  over time from the hydration process of concrete is plotted from three concrete cylindrical samples into an averaged fitted curve, displayed in Figure 64. This plotted data is computed with the calculated effect of the time-dependent deformations on the wave velocity in Figure 63. The resulting relation, shown in Figure 65, is found for all considered time-dependent factors by use of analytical calculations and laboratory tests.

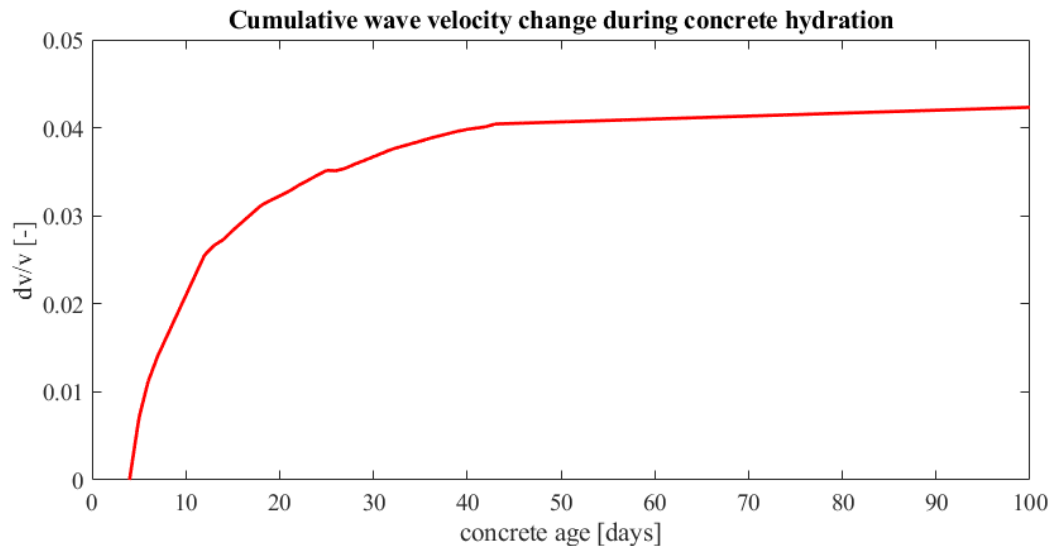


**Figure 64: Fitted curve of the wave-velocity development during concrete hydration derived from the concrete hydration test**

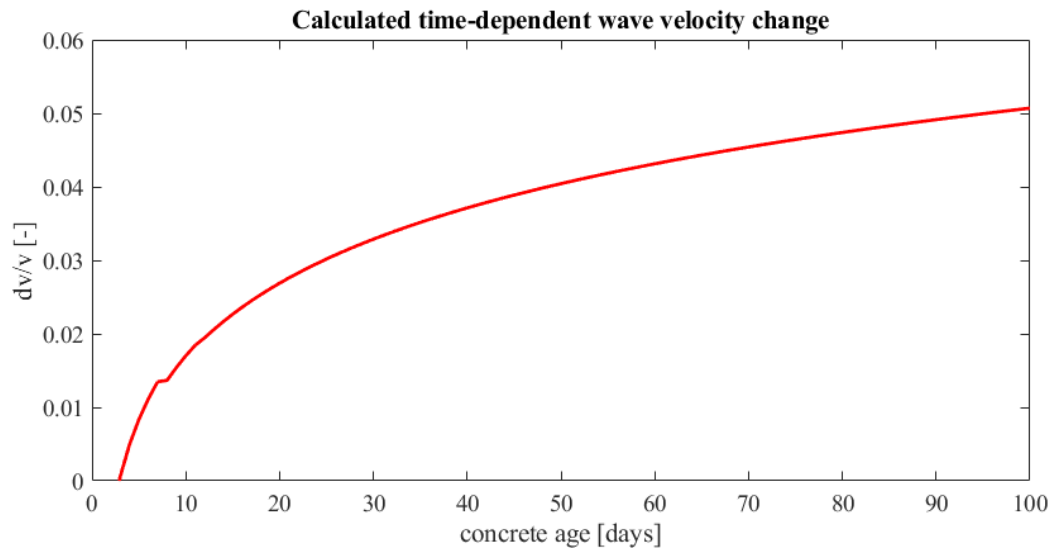


**Figure 65: Total wave-velocity change over concrete age due to time-dependent factors, including creep, shrinkage and concrete hydration**

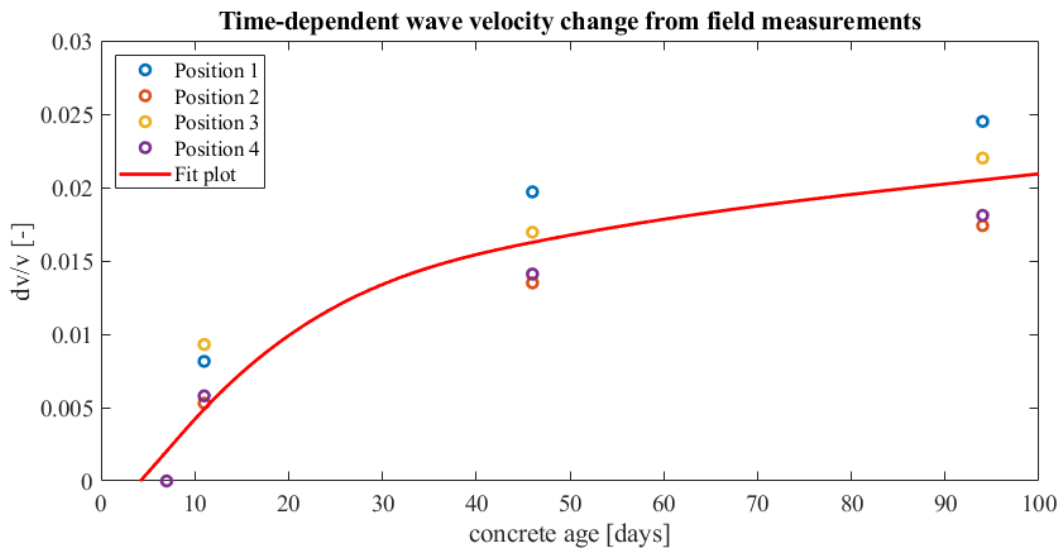


**Figure 66: Approximated relation between  $dv/v$  and concrete structure age from Measurement 2 to Measurement 5 at all four sensor group positions**

In Figure 66, the corresponding time-dependent  $dv/v$ -component is illustrated over the concrete age from the time of casting. The dots within the graph represent the change in wave velocity  $dv/v$  between corresponding field measurements at the four sensor group positions. From these data points, a fitted curve is computed to draw the development of  $dv/v$  as the concrete ages and time-dependent deformation on the structure progresses. For the analysis of the time-dependent factors on the  $dv/v$ , only Measurement 2 to Measurement 5 are considered, as data from Measurement 1 is inadequate due to underdeveloped concrete and cross-correlation between Measurement 5 and later measurements showed very low reliability.

Finally, two graphs are presented with both showing the relation between concrete age and the change in wave velocity due to the stiffness development of young concrete and time-dependent deformation. With one graph resulting from analytical derivation (Figure 65) and the other graph resulting from approximation of measured field data (Figure 66). One can observe that both graphs roughly follow the same logarithmic function, which indicates similarities in how time-dependent factors affect the velocity

of the wave signals in prestressed cast-in-situ concrete structures and concrete samples in the laboratory. However, there is a disparity in values of  $dv/v$  when the analytical results and experimental results are compared. Within the same time span, the wave velocity of the wave signal within the concrete bridge structure is expected to increase twice as much than what is measured. The definitive cause for the disparity is unclear, however, some important aspects from the manner of derivation are likely to have influenced the results. The following main inconsistencies have likely caused compatibility issues for a direct comparison of the two obtained graphs:

- The concrete cylinders used for measuring the hydration process of young concrete consists of a different concrete mix than the one used for casting the measured concrete structure. Therefore, the use of the fitted curve (Figure 64), which shows the effect of the development of young concrete on the velocity of the wave signal, may not be valid as a direct reference.
- The conditions around hydration of the measured concrete structure are different from those of the concrete cylinders. The concrete bridge structure is located outdoors and exposed to various environmental factors, while the concrete cylinders samples are stored indoors inside a laboratory. The variance in temperature and ambient humidity are likely to affect the strength development of the concrete structure in comparison to the laboratory test samples.
- The samples used in the creep tests are made of geopolymer concrete instead of ordinary concrete. Thus, the relation, drawn in Figure 62, between time-dependent deformation and wave velocity change may not be accurate for assessment of the concrete structure which consists of ordinary concrete.

## 7 Discussion

At the end, the all encapsulating question on whether CWI can be used to monitor stress changes in concrete structures with cast-in SA is evaluated. From laboratory tests it has been established that stresses in concrete can most certainly be ascertained with the use of CWI in combinations with embedded SA. However, applying the same principle to a large concrete structure in service might not be as viable. The conditions of field measurements are far more dynamic and unpredictable in comparison to the controlled environment in the laboratory. As such, the simplicity of denoting CWI results to a single factor is lost. One can deduce the influencing factors by determining and exploring the actors on the evaluated medium during assessment. This procedure of isolating various acting factors has a major drawback. Namely, it requires extensive prerequisite knowledge on the conditions of the structure and therefore the procedure is inaccessible to the unversed.

### 7.1 Cycle skipping prevention

Another bit of discourse is the manner in which cycle skipping in the CWI analysis is prevented, as explained in Section 3.4 and applied in Section 4.1.1. This data correcting method requires extensive user interference during post-processing, which then takes in question the authenticity of the analysis results. In worst cases, this manipulation of results can do more harm than good. Thus, attentive and informed handling of the data is required.

### 7.2 CWI data processing

The first thing to consider for data processing in this study is the assumption made about the behavior of waves in a heterogeneous medium and the consequences thereof on the wave signal. In Section 2.6, it was established that only P-waves are considered in this study as sensors are positioned as such, that perturbation from stress changes are parallel to the direction of the wave propagation. This statement is a simplification however, as the wave signal travels a scattered path through the medium and thus experiences constant redirection of propagation direction. In reality, concrete as a viscoelastic material, facilitates both P-waves and S-waves, which interact differently to longitudinal stress changes.

This study has attempted to include the most dominant factors affecting the wave propagation velocity in CWI data of a concrete bridge structure during its construction. However, not all factors are considered. For example, temperature has shown to affect wave velocity in past studies [1] and in this study (Section 5.3.1). As the concrete structure in question is situated outdoors, it is exposed to temperature changes from day-night cycles as well as seasonal passage. The measurements on the concrete structure are conducted over several months from summer to winter, which causes a discrepancy in environmental conditions between measurements. Even during the measurements, variance in temperature is present as the measuring act itself takes multiple hours, during which the temperature changes. As the measured element is considerably thick, the surface temperature is different from the internal temperature of the structure, where the SA is embedded, creating a temperature gradient within the structure. These factors make temperature and other environmental factors increasingly complex components to consider in CWI.

The time-dependent factors, such as creep deformation and concrete hydration, are assessed with laboratory tests using non-identical samples. The concrete hydration tests are done with concrete cylinders with a different mix design and geopolymer concrete is tested for creep deformation instead of ordinary concrete. The mechanical behavior of the test samples is expected to be quite similar to that of the concrete structure under the specified conditions, but unforeseen deviations in the results are entirely possible.

The  $dv/v$ -component associated with time-dependent factors, as determined in Section 6.1.2, is derived by subtracting the projected stress component from the averaged wave-velocity change of the sensor pairs, shown in Figure 56, and is considered constant over the structure cross-section. In regards to concrete hydration, in reality, concrete does not hydrate uniformly over the cross-section depending on the dimensions of the element. Thick concrete elements do not hydrate evenly as the trapped hydration heat in the internal volume of the element causes the hydration process to accelerate. In this study, this variance in concrete maturity is not considered as all projected values are approximations.

The transition from a 3D configuration to a 2D configuration of the CWI's  $dv/v$ -values is used to draw a clearer comparison with the mechanical model of the concrete structure, as shown in Section 6.1.2. One could argue that this act is an oversimplification of the actual situation as the structure is not homogeneous in the lateral direction of the bridge span. But as this study operates with approximations, validation can be found for a more simplified model.

Evaluation on stresses in the structure is exclusively applied to forces in the longitudinal direction, i.e. shear forces are not considered. However, stresses perpendicular to the wave propagation direction certainly affect the wave velocity [4]. For this study the effects of shear forces are not considered in the CWI results as the additional variables in the assessment would make calculations more complex. Even though shear forces are excluded in this study, their significance on the results is present and should be borne in mind.

### **7.3 Structural analysis**

A point of contention in the structural analysis is the interaction between eccentric post-tensioning and the self-weight loading while the structure is still supported by the formwork and shoring. In the analytical derivation of the cross-sectional stresses in the bridge structure, the assumption is made that bending moments generated from the draping of the prestressing tendons during application of 20% of the total prestressing force are balanced by the self-weight loading, resulting in no residual stresses due to bending moments. Correspondingly, at 100% applied prestressing force the assumption is generally made that the internal forces due to prestress eccentricity outweigh the self-weight loading and carry the structure self-weight entirely, but in reality the mechanical conditions are much more complex. The derived displacement field shows that in such a case the structure deflects downwards at certain areas due to the interaction of loads. It is therefore more likely that the formwork and shoring still provide counterbalancing force on to the structure to prevent downwards displacement. As such, a variance in bending moment distribution is calculated between approximated minimal displacement and full engagement of the self-weight loading. Even with these additional considerations, the derived bending moment distribution might not be completely accurate, as the soil underneath the shoring has a certain elasticity and affects the displacement field of the structure, which is not considered for this study.

### **7.4 Recommendations for future studies**

At the end of the study, a resemblance of the desired results has been found, but these findings are not without the necessary assumptions. The majority of these assumptions stem from the uncertainties and dynamic circumstances surrounding the field measurements on the concrete structure. For future studies, actions and measures to keep uncertainties to a minimum are highly advised. Measurements should for instance be done more regularly with a maximum interval of a few days. This is especially advised when dealing with young concrete as various time-dependent factors have highly significant effects on the medium. With more frequently acquired data, the accumulation of unknown factors is limited. A good modification would be to automatize the measuring procedure, so the requirement for human presence is kept to a minimum, as there might be limited options for direct involvement during construction.

## 8 Conclusions

Coda Wave Interferometry in combination with Smart Aggregate has great prospects to be a valuable asset in the assessment of concrete elements and structures. This study has explored the application of this monitoring system for the evaluation of various mechanical properties of concrete structures. Individually, the characteristic mechanical properties of concrete under certain conditions such as concrete hydration, compressive loading and creep can be assessed by means of assessing the acoustoelastic properties of the material. It is when the various factors act on the medium simultaneously, that appraisal becomes increasingly complicated. As such, the technique in its current stage of development still has low reliability as a standalone monitoring tool for precise assessment of stresses in large complex concrete structures and might be more applicable as a general control instrument in conjunction with other monitoring methods.

Finally, the conclusive findings of this study on Coda Wave Interferometry on concrete elements with embedded Smart Aggregate are summarized by the research sub-questions:

How can Coda Wave Interferometry be used to monitor stress changes in concrete structures with embedded Smart Aggregate?

- With the use of a representative sample, the relation between wave propagation velocity and stresses can be ascertained for a particular concrete medium.
- The wave propagation velocity has a near-linear relation with uniaxial compressive loading in concrete. Non-linearity sets in with uniaxial compressive loading to near failure. The wave propagation velocity increases with an increase of compressive stresses on the medium. The increase in wave velocity diminishes as the loading increases to near concrete compressive strength. The same relation is observed inversed during unloading and remains the same over a second loading cycle.
- Initial loading and fully unloading after loading concrete near its compressive strength causes deviations in the signal's waveform. This phenomenon is likely caused by the formation and opening of cracks in the microstructure of the material and has detrimental effects for cross-correlation between wave signals.
- By determining the additional factors acting on the structure and their impact on the wave propagation velocity, the effects of a change in stress-state on the wave propagation velocity can be isolated and evaluated.

Which acting factors affect the acoustoelastic properties of the concrete structure during the construction phase and how can the factors acting on the structure be assessed with Coda Wave Interferometry and embedded Smart Aggregate?

- The most prominent factors acting on the acoustoelastic properties of the concrete structure during the construction phase are found to be time-related, including but not limited to creep, shrinkage and concrete hydration. The impact of these factors on the wave propagation velocity can be assessed with representative laboratory tests.
- The hydration process of young concrete has a logarithmic relation with the wave propagation velocity. The acoustoelastic properties of young concrete elements continue to evolve as the stiffness of the material develops. The wave velocity of the signal traveling through the medium increases during the hydration process. An increase is observed in concrete samples to up to 40 days old.

- The signal wave velocity decreases in geopolymer concrete as it deforms due to creep. As geopolymer elements are compacted over time from a constant load, the wave velocity decreases with a near linear relation.
- Variation in ambient temperature changes the signal's waveform. These changes to the waveform have detrimental effects on the ability to cross-correlate two comparative wave signals.
- Recently cast concrete structures have highly volatile acoustoelastic properties, which evolve over time. For proper assessment of the structure during its early age, frequent measurements are required.
- Concrete structures continue to experience changes to its acoustoelastic properties without the addition of permanent changes to the loading conditions. The cause is highly likely related to cyclic exposure to external factors, such as the environment and construction proceedings.

How do the results from the experimental Coda Wave Interferometry translate and compare to a structural analysis of the concrete structure?

- Many dissimilarities are established between analytical results from the structural analysis and experimental results from Coda Wave Interferometry in regards to the changes in stress-state of the monitored structure. However, as the conditions of the monitored structure during the construction phase are highly complex, the structural analysis involves its own approximations. This results in an additional layer of uncertainty to the comparison. Nevertheless, the study shows that stress gradients within the structure are detectable and the derived stress distributions from the Coda Wave Interferometry results do reflect the analytically derived stress distributions, if certain conditions are assumed.
- The summation of the considered time-related factors acting on the acoustoelastic properties of the concrete structure roughly reflects the analytically derived results in conjunction with the laboratory test results. The comparison does not provide an exact match. But considering the non-identical conditions, the discrepancies are to be expected.
- Exact comparisons between analytical results of a structural analysis and experimental Coda Wave Interferometry results prove to have low reliability with the methodology used in this study. Conclusive ascertainment of the stress-state of the structure in this manner is therefore not feasible.

The biggest challenge encountered in this study is establishing the proper methodology for Coda Wave Interferometry assessment by utilizing Smart Aggregate. Before any monitoring is done an extensive preliminary plan of operations is required for effective post-processing of the acquired data. During the post-processing, prerequisite knowledge of the behavior of the material is required as conditions of the structure become more complex.

The complexity of analyzing large concrete structures with Coda Wave Interferometry requires the aid of additional assessment methods, such as laboratory testing. These additional ventures serve to establish the relation between acoustoelastic effects of the material and the mechanical properties. Ideally, future acquisition of this information is possible without experimental endeavors. As this form of monitoring concrete structure is still in its infancy and in development, the instalment of a general directory with the acoustoelastic specifics of commercial concrete mixes is plausible in the near future.

# References

- [1] É. Larose, J. de Rosny, L. Margerin en D. Anache, „Observation of multiple scattering of kHz vibrations in a concrete structure and application to monitoring weak changes,” vol. 73, 2006.
- [2] É. Larose en S. Hall, „Monitoring stress related velocity variation in concrete with a  $2.10^{-5}$  relative resolution using diffuse ultrasound,” vol. 125, 2009.
- [3] T. Planès en É. Larose, „A review of ultrasonic Coda Wave Interferometry in concrete,” vol. 53, 2013.
- [4] A. Guz en F. Makhort, „The Physical Fundamentals Of The Ultrasonic Nondestructive Stress Analysis Of Solids,” vol. 36, 2000.
- [5] S. C. Stähler, C. Sens-Schönfelder en E. Niederleithinger, „Monitoring stress changes in a concrete bridge with coda wave interferometry,” vol. 129, 2011.
- [6] F. D. Murnaghan, „Finite Deformation of an Elastic Solid,” 1951.
- [7] Wikipedia, „Time of flight,” [Online]. Available: [https://en.wikipedia.org/wiki/Time\\_of\\_flight](https://en.wikipedia.org/wiki/Time_of_flight). [Opened 11 October 2021].
- [8] ISO 1920-7, „Testing concrete Part 7: Non-destructive tests on hardened concrete,” 2004.
- [9] S. W. Smith, The Scientist and Engineer's Guide to Digital Signal Processing, 1999.
- [10] V. Malhotra en N. Carino, „Handbook on Nondestructive Testing of Concrete,” 2004.
- [11] Y. Wang, Seismic Inverse Q Filtering, 2009.
- [12] Proceq, „Operating Instructions,” 2017.
- [13] ASTM D2845, „Standard Test Method for Laboratory Determination of Pulse Velocities and Ultrasonic Elastic Constants of Rock,” 2008.
- [14] I. Lillamand, J.-F. Chaix, M.-A. Ploix en V. Garnier, „Acoustoelastic effect in concrete material under uni-axial compressive loading,” vol. 43, 2010.
- [15] R. Snieder, „The Theory of Coda Wave Interferometry,” vol. 163, 2006.
- [16] A. Obermann, T. Planès, E. Larose, C. Sens-Schönfelder en M. Campillo, „Depth sensitivity of seismic coda waves to velocity perturbations in an elastic heterogeneous medium,” vol. 194, 2013.

- [17] G. Milone, „Numerical Study of Stress Identification in Concrete using Coda-Wave Interferometry,” 2019.
- [18] C. Kevinly, „Application of coda-wave interferometry on concrete structures by utilizing smart aggregates,” 2018.
- [19] A. Obermann, T. Planès, C. Hadziioannou en M. Campillo, „Lapse-time-dependent coda-wave depth sensitivity to local velocity perturbations in 3-D heterogeneous elastic media,” vol. 207, 2016.
- [20] C. Pacheco en R. Snieder, „Time-lapse travelttime change of singly scattered acoustic waves,” vol. 165, nr. 2, 2006.
- [21] J. Wu, Q. Kong, W. Li en I. Lim, „Interlayer Slide Detection Using Piezoceramic Smart Aggregates Based on Active Sensing Approach,” 2017.
- [22] The MathWorks, Inc., „MathWorks - MATLAB & Simulink,” [Online]. Available: <https://nl.mathworks.com/products/matlab.html>. [Opened 25 November 2021].
- [23] T. J. Boerrigter, „Coda Wave Interferometry Analysis for Brittle Rock Deformation during Uniaxial Compression,” 2017.
- [24] A. Carpinteri, J. Xu, G. Lacidogna en A. Manuello, „Reliable onset time determination and source location of acoustic emissions in concrete structures,” vol. 34, 2011.
- [25] NEN-EN 1992-1-1, „Eurocode 2: Design of concrete structures - Part 1-1: General rules and rules for buildings,” 2004.
- [26] Wikipedia, „Creep and shrinkage of concrete,” [Online]. Available: [https://en.wikipedia.org/wiki/Creep\\_and\\_shrinkage\\_of\\_concrete](https://en.wikipedia.org/wiki/Creep_and_shrinkage_of_concrete). [Opened 25 November 2021].
- [27] EurocodeApplied, „Eurocode 2: Table of concrete design properties,” [Online]. Available: <https://eurocodeapplied.com/design/en1992/concrete-design-properties>. [Opened 16 December 2021].
- [28] C. Du en Y. Yang, „Experimental investigation on crack detection using imbedded smart aggregate,” 2019.
- [29] Cybernet Systems Co. Ltd., „Maplesoft - Software for Mathematics, Online Learning, Engineering,” [Online]. Available: <https://www.maplesoft.com/>. [Opened 25 November 2021].
- [30] EurocodeApplied, „Eurocode 2: Concrete creep coefficient & shrinkage strain,” [Online]. Available: <https://eurocodeapplied.com/design/en1992/creep-shrinkage>. [Opened 25 November 2021].

## A. MATLAB-script for data reading and CWI computation

```
% This script picks first arrival and does CWI
% Fengqiao.Zhang, Oct.14, 2020
% edited by Danny Fu, Oct 30, 2021

clc;
close all;
clf;
clearvars;
set(0,'DefaultAxesFontName','Times New Roman');
set(0,'DefaultTextFontName','Times New Roman');
set(0,'DefaultAxesFontSize',14); set(0,'DefaultTextFontSize',14);
set(0,'defaultlinelength',2);
addpath('E:\TUD\Thesis\Matlabcodes origineel');

%% read measurement
load('E:\TUD\Thesis\pre_read_results','alldata');

% information
Position(1).Day(1).src = 0:7; Position(1).Day(1).info = 1557:1564;
%100V stacking 10
Position(2).Day(1).src = 0:11; Position(2).Day(1).info = [1572:1574
1576:1584];%100V stacking 10
Position(3).Day(1).src = 0:13; Position(3).Day(1).info = 1590:1603;
%200V stacking 30
Position(4).Day(1).src = 0:11; Position(4).Day(1).info = 1610:1621;
%100V stacking 30
Position(1).Day(2).src = 0:7; Position(1).Day(2).info = 1666:1673;
%100V stacking 10
Position(2).Day(2).src = 0:11; Position(2).Day(2).info = [1674
1677:1687]; %100V stacking 30
Position(3).Day(2).src = 0:13; Position(3).Day(2).info = 1689:1702;
%200V stacking 30
Position(4).Day(2).src = 0:11; Position(4).Day(2).info = 1703:1714;
%100V stacking 30
Position(1).Day(3).src = 0:7; Position(1).Day(3).info = [1715
1717:1723]; %100V stacking 10
Position(2).Day(3).src = 0:11; Position(2).Day(3).info = 1726:1737;
%100V stacking 10
Position(3).Day(3).src = 0:13; Position(3).Day(3).info = 1738:1751;
%200V stacking 10
Position(4).Day(3).src = 0:11; Position(4).Day(3).info = 1703:1714;
%no measurement at position 4 on day 3, day 2 measurements used instead
Position(1).Day(4).src = 0:7; Position(1).Day(4).info = 1794:1801;
%100V stacking 10
Position(2).Day(4).src = 0:11; Position(2).Day(4).info = 1782:1793;
%100V stacking 10
Position(3).Day(4).src = 0:13; Position(3).Day(4).info = 1767:1780;
%200V stacking 10
Position(4).Day(4).src = 0:11; Position(4).Day(4).info = 1755:1766;
%100V stacking 10
Position(1).Day(5).src = 0:7; Position(1).Day(5).info = 1864:1871;
%100V stacking 10
```

```

Position(2).Day(5).src = 0:11; Position(2).Day(5).info = 1872:1883;
%100V stacking 10
Position(3).Day(5).src = 0:13; Position(3).Day(5).info = 1885:1898;
%200V stacking 10
Position(4).Day(5).src = 0:11; Position(4).Day(5).info = 1899:1910;
%100V stacking 10

Position(1).Day(6).src = 0:7; Position(1).Day(6).info = [2140:2144
2146:2148]; %100V stacking 10
Position(2).Day(6).src = 0:11; Position(2).Day(6).info = [2150:2154
2156 2158 2164 2159 2162 2160 2161]; %100V stacking 10
Position(3).Day(6).src = 0:13; Position(3).Day(6).info = [2166:2175
2177:2180]; %200V stacking 10
Position(4).Day(6).src = 0:11; Position(4).Day(6).info = 2181:2192;
%100V stacking 10
Position(1).Day(7).src = 0:7; Position(1).Day(7).info = 2194:2201;
%100V stacking 10
Position(2).Day(7).src = 0:11; Position(2).Day(7).info = 2203:2214;
%100V stacking 10
Position(3).Day(7).src = 0:13; Position(3).Day(7).info = 2215:2228;
%200V stacking 10
Position(4).Day(7).src = 0:11; Position(4).Day(7).info = 2229:2240;
%100V stacking 10

Position(1).Day(8).src = 0:7; Position(1).Day(8).info = 2608:2615;
%100V stacking 5
Position(2).Day(8).src = 0:11; Position(2).Day(8).info = [2630:2634
2636 2635 2637:2641]; %200V stacking 5
Position(3).Day(8).src = 0:13; Position(3).Day(8).info = 2645:2658;
%200V stacking 5
Position(4).Day(8).src = 0:11; Position(4).Day(8).info = [2661:2666
2668 2671 2670 2672:2674]; %200V stacking 5

%special cases for Day 8
Position(1).Day(9).src = 0:7; Position(1).Day(9).info = 2600:2607;
%100V stacking 5, load on span 1
Position(2).Day(9).src = 0:6; Position(2).Day(9).info = 2623:2629;
%200V stacking 5, load on sensor location
Position(4).Day(9).src = 0; Position(4).Day(9).info = 2675;
%200V stacking 5, load on span 3

% DAY1(cast) 2020-09-15 20:40-02:31
% DAY2 2020-09-21 11:54-16:39
% DAY3 2020-09-25 20:17-22:17
% DAY4 2020-10-30 12:21-14:08
% DAY5 2020-12-17 13:32-15:42
% DAY6 2021-08-31 12:08-16:33
% DAY7 2021-09-02 11:44-15:45
% DAY8 2021-10-16 12:05-19:30

% index from the file
src = zeros(1,length(alldata));
info = zeros(1,length(alldata));
for ii = 1:length(alldata)
    src(ii) = alldata(ii).src;
    info(ii) = alldata(ii).info;
end

%% select first arrival
for ii = 1:length(alldata)

```

```

for jj = 1:length(alldata(ii).ch)
    sig = alldata(ii).wave(:,jj);
    t = alldata(ii).time;
    sig(t<4*1e-5) = 0;
    win = find(t>3.5e-4,1);
    pretri = round(win/2);
    [AIC,arvt] = AIC_pick(sig,t,pretri,win,0);
    alldata(ii).arvt(jj) = arvt;
end
end

%% take the example to show the result
pos = 1; % select the position of measurement 1-4
reclg = 8; % how many sensors at that position (pos1=8, pos2=12, pos3=14,
pos4=12)
id = 1; % which measurement is taken from that position (which sender)
recid = 5; % select the receiver
stest = 3; % stressed test day to compare
rtest = 2; % reference test, day 2+

for day = 2:8
    srcv = Position(pos).Day(day).src(id);
    infov = Position(pos).Day(day).info(id);

    ind = find(src==srcv&info==infov);

    t = alldata(ind).time;
    ch = alldata(ind).ch;
    sig = alldata(ind).wave;
    arvt = alldata(ind).arvt;

    % plot waves
    rg = max(abs(sig(:)));
    figure(day);clf;hold on;
    for ii = 1:reclg
        is = find(t==arvt); % arvt is the picked arrival time, t is the
time series of the signal. This line finds the onset point where noise ends
        dA = mean(sig(1:is,ii)); % sig is the amplitude series of the
signal. This line calculates the average noise amplitude
        sig_shift = sig(:,ii)-dA; % this line shift the signal
        subplot(reclg/2,2,ii);hold on;
        plot(t,sig_shift,'k-');
        plot(arvt(ii)*[1 1],[-1 1]*rg,'r:');
        xlabel('time [s]');
        ylabel('amplitude [V]');
        ylim([-1 1]*rg);
        title(['P' num2str(pos) ',D' num2str(day) ': S' num2str(srcv) '-R'
num2str(ch(ii))]);
        box on;
    end
end

%% coda wave interferometry
for day = 2:8
    srcv = Position(pos).Day(day).src(id);
    infov = Position(pos).Day(day).info(id);

    ind = find(src==srcv&info==infov);

    Day(day).t = alldata(ind).time;

```

```

    Day(day).ch      = alldata(ind).ch(1:reclg);
    Day(day).sig     = alldata(ind).wave(:,1:reclg);
    Day(day).arvt   = alldata(ind).arvt(1:reclg);
    Day(day).src     = srcv;
end

% select reference
t0      = Day(rtest).arvt(recid);
ref     = Day(rtest).sig(:,recid);
ch      = Day(rtest).ch(recid);
t       = Day(rtest).t;
dt      = t(2)-t(1);

% select signal
sig     = Day(stest).sig(:,recid);

% shift signal to correct misaligned axis
is      = find(t==arvt); % arvt is the picked arrival time, t is the time
series of the signal. This line finds the onset point where noise ends
dB      = mean(ref(1:is)); % ref is the amplitude series of the reference.
This line calculates the average noise amplitude
ref_shift = ref(:)-dB; % this line shift the reference
dA      = mean(sig(1:is)); % sig is the amplitude series of the signal. This
line calculates the average noise amplitude
sig_shift = sig(:)-dA; % this line shift the signal

%% plot reference signal and compressed signal
rg      = max(abs([ref_shift;sig_shift]));
figure(10);clf;hold on;
plot(t,ref_shift,'b')
plot(t,sig_shift,'r')
plot(t0*[1 1],[-1 1]*rg,'k:');
xlabel('time [s]');
ylabel('amplitude [V]');
ylim([-1 1]*rg);
title(['P' num2str(pos) ': S' num2str(Day(rtest).src) '-R' num2str(ch)]);
box on;
legend('Reference','Comparative','First arrival')

% make time unique =====
[tu,kp] = unique(t); % the first point is taken
refu    = ref(kp);
sigu    = sig(kp);
dtu     = tu(2)-tu(1);

% shift signal again after making time unique
isu     = find(tu==arvt); % arvt is the picked arrival time, tu is the
time series of the signal. This line finds the onset point where noise ends
dBu     = mean(refu(1:isu)); % ref is the amplitude series of the reference.
This line calculates the average noise amplitude
refu_shift = refu(1:length(tu))-dBu; % shift the reference
dAu      = mean(sigu(1:isu)); % sigu is the amplitude series of the signal.
This line calculates the average noise amplitude
sigu_shift = sigu(1:length(tu))-dAu; % shift the signal

% stretching
% define window
f       = 88; % [kHz], 88 for pos1/3, 50 for pos 2/4
p       = 1/(f*1e3); % [s]

```

```

wndlg      = 8*p;           % window length in periods, 8 for pos 1/3, 5 for pos
2/4
wndst      = t0:wndlg/2:(max(tu)-wndlg); % select start of windows, with
half overlapped
% choose which window is the start of the coda wave, 1 for window directly
after first arrival
wid_coda   = 1;           % starting window for stretching display
wid_avg    = 1;           % calculate averages from nth window for first
arrival errors

% stretching
epsrange = 2.5e-2;
epsilon   = (-epsrange:1e-4:epsrange); % epsilon range
EPS       = zeros(1,length(wndst));
CC        = zeros(1,length(wndst));
COEF_CORR= zeros(length(epsilon),length(wndst));

% with cycling skipping correction
[COEF_CORR,CC,EPS] =
stretching_calculation_dfu(refu_shift,sigu_shift,tu,dtu,epsilon,wndst,wndlg
); % stretching script from Hao Cheng

% without cycle skipping correction
for ii = 1:length(wndst)
    tid1 = fix(wndst(ii)/dtu); % start point of each window
    tid2 = tid1+fix(wndlg/dtu); % end point of each window
    time_window = tid1:tid2; % window range
    [eps,cc,coef_corr,~] =
stretching_LCPC(sigu,refu,tu,epsilon,time_window,0); % stretching
    [pk,loc] = findpeaks(coef_corr); %find highest epsilon from
stretching
    [pkm,idm] = max(pk);
    EPS(ii) = epsilon(loc(idm));
    CC(ii) = pk(idm);
    COEF_CORR(:,ii) = coef_corr;
end

%% find relevant stretching windows
wid = find(CC > 0.5); % find indices of stretching windows
above CC threshold
cod = find(wid >= wid_coda); % find indices of stretching windows
above CC threshold in coda wave
avg = find(wid >= wid_avg);
CC_avg = mean(CC(wid(avg))); % average CC of stretching windows in
coda above CC threshold
EPS_avg = mean(EPS(wid(avg)))*1000; % average epsilon of stretching windows
in coda above CC threshold
wid1 = wid(cod(1)); % first stretching window in coda above
CC threshold

%% plots
figure(11);clf;
subplot(2,1,1);hold on;
plot(tu,refu_shift,'b');
plot(tu,sigu_shift,'r');
plot(t0*[1 1],[-1 1]*rg,'k:');
plot(wndst(wid1)*[1 1],[-1 1]*rg,'m:');
plot(wndst(wid1+1)*[1 1],[-1 1]*rg,'m:');
xlabel('time [s]');
xlim(tu([1 end]));

```

```

ylabel('amplitude [V]');
ylim([-1 1]*rg);
title(['P' num2str(pos) ': S' num2str(Day(rtest).src) '-R' num2str(ch)]);
box on;
leg_ref = sprintf('Reference (Day %i)', rtest);
leg_com = sprintf('Comparative (Day %i)', stest);
legend(leg_ref,leg_com,'First arrival','Stretching window');
subplot(2,1,2);hold on;
yyaxis left;
plot(wndst,EPS);
xlabel('time [s]');
xlim(tu([1 end]));
ylabel('epsilon [-]');
ylim([-epsrange epsrange]);
plot(t0*[1 1],[-1 1]*epsrange,'k:');
plot(wndst(wid1)*[1 1],[-1 1]*epsrange,'m:');
plot(wndst(wid1+1)*[1 1],[-1 1]*epsrange,'m:');
yyaxis right;
plot(wndst,CC);
ylim([0 1]);
ylabel('CC [-]');
box on;

figure(12);clf;
subplot(1,2,1);hold on;
pt = find(tu>=wndst(wid1)&tu<wndst(wid1+1));
plot(tu,refu_shift,'b');
plot(tu,sigu_shift,'r');
xlabel('time [s]');
ylabel('amplitude [V]');
xlim(tu(pt([1 end])));
title(['P' num2str(pos) ': S' num2str(Day(rtest).src) '-R' num2str(ch)]);
box on;
subplot(1,2,2);hold on;
tu2=tu*(1+EPS(wid1));
synt=interp1(tu2,sigu_shift,tu,'spline');
plot(tu,refu_shift,'b');
plot(tu,synt,'r');
xlabel('time [s]');
ylabel('amplitude [V]');
xlim(tu(pt([1 end])));
title(['?=' num2str(EPS_avg,'%1f') '% ; CC=' num2str(CC_avg,'%2f')]);
linkaxes([subplot(1,2,1),subplot(1,2,2)],'y');
box on;

figure(13);clf;
plot(epsilon,COEF_CORR(:,wid1),'k');
xlabel('epsilon [-]');
ylabel('CC [-]');
ylim([-1 1]);
box on;

%% END

```

## B. FFT analysis

The dominant frequency of the wave signal is determined with FFT analysis. The wave signal is converted from the time domain to the frequency domain. From there the dominant frequency is determined from all available data at a given position whilst taking the scattering regime into consideration. From the analysis of the data at Position 1 (Figure 67) and Position 3 (Figure 69) one observes a peak at roughly 88 kHz. Position 3's analysis shows an additional small peak at 40 kHz, but this is neglected in favor of the more consistent higher frequency. Analysis of Position 2 (Figure 68) and Position 4 (Figure 70) show results with peaks at roughly 50 kHz and 110 kHz. In these instances the lower frequency of 50 kHz is set as dominant as a high frequency of 110 kHz is associated with excess scattering of the signal. The relevancy of the dominant wave frequency comes with determining the stretching window for CWI, as ideally the stretching window length is a product of wave periods.

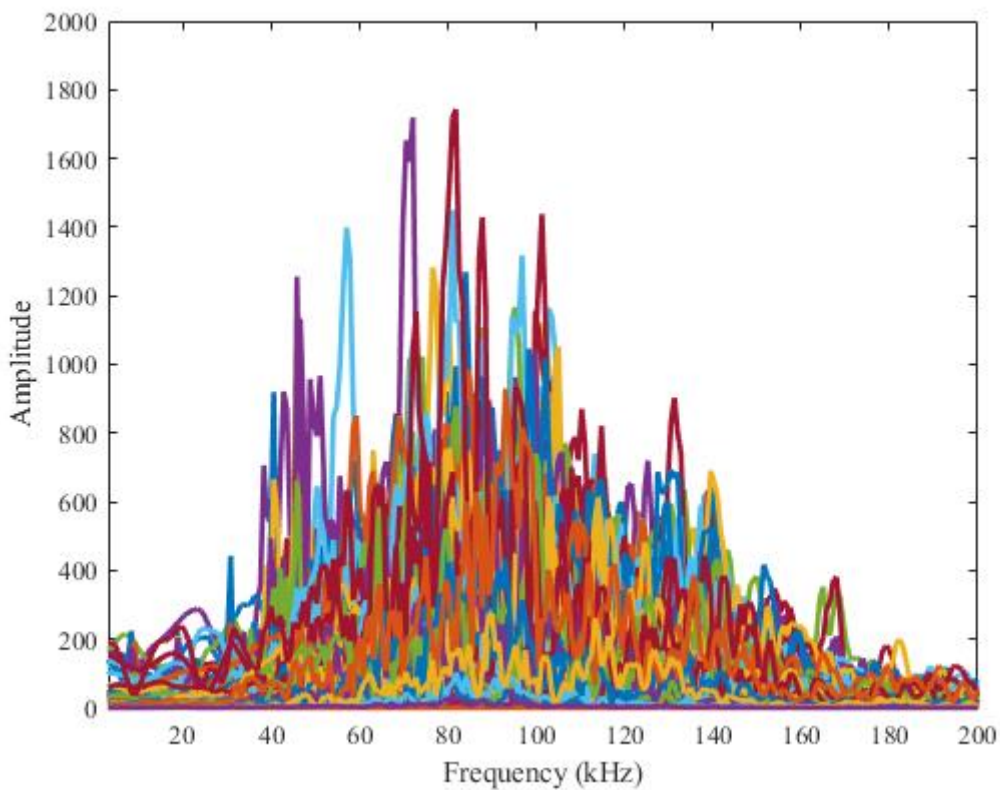


Figure 67: FFT analysis of measured wave signals from all principal sensor pairs at Position 1 from all field measurements

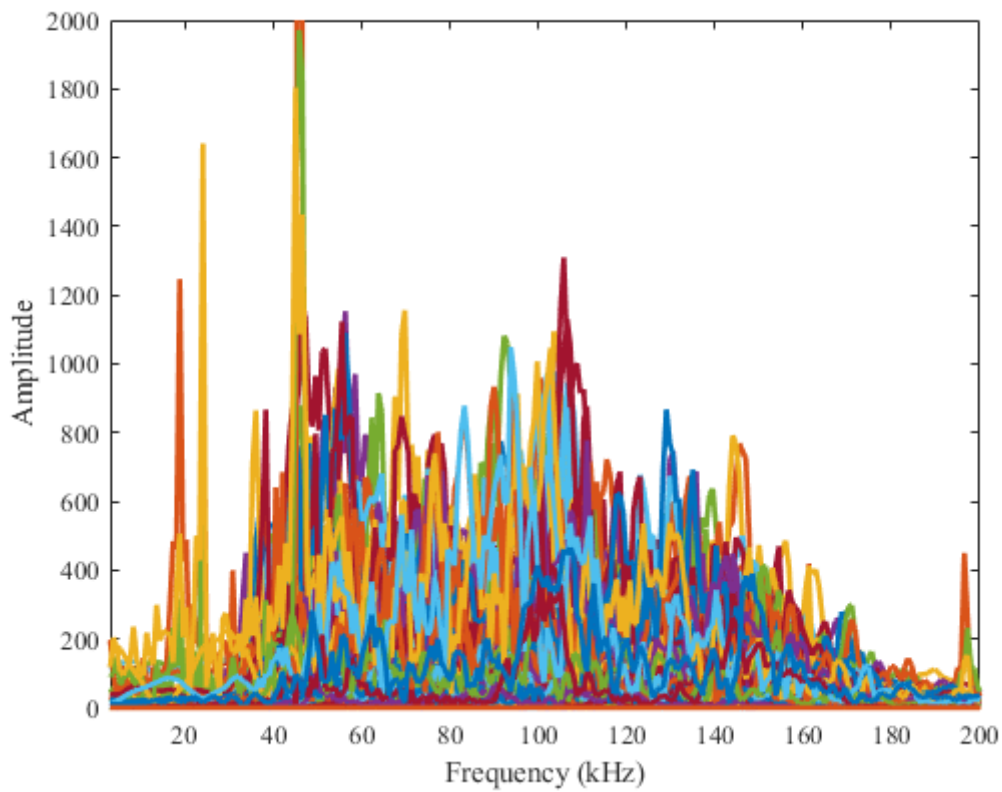


Figure 68: FFT analysis of measured wave signals from all principal sensor pairs at Position 2 from all field measurements

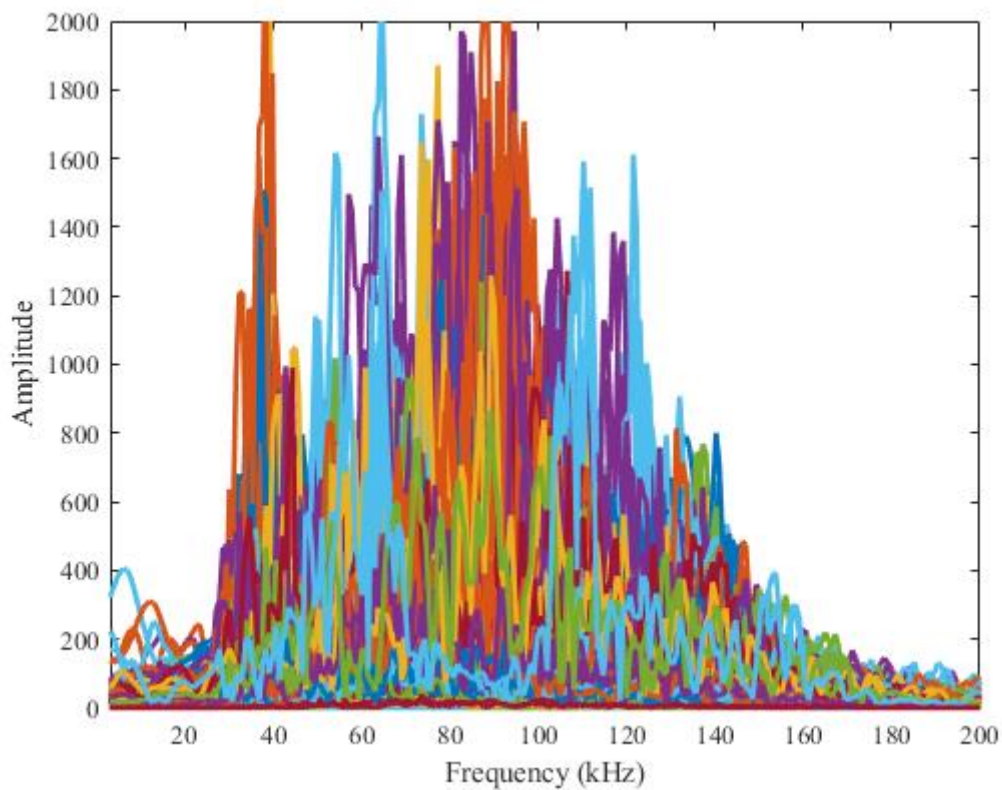


Figure 69: FFT analysis of measured wave signals from all principal sensor pairs at Position 3 from all field measurements

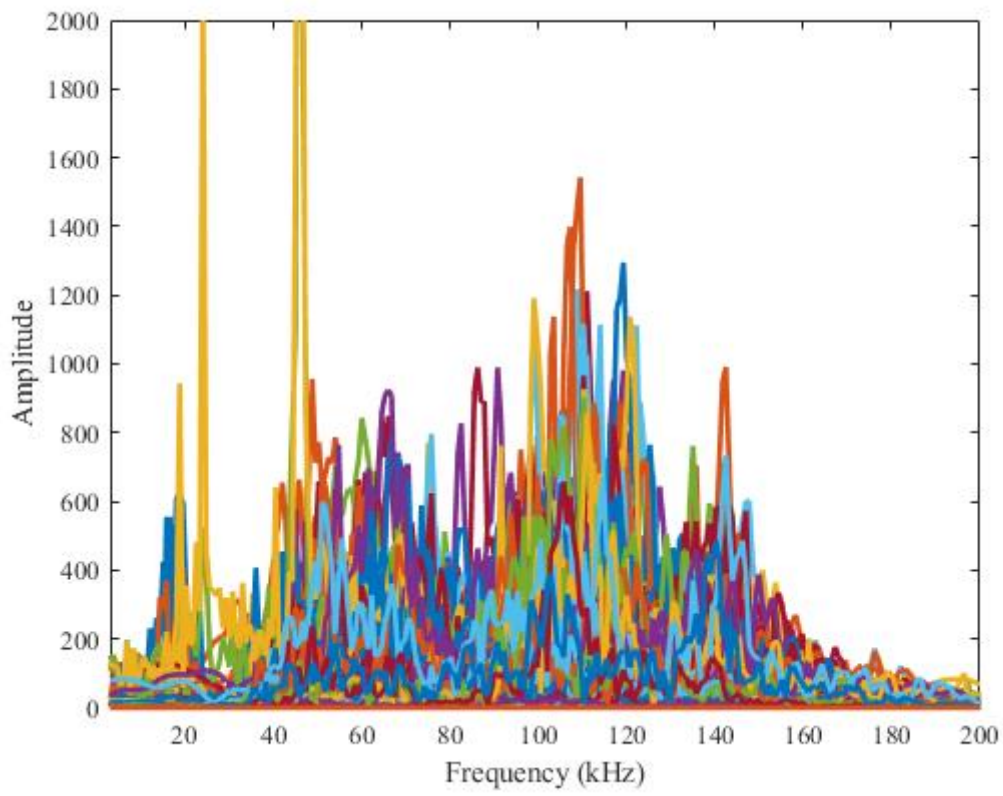


Figure 70: FFT analysis of measured wave signals from all principal sensor pairs at Position 4 from all field measurements

## C. Cycle skipping correction

The effects of the modified MATLAB-script (Appendix A) with cycle skipping prevention are shown in the following figures. The wave-velocity change  $dv/v$  is plotted over the travel time of the wave signal. For each position on the bridge, three graphs are shown. The graphs illustrate the plotted wave-velocity change utilizing the original MATLAB-script, the wave-velocity change with the modified MATLAB-script and finally the results by manually correcting the outliers of the modified script, as explained in Section 4.1.1.

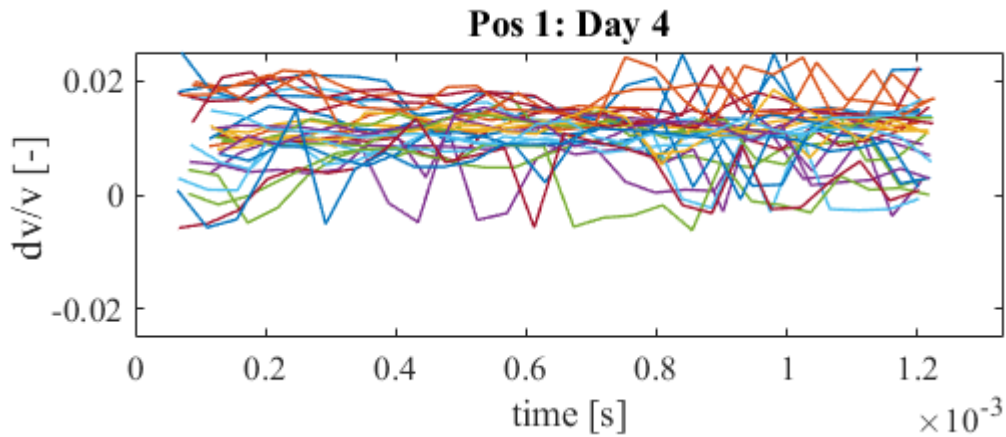


Figure 71: Corrected  $dv/v$  over time of CWI between Measurement 3 and Measurement 4 at Position 1 with cycle skipping prevention and outlier correction

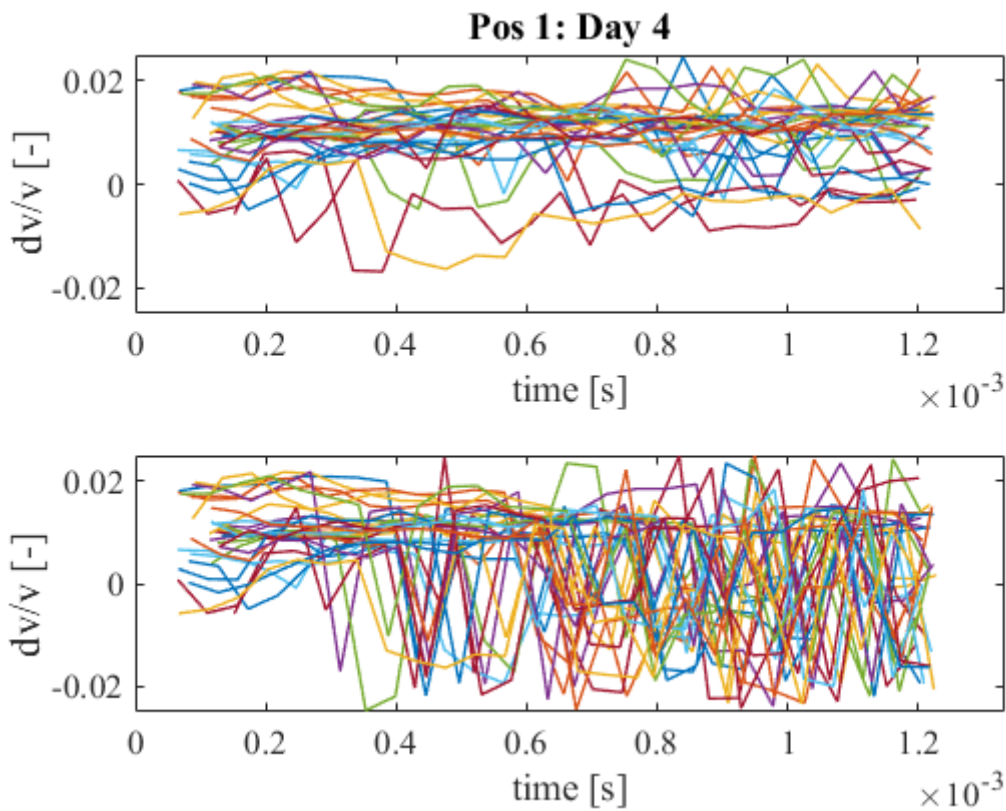


Figure 72: Comparison of  $dv/v$  over time of CWI between Measurement 3 and Measurement 4 at Position 1 between original script (bottom) and script with cycle skipping prevention (top)

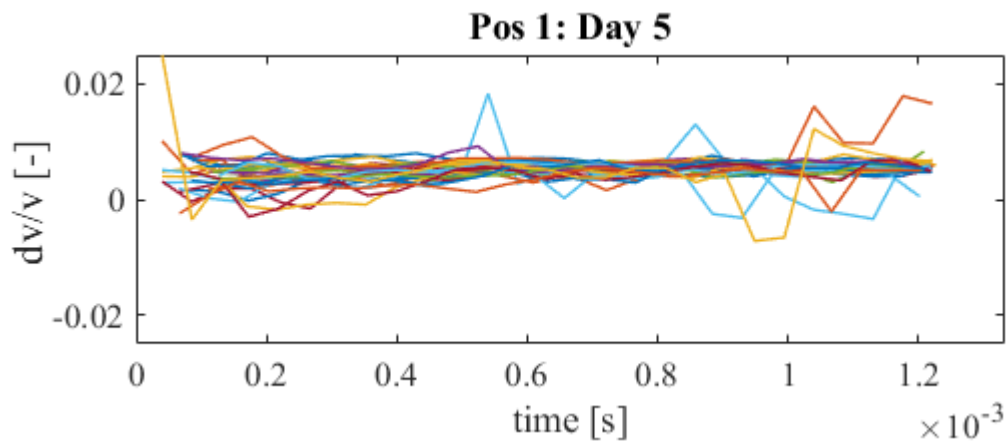


Figure 73: Corrected  $dv/v$  over time of CWI between Measurement 4 and Measurement 5 at Position 1 with cycle skipping prevention and outlier correction

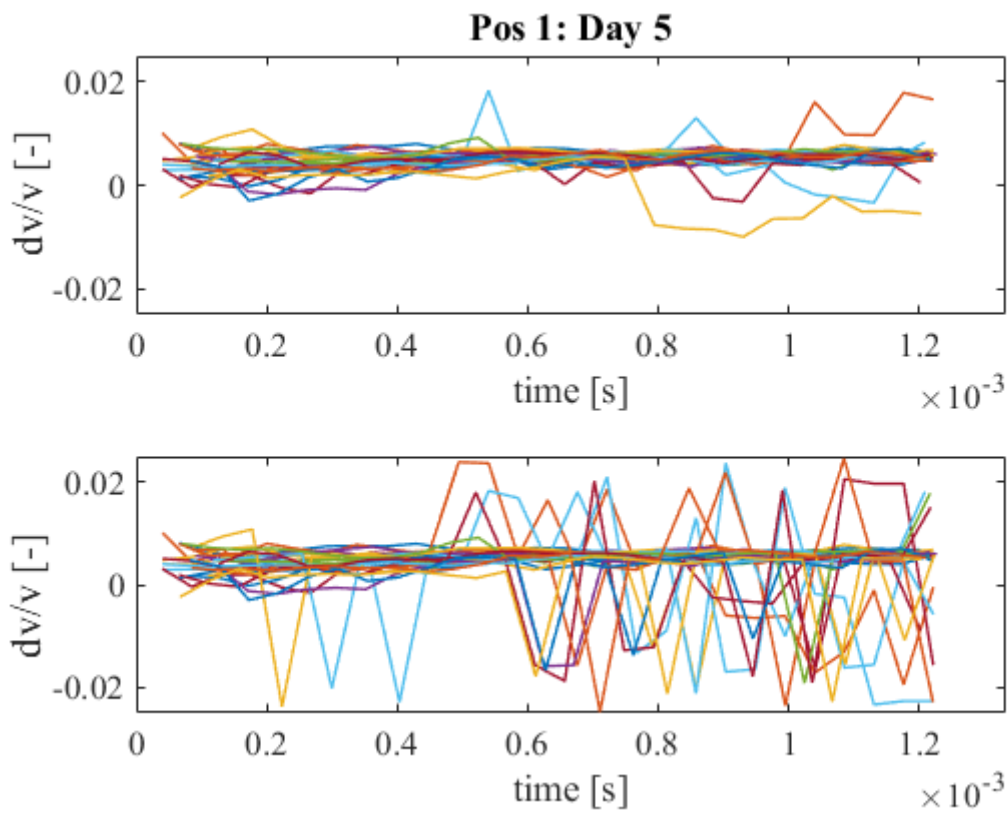


Figure 74: Comparison of  $dv/v$  over time of CWI between Measurement 4 and Measurement 5 at Position 1 between original script (bottom) and script with cycle skipping prevention (top)

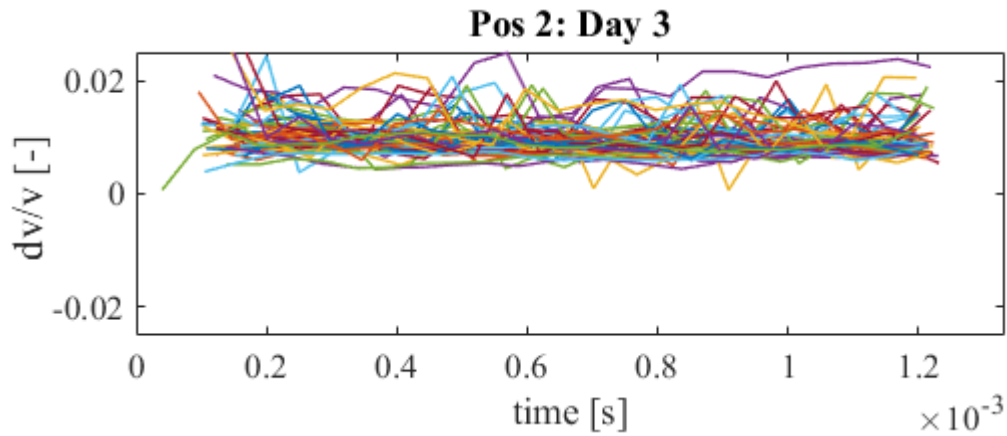


Figure 75: Corrected  $dv/v$  over time of CWI between Measurement 2 and Measurement 3 at Position 2 with cycle skipping prevention and outlier correction

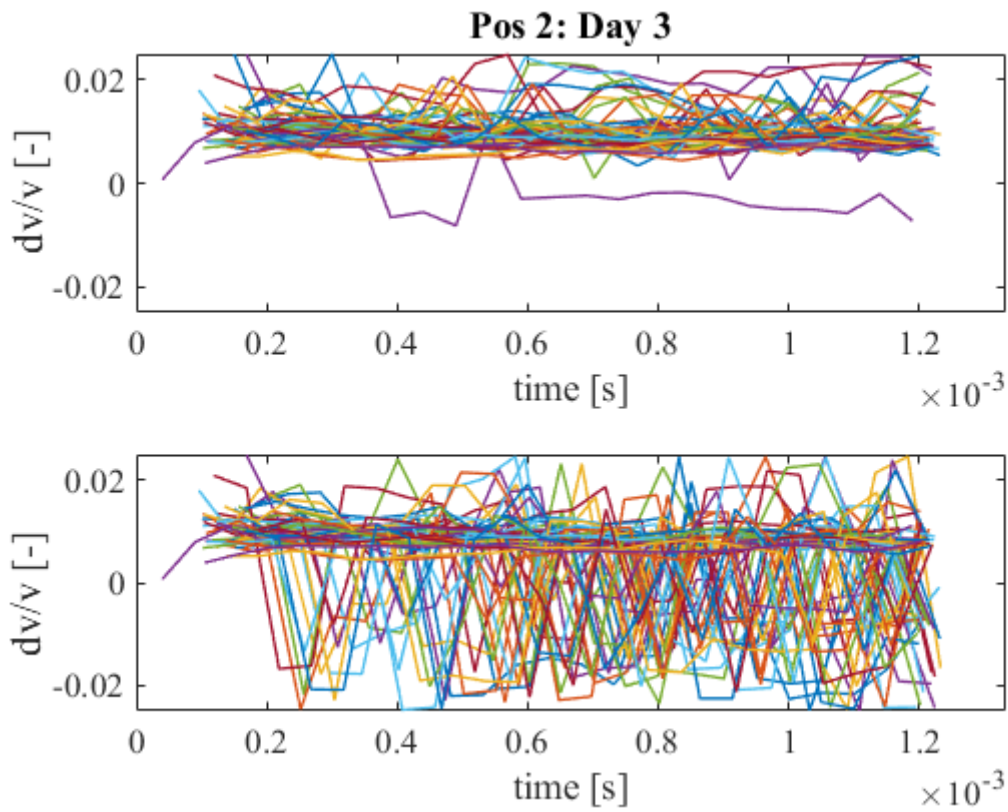


Figure 76: Comparison of  $dv/v$  over time of CWI between Measurement 2 and Measurement 3 at Position 2 between original script (bottom) and script with cycle skipping prevention (top)

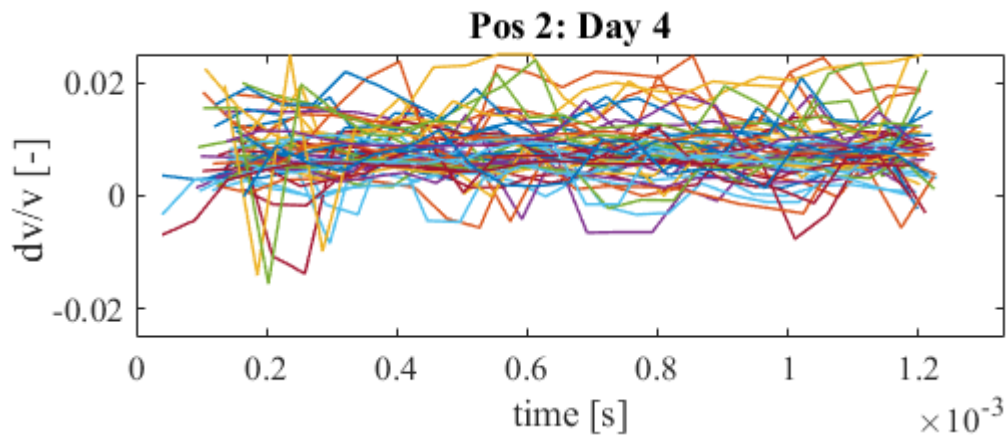


Figure 77: Corrected  $dv/v$  over time of CWI between Measurement 3 and Measurement 4 at Position 2 with cycle skipping prevention and outlier correction

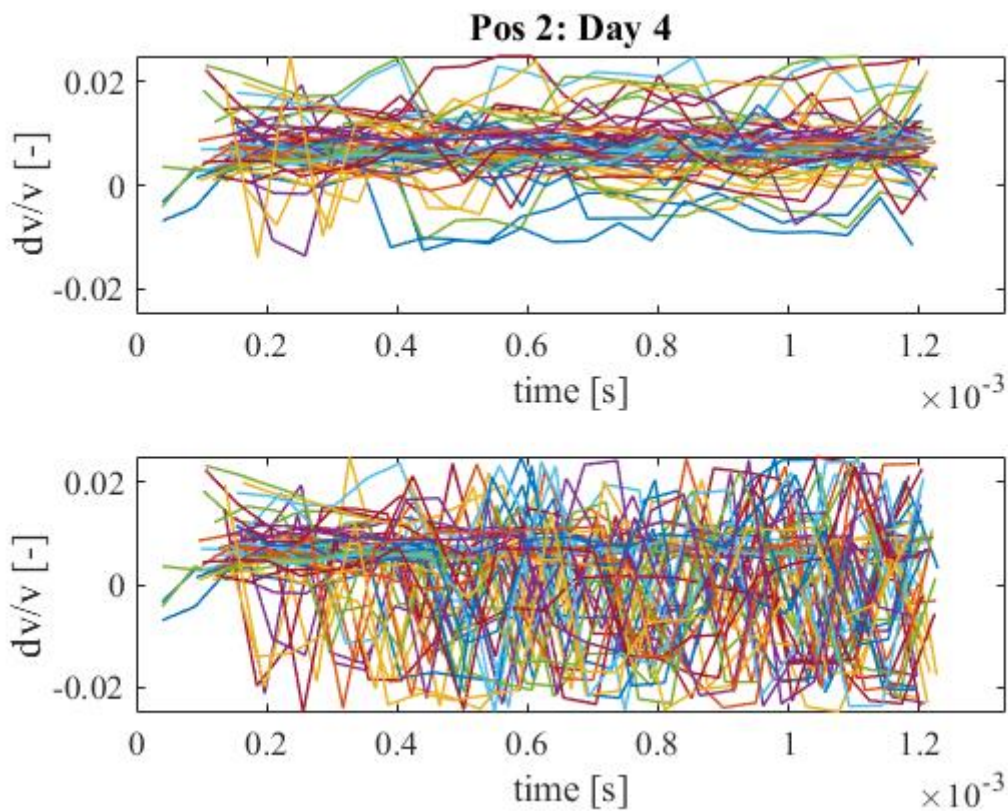


Figure 78: Comparison of  $dv/v$  over time of CWI between Measurement 3 and Measurement 4 at Position 2 between original script (bottom) and script with cycle skipping prevention (top)

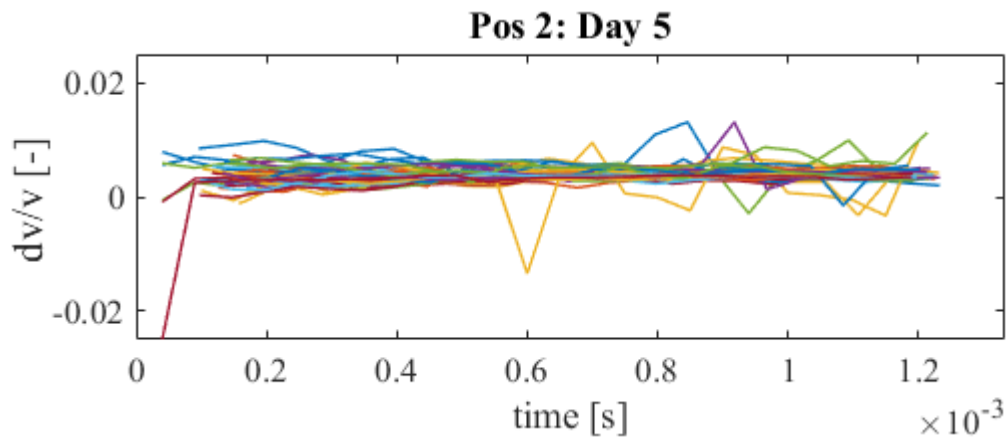


Figure 79: Corrected  $dv/v$  over time of CWI between Measurement 4 and Measurement 5 at Position 2 with cycle skipping prevention and outlier correction

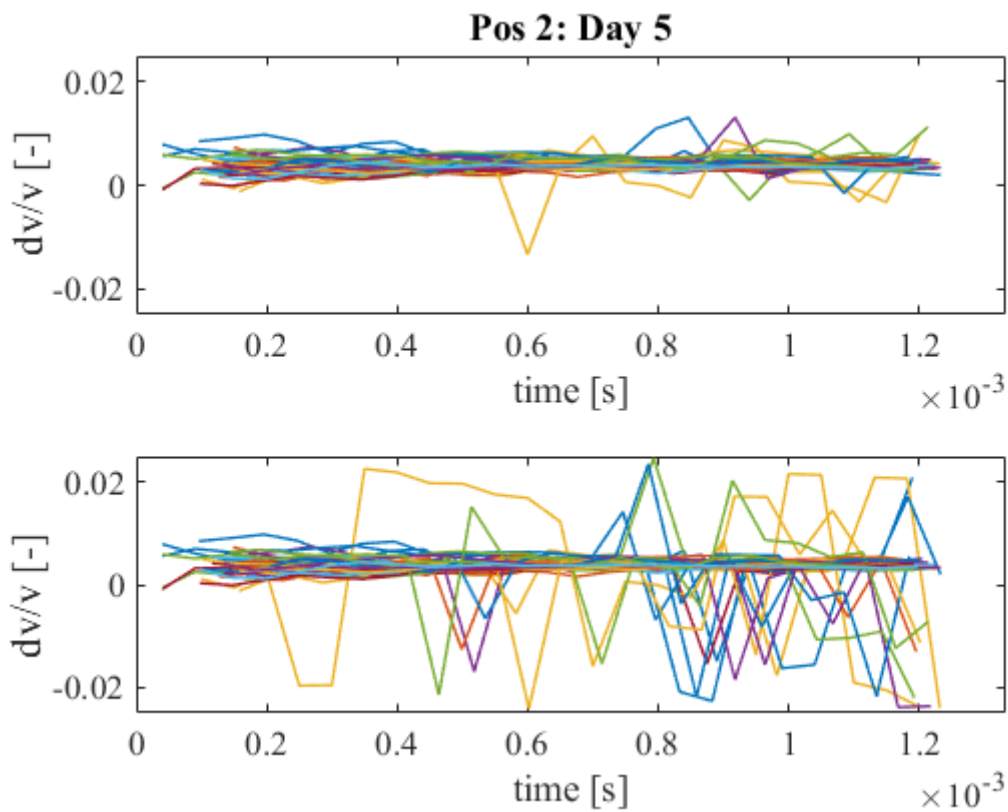


Figure 80: Comparison of  $dv/v$  over time of CWI between Measurement 4 and Measurement 5 at Position 2 between original script (bottom) and script with cycle skipping prevention (top)

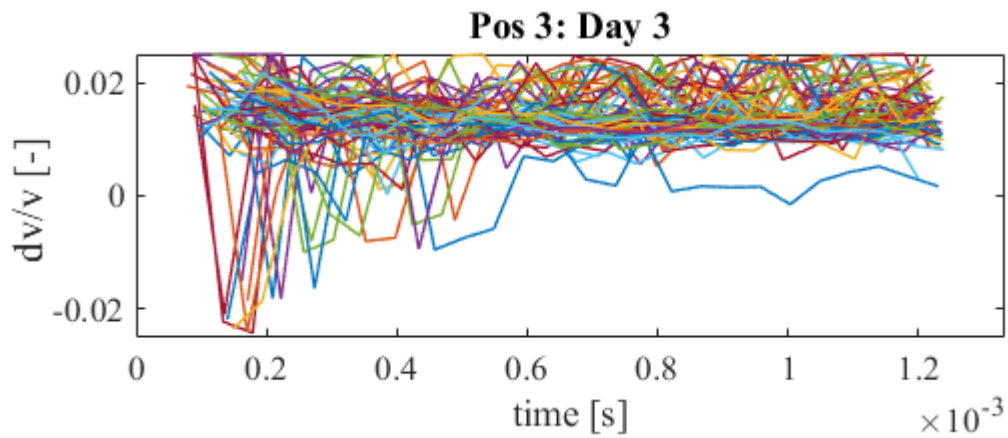


Figure 81: Corrected  $dv/v$  over time of CWI between Measurement 2 and Measurement 3 at Position 3 with cycle skipping prevention and outlier correction

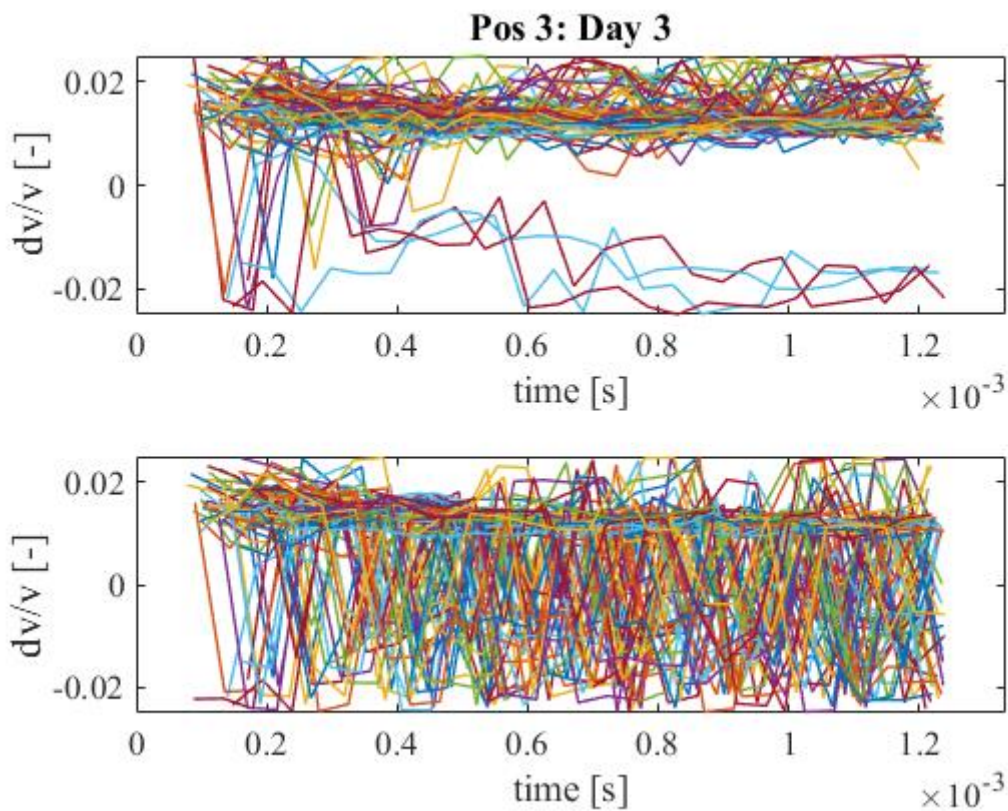


Figure 82: Comparison of  $dv/v$  over time of CWI between Measurement 2 and Measurement 3 at Position 3 between original script (bottom) and script with cycle skipping prevention (top)

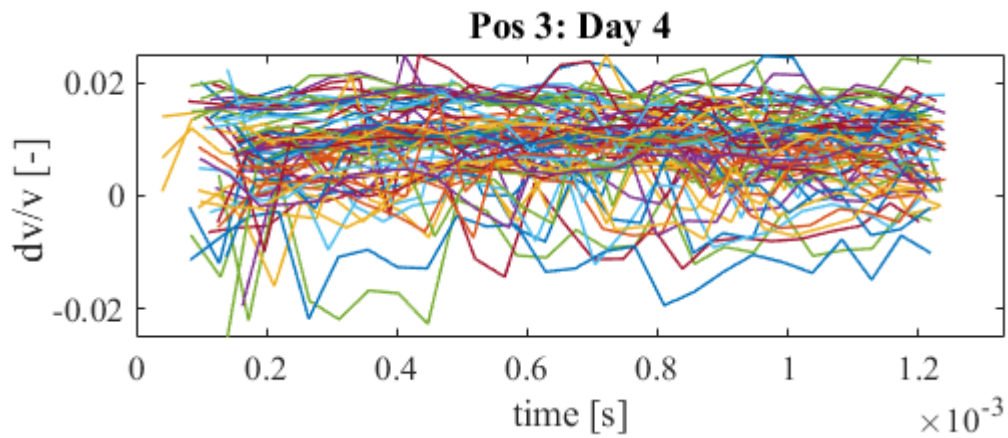


Figure 83: Corrected  $dv/v$  over time of CWI between Measurement 3 and Measurement 4 at Position 3 with cycle skipping prevention and outlier correction

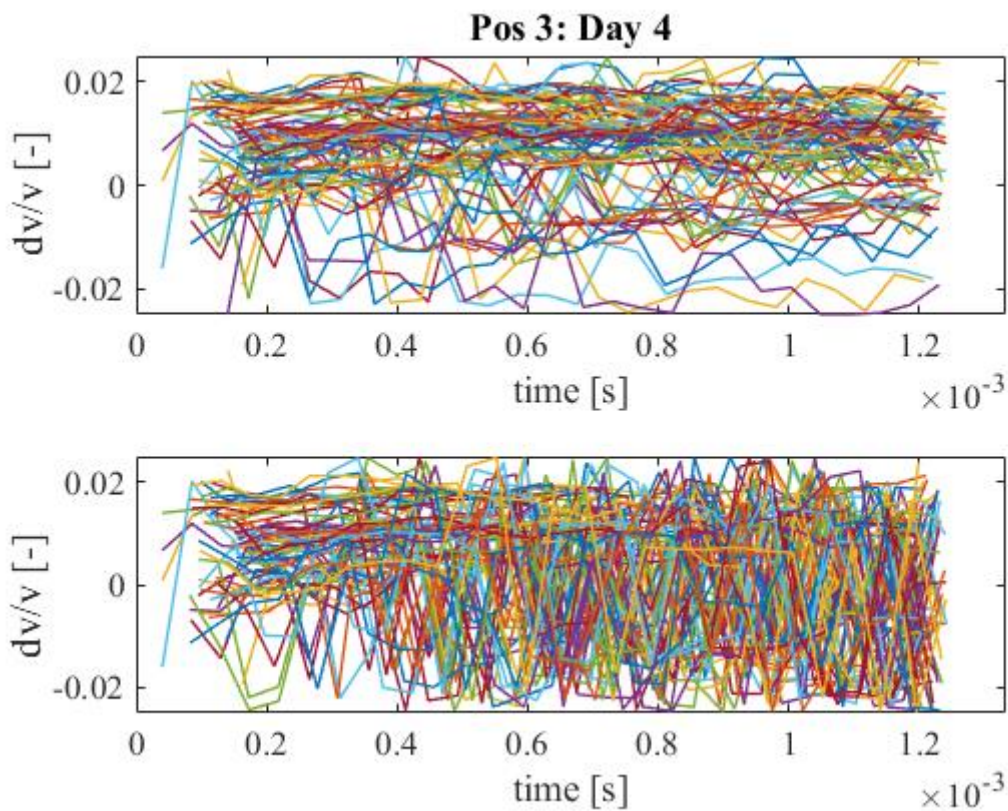


Figure 84: Comparison of  $dv/v$  over time of CWI between Measurement 3 and Measurement 4 at Position 3 between original script (bottom) and script with cycle skipping prevention (top)

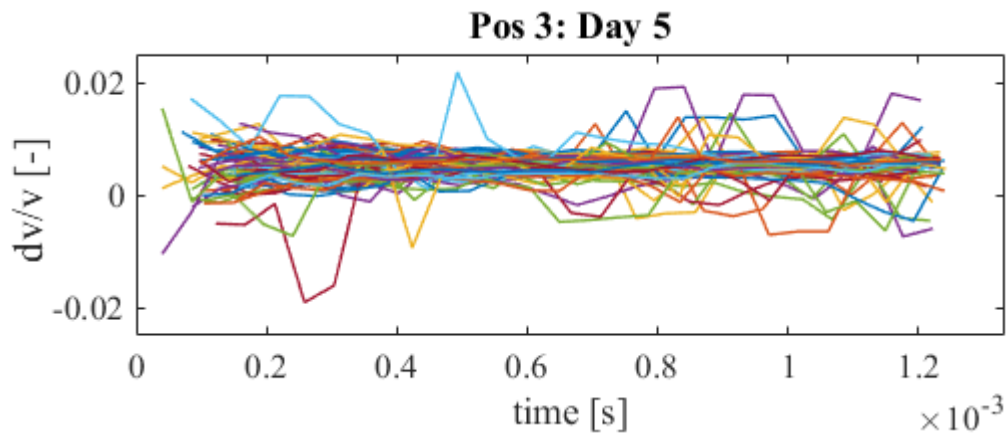


Figure 85: Corrected  $dv/v$  over time of CWI between Measurement 4 and Measurement 5 at Position 3 with cycle skipping prevention and outlier correction

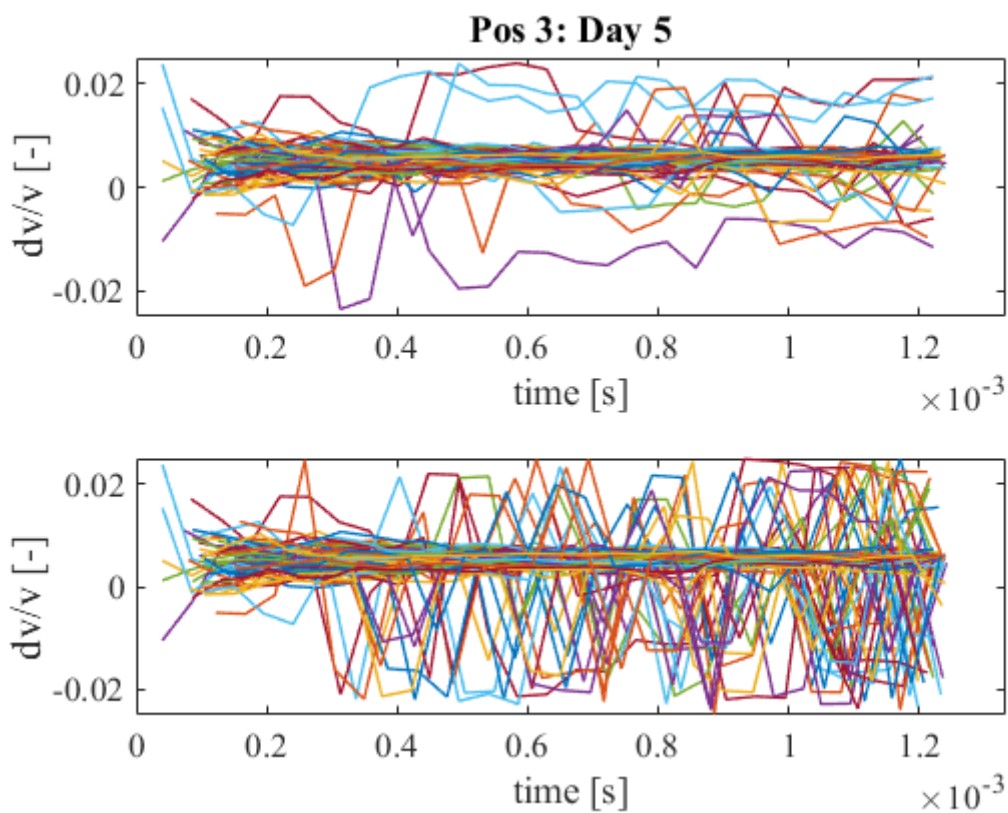


Figure 86: Comparison of  $dv/v$  over time of CWI between Measurement 4 and Measurement 5 at Position 3 between original script (bottom) and script with cycle skipping prevention (top)

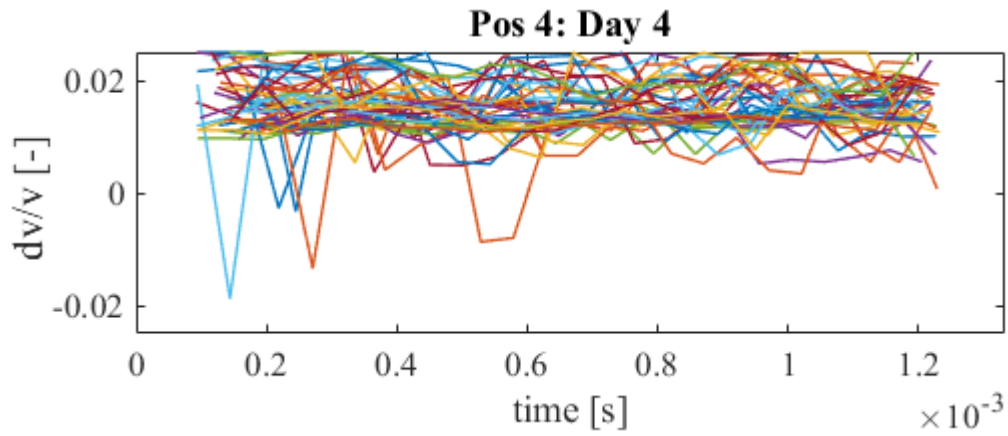


Figure 87: Corrected  $dv/v$  over time of CWI between Measurement 2 and Measurement 4 at Position 4 with cycle skipping prevention and outlier correction

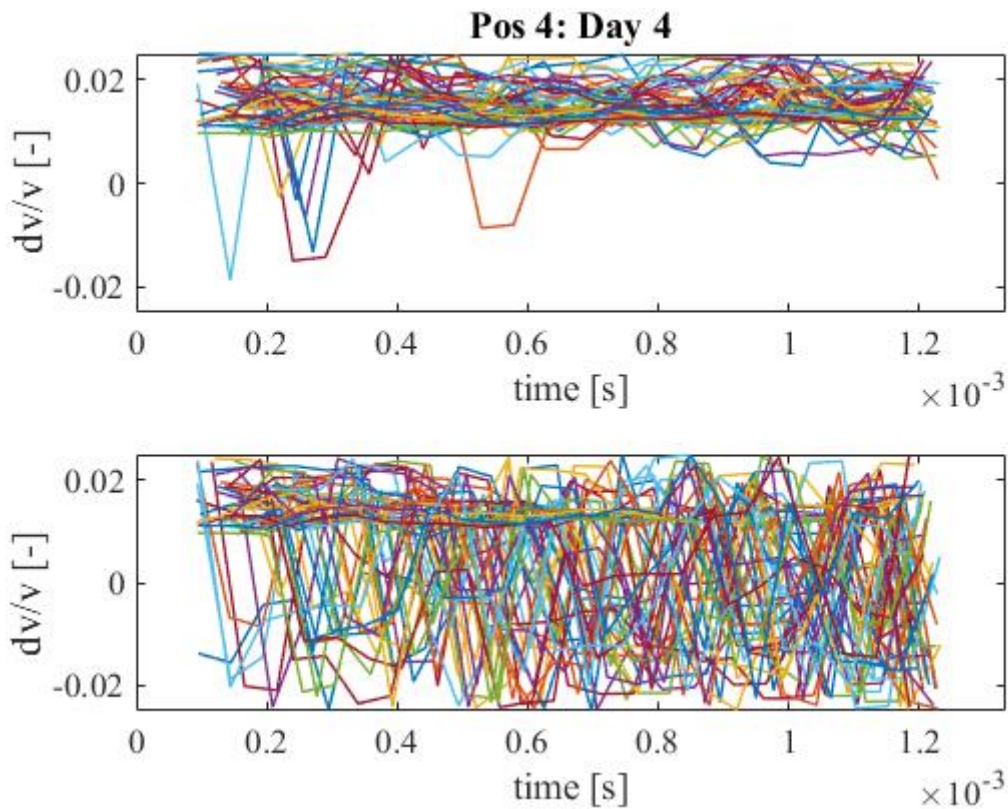


Figure 88: Comparison of  $dv/v$  over time of CWI between Measurement 2 and Measurement 4 at Position 4 between original script (bottom) and script with cycle skipping prevention (top)

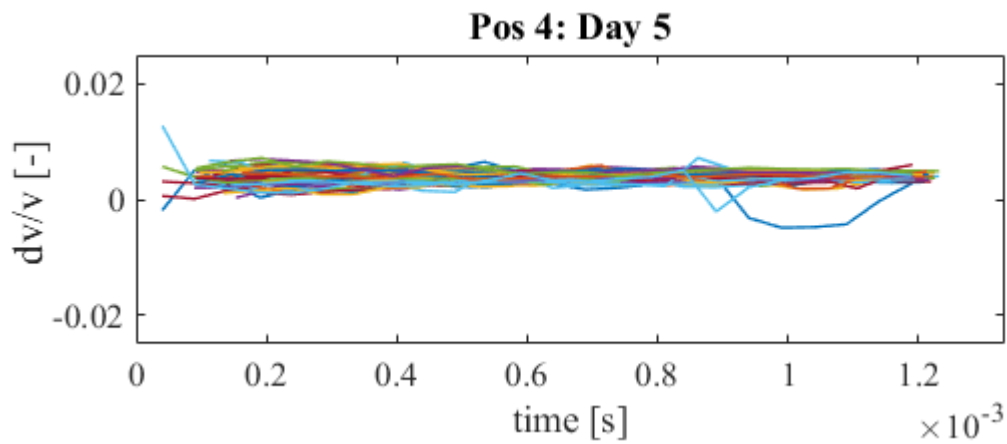


Figure 89: Corrected  $dv/v$  over time of CWI between Measurement 4 and Measurement 5 at Position 4 with cycle skipping prevention and outlier correction

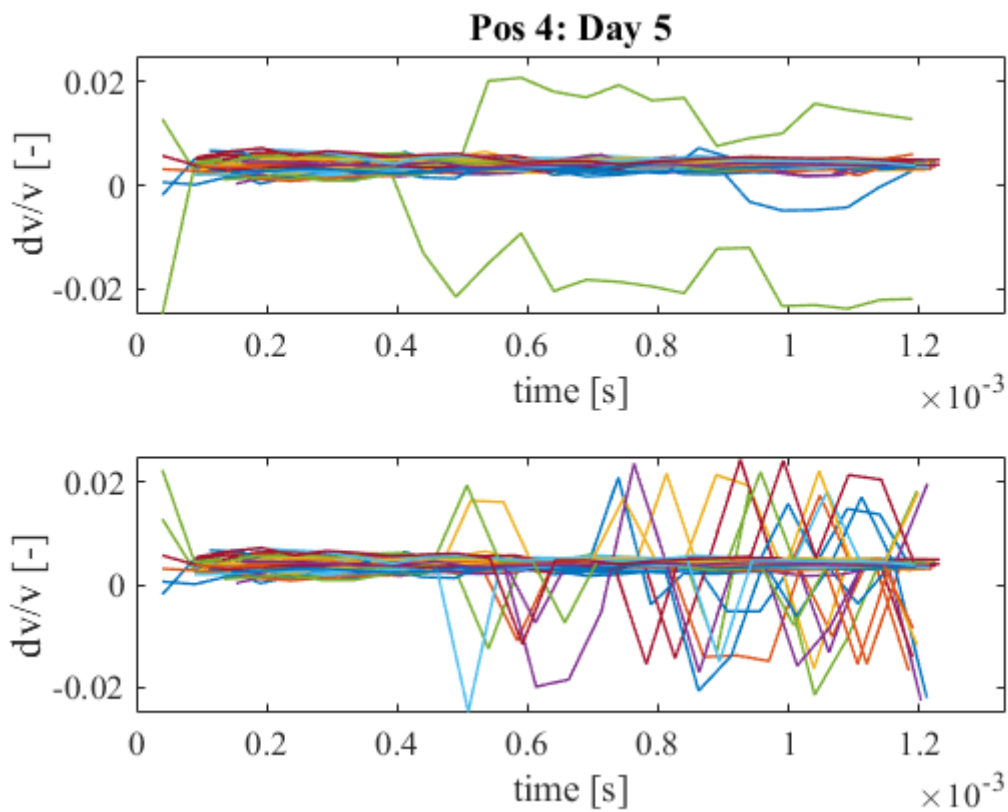


Figure 90: Comparison of  $dv/v$  over time of CWI between Measurement 4 and Measurement 5 at Position 4 between original script (bottom) and script with cycle skipping prevention (top)

## D. CWI results of field measurements

When comparisons are drawn between the CWI results of early measurements and later measurement, one observes clear differences in variance in  $dv/v$  and  $CC$ . From CWI of early measurements,  $dv/v$  and  $CC$  are very turbulent with inconsistent  $dv/v$ -values and frequent low  $CC$ . On the other hand, the outputs from CWI of later measurements are more consistent with significantly higher  $CC$ , despite the increase in time lapse between the later measurements. The CWI results of later measurements are consequently more reliable. This holds true as long as the time between measurements remain proportional, e.g. a time period within two months.

The suboptimal CWI results of early measurements are most likely related to the relatively volatile properties of young concrete. Due to the many possible parameters affecting the acoustoelastic properties of the medium in an exposed environment, a definitive cause is hard to pinpoint. With the given circumstances, the most probable cause is the continued concrete hydration during the early measurements, which has finalized during the later measurements. When there is a long time period in between measurements the evolving properties of maturing concrete and the environmental exposure cause complications for cross-correlation between the measured wave signals.

As the CWI results of Measurement 6, Measurement 7 and Measurement 8 are obtained from measurements in relatively quick succession, cross-correlation between the signals return good comprehensive results, as shown by the consistent  $dv/v$  and high  $CC$ .

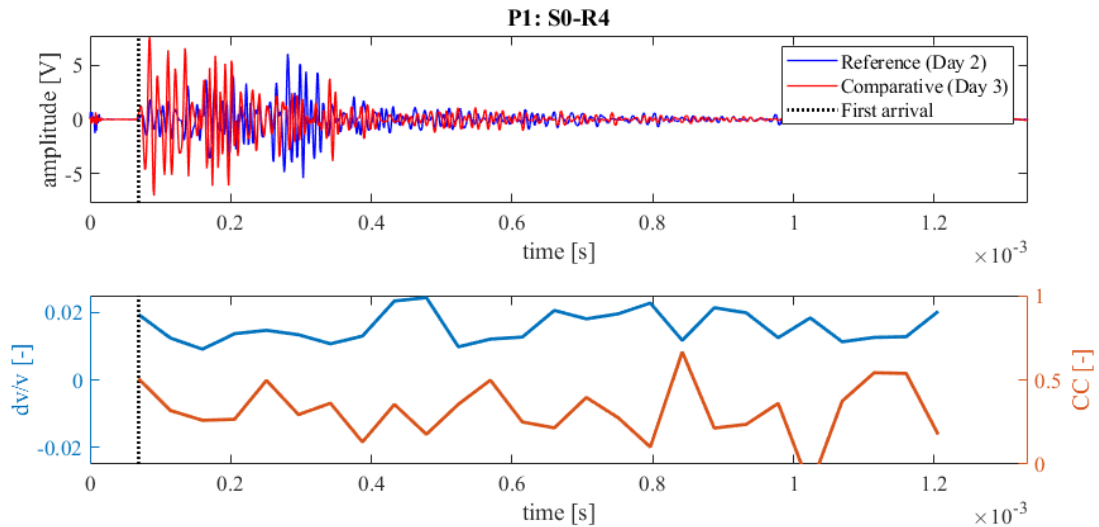


Figure 91: Wave signals of Measurement 2 (blue) and Measurement 3 (red) between principal sensor pair Source S0 and Receiver S4 at Position 1 (top),  $dv/v$  (blue) and  $CC$  (orange) results from CWI over the signal travel time divided in stretching windows (bottom)

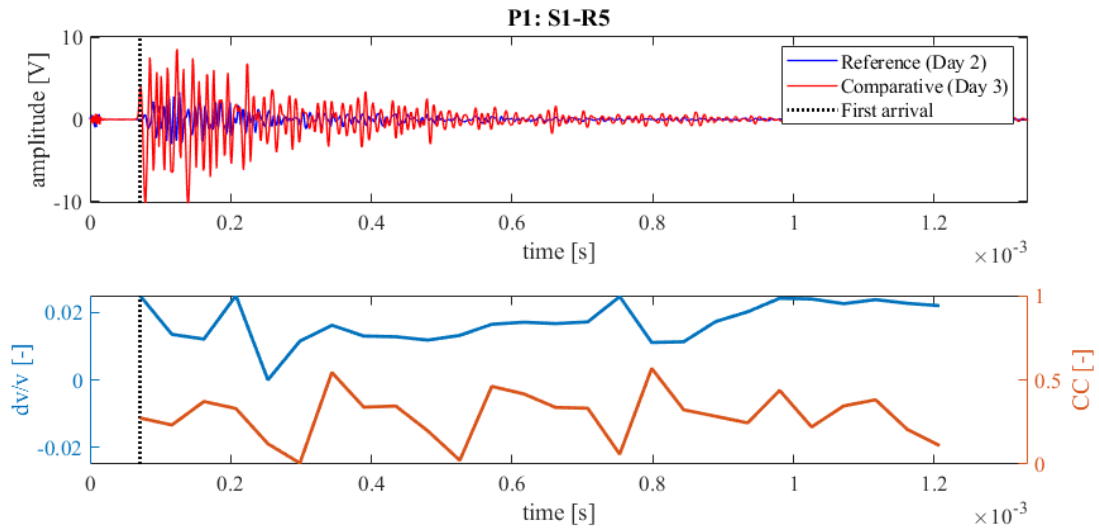


Figure 92: Wave signals of Measurement 2 (blue) and Measurement 3 (red) between principal sensor pair Source S1 and Receiver S5 at Position 1 (top),  $dv/v$  (blue) and CC (orange) results from CWI over the signal travel time divided in stretching windows (bottom)

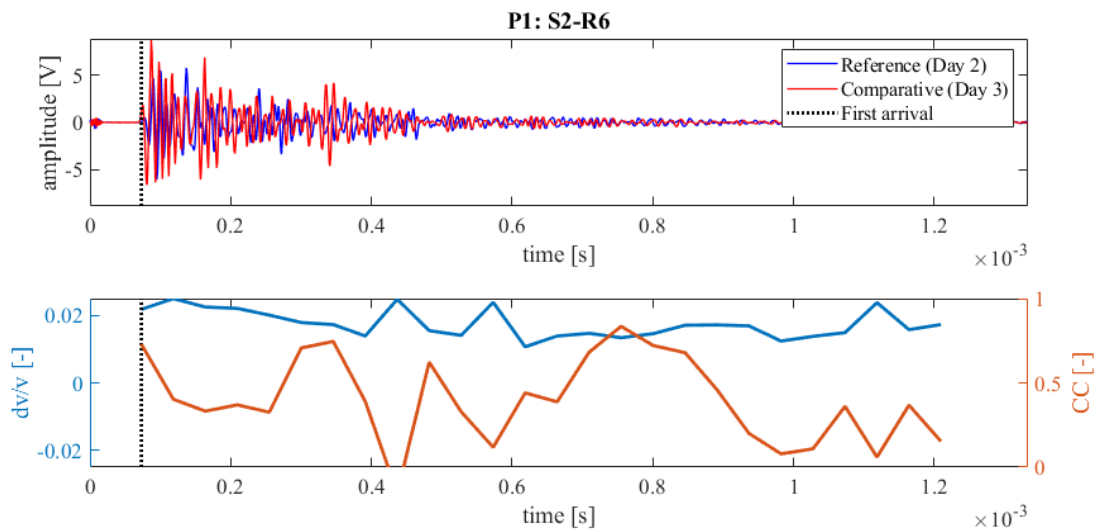


Figure 93: Wave signals of Measurement 2 (blue) and Measurement 3 (red) between principal sensor pair Source S2 and Receiver S6 at Position 1 (top),  $dv/v$  (blue) and CC (orange) results from CWI over the signal travel time divided in stretching windows (bottom)

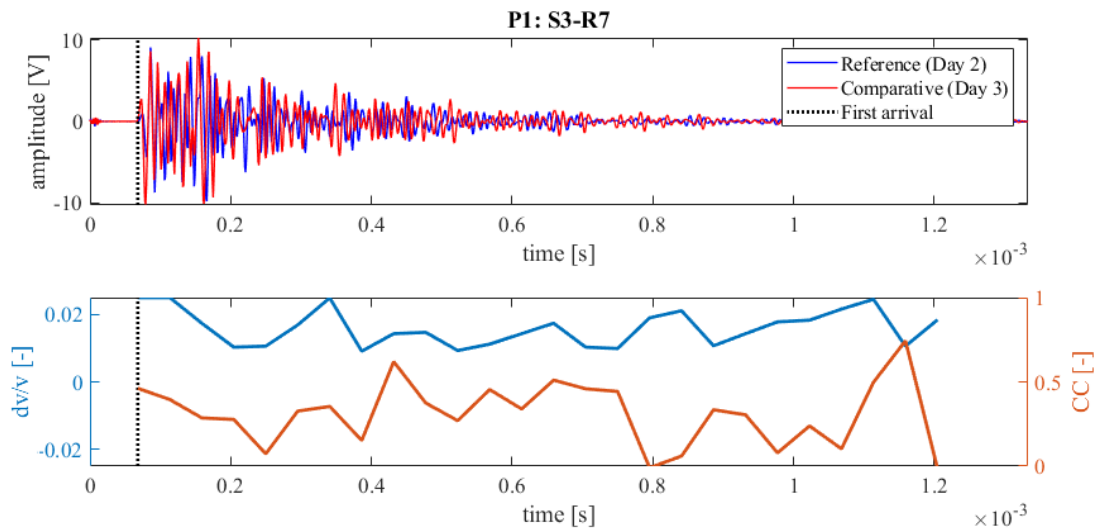


Figure 94: Wave signals of Measurement 2 (blue) and Measurement 3 (red) between principal sensor pair Source S3 and Receiver S7 at Position 1 (top),  $dv/v$  (blue) and  $CC$  (orange) results from CWI over the signal travel time divided in stretching windows (bottom)

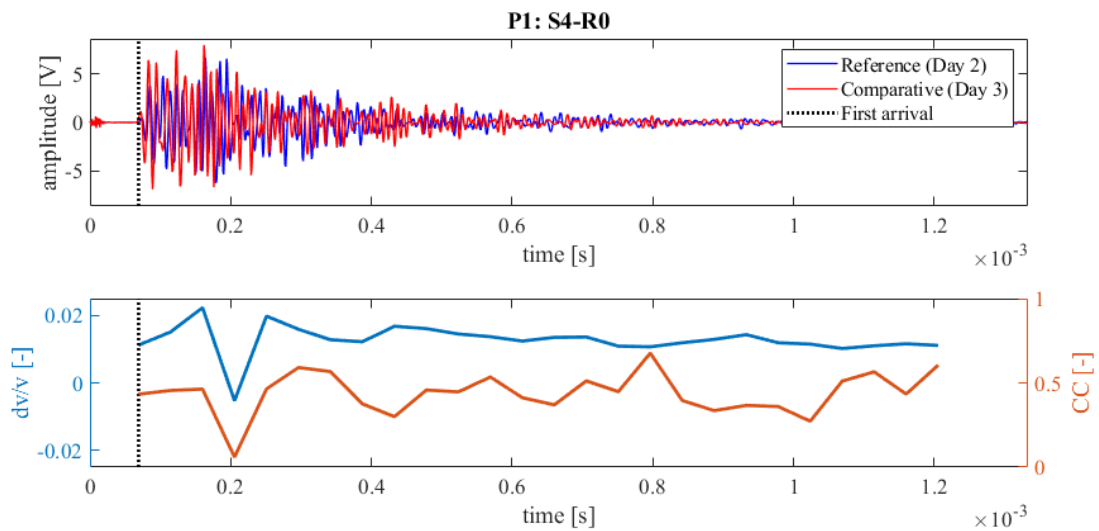


Figure 95: Wave signals of Measurement 2 (blue) and Measurement 3 (red) between principal sensor pair Source S4 and Receiver S0 at Position 1 (top),  $dv/v$  (blue) and  $CC$  (orange) results from CWI over the signal travel time divided in stretching windows (bottom)

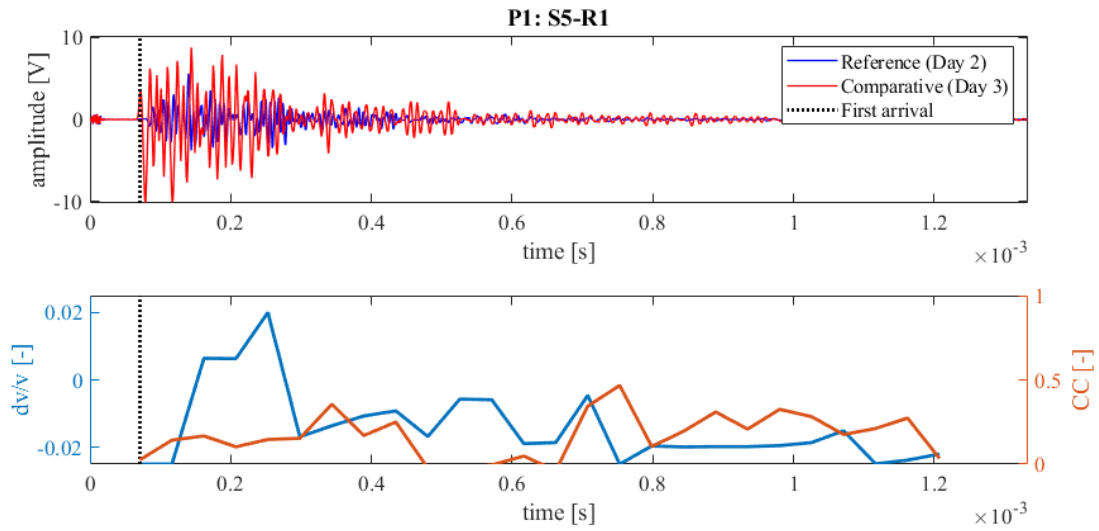


Figure 96: Wave signals of Measurement 2 (blue) and Measurement 3 (red) between principal sensor pair Source S5 and Receiver S1 at Position 1 (top),  $dv/v$  (blue) and CC (orange) results from CWI over the signal travel time divided in stretching windows (bottom)

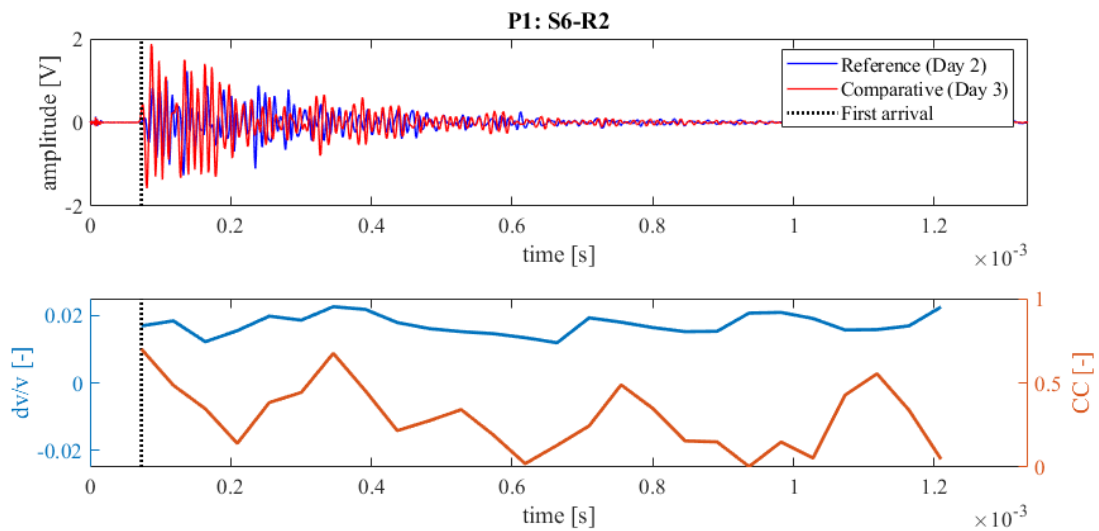


Figure 97: Wave signals of Measurement 2 (blue) and Measurement 3 (red) between principal sensor pair Source S6 and Receiver S2 at Position 1 (top),  $dv/v$  (blue) and CC (orange) results from CWI over the signal travel time divided in stretching windows (bottom)

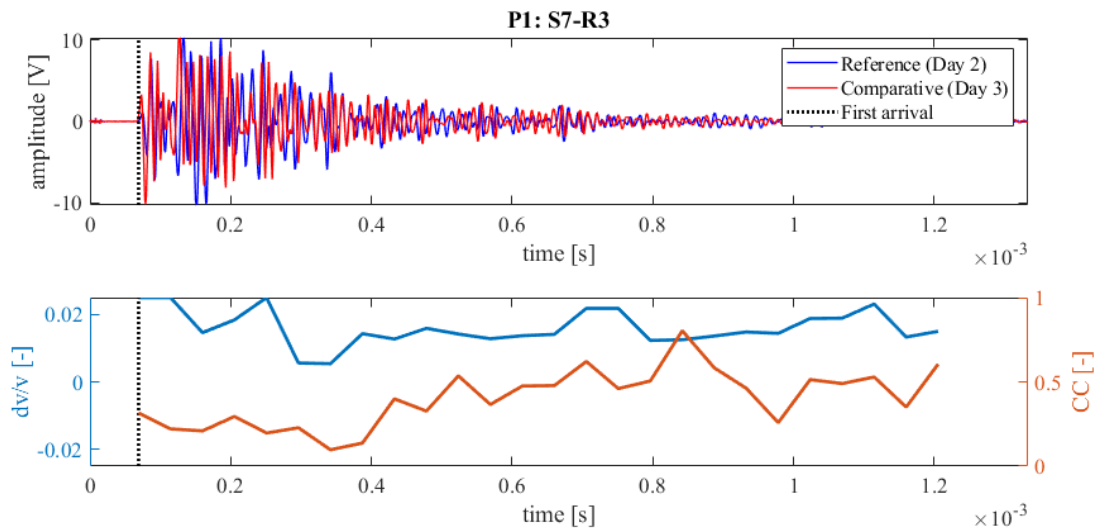


Figure 98: Wave signals of Measurement 2 (blue) and Measurement 3 (red) between principal sensor pair Source S7 and Receiver S3 at Position 1 (top),  $dv/v$  (blue) and CC (orange) results from CWI over the signal travel time divided in stretching windows (bottom)

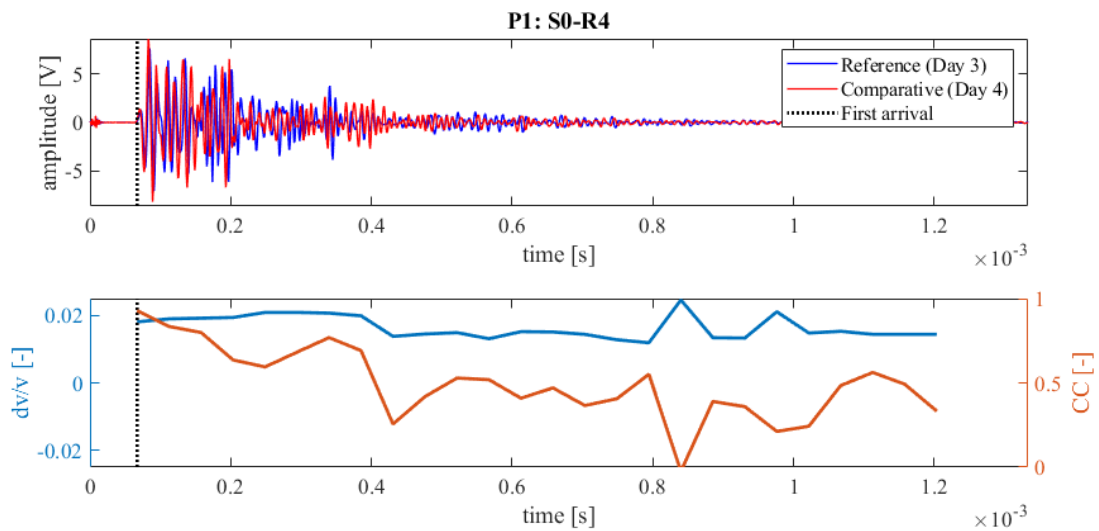


Figure 99: Wave signals of Measurement 3 (blue) and Measurement 4 (red) between principal sensor pair Source S0 and Receiver S4 at Position 1 (top),  $dv/v$  (blue) and CC (orange) results from CWI over the signal travel time divided in stretching windows (bottom)

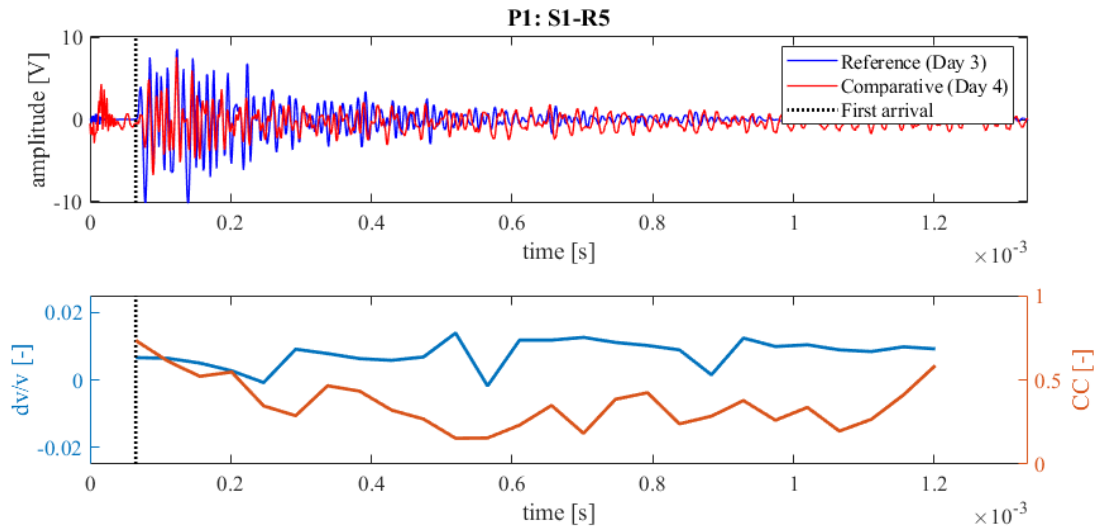


Figure 100: Wave signals of Measurement 3 (blue) and Measurement 4 (red) between principal sensor pair Source S1 and Receiver S5 at Position 1 (top),  $dv/v$  (blue) and CC (orange) results from CWI over the signal travel time divided in stretching windows (bottom)

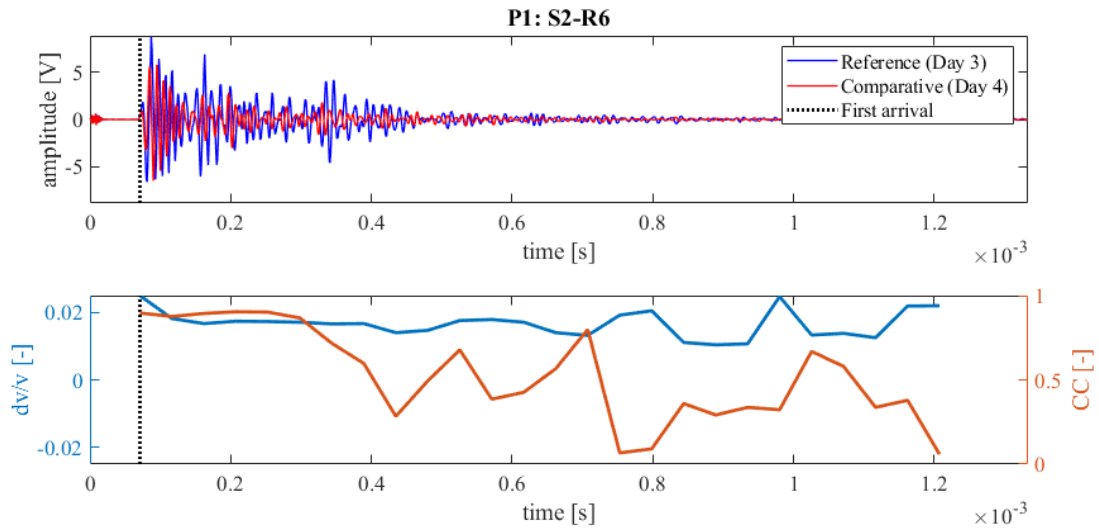


Figure 101: Wave signals of Measurement 3 (blue) and Measurement 4 (red) between principal sensor pair Source S2 and Receiver S6 at Position 1 (top),  $dv/v$  (blue) and CC (orange) results from CWI over the signal travel time divided in stretching windows (bottom)

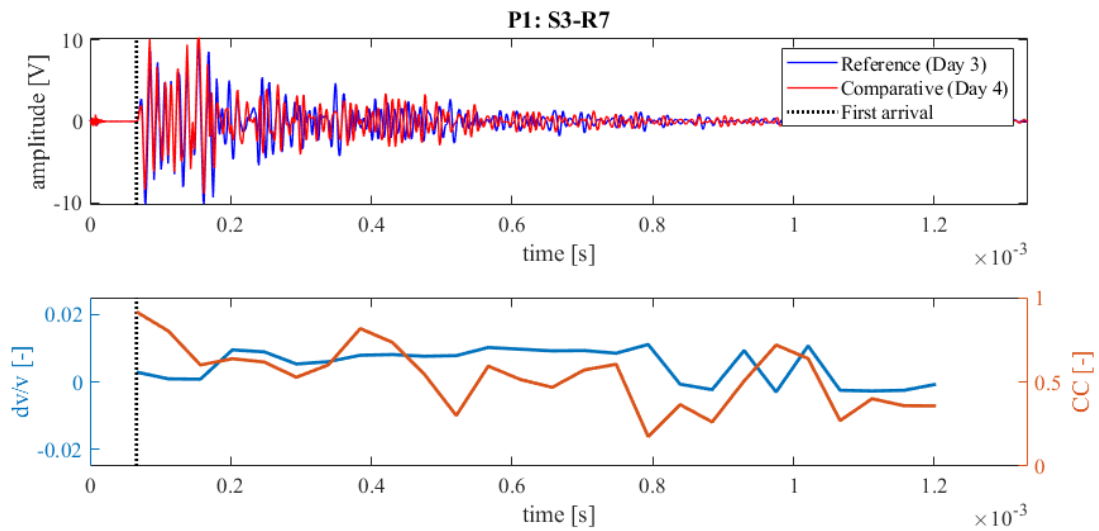


Figure 102: Wave signals of Measurement 3 (blue) and Measurement 4 (red) between principal sensor pair Source S3 and Receiver S7 at Position 1 (top),  $dv/v$  (blue) and  $CC$  (orange) results from CWI over the signal travel time divided in stretching windows (bottom)

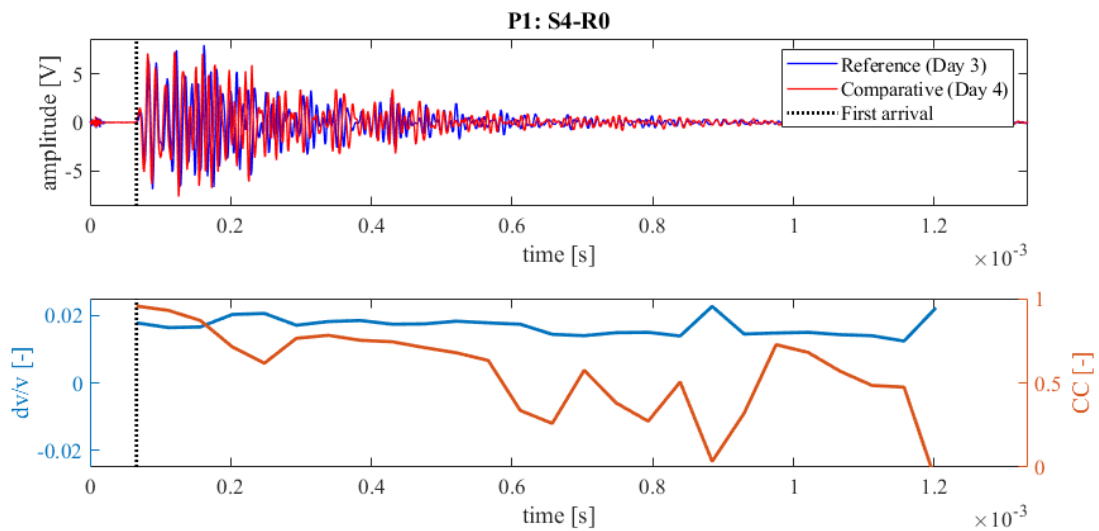


Figure 103: Wave signals of Measurement 3 (blue) and Measurement 4 (red) between principal sensor pair Source S4 and Receiver S0 at Position 1 (top),  $dv/v$  (blue) and  $CC$  (orange) results from CWI over the signal travel time divided in stretching windows (bottom)

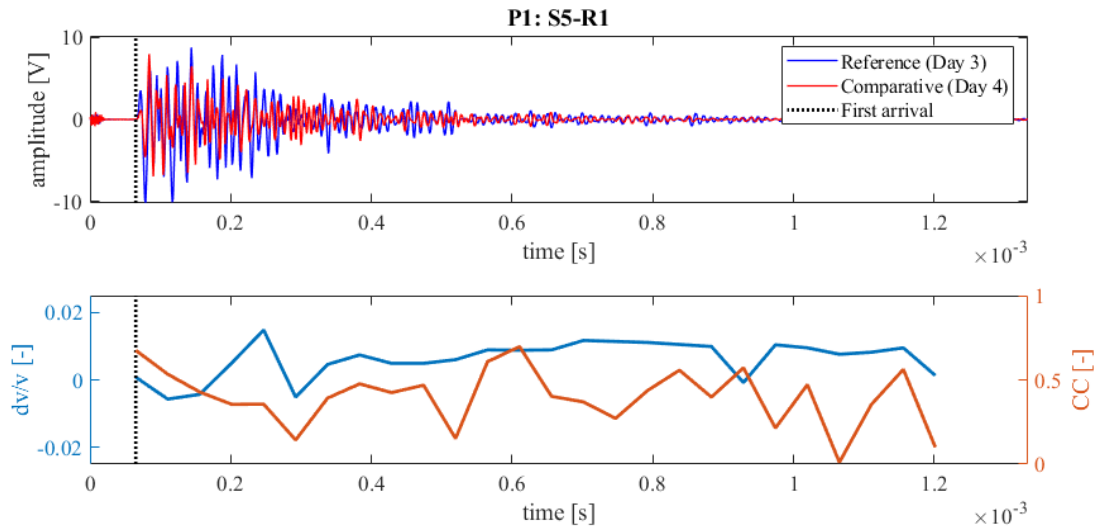


Figure 104: Wave signals of Measurement 3 (blue) and Measurement 4 (red) between principal sensor pair Source S5 and Receiver S1 at Position 1 (top),  $dv/v$  (blue) and  $CC$  (orange) results from CWI over the signal travel time divided in stretching windows (bottom)

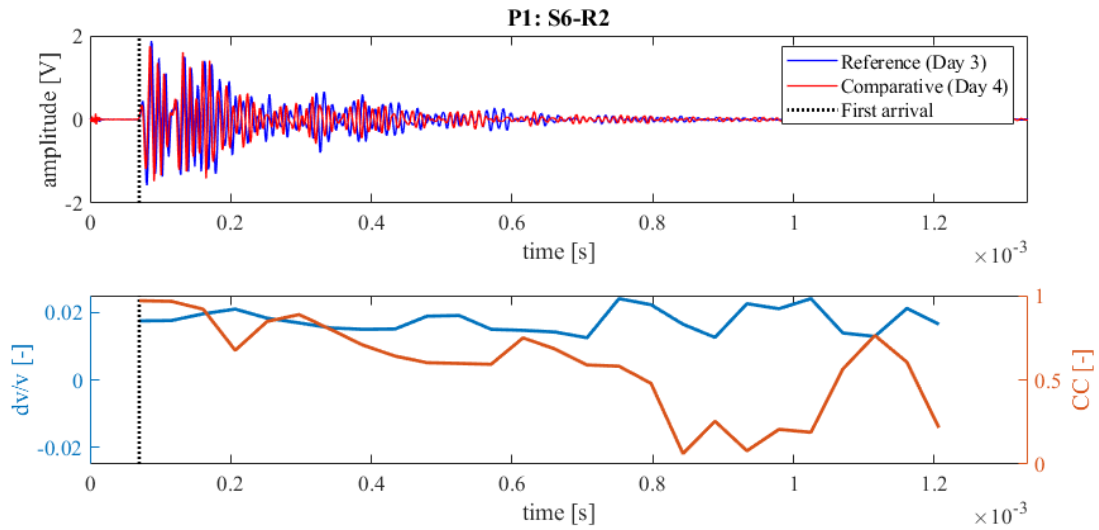


Figure 105: Wave signals of Measurement 3 (blue) and Measurement 4 (red) between principal sensor pair Source S6 and Receiver S2 at Position 1 (top),  $dv/v$  (blue) and  $CC$  (orange) results from CWI over the signal travel time divided in stretching windows (bottom)

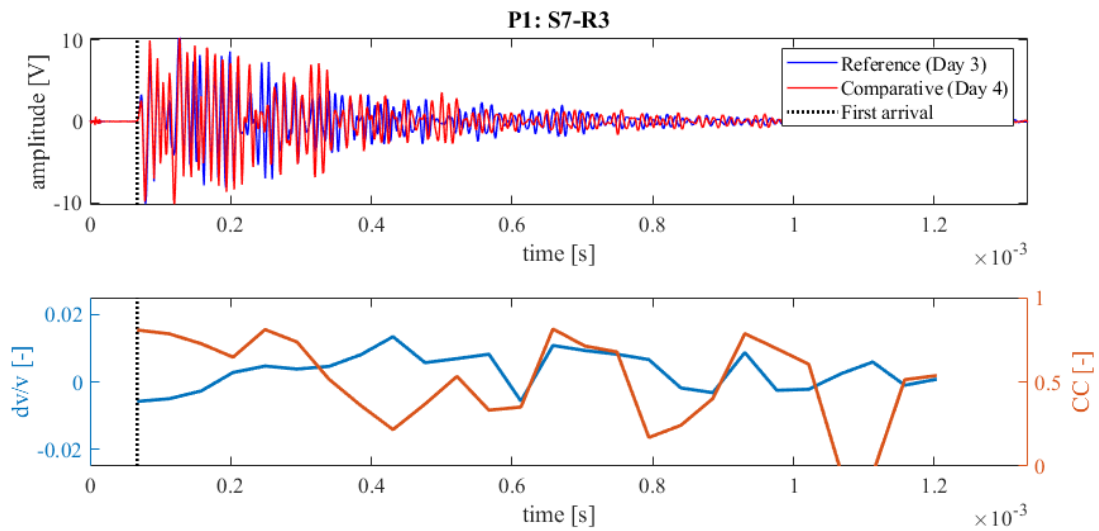


Figure 106: Wave signals of Measurement 3 (blue) and Measurement 4 (red) between principal sensor pair Source S7 and Receiver S3 at Position 1 (top),  $dv/v$  (blue) and CC (orange) results from CWI over the signal travel time divided in stretching windows (bottom)

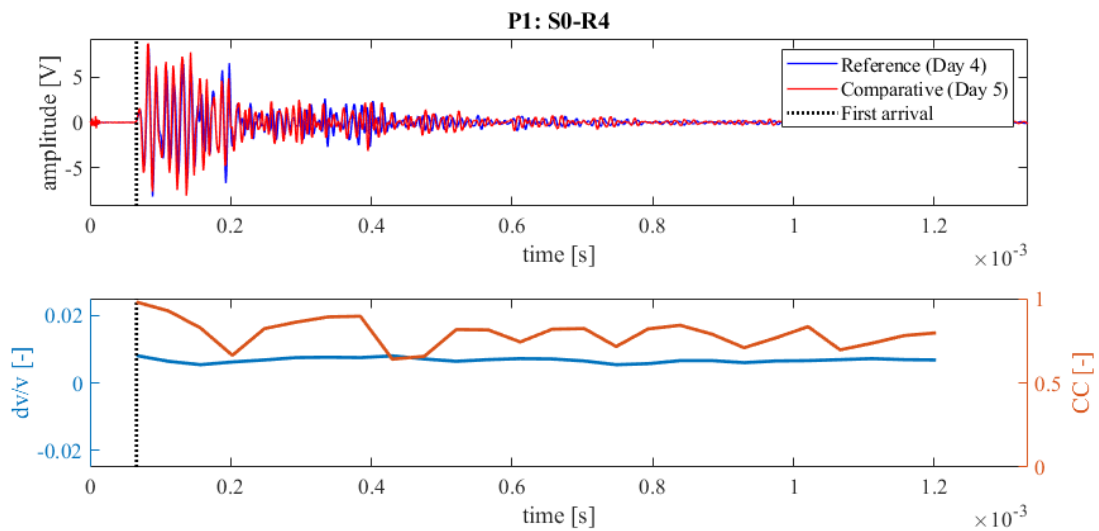


Figure 107: Wave signals of Measurement 4 (blue) and Measurement 5 (red) between principal sensor pair Source S0 and Receiver S4 at Position 1 (top),  $dv/v$  (blue) and CC (orange) results from CWI over the signal travel time divided in stretching windows (bottom)

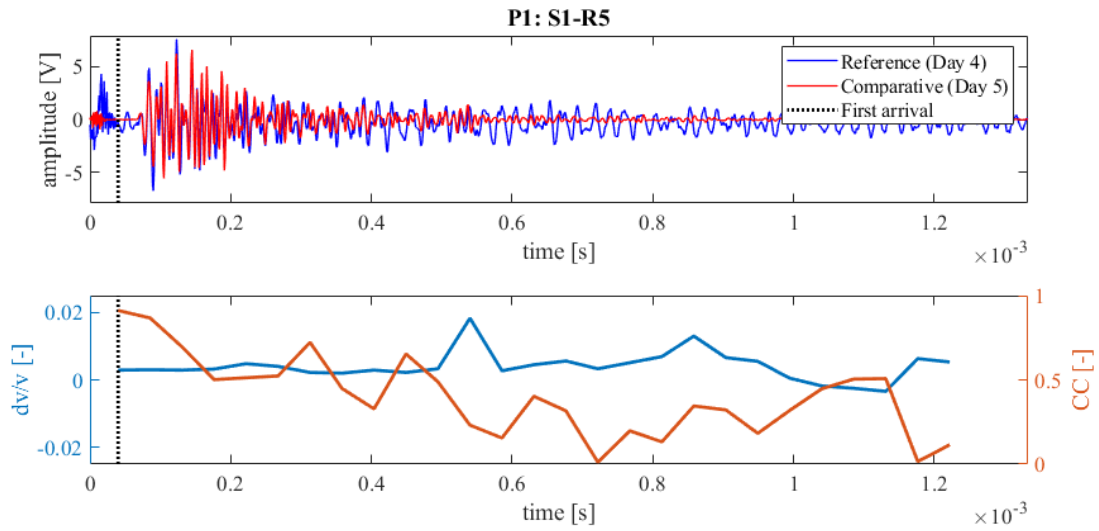


Figure 108: Wave signals of Measurement 4 (blue) and Measurement 5 (red) between principal sensor pair Source S1 and Receiver S5 at Position 1 (top),  $dv/v$  (blue) and  $CC$  (orange) results from CWI over the signal travel time divided in stretching windows (bottom)

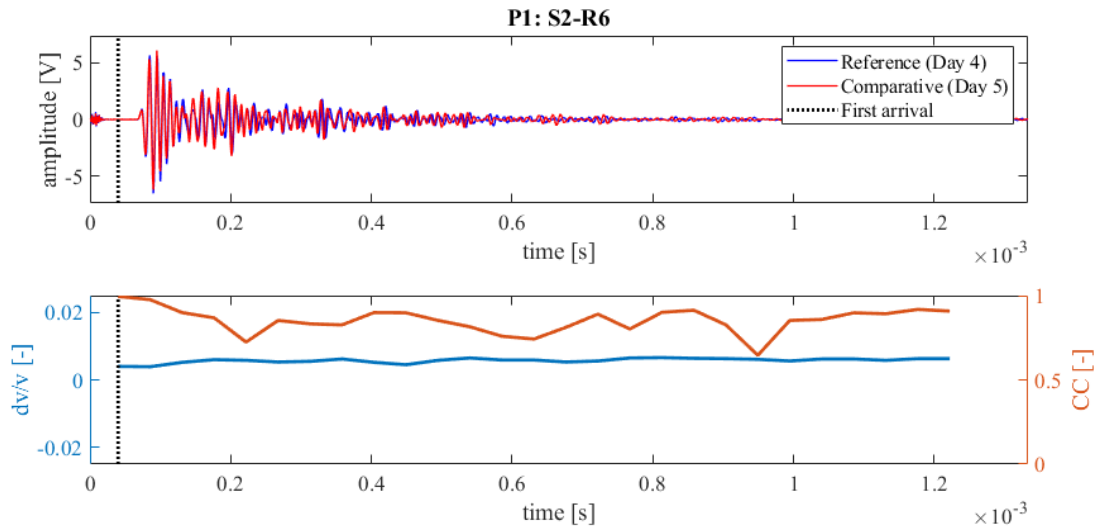


Figure 109: Wave signals of Measurement 4 (blue) and Measurement 5 (red) between principal sensor pair Source S2 and Receiver S6 at Position 1 (top),  $dv/v$  (blue) and  $CC$  (orange) results from CWI over the signal travel time divided in stretching windows (bottom)

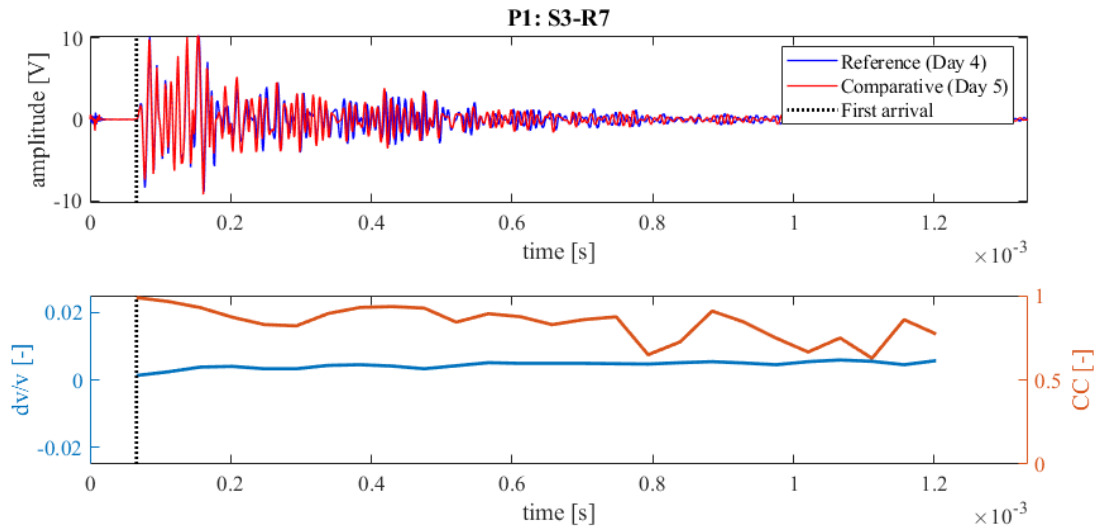


Figure 110: Wave signals of Measurement 4 (blue) and Measurement 5 (red) between principal sensor pair Source S3 and Receiver S7 at Position 1 (top),  $dv/v$  (blue) and  $CC$  (orange) results from CWI over the signal travel time divided in stretching windows (bottom)

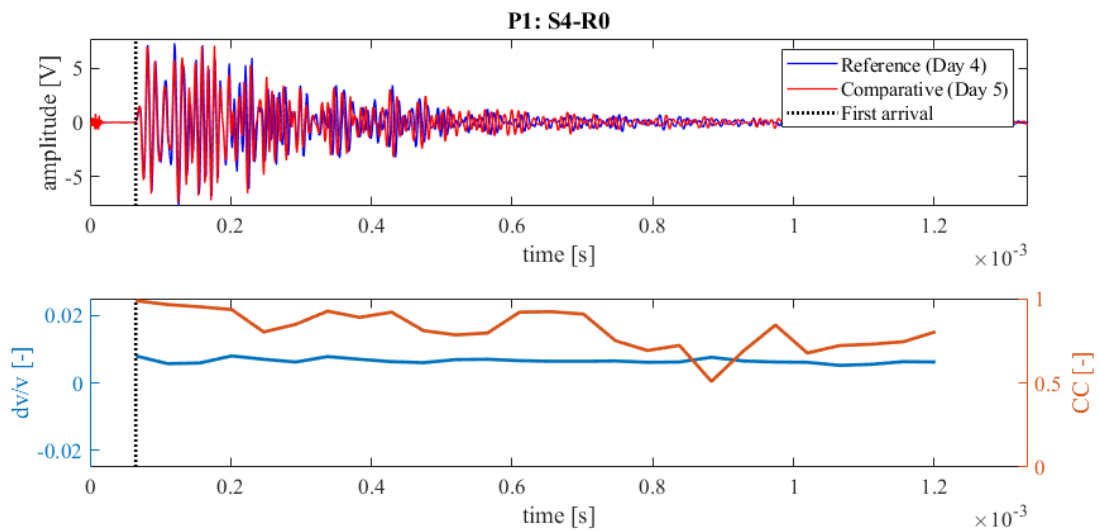


Figure 111: Wave signals of Measurement 4 (blue) and Measurement 5 (red) between principal sensor pair Source S4 and Receiver S0 at Position 1 (top),  $dv/v$  (blue) and  $CC$  (orange) results from CWI over the signal travel time divided in stretching windows (bottom)

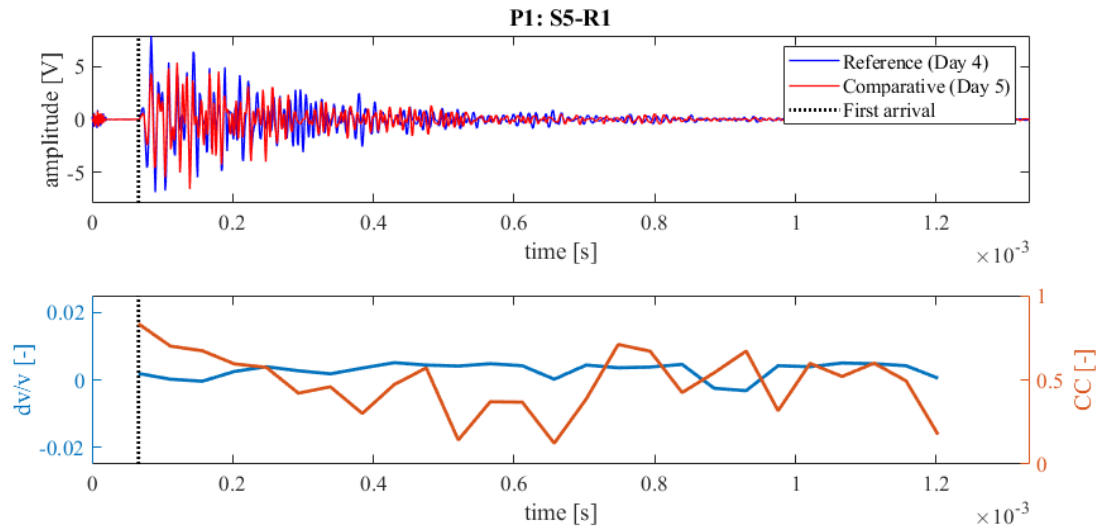


Figure 112: Wave signals of Measurement 4 (blue) and Measurement 5 (red) between principal sensor pair Source S5 and Receiver S1 at Position 1 (top),  $dv/v$  (blue) and  $CC$  (orange) results from CWI over the signal travel time divided in stretching windows (bottom)

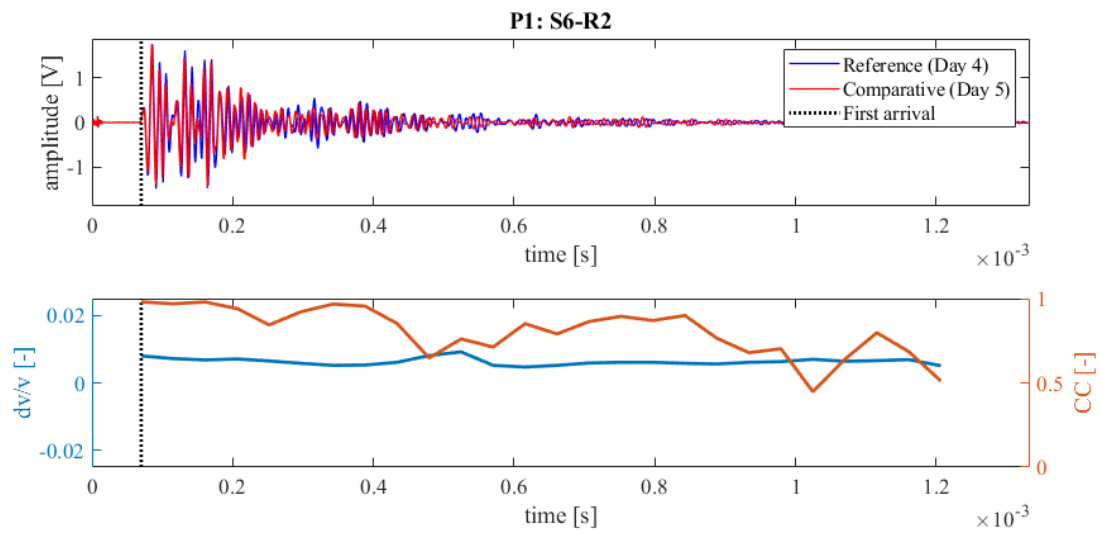


Figure 113: Wave signals of Measurement 4 (blue) and Measurement 5 (red) between principal sensor pair Source S6 and Receiver S2 at Position 1 (top),  $dv/v$  (blue) and  $CC$  (orange) results from CWI over the signal travel time divided in stretching windows (bottom)

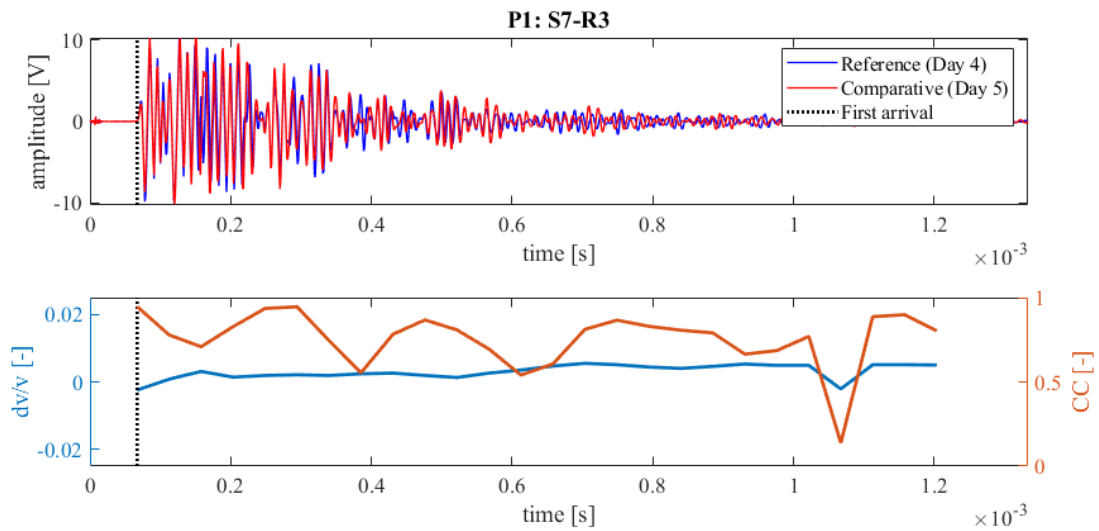


Figure 114: Wave signals of Measurement 4 (blue) and Measurement 5 (red) between principal sensor pair Source S7 and Receiver S3 at Position 1 (top),  $dv/v$  (blue) and CC (orange) results from CWI over the signal travel time divided in stretching windows (bottom)

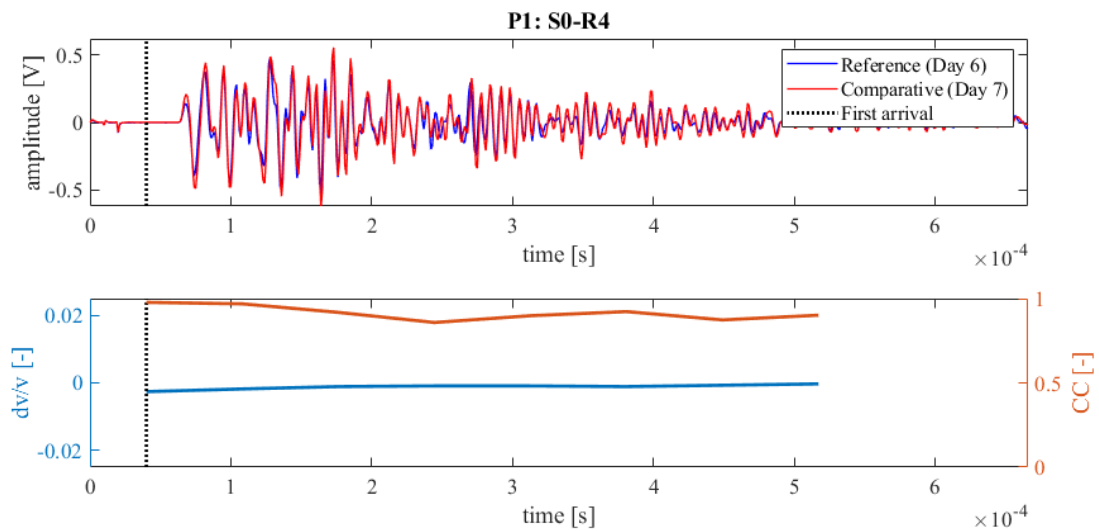


Figure 115: Wave signals of Measurement 6 (blue) and Measurement 7 (red) between principal sensor pair Source S0 and Receiver S4 at Position 1 (top),  $dv/v$  (blue) and CC (orange) results from CWI over the signal travel time divided in stretching windows (bottom)

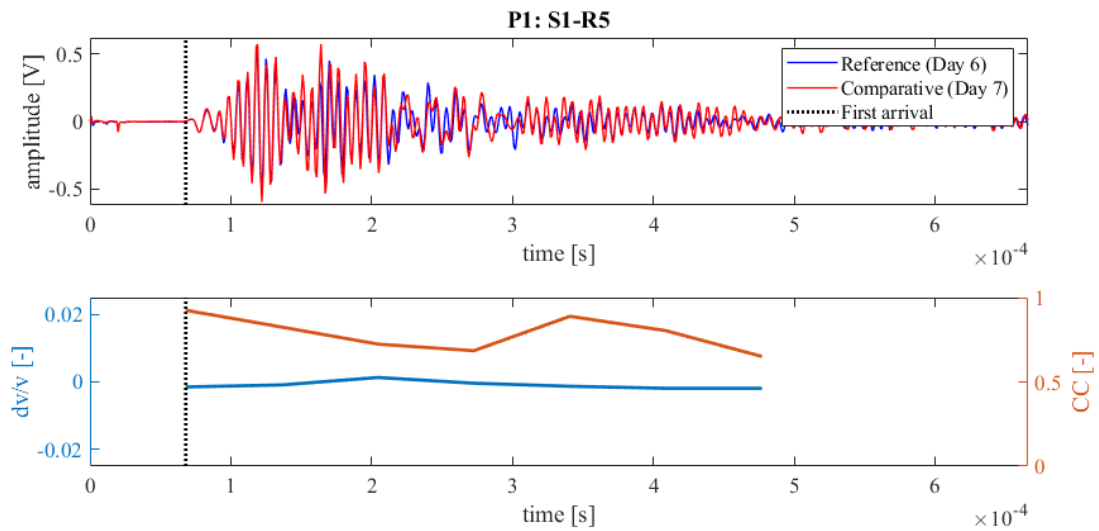


Figure 116: Wave signals of Measurement 6 (blue) and Measurement 7 (red) between principal sensor pair Source S1 and Receiver S5 at Position 1 (top),  $dv/v$  (blue) and CC (orange) results from CWI over the signal travel time divided in stretching windows (bottom)

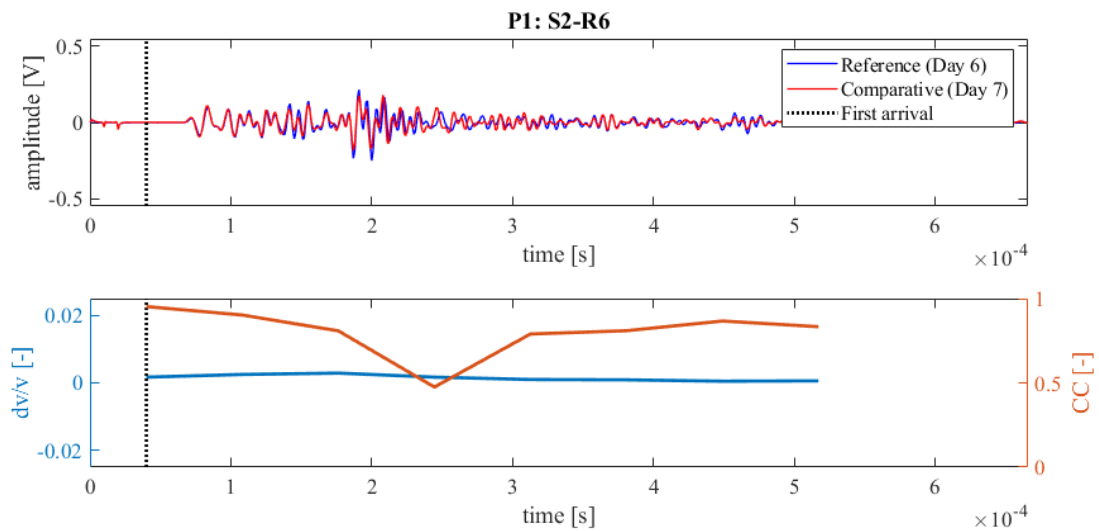


Figure 117: Wave signals of Measurement 6 (blue) and Measurement 7 (red) between principal sensor pair Source S2 and Receiver S6 at Position 1 (top),  $dv/v$  (blue) and CC (orange) results from CWI over the signal travel time divided in stretching windows (bottom)

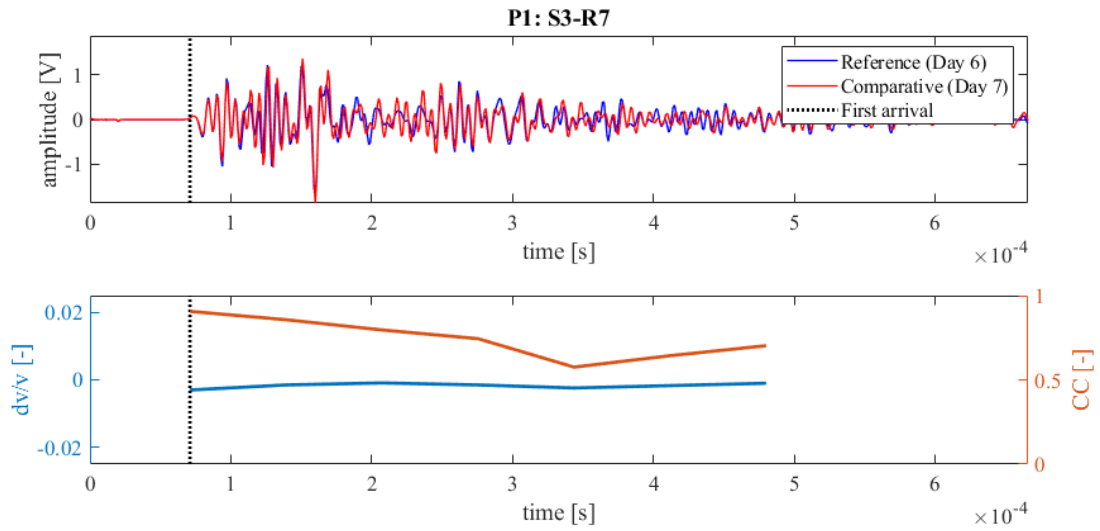


Figure 118: Wave signals of Measurement 6 (blue) and Measurement 7 (red) between principal sensor pair Source S3 and Receiver S7 at Position 1 (top),  $dv/v$  (blue) and  $CC$  (orange) results from CWI over the signal travel time divided in stretching windows (bottom)

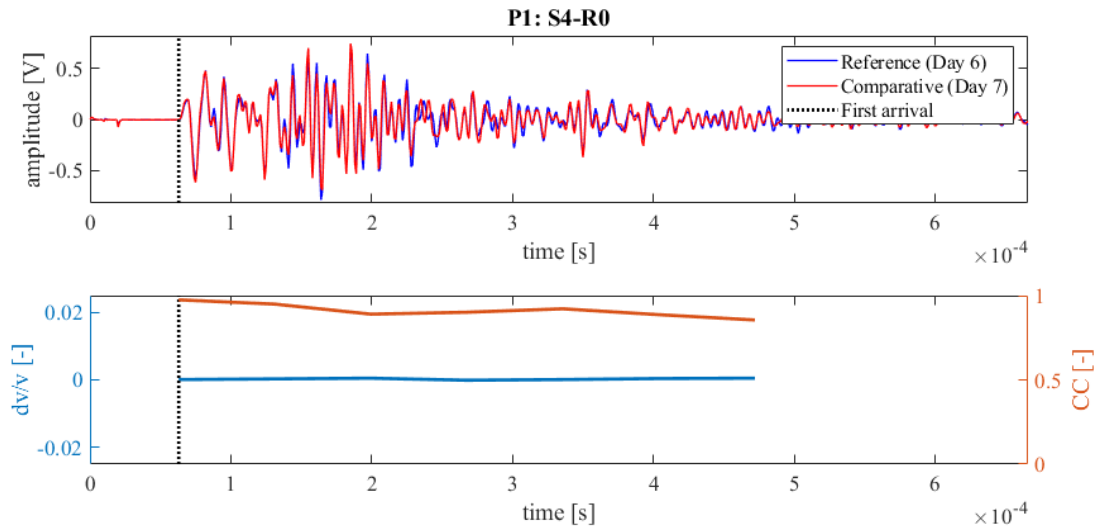


Figure 119: Wave signals of Measurement 6 (blue) and Measurement 7 (red) between principal sensor pair Source S4 and Receiver S0 at Position 1 (top),  $dv/v$  (blue) and  $CC$  (orange) results from CWI over the signal travel time divided in stretching windows (bottom)

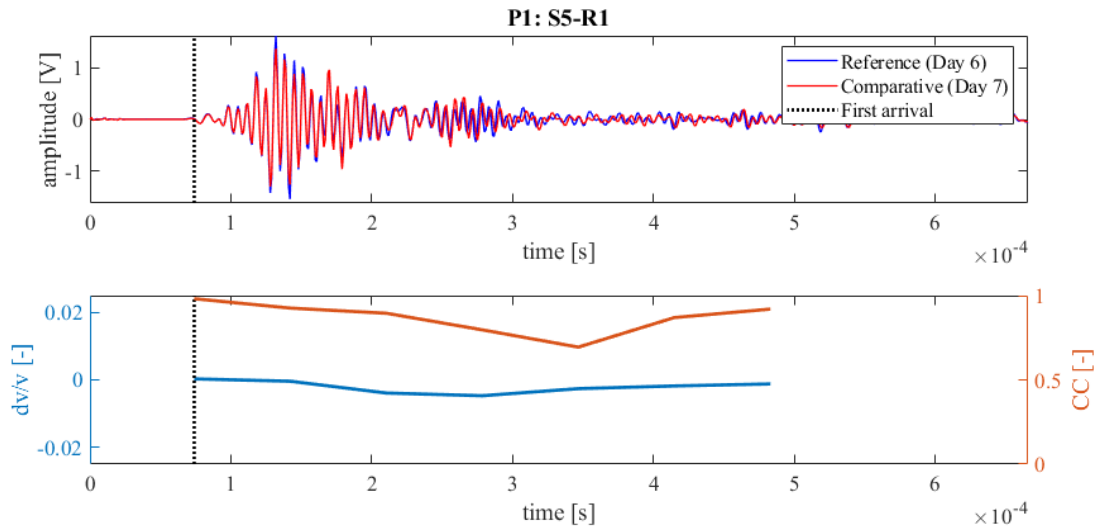


Figure 120: Wave signals of Measurement 6 (blue) and Measurement 7 (red) between principal sensor pair Source S5 and Receiver S1 at Position 1 (top),  $dv/v$  (blue) and  $CC$  (orange) results from CWI over the signal travel time divided in stretching windows (bottom)

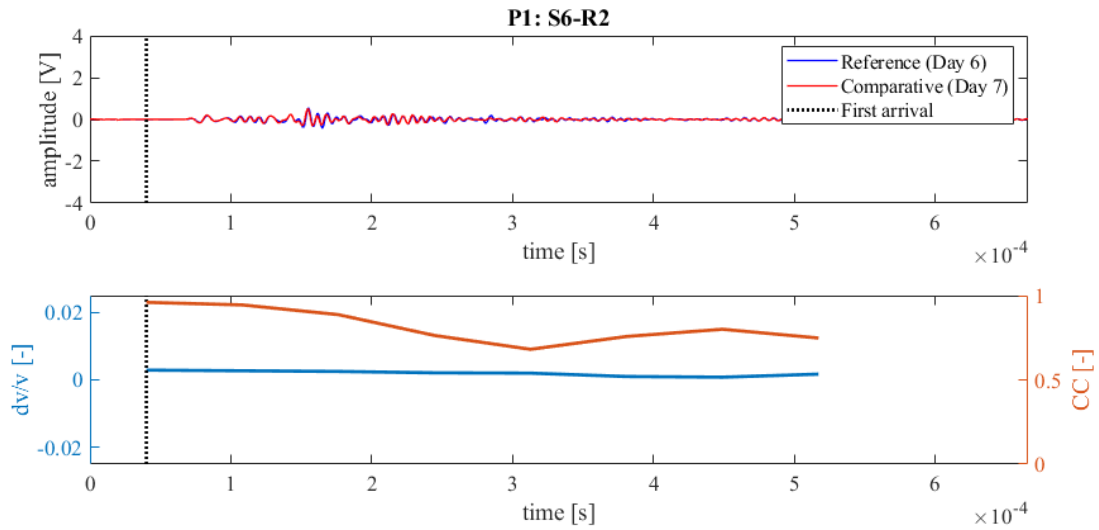


Figure 121: Wave signals of Measurement 6 (blue) and Measurement 7 (red) between principal sensor pair Source S6 and Receiver S2 at Position 1 (top),  $dv/v$  (blue) and  $CC$  (orange) results from CWI over the signal travel time divided in stretching windows (bottom)

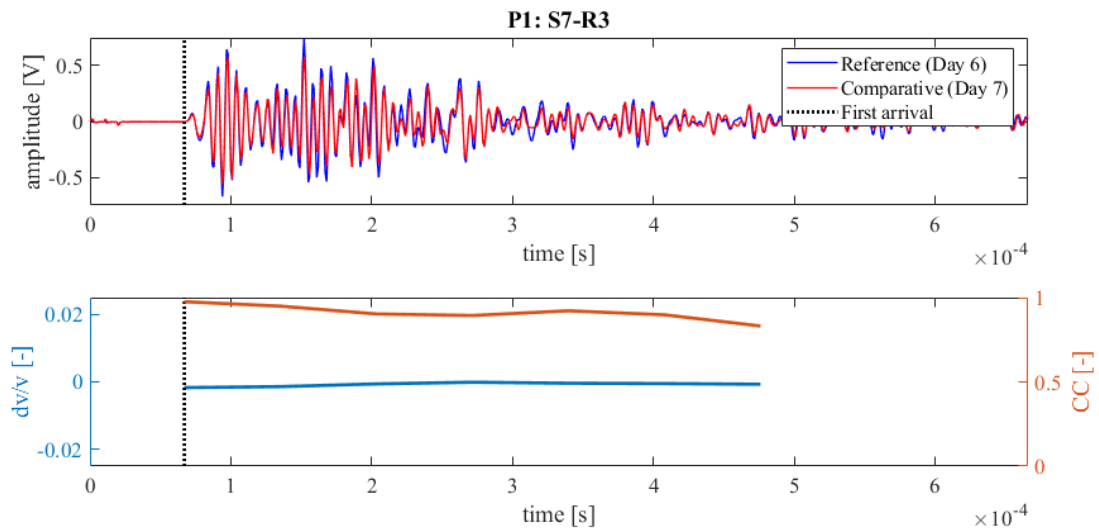


Figure 122: Wave signals of Measurement 6 (blue) and Measurement 7 (red) between principal sensor pair Source S7 and Receiver S3 at Position 1 (top),  $dv/v$  (blue) and  $CC$  (orange) results from CWI over the signal travel time divided in stretching windows (bottom)

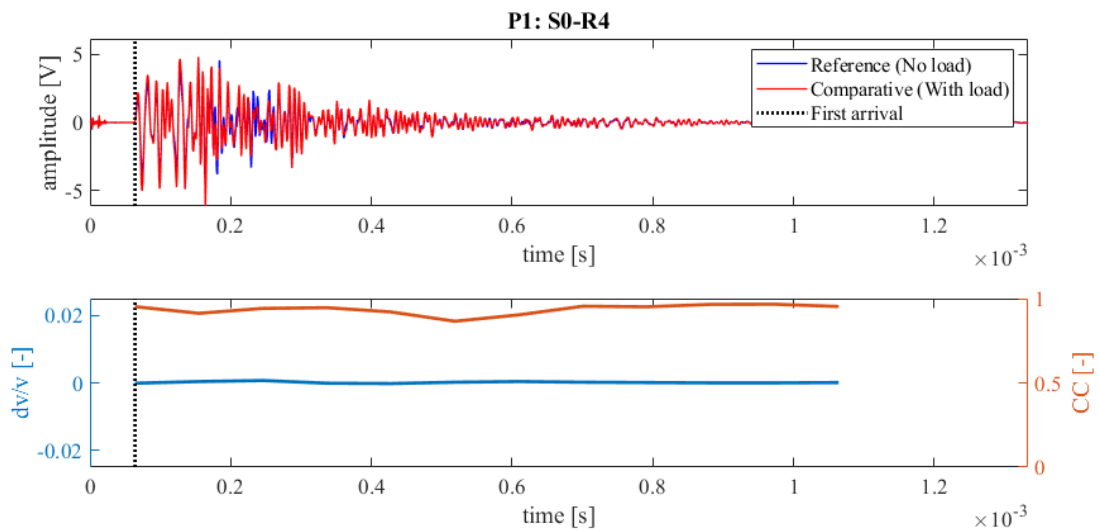


Figure 123: Wave signals of Measurement 8 without lorry load (blue) and with lorry load (red) between principal sensor pair Source S0 and Receiver S4 at Position 1 (top),  $dv/v$  (blue) and  $CC$  (orange) results from CWI over the signal travel time divided in stretching windows (bottom)

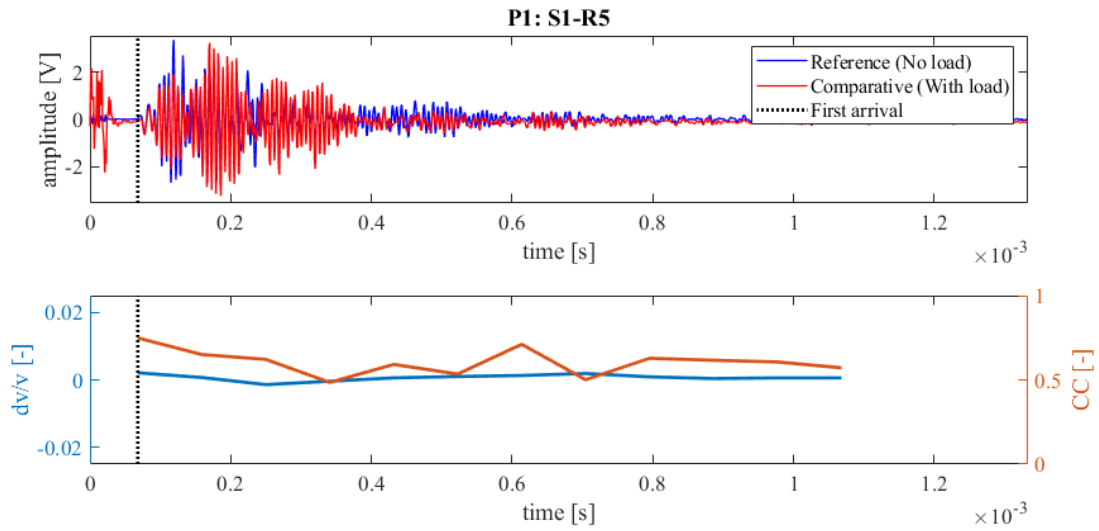


Figure 124: Wave signals of Measurement 8 without lorry load (blue) and with lorry load (red) between principal sensor pair Source S1 and Receiver S5 at Position 1 (top),  $dv/v$  (blue) and  $CC$  (orange) results from CWI over the signal travel time divided in stretching windows (bottom)

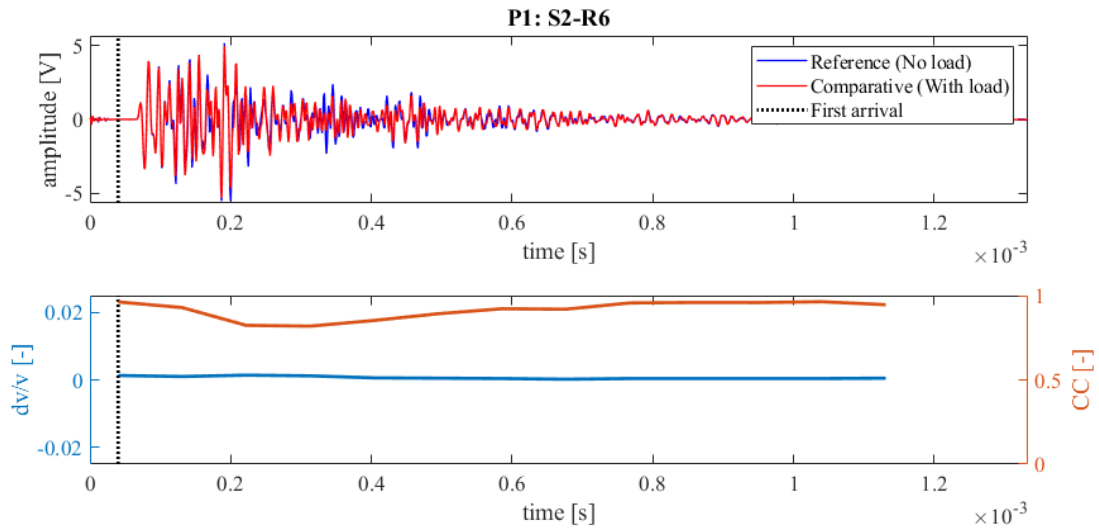


Figure 125: Wave signals of Measurement 8 without lorry load (blue) and with lorry load (red) between principal sensor pair Source S2 and Receiver S6 at Position 1 (top),  $dv/v$  (blue) and  $CC$  (orange) results from CWI over the signal travel time divided in stretching windows (bottom)

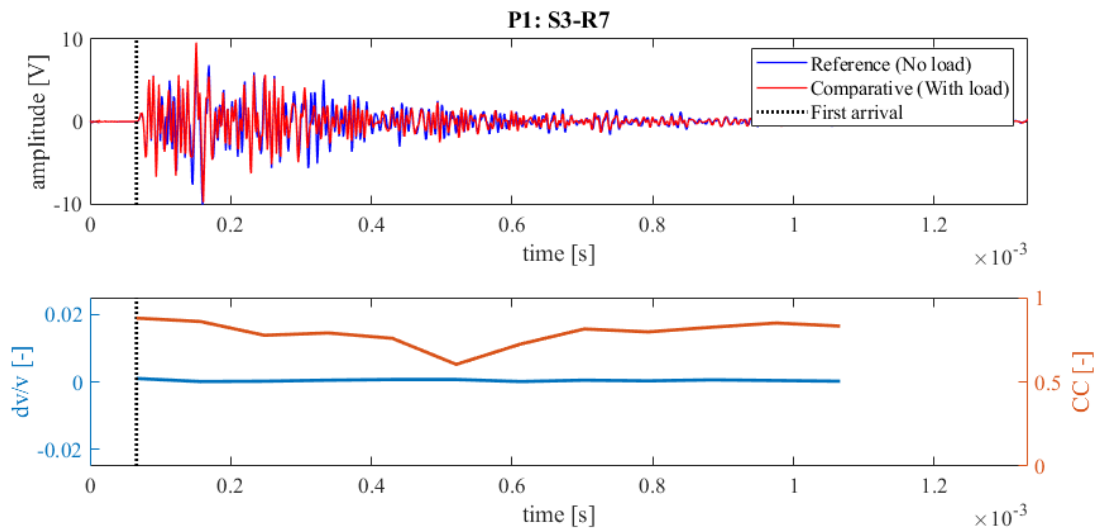


Figure 126: Wave signals of Measurement 8 without lorry load (blue) and with lorry load (red) between principal sensor pair Source S3 and Receiver S7 at Position 1 (top),  $dv/v$  (blue) and  $CC$  (orange) results from CWI over the signal travel time divided in stretching windows (bottom)

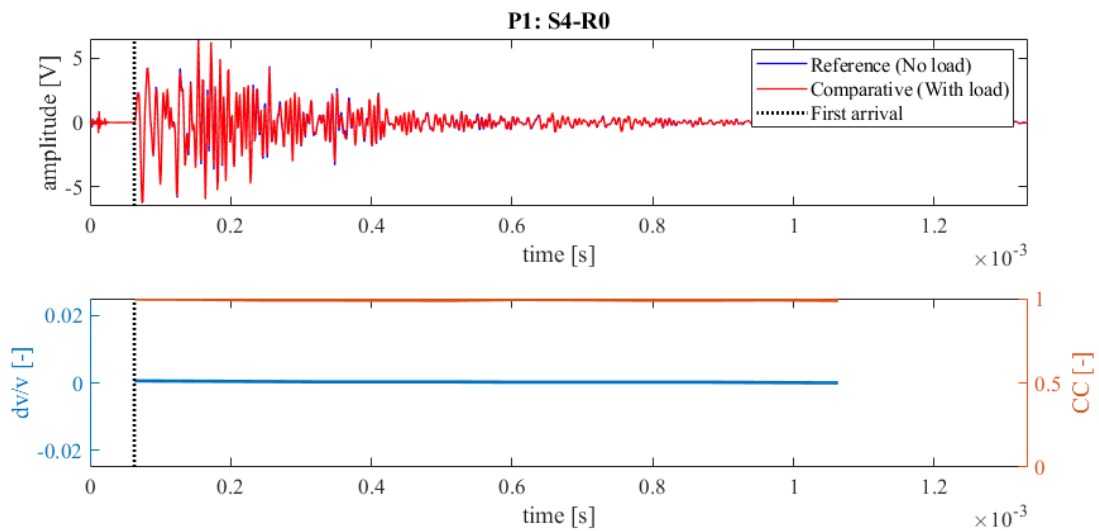


Figure 127: Wave signals of Measurement 8 without lorry load (blue) and with lorry load (red) between principal sensor pair Source S4 and Receiver S0 at Position 1 (top),  $dv/v$  (blue) and  $CC$  (orange) results from CWI over the signal travel time divided in stretching windows (bottom)

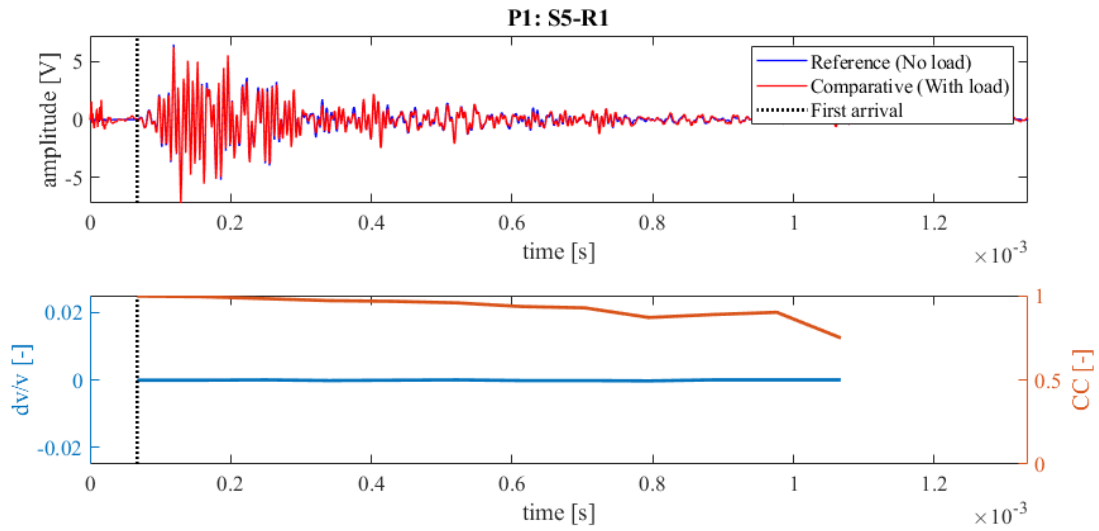


Figure 128: Wave signals of Measurement 8 without lorry load (blue) and with lorry load (red) between principal sensor pair Source S5 and Receiver S1 at Position 1 (top),  $dv/v$  (blue) and  $CC$  (orange) results from CWI over the signal travel time divided in stretching windows (bottom)

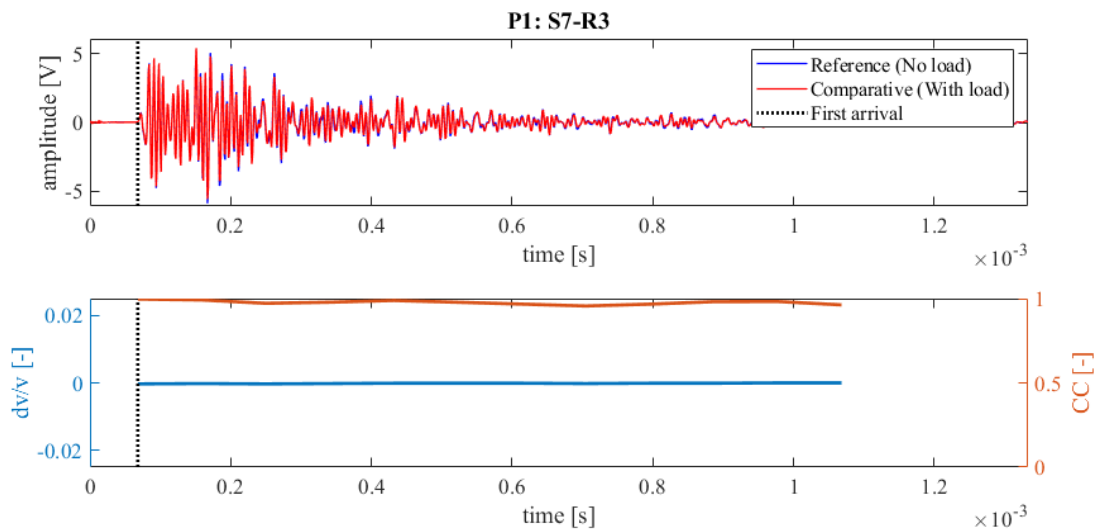


Figure 129: Wave signals of Measurement 8 without lorry load (blue) and with lorry load (red) between principal sensor pair Source S7 and Receiver S3 at Position 1 (top),  $dv/v$  (blue) and  $CC$  (orange) results from CWI over the signal travel time divided in stretching windows (bottom)

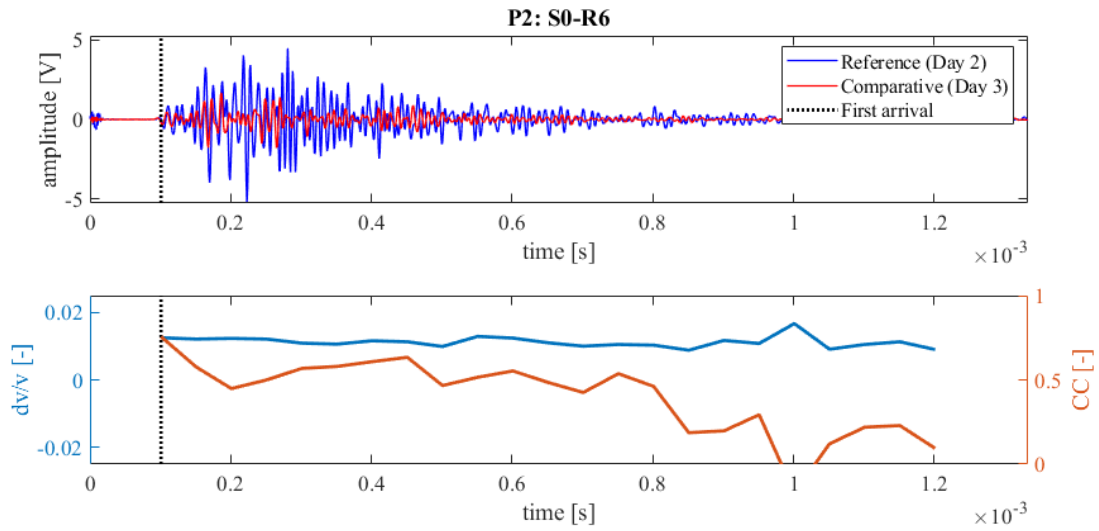


Figure 130: Wave signals of Measurement 2 (blue) and Measurement 3 (red) between principal sensor pair Source S0 and Receiver S6 at Position 2 (top),  $dv/v$  (blue) and  $CC$  (orange) results from CWI over the signal travel time divided in stretching windows (bottom)

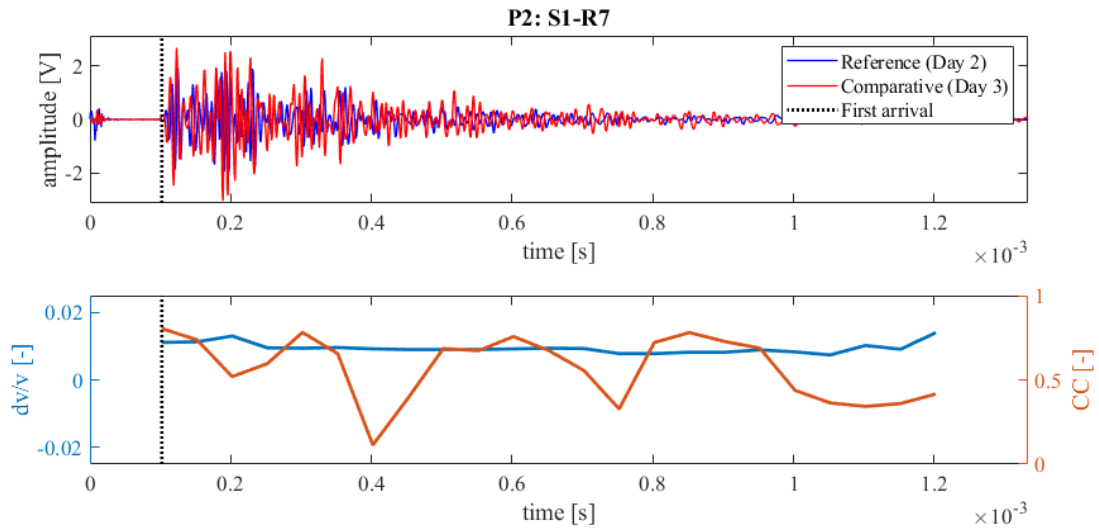


Figure 131: Wave signals of Measurement 2 (blue) and Measurement 3 (red) between principal sensor pair Source S1 and Receiver S7 at Position 2 (top),  $dv/v$  (blue) and  $CC$  (orange) results from CWI over the signal travel time divided in stretching windows (bottom)

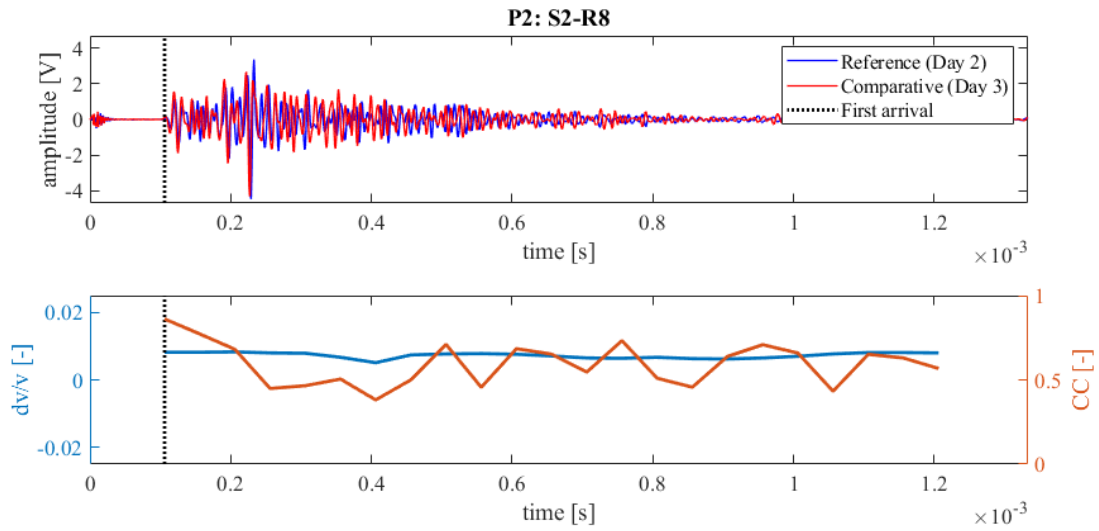


Figure 132: Wave signals of Measurement 2 (blue) and Measurement 3 (red) between principal sensor pair Source S2 and Receiver S8 at Position 2 (top),  $dv/v$  (blue) and  $CC$  (orange) results from CWI over the signal travel time divided in stretching windows (bottom)

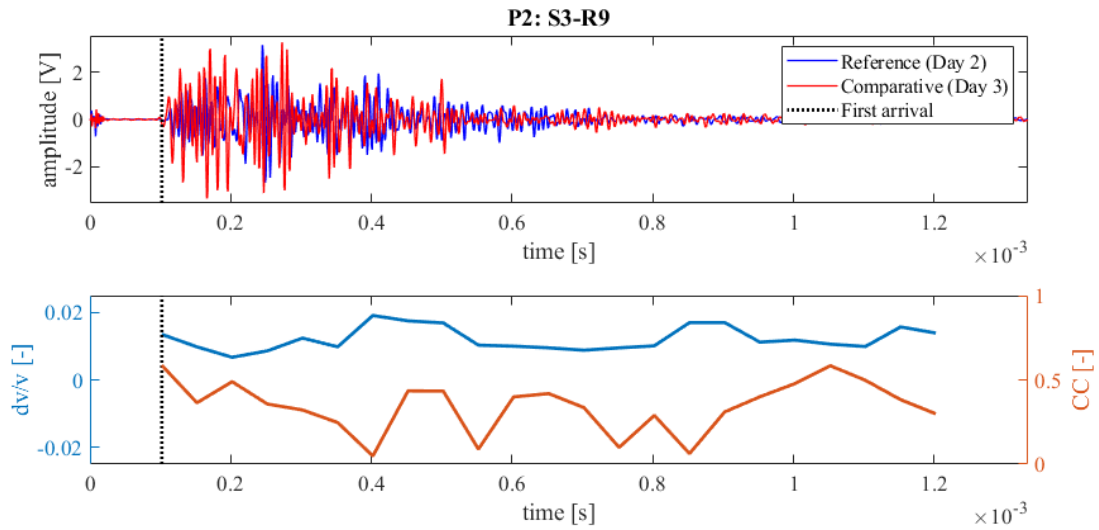


Figure 133: Wave signals of Measurement 2 (blue) and Measurement 3 (red) between principal sensor pair Source S3 and Receiver S9 at Position 2 (top),  $dv/v$  (blue) and  $CC$  (orange) results from CWI over the signal travel time divided in stretching windows (bottom)

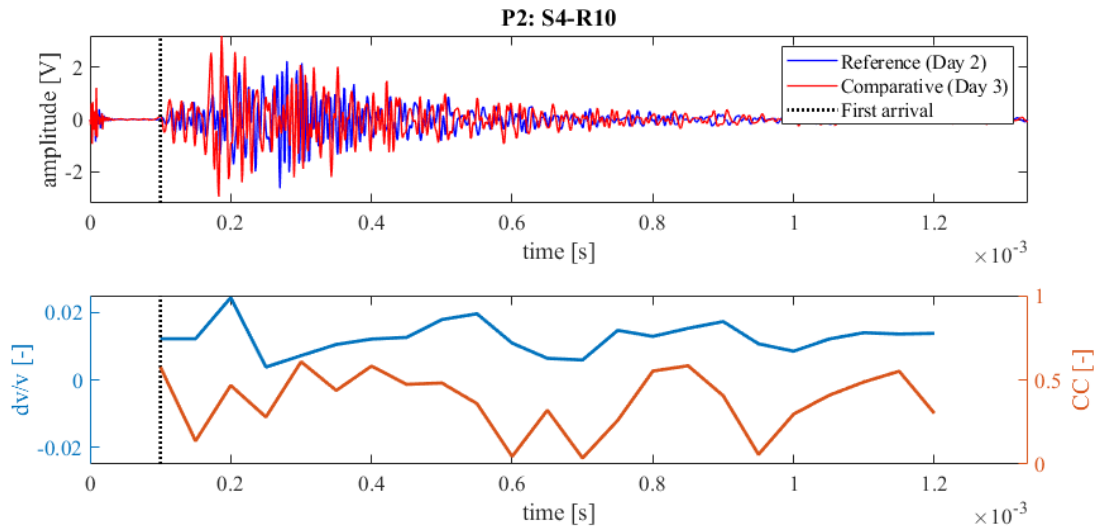


Figure 134: Wave signals of Measurement 2 (blue) and Measurement 3 (red) between principal sensor pair Source S4 and Receiver S10 at Position 2 (top),  $dv/v$  (blue) and  $CC$  (orange) results from CWI over the signal travel time divided in stretching windows (bottom)

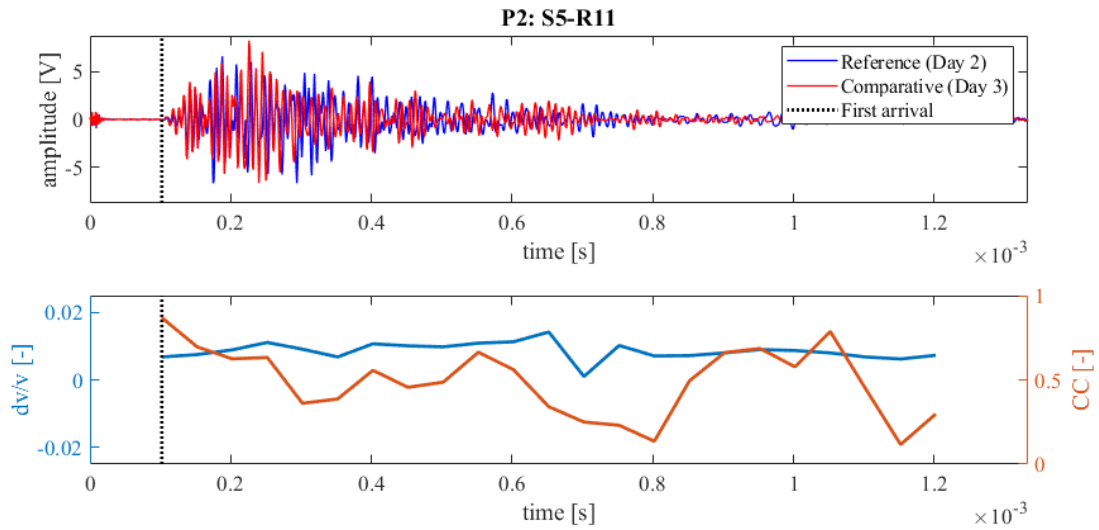


Figure 135: Wave signals of Measurement 2 (blue) and Measurement 3 (red) between principal sensor pair Source S5 and Receiver S11 at Position 2 (top),  $dv/v$  (blue) and  $CC$  (orange) results from CWI over the signal travel time divided in stretching windows (bottom)

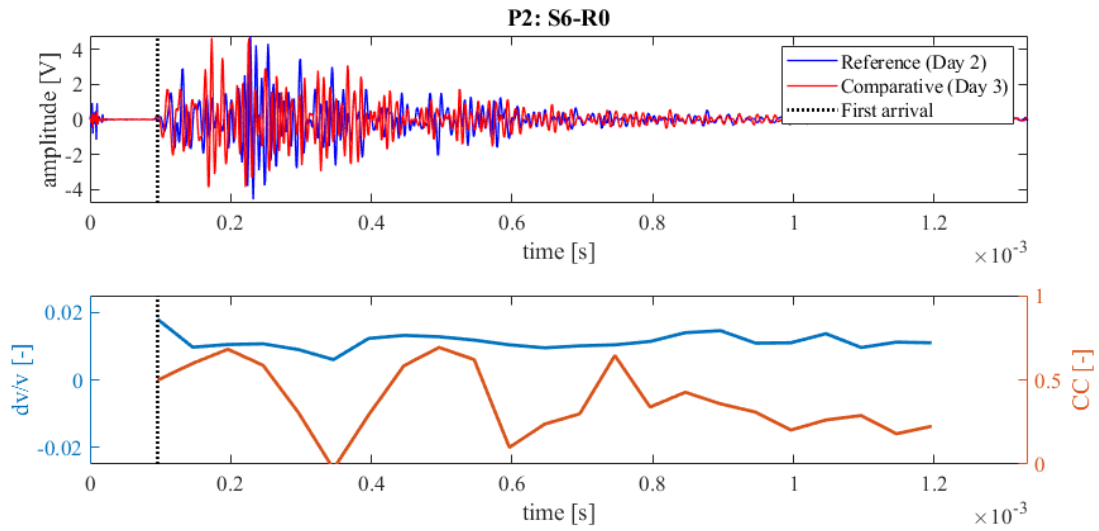


Figure 136: Wave signals of Measurement 2 (blue) and Measurement 3 (red) between principal sensor pair Source S6 and Receiver S0 at Position 2 (top),  $dv/v$  (blue) and  $CC$  (orange) results from CWI over the signal travel time divided in stretching windows (bottom)

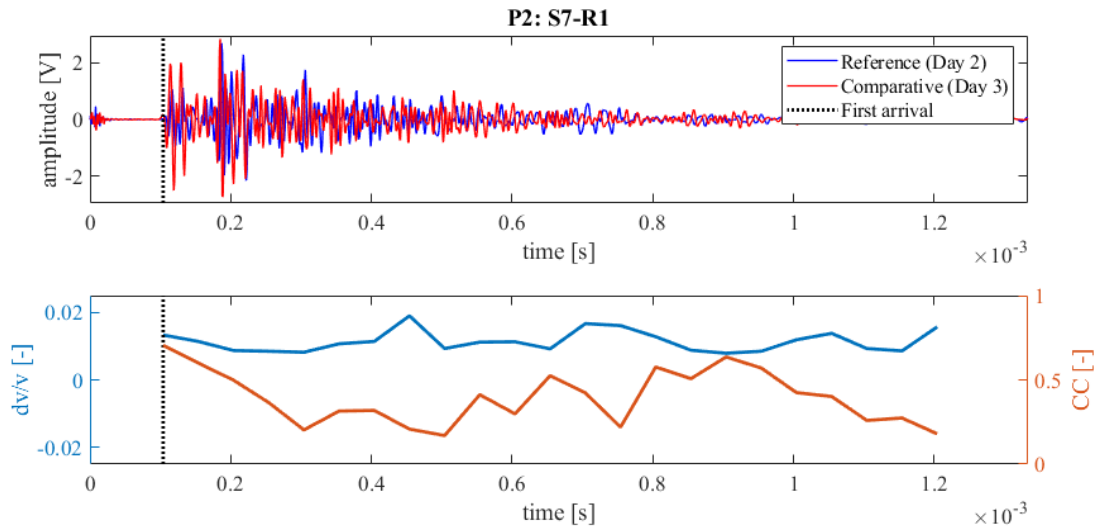


Figure 137: Wave signals of Measurement 2 (blue) and Measurement 3 (red) between principal sensor pair Source S7 and Receiver S1 at Position 2 (top),  $dv/v$  (blue) and  $CC$  (orange) results from CWI over the signal travel time divided in stretching windows (bottom)

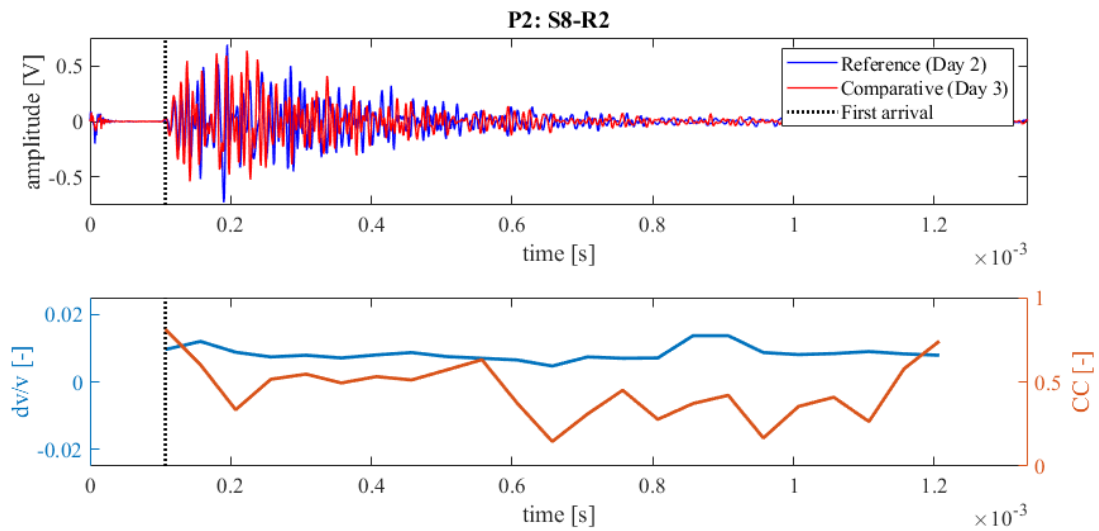


Figure 138: Wave signals of Measurement 2 (blue) and Measurement 3 (red) between principal sensor pair Source S8 and Receiver S2 at Position 2 (top),  $dv/v$  (blue) and  $CC$  (orange) results from CWI over the signal travel time divided in stretching windows (bottom)

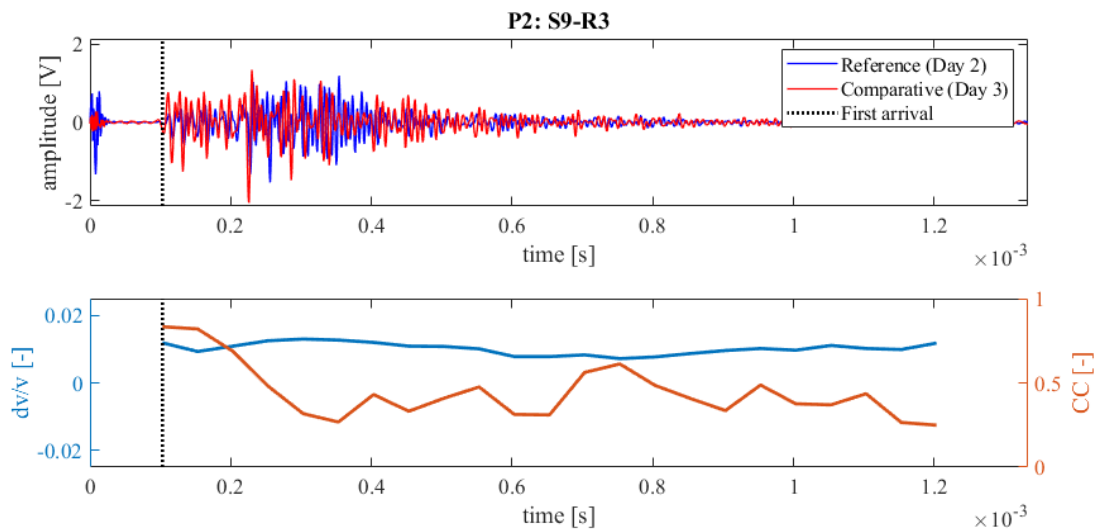


Figure 139: Wave signals of Measurement 2 (blue) and Measurement 3 (red) between principal sensor pair Source S9 and Receiver S3 at Position 2 (top),  $dv/v$  (blue) and  $CC$  (orange) results from CWI over the signal travel time divided in stretching windows (bottom)

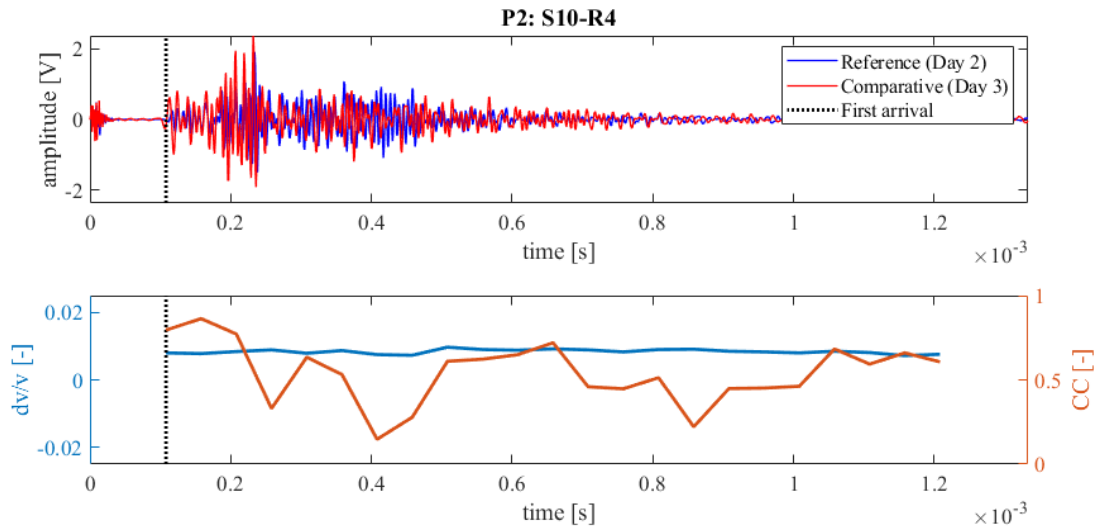


Figure 140: Wave signals of Measurement 2 (blue) and Measurement 3 (red) between principal sensor pair Source S10 and Receiver S4 at Position 2 (top),  $dv/v$  (blue) and  $CC$  (orange) results from CWI over the signal travel time divided in stretching windows (bottom)

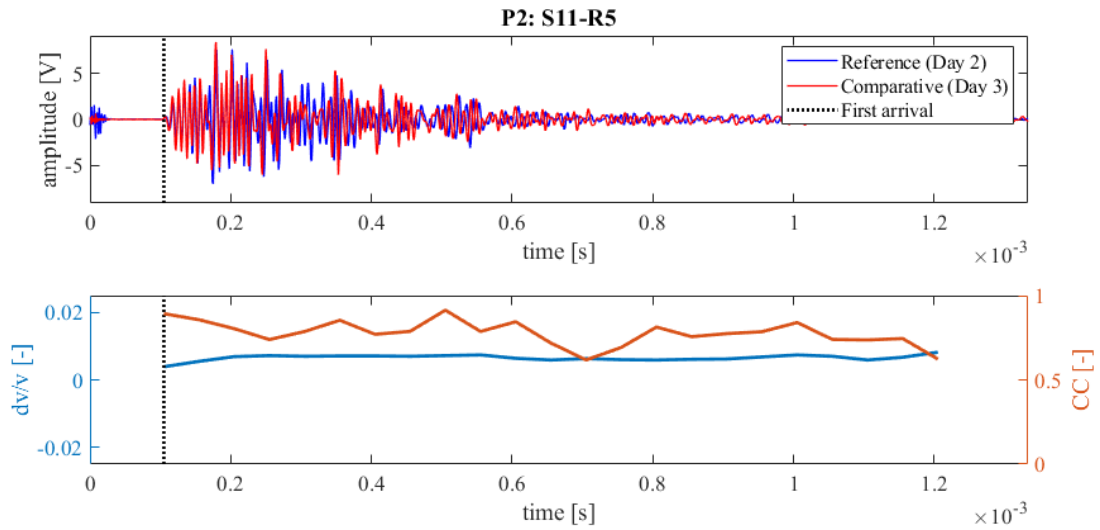


Figure 141: Wave signals of Measurement 2 (blue) and Measurement 3 (red) between principal sensor pair Source S11 and Receiver S5 at Position 2 (top),  $dv/v$  (blue) and  $CC$  (orange) results from CWI over the signal travel time divided in stretching windows (bottom)

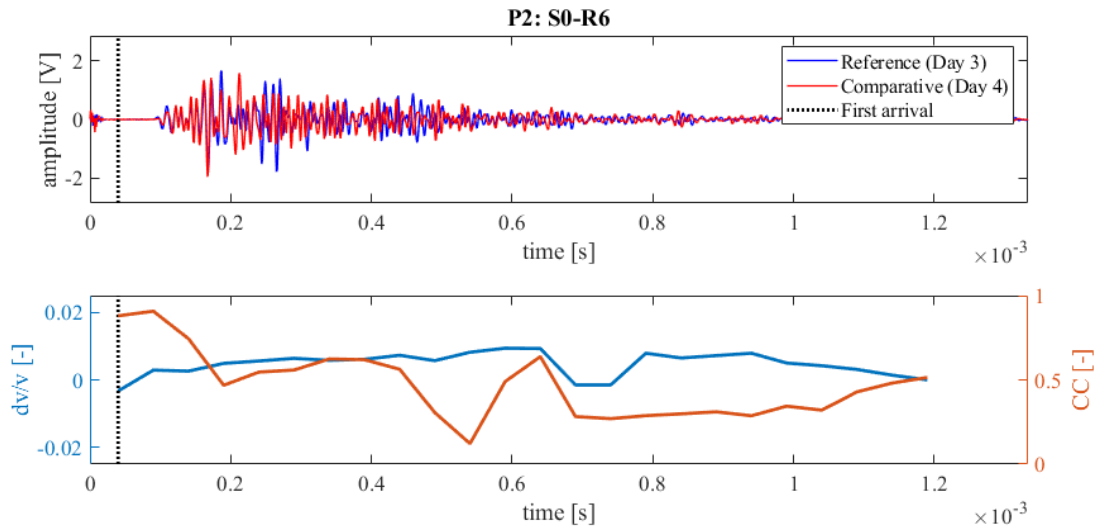


Figure 142: Wave signals of Measurement 3 (blue) and Measurement 4 (red) between principal sensor pair Source S0 and Receiver S6 at Position 2 (top),  $dv/v$  (blue) and  $CC$  (orange) results from CWI over the signal travel time divided in stretching windows (bottom)

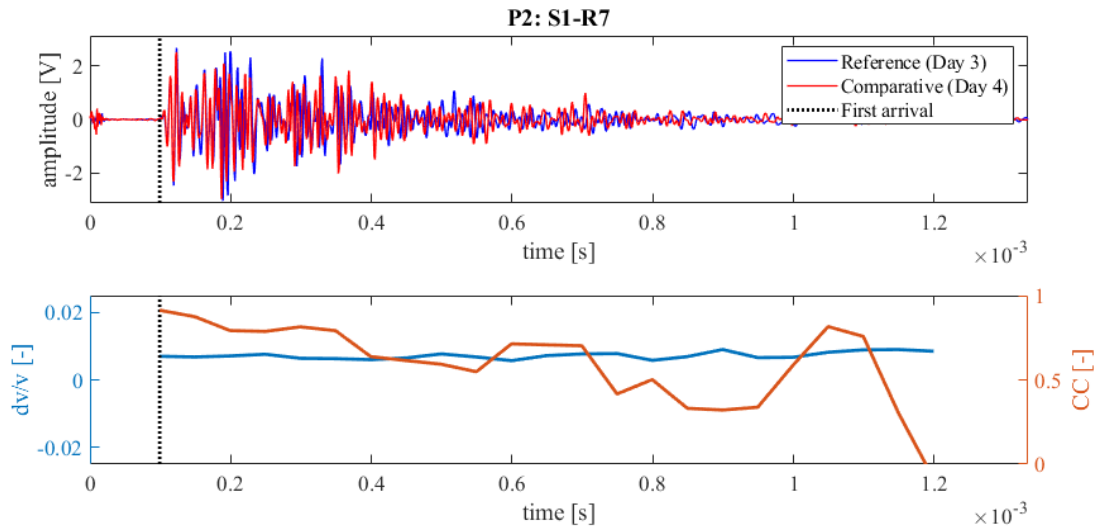


Figure 143: Wave signals of Measurement 3 (blue) and Measurement 4 (red) between principal sensor pair Source S1 and Receiver S7 at Position 2 (top),  $dv/v$  (blue) and  $CC$  (orange) results from CWI over the signal travel time divided in stretching windows (bottom)

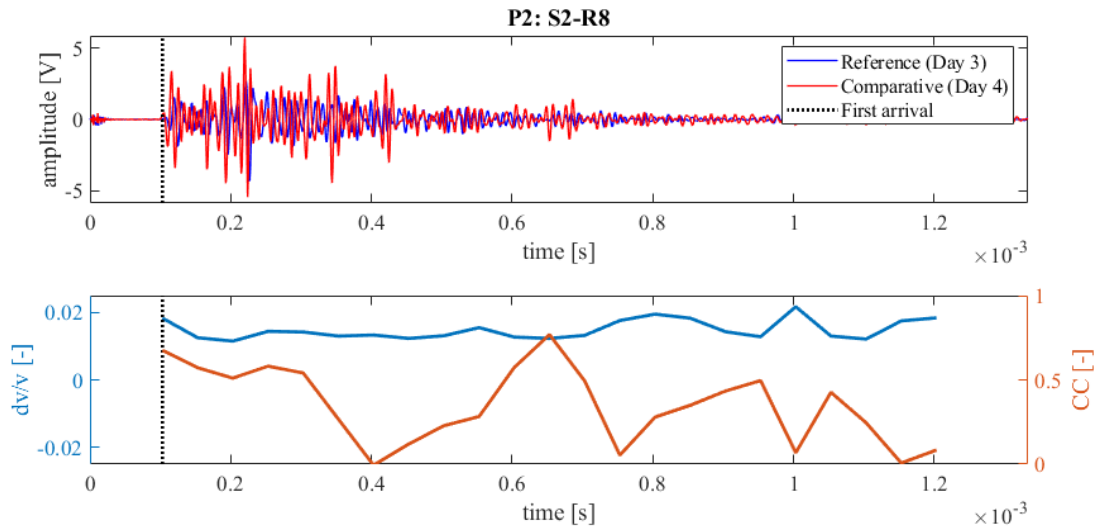


Figure 144: Wave signals of Measurement 3 (blue) and Measurement 4 (red) between principal sensor pair Source S2 and Receiver S8 at Position 2 (top),  $dv/v$  (blue) and  $CC$  (orange) results from CWI over the signal travel time divided in stretching windows (bottom)

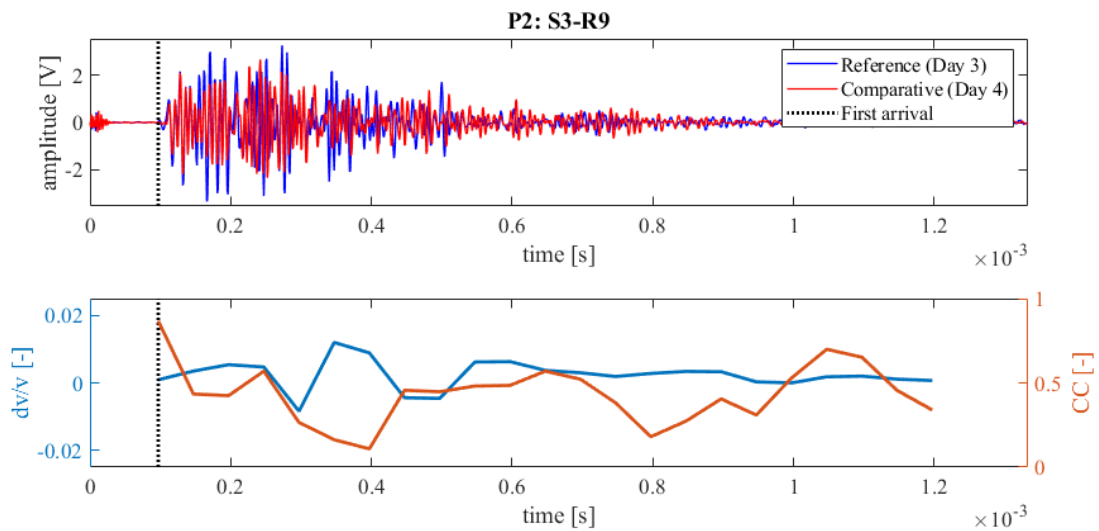


Figure 145: Wave signals of Measurement 3 (blue) and Measurement 4 (red) between principal sensor pair Source S3 and Receiver S9 at Position 2 (top),  $dv/v$  (blue) and  $CC$  (orange) results from CWI over the signal travel time divided in stretching windows (bottom)

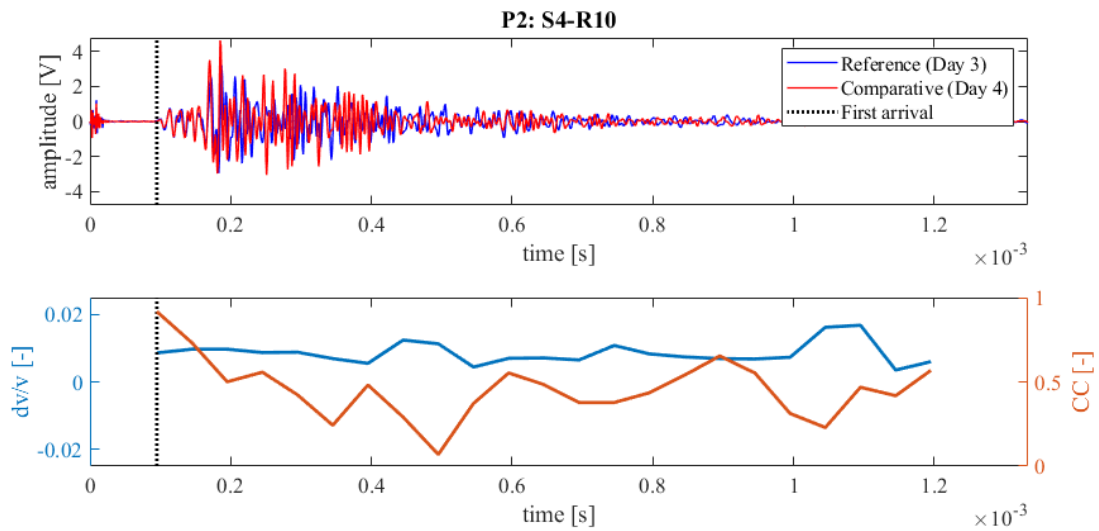


Figure 146: Wave signals of Measurement 3 (blue) and Measurement 4 (red) between principal sensor pair Source S4 and Receiver S10 at Position 2 (top),  $dv/v$  (blue) and CC (orange) results from CWI over the signal travel time divided in stretching windows (bottom)

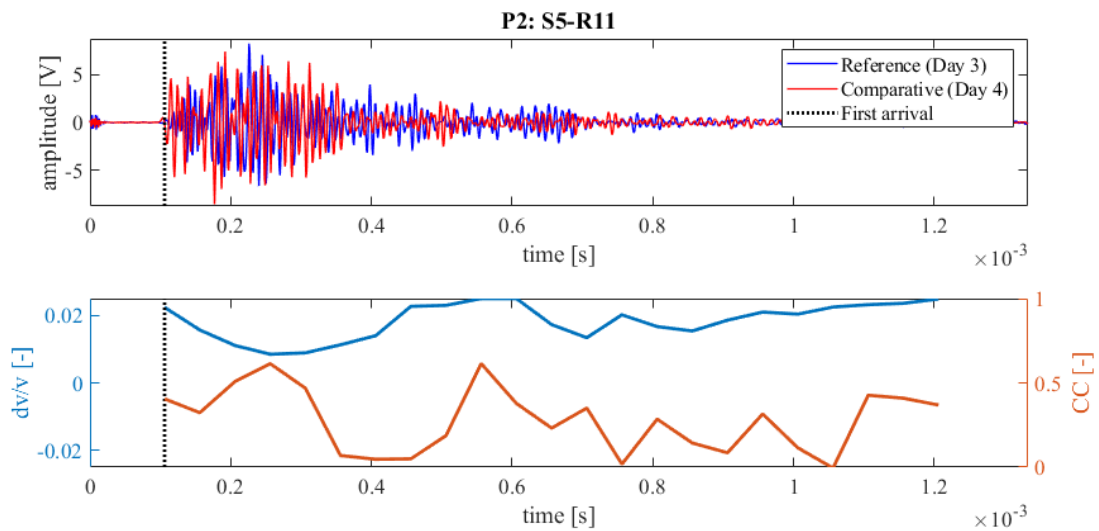


Figure 147: Wave signals of Measurement 3 (blue) and Measurement 4 (red) between principal sensor pair Source S5 and Receiver S11 at Position 2 (top),  $dv/v$  (blue) and CC (orange) results from CWI over the signal travel time divided in stretching windows (bottom)

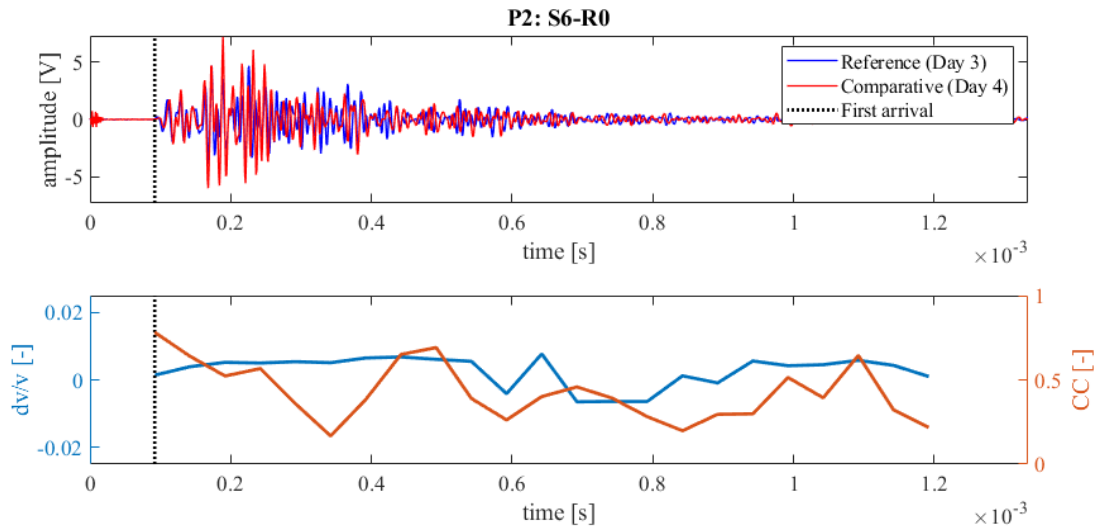


Figure 148: Wave signals of Measurement 3 (blue) and Measurement 4 (red) between principal sensor pair Source S6 and Receiver S0 at Position 2 (top),  $dv/v$  (blue) and  $CC$  (orange) results from CWI over the signal travel time divided in stretching windows (bottom)

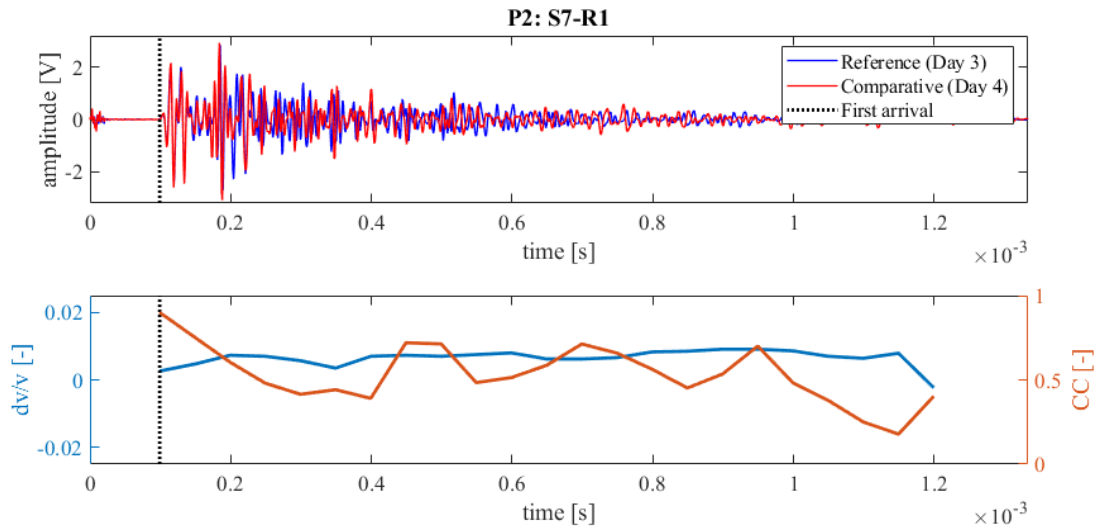


Figure 149: Wave signals of Measurement 3 (blue) and Measurement 4 (red) between principal sensor pair Source S7 and Receiver S1 at Position 2 (top),  $dv/v$  (blue) and  $CC$  (orange) results from CWI over the signal travel time divided in stretching windows (bottom)

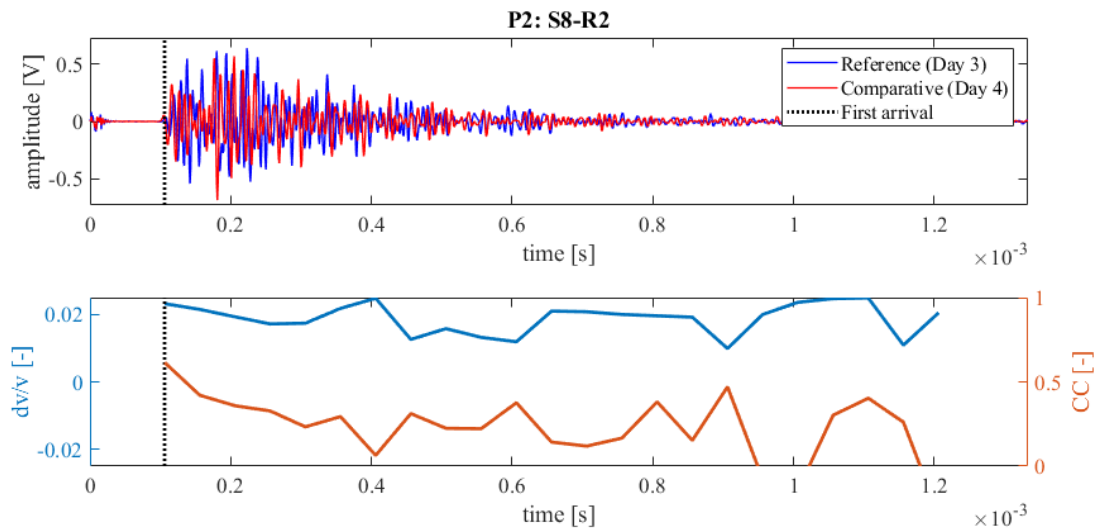


Figure 150: Wave signals of Measurement 3 (blue) and Measurement 4 (red) between principal sensor pair Source S8 and Receiver S2 at Position 2 (top),  $dv/v$  (blue) and  $CC$  (orange) results from CWI over the signal travel time divided in stretching windows (bottom)

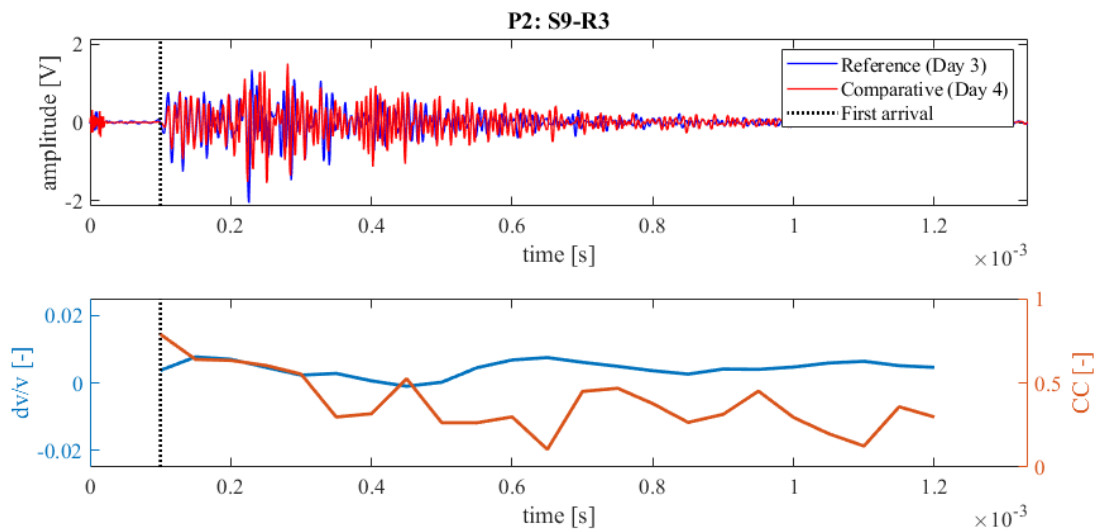
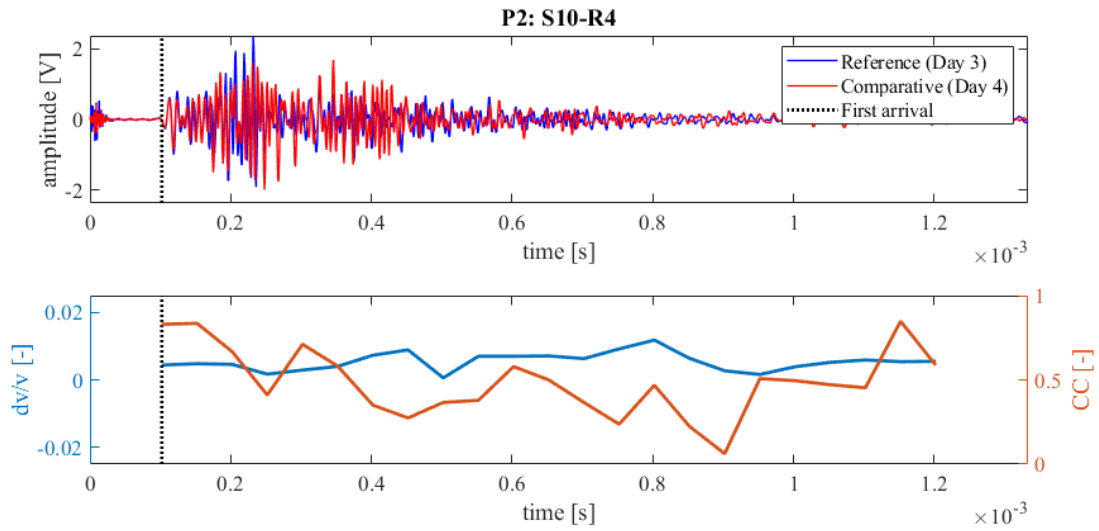
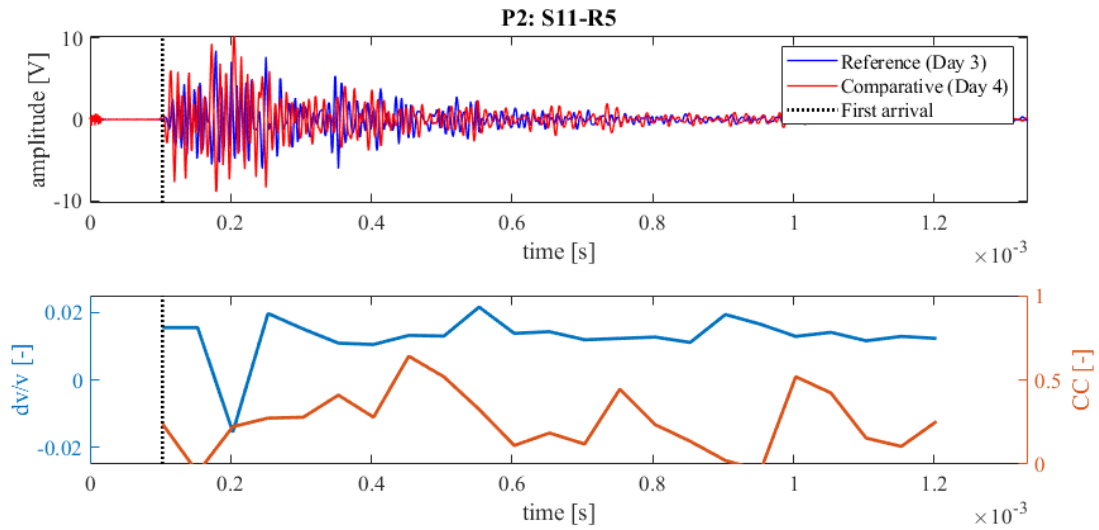


Figure 151: Wave signals of Measurement 3 (blue) and Measurement 4 (red) between principal sensor pair Source S9 and Receiver S3 at Position 2 (top),  $dv/v$  (blue) and  $CC$  (orange) results from CWI over the signal travel time divided in stretching windows (bottom)



**Figure 152: Wave signals of Measurement 3 (blue) and Measurement 4 (red) between principal sensor pair Source S10 and Receiver S4 at Position 2 (top),  $dv/v$  (blue) and CC (orange) results from CWI over the signal travel time divided in stretching windows (bottom)**



**Figure 153: Wave signals of Measurement 3 (blue) and Measurement 4 (red) between principal sensor pair Source S11 and Receiver S5 at Position 2 (top),  $dv/v$  (blue) and CC (orange) results from CWI over the signal travel time divided in stretching windows (bottom)**

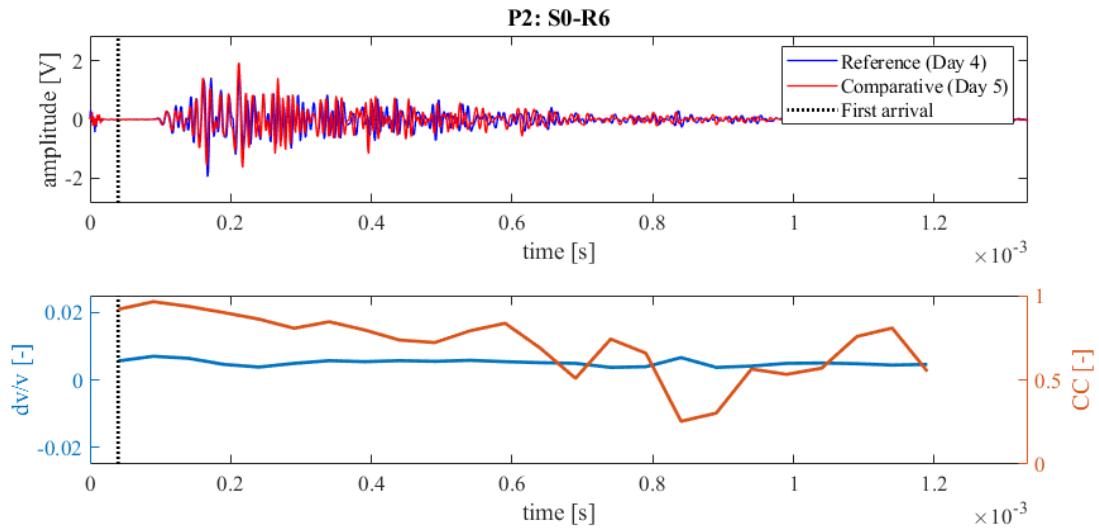


Figure 154: Wave signals of Measurement 4 (blue) and Measurement 5 (red) between principal sensor pair Source S0 and Receiver S6 at Position 2 (top),  $dv/v$  (blue) and  $CC$  (orange) results from CWI over the signal travel time divided in stretching windows (bottom)

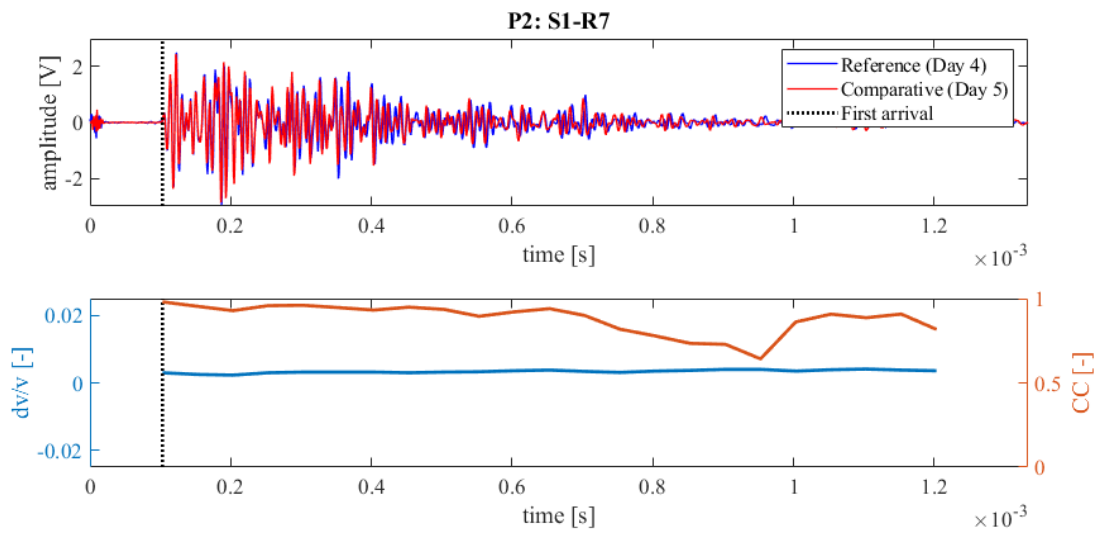


Figure 155: Wave signals of Measurement 4 (blue) and Measurement 5 (red) between principal sensor pair Source S1 and Receiver S7 at Position 2 (top),  $dv/v$  (blue) and  $CC$  (orange) results from CWI over the signal travel time divided in stretching windows (bottom)

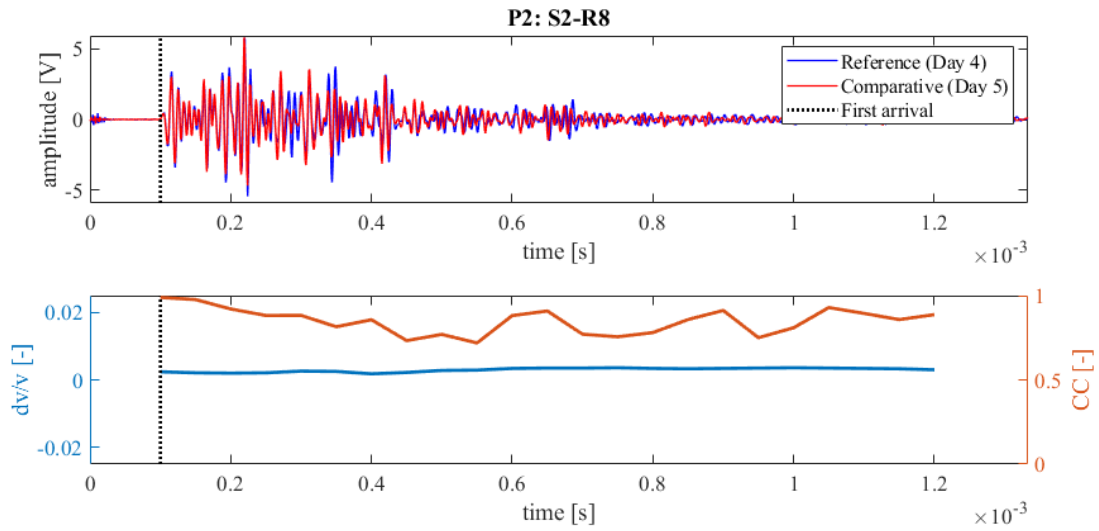


Figure 156: Wave signals of Measurement 4 (blue) and Measurement 5 (red) between principal sensor pair Source S2 and Receiver S8 at Position 2 (top),  $dv/v$  (blue) and  $CC$  (orange) results from CWI over the signal travel time divided in stretching windows (bottom)

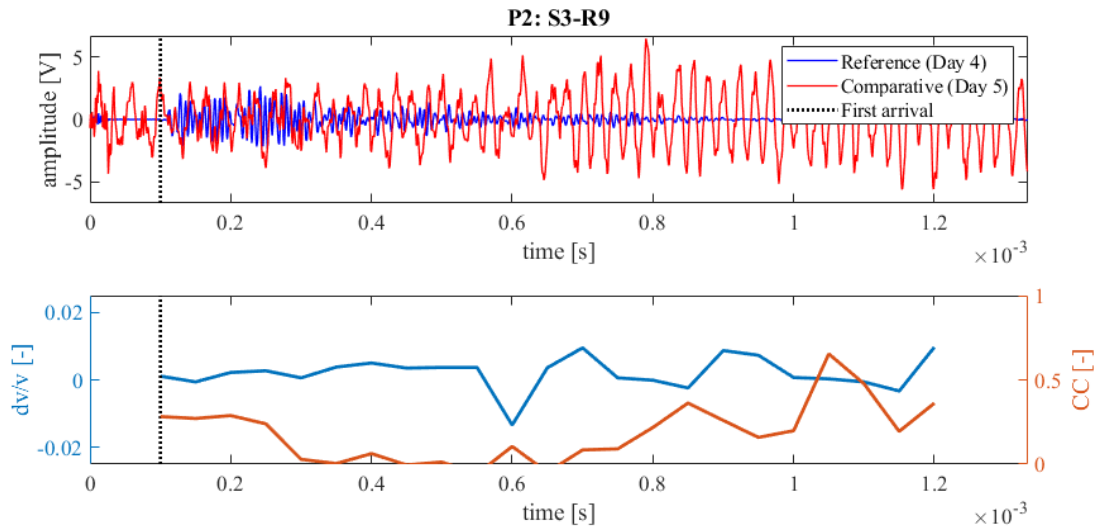


Figure 157: Wave signals of Measurement 4 (blue) and Measurement 5 (red) between principal sensor pair Source S3 and Receiver S9 at Position 2 (top),  $dv/v$  (blue) and  $CC$  (orange) results from CWI over the signal travel time divided in stretching windows (bottom)

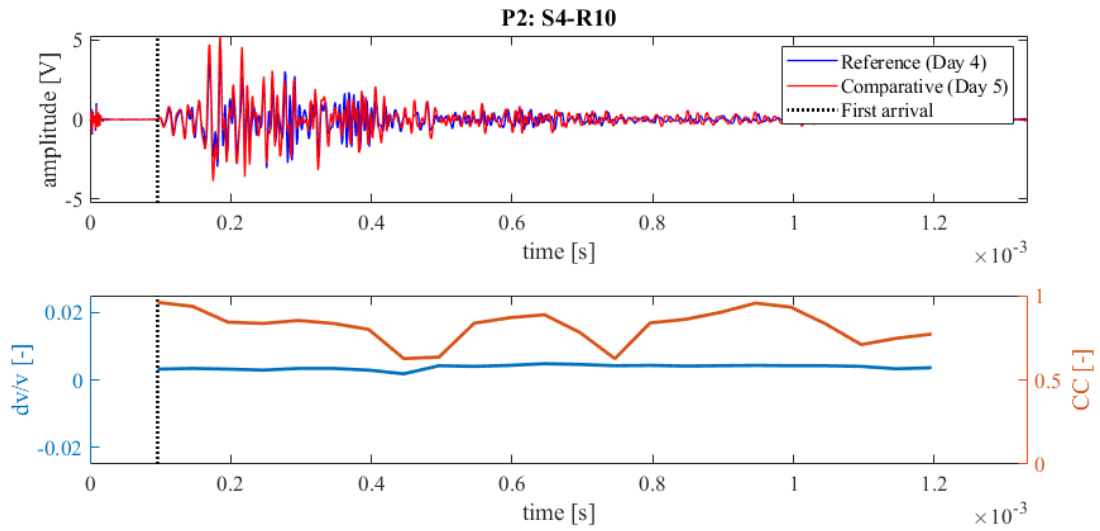


Figure 158: Wave signals of Measurement 4 (blue) and Measurement 5 (red) between principal sensor pair Source S4 and Receiver S10 at Position 2 (top),  $dv/v$  (blue) and  $CC$  (orange) results from CWI over the signal travel time divided in stretching windows (bottom)

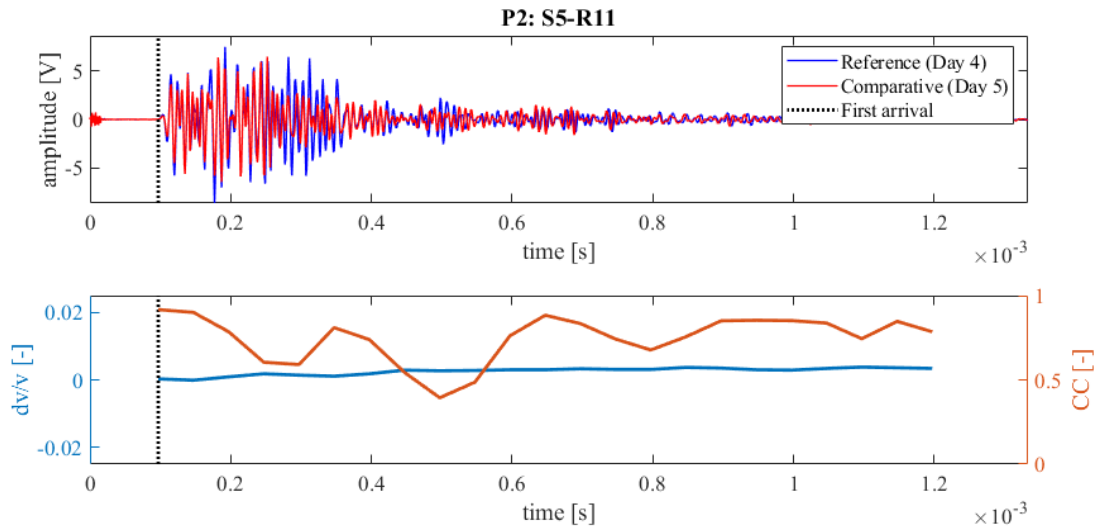


Figure 159: Wave signals of Measurement 4 (blue) and Measurement 5 (red) between principal sensor pair Source S5 and Receiver S11 at Position 2 (top),  $dv/v$  (blue) and  $CC$  (orange) results from CWI over the signal travel time divided in stretching windows (bottom)

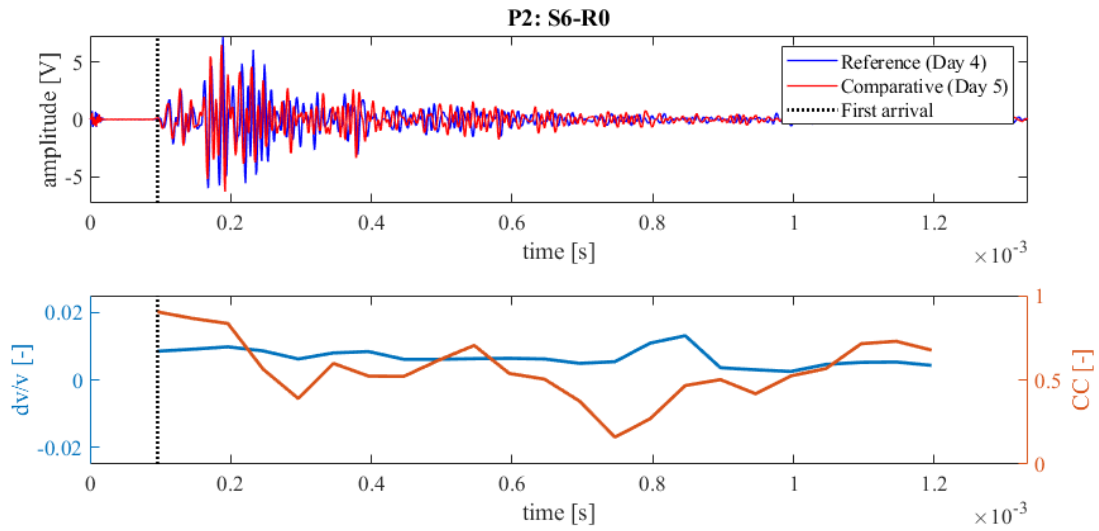


Figure 160: Wave signals of Measurement 4 (blue) and Measurement 5 (red) between principal sensor pair Source S6 and Receiver S0 at Position 2 (top),  $dv/v$  (blue) and  $CC$  (orange) results from CWI over the signal travel time divided in stretching windows (bottom)

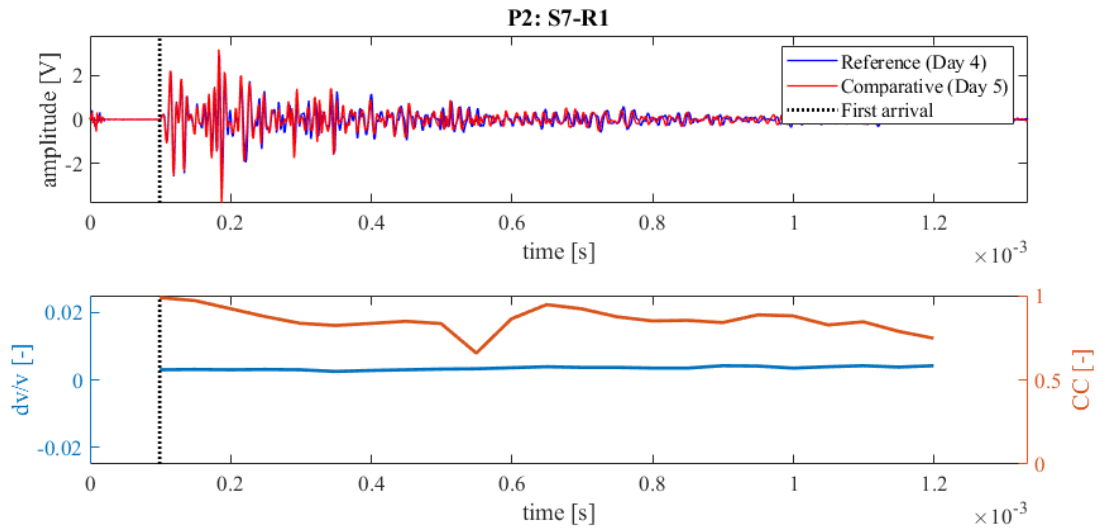


Figure 161: Wave signals of Measurement 4 (blue) and Measurement 5 (red) between principal sensor pair Source S7 and Receiver S1 at Position 2 (top),  $dv/v$  (blue) and  $CC$  (orange) results from CWI over the signal travel time divided in stretching windows (bottom)

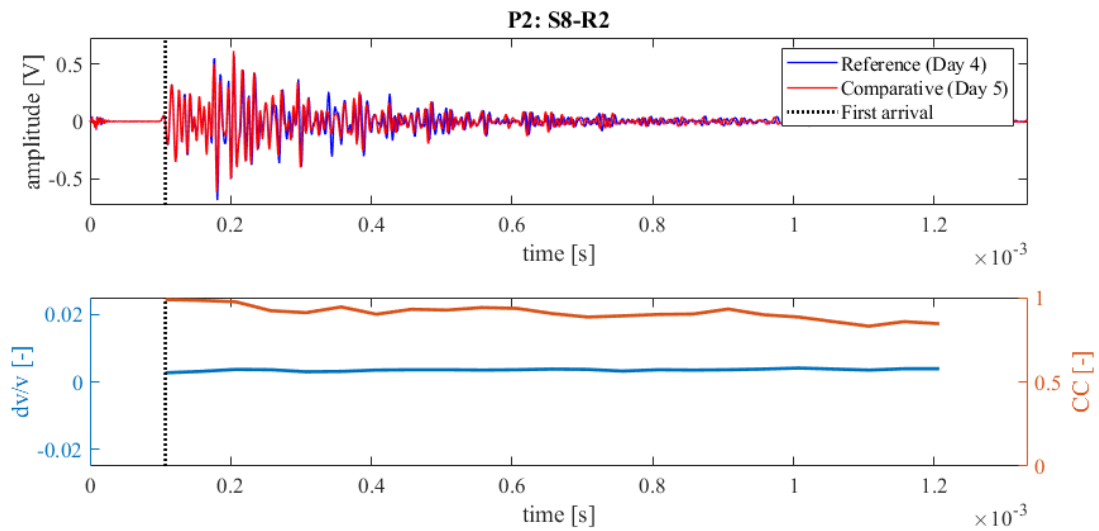


Figure 162: Wave signals of Measurement 4 (blue) and Measurement 5 (red) between principal sensor pair Source S8 and Receiver S2 at Position 2 (top),  $dv/v$  (blue) and  $CC$  (orange) results from CWI over the signal travel time divided in stretching windows (bottom)

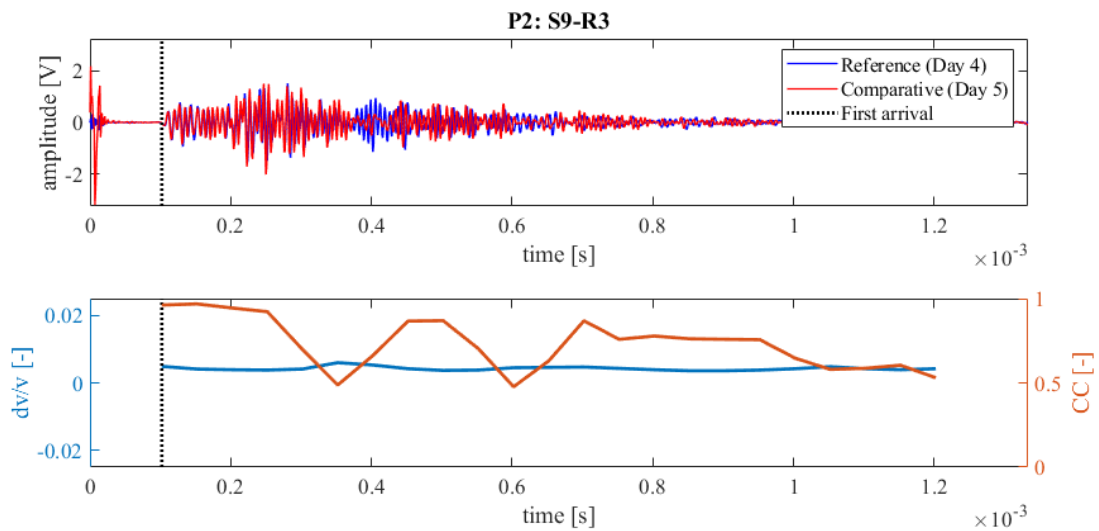


Figure 163: Wave signals of Measurement 4 (blue) and Measurement 5 (red) between principal sensor pair Source S9 and Receiver S3 at Position 2 (top),  $dv/v$  (blue) and  $CC$  (orange) results from CWI over the signal travel time divided in stretching windows (bottom)

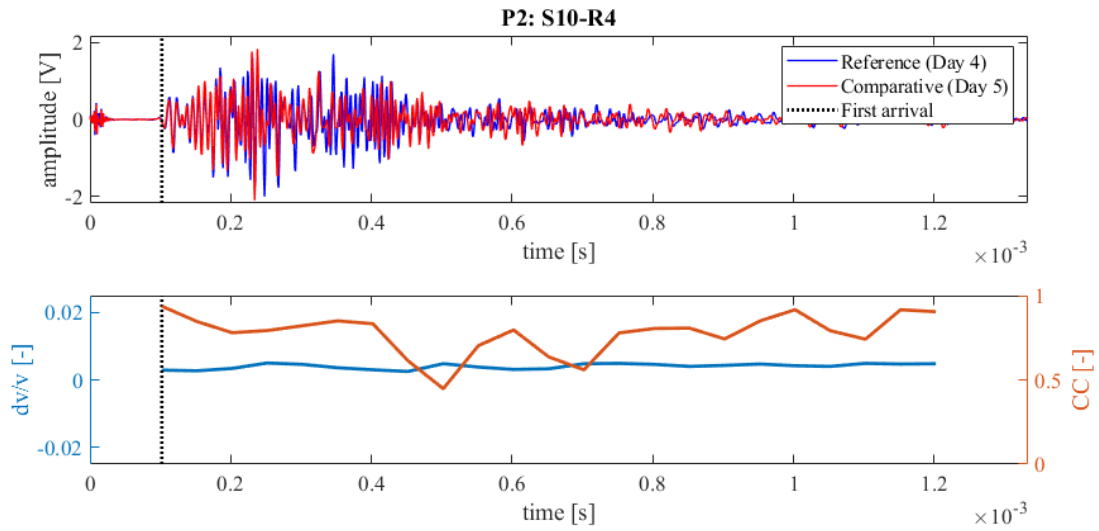


Figure 164: Wave signals of Measurement 4 (blue) and Measurement 5 (red) between principal sensor pair Source S10 and Receiver S4 at Position 2 (top),  $dv/v$  (blue) and  $CC$  (orange) results from CWI over the signal travel time divided in stretching windows (bottom)

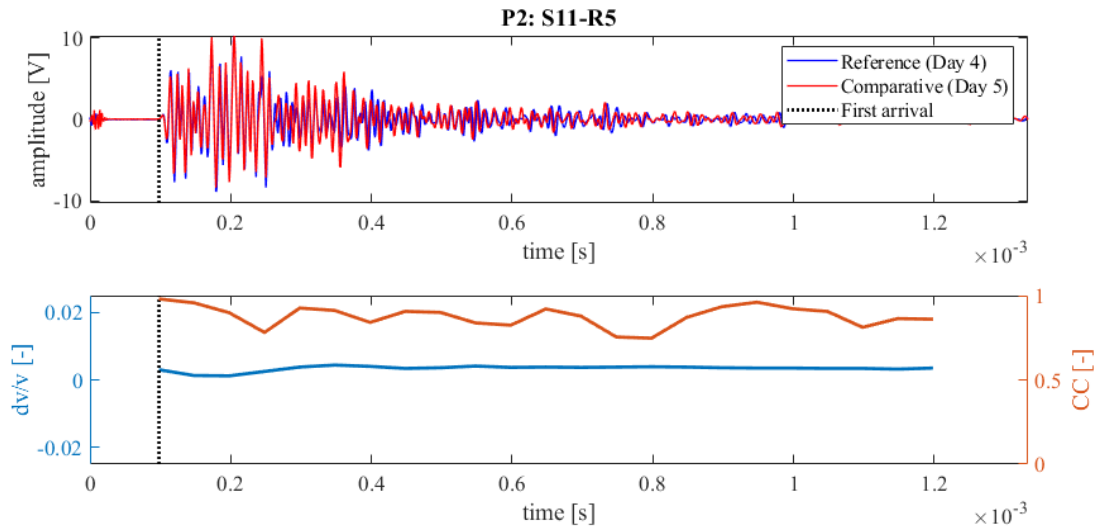


Figure 165: Wave signals of Measurement 4 (blue) and Measurement 5 (red) between principal sensor pair Source S11 and Receiver S5 at Position 2 (top),  $dv/v$  (blue) and  $CC$  (orange) results from CWI over the signal travel time divided in stretching windows (bottom)

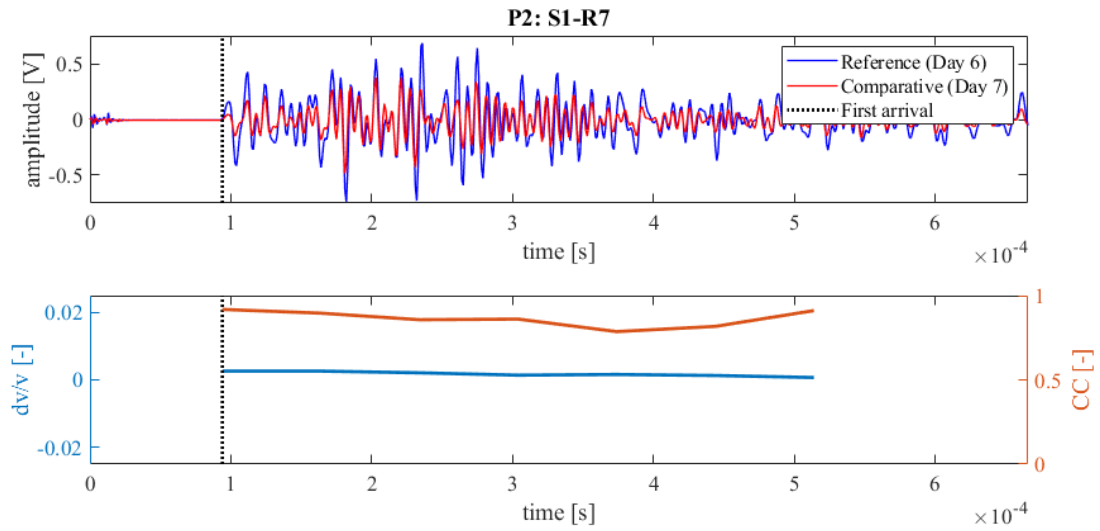


Figure 166: Wave signals of Measurement 6 (blue) and Measurement 7 (red) between principal sensor pair Source S1 and Receiver S7 at Position 2 (top),  $dv/v$  (blue) and  $CC$  (orange) results from CWI over the signal travel time divided in stretching windows (bottom)

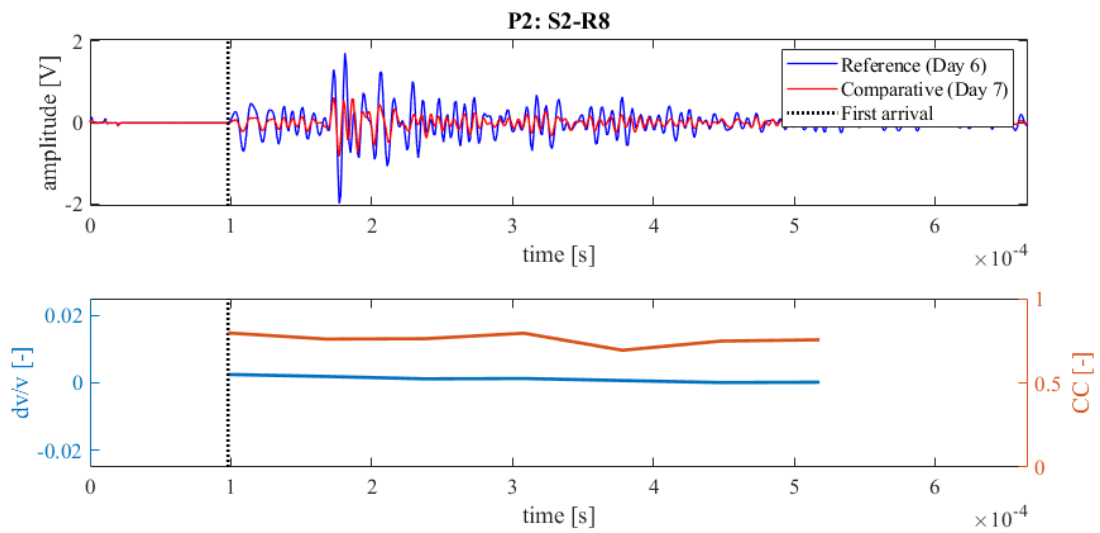


Figure 167: Wave signals of Measurement 6 (blue) and Measurement 7 (red) between principal sensor pair Source S2 and Receiver S8 at Position 2 (top),  $dv/v$  (blue) and  $CC$  (orange) results from CWI over the signal travel time divided in stretching windows (bottom)

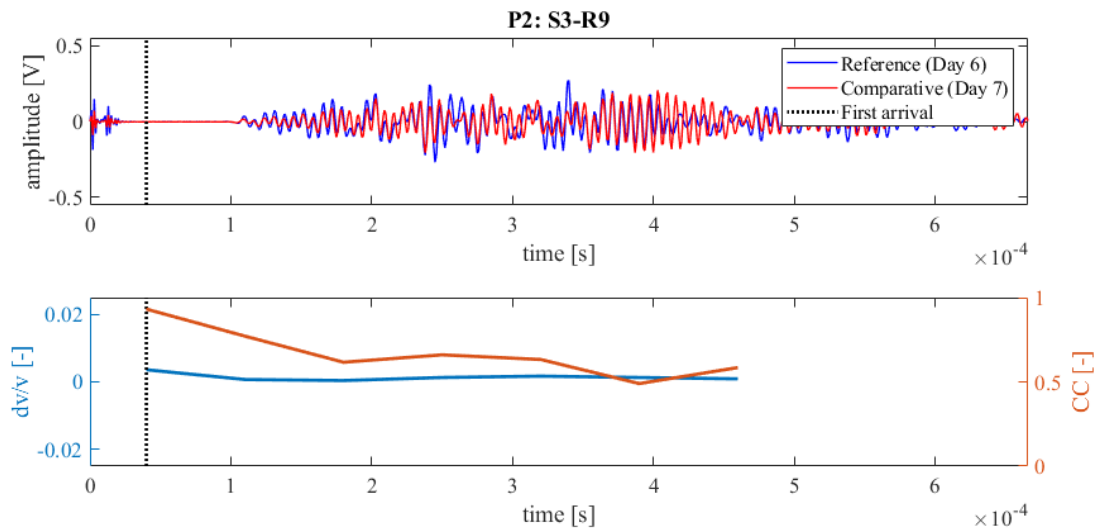


Figure 168: Wave signals of Measurement 6 (blue) and Measurement 7 (red) between principal sensor pair Source S3 and Receiver S9 at Position 2 (top),  $dv/v$  (blue) and  $CC$  (orange) results from CWI over the signal travel time divided in stretching windows (bottom)

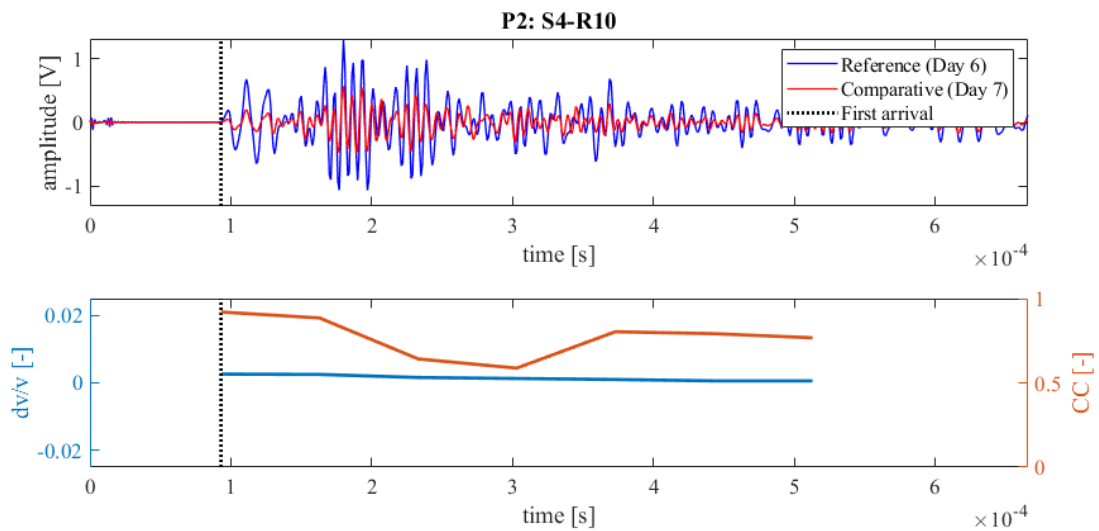


Figure 169: Wave signals of Measurement 6 (blue) and Measurement 7 (red) between principal sensor pair Source S4 and Receiver S10 at Position 2 (top),  $dv/v$  (blue) and  $CC$  (orange) results from CWI over the signal travel time divided in stretching windows (bottom)

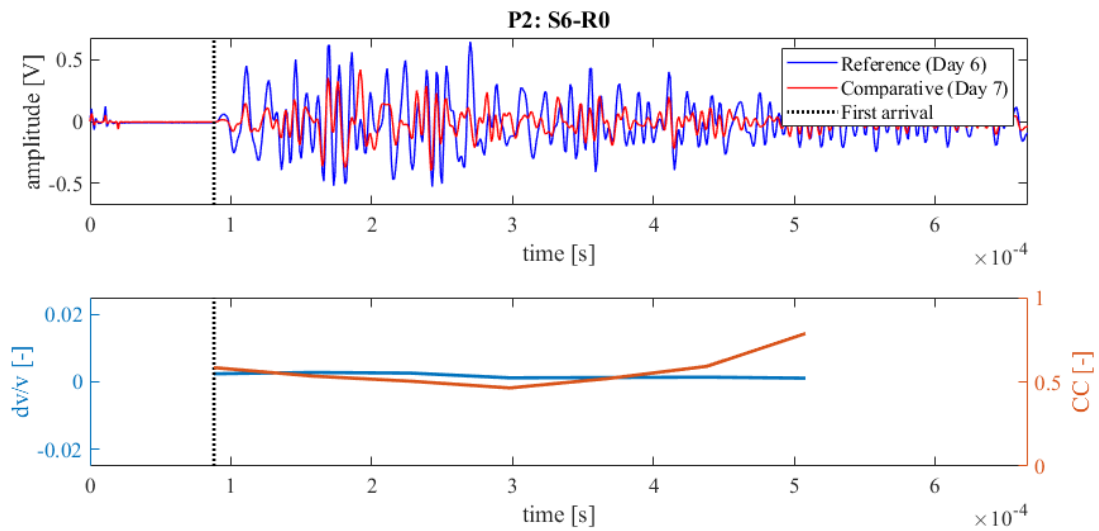


Figure 170: Wave signals of Measurement 6 (blue) and Measurement 7 (red) between principal sensor pair Source S6 and Receiver S0 at Position 2 (top),  $dv/v$  (blue) and  $CC$  (orange) results from CWI over the signal travel time divided in stretching windows (bottom)

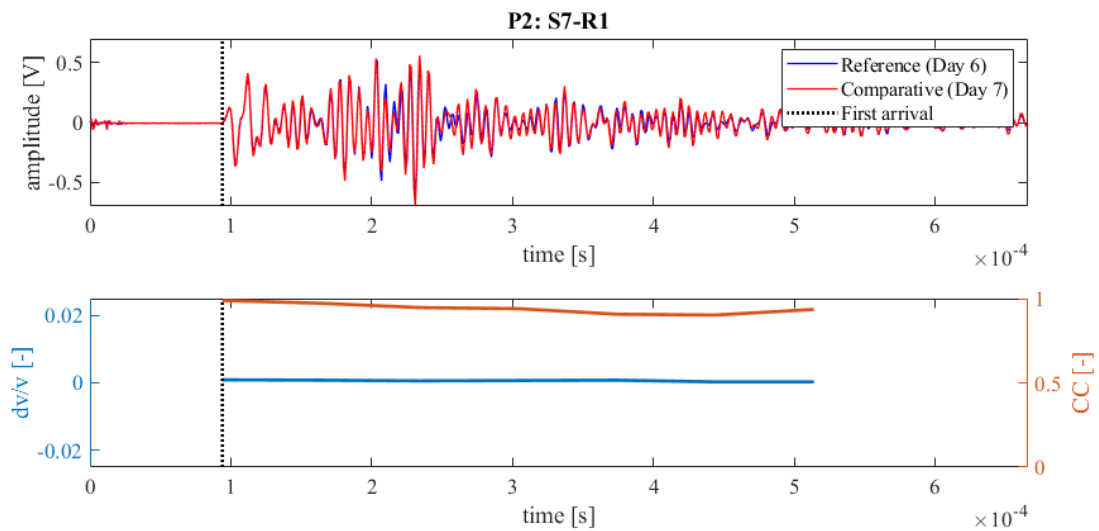


Figure 171: Wave signals of Measurement 6 (blue) and Measurement 7 (red) between principal sensor pair Source S7 and Receiver S1 at Position 2 (top),  $dv/v$  (blue) and  $CC$  (orange) results from CWI over the signal travel time divided in stretching windows (bottom)

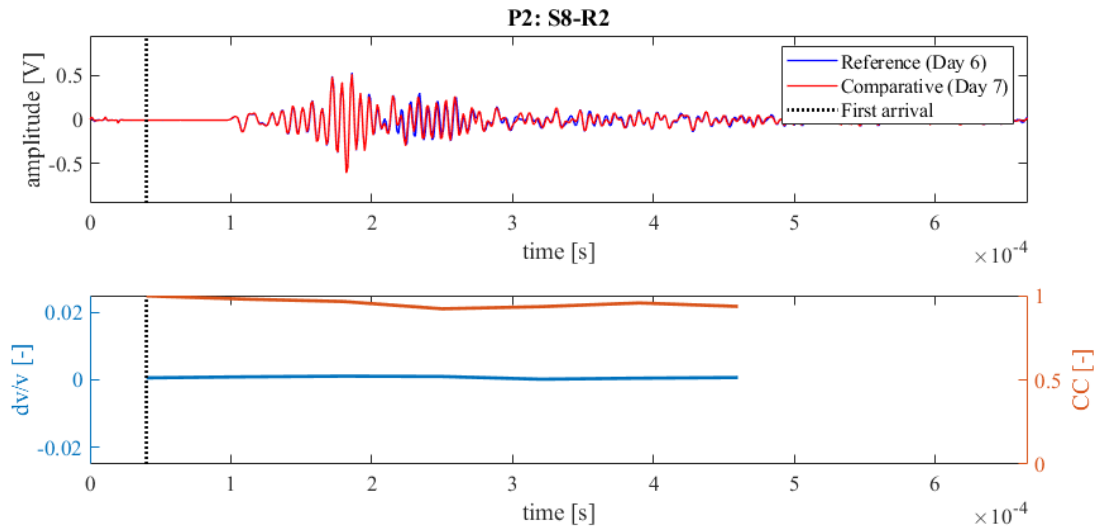


Figure 172: Wave signals of Measurement 6 (blue) and Measurement 7 (red) between principal sensor pair Source S8 and Receiver S2 at Position 2 (top),  $dv/v$  (blue) and CC (orange) results from CWI over the signal travel time divided in stretching windows (bottom)

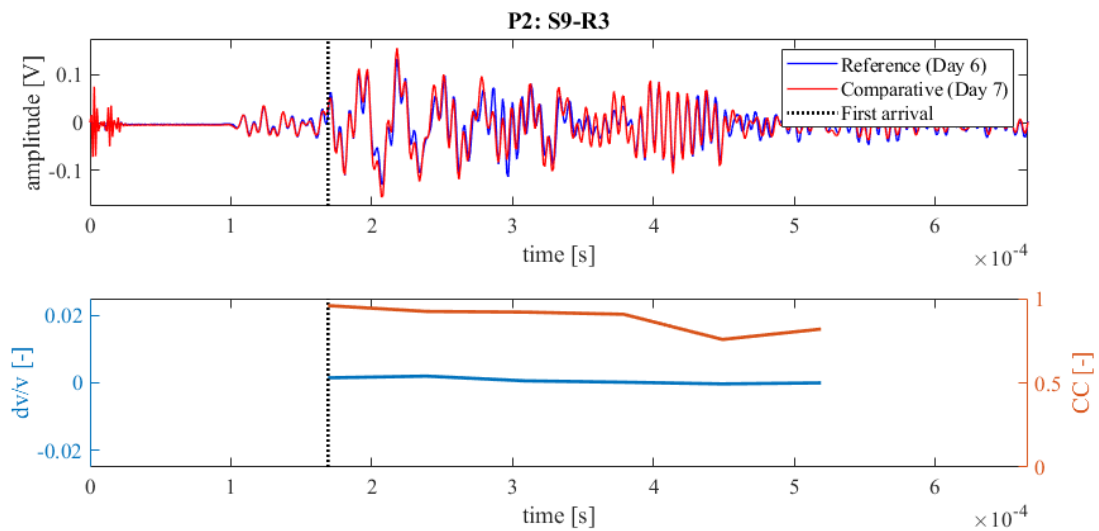


Figure 173: Wave signals of Measurement 6 (blue) and Measurement 7 (red) between principal sensor pair Source S9 and Receiver S3 at Position 2 (top),  $dv/v$  (blue) and CC (orange) results from CWI over the signal travel time divided in stretching windows (bottom)

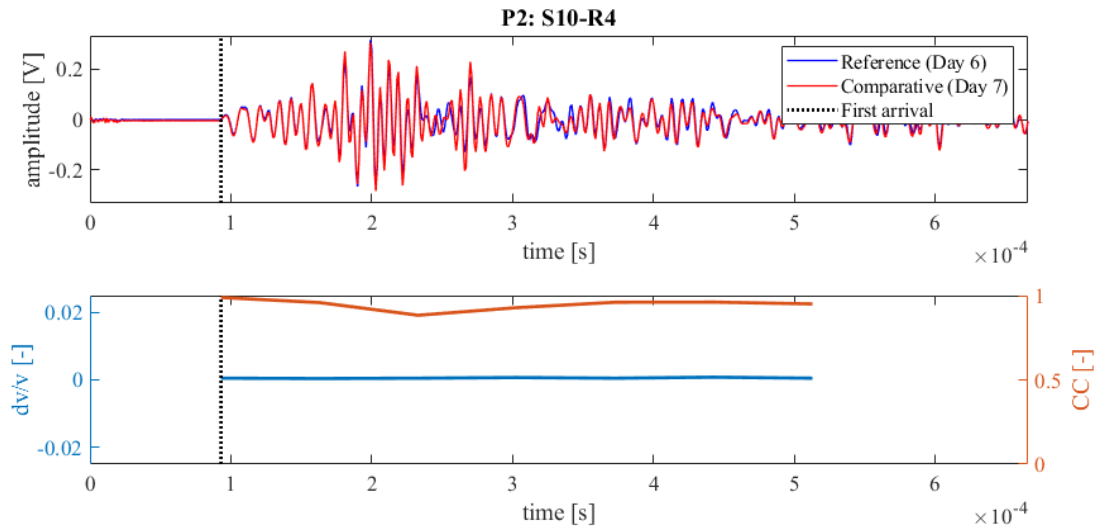


Figure 174: Wave signals of Measurement 6 (blue) and Measurement 7 (red) between principal sensor pair Source S10 and Receiver S4 at Position 2 (top),  $dv/v$  (blue) and  $CC$  (orange) results from CWI over the signal travel time divided in stretching windows (bottom)

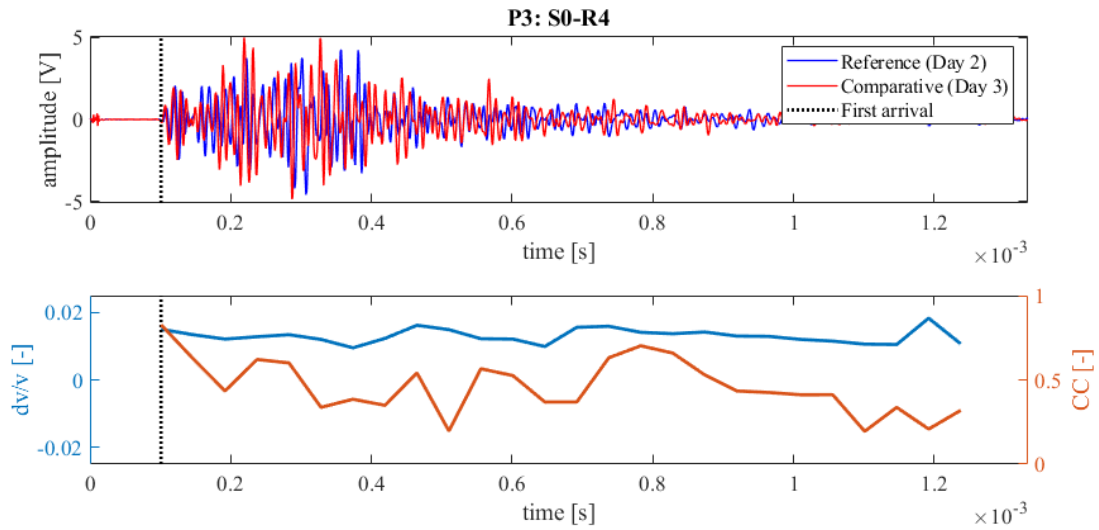


Figure 175: Wave signals of Measurement 2 (blue) and Measurement 3 (red) between principal sensor pair Source S0 and Receiver S4 at Position 3 (top),  $dv/v$  (blue) and  $CC$  (orange) results from CWI over the signal travel time divided in stretching windows (bottom)

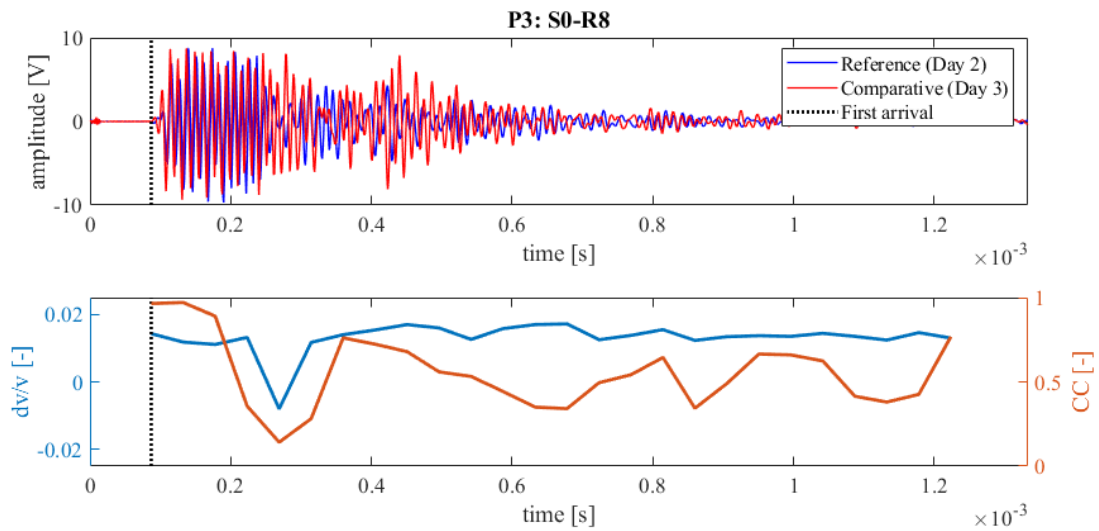


Figure 176: Wave signals of Measurement 2 (blue) and Measurement 3 (red) between principal sensor pair Source S0 and Receiver S8 at Position 3 (top),  $dv/v$  (blue) and  $CC$  (orange) results from CWI over the signal travel time divided in stretching windows (bottom)

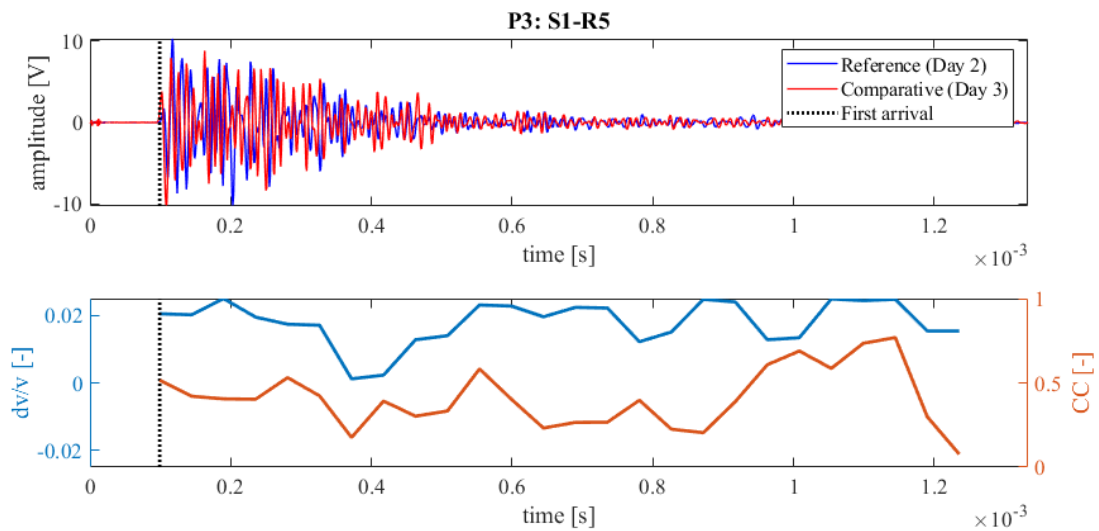


Figure 177: Wave signals of Measurement 2 (blue) and Measurement 3 (red) between principal sensor pair Source S1 and Receiver S5 at Position 3 (top),  $dv/v$  (blue) and  $CC$  (orange) results from CWI over the signal travel time divided in stretching windows (bottom)

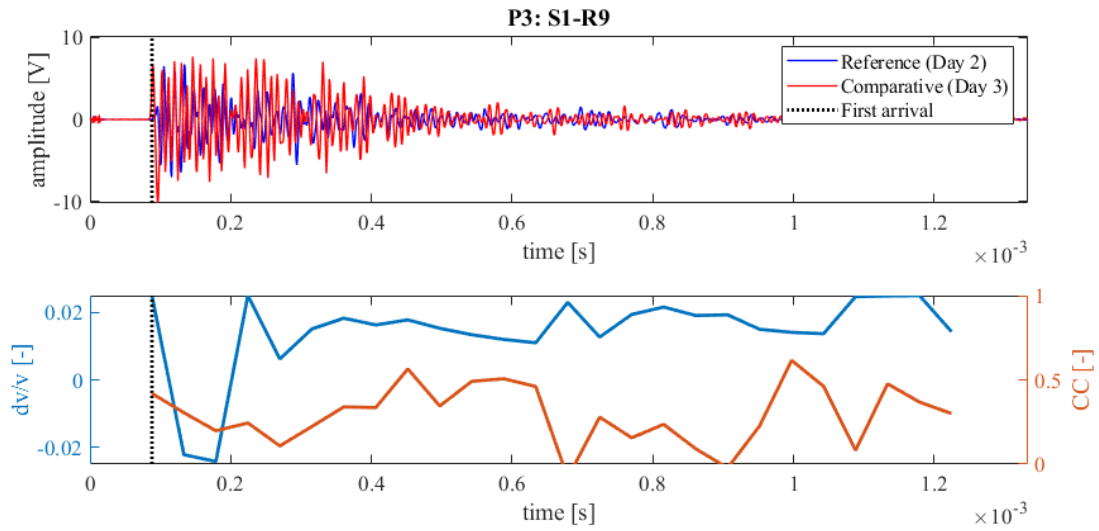


Figure 178: Wave signals of Measurement 2 (blue) and Measurement 3 (red) between principal sensor pair Source S1 and Receiver S9 at Position 3 (top),  $dv/v$  (blue) and  $CC$  (orange) results from CWI over the signal travel time divided in stretching windows (bottom)

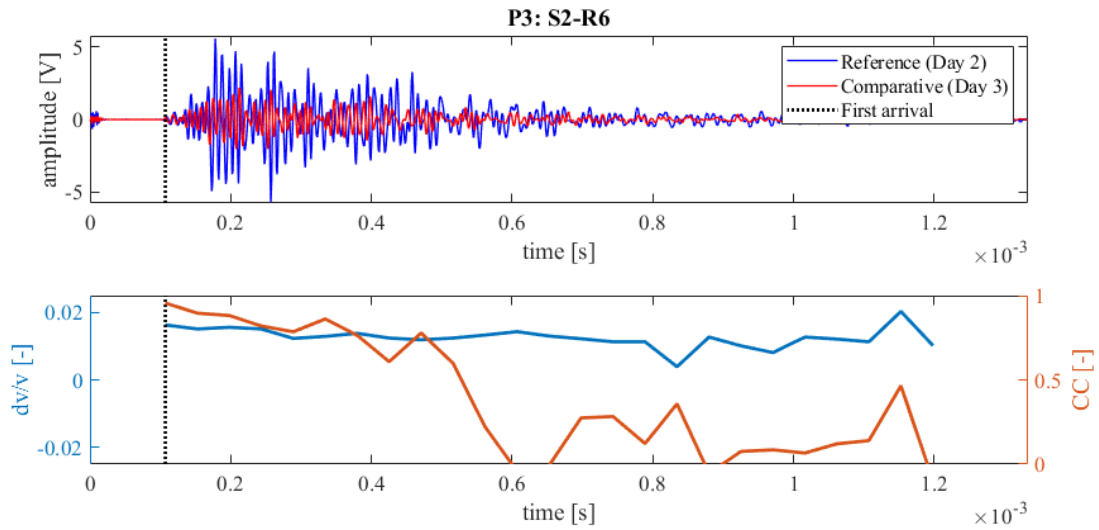


Figure 179: Wave signals of Measurement 2 (blue) and Measurement 3 (red) between principal sensor pair Source S2 and Receiver S6 at Position 3 (top),  $dv/v$  (blue) and  $CC$  (orange) results from CWI over the signal travel time divided in stretching windows (bottom)

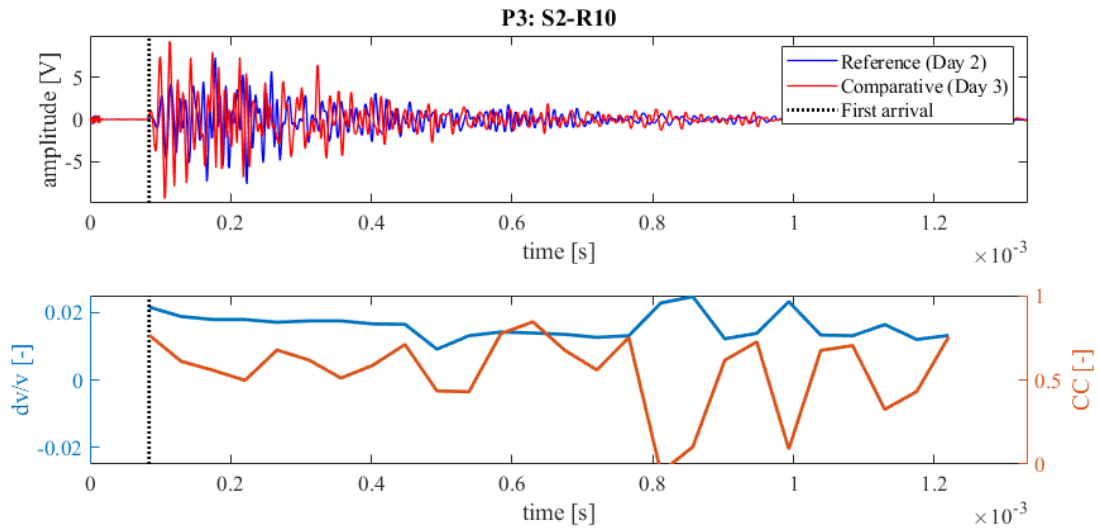


Figure 180: Wave signals of Measurement 2 (blue) and Measurement 3 (red) between principal sensor pair Source S2 and Receiver S10 at Position 3 (top),  $dv/v$  (blue) and  $CC$  (orange) results from CWI over the signal travel time divided in stretching windows (bottom)

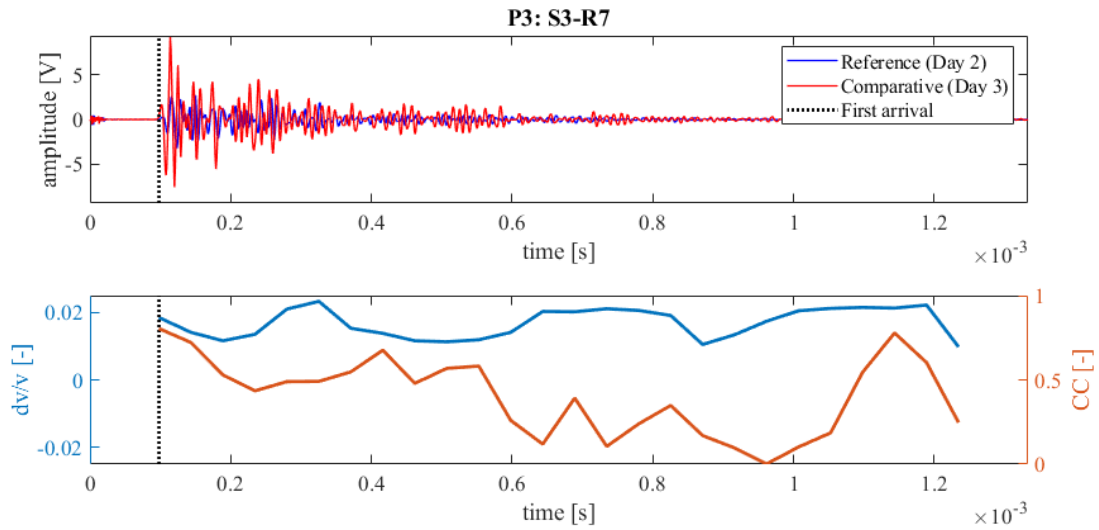


Figure 181: Wave signals of Measurement 2 (blue) and Measurement 3 (red) between principal sensor pair Source S3 and Receiver S7 at Position 3 (top),  $dv/v$  (blue) and  $CC$  (orange) results from CWI over the signal travel time divided in stretching windows (bottom)

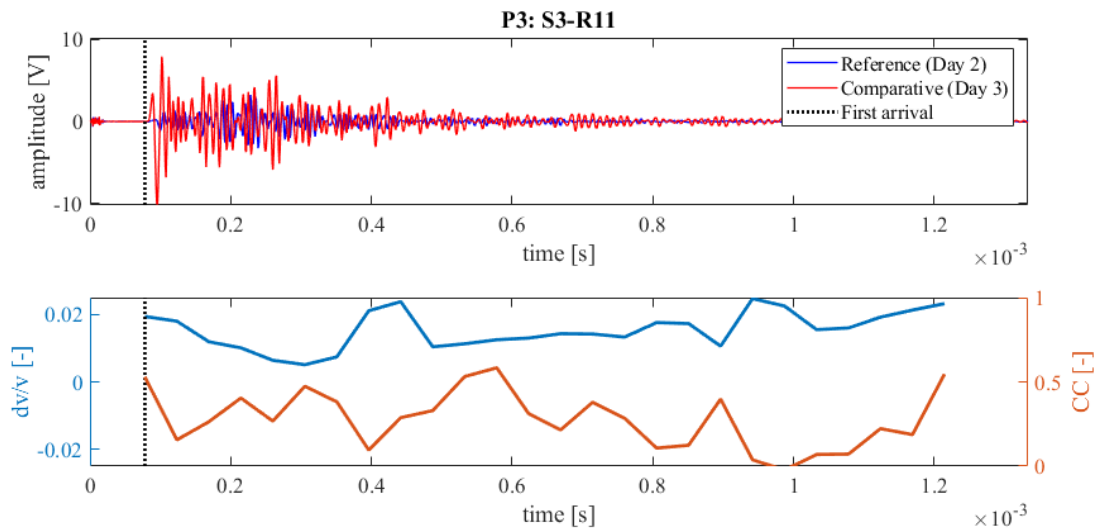


Figure 182: Wave signals of Measurement 2 (blue) and Measurement 3 (red) between principal sensor pair Source S3 and Receiver S11 at Position 3 (top),  $dv/v$  (blue) and  $CC$  (orange) results from CWI over the signal travel time divided in stretching windows (bottom)

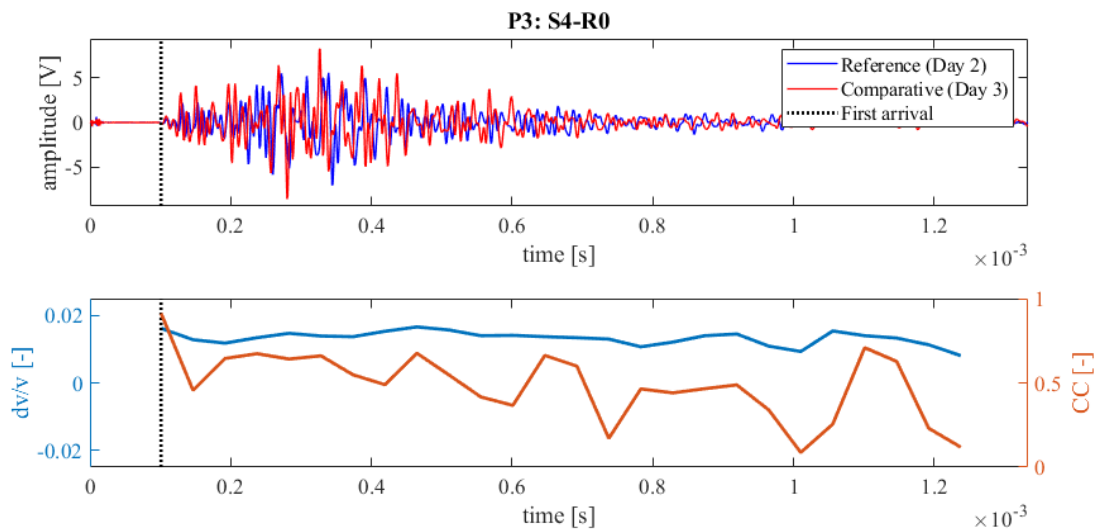


Figure 183: Wave signals of Measurement 2 (blue) and Measurement 3 (red) between principal sensor pair Source S4 and Receiver S0 at Position 3 (top),  $dv/v$  (blue) and  $CC$  (orange) results from CWI over the signal travel time divided in stretching windows (bottom)

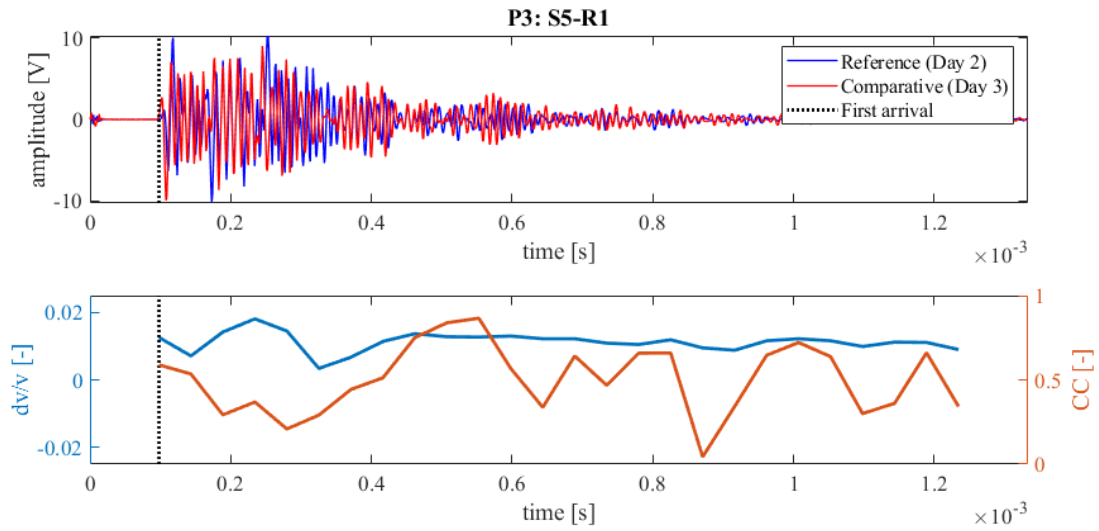


Figure 184: Wave signals of Measurement 2 (blue) and Measurement 3 (red) between principal sensor pair Source S5 and Receiver S1 at Position 3 (top),  $dv/v$  (blue) and  $CC$  (orange) results from CWI over the signal travel time divided in stretching windows (bottom)

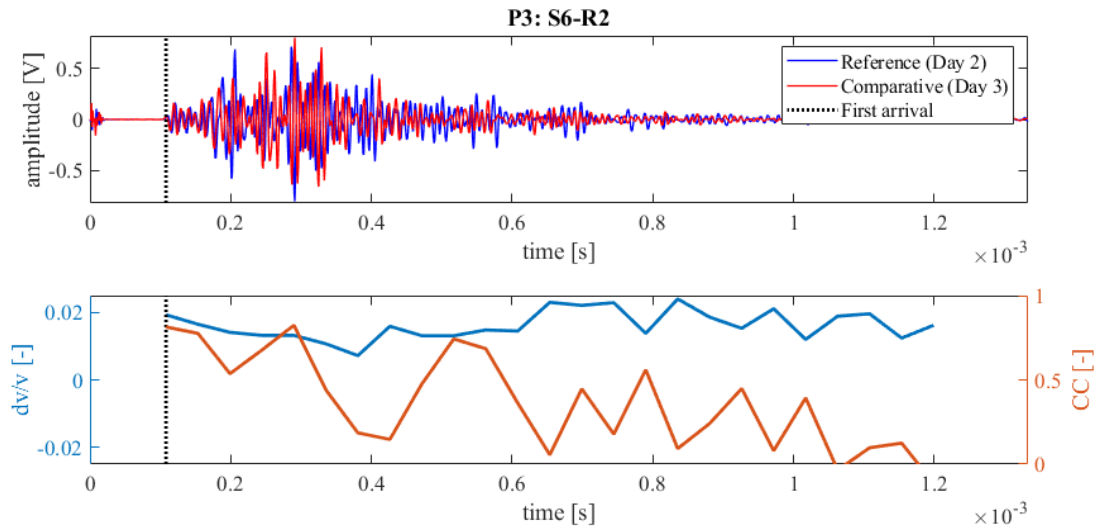


Figure 185: Wave signals of Measurement 2 (blue) and Measurement 3 (red) between principal sensor pair Source S6 and Receiver S2 at Position 3 (top),  $dv/v$  (blue) and  $CC$  (orange) results from CWI over the signal travel time divided in stretching windows (bottom)

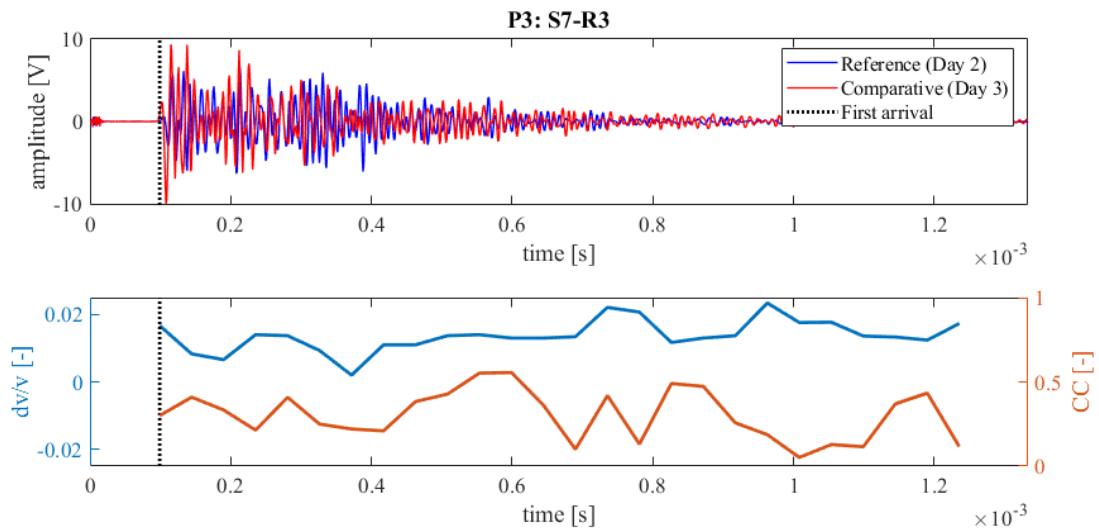


Figure 186: Wave signals of Measurement 2 (blue) and Measurement 3 (red) between principal sensor pair Source S7 and Receiver S3 at Position 3 (top),  $dv/v$  (blue) and CC (orange) results from CWI over the signal travel time divided in stretching windows (bottom)

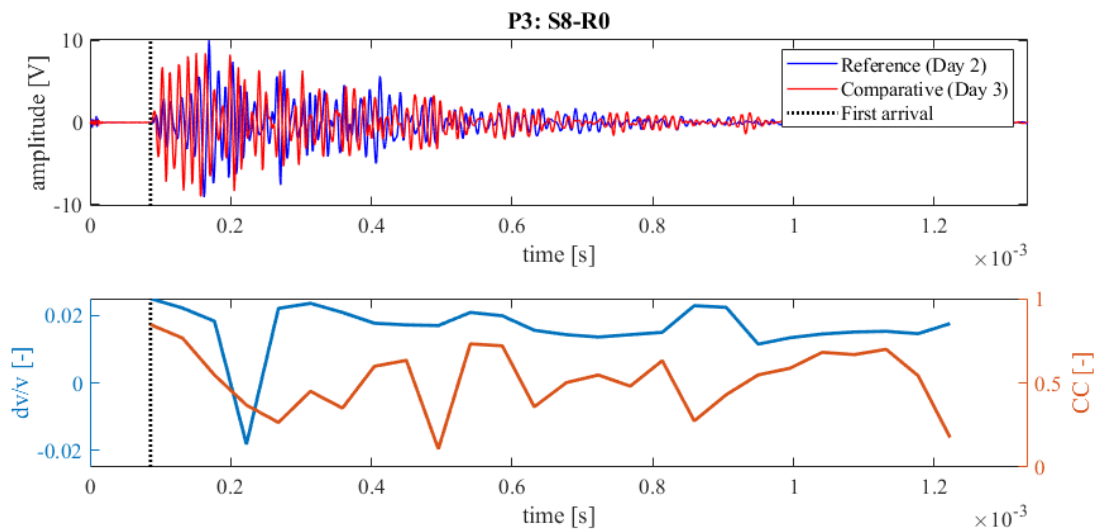


Figure 187: Wave signals of Measurement 2 (blue) and Measurement 3 (red) between principal sensor pair Source S8 and Receiver S0 at Position 3 (top),  $dv/v$  (blue) and CC (orange) results from CWI over the signal travel time divided in stretching windows (bottom)

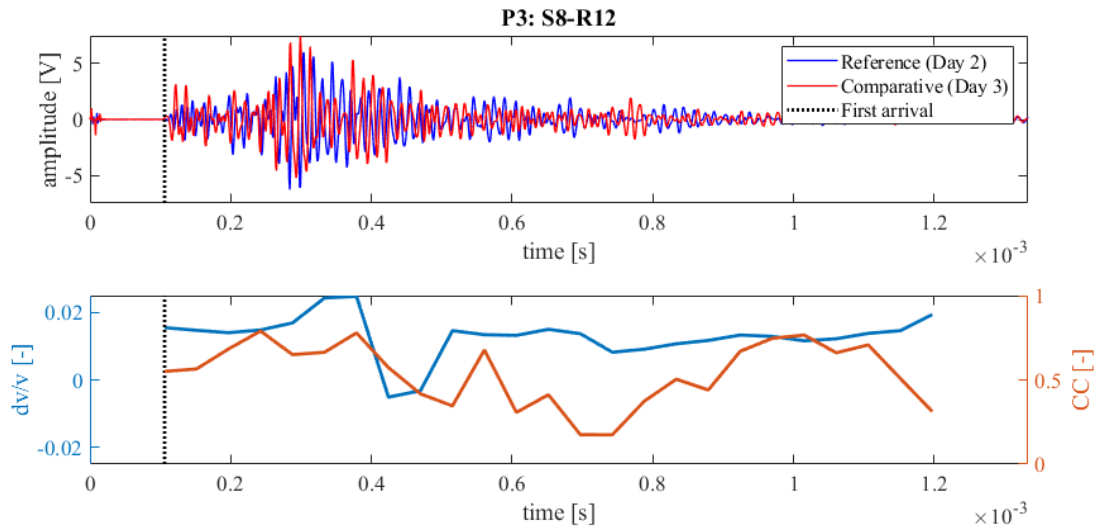


Figure 188: Wave signals of Measurement 2 (blue) and Measurement 3 (red) between principal sensor pair Source S8 and Receiver S12 at Position 3 (top),  $dv/v$  (blue) and  $CC$  (orange) results from CWI over the signal travel time divided in stretching windows (bottom)

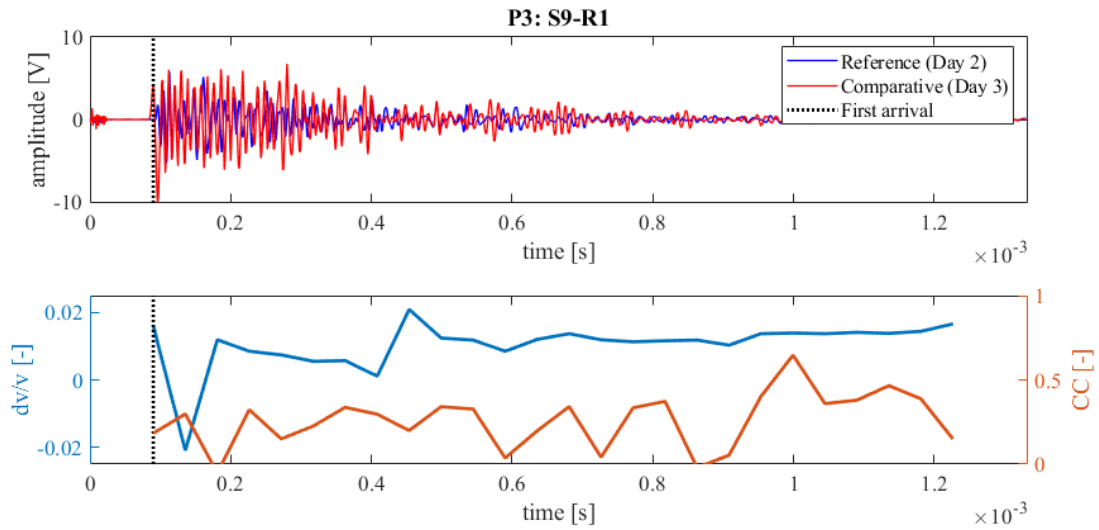


Figure 189: Wave signals of Measurement 2 (blue) and Measurement 3 (red) between principal sensor pair Source S9 and Receiver S1 at Position 3 (top),  $dv/v$  (blue) and  $CC$  (orange) results from CWI over the signal travel time divided in stretching windows (bottom)

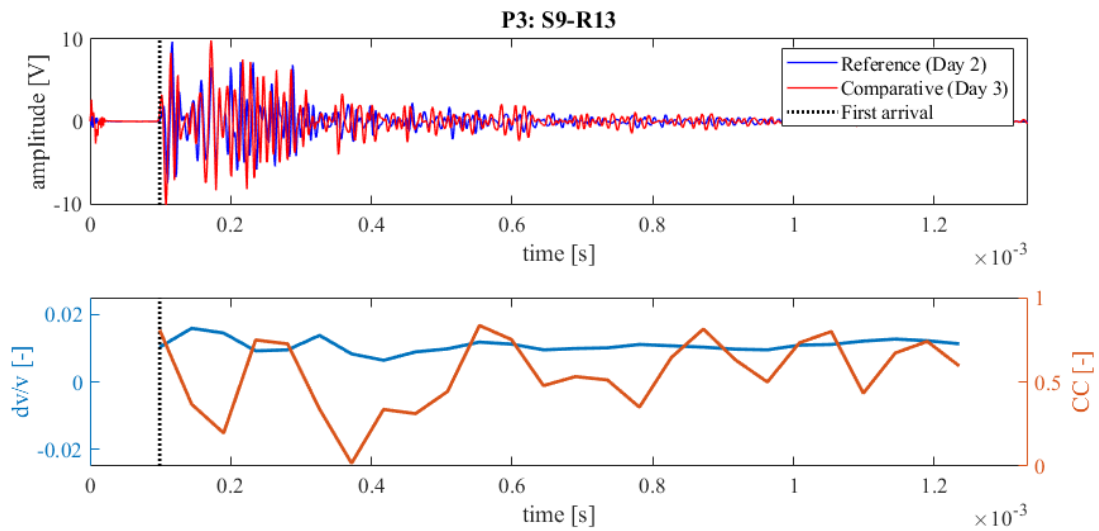


Figure 190: Wave signals of Measurement 2 (blue) and Measurement 3 (red) between principal sensor pair Source S9 and Receiver S13 at Position 3 (top),  $dv/v$  (blue) and  $CC$  (orange) results from CWI over the signal travel time divided in stretching windows (bottom)

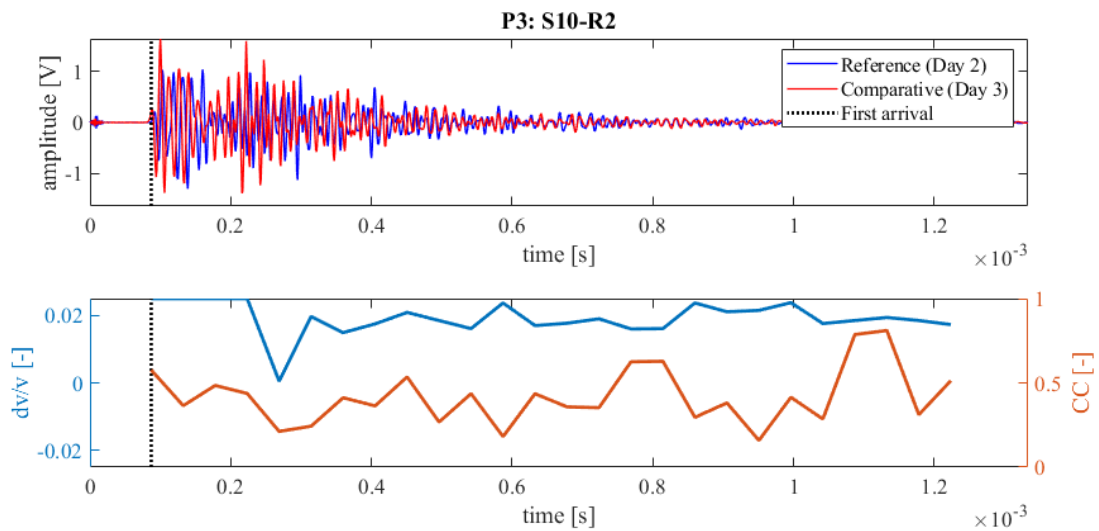
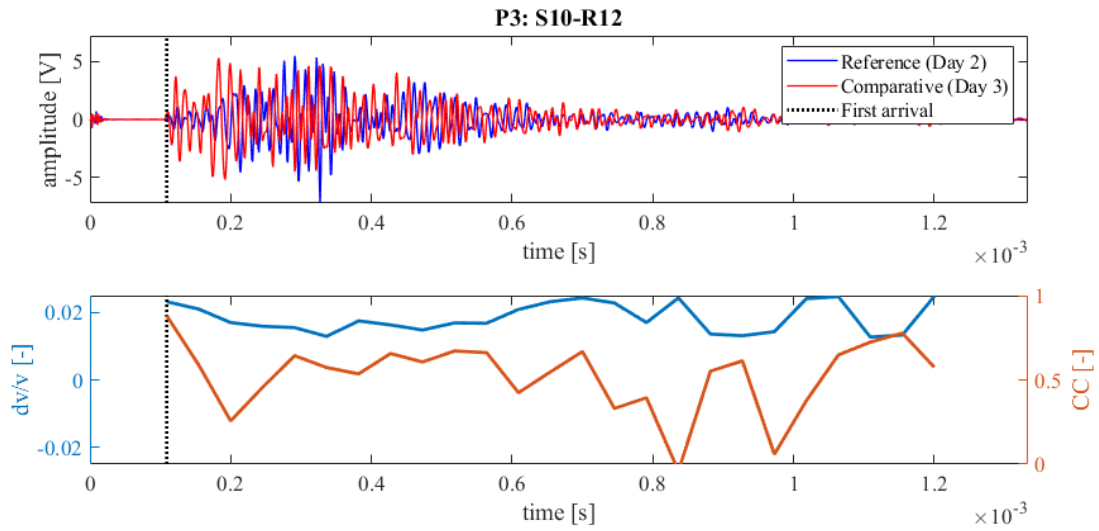
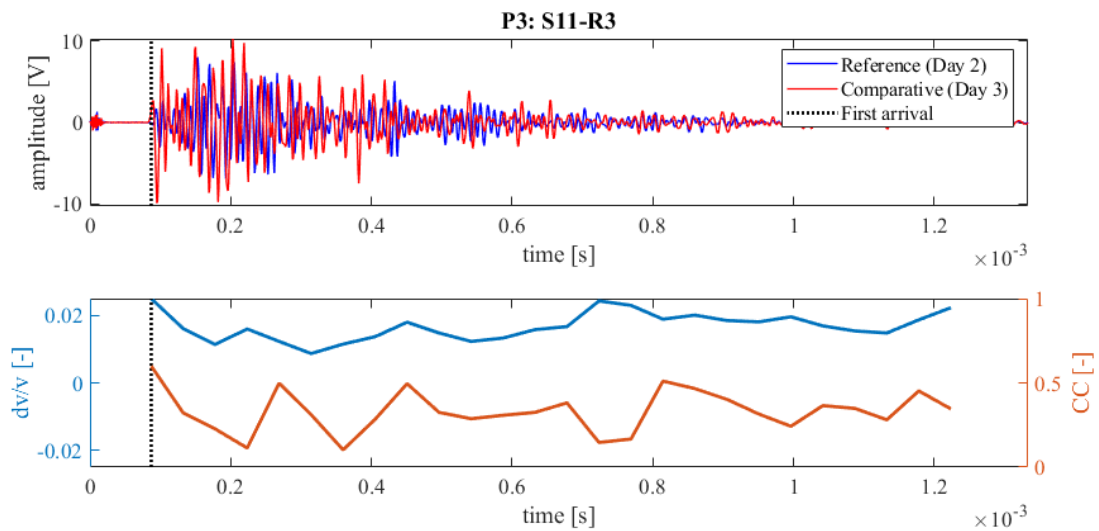


Figure 191: Wave signals of Measurement 2 (blue) and Measurement 3 (red) between principal sensor pair Source S10 and Receiver S2 at Position 3 (top),  $dv/v$  (blue) and  $CC$  (orange) results from CWI over the signal travel time divided in stretching windows (bottom)



**Figure 192: Wave signals of Measurement 2 (blue) and Measurement 3 (red) between principal sensor pair Source S10 and Receiver S12 at Position 3 (top),  $dv/v$  (blue) and CC (orange) results from CWI over the signal travel time divided in stretching windows (bottom)**



**Figure 193: Wave signals of Measurement 2 (blue) and Measurement 3 (red) between principal sensor pair Source S11 and Receiver S3 at Position 3 (top),  $dv/v$  (blue) and CC (orange) results from CWI over the signal travel time divided in stretching windows (bottom)**

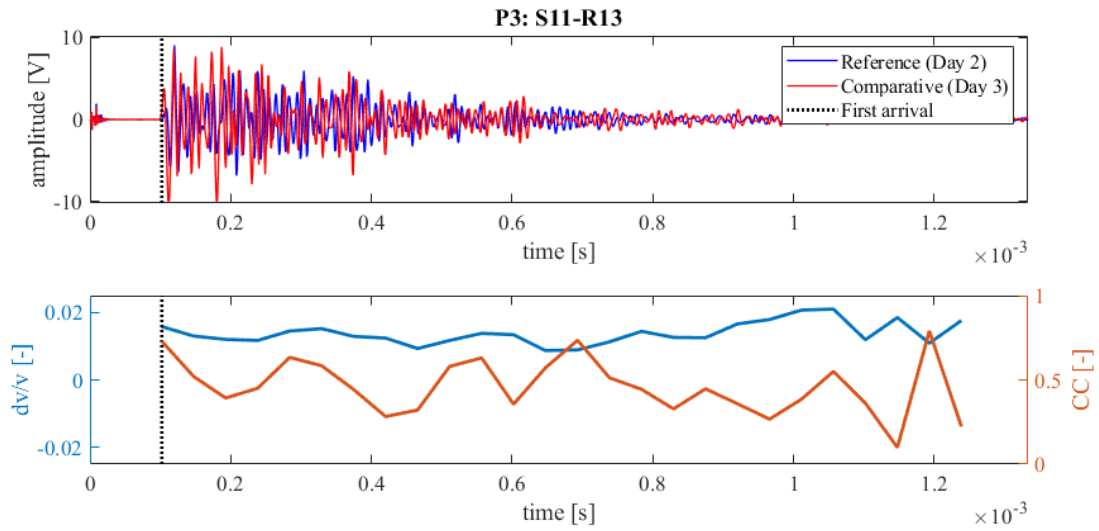


Figure 194: Wave signals of Measurement 2 (blue) and Measurement 3 (red) between principal sensor pair Source S11 and Receiver S13 at Position 3 (top),  $dv/v$  (blue) and  $CC$  (orange) results from CWI over the signal travel time divided in stretching windows (bottom)

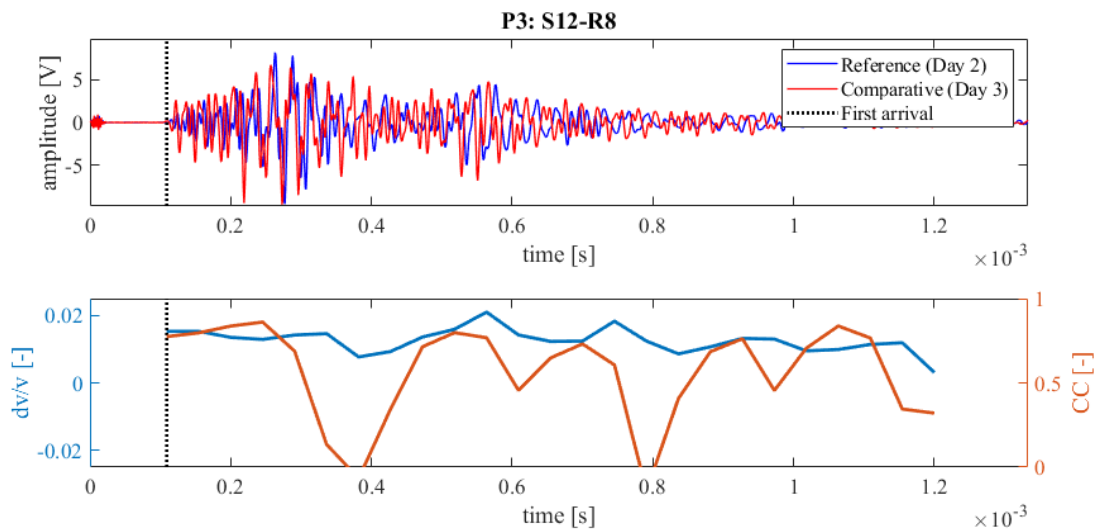
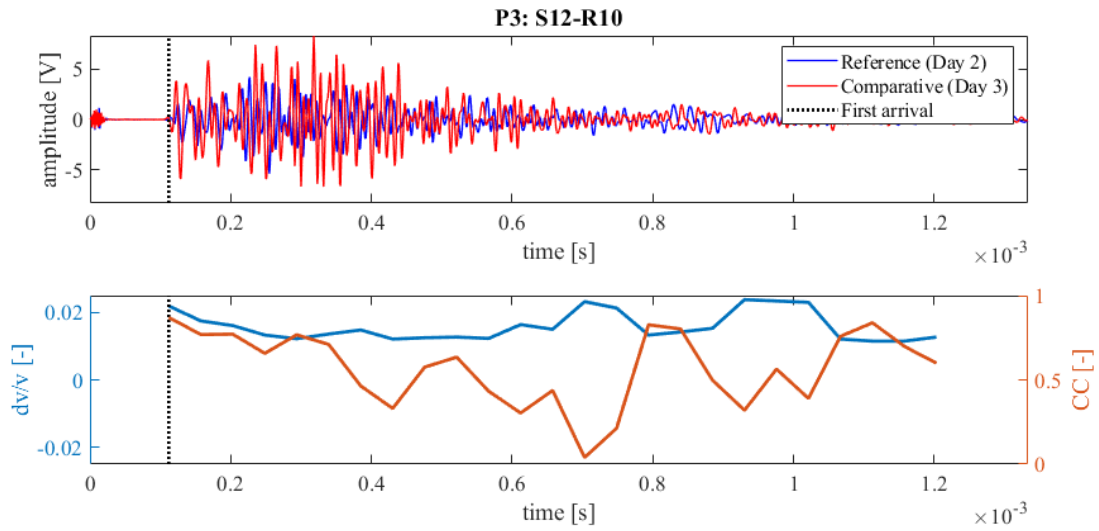
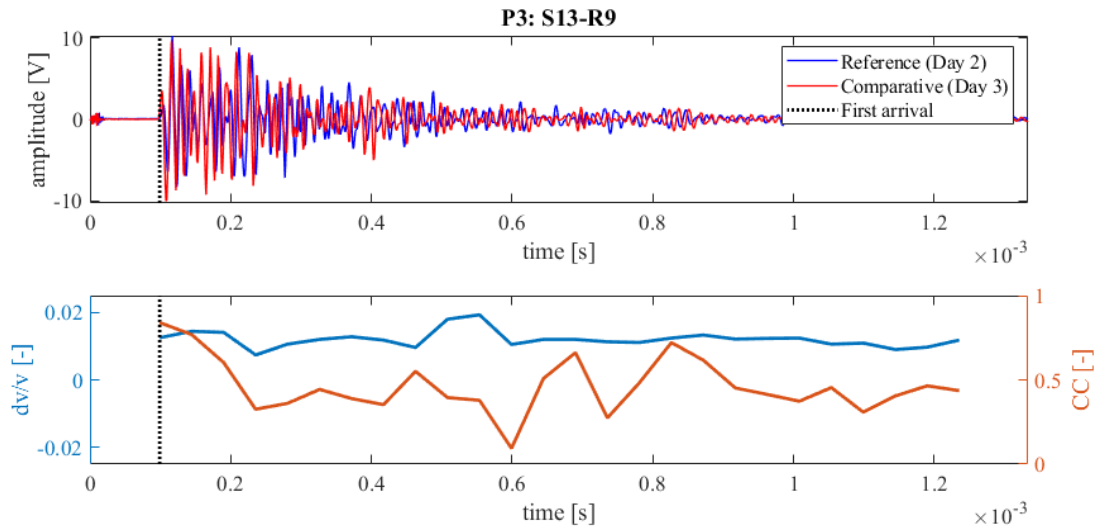


Figure 195: Wave signals of Measurement 2 (blue) and Measurement 3 (red) between principal sensor pair Source S12 and Receiver S8 at Position 3 (top),  $dv/v$  (blue) and  $CC$  (orange) results from CWI over the signal travel time divided in stretching windows (bottom)



**Figure 196: Wave signals of Measurement 2 (blue) and Measurement 3 (red) between principal sensor pair Source S12 and Receiver S10 at Position 3 (top),  $dv/v$  (blue) and CC (orange) results from CWI over the signal travel time divided in stretching windows (bottom)**



**Figure 197: Wave signals of Measurement 2 (blue) and Measurement 3 (red) between principal sensor pair Source S13 and Receiver S9 at Position 3 (top),  $dv/v$  (blue) and CC (orange) results from CWI over the signal travel time divided in stretching windows (bottom)**

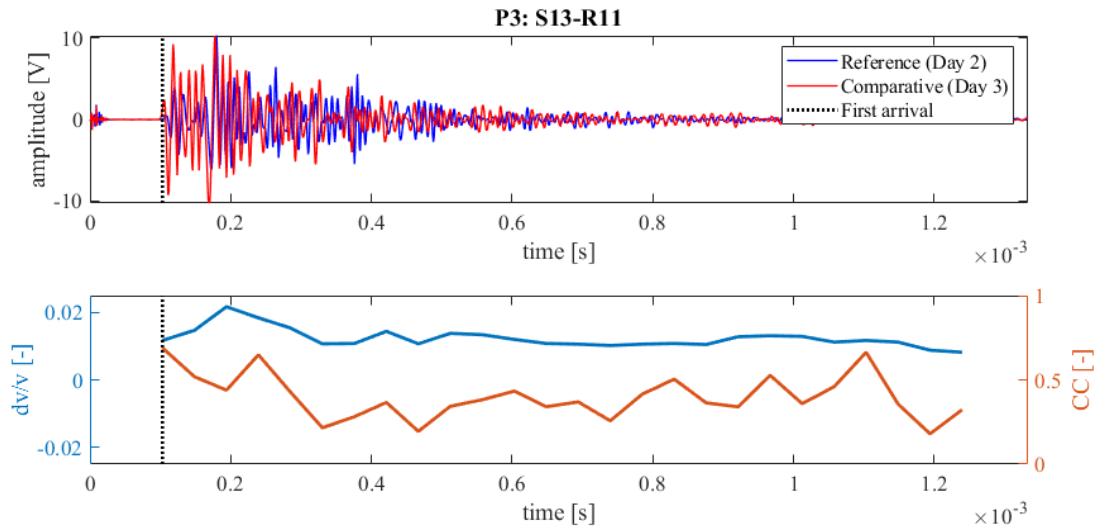


Figure 198: Wave signals of Measurement 2 (blue) and Measurement 3 (red) between principal sensor pair Source S13 and Receiver S11 at Position 3 (top),  $dv/v$  (blue) and  $CC$  (orange) results from CWI over the signal travel time divided in stretching windows (bottom)

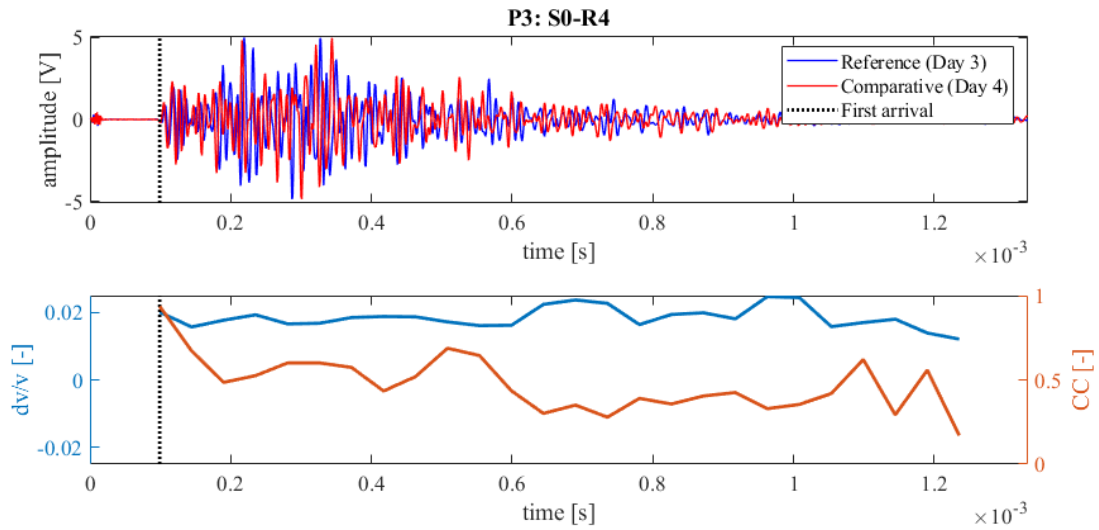


Figure 199: Wave signals of Measurement 3 (blue) and Measurement 4 (red) between principal sensor pair Source S0 and Receiver S4 at Position 3 (top),  $dv/v$  (blue) and  $CC$  (orange) results from CWI over the signal travel time divided in stretching windows (bottom)

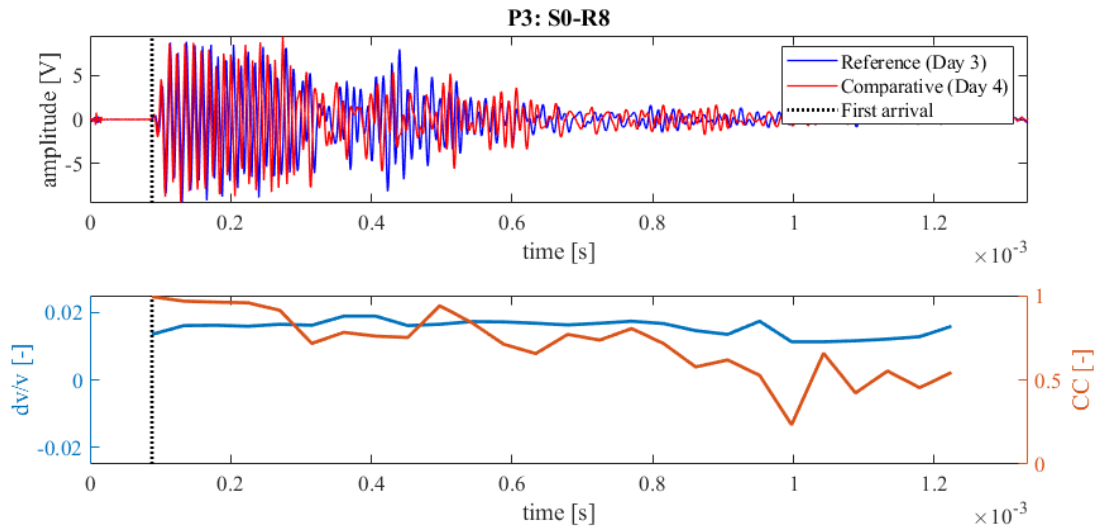


Figure 200: Wave signals of Measurement 3 (blue) and Measurement 4 (red) between principal sensor pair Source S0 and Receiver S8 at Position 3 (top),  $dv/v$  (blue) and CC (orange) results from CWI over the signal travel time divided in stretching windows (bottom)

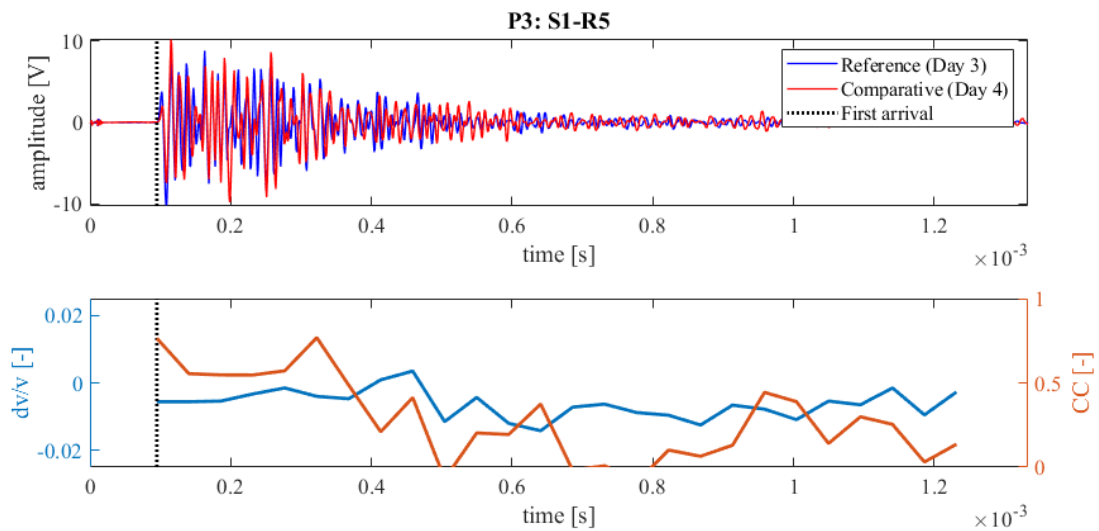


Figure 201: Wave signals of Measurement 3 (blue) and Measurement 4 (red) between principal sensor pair Source S1 and Receiver S5 at Position 3 (top),  $dv/v$  (blue) and CC (orange) results from CWI over the signal travel time divided in stretching windows (bottom)

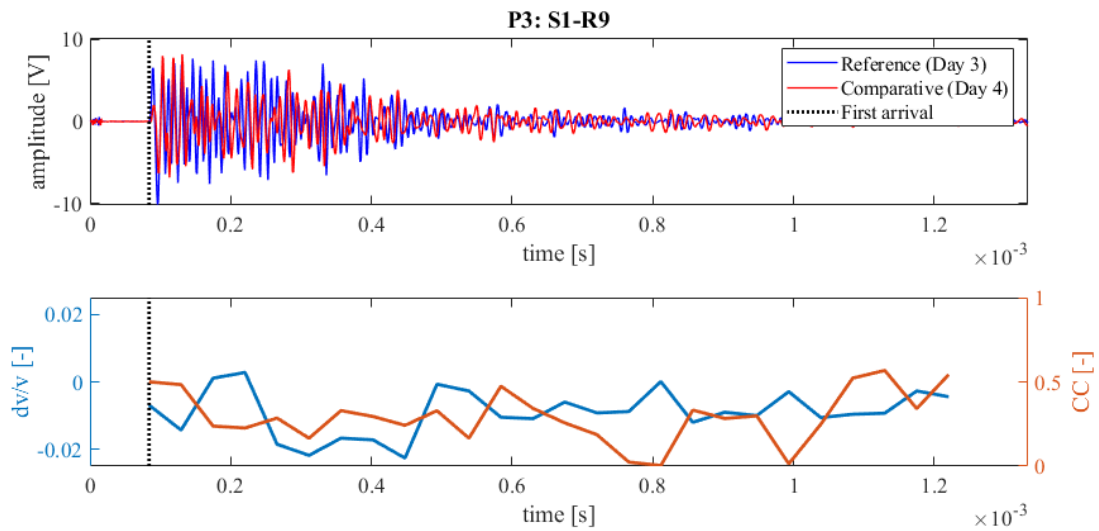


Figure 202: Wave signals of Measurement 3 (blue) and Measurement 4 (red) between principal sensor pair Source S1 and Receiver S9 at Position 3 (top),  $dv/v$  (blue) and CC (orange) results from CWI over the signal travel time divided in stretching windows (bottom)

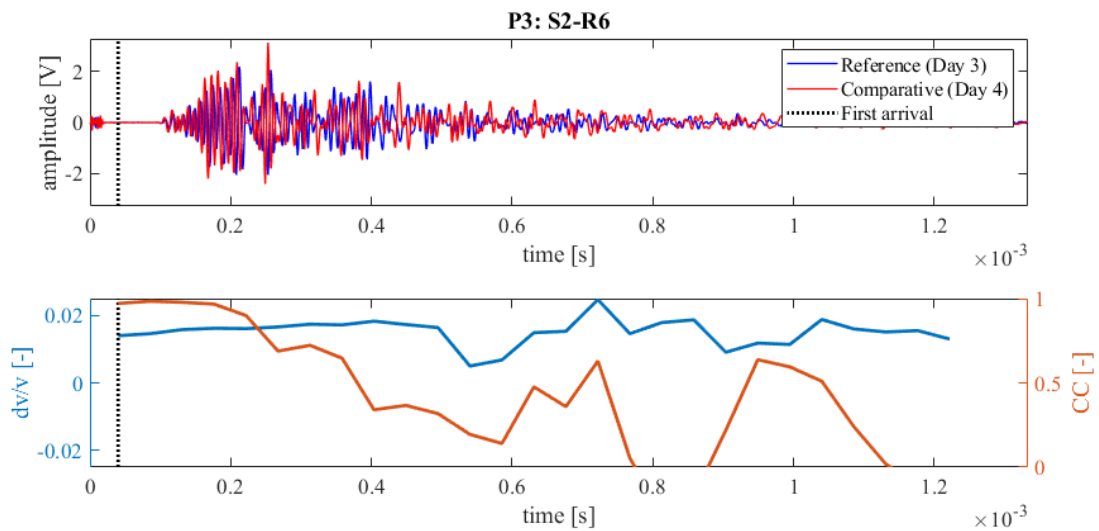


Figure 203: Wave signals of Measurement 3 (blue) and Measurement 4 (red) between principal sensor pair Source S2 and Receiver S6 at Position 3 (top),  $dv/v$  (blue) and CC (orange) results from CWI over the signal travel time divided in stretching windows (bottom)

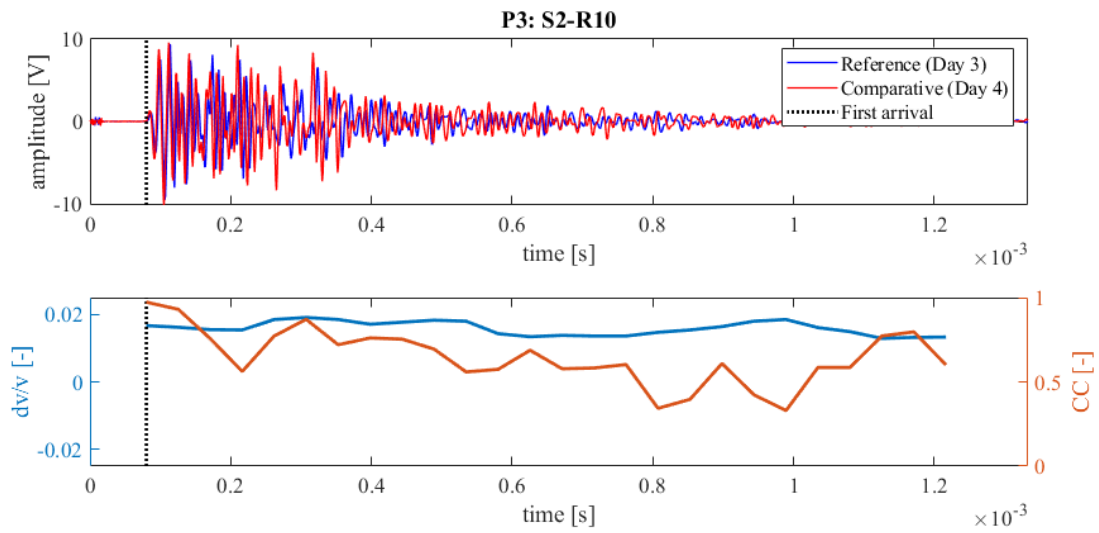


Figure 204: Wave signals of Measurement 3 (blue) and Measurement 4 (red) between principal sensor pair Source S2 and Receiver S10 at Position 3 (top),  $dv/v$  (blue) and  $CC$  (orange) results from CWI over the signal travel time divided in stretching windows (bottom)

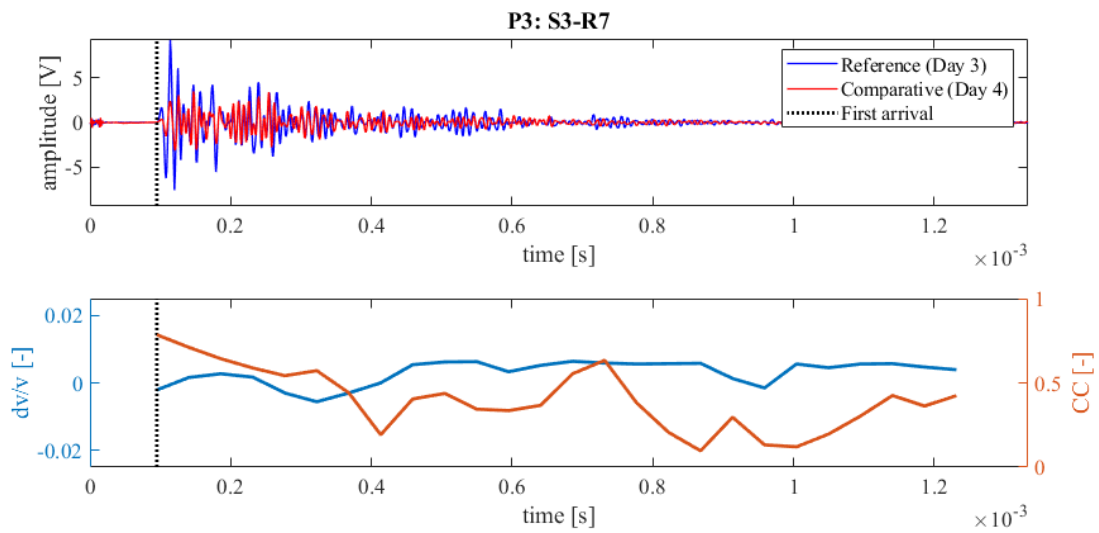


Figure 205: Wave signals of Measurement 3 (blue) and Measurement 4 (red) between principal sensor pair Source S3 and Receiver S7 at Position 3 (top),  $dv/v$  (blue) and  $CC$  (orange) results from CWI over the signal travel time divided in stretching windows (bottom)

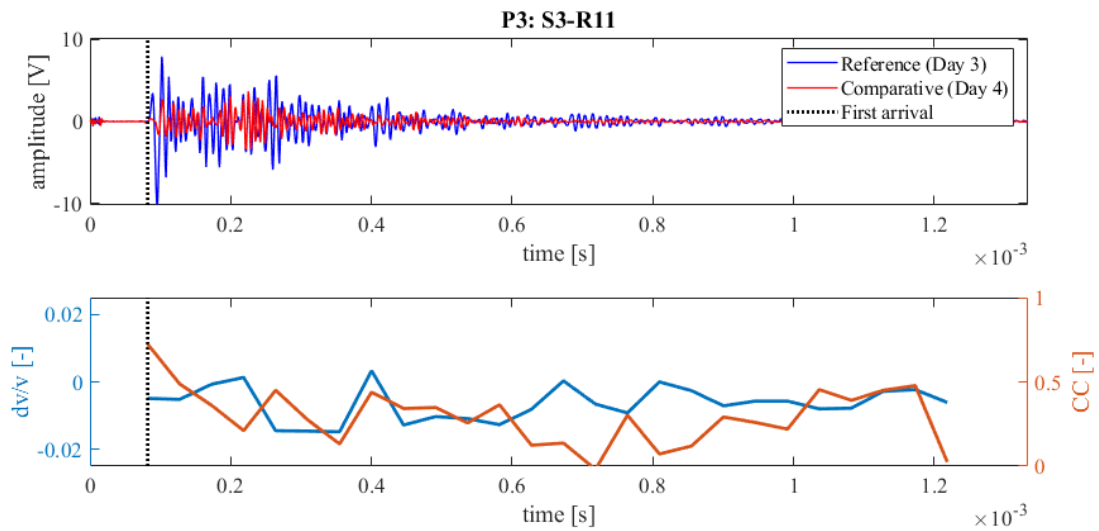


Figure 206: Wave signals of Measurement 3 (blue) and Measurement 4 (red) between principal sensor pair Source S3 and Receiver S11 at Position 3 (top),  $dv/v$  (blue) and  $CC$  (orange) results from CWI over the signal travel time divided in stretching windows (bottom)

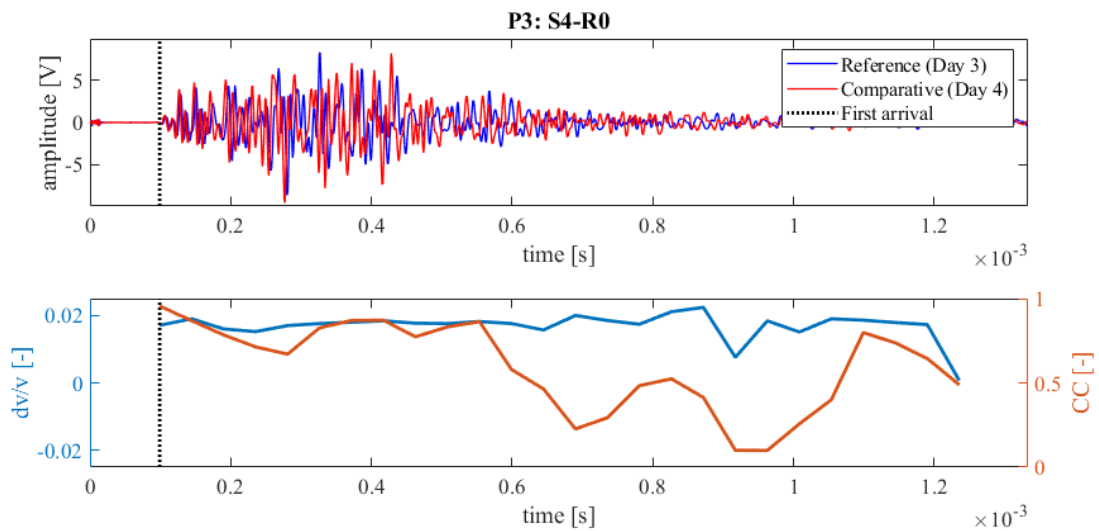


Figure 207: Wave signals of Measurement 3 (blue) and Measurement 4 (red) between principal sensor pair Source S4 and Receiver S0 at Position 3 (top),  $dv/v$  (blue) and  $CC$  (orange) results from CWI over the signal travel time divided in stretching windows (bottom)

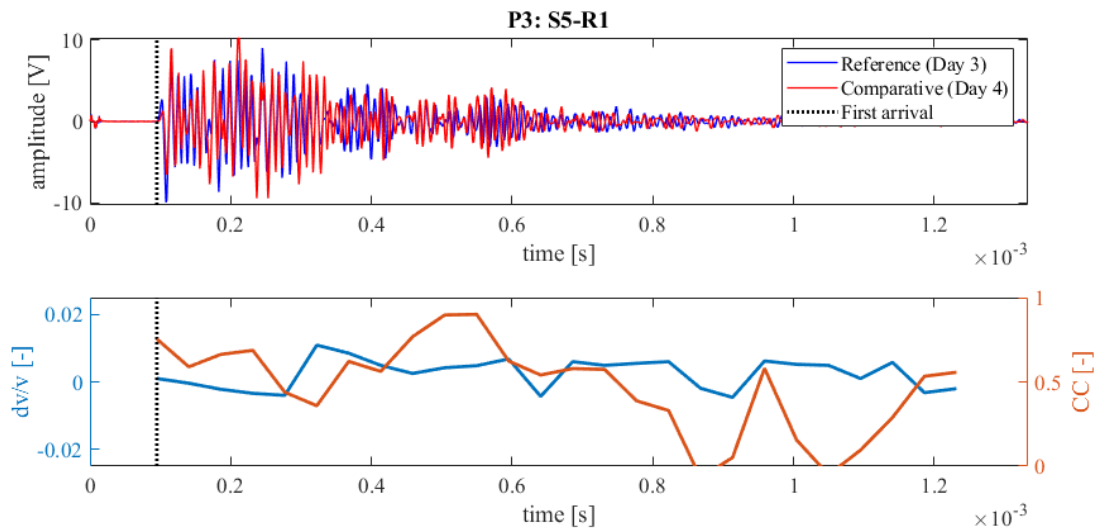


Figure 208: Wave signals of Measurement 3 (blue) and Measurement 4 (red) between principal sensor pair Source S5 and Receiver S1 at Position 3 (top),  $dv/v$  (blue) and CC (orange) results from CWI over the signal travel time divided in stretching windows (bottom)

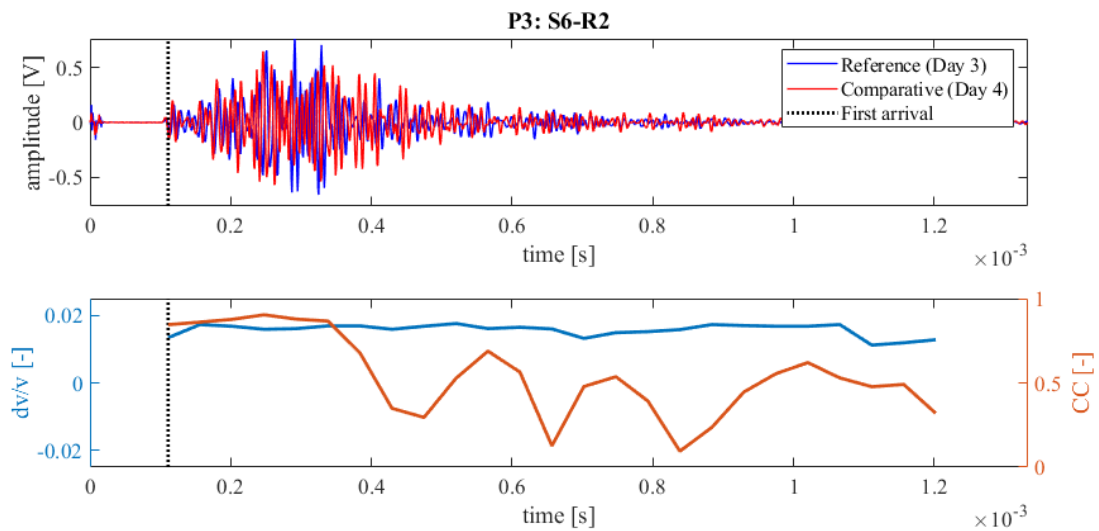


Figure 209: Wave signals of Measurement 3 (blue) and Measurement 4 (red) between principal sensor pair Source S6 and Receiver S2 at Position 3 (top),  $dv/v$  (blue) and CC (orange) results from CWI over the signal travel time divided in stretching windows (bottom)

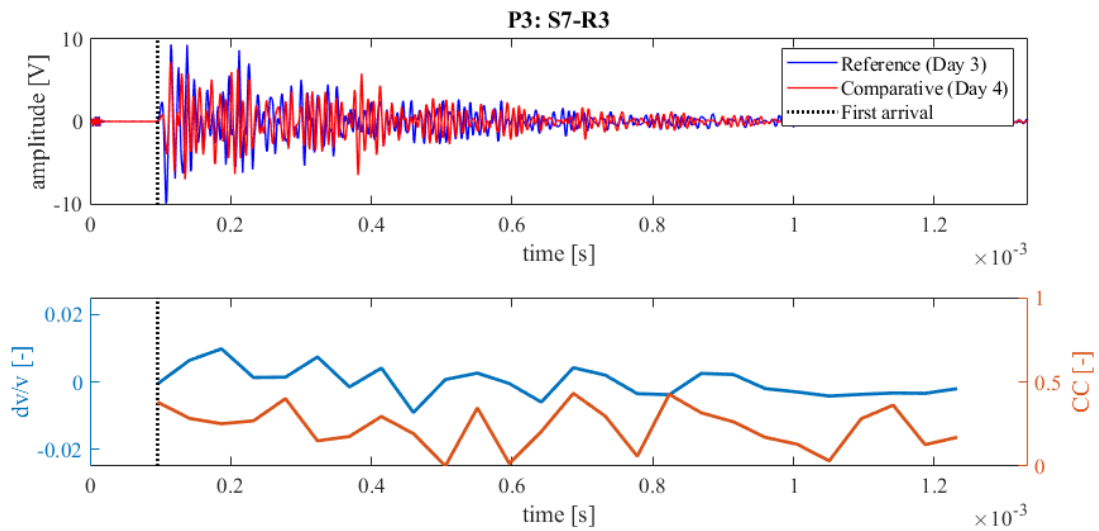


Figure 210: Wave signals of Measurement 3 (blue) and Measurement 4 (red) between principal sensor pair Source S7 and Receiver S3 at Position 3 (top),  $dv/v$  (blue) and  $CC$  (orange) results from CWI over the signal travel time divided in stretching windows (bottom)

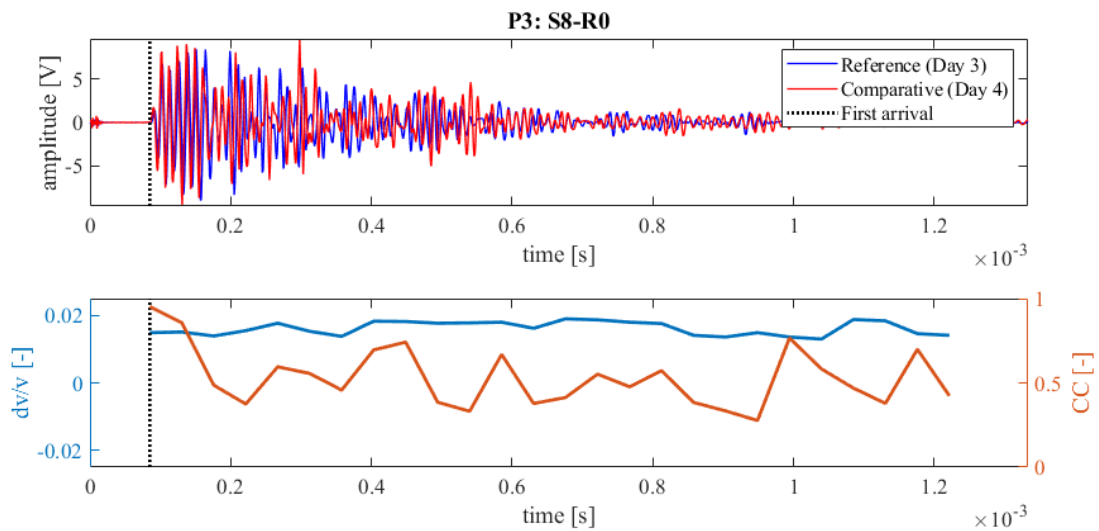
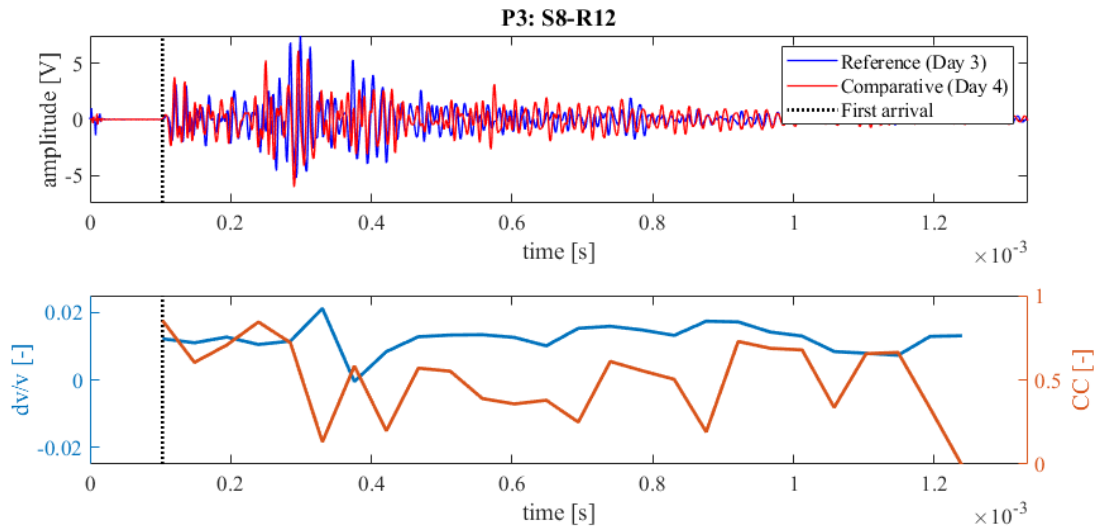
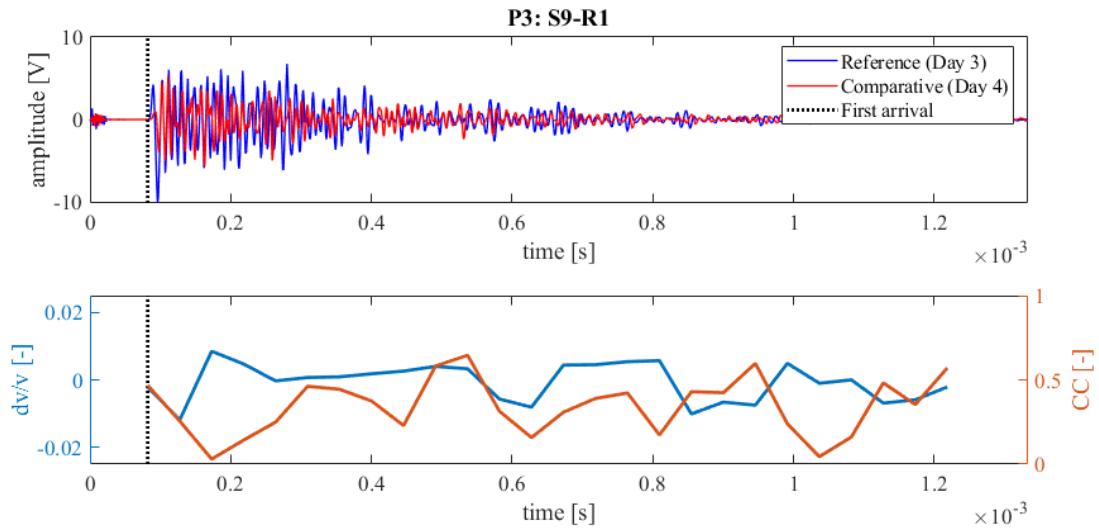


Figure 211: Wave signals of Measurement 3 (blue) and Measurement 4 (red) between principal sensor pair Source S8 and Receiver S0 at Position 3 (top),  $dv/v$  (blue) and  $CC$  (orange) results from CWI over the signal travel time divided in stretching windows (bottom)



**Figure 212: Wave signals of Measurement 3 (blue) and Measurement 4 (red) between principal sensor pair Source S8 and Receiver S12 at Position 3 (top),  $dv/v$  (blue) and  $CC$  (orange) results from CWI over the signal travel time divided in stretching windows (bottom)**



**Figure 213: Wave signals of Measurement 3 (blue) and Measurement 4 (red) between principal sensor pair Source S9 and Receiver S1 at Position 3 (top),  $dv/v$  (blue) and  $CC$  (orange) results from CWI over the signal travel time divided in stretching windows (bottom)**

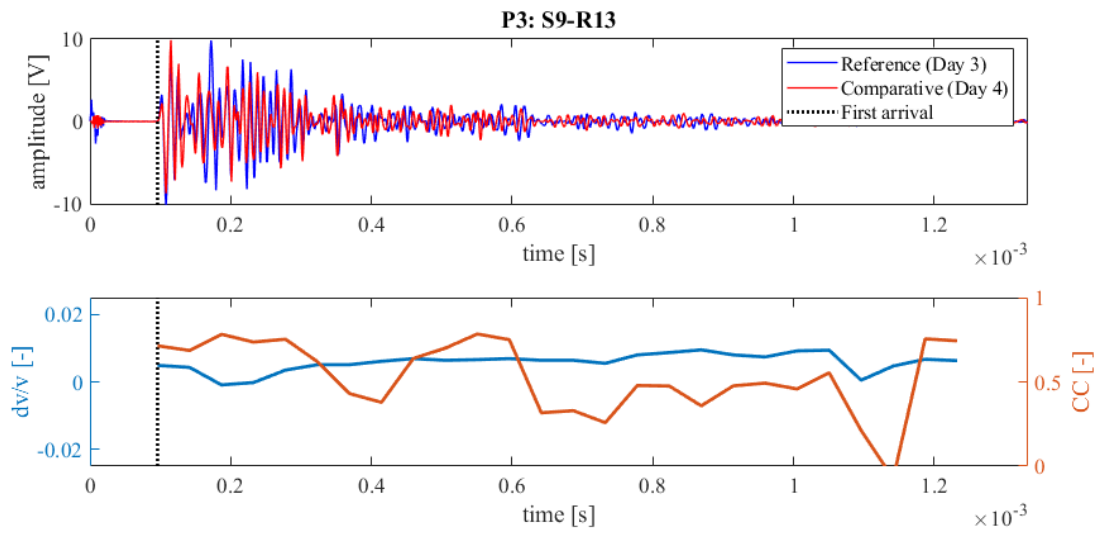


Figure 214: Wave signals of Measurement 3 (blue) and Measurement 4 (red) between principal sensor pair Source S9 and Receiver S13 at Position 3 (top),  $dv/v$  (blue) and  $CC$  (orange) results from CWI over the signal travel time divided in stretching windows (bottom)

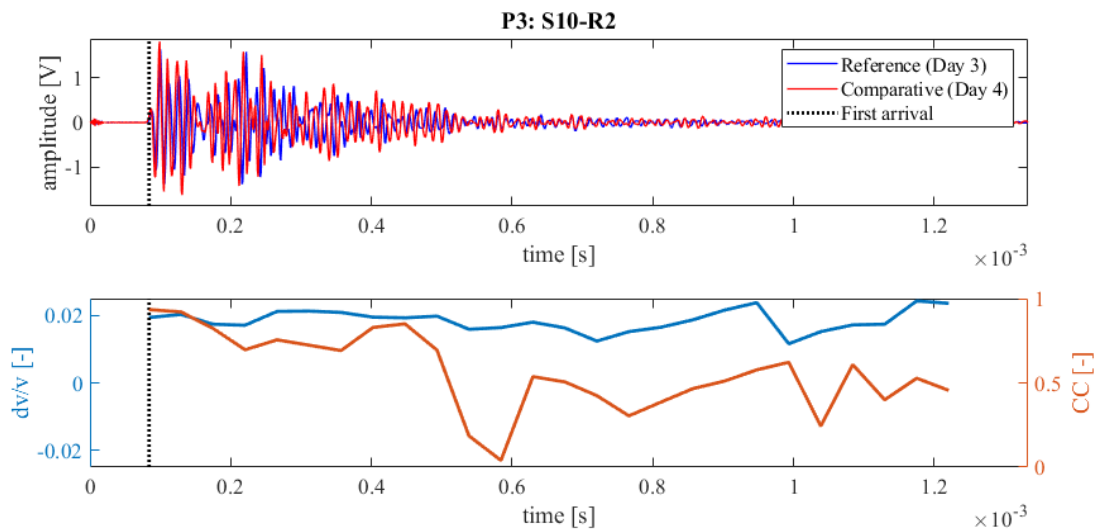
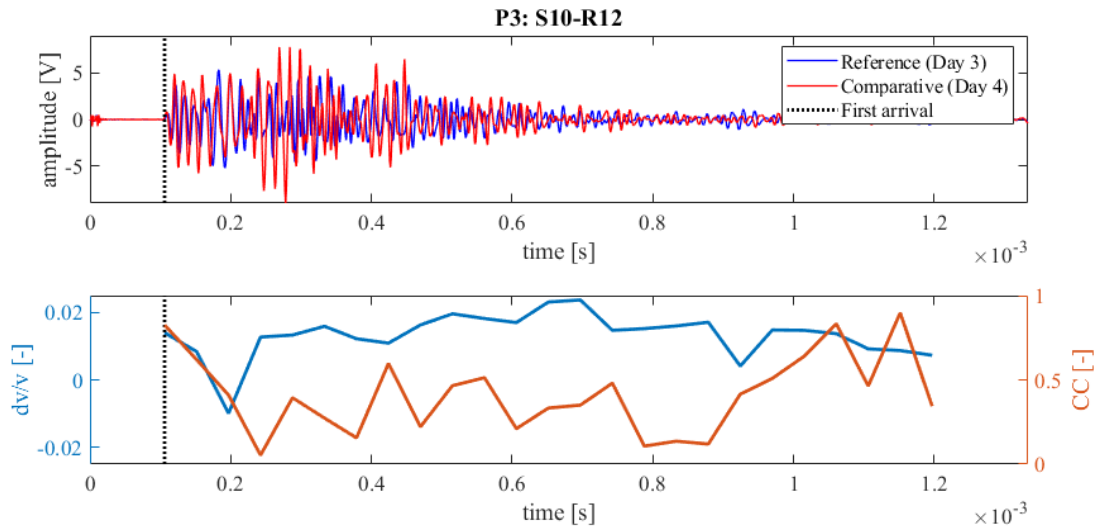
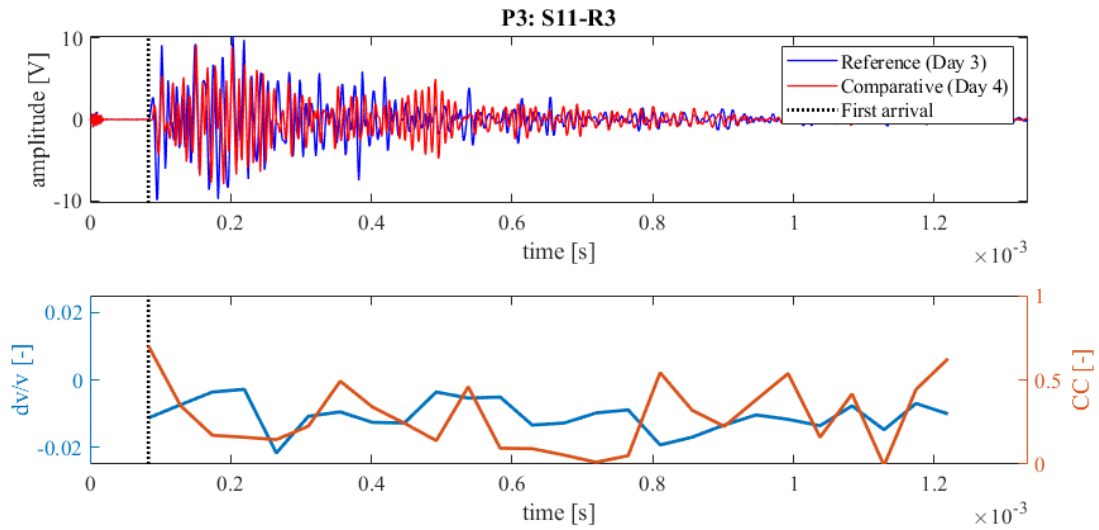


Figure 215: Wave signals of Measurement 3 (blue) and Measurement 4 (red) between principal sensor pair Source S10 and Receiver S2 at Position 3 (top),  $dv/v$  (blue) and  $CC$  (orange) results from CWI over the signal travel time divided in stretching windows (bottom)



**Figure 216:** Wave signals of Measurement 3 (blue) and Measurement 4 (red) between principal sensor pair Source S10 and Receiver S12 at Position 3 (top),  $dv/v$  (blue) and  $CC$  (orange) results from CWI over the signal travel time divided in stretching windows (bottom)



**Figure 217:** Wave signals of Measurement 3 (blue) and Measurement 4 (red) between principal sensor pair Source S11 and Receiver S3 at Position 3 (top),  $dv/v$  (blue) and  $CC$  (orange) results from CWI over the signal travel time divided in stretching windows (bottom)

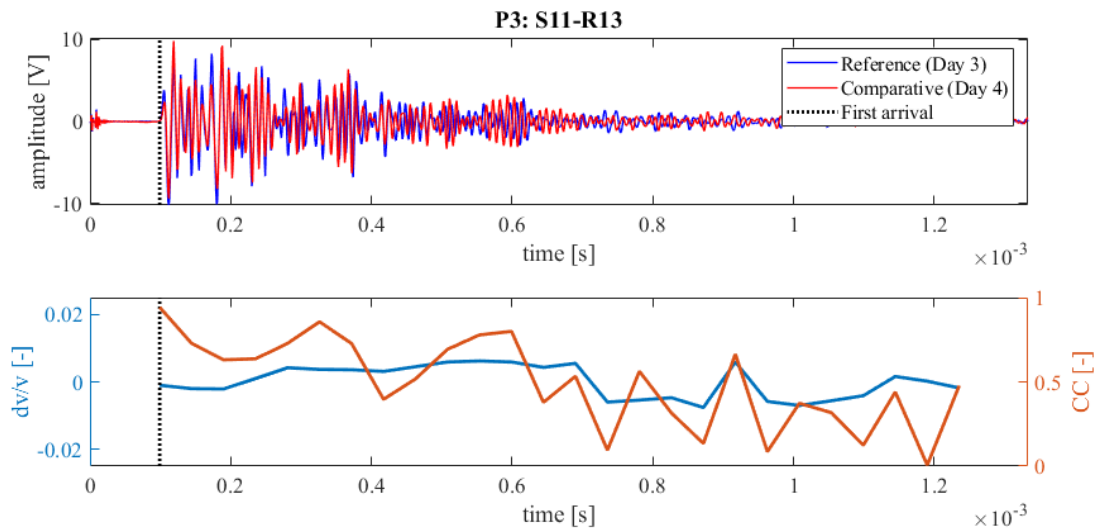


Figure 218: Wave signals of Measurement 3 (blue) and Measurement 4 (red) between principal sensor pair Source S11 and Receiver S13 at Position 3 (top),  $dv/v$  (blue) and CC (orange) results from CWI over the signal travel time divided in stretching windows (bottom)

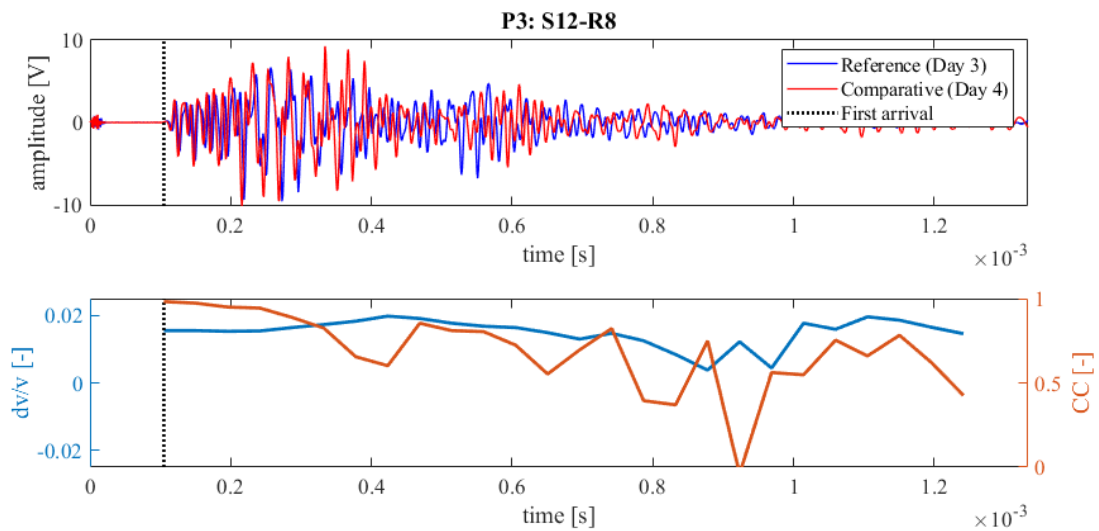


Figure 219: Wave signals of Measurement 3 (blue) and Measurement 4 (red) between principal sensor pair Source S12 and Receiver S8 at Position 3 (top),  $dv/v$  (blue) and CC (orange) results from CWI over the signal travel time divided in stretching windows (bottom)

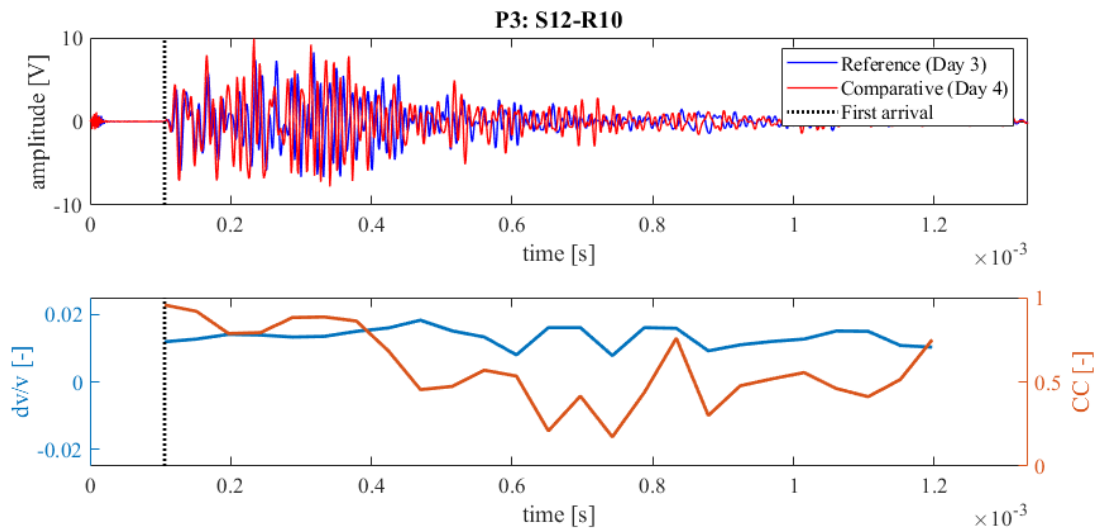


Figure 220: Wave signals of Measurement 3 (blue) and Measurement 4 (red) between principal sensor pair Source S12 and Receiver S10 at Position 3 (top),  $dv/v$  (blue) and  $CC$  (orange) results from CWI over the signal travel time divided in stretching windows (bottom)

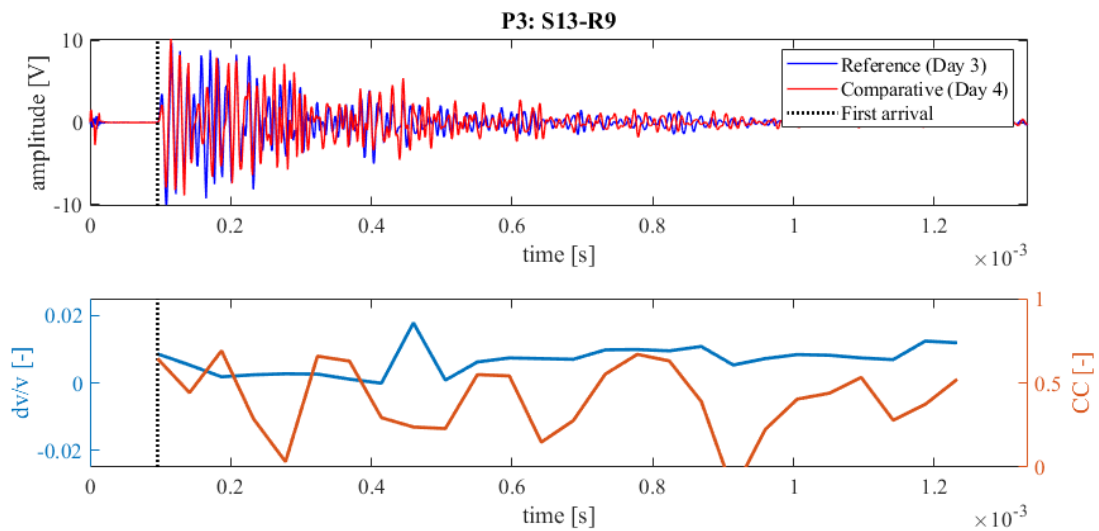


Figure 221: Wave signals of Measurement 3 (blue) and Measurement 4 (red) between principal sensor pair Source S13 and Receiver S9 at Position 3 (top),  $dv/v$  (blue) and  $CC$  (orange) results from CWI over the signal travel time divided in stretching windows (bottom)

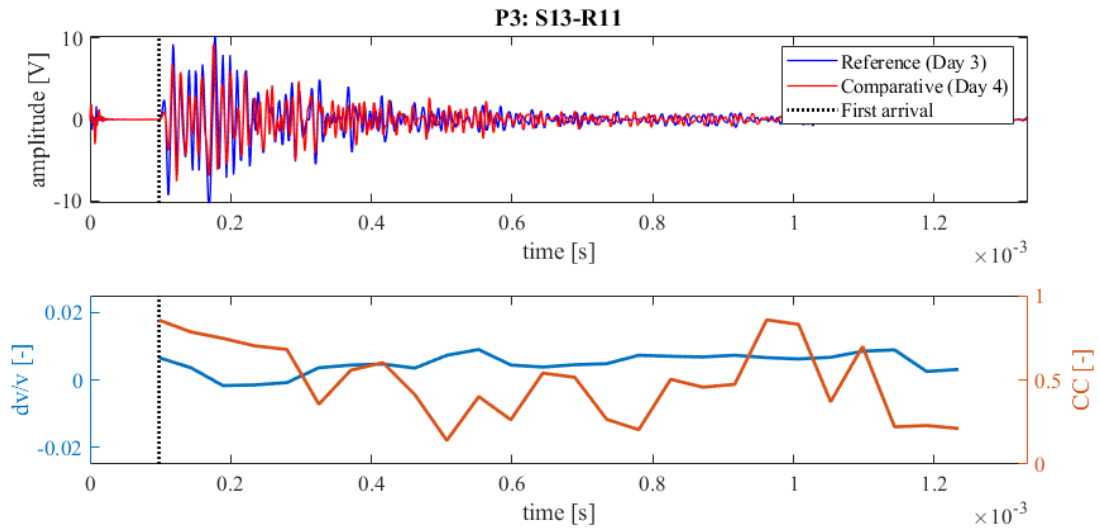


Figure 222: Wave signals of Measurement 3 (blue) and Measurement 4 (red) between principal sensor pair Source S13 and Receiver S11 at Position 3 (top),  $dv/v$  (blue) and  $CC$  (orange) results from CWI over the signal travel time divided in stretching windows (bottom)

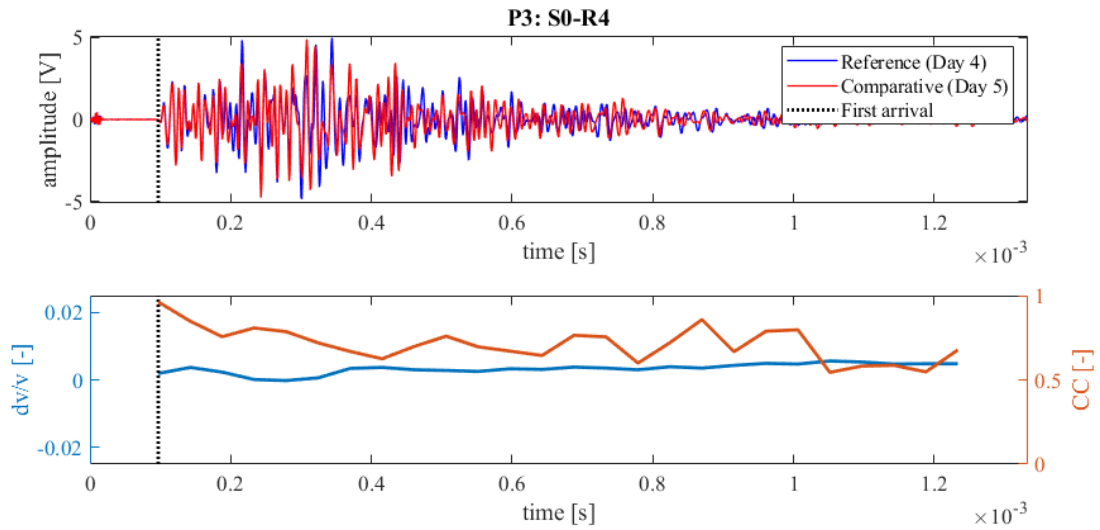


Figure 223: Wave signals of Measurement 4 (blue) and Measurement 5 (red) between principal sensor pair Source S0 and Receiver S4 at Position 3 (top),  $dv/v$  (blue) and  $CC$  (orange) results from CWI over the signal travel time divided in stretching windows (bottom)

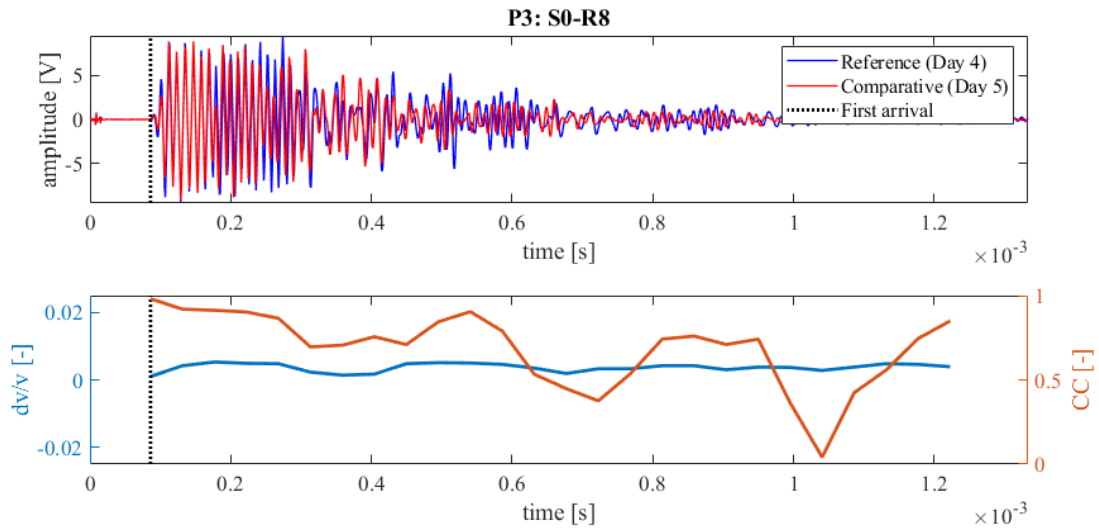


Figure 224: Wave signals of Measurement 4 (blue) and Measurement 5 (red) between principal sensor pair Source S0 and Receiver S8 at Position 3 (top),  $dv/v$  (blue) and  $CC$  (orange) results from CWI over the signal travel time divided in stretching windows (bottom)

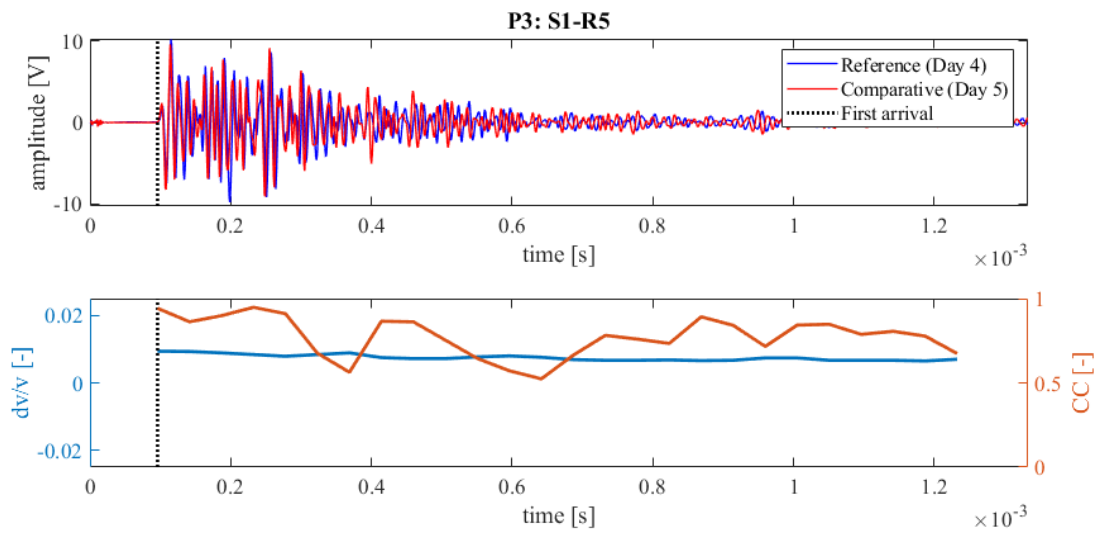


Figure 225: Wave signals of Measurement 4 (blue) and Measurement 5 (red) between principal sensor pair Source S1 and Receiver S5 at Position 3 (top),  $dv/v$  (blue) and  $CC$  (orange) results from CWI over the signal travel time divided in stretching windows (bottom)

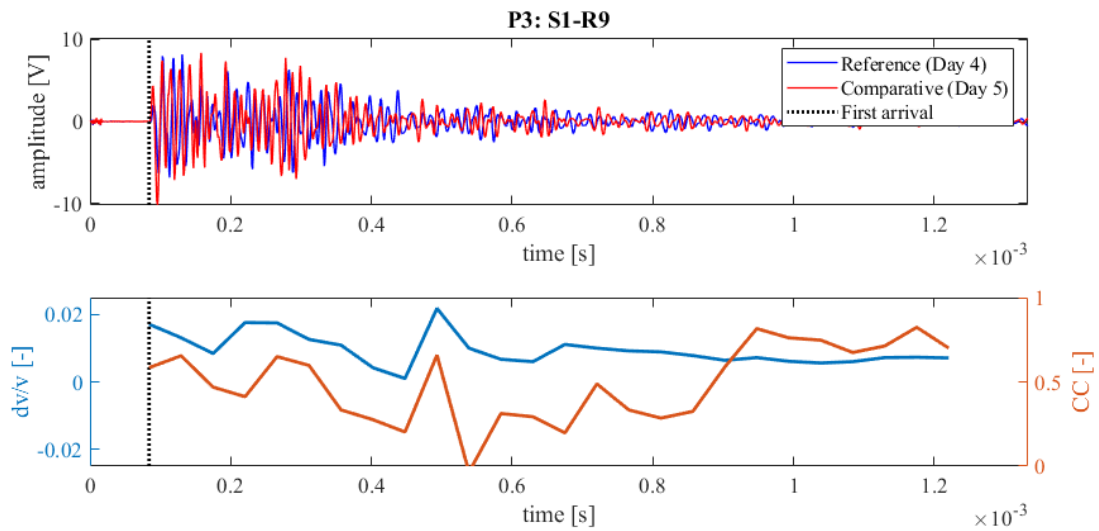


Figure 226: Wave signals of Measurement 4 (blue) and Measurement 5 (red) between principal sensor pair Source S1 and Receiver S9 at Position 3 (top),  $dv/v$  (blue) and  $CC$  (orange) results from CWI over the signal travel time divided in stretching windows (bottom)

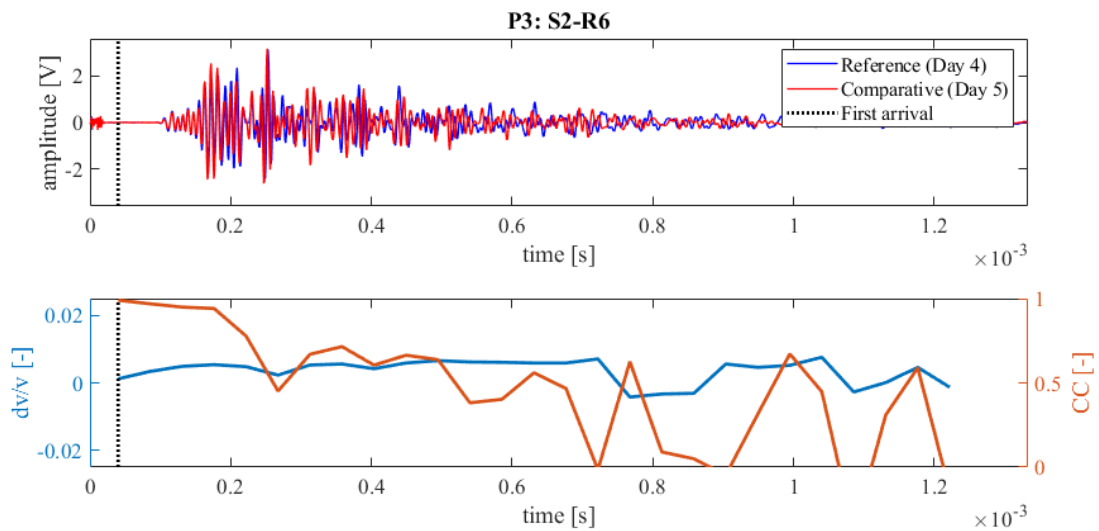


Figure 227: Wave signals of Measurement 4 (blue) and Measurement 5 (red) between principal sensor pair Source S2 and Receiver S6 at Position 3 (top),  $dv/v$  (blue) and  $CC$  (orange) results from CWI over the signal travel time divided in stretching windows (bottom)

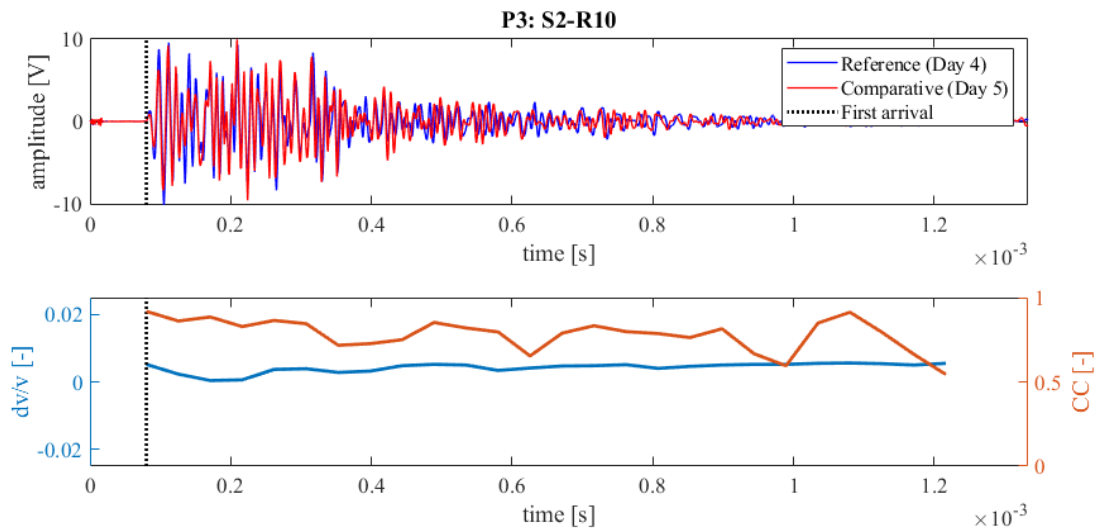


Figure 228: Wave signals of Measurement 4 (blue) and Measurement 5 (red) between principal sensor pair Source S2 and Receiver S10 at Position 3 (top),  $dv/v$  (blue) and  $CC$  (orange) results from CWI over the signal travel time divided in stretching windows (bottom)

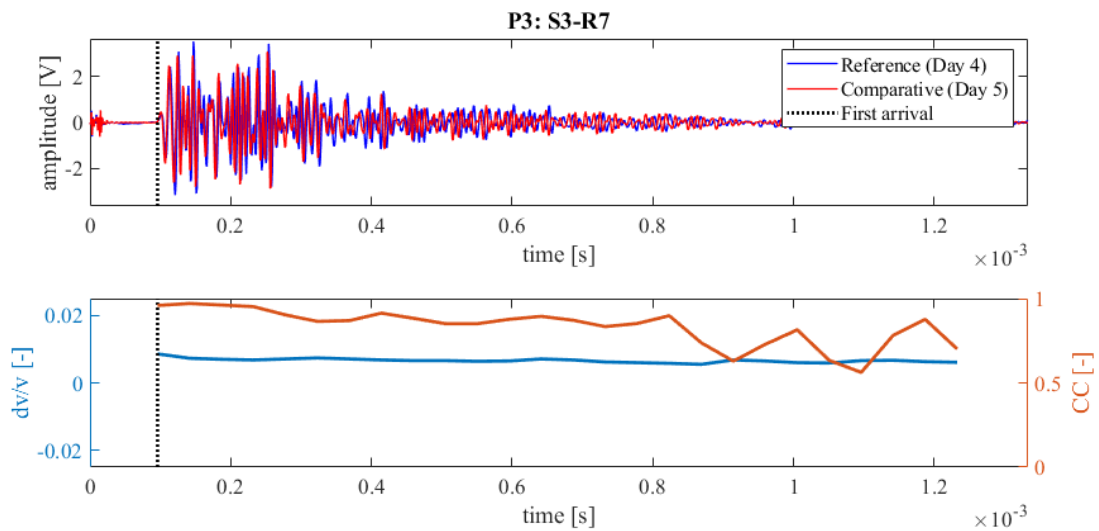


Figure 229: Wave signals of Measurement 4 (blue) and Measurement 5 (red) between principal sensor pair Source S3 and Receiver S7 at Position 3 (top),  $dv/v$  (blue) and  $CC$  (orange) results from CWI over the signal travel time divided in stretching windows (bottom)

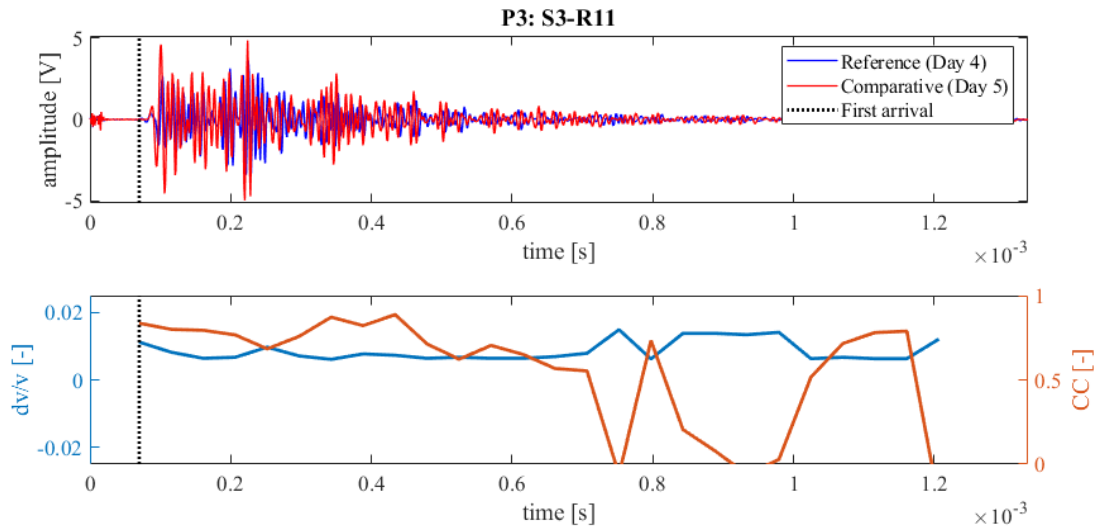


Figure 230: Wave signals of Measurement 4 (blue) and Measurement 5 (red) between principal sensor pair Source S3 and Receiver S11 at Position 3 (top),  $dv/v$  (blue) and  $CC$  (orange) results from CWI over the signal travel time divided in stretching windows (bottom)

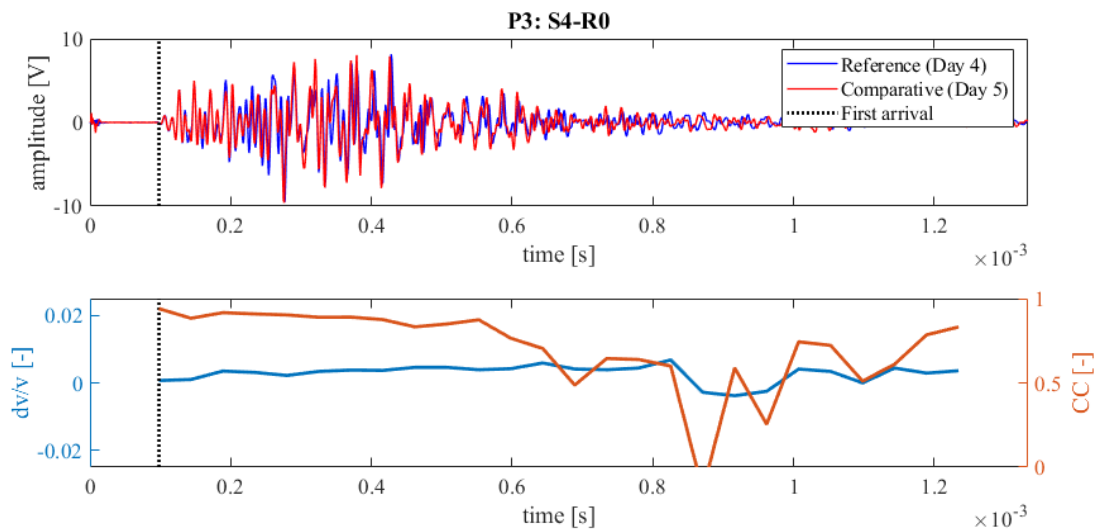


Figure 231: Wave signals of Measurement 4 (blue) and Measurement 5 (red) between principal sensor pair Source S4 and Receiver S0 at Position 3 (top),  $dv/v$  (blue) and  $CC$  (orange) results from CWI over the signal travel time divided in stretching windows (bottom)

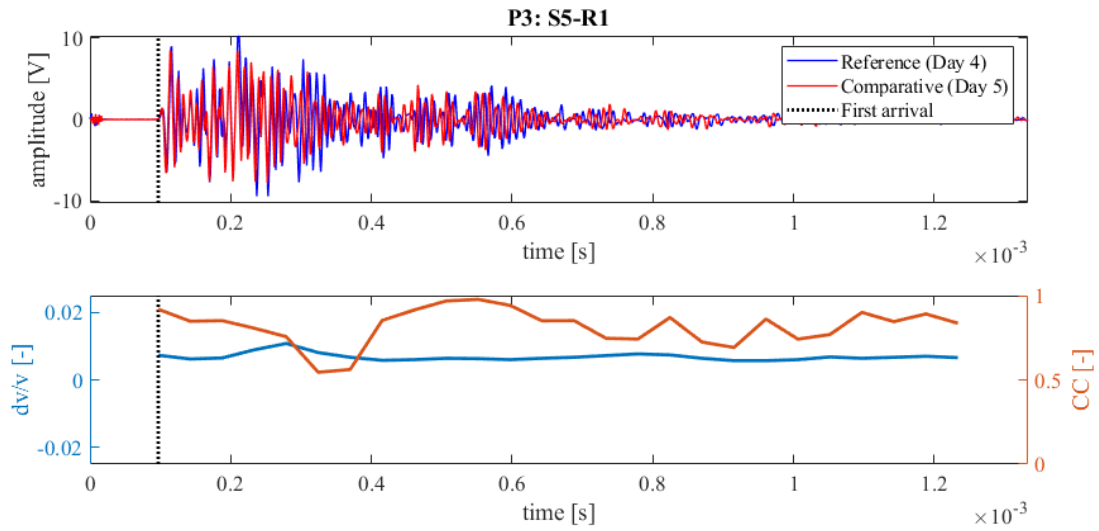


Figure 232: Wave signals of Measurement 4 (blue) and Measurement 5 (red) between principal sensor pair Source S5 and Receiver S1 at Position 3 (top),  $dv/v$  (blue) and  $CC$  (orange) results from CWI over the signal travel time divided in stretching windows (bottom)

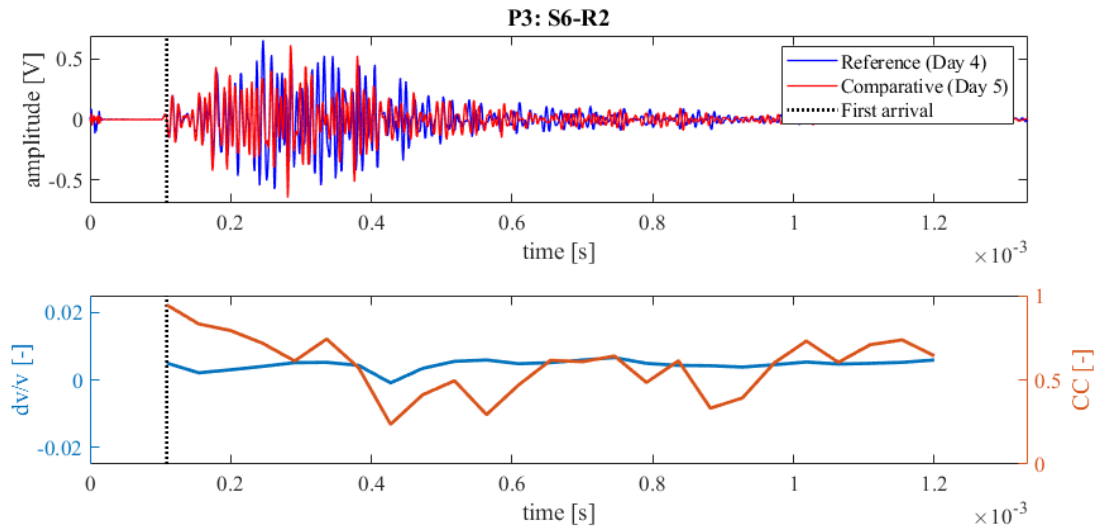


Figure 233: Wave signals of Measurement 4 (blue) and Measurement 5 (red) between principal sensor pair Source S6 and Receiver S2 at Position 3 (top),  $dv/v$  (blue) and  $CC$  (orange) results from CWI over the signal travel time divided in stretching windows (bottom)

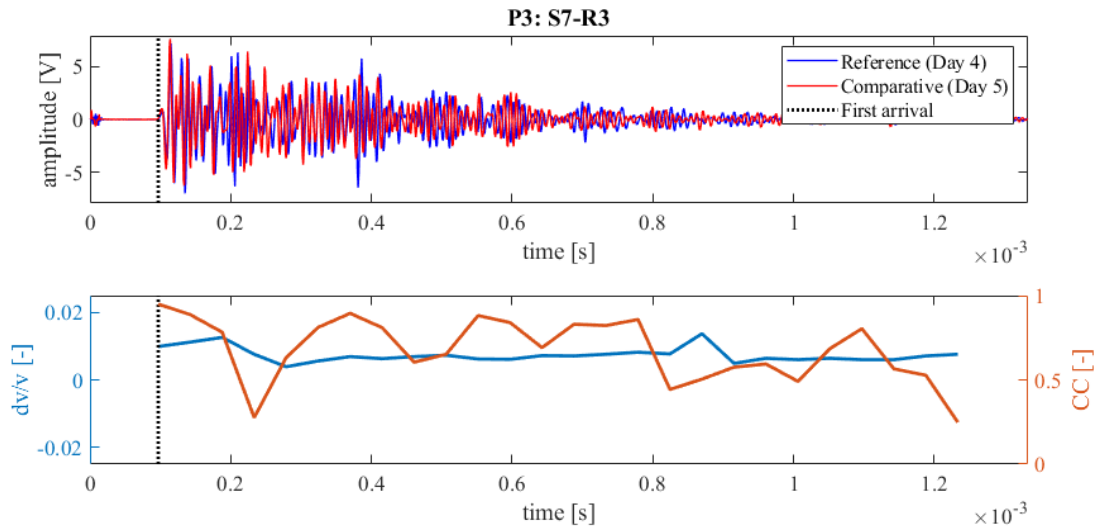


Figure 234: Wave signals of Measurement 4 (blue) and Measurement 5 (red) between principal sensor pair Source S7 and Receiver S3 at Position 3 (top),  $dv/v$  (blue) and  $CC$  (orange) results from CWI over the signal travel time divided in stretching windows (bottom)

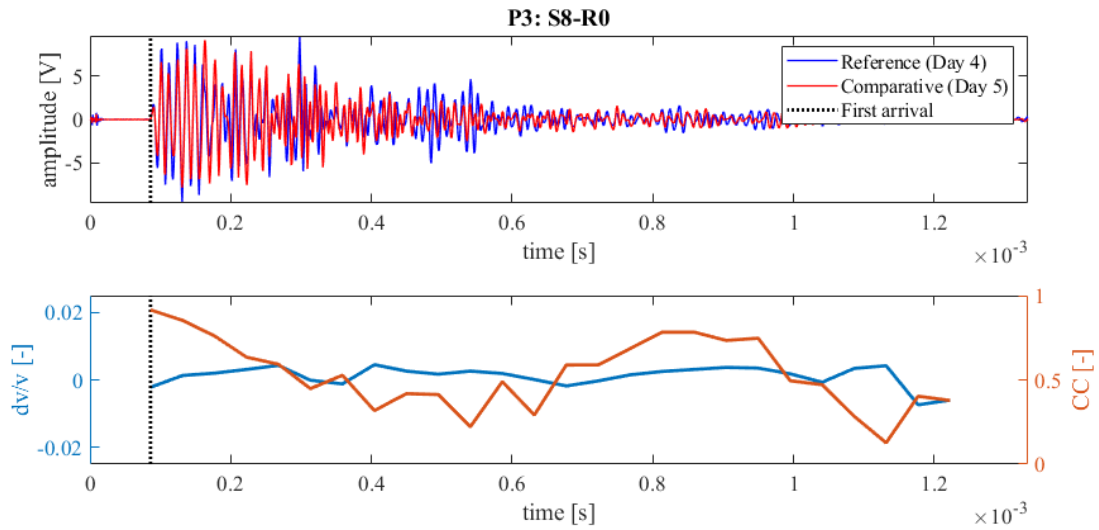


Figure 235: Wave signals of Measurement 4 (blue) and Measurement 5 (red) between principal sensor pair Source S8 and Receiver S0 at Position 3 (top),  $dv/v$  (blue) and  $CC$  (orange) results from CWI over the signal travel time divided in stretching windows (bottom)

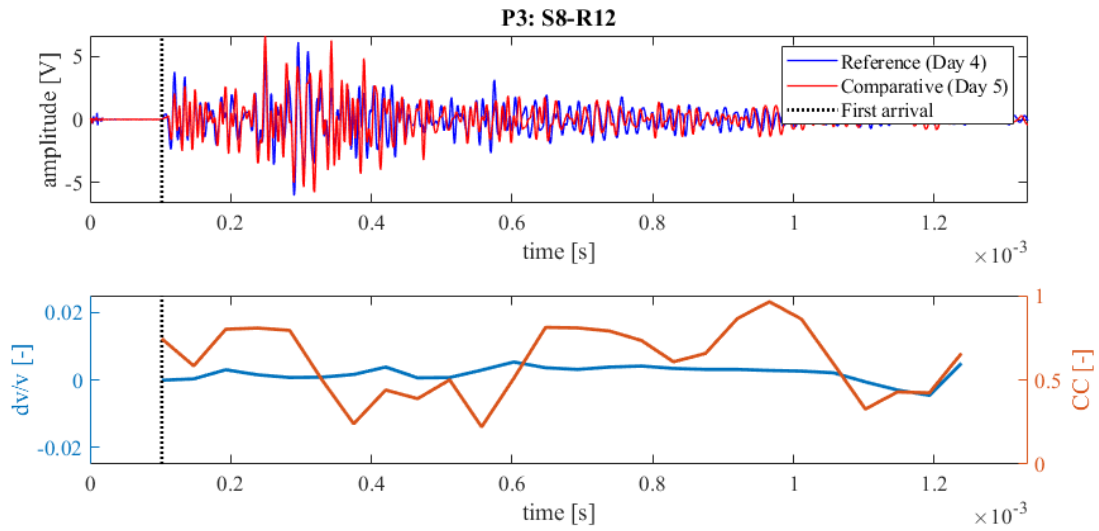


Figure 236: Wave signals of Measurement 4 (blue) and Measurement 5 (red) between principal sensor pair Source S8 and Receiver S12 at Position 3 (top),  $dv/v$  (blue) and  $CC$  (orange) results from CWI over the signal travel time divided in stretching windows (bottom)

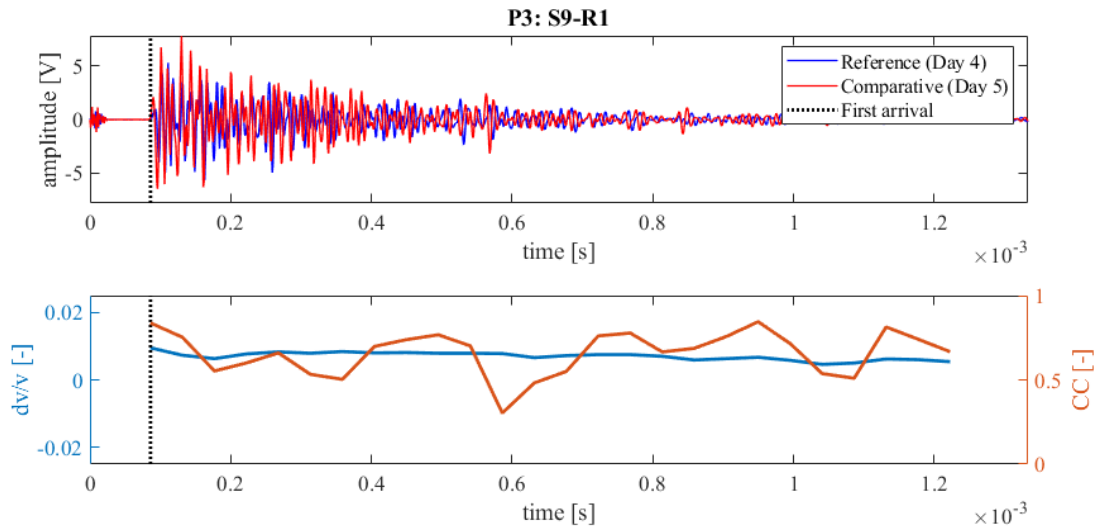


Figure 237: Wave signals of Measurement 4 (blue) and Measurement 5 (red) between principal sensor pair Source S9 and Receiver S1 at Position 3 (top),  $dv/v$  (blue) and  $CC$  (orange) results from CWI over the signal travel time divided in stretching windows (bottom)

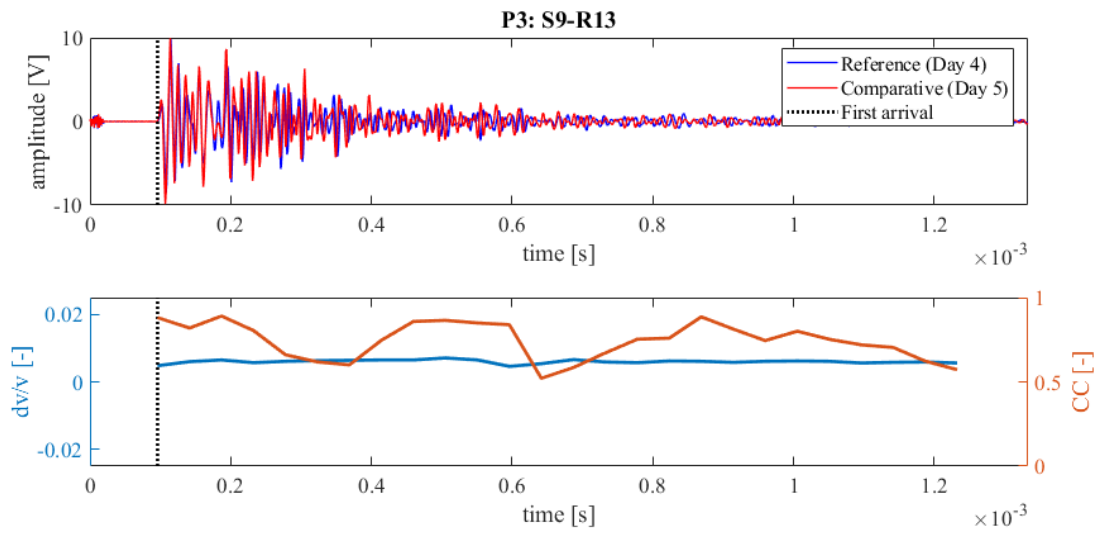


Figure 238: Wave signals of Measurement 4 (blue) and Measurement 5 (red) between principal sensor pair Source S9 and Receiver S13 at Position 3 (top),  $dv/v$  (blue) and  $CC$  (orange) results from CWI over the signal travel time divided in stretching windows (bottom)

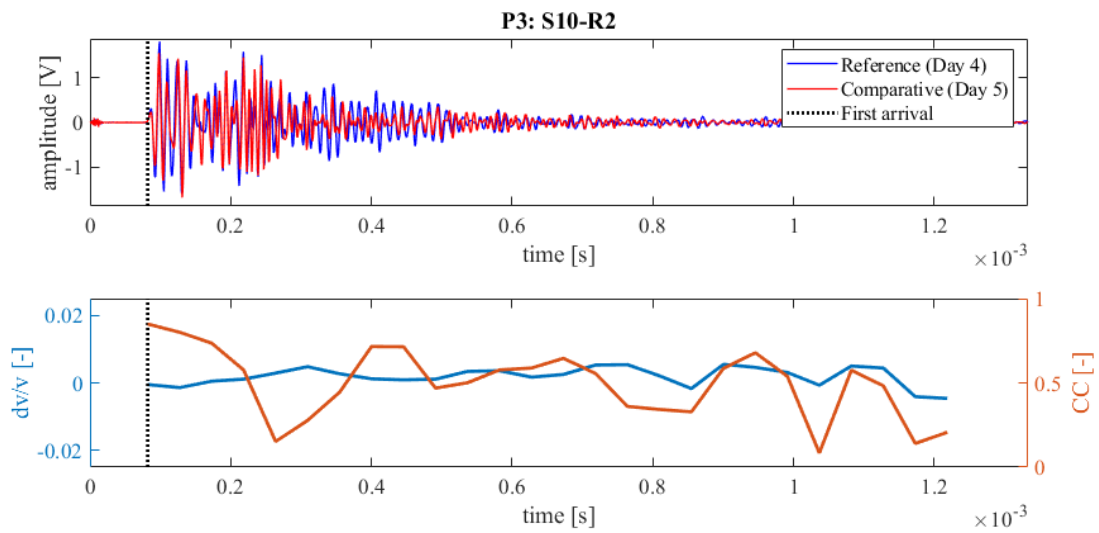
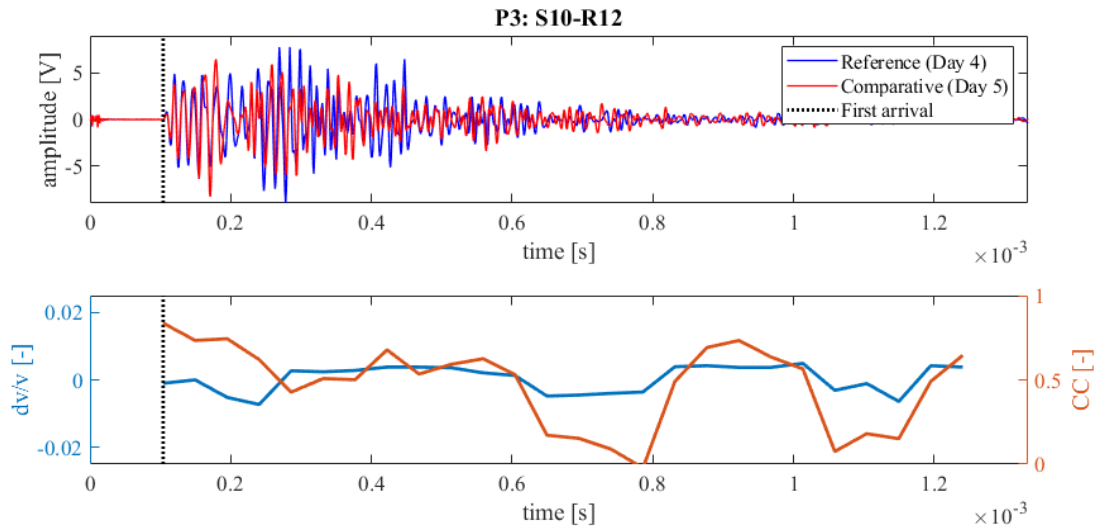
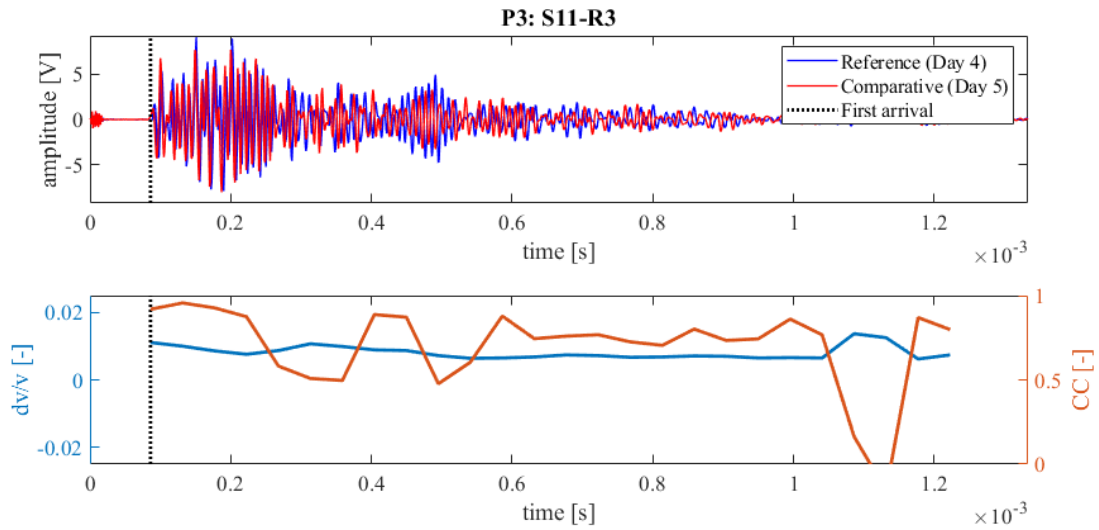


Figure 239: Wave signals of Measurement 4 (blue) and Measurement 5 (red) between principal sensor pair Source S10 and Receiver S2 at Position 3 (top),  $dv/v$  (blue) and  $CC$  (orange) results from CWI over the signal travel time divided in stretching windows (bottom)



**Figure 240: Wave signals of Measurement 4 (blue) and Measurement 5 (red) between principal sensor pair Source S10 and Receiver S12 at Position 3 (top),  $dv/v$  (blue) and CC (orange) results from CWI over the signal travel time divided in stretching windows (bottom)**



**Figure 241: Wave signals of Measurement 4 (blue) and Measurement 5 (red) between principal sensor pair Source S11 and Receiver S3 at Position 3 (top),  $dv/v$  (blue) and CC (orange) results from CWI over the signal travel time divided in stretching windows (bottom)**

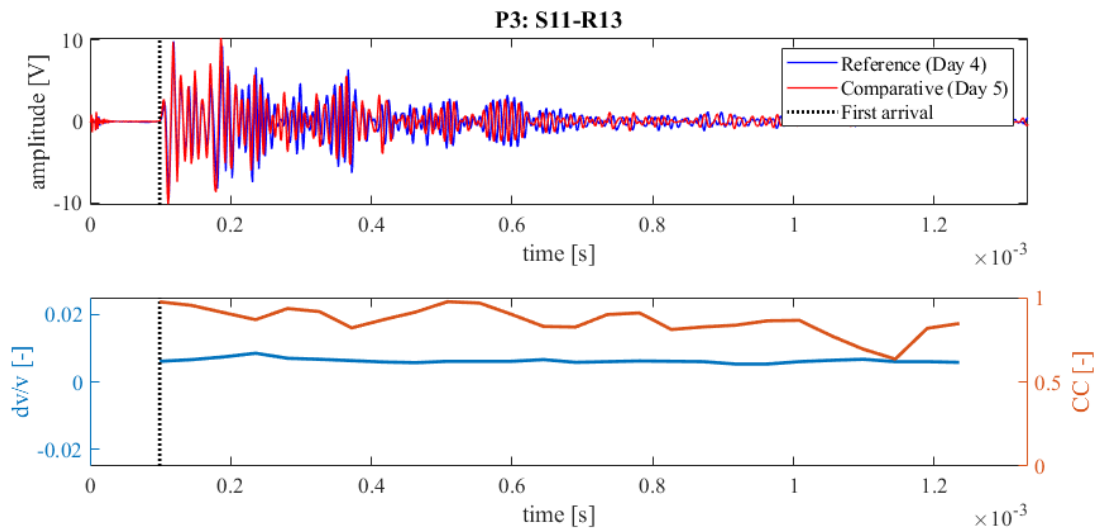


Figure 242: Wave signals of Measurement 4 (blue) and Measurement 5 (red) between principal sensor pair Source S11 and Receiver S13 at Position 3 (top),  $dv/v$  (blue) and  $CC$  (orange) results from CWI over the signal travel time divided in stretching windows (bottom)

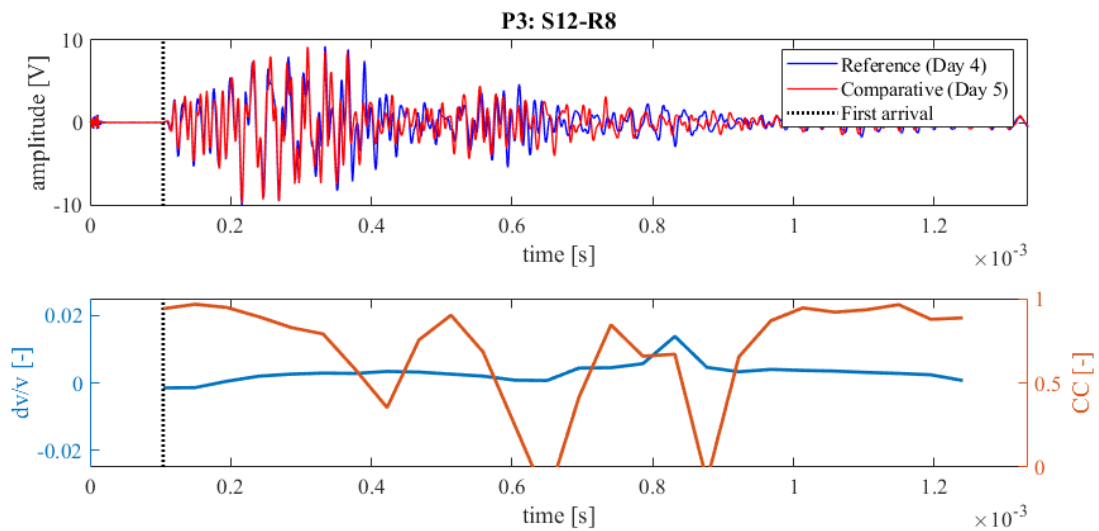


Figure 243: Wave signals of Measurement 4 (blue) and Measurement 5 (red) between principal sensor pair Source S12 and Receiver S8 at Position 3 (top),  $dv/v$  (blue) and  $CC$  (orange) results from CWI over the signal travel time divided in stretching windows (bottom)

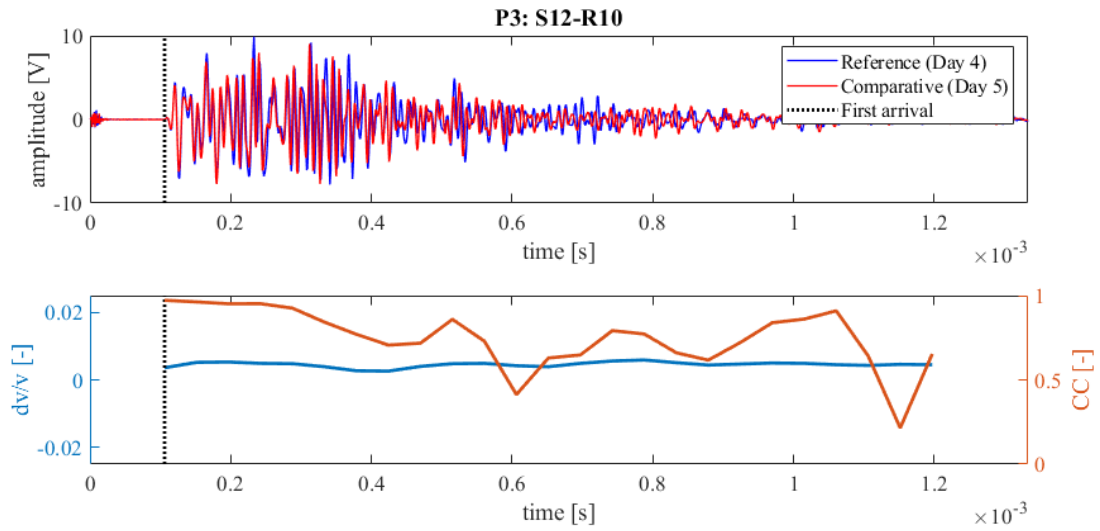


Figure 244: Wave signals of Measurement 4 (blue) and Measurement 5 (red) between principal sensor pair Source S12 and Receiver S10 at Position 3 (top),  $dv/v$  (blue) and  $CC$  (orange) results from CWI over the signal travel time divided in stretching windows (bottom)

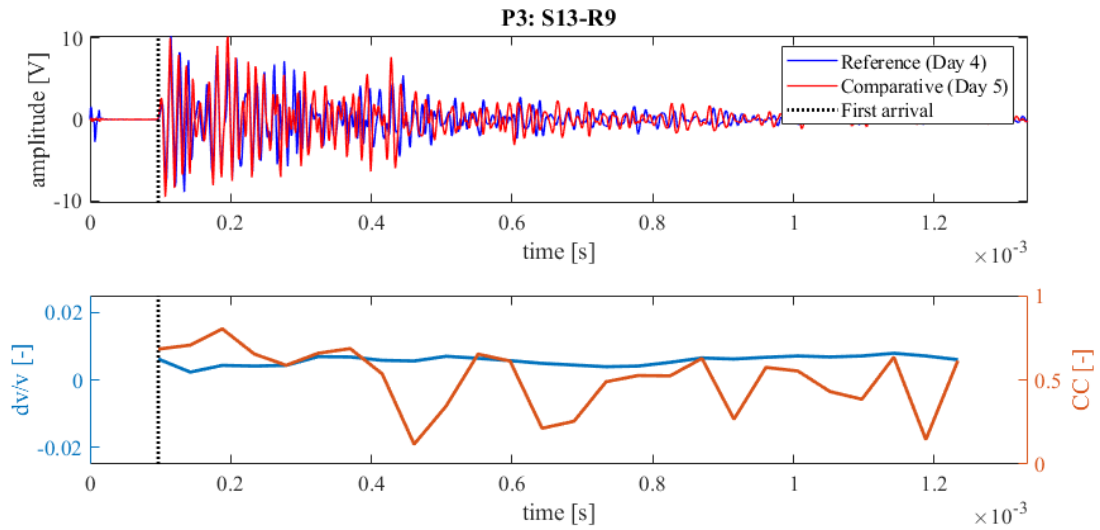


Figure 245: Wave signals of Measurement 4 (blue) and Measurement 5 (red) between principal sensor pair Source S13 and Receiver S9 at Position 3 (top),  $dv/v$  (blue) and  $CC$  (orange) results from CWI over the signal travel time divided in stretching windows (bottom)

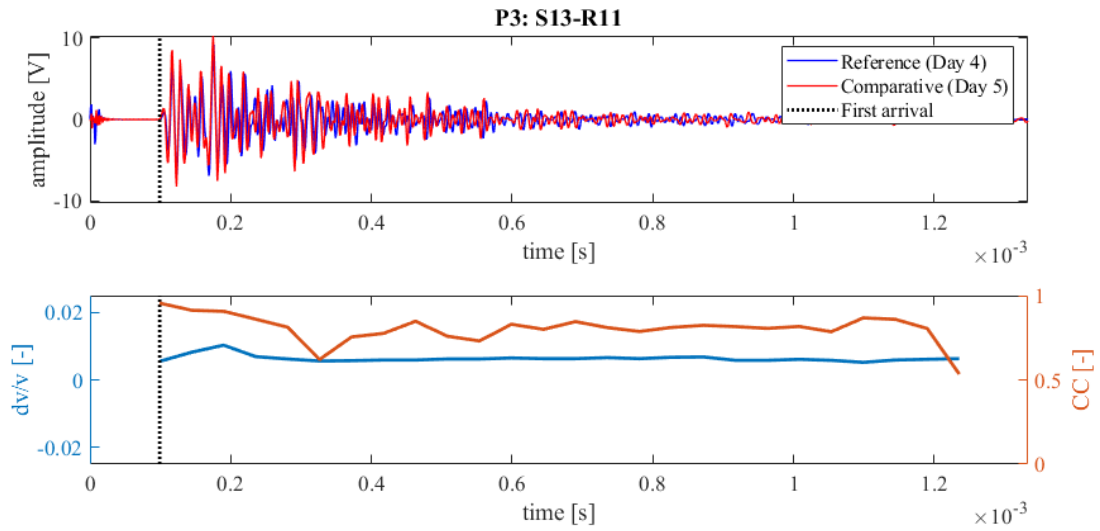


Figure 246: Wave signals of Measurement 4 (blue) and Measurement 5 (red) between principal sensor pair Source S13 and Receiver S11 at Position 3 (top),  $dv/v$  (blue) and  $CC$  (orange) results from CWI over the signal travel time divided in stretching windows (bottom)

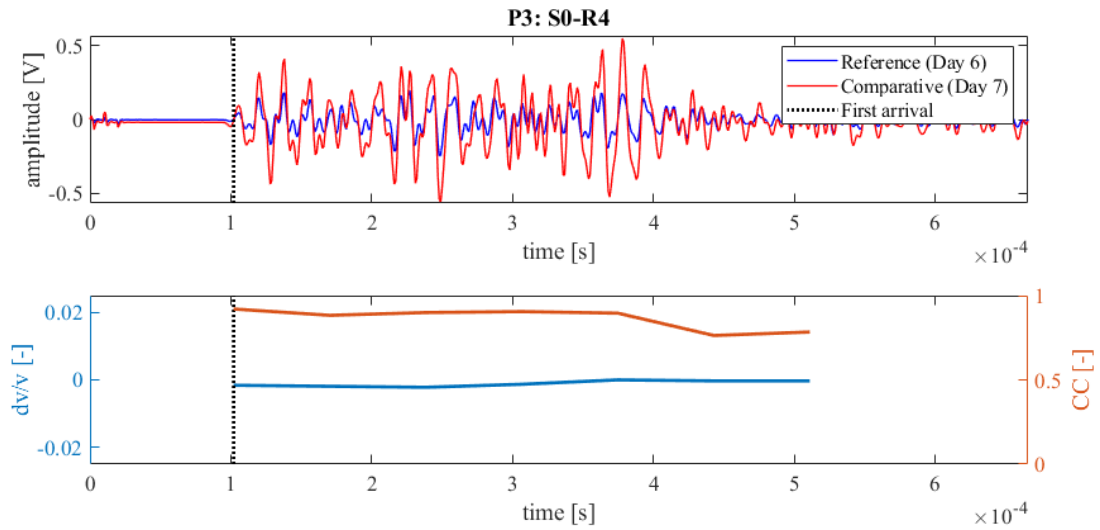


Figure 247: Wave signals of Measurement 6 (blue) and Measurement 7 (red) between principal sensor pair Source S0 and Receiver S4 at Position 3 (top),  $dv/v$  (blue) and  $CC$  (orange) results from CWI over the signal travel time divided in stretching windows (bottom)

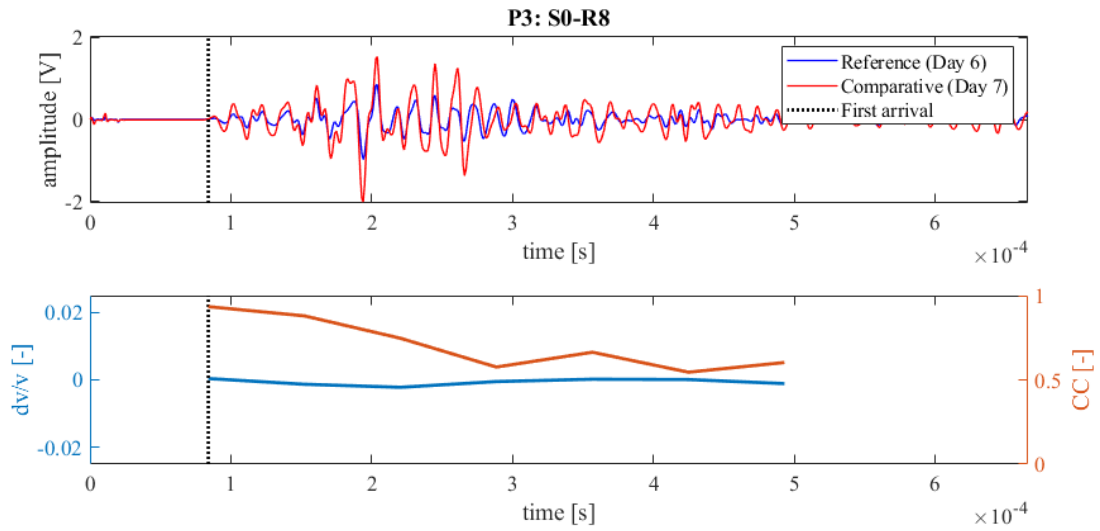


Figure 248: Wave signals of Measurement 6 (blue) and Measurement 7 (red) between principal sensor pair Source S0 and Receiver S8 at Position 3 (top),  $dv/v$  (blue) and CC (orange) results from CWI over the signal travel time divided in stretching windows (bottom)

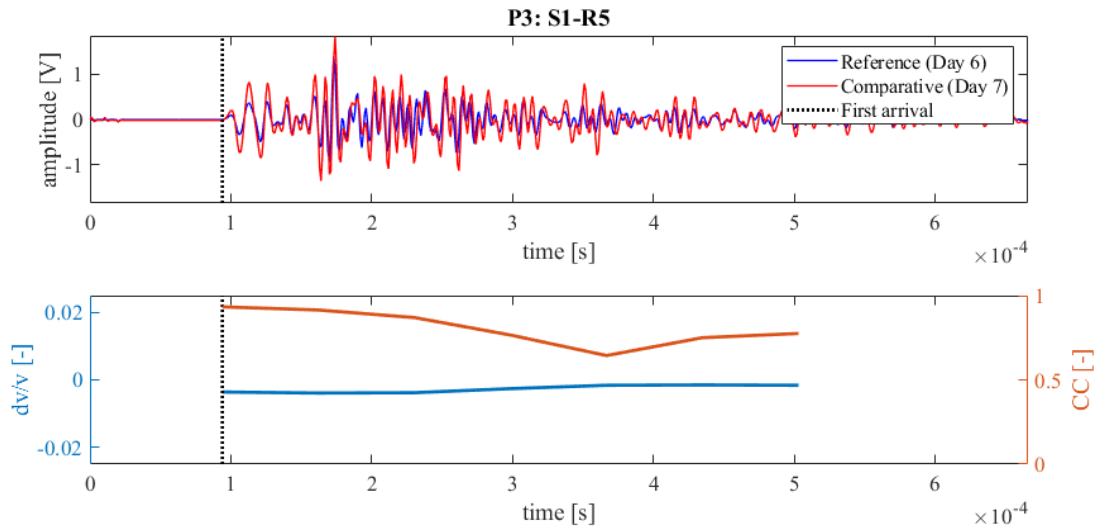


Figure 249: Wave signals of Measurement 6 (blue) and Measurement 7 (red) between principal sensor pair Source S1 and Receiver S5 at Position 3 (top),  $dv/v$  (blue) and CC (orange) results from CWI over the signal travel time divided in stretching windows (bottom)

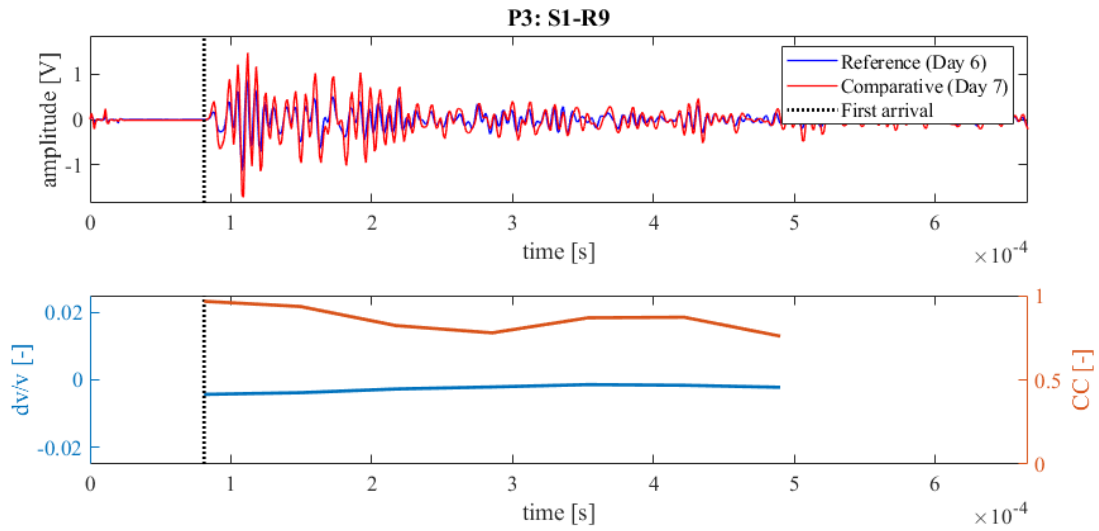


Figure 250: Wave signals of Measurement 6 (blue) and Measurement 7 (red) between principal sensor pair Source S1 and Receiver S9 at Position 3 (top),  $dv/v$  (blue) and CC (orange) results from CWI over the signal travel time divided in stretching windows (bottom)

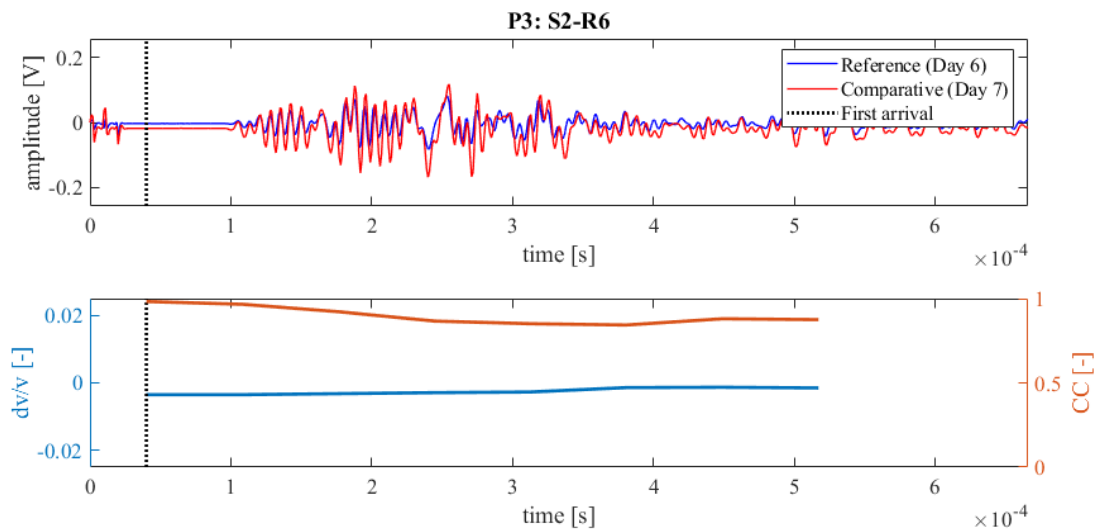


Figure 251: Wave signals of Measurement 6 (blue) and Measurement 7 (red) between principal sensor pair Source S2 and Receiver S6 at Position 3 (top),  $dv/v$  (blue) and CC (orange) results from CWI over the signal travel time divided in stretching windows (bottom)

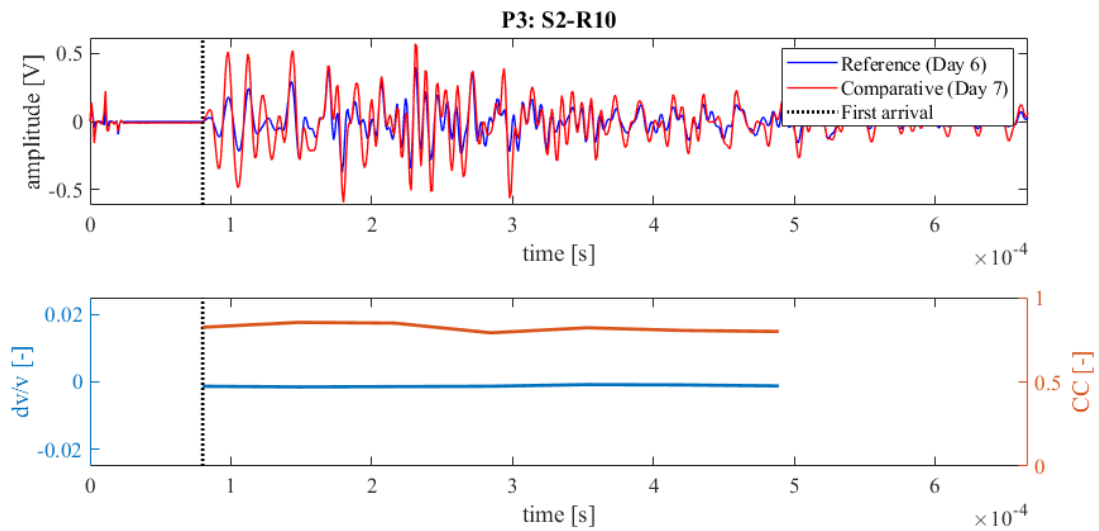


Figure 252: Wave signals of Measurement 6 (blue) and Measurement 7 (red) between principal sensor pair Source S2 and Receiver S10 at Position 3 (top),  $dv/v$  (blue) and CC (orange) results from CWI over the signal travel time divided in stretching windows (bottom)

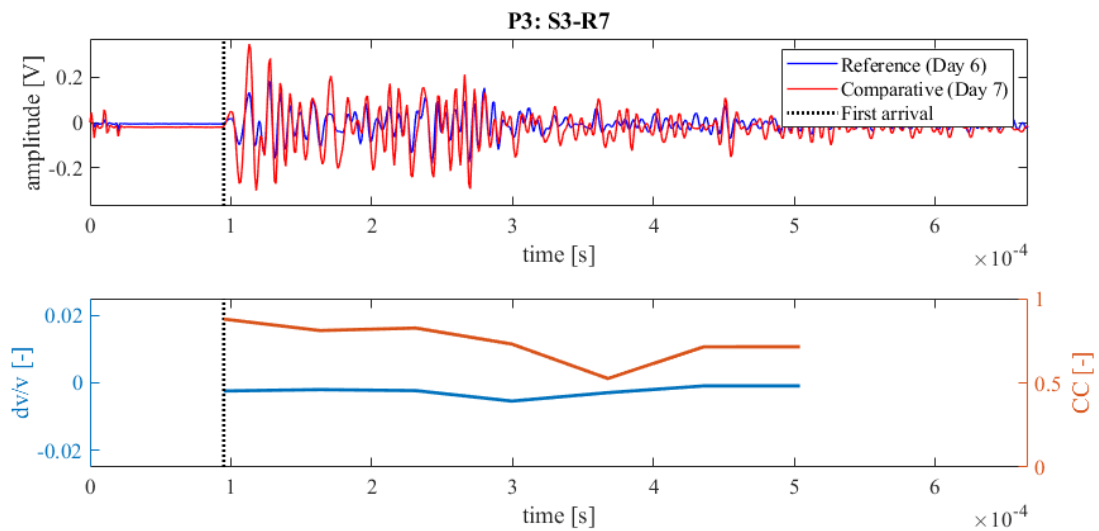


Figure 253: Wave signals of Measurement 6 (blue) and Measurement 7 (red) between principal sensor pair Source S3 and Receiver S7 at Position 3 (top),  $dv/v$  (blue) and CC (orange) results from CWI over the signal travel time divided in stretching windows (bottom)

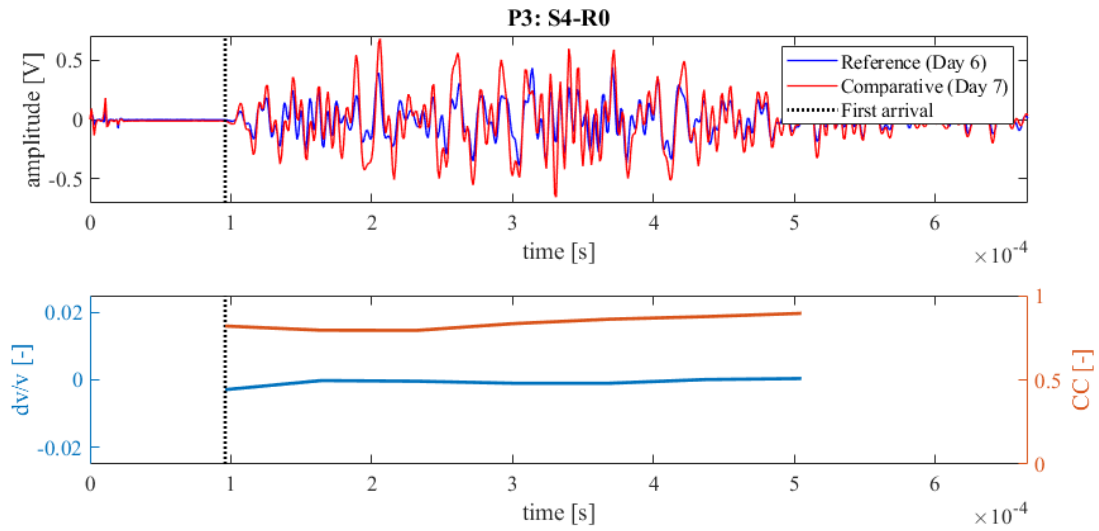


Figure 254: Wave signals of Measurement 6 (blue) and Measurement 7 (red) between principal sensor pair Source S4 and Receiver S0 at Position 3 (top),  $dv/v$  (blue) and CC (orange) results from CWI over the signal travel time divided in stretching windows (bottom)

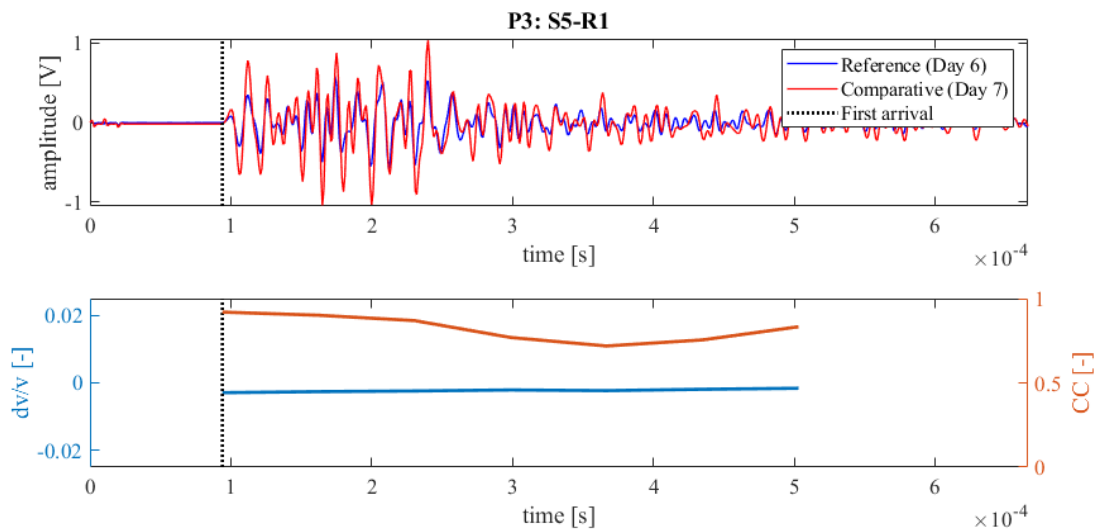


Figure 255: Wave signals of Measurement 6 (blue) and Measurement 7 (red) between principal sensor pair Source S5 and Receiver S1 at Position 3 (top),  $dv/v$  (blue) and CC (orange) results from CWI over the signal travel time divided in stretching windows (bottom)

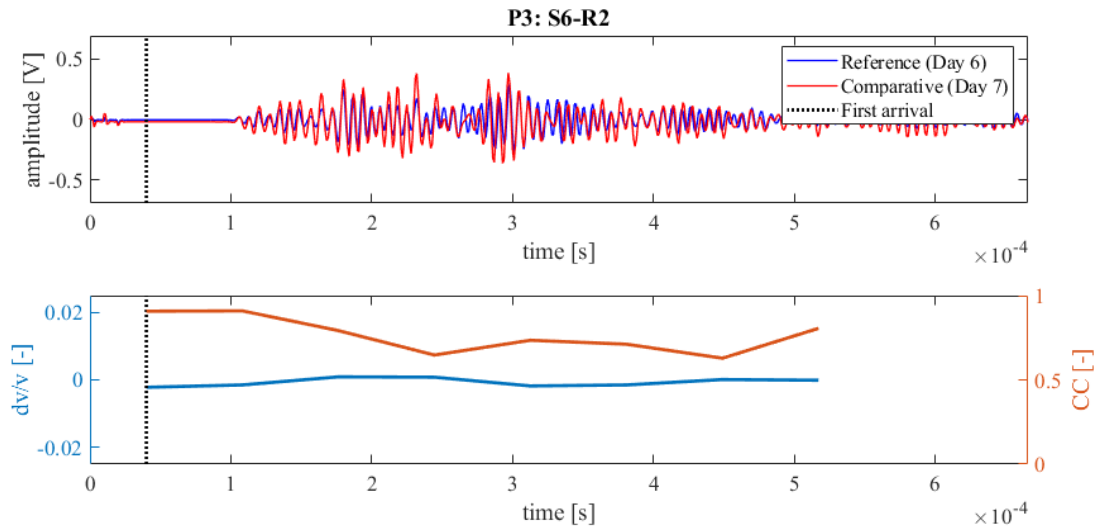


Figure 256: Wave signals of Measurement 6 (blue) and Measurement 7 (red) between principal sensor pair Source S6 and Receiver S2 at Position 3 (top),  $dv/v$  (blue) and  $CC$  (orange) results from CWI over the signal travel time divided in stretching windows (bottom)

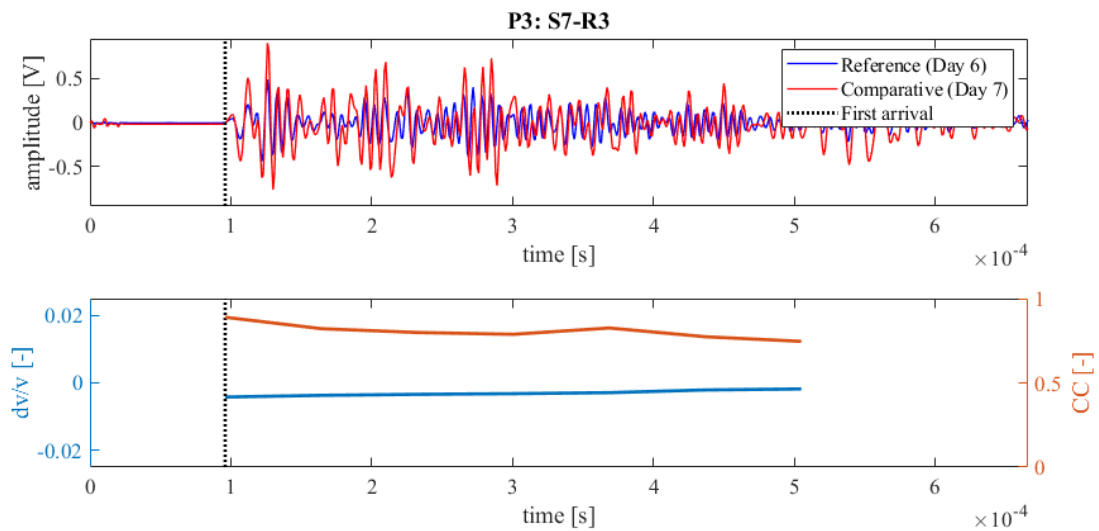


Figure 257: Wave signals of Measurement 6 (blue) and Measurement 7 (red) between principal sensor pair Source S7 and Receiver S3 at Position 3 (top),  $dv/v$  (blue) and  $CC$  (orange) results from CWI over the signal travel time divided in stretching windows (bottom)

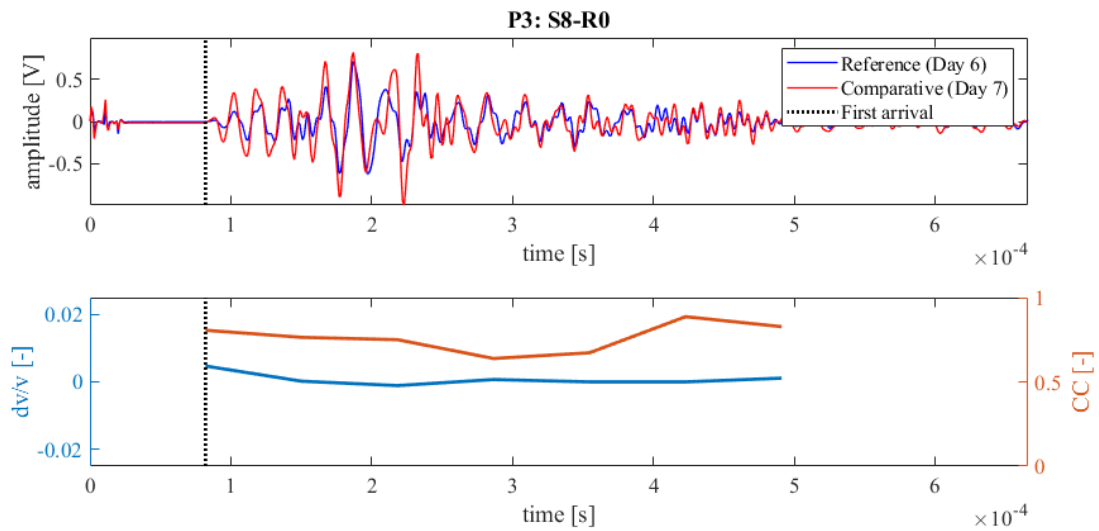


Figure 258: Wave signals of Measurement 6 (blue) and Measurement 7 (red) between principal sensor pair Source S8 and Receiver S0 at Position 3 (top),  $dv/v$  (blue) and CC (orange) results from CWI over the signal travel time divided in stretching windows (bottom)

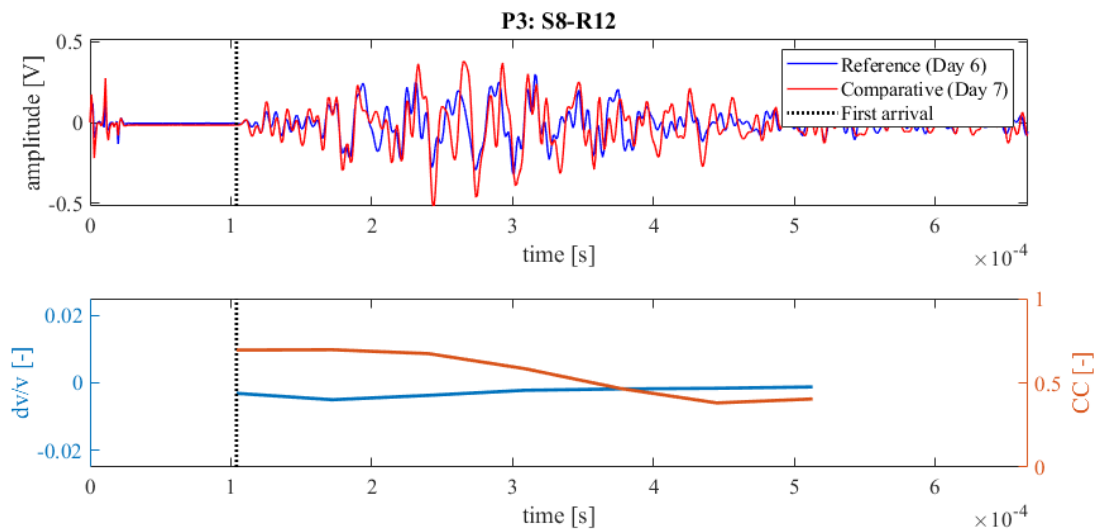


Figure 259: Wave signals of Measurement 6 (blue) and Measurement 7 (red) between principal sensor pair Source S8 and Receiver S12 at Position 3 (top),  $dv/v$  (blue) and CC (orange) results from CWI over the signal travel time divided in stretching windows (bottom)

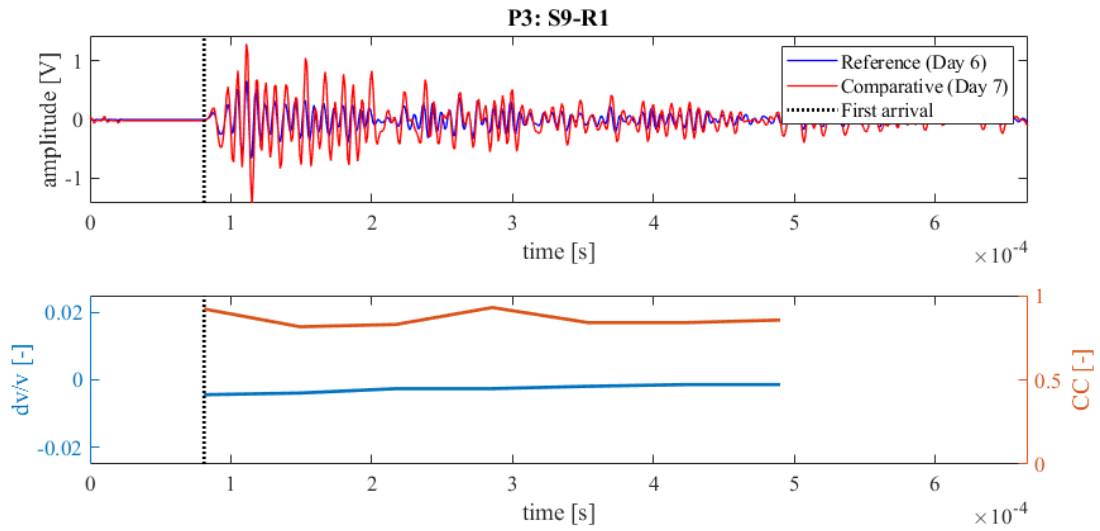


Figure 260: Wave signals of Measurement 6 (blue) and Measurement 7 (red) between principal sensor pair Source S9 and Receiver S1 at Position 3 (top),  $dv/v$  (blue) and  $CC$  (orange) results from CWI over the signal travel time divided in stretching windows (bottom)

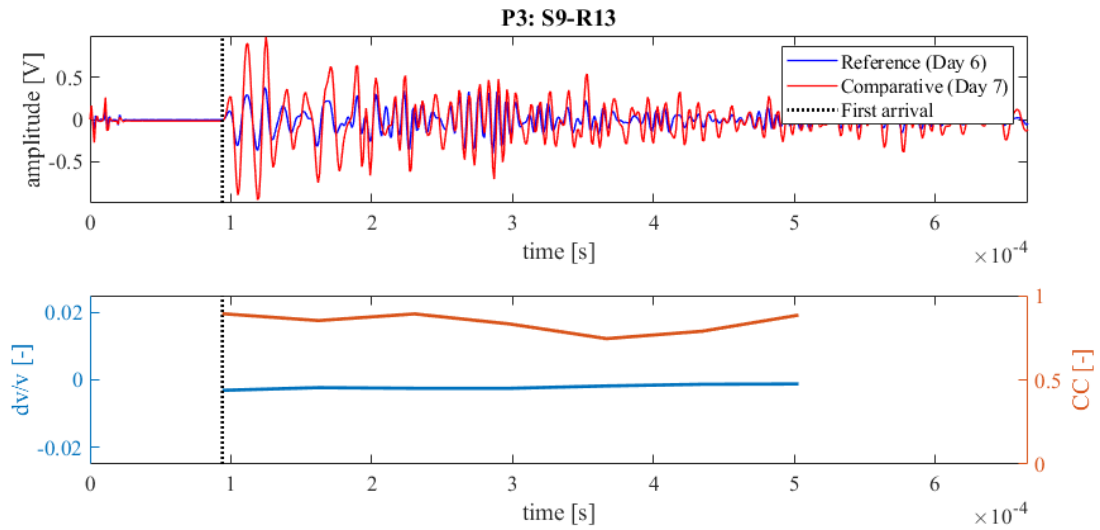


Figure 261: Wave signals of Measurement 6 (blue) and Measurement 7 (red) between principal sensor pair Source S9 and Receiver S13 at Position 3 (top),  $dv/v$  (blue) and  $CC$  (orange) results from CWI over the signal travel time divided in stretching windows (bottom)

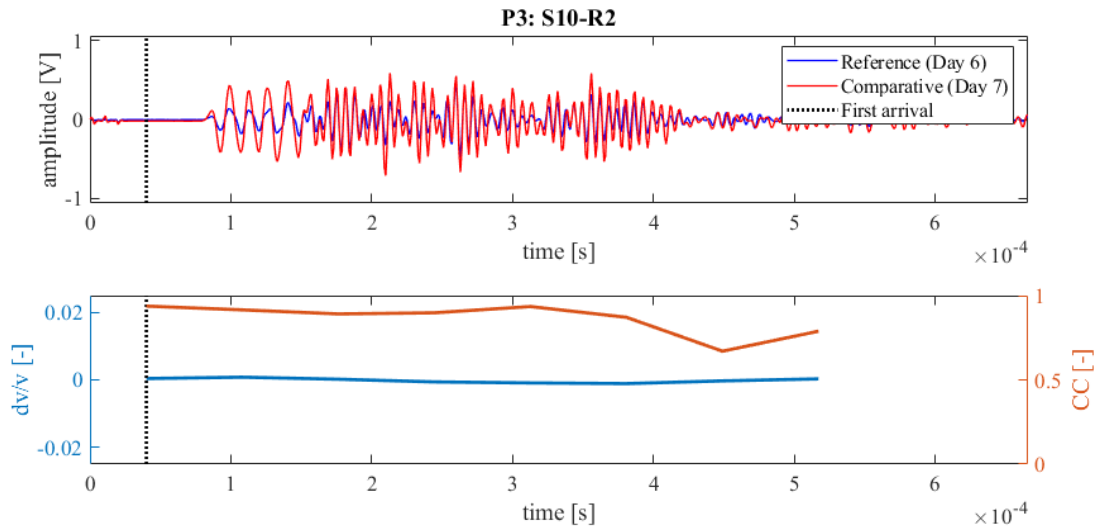


Figure 262: Wave signals of Measurement 6 (blue) and Measurement 7 (red) between principal sensor pair Source S10 and Receiver S2 at Position 3 (top),  $dv/v$  (blue) and  $CC$  (orange) results from CWI over the signal travel time divided in stretching windows (bottom)

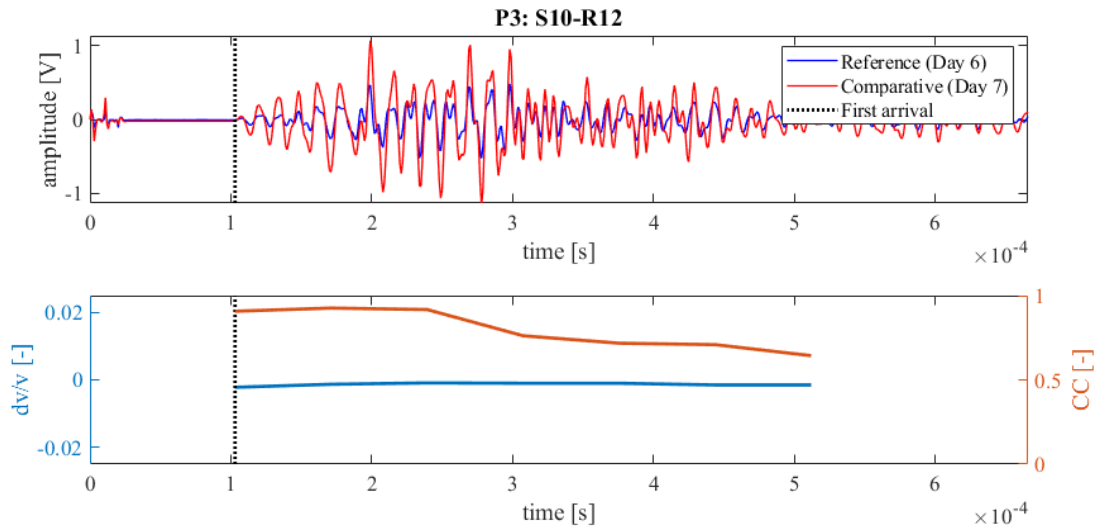


Figure 263: Wave signals of Measurement 6 (blue) and Measurement 7 (red) between principal sensor pair Source S10 and Receiver S12 at Position 3 (top),  $dv/v$  (blue) and  $CC$  (orange) results from CWI over the signal travel time divided in stretching windows (bottom)

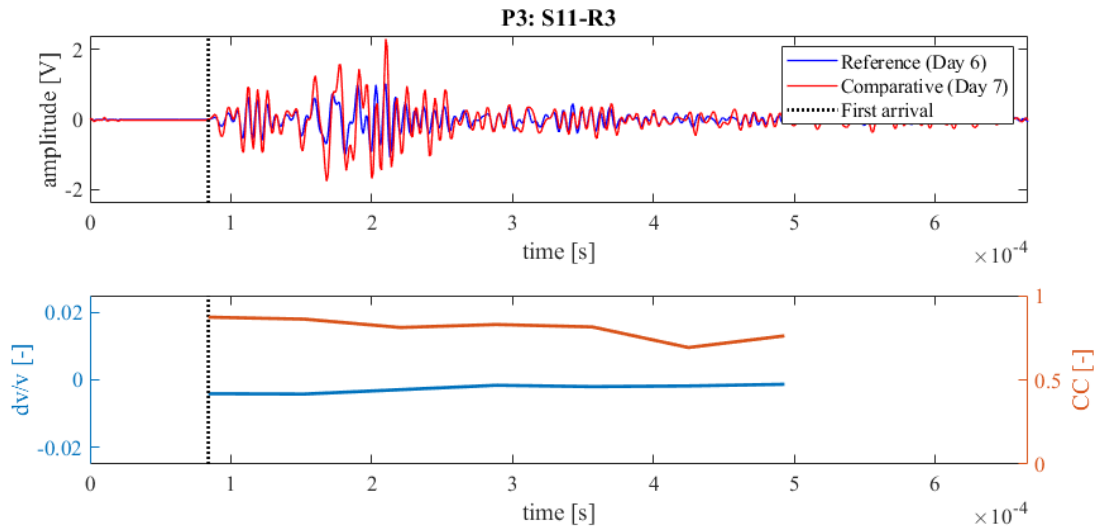


Figure 264: Wave signals of Measurement 6 (blue) and Measurement 7 (red) between principal sensor pair Source S11 and Receiver S3 at Position 3 (top),  $dv/v$  (blue) and CC (orange) results from CWI over the signal travel time divided in stretching windows (bottom)

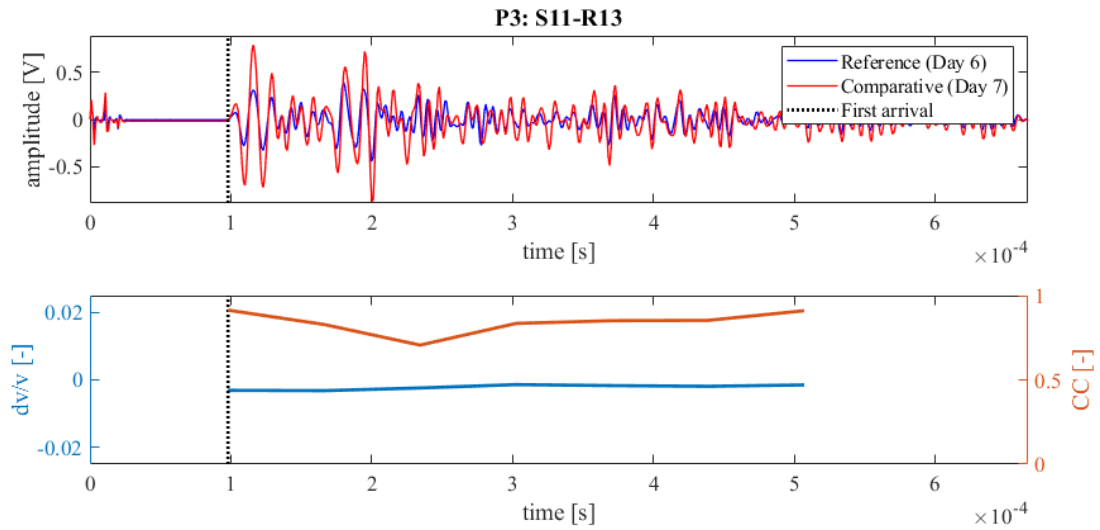


Figure 265: Wave signals of Measurement 6 (blue) and Measurement 7 (red) between principal sensor pair Source S11 and Receiver S13 at Position 3 (top),  $dv/v$  (blue) and CC (orange) results from CWI over the signal travel time divided in stretching windows (bottom)

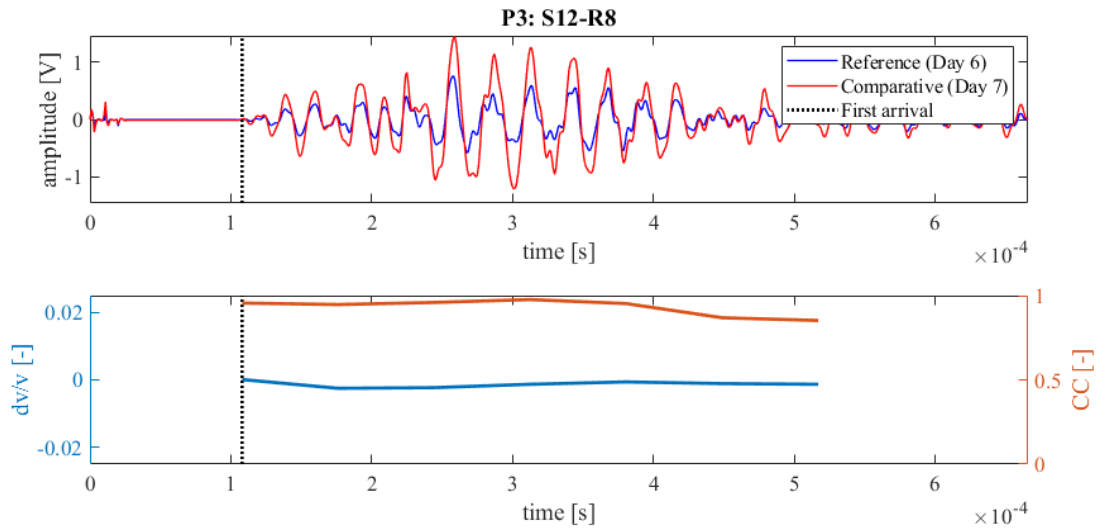


Figure 266: Wave signals of Measurement 6 (blue) and Measurement 7 (red) between principal sensor pair Source S12 and Receiver S8 at Position 3 (top),  $dv/v$  (blue) and CC (orange) results from CWI over the signal travel time divided in stretching windows (bottom)

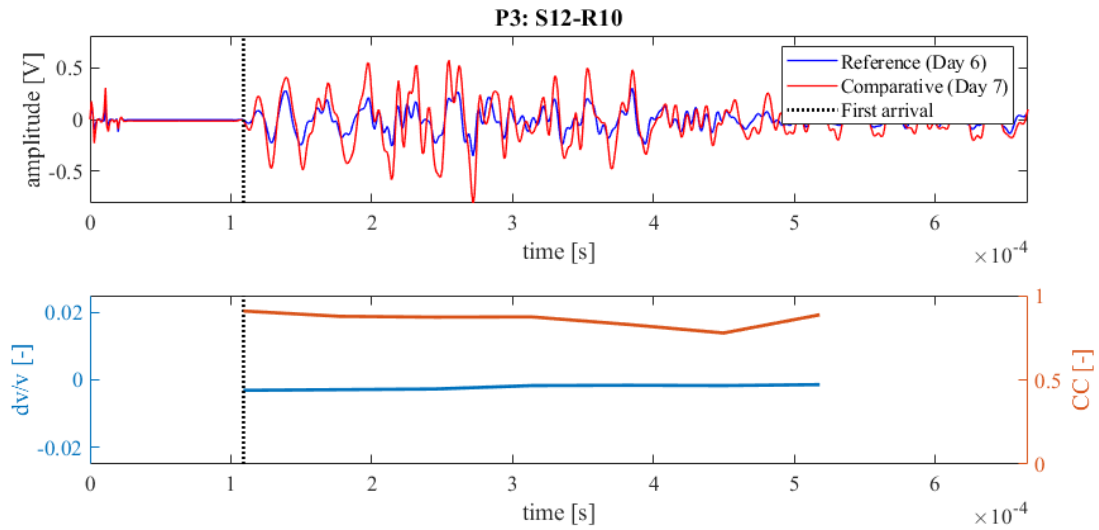


Figure 267: Wave signals of Measurement 6 (blue) and Measurement 7 (red) between principal sensor pair Source S12 and Receiver S10 at Position 3 (top),  $dv/v$  (blue) and CC (orange) results from CWI over the signal travel time divided in stretching windows (bottom)

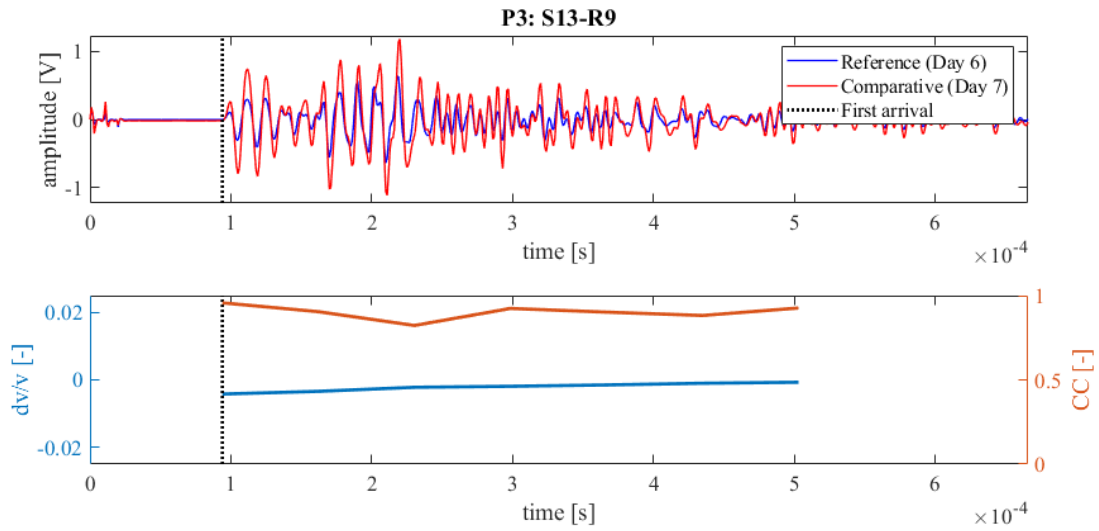


Figure 268: Wave signals of Measurement 6 (blue) and Measurement 7 (red) between principal sensor pair Source S13 and Receiver S9 at Position 3 (top),  $dv/v$  (blue) and CC (orange) results from CWI over the signal travel time divided in stretching windows (bottom)

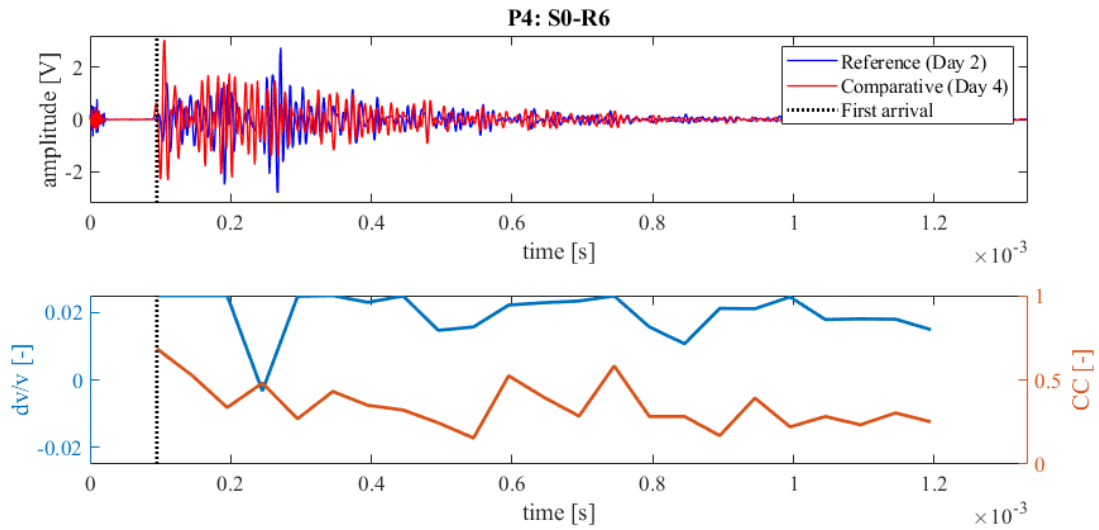


Figure 269: Wave signals of Measurement 2 (blue) and Measurement 4 (red) between principal sensor pair Source S0 and Receiver S6 at Position 4 (top),  $dv/v$  (blue) and CC (orange) results from CWI over the signal travel time divided in stretching windows (bottom)

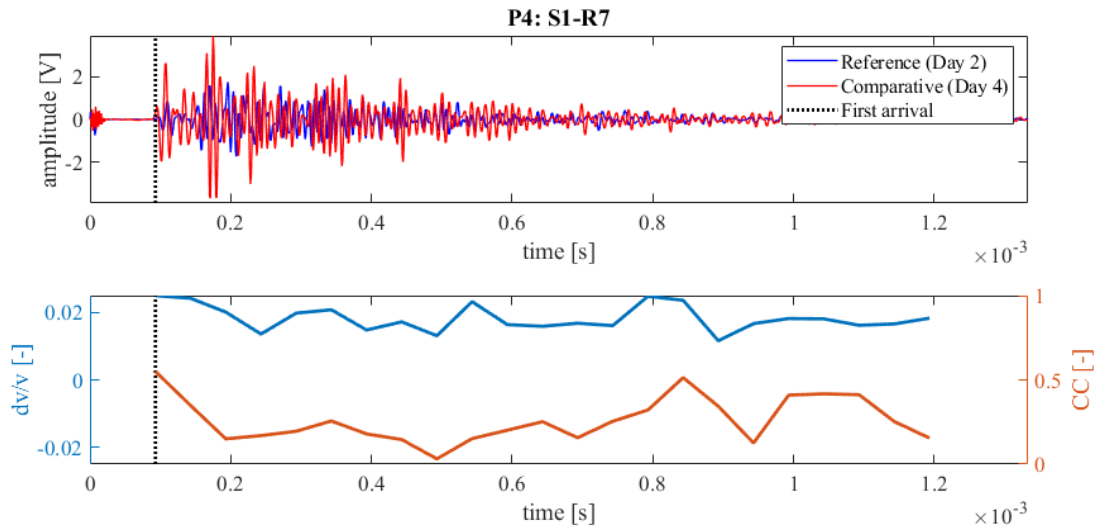


Figure 270: Wave signals of Measurement 2 (blue) and Measurement 4 (red) between principal sensor pair Source S1 and Receiver S7 at Position 4 (top),  $dv/v$  (blue) and  $CC$  (orange) results from CWI over the signal travel time divided in stretching windows (bottom)

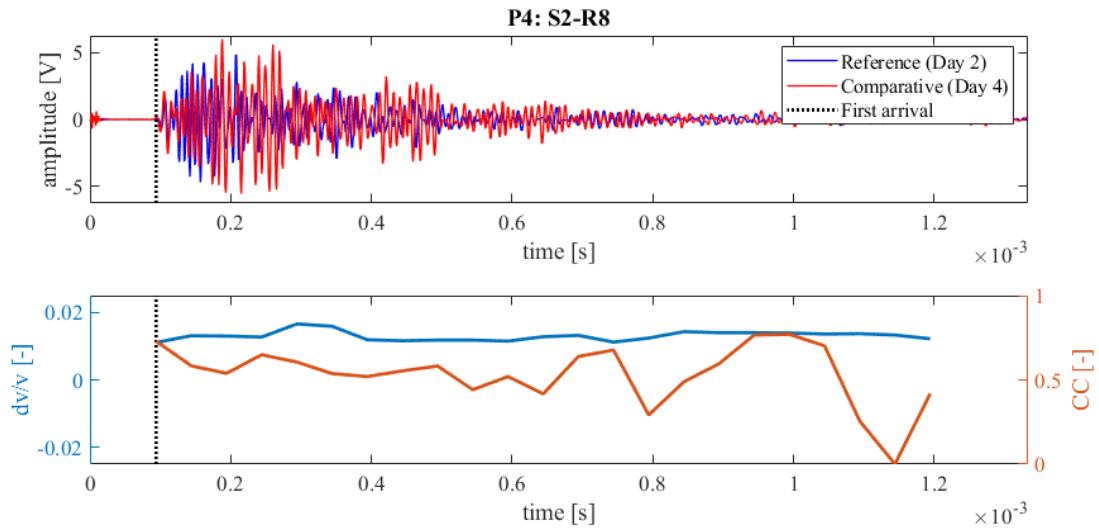


Figure 271: Wave signals of Measurement 2 (blue) and Measurement 4 (red) between principal sensor pair Source S2 and Receiver S8 at Position 4 (top),  $dv/v$  (blue) and  $CC$  (orange) results from CWI over the signal travel time divided in stretching windows (bottom)

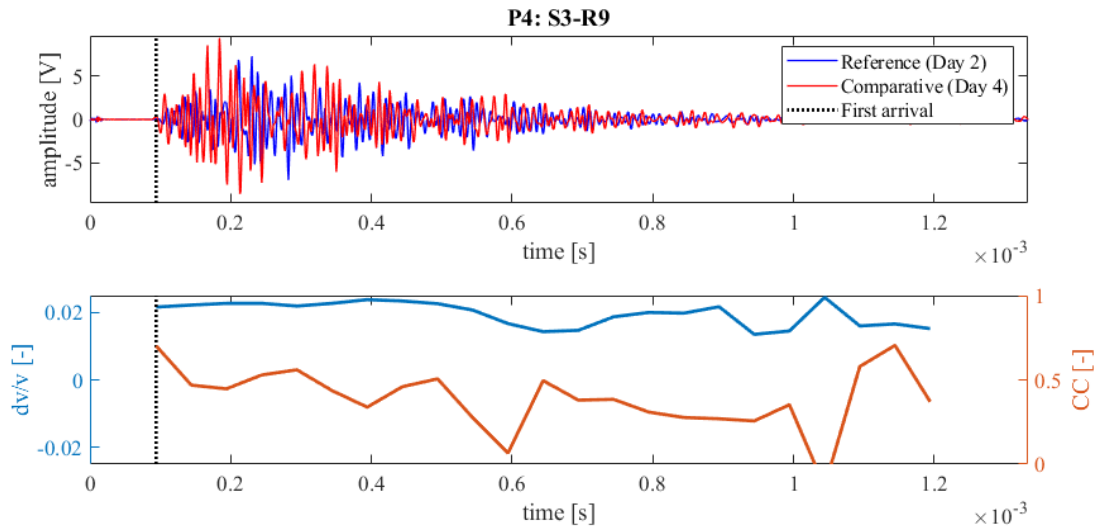


Figure 272: Wave signals of Measurement 2 (blue) and Measurement 4 (red) between principal sensor pair Source S3 and Receiver S9 at Position 4 (top),  $dv/v$  (blue) and  $CC$  (orange) results from CWI over the signal travel time divided in stretching windows (bottom)

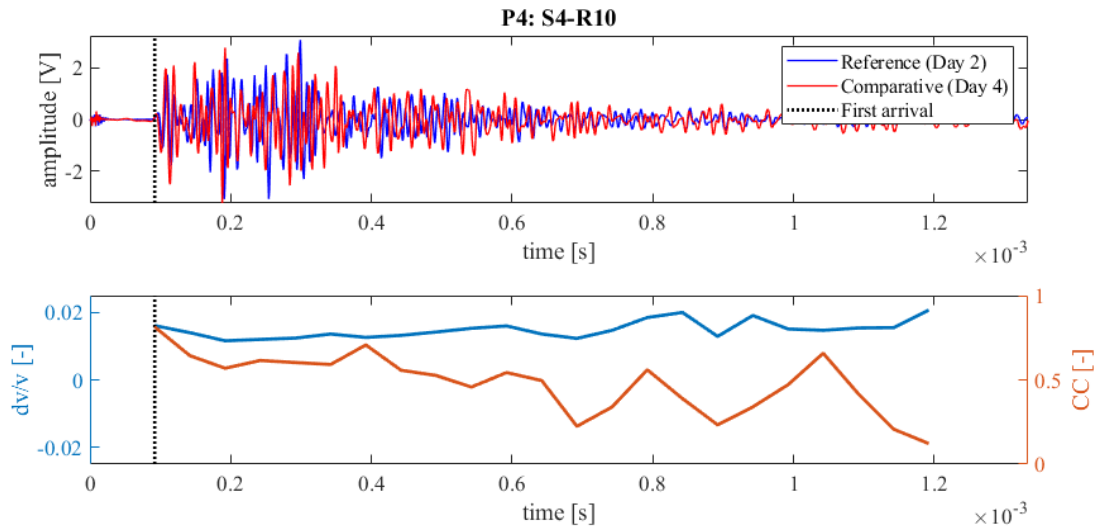


Figure 273: Wave signals of Measurement 2 (blue) and Measurement 4 (red) between principal sensor pair Source S4 and Receiver S10 at Position 4 (top),  $dv/v$  (blue) and  $CC$  (orange) results from CWI over the signal travel time divided in stretching windows (bottom)

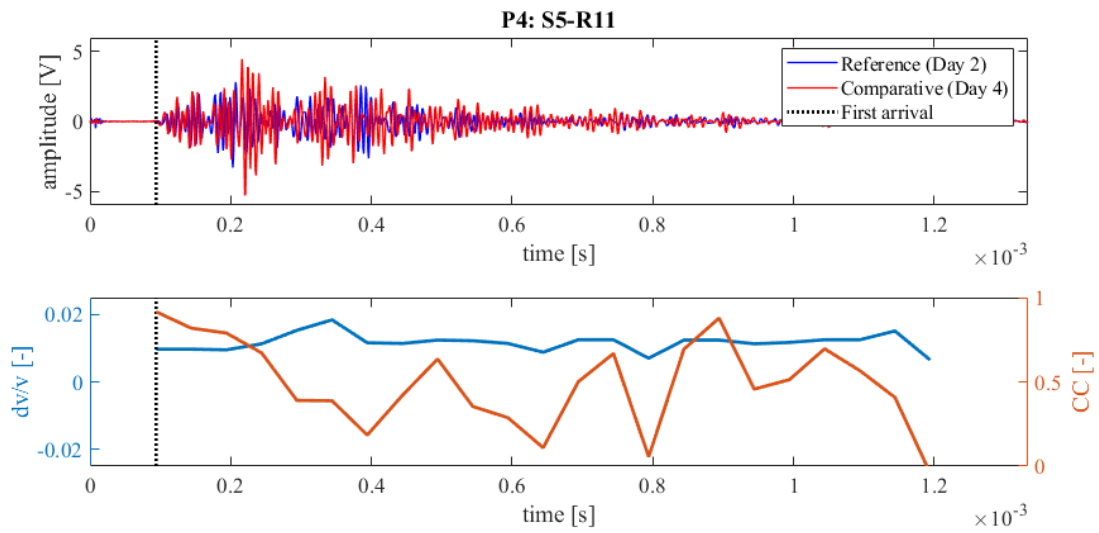


Figure 274: Wave signals of Measurement 2 (blue) and Measurement 4 (red) between principal sensor pair Source S5 and Receiver S11 at Position 4 (top),  $dv/v$  (blue) and  $CC$  (orange) results from CWI over the signal travel time divided in stretching windows (bottom)

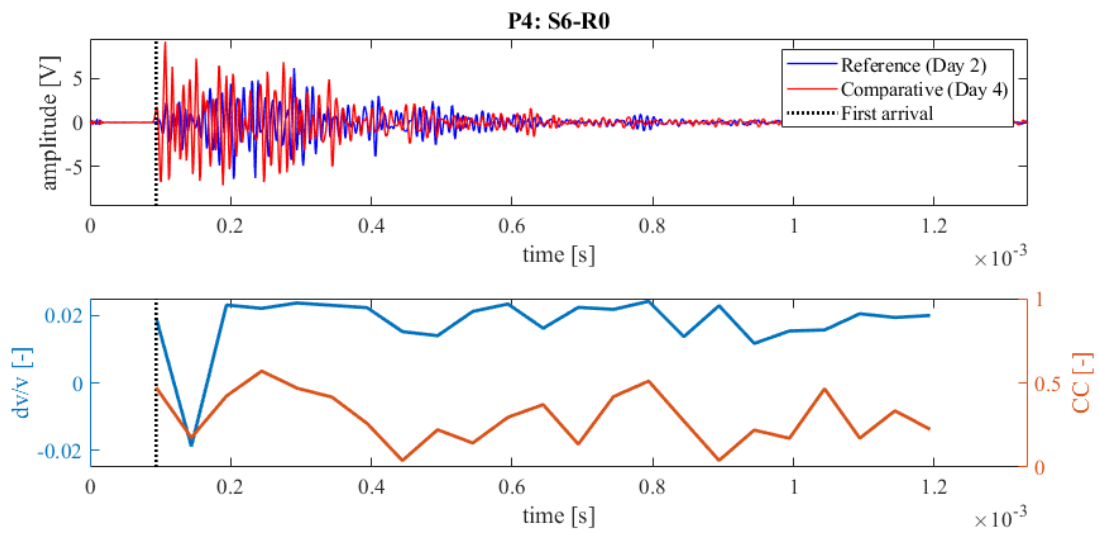


Figure 275: Wave signals of Measurement 2 (blue) and Measurement 4 (red) between principal sensor pair Source S6 and Receiver S0 at Position 4 (top),  $dv/v$  (blue) and  $CC$  (orange) results from CWI over the signal travel time divided in stretching windows (bottom)

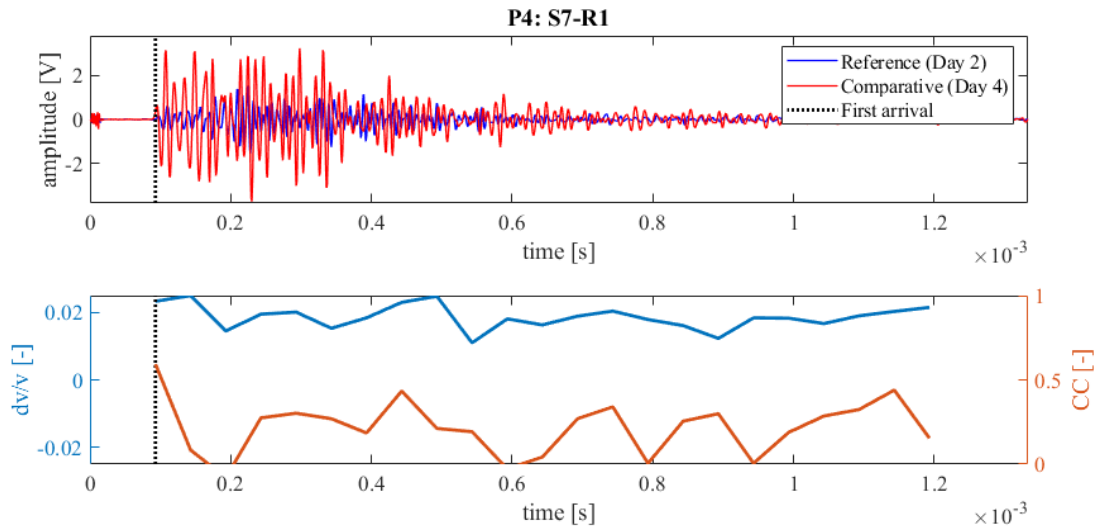


Figure 276: Wave signals of Measurement 2 (blue) and Measurement 4 (red) between principal sensor pair Source S7 and Receiver S1 at Position 4 (top),  $dv/v$  (blue) and  $CC$  (orange) results from CWI over the signal travel time divided in stretching windows (bottom)

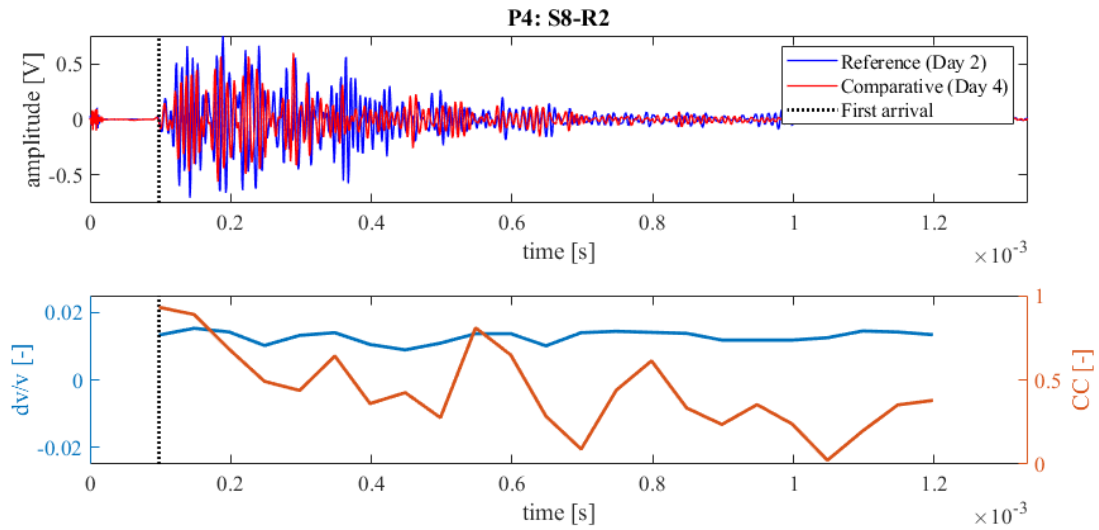


Figure 277: Wave signals of Measurement 2 (blue) and Measurement 4 (red) between principal sensor pair Source S8 and Receiver S2 at Position 4 (top),  $dv/v$  (blue) and  $CC$  (orange) results from CWI over the signal travel time divided in stretching windows (bottom)

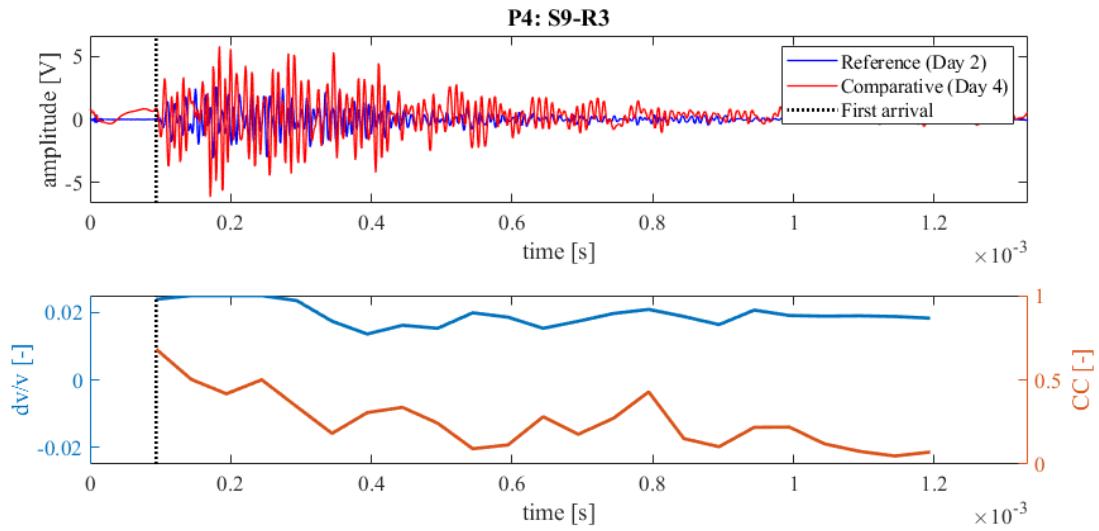


Figure 278: Wave signals of Measurement 2 (blue) and Measurement 4 (red) between principal sensor pair Source S9 and Receiver S3 at Position 4 (top),  $dv/v$  (blue) and  $CC$  (orange) results from CWI over the signal travel time divided in stretching windows (bottom)

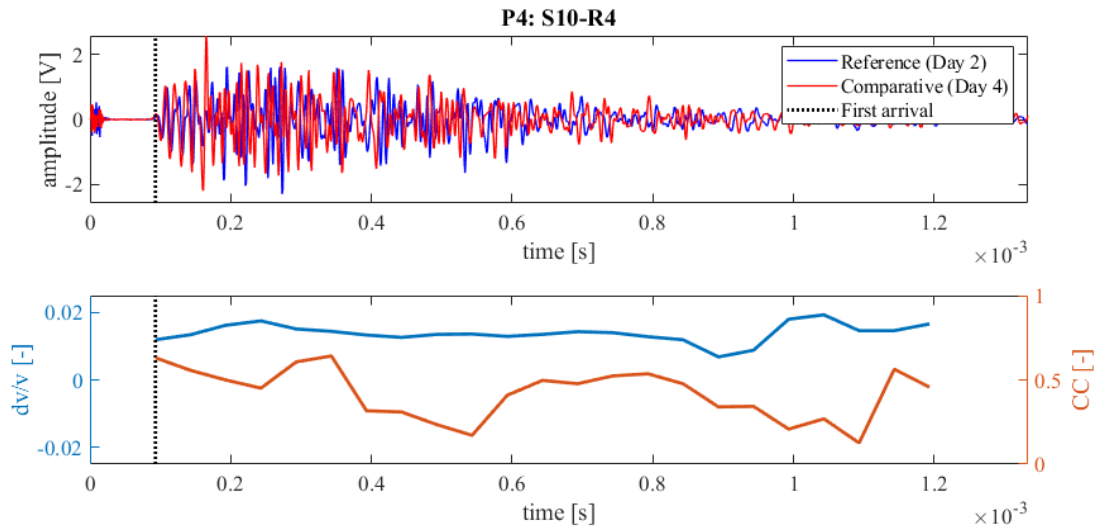


Figure 279: Wave signals of Measurement 2 (blue) and Measurement 4 (red) between principal sensor pair Source S10 and Receiver S4 at Position 4 (top),  $dv/v$  (blue) and  $CC$  (orange) results from CWI over the signal travel time divided in stretching windows (bottom)

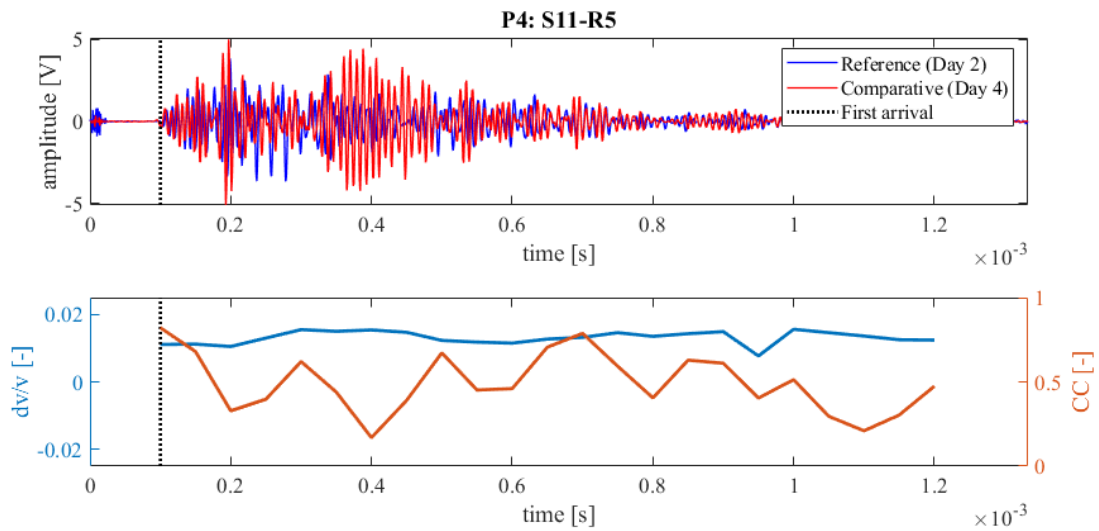


Figure 280: Wave signals of Measurement 2 (blue) and Measurement 4 (red) between principal sensor pair Source S11 and Receiver S5 at Position 4 (top),  $dv/v$  (blue) and  $CC$  (orange) results from CWI over the signal travel time divided in stretching windows (bottom)

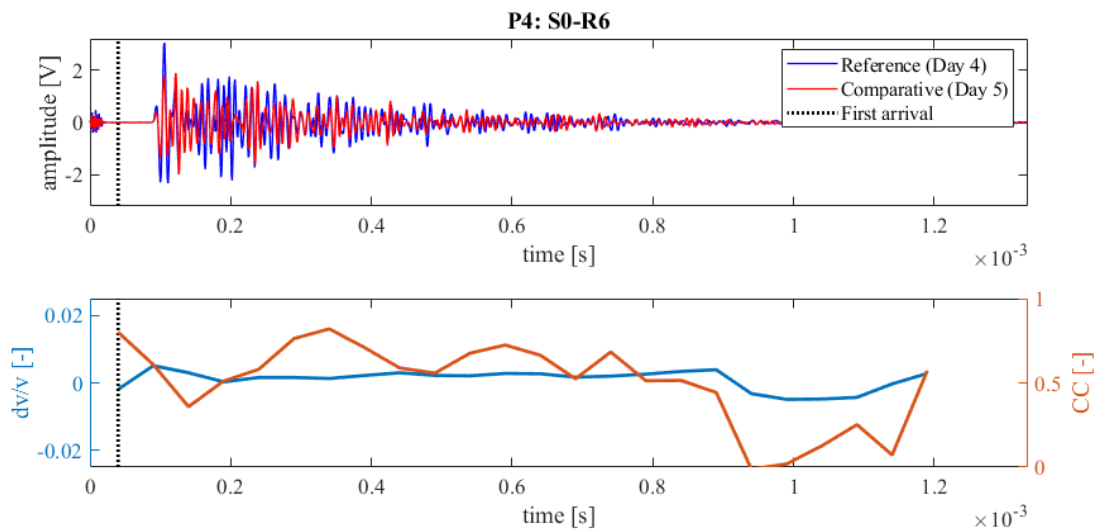


Figure 281: Wave signals of Measurement 4 (blue) and Measurement 5 (red) between principal sensor pair Source S0 and Receiver S6 at Position 4 (top),  $dv/v$  (blue) and  $CC$  (orange) results from CWI over the signal travel time divided in stretching windows (bottom)

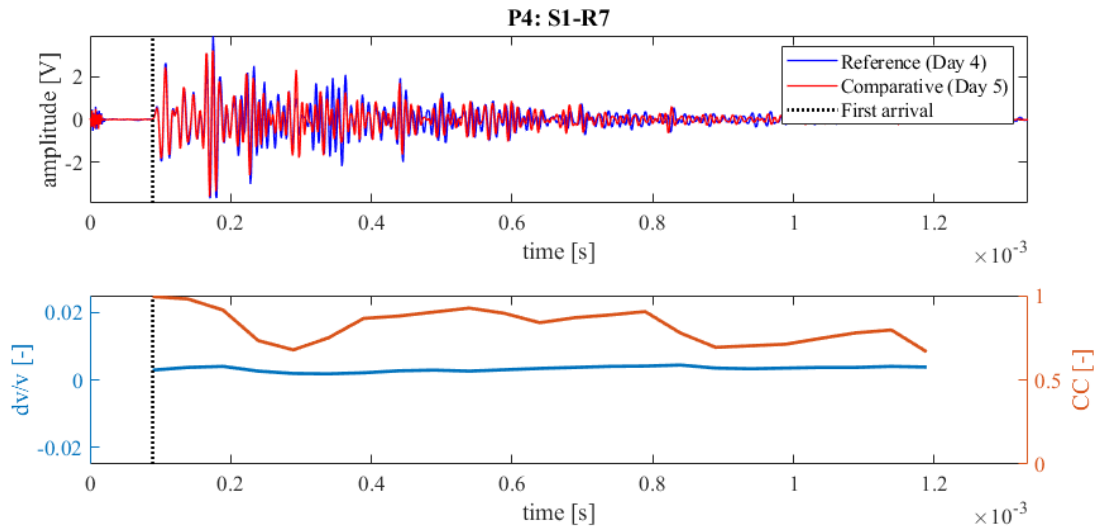


Figure 282: Wave signals of Measurement 4 (blue) and Measurement 5 (red) between principal sensor pair Source S1 and Receiver S7 at Position 4 (top),  $dv/v$  (blue) and  $CC$  (orange) results from CWI over the signal travel time divided in stretching windows (bottom)

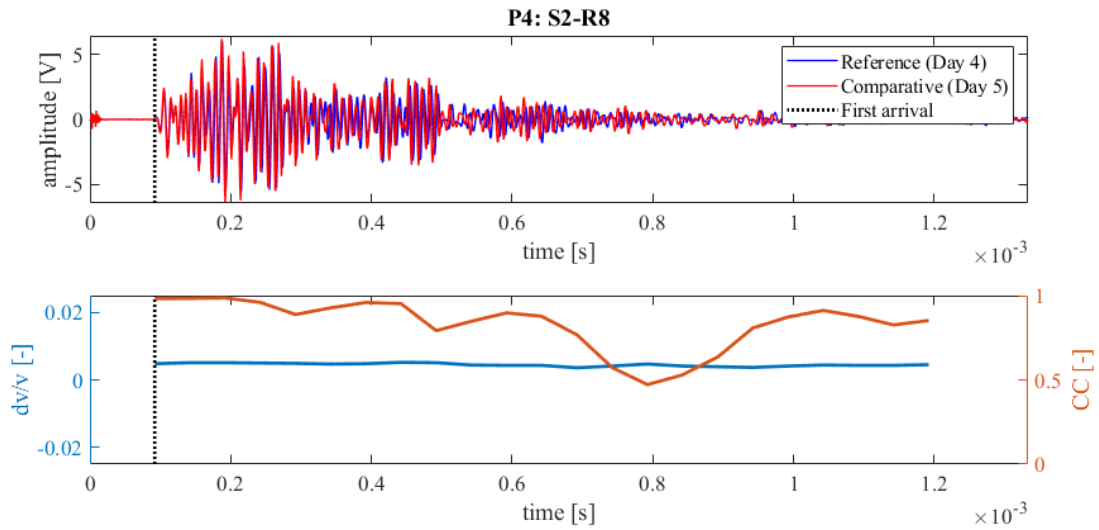


Figure 283: Wave signals of Measurement 4 (blue) and Measurement 5 (red) between principal sensor pair Source S2 and Receiver S8 at Position 4 (top),  $dv/v$  (blue) and  $CC$  (orange) results from CWI over the signal travel time divided in stretching windows (bottom)

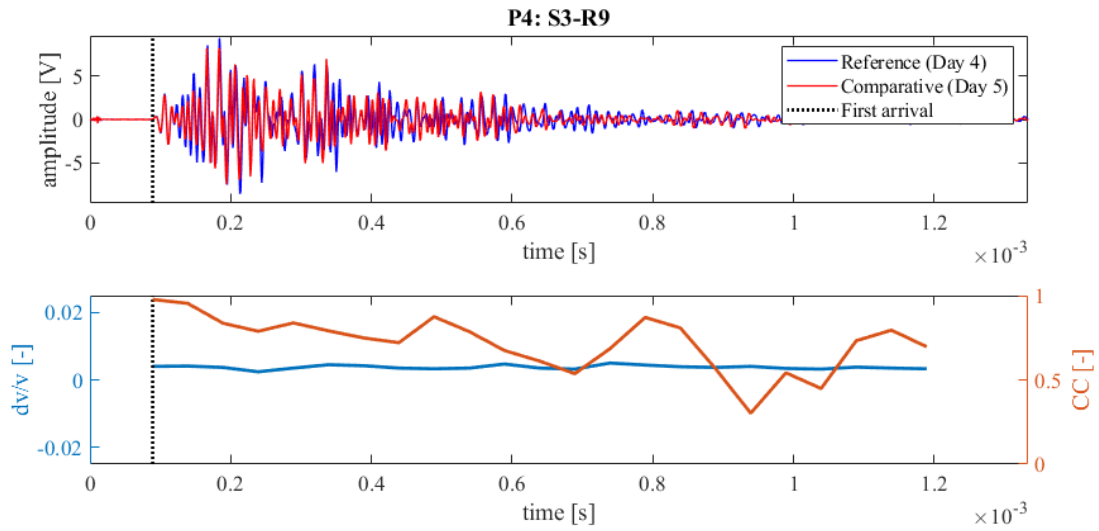


Figure 284: Wave signals of Measurement 4 (blue) and Measurement 5 (red) between principal sensor pair Source S3 and Receiver S9 at Position 4 (top),  $dv/v$  (blue) and  $CC$  (orange) results from CWI over the signal travel time divided in stretching windows (bottom)

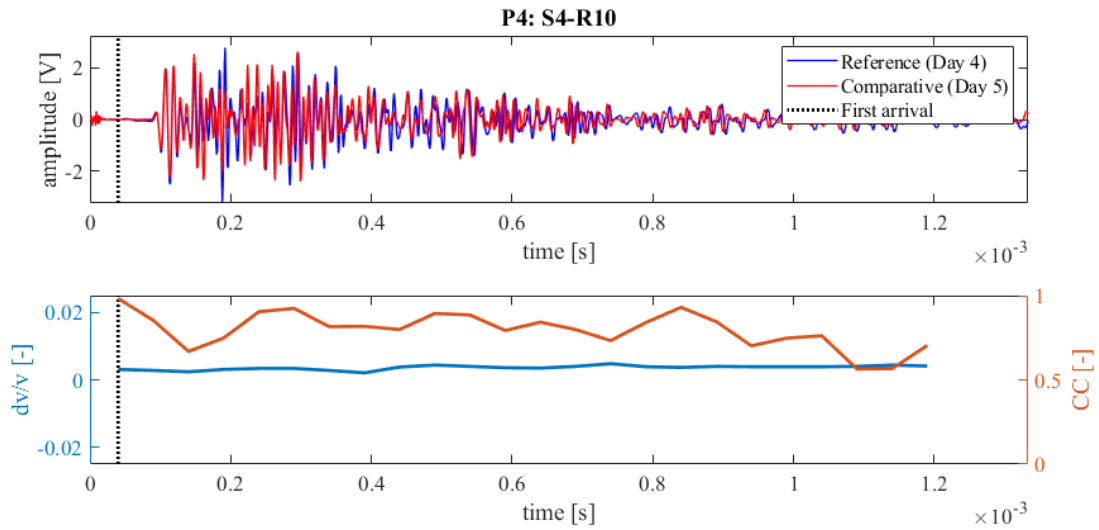


Figure 285: Wave signals of Measurement 4 (blue) and Measurement 5 (red) between principal sensor pair Source S4 and Receiver S10 at Position 4 (top),  $dv/v$  (blue) and  $CC$  (orange) results from CWI over the signal travel time divided in stretching windows (bottom)

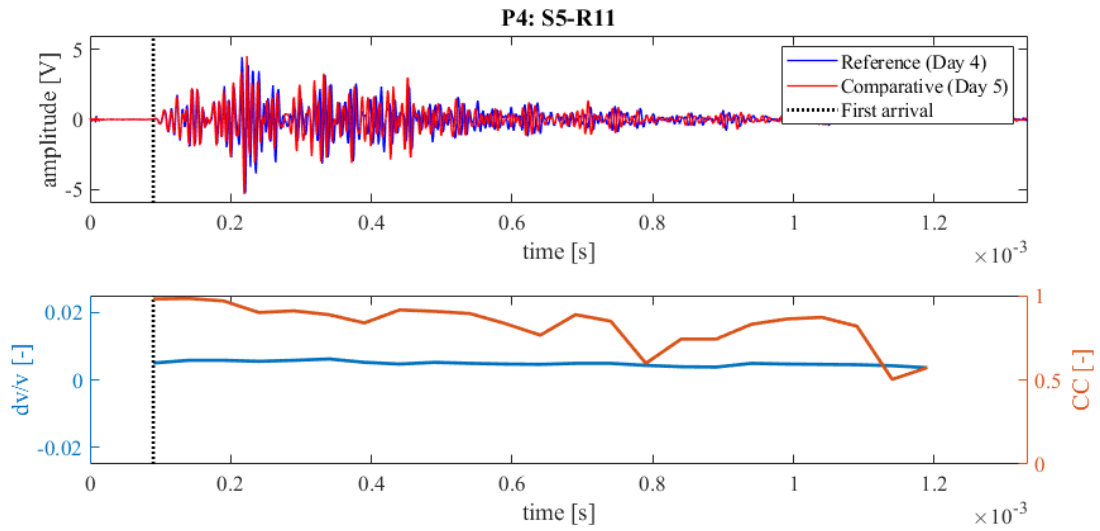


Figure 286: Wave signals of Measurement 4 (blue) and Measurement 5 (red) between principal sensor pair Source S5 and Receiver S11 at Position 4 (top),  $dv/v$  (blue) and  $CC$  (orange) results from CWI over the signal travel time divided in stretching windows (bottom)

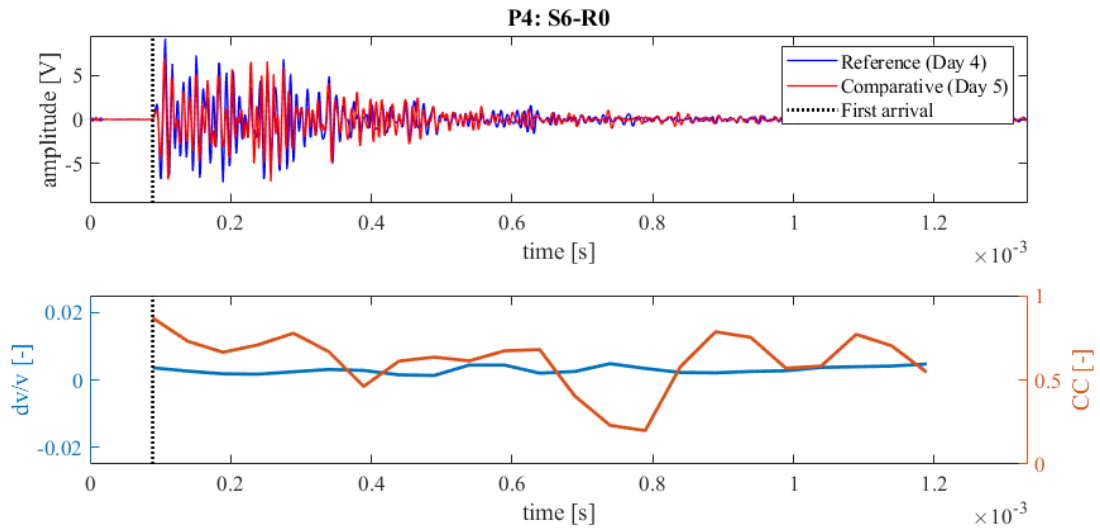


Figure 287: Wave signals of Measurement 4 (blue) and Measurement 5 (red) between principal sensor pair Source S6 and Receiver S0 at Position 4 (top),  $dv/v$  (blue) and  $CC$  (orange) results from CWI over the signal travel time divided in stretching windows (bottom)

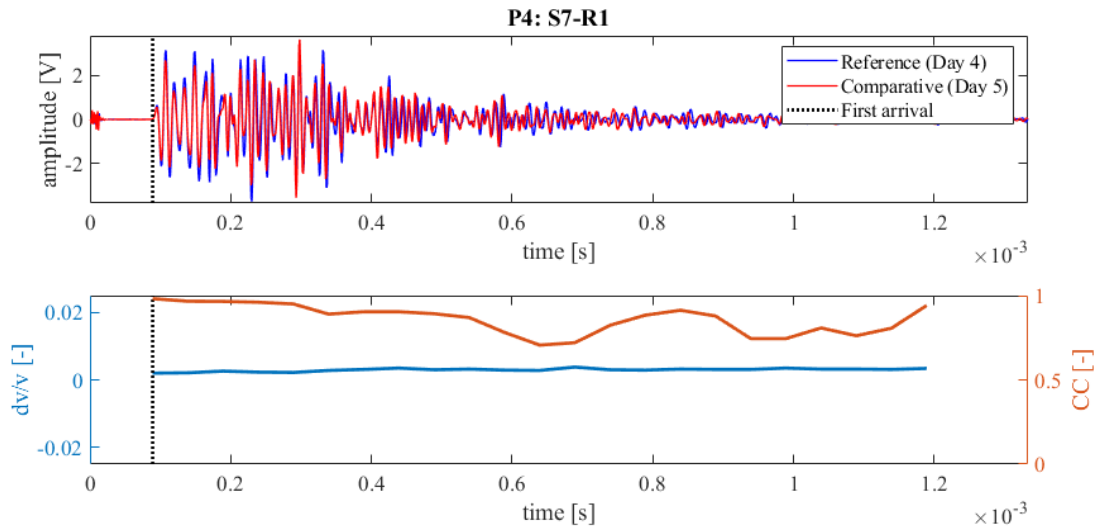


Figure 288: Wave signals of Measurement 4 (blue) and Measurement 5 (red) between principal sensor pair Source S7 and Receiver S1 at Position 4 (top),  $dv/v$  (blue) and  $CC$  (orange) results from CWI over the signal travel time divided in stretching windows (bottom)

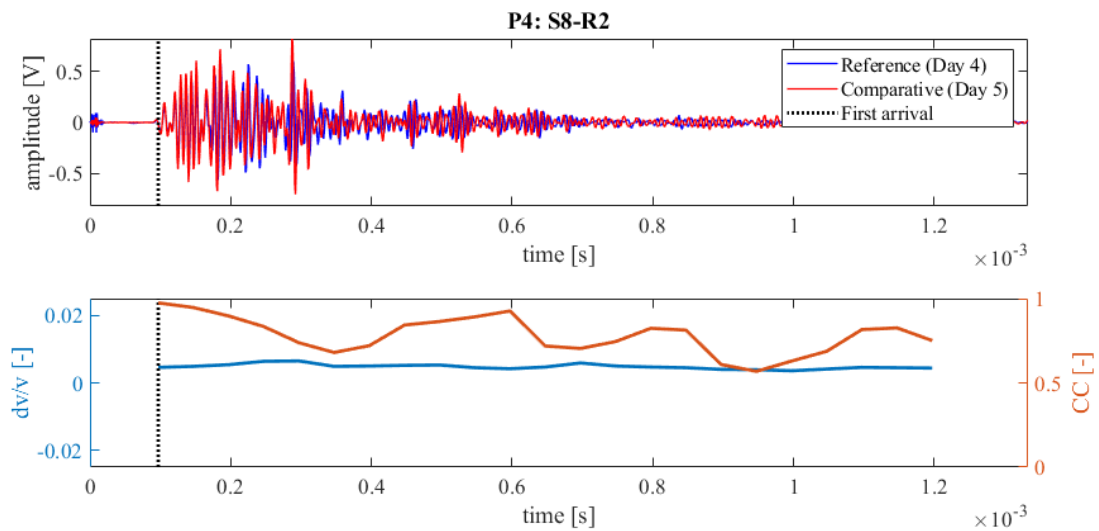


Figure 289: Wave signals of Measurement 4 (blue) and Measurement 5 (red) between principal sensor pair Source S8 and Receiver S2 at Position 4 (top),  $dv/v$  (blue) and  $CC$  (orange) results from CWI over the signal travel time divided in stretching windows (bottom)

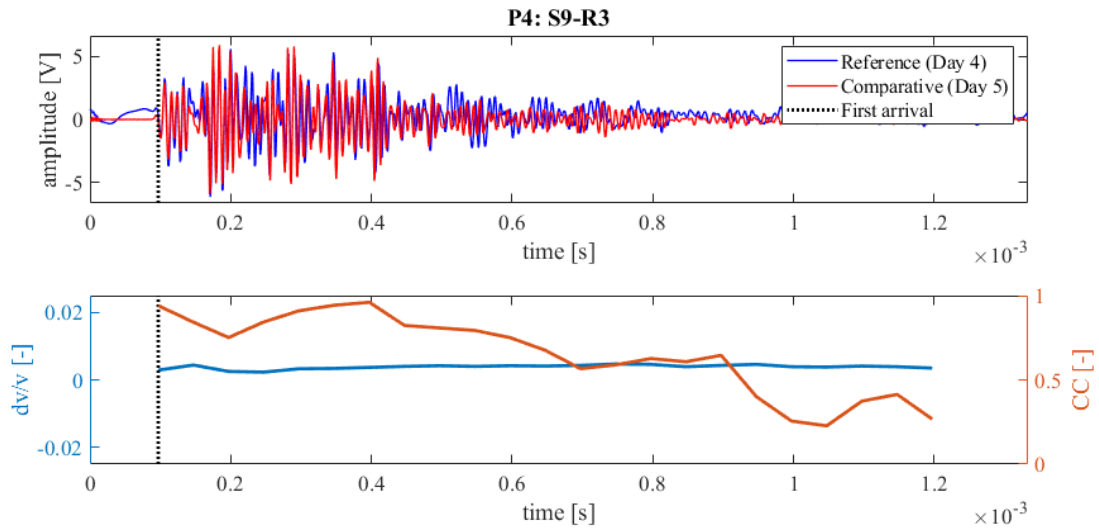


Figure 290: Wave signals of Measurement 4 (blue) and Measurement 5 (red) between principal sensor pair Source S9 and Receiver S3 at Position 4 (top),  $dv/v$  (blue) and  $CC$  (orange) results from CWI over the signal travel time divided in stretching windows (bottom)

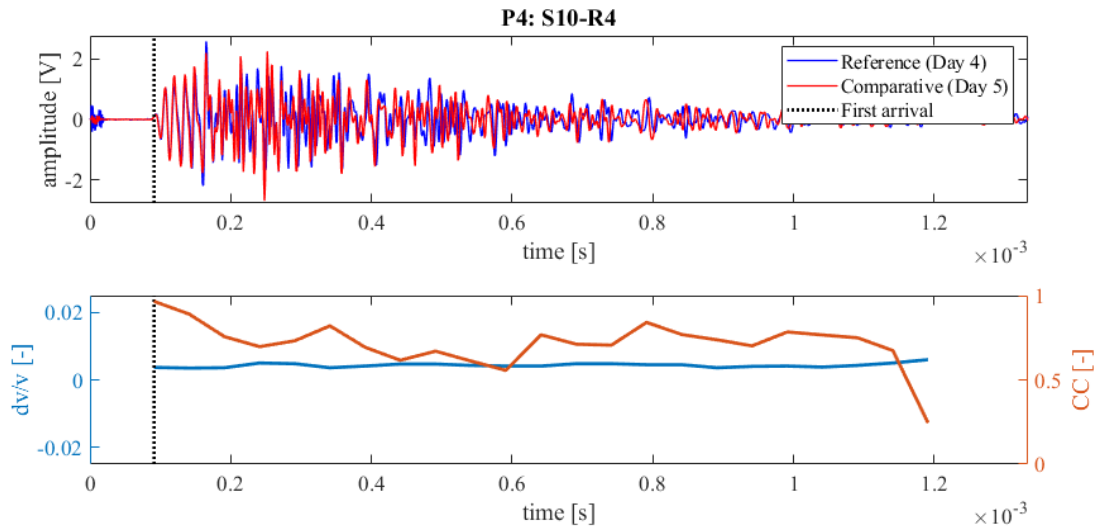


Figure 291: Wave signals of Measurement 4 (blue) and Measurement 5 (red) between principal sensor pair Source S10 and Receiver S4 at Position 4 (top),  $dv/v$  (blue) and  $CC$  (orange) results from CWI over the signal travel time divided in stretching windows (bottom)

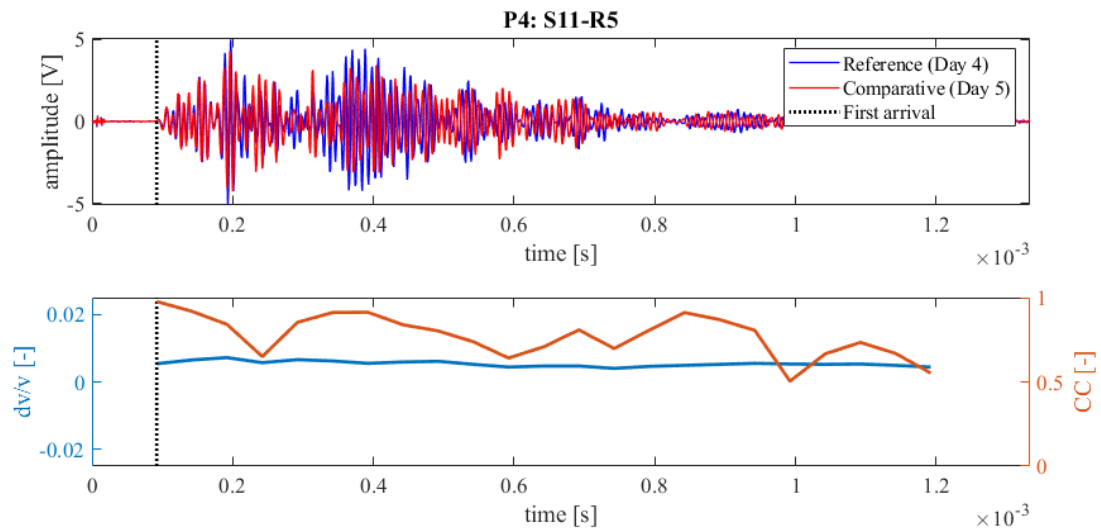


Figure 292: Wave signals of Measurement 4 (blue) and Measurement 5 (red) between principal sensor pair Source S11 and Receiver S5 at Position 4 (top),  $dv/v$  (blue) and  $CC$  (orange) results from CWI over the signal travel time divided in stretching windows (bottom)

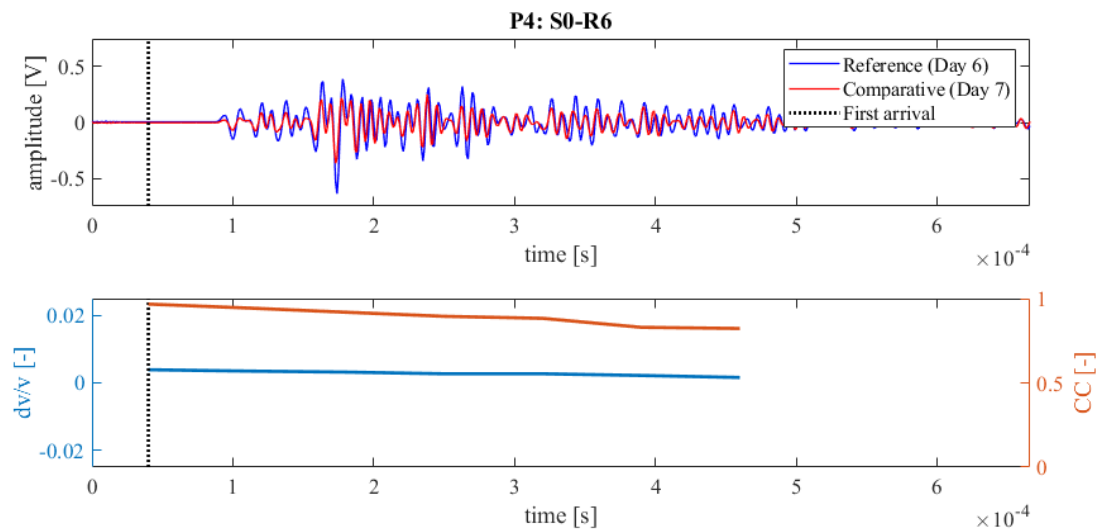


Figure 293: Wave signals of Measurement 6 (blue) and Measurement 7 (red) between principal sensor pair Source S0 and Receiver S6 at Position 4 (top),  $dv/v$  (blue) and  $CC$  (orange) results from CWI over the signal travel time divided in stretching windows (bottom)

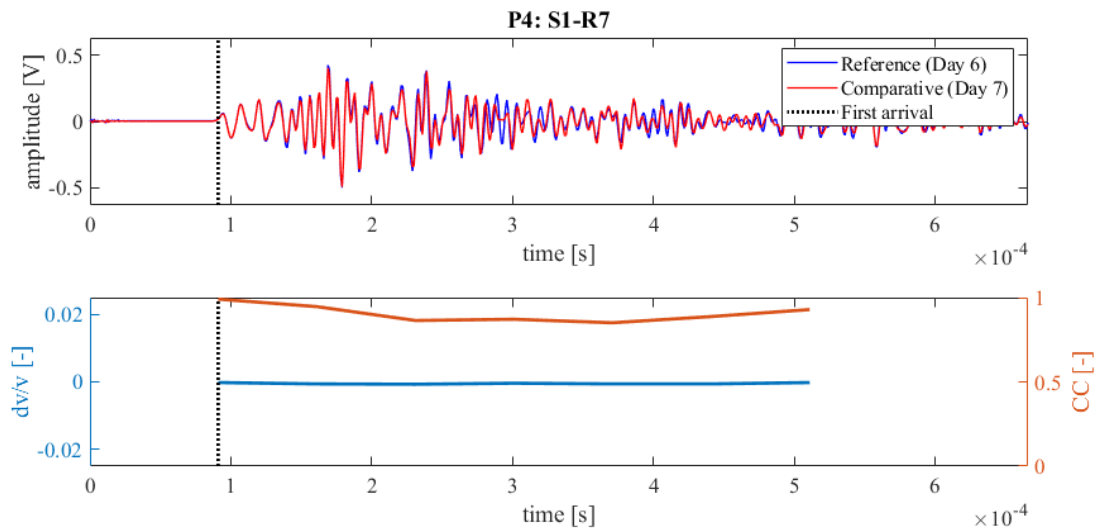


Figure 294: Wave signals of Measurement 6 (blue) and Measurement 7 (red) between principal sensor pair Source S1 and Receiver S7 at Position 4 (top),  $dv/v$  (blue) and  $CC$  (orange) results from CWI over the signal travel time divided in stretching windows (bottom)

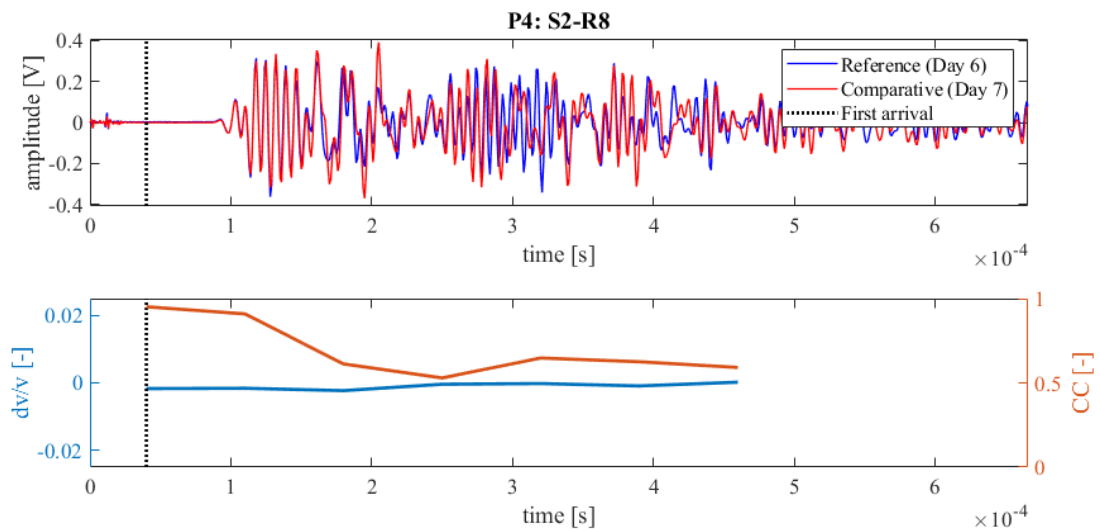
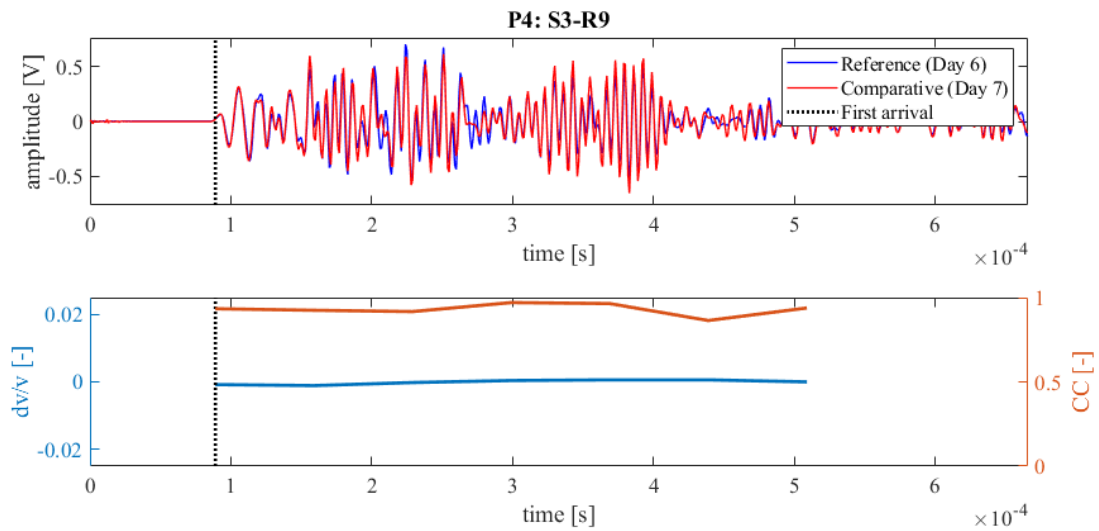
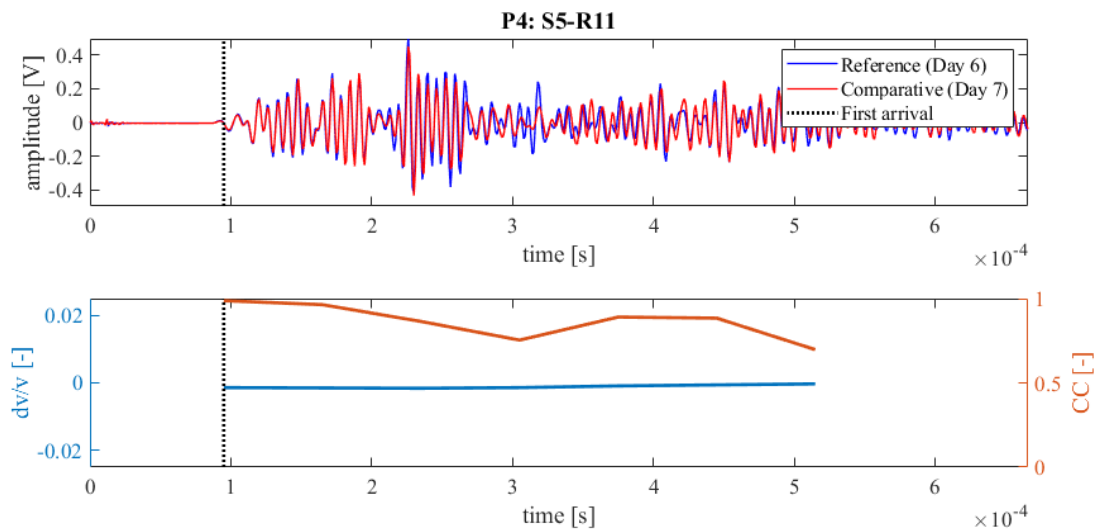


Figure 295: Wave signals of Measurement 6 (blue) and Measurement 7 (red) between principal sensor pair Source S2 and Receiver S8 at Position 4 (top),  $dv/v$  (blue) and  $CC$  (orange) results from CWI over the signal travel time divided in stretching windows (bottom)



**Figure 296: Wave signals of Measurement 6 (blue) and Measurement 7 (red) between principal sensor pair Source S3 and Receiver S9 at Position 4 (top),  $dv/v$  (blue) and  $CC$  (orange) results from CWI over the signal travel time divided in stretching windows (bottom)**



**Figure 297: Wave signals of Measurement 6 (blue) and Measurement 7 (red) between principal sensor pair Source S5 and Receiver S11 at Position 4 (top),  $dv/v$  (blue) and  $CC$  (orange) results from CWI over the signal travel time divided in stretching windows (bottom)**

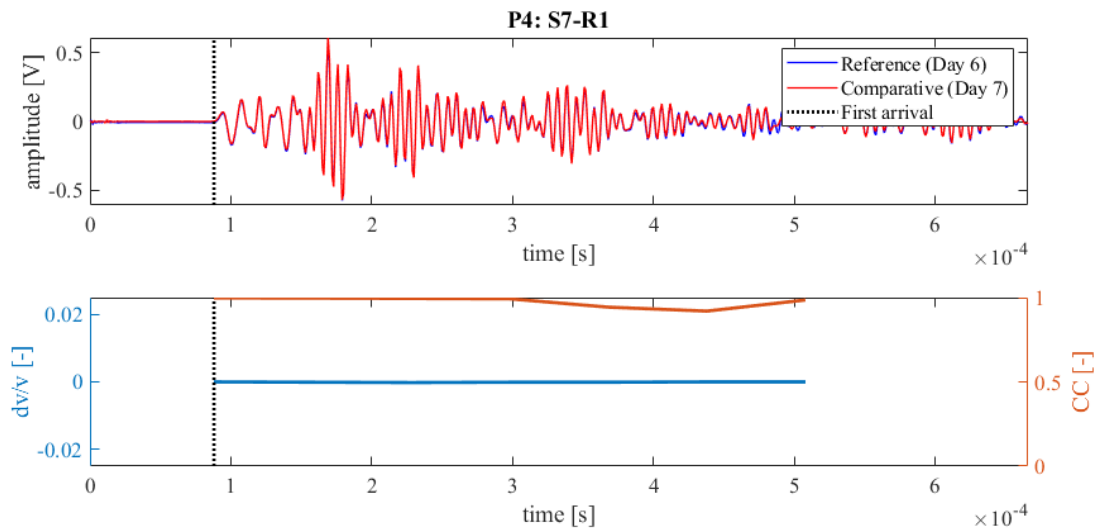


Figure 298: Wave signals of Measurement 6 (blue) and Measurement 7 (red) between principal sensor pair Source S7 and Receiver S1 at Position 4 (top),  $dv/v$  (blue) and  $CC$  (orange) results from CWI over the signal travel time divided in stretching windows (bottom)

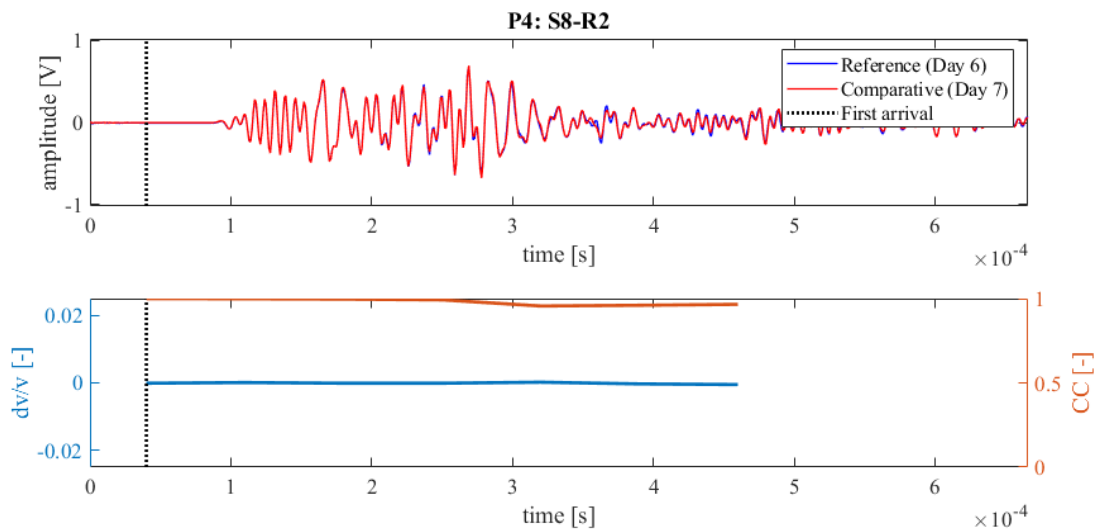


Figure 299: Wave signals of Measurement 6 (blue) and Measurement 7 (red) between principal sensor pair Source S8 and Receiver S2 at Position 4 (top),  $dv/v$  (blue) and  $CC$  (orange) results from CWI over the signal travel time divided in stretching windows (bottom)

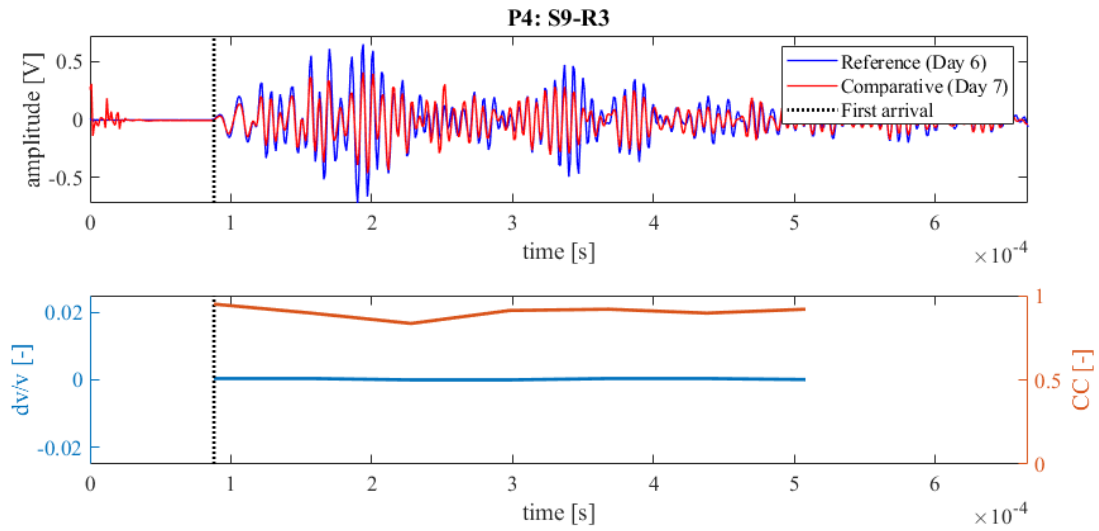


Figure 300: Wave signals of Measurement 6 (blue) and Measurement 7 (red) between principal sensor pair Source S9 and Receiver S3 at Position 4 (top),  $dv/v$  (blue) and CC (orange) results from CWI over the signal travel time divided in stretching windows (bottom)

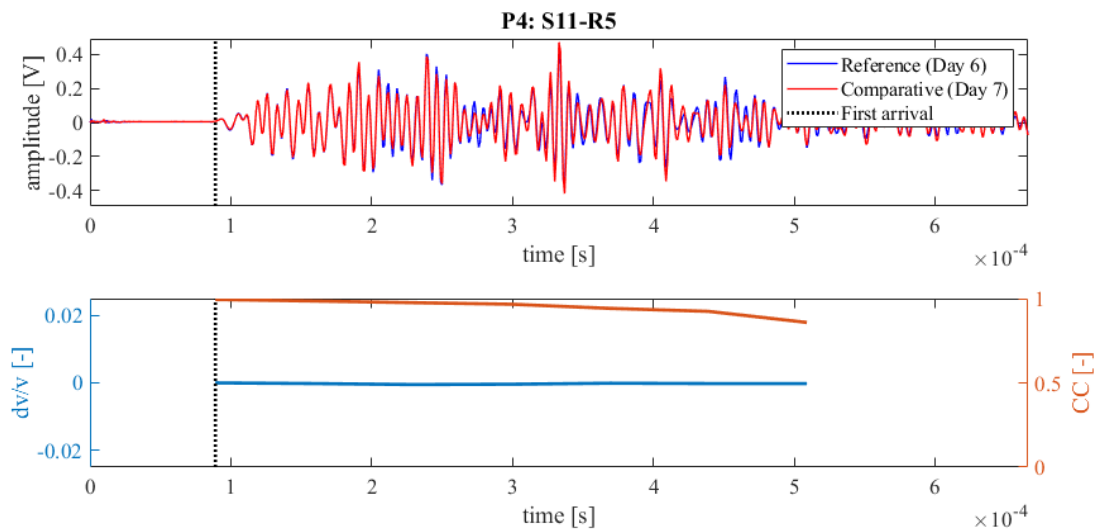


Figure 301: Wave signals of Measurement 6 (blue) and Measurement 7 (red) between principal sensor pair Source S11 and Receiver S5 at Position 4 (top),  $dv/v$  (blue) and CC (orange) results from CWI over the signal travel time divided in stretching windows (bottom)

## E. CWI results of concrete hydration tests

The CWI results from the concrete hydration tests are obtained from concrete cylindrical samples with embedded SA and are kept in a controlled environment. The measuring schedule is shown in Table 20. The CWI results show a clear discrepancy in the two first measurements. This is when the concrete is at its youngest. After the initial measurements, minimal deviations in the signal's waveform are observed. As the concrete ages, the discrepancies lower in magnitude, as does the  $dv/v$ . This trend holds true for all three tested concrete cylinders, Cylinder 3, Cylinder 4 and Cylinder 5. It is important to note that the concrete mix design of the three test cylinders is not identical to the mix design from which the assessed concrete bridge consists of.

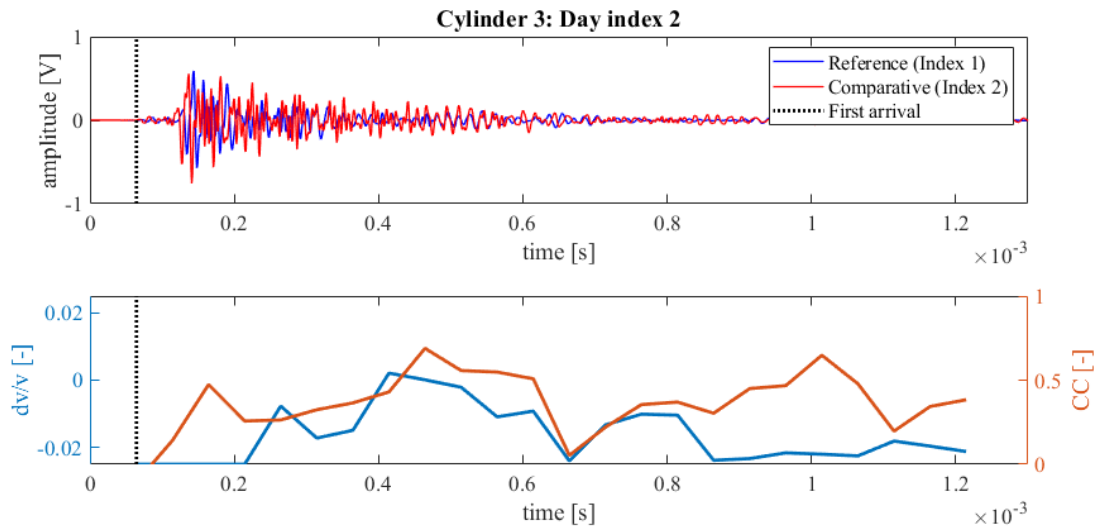


Figure 302: Wave signals of Measurement 1 (blue) and Measurement 2 (red) of concrete hydration test Cylinder 3 (top),  $dv/v$  (blue) and CC (orange) results from CWI over the signal travel time divided in stretching windows (bottom)

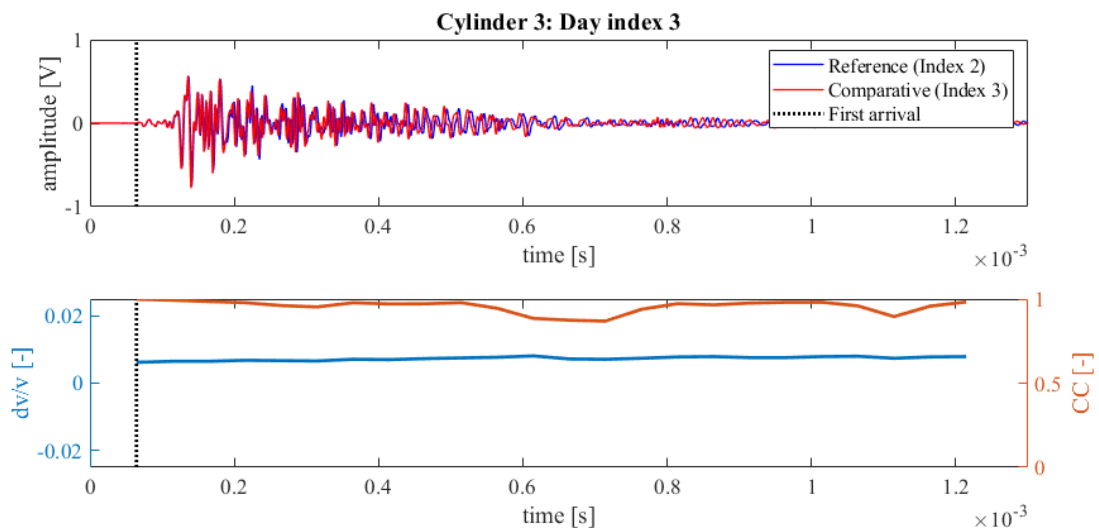
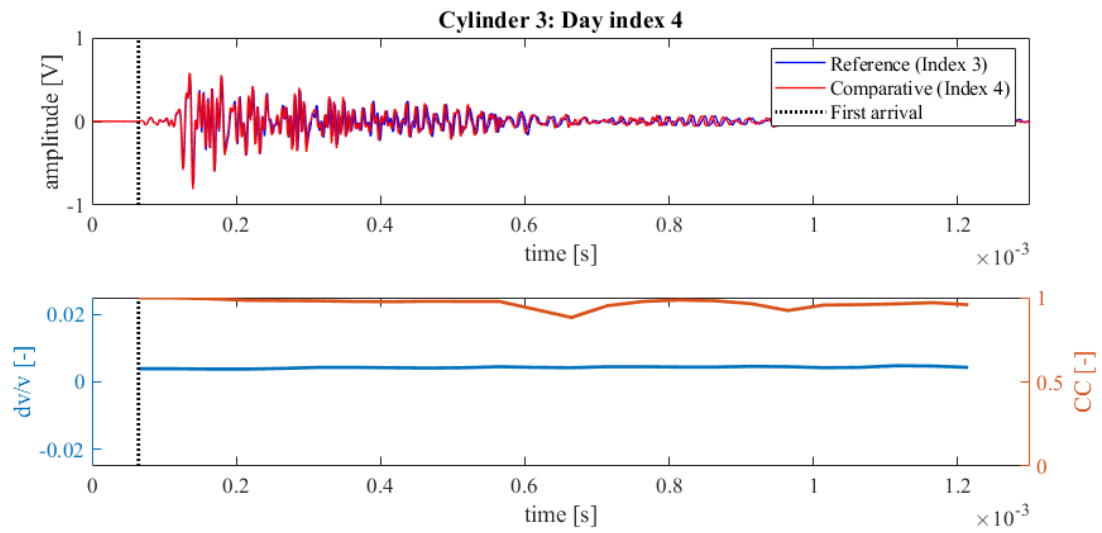
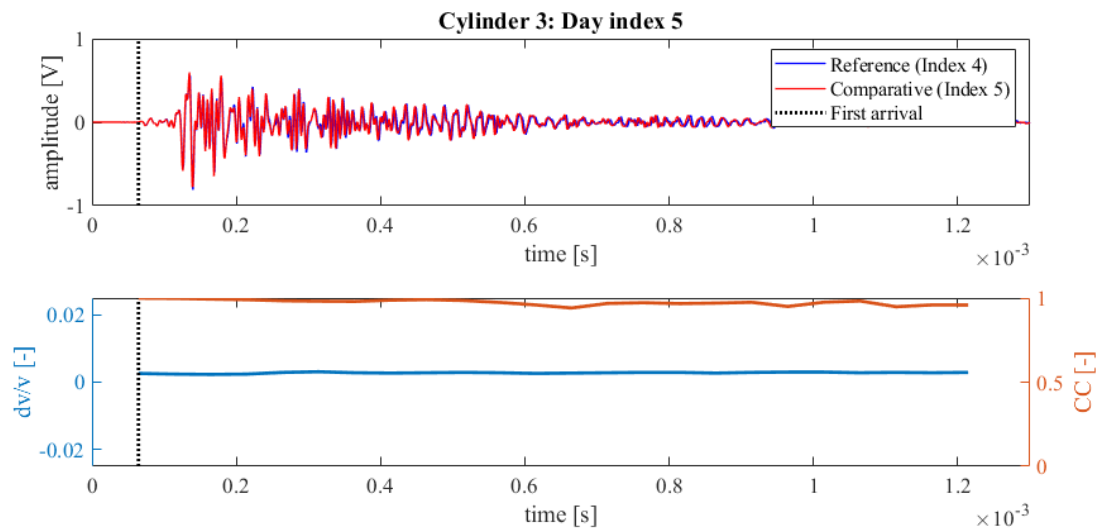


Figure 303: Wave signals of Measurement 2 (blue) and Measurement 3 (red) of concrete hydration test Cylinder 3 (top),  $dv/v$  (blue) and CC (orange) results from CWI over the signal travel time divided in stretching windows (bottom)



**Figure 304: Wave signals of Measurement 3 (blue) and Measurement 4 (red) of concrete hydration test Cylinder 3 (top),  $dv/v$  (blue) and CC (orange) results from CWI over the signal travel time divided in stretching windows (bottom)**



**Figure 305: Wave signals of Measurement 4 (blue) and Measurement 5 (red) of concrete hydration test Cylinder 3 (top),  $dv/v$  (blue) and CC (orange) results from CWI over the signal travel time divided in stretching windows (bottom)**

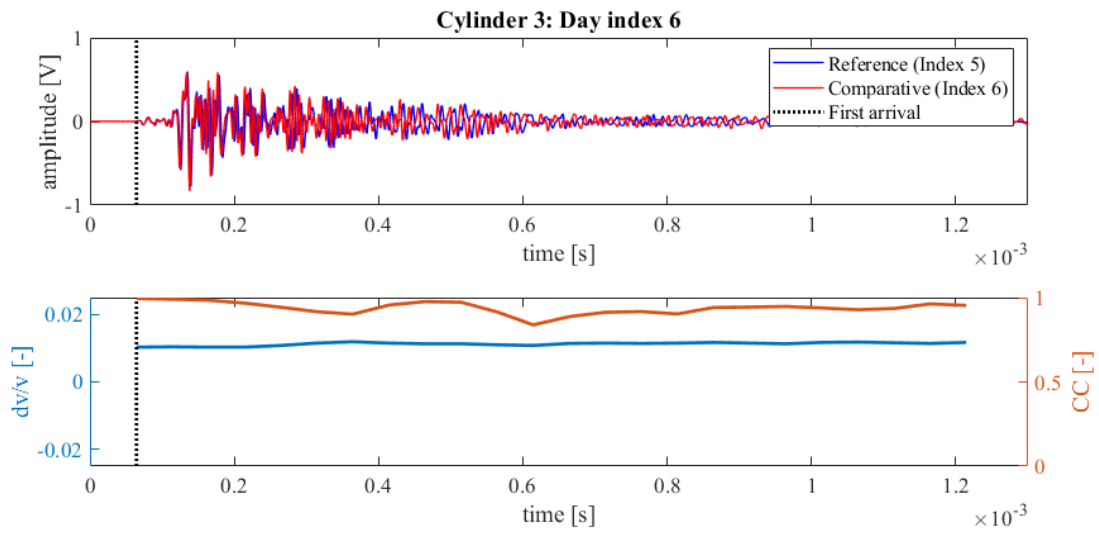


Figure 306: Wave signals of Measurement 5 (blue) and Measurement 6 (red) of concrete hydration test Cylinder 3 (top),  $dv/v$  (blue) and  $CC$  (orange) results from CWI over the signal travel time divided in stretching windows (bottom)

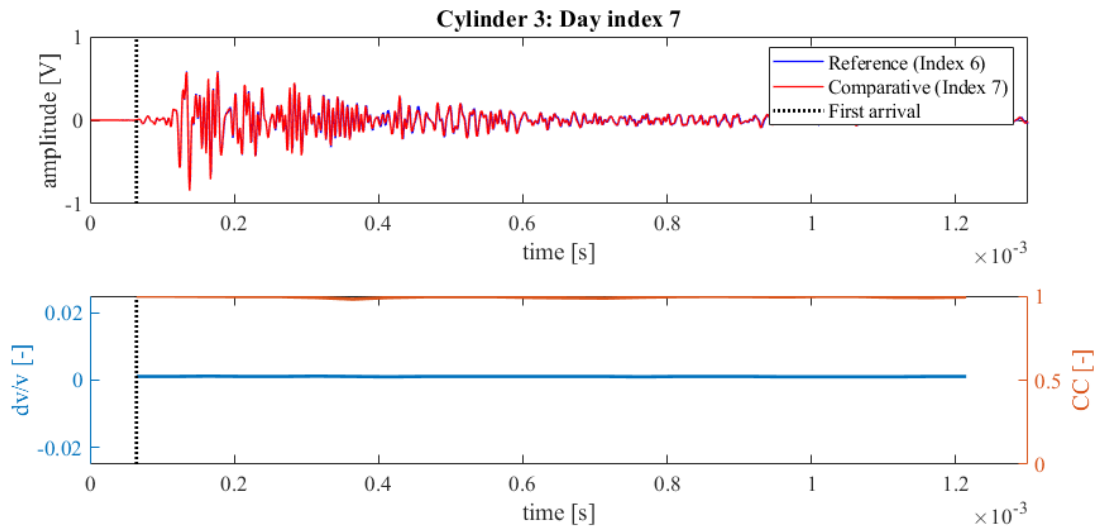


Figure 307: Wave signals of Measurement 6 (blue) and Measurement 7 (red) of concrete hydration test Cylinder 3 (top),  $dv/v$  (blue) and  $CC$  (orange) results from CWI over the signal travel time divided in stretching windows (bottom)

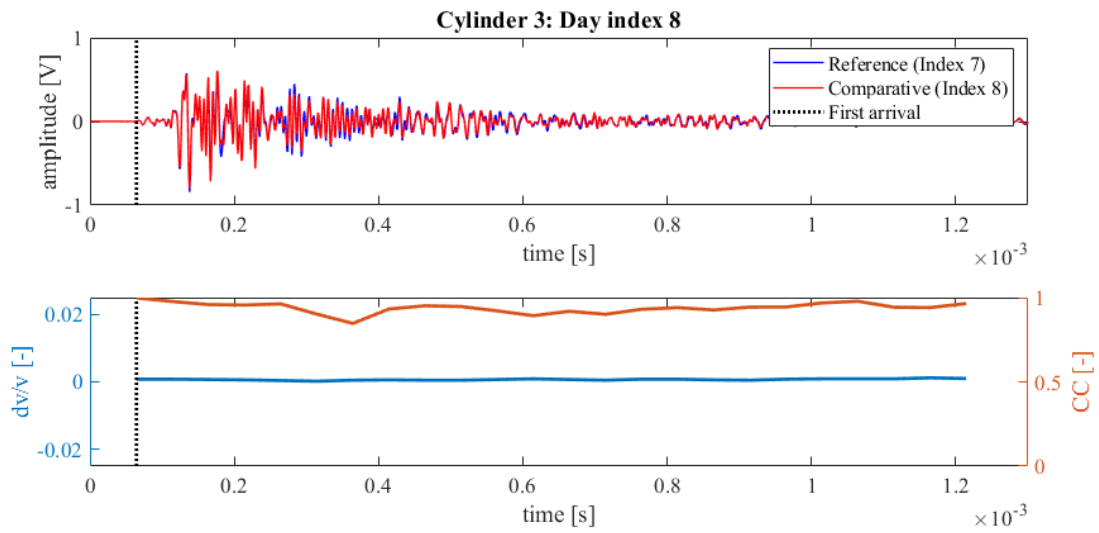


Figure 308: Wave signals of Measurement 7 (blue) and Measurement 8 (red) of concrete hydration test Cylinder 3 (top),  $dv/v$  (blue) and CC (orange) results from CWI over the signal travel time divided in stretching windows (bottom)

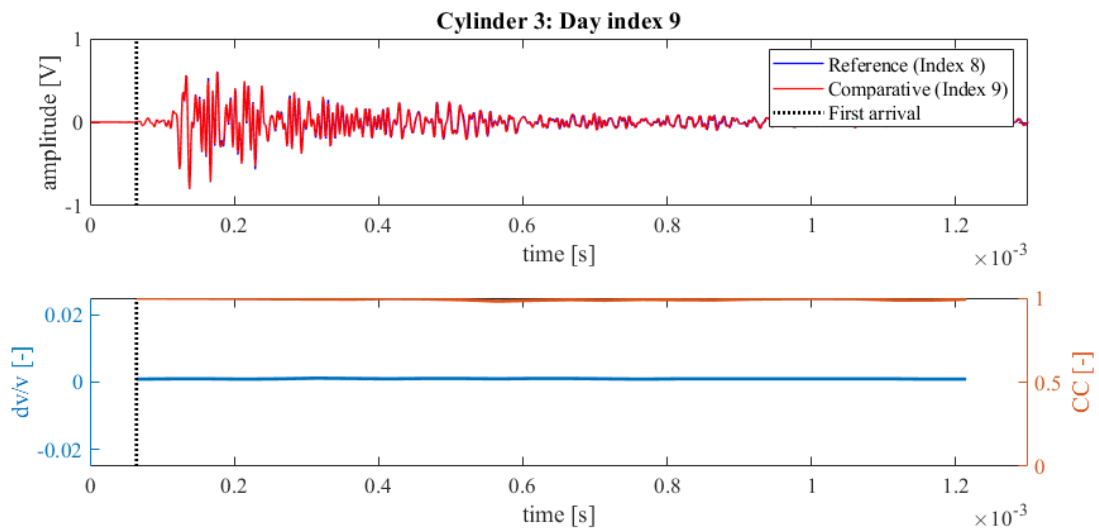


Figure 309: Wave signals of Measurement 8 (blue) and Measurement 9 (red) of concrete hydration test Cylinder 3 (top),  $dv/v$  (blue) and CC (orange) results from CWI over the signal travel time divided in stretching windows (bottom)

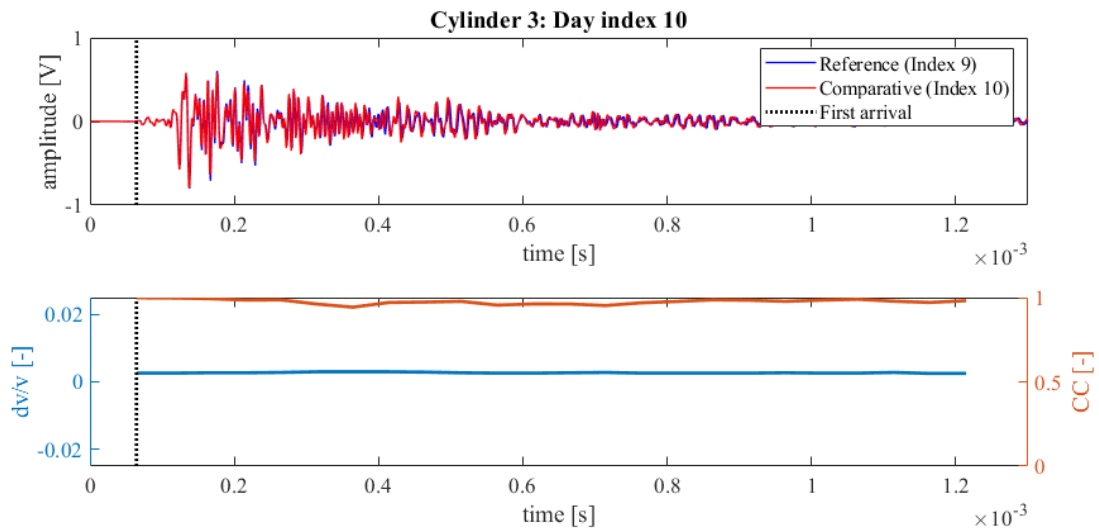


Figure 310: Wave signals of Measurement 9 (blue) and Measurement 10 (red) of concrete hydration test Cylinder 3 (top),  $dv/v$  (blue) and  $CC$  (orange) results from CWI over the signal travel time divided in stretching windows (bottom)

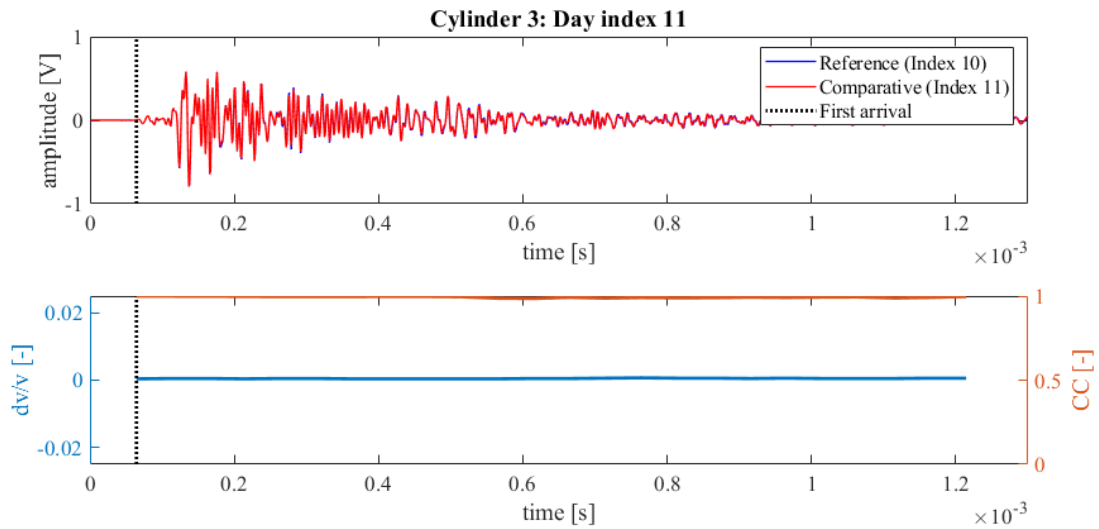
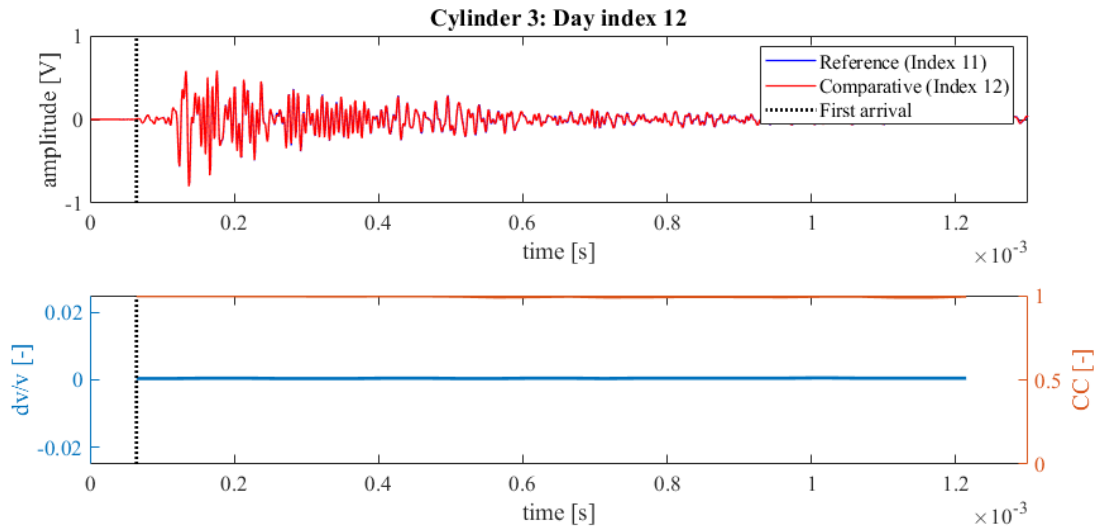
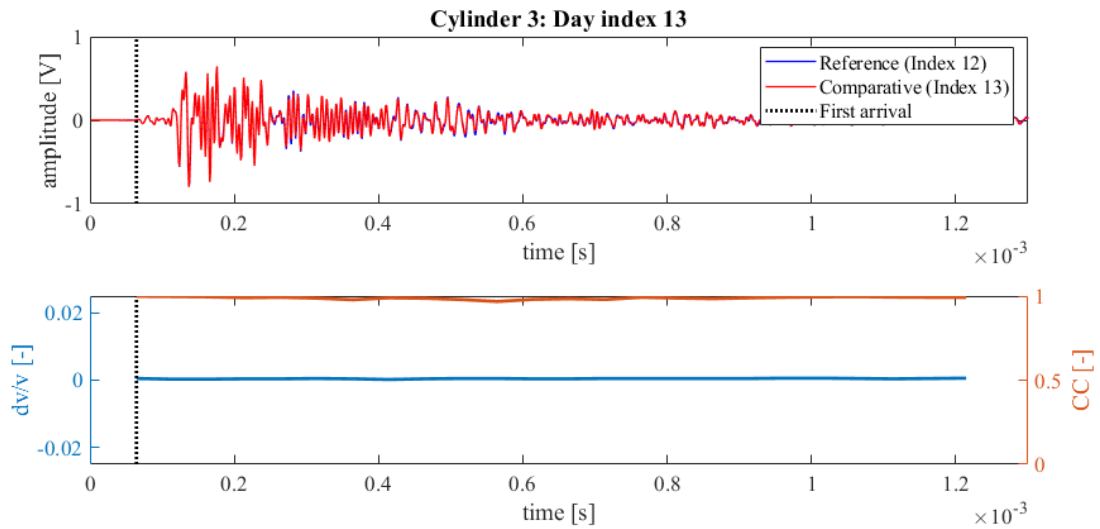


Figure 311: Wave signals of Measurement 10 (blue) and Measurement 11 (red) of concrete hydration test Cylinder 3 (top),  $dv/v$  (blue) and  $CC$  (orange) results from CWI over the signal travel time divided in stretching windows (bottom)



**Figure 312: Wave signals of Measurement 11 (blue) and Measurement 12 (red) of concrete hydration test Cylinder 3 (top),  $dv/v$  (blue) and CC (orange) results from CWI over the signal travel time divided in stretching windows (bottom)**



**Figure 313: Wave signals of Measurement 12 (blue) and Measurement 13 (red) of concrete hydration test Cylinder 3 (top),  $dv/v$  (blue) and CC (orange) results from CWI over the signal travel time divided in stretching windows (bottom)**

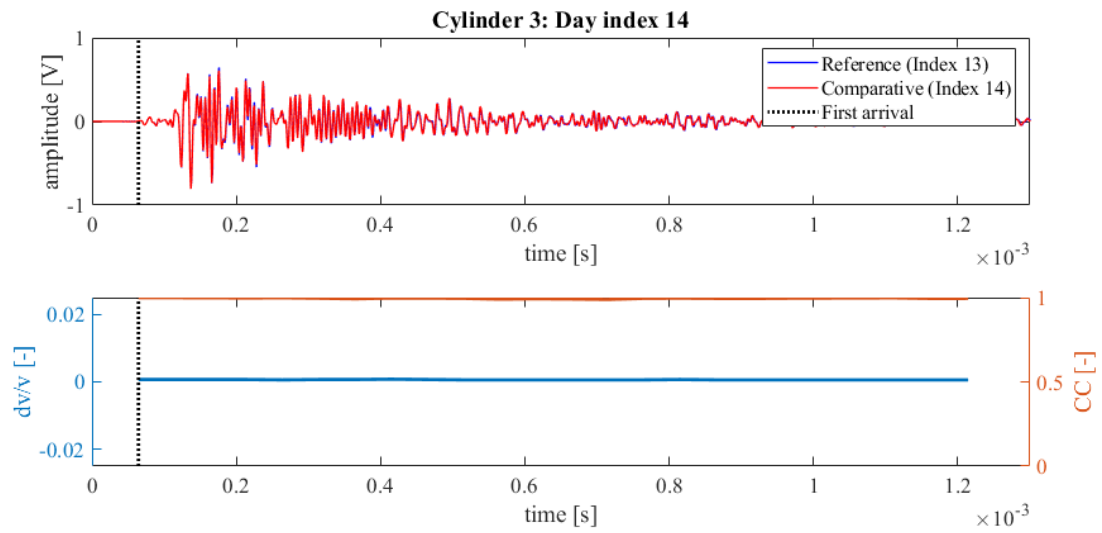


Figure 314: Wave signals of Measurement 13 (blue) and Measurement 14 (red) of concrete hydration test Cylinder 3 (top),  $dv/v$  (blue) and CC (orange) results from CWI over the signal travel time divided in stretching windows (bottom)

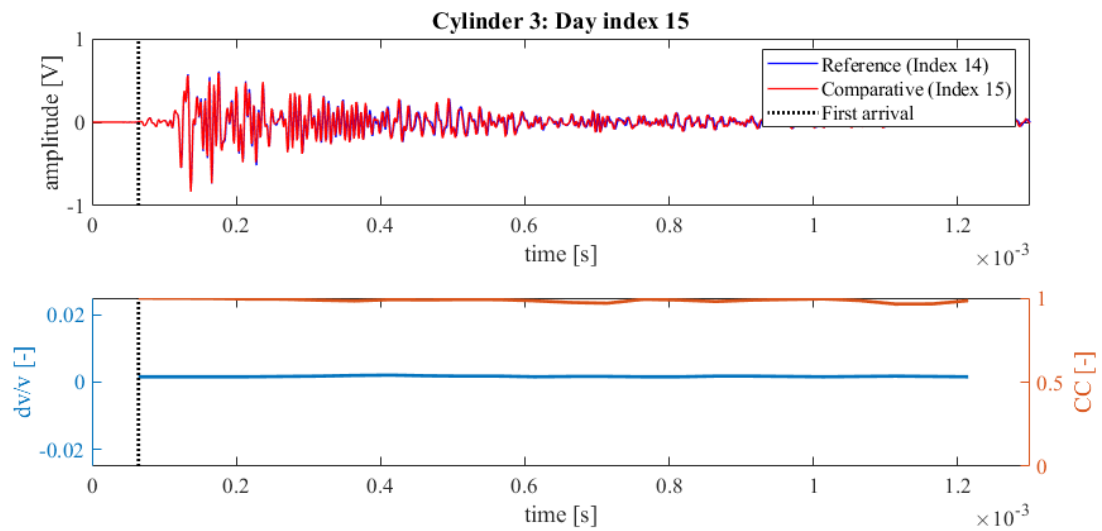


Figure 315: Wave signals of Measurement 14 (blue) and Measurement 15 (red) of concrete hydration test Cylinder 3 (top),  $dv/v$  (blue) and CC (orange) results from CWI over the signal travel time divided in stretching windows (bottom)

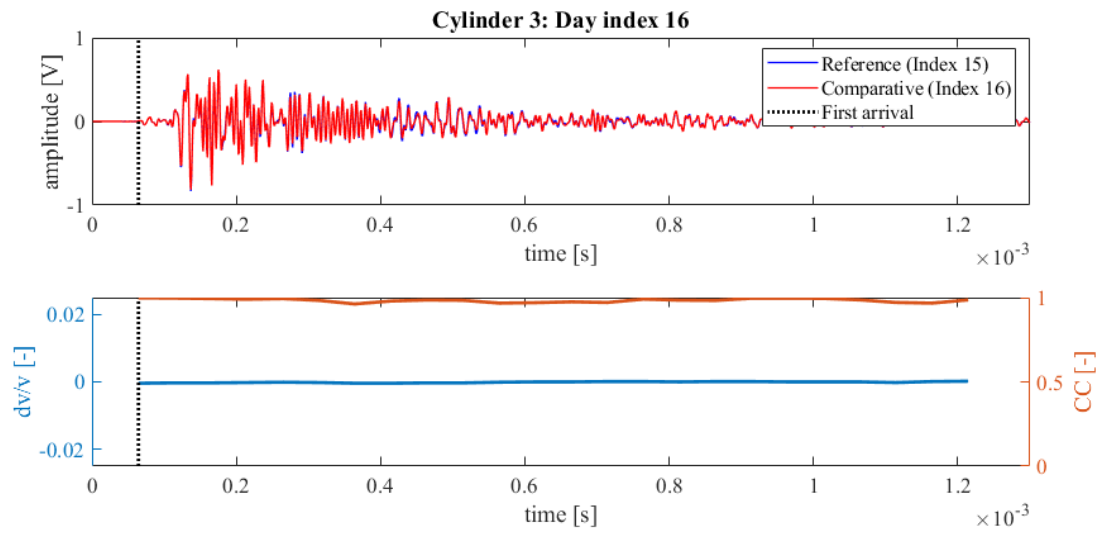


Figure 316: Wave signals of Measurement 15 (blue) and Measurement 16 (red) of concrete hydration test Cylinder 3 (top),  $dv/v$  (blue) and CC (orange) results from CWI over the signal travel time divided in stretching windows (bottom)

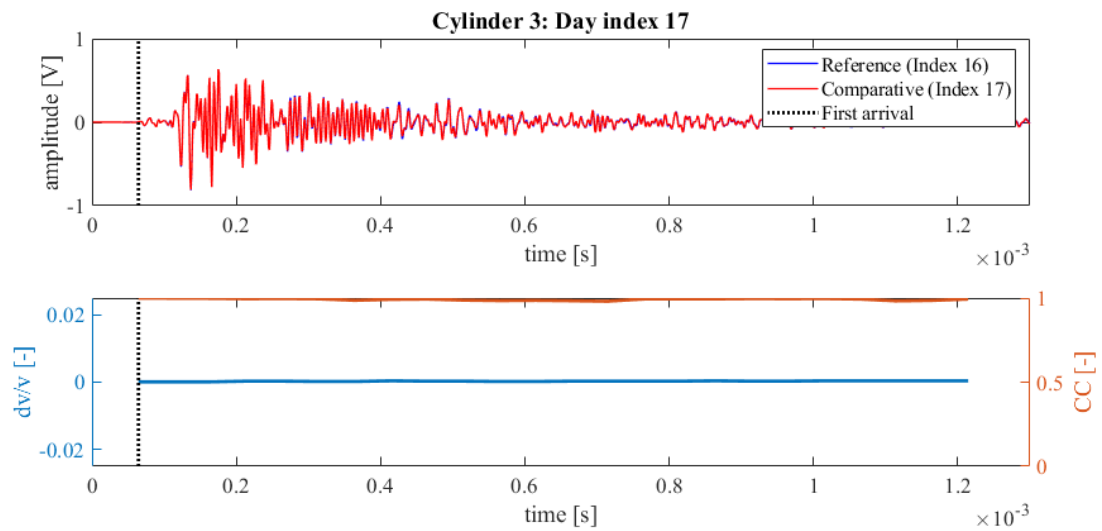


Figure 317: Wave signals of Measurement 16 (blue) and Measurement 17 (red) of concrete hydration test Cylinder 3 (top),  $dv/v$  (blue) and CC (orange) results from CWI over the signal travel time divided in stretching windows (bottom)

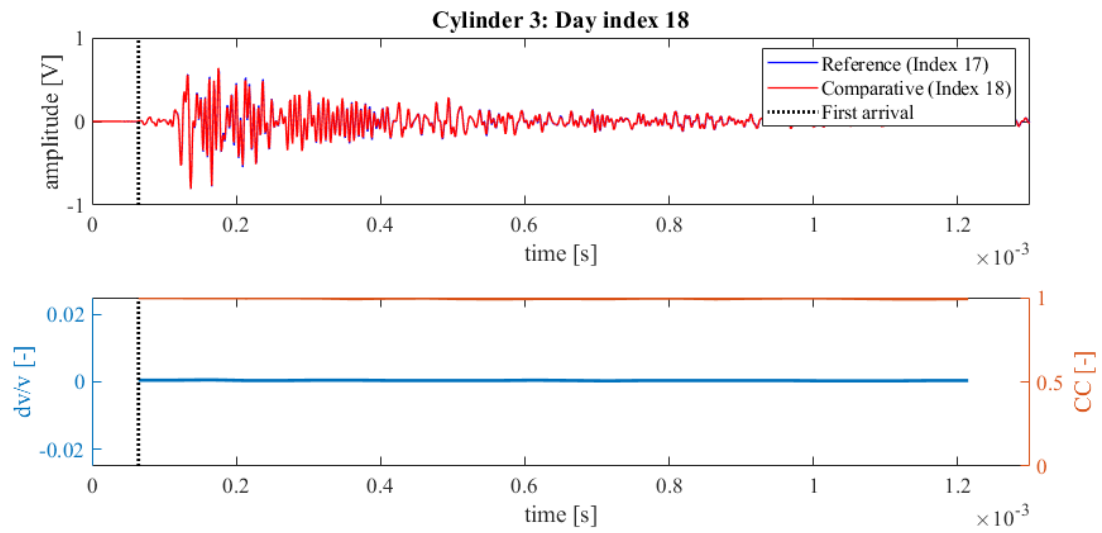


Figure 318: Wave signals of Measurement 17 (blue) and Measurement 18 (red) of concrete hydration test Cylinder 3 (top),  $dv/v$  (blue) and  $CC$  (orange) results from CWI over the signal travel time divided in stretching windows (bottom)

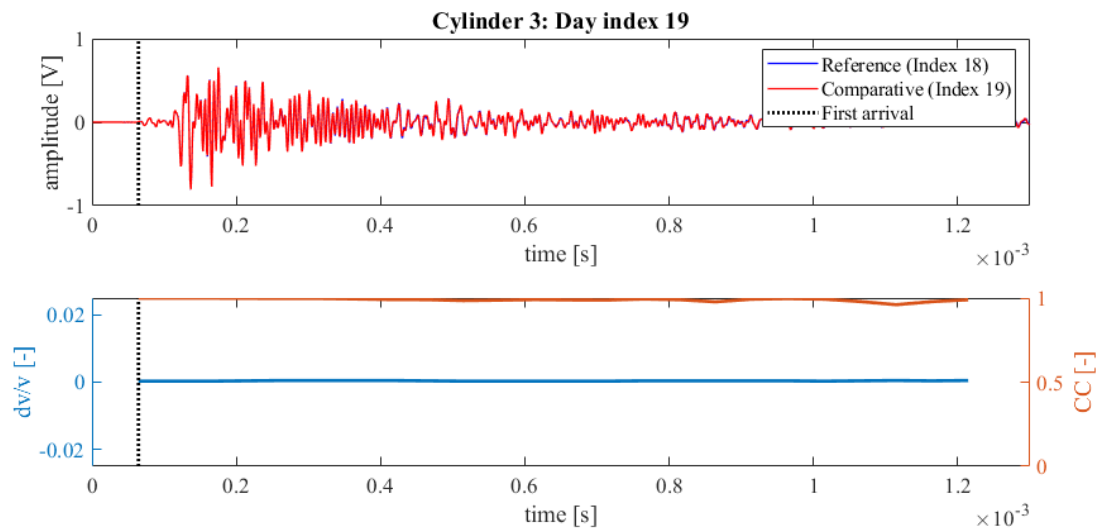


Figure 319: Wave signals of Measurement 18 (blue) and Measurement 19 (red) of concrete hydration test Cylinder 3 (top),  $dv/v$  (blue) and  $CC$  (orange) results from CWI over the signal travel time divided in stretching windows (bottom)

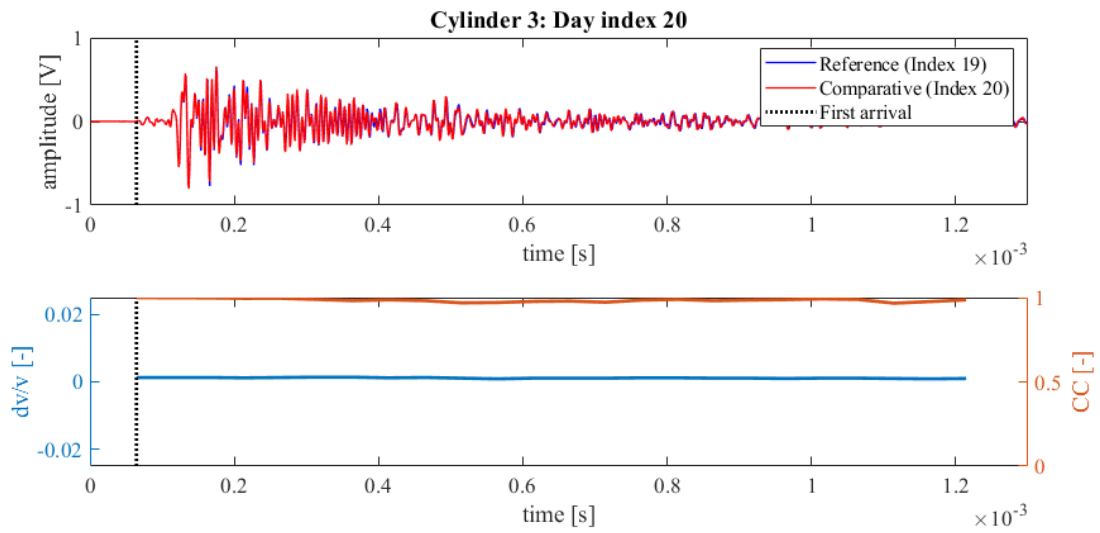


Figure 320: Wave signals of Measurement 19 (blue) and Measurement 20 (red) of concrete hydration test Cylinder 3 (top),  $dv/v$  (blue) and CC (orange) results from CWI over the signal travel time divided in stretching windows (bottom)

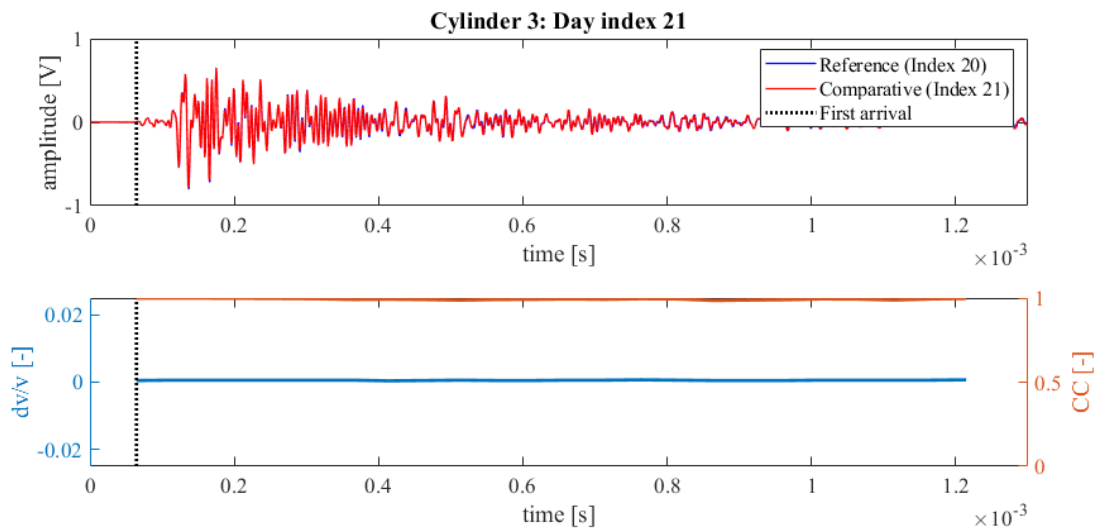


Figure 321: Wave signals of Measurement 20 (blue) and Measurement 21 (red) of concrete hydration test Cylinder 3 (top),  $dv/v$  (blue) and CC (orange) results from CWI over the signal travel time divided in stretching windows (bottom)

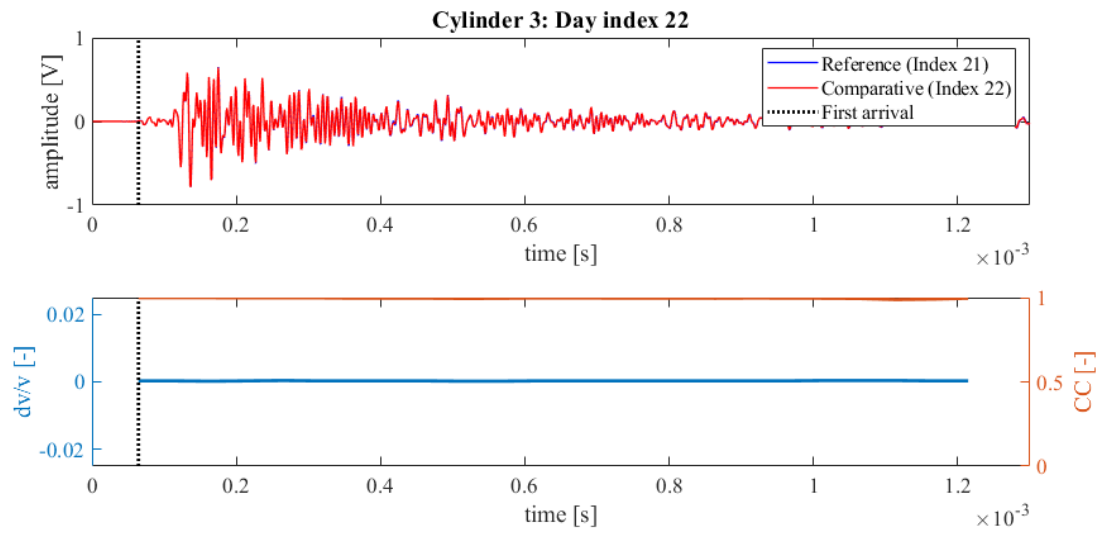


Figure 322: Wave signals of Measurement 21 (blue) and Measurement 22 (red) of concrete hydration test Cylinder 3 (top),  $dv/v$  (blue) and  $CC$  (orange) results from CWI over the signal travel time divided in stretching windows (bottom)

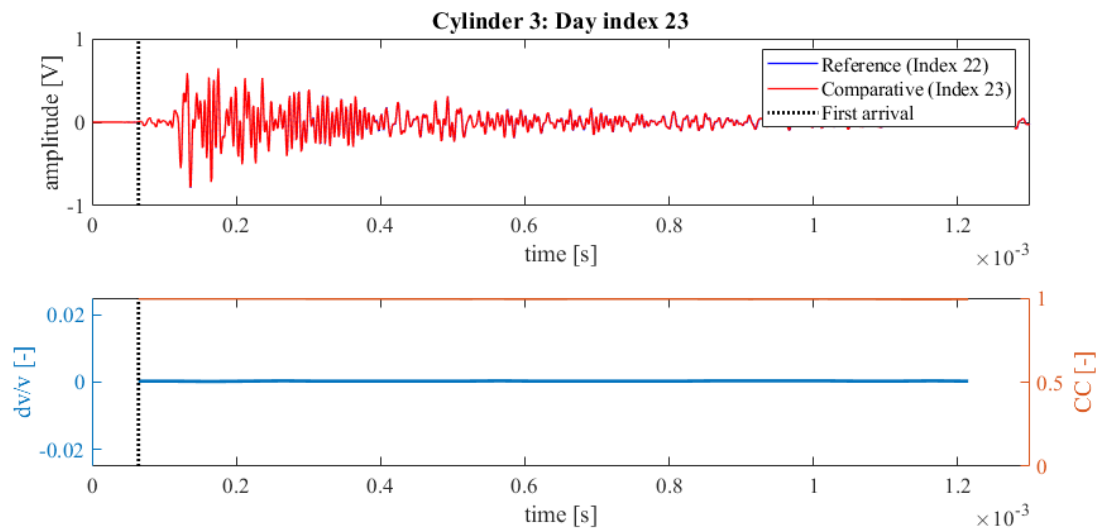


Figure 323: Wave signals of Measurement 22 (blue) and Measurement 23 (red) of concrete hydration test Cylinder 3 (top),  $dv/v$  (blue) and  $CC$  (orange) results from CWI over the signal travel time divided in stretching windows (bottom)

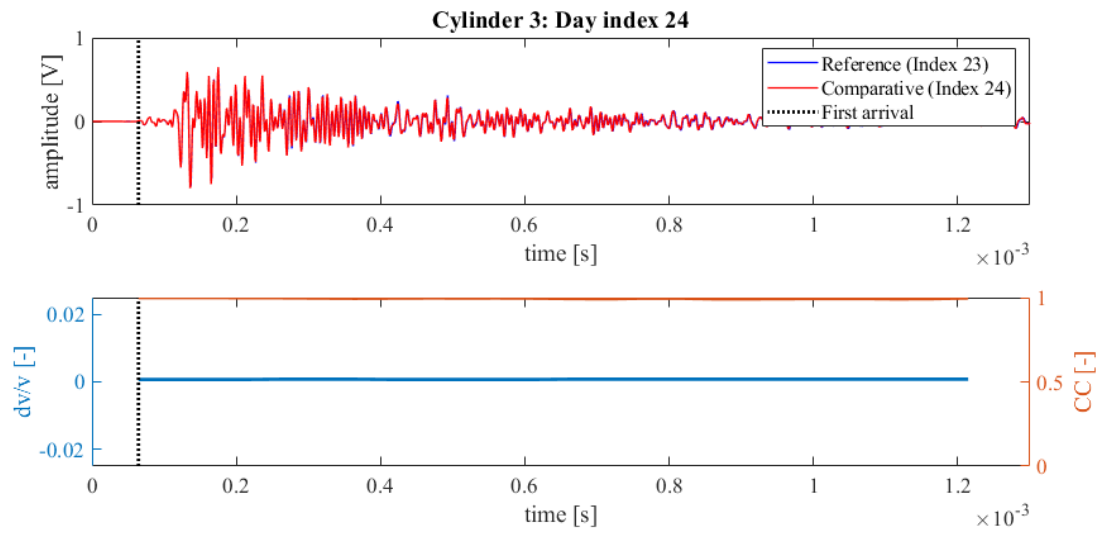


Figure 324: Wave signals of Measurement 23 (blue) and Measurement 24 (red) of concrete hydration test Cylinder 3 (top),  $dv/v$  (blue) and  $CC$  (orange) results from CWI over the signal travel time divided in stretching windows (bottom)

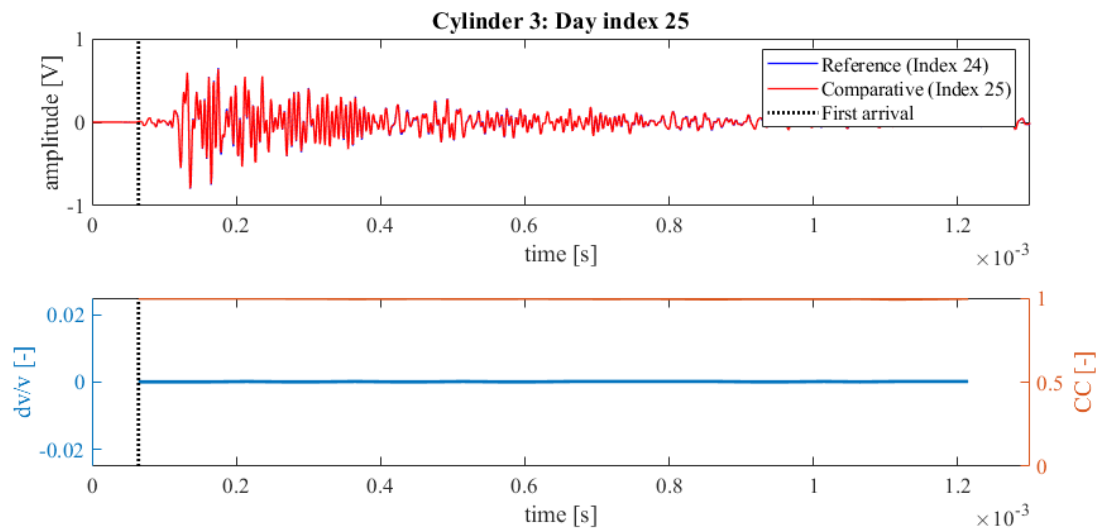


Figure 325: Wave signals of Measurement 24 (blue) and Measurement 25 (red) of concrete hydration test Cylinder 3 (top),  $dv/v$  (blue) and  $CC$  (orange) results from CWI over the signal travel time divided in stretching windows (bottom)

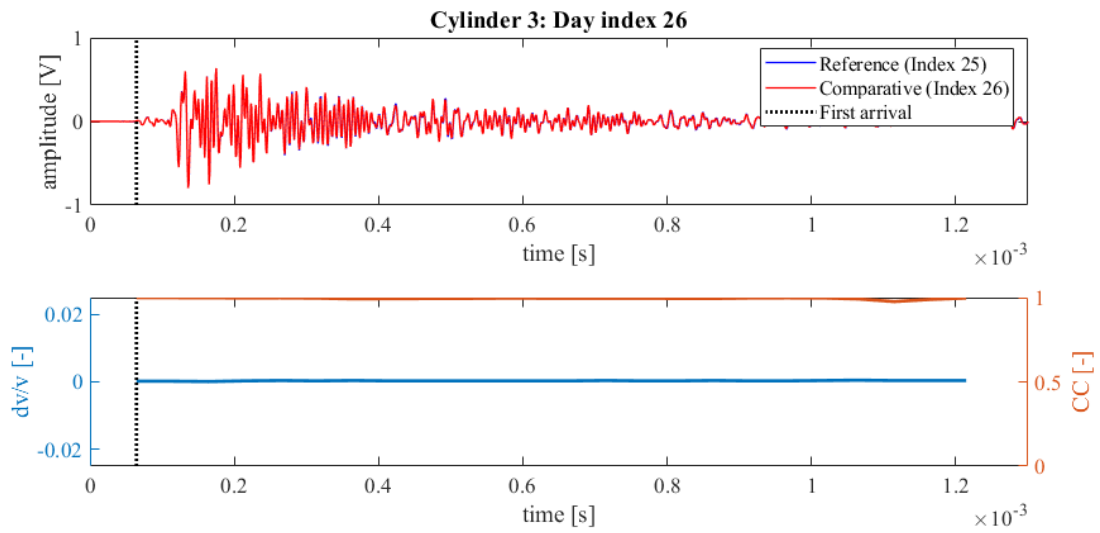


Figure 326: Wave signals of Measurement 25 (blue) and Measurement 26 (red) of concrete hydration test Cylinder 3 (top),  $dv/v$  (blue) and  $CC$  (orange) results from CWI over the signal travel time divided in stretching windows (bottom)

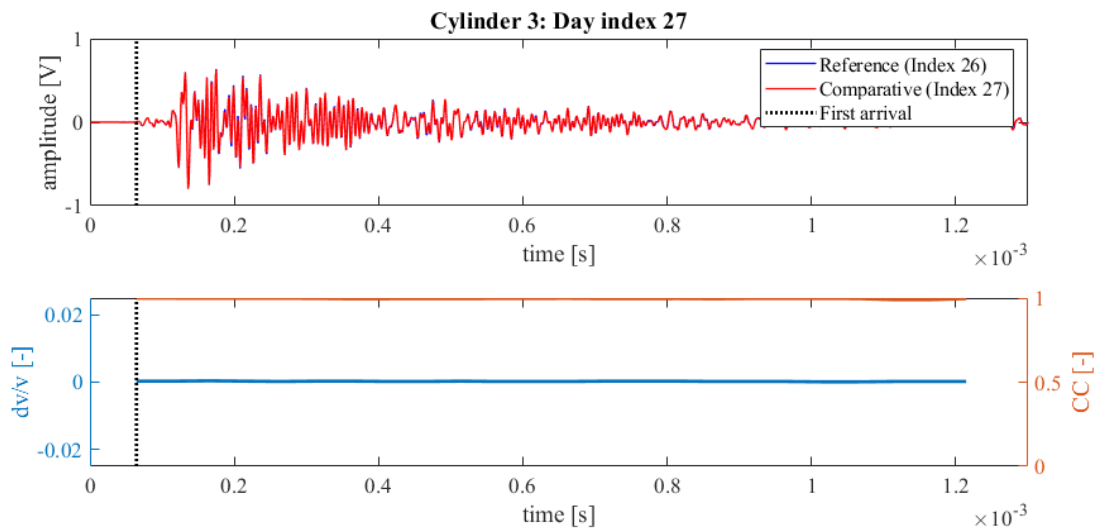
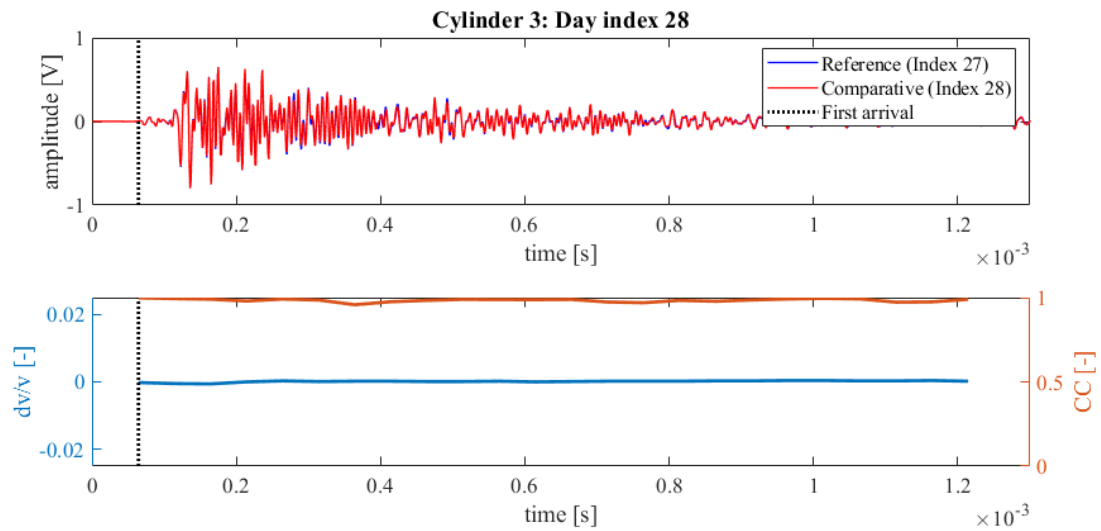
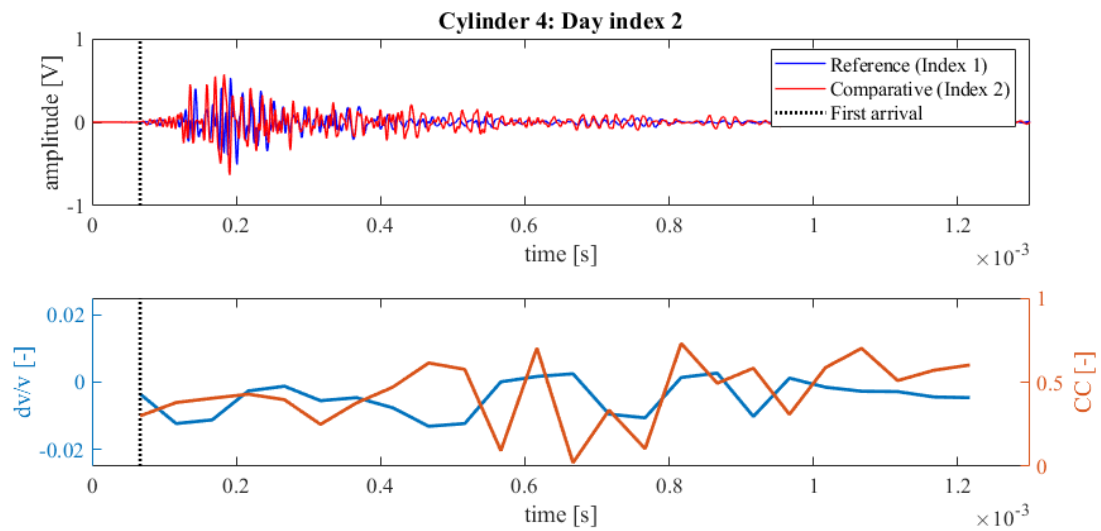


Figure 327: Wave signals of Measurement 26 (blue) and Measurement 27 (red) of concrete hydration test Cylinder 3 (top),  $dv/v$  (blue) and  $CC$  (orange) results from CWI over the signal travel time divided in stretching windows (bottom)



**Figure 328: Wave signals of Measurement 27 (blue) and Measurement 28 (red) of concrete hydration test Cylinder 3 (top),  $dv/v$  (blue) and CC (orange) results from CWI over the signal travel time divided in stretching windows (bottom)**



**Figure 329: Wave signals of Measurement 1 (blue) and Measurement 2 (red) of concrete hydration test Cylinder 4 (top),  $dv/v$  (blue) and CC (orange) results from CWI over the signal travel time divided in stretching windows (bottom)**

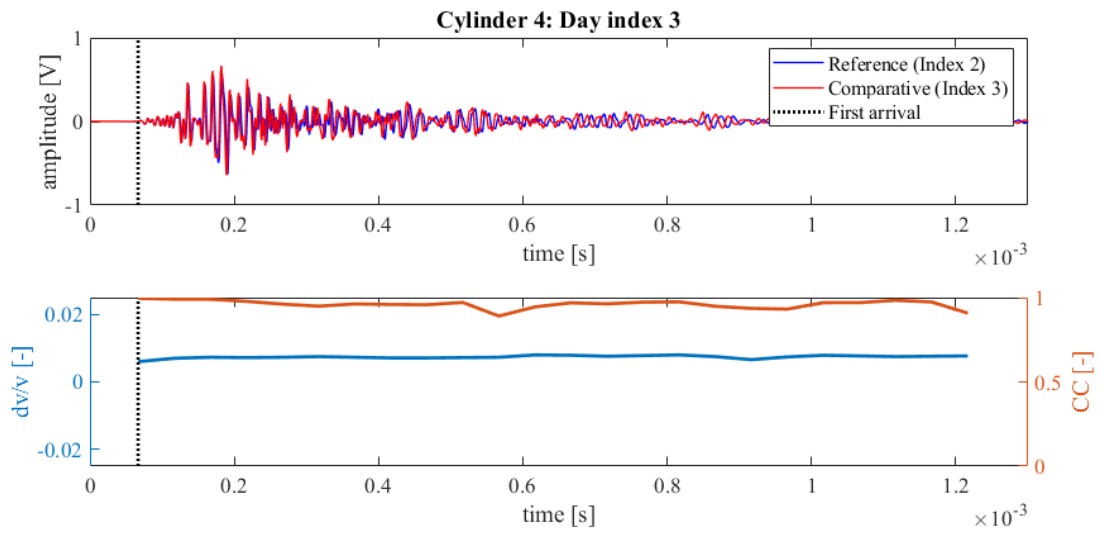


Figure 330: Wave signals of Measurement 2 (blue) and Measurement 3 (red) of concrete hydration test Cylinder 4 (top),  $dv/v$  (blue) and  $CC$  (orange) results from CWI over the signal travel time divided in stretching windows (bottom)

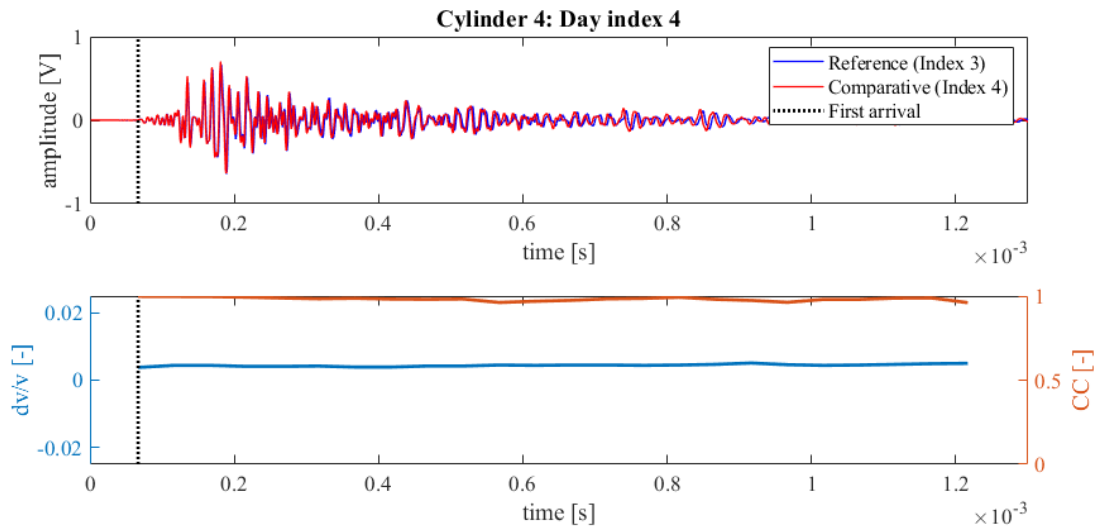


Figure 331: Wave signals of Measurement 3 (blue) and Measurement 4 (red) of concrete hydration test Cylinder 4 (top),  $dv/v$  (blue) and  $CC$  (orange) results from CWI over the signal travel time divided in stretching windows (bottom)

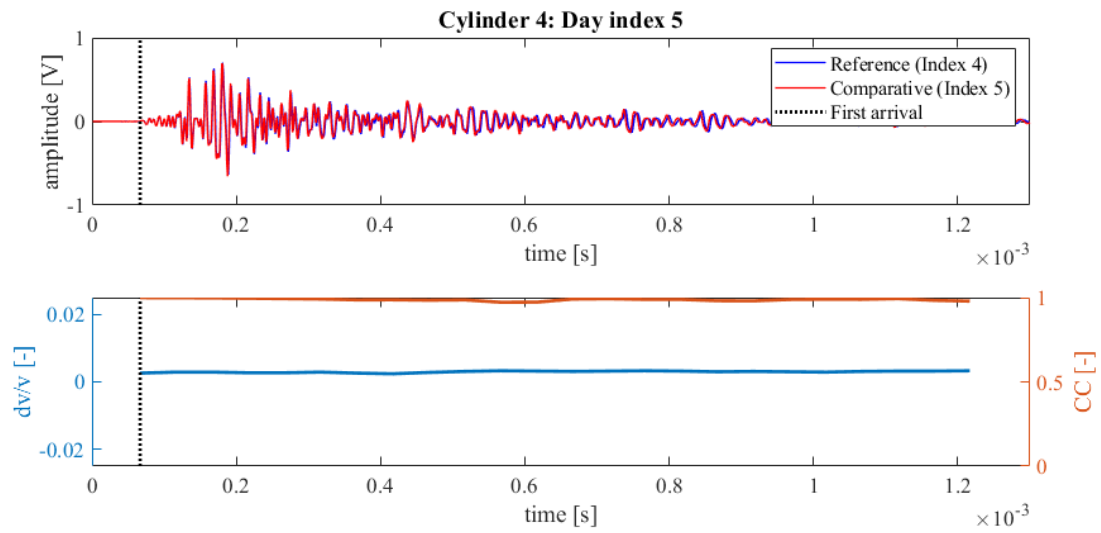


Figure 332: Wave signals of Measurement 4 (blue) and Measurement 5 (red) of concrete hydration test Cylinder 4 (top),  $dv/v$  (blue) and  $CC$  (orange) results from CWI over the signal travel time divided in stretching windows (bottom)

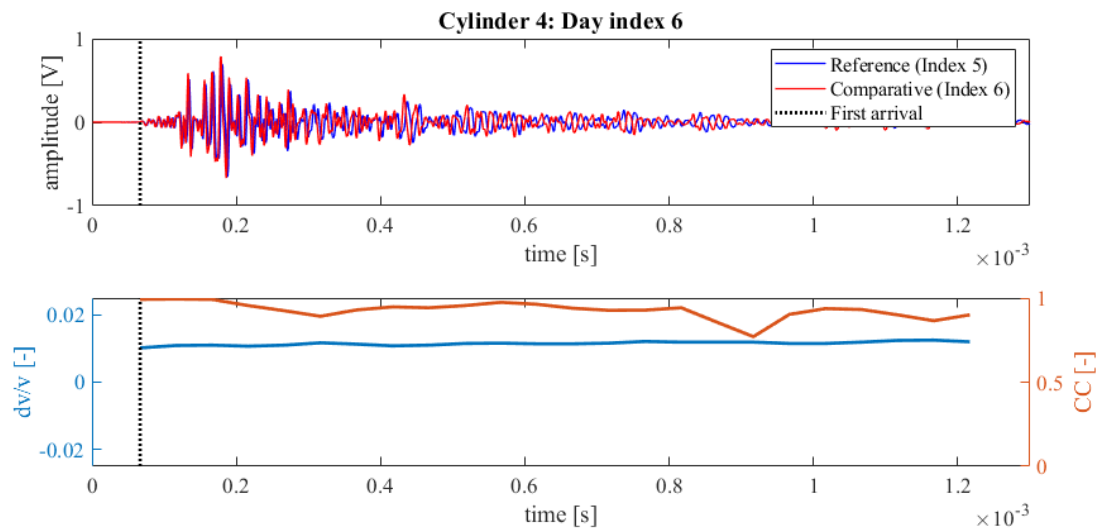


Figure 333: Wave signals of Measurement 5 (blue) and Measurement 6 (red) of concrete hydration test Cylinder 4 (top),  $dv/v$  (blue) and  $CC$  (orange) results from CWI over the signal travel time divided in stretching windows (bottom)

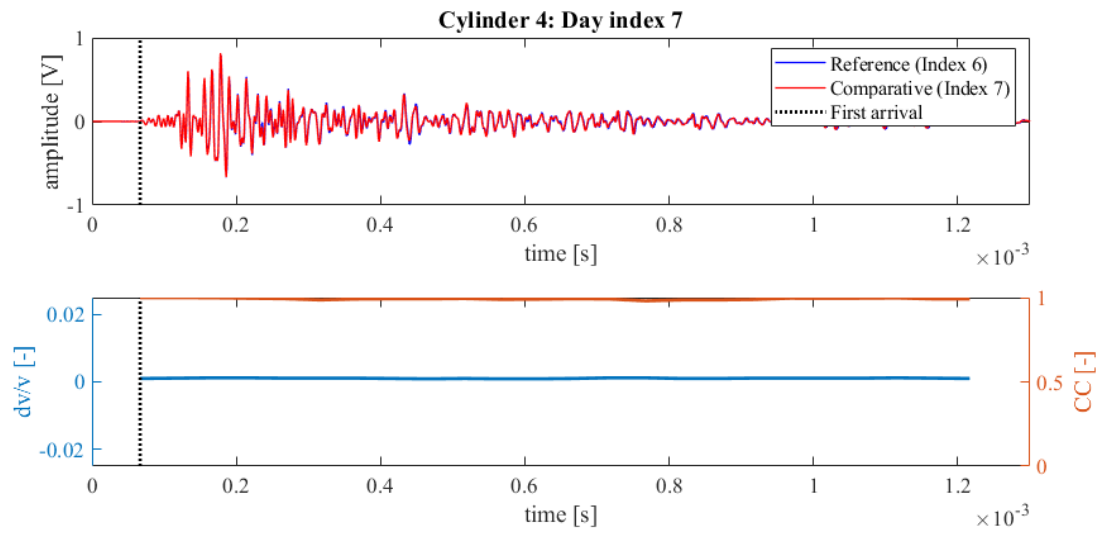


Figure 334: Wave signals of Measurement 6 (blue) and Measurement 7 (red) of concrete hydration test Cylinder 4 (top),  $dv/v$  (blue) and  $CC$  (orange) results from CWI over the signal travel time divided in stretching windows (bottom)

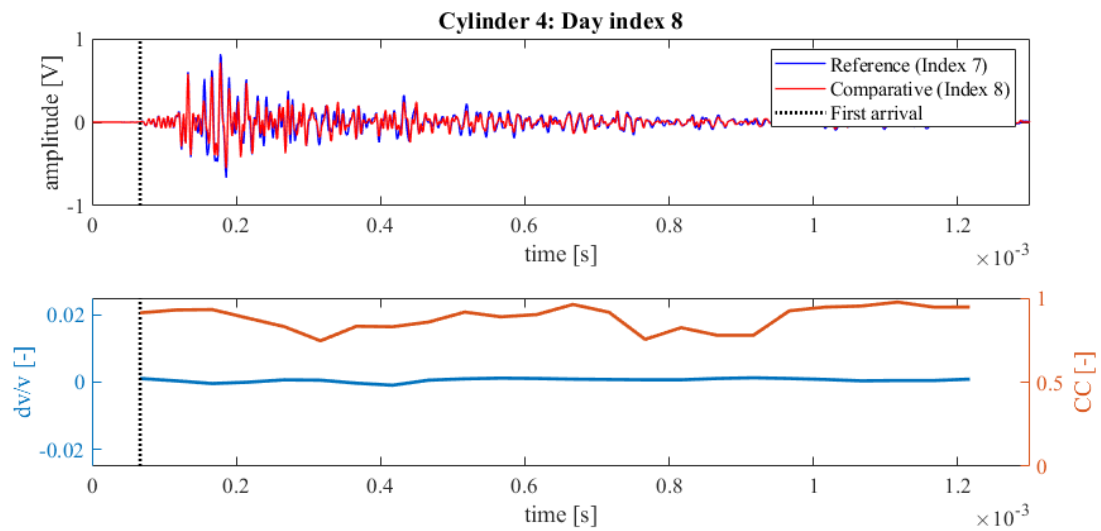


Figure 335: Wave signals of Measurement 7 (blue) and Measurement 8 (red) of concrete hydration test Cylinder 4 (top),  $dv/v$  (blue) and  $CC$  (orange) results from CWI over the signal travel time divided in stretching windows (bottom)

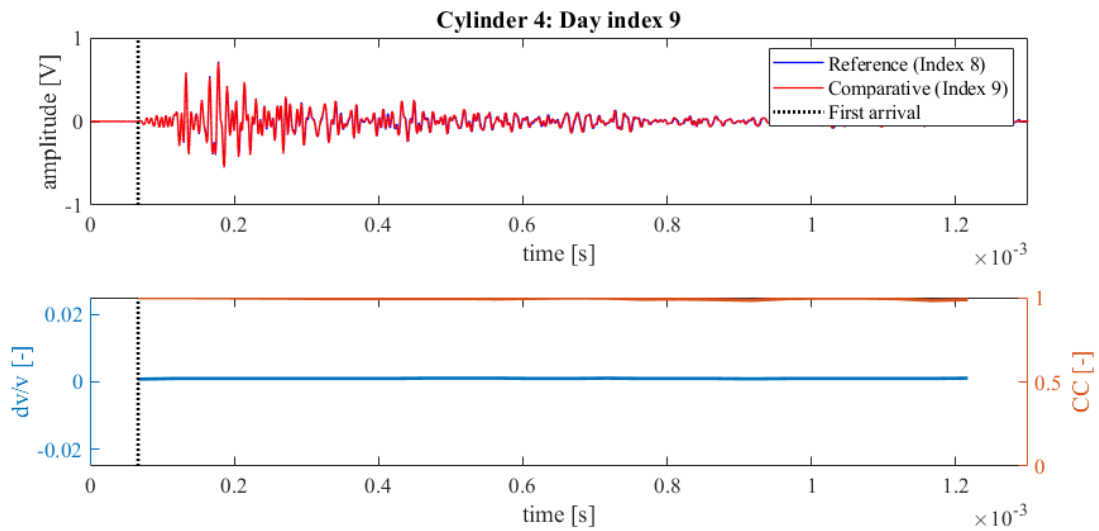


Figure 336: Wave signals of Measurement 8 (blue) and Measurement 9 (red) of concrete hydration test Cylinder 4 (top),  $dv/v$  (blue) and  $CC$  (orange) results from CWI over the signal travel time divided in stretching windows (bottom)

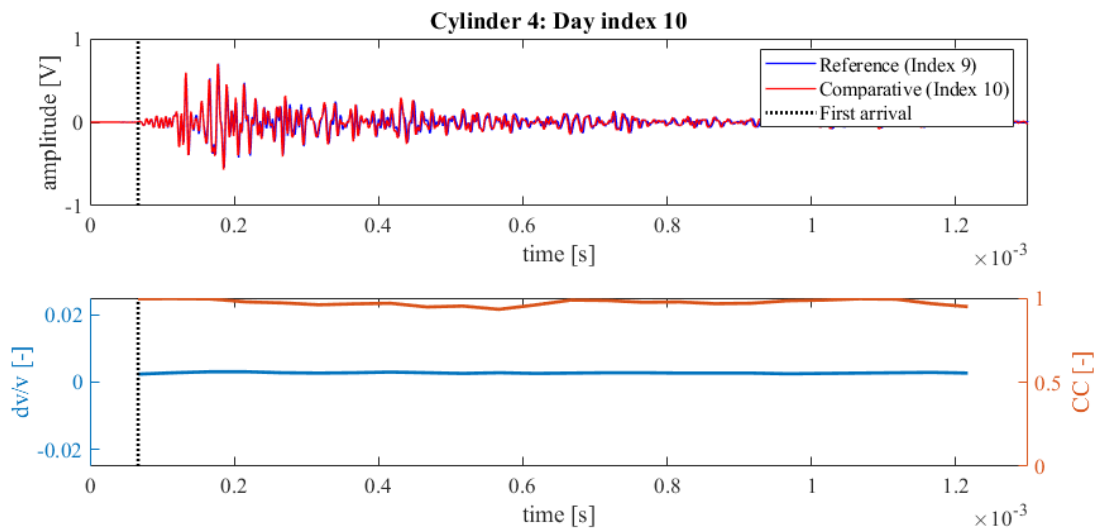
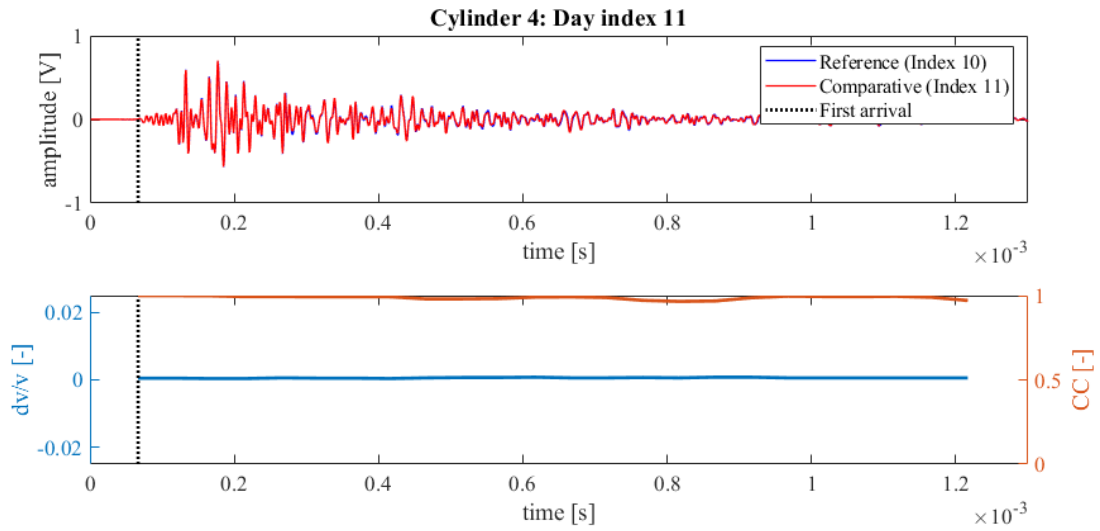
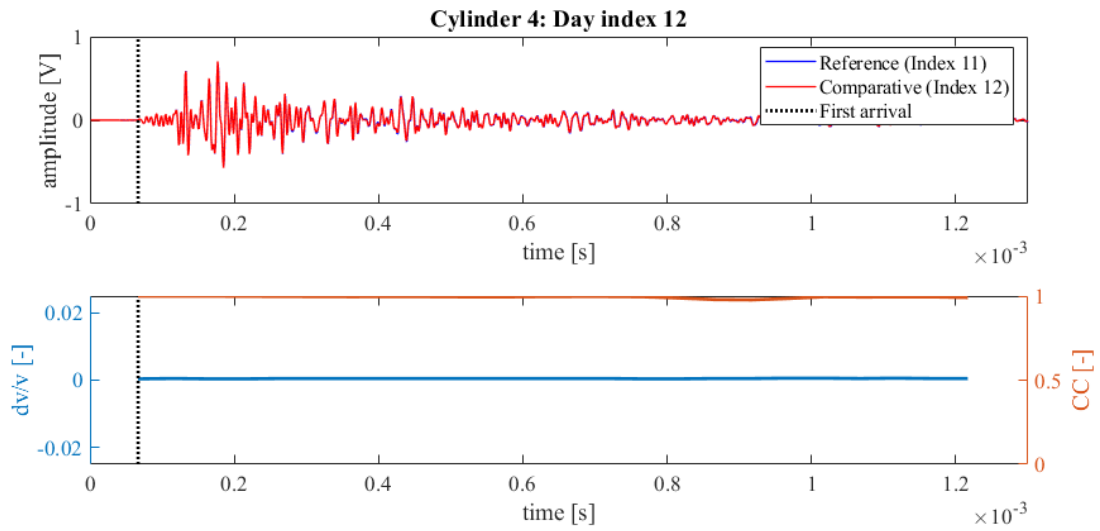


Figure 337: Wave signals of Measurement 9 (blue) and Measurement 10 (red) of concrete hydration test Cylinder 4 (top),  $dv/v$  (blue) and  $CC$  (orange) results from CWI over the signal travel time divided in stretching windows (bottom)



**Figure 338: Wave signals of Measurement 10 (blue) and Measurement 11 (red) of concrete hydration test Cylinder 4 (top),  $dv/v$  (blue) and  $CC$  (orange) results from CWI over the signal travel time divided in stretching windows (bottom)**



**Figure 339: Wave signals of Measurement 11 (blue) and Measurement 12 (red) of concrete hydration test Cylinder 4 (top),  $dv/v$  (blue) and  $CC$  (orange) results from CWI over the signal travel time divided in stretching windows (bottom)**

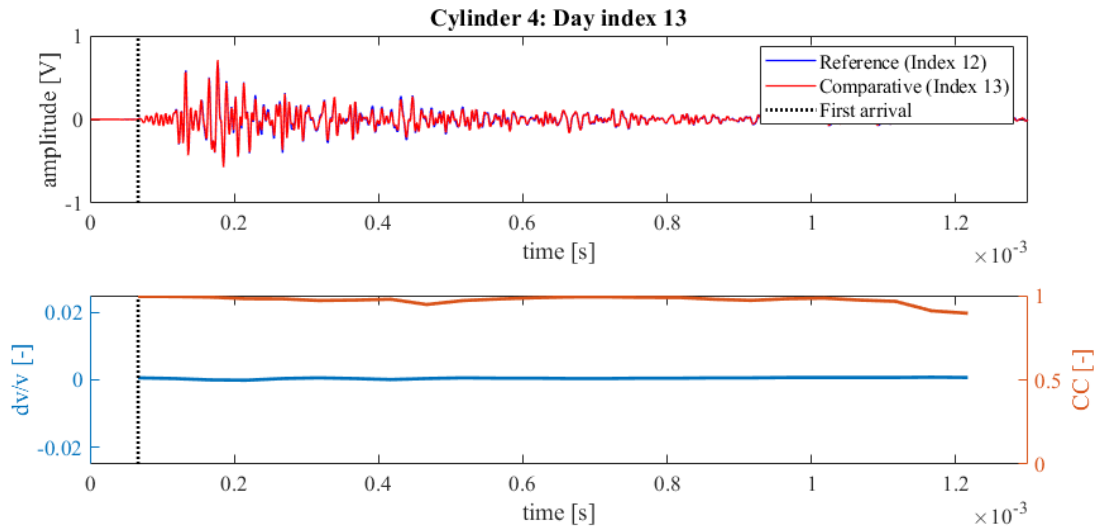


**Figure 340: Wave signals of Measurement 12 (blue) and Measurement 13 (red) of concrete hydration test Cylinder 4 (top),  $dv/v$  (blue) and CC (orange) results from CWI over the signal travel time divided in stretching windows (bottom)**

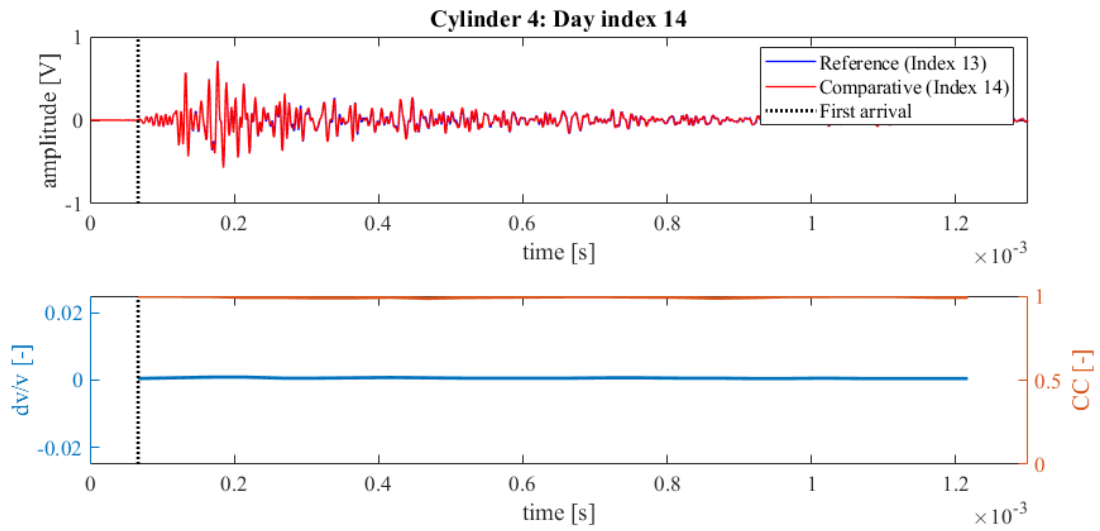


**Figure 341: Wave signals of Measurement 13 (blue) and Measurement 14 (red) of concrete hydration test Cylinder 4 (top),  $dv/v$  (blue) and CC (orange) results from CWI over the signal travel time divided in stretching windows (bottom)**

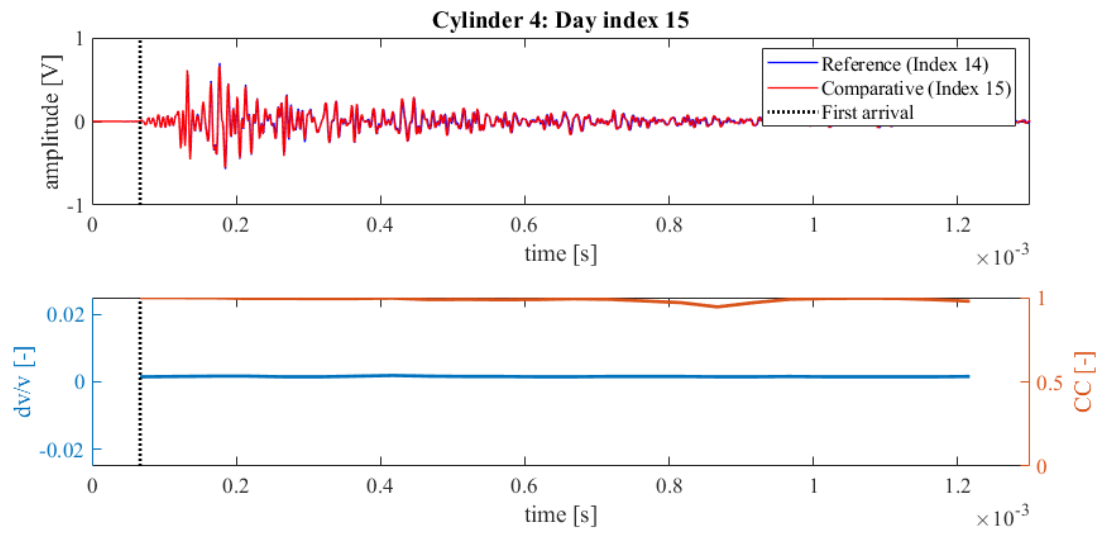


Figure 342: Wave signals of Measurement 14 (blue) and Measurement 15 (red) of concrete hydration test Cylinder 4 (top),  $dv/v$  (blue) and  $CC$  (orange) results from CWI over the signal travel time divided in stretching windows (bottom)

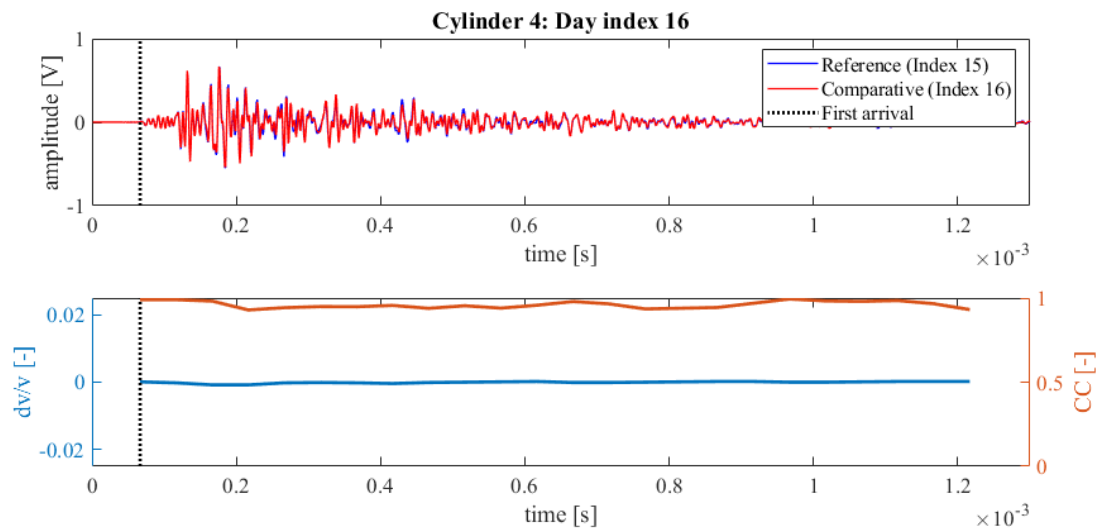


Figure 343: Wave signals of Measurement 15 (blue) and Measurement 16 (red) of concrete hydration test Cylinder 4 (top),  $dv/v$  (blue) and  $CC$  (orange) results from CWI over the signal travel time divided in stretching windows (bottom)

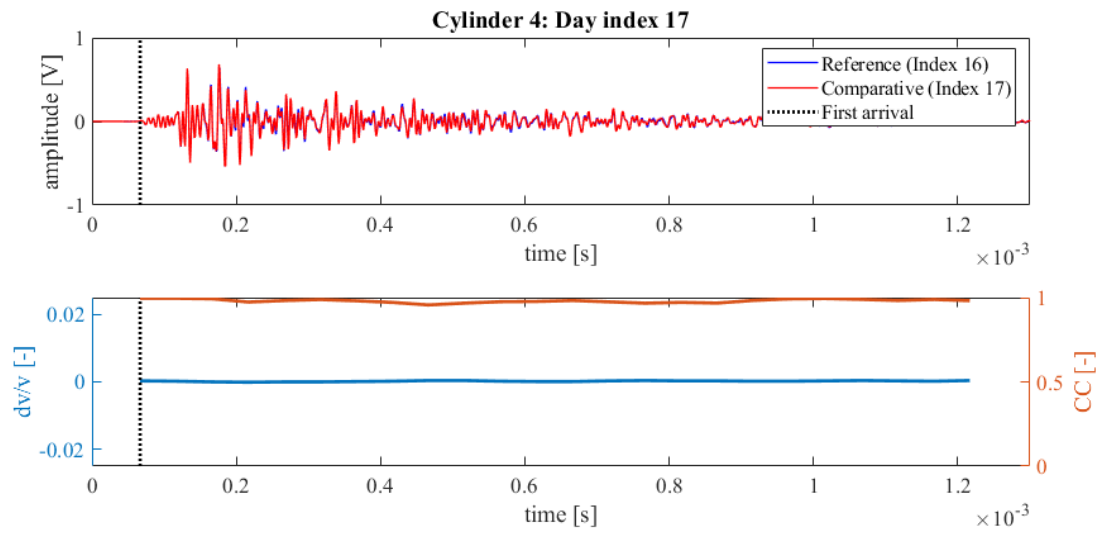


Figure 344: Wave signals of Measurement 16 (blue) and Measurement 17 (red) of concrete hydration test Cylinder 4 (top),  $dv/v$  (blue) and  $CC$  (orange) results from CWI over the signal travel time divided in stretching windows (bottom)

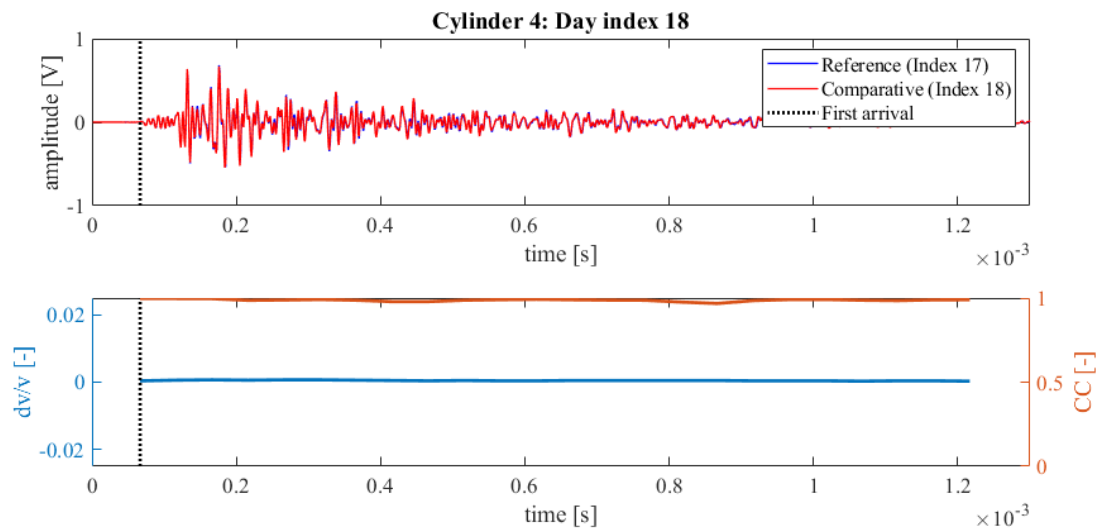
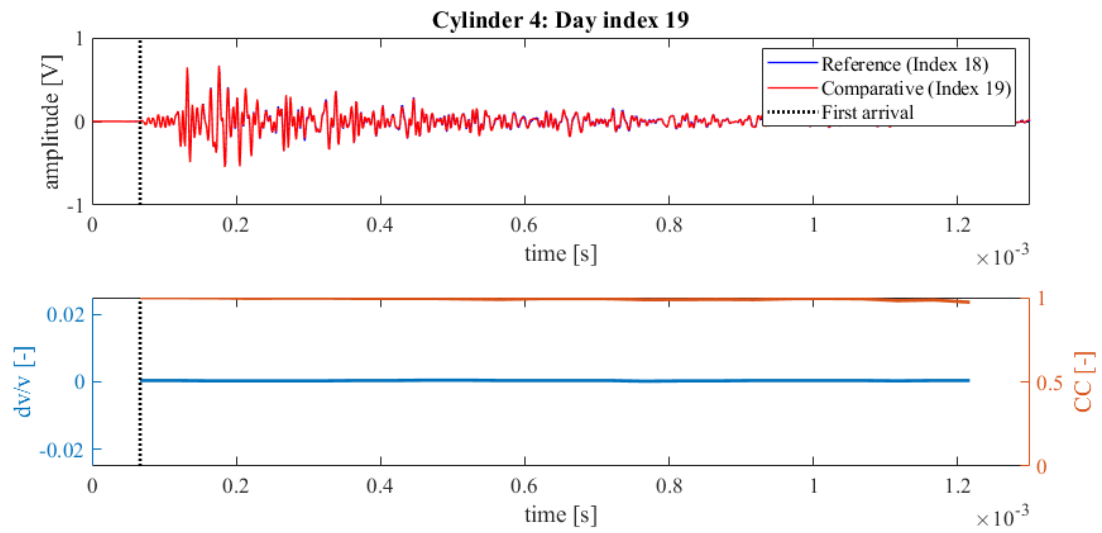
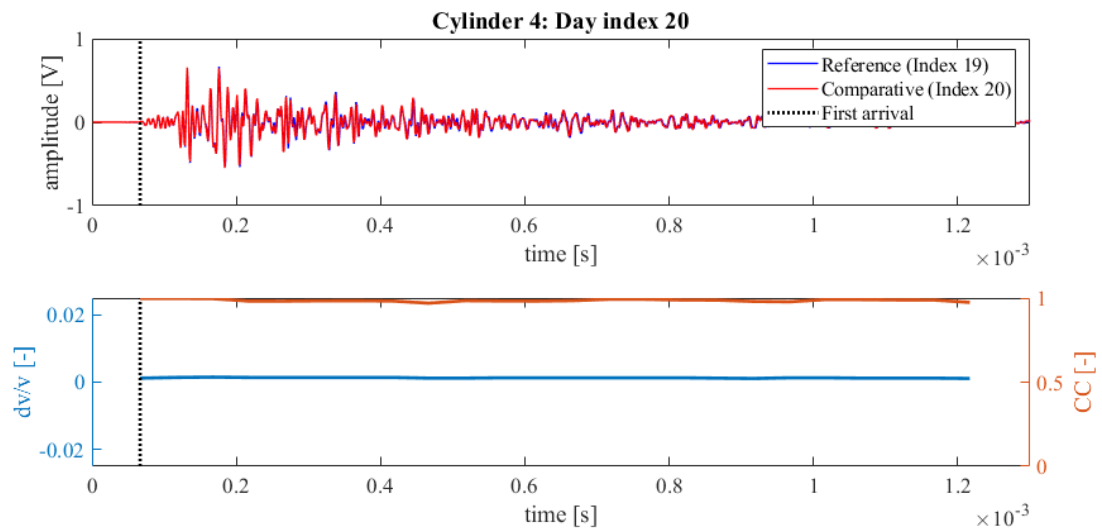


Figure 345: Wave signals of Measurement 17 (blue) and Measurement 18 (red) of concrete hydration test Cylinder 4 (top),  $dv/v$  (blue) and  $CC$  (orange) results from CWI over the signal travel time divided in stretching windows (bottom)



**Figure 346:** Wave signals of Measurement 18 (blue) and Measurement 19 (red) of concrete hydration test Cylinder 4 (top),  $dv/v$  (blue) and CC (orange) results from CWI over the signal travel time divided in stretching windows (bottom)



**Figure 347:** Wave signals of Measurement 19 (blue) and Measurement 20 (red) of concrete hydration test Cylinder 4 (top),  $dv/v$  (blue) and CC (orange) results from CWI over the signal travel time divided in stretching windows (bottom)

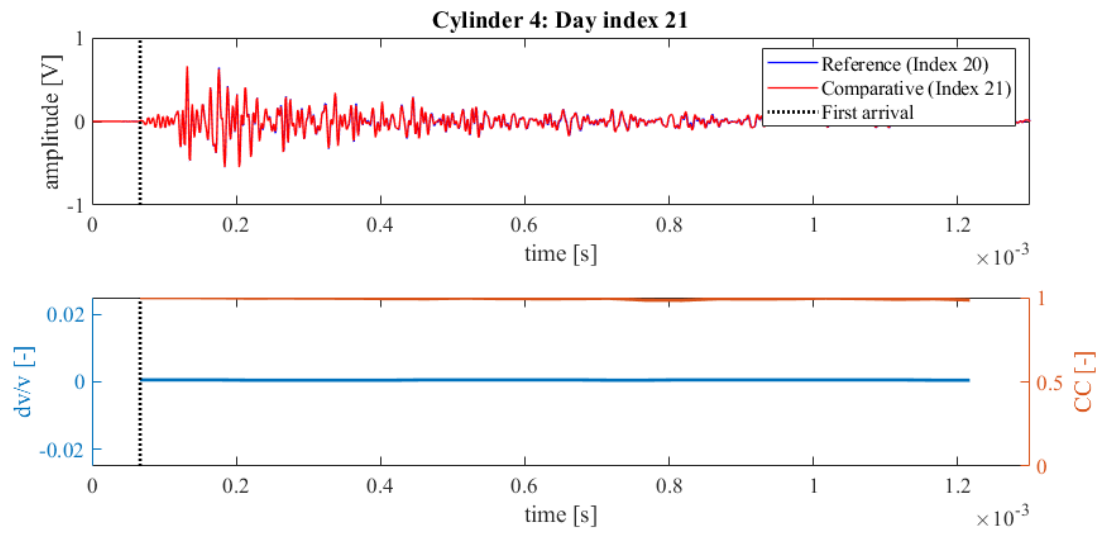


**Figure 348: Wave signals of Measurement 20 (blue) and Measurement 21 (red) of concrete hydration test Cylinder 4 (top),  $dv/v$  (blue) and CC (orange) results from CWI over the signal travel time divided in stretching windows (bottom)**

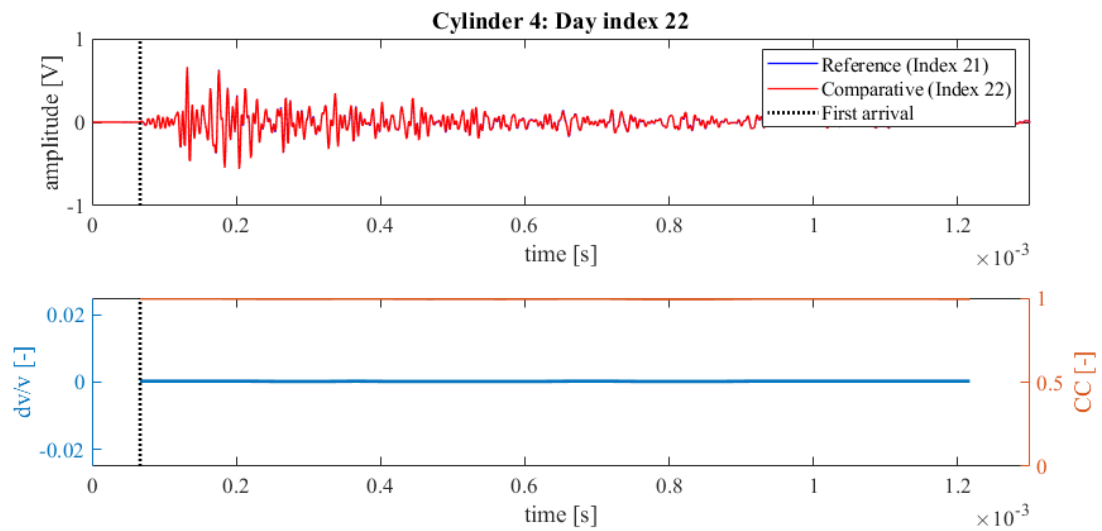


**Figure 349: Wave signals of Measurement 21 (blue) and Measurement 22 (red) of concrete hydration test Cylinder 4 (top),  $dv/v$  (blue) and CC (orange) results from CWI over the signal travel time divided in stretching windows (bottom)**

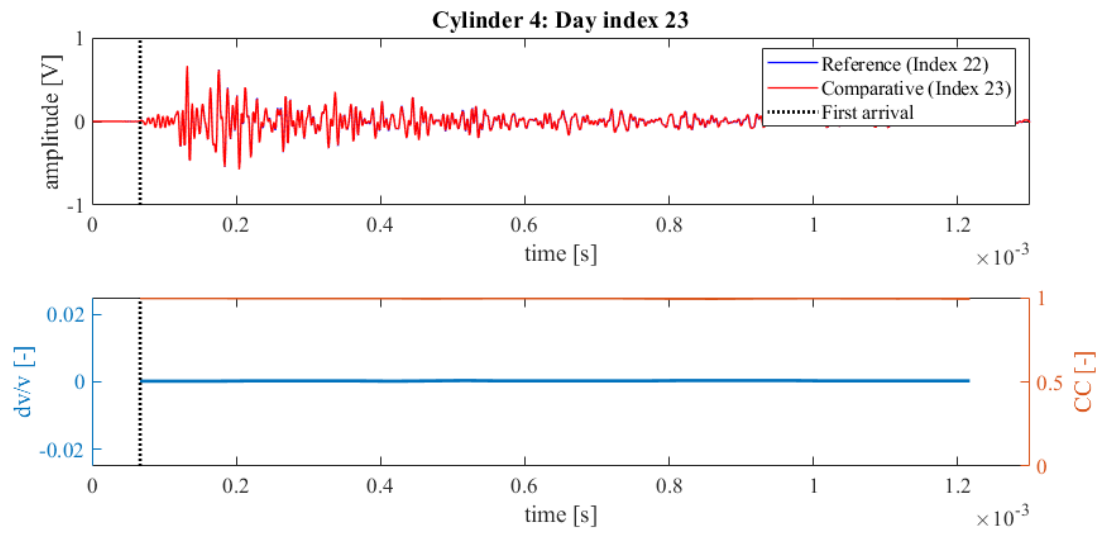


Figure 350: Wave signals of Measurement 22 (blue) and Measurement 23 (red) of concrete hydration test Cylinder 4 (top),  $dv/v$  (blue) and  $CC$  (orange) results from CWI over the signal travel time divided in stretching windows (bottom)

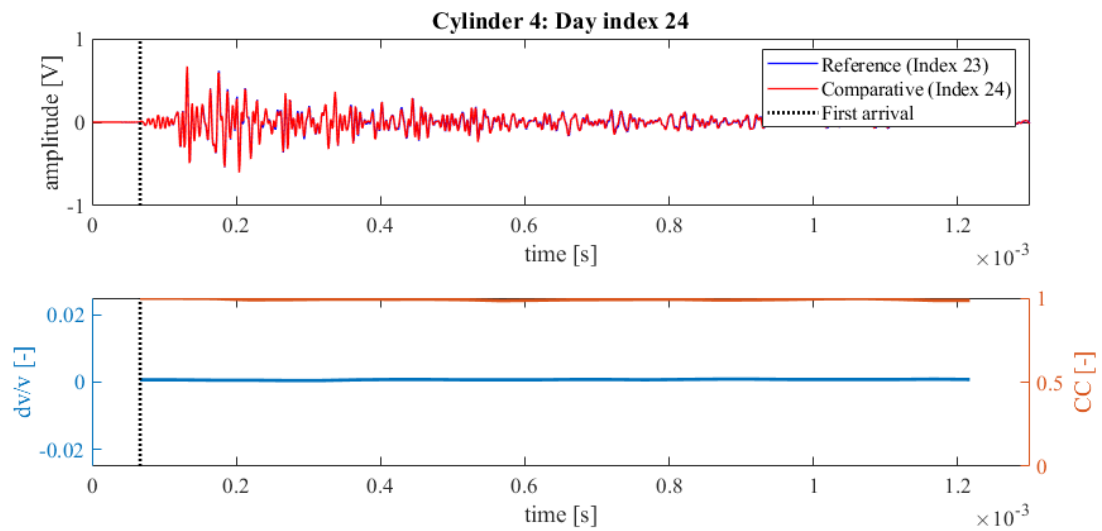
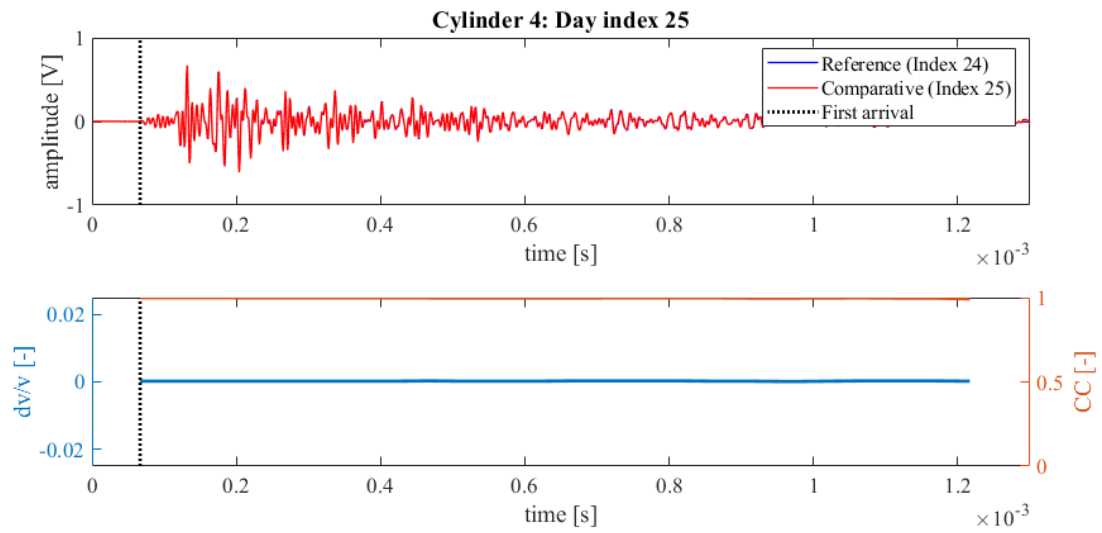
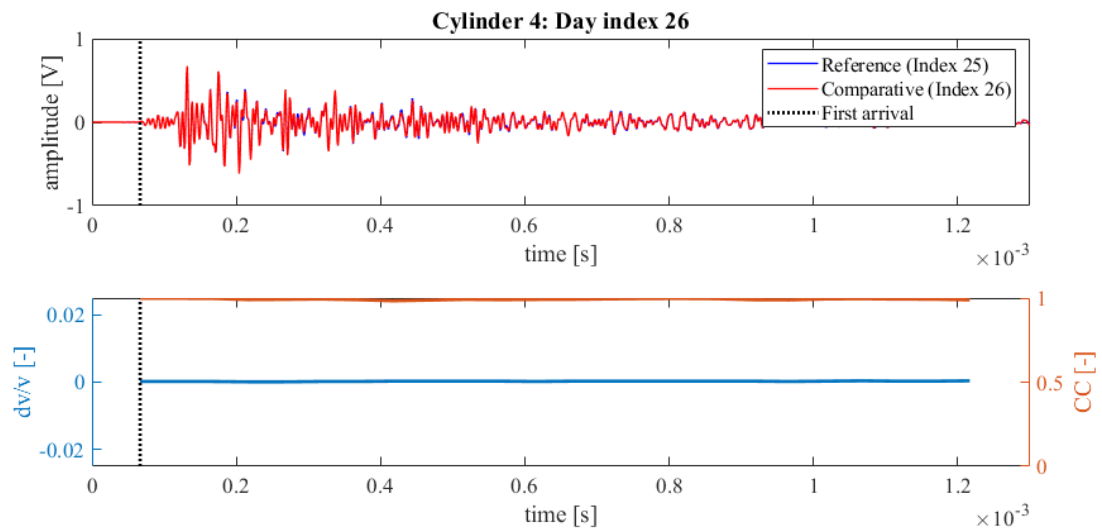


Figure 351: Wave signals of Measurement 23 (blue) and Measurement 24 (red) of concrete hydration test Cylinder 4 (top),  $dv/v$  (blue) and  $CC$  (orange) results from CWI over the signal travel time divided in stretching windows (bottom)



**Figure 352: Wave signals of Measurement 24 (blue) and Measurement 25 (red) of concrete hydration test Cylinder 4 (top),  $dv/v$  (blue) and CC (orange) results from CWI over the signal travel time divided in stretching windows (bottom)**



**Figure 353: Wave signals of Measurement 25 (blue) and Measurement 26 (red) of concrete hydration test Cylinder 4 (top),  $dv/v$  (blue) and CC (orange) results from CWI over the signal travel time divided in stretching windows (bottom)**

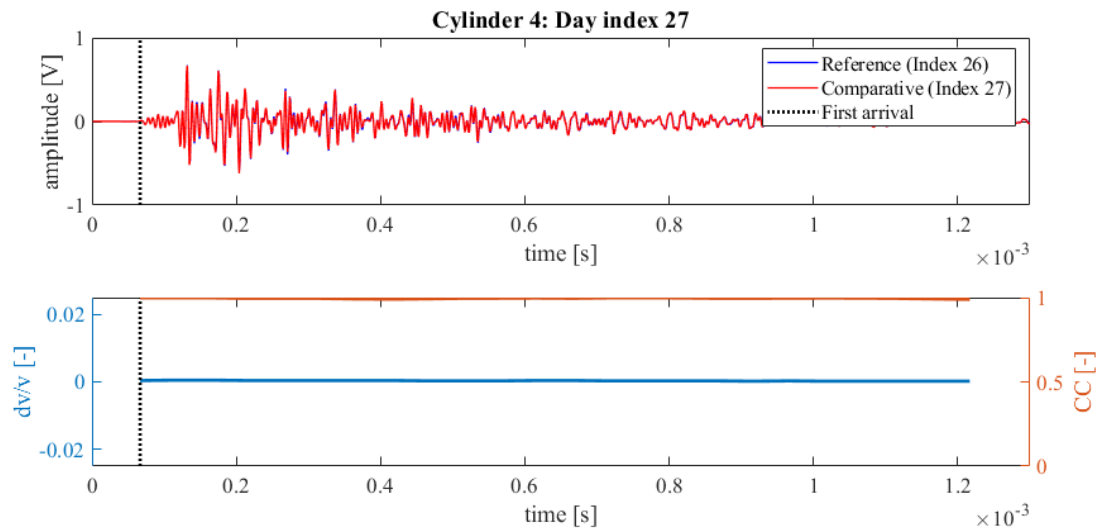


**Figure 354: Wave signals of Measurement 26 (blue) and Measurement 27 (red) of concrete hydration test Cylinder 4 (top),  $dv/v$  (blue) and CC (orange) results from CWI over the signal travel time divided in stretching windows (bottom)**

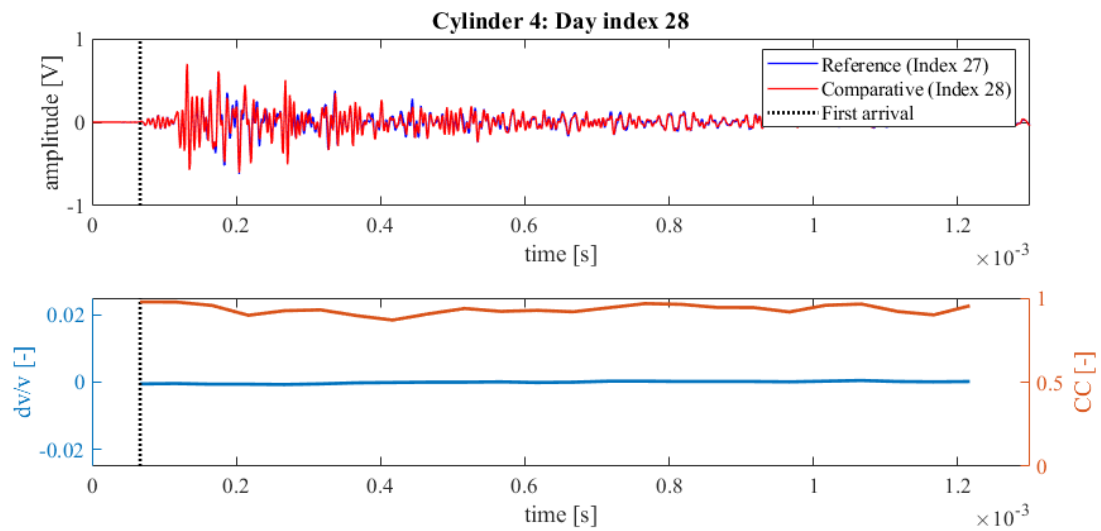


**Figure 355: Wave signals of Measurement 27 (blue) and Measurement 28 (red) of concrete hydration test Cylinder 4 (top),  $dv/v$  (blue) and CC (orange) results from CWI over the signal travel time divided in stretching windows (bottom)**

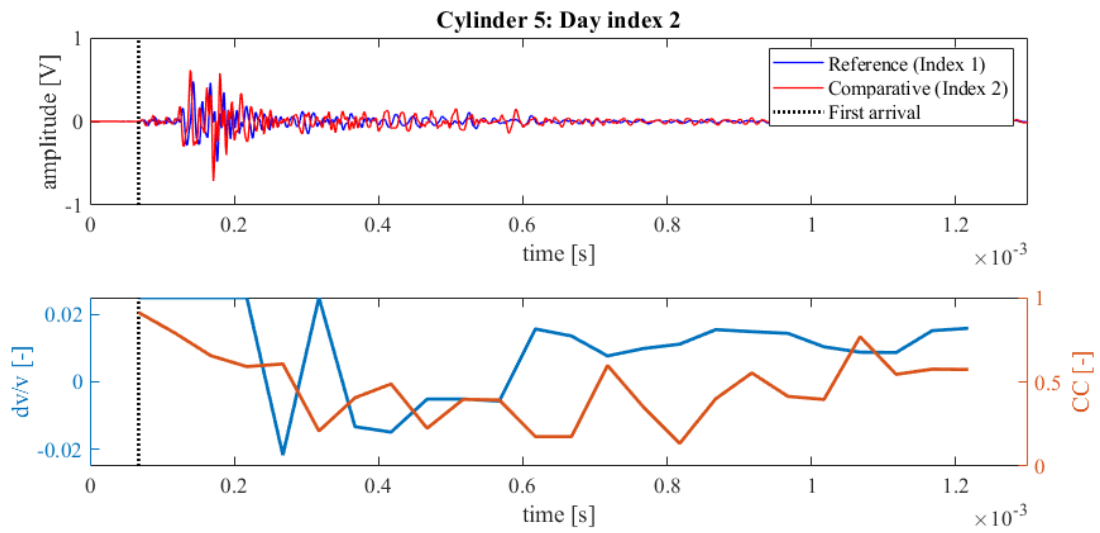


Figure 356: Wave signals of Measurement 1 (blue) and Measurement 2 (red) of concrete hydration test Cylinder 5 (top),  $dv/v$  (blue) and CC (orange) results from CWI over the signal travel time divided in stretching windows (bottom)

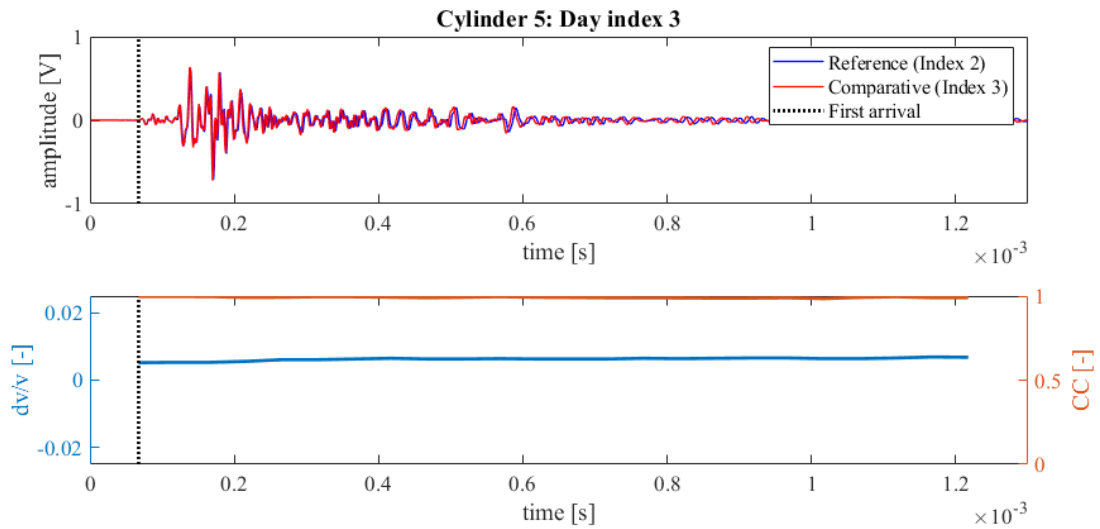


Figure 357: Wave signals of Measurement 2 (blue) and Measurement 3 (red) of concrete hydration test Cylinder 5 (top),  $dv/v$  (blue) and CC (orange) results from CWI over the signal travel time divided in stretching windows (bottom)

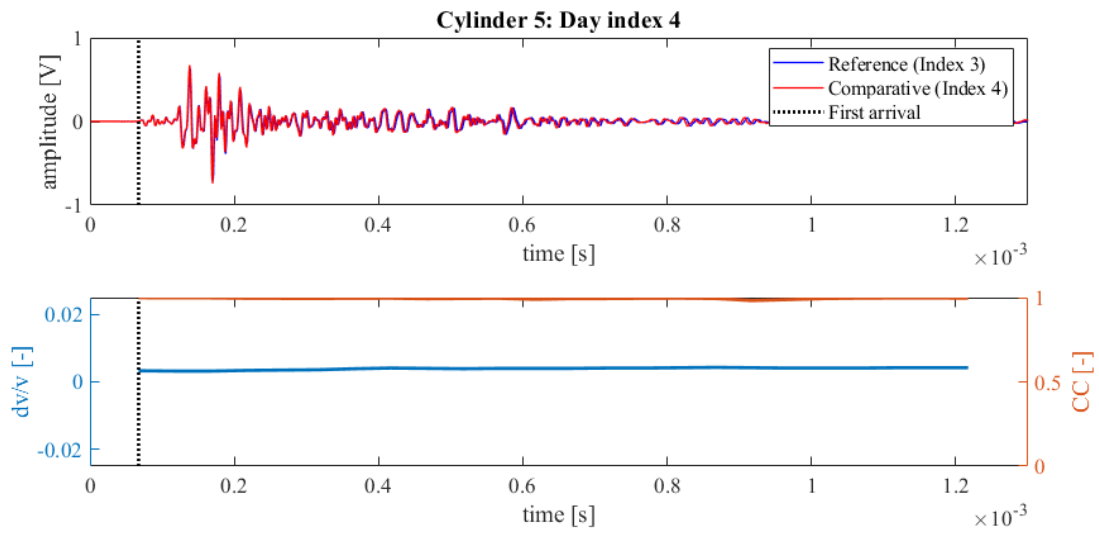


Figure 358: Wave signals of Measurement 3 (blue) and Measurement 4 (red) of concrete hydration test Cylinder 5 (top),  $dv/v$  (blue) and  $CC$  (orange) results from CWI over the signal travel time divided in stretching windows (bottom)

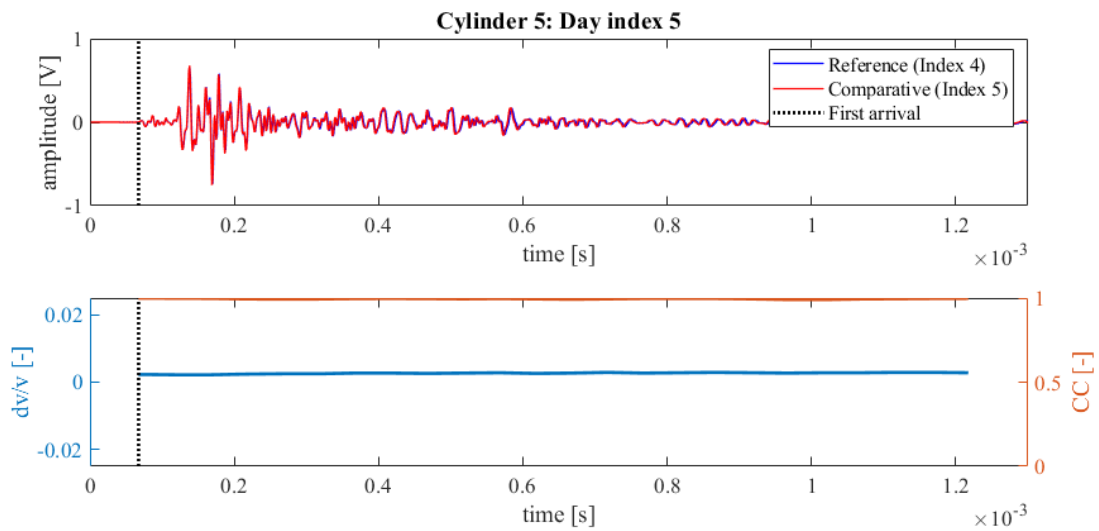


Figure 359: Wave signals of Measurement 4 (blue) and Measurement 5 (red) of concrete hydration test Cylinder 5 (top),  $dv/v$  (blue) and  $CC$  (orange) results from CWI over the signal travel time divided in stretching windows (bottom)

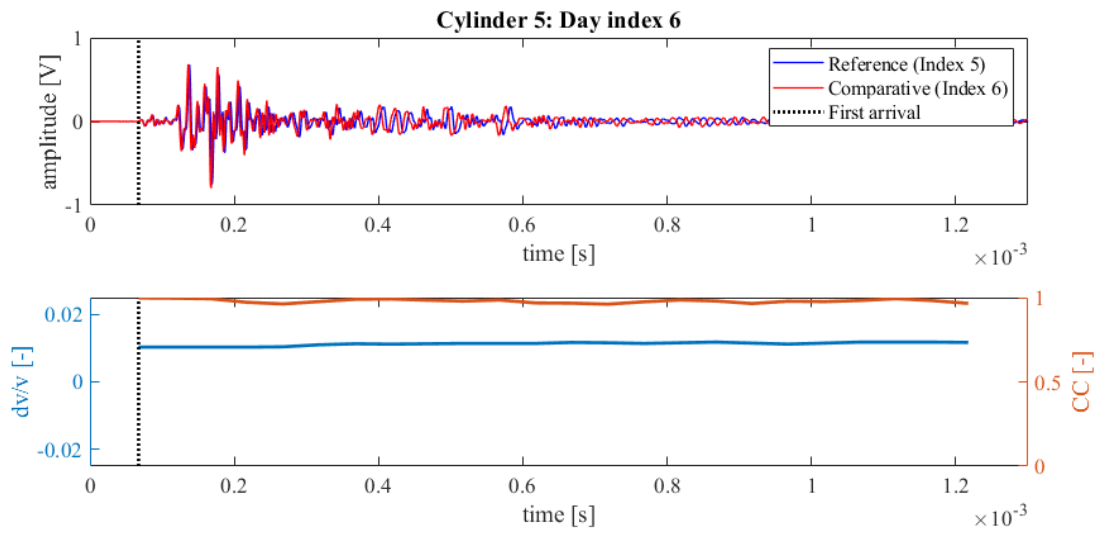


Figure 360: Wave signals of Measurement 5 (blue) and Measurement 6 (red) of concrete hydration test Cylinder 5 (top),  $dv/v$  (blue) and  $CC$  (orange) results from CWI over the signal travel time divided in stretching windows (bottom)

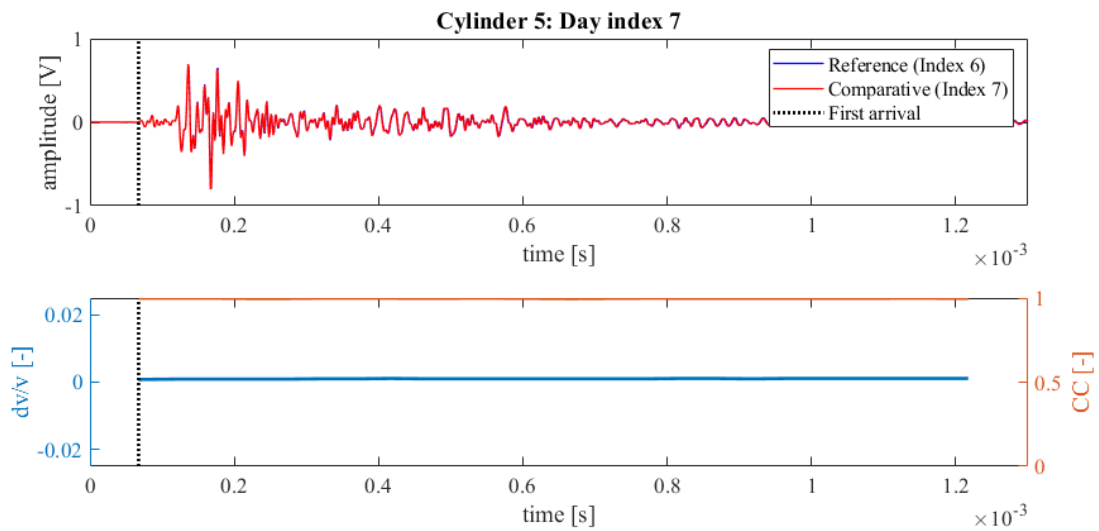


Figure 361: Wave signals of Measurement 6 (blue) and Measurement 7 (red) of concrete hydration test Cylinder 5 (top),  $dv/v$  (blue) and  $CC$  (orange) results from CWI over the signal travel time divided in stretching windows (bottom)

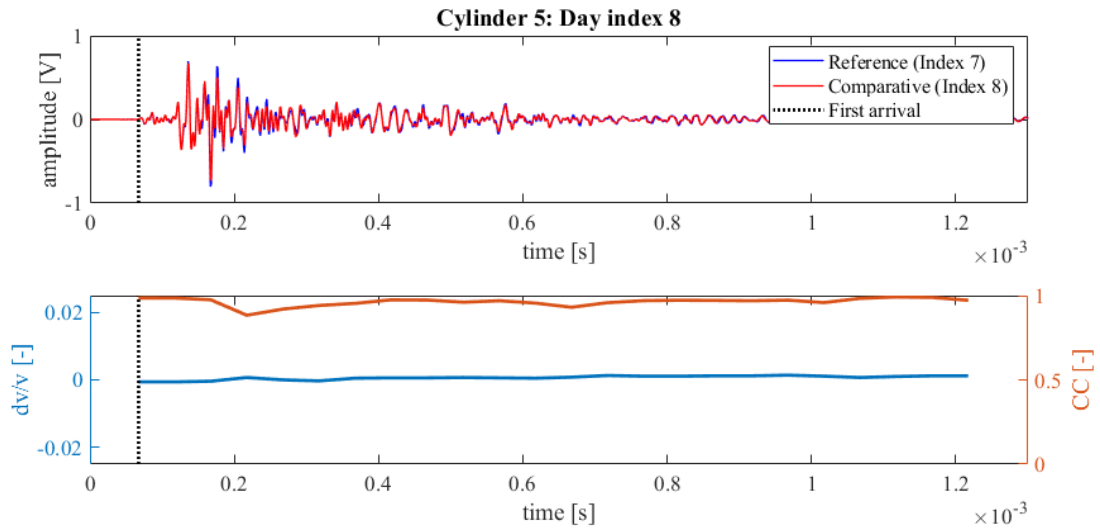


Figure 362: Wave signals of Measurement 7 (blue) and Measurement 8 (red) of concrete hydration test Cylinder 5 (top),  $dv/v$  (blue) and  $CC$  (orange) results from CWI over the signal travel time divided in stretching windows (bottom)

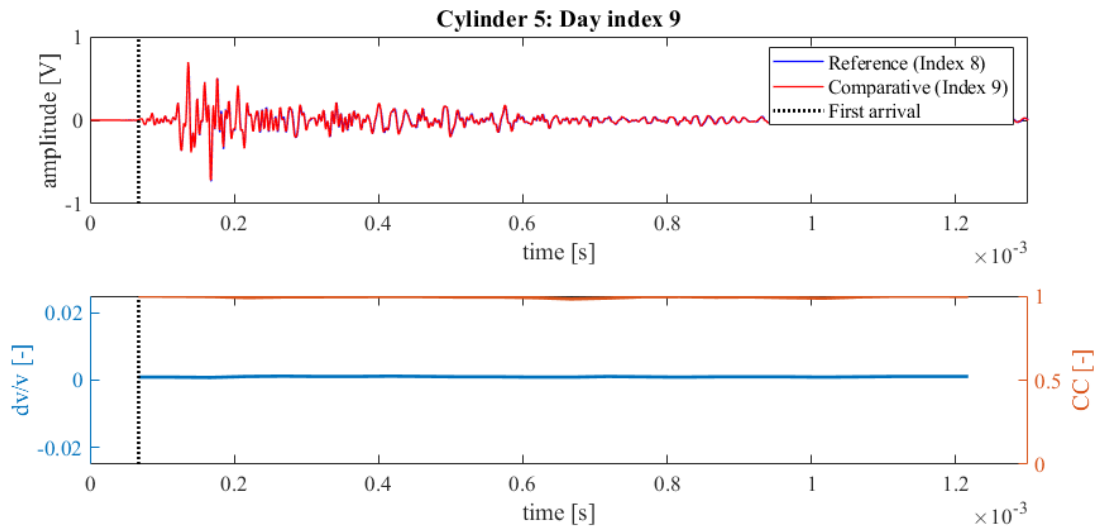
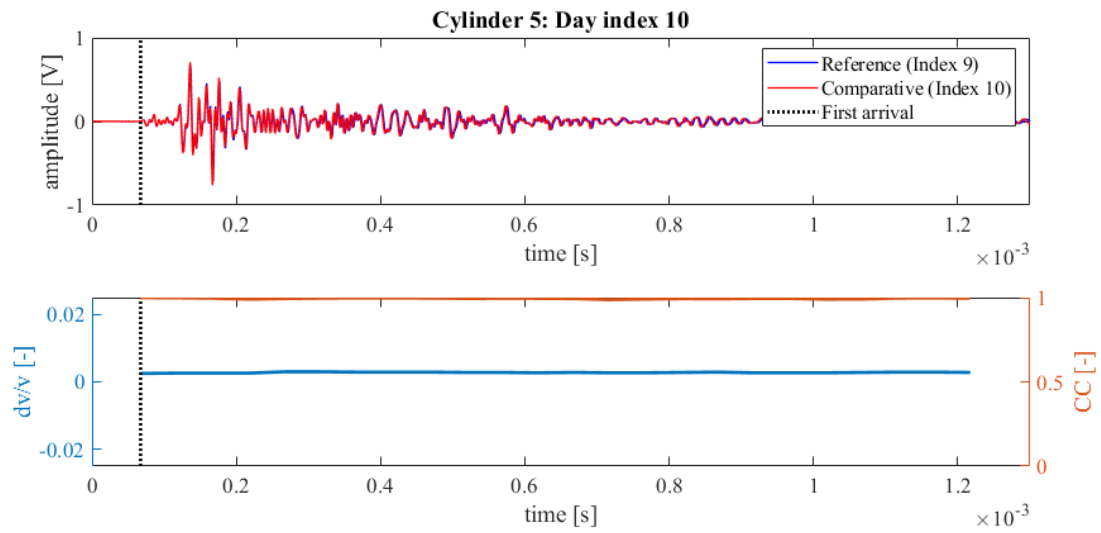
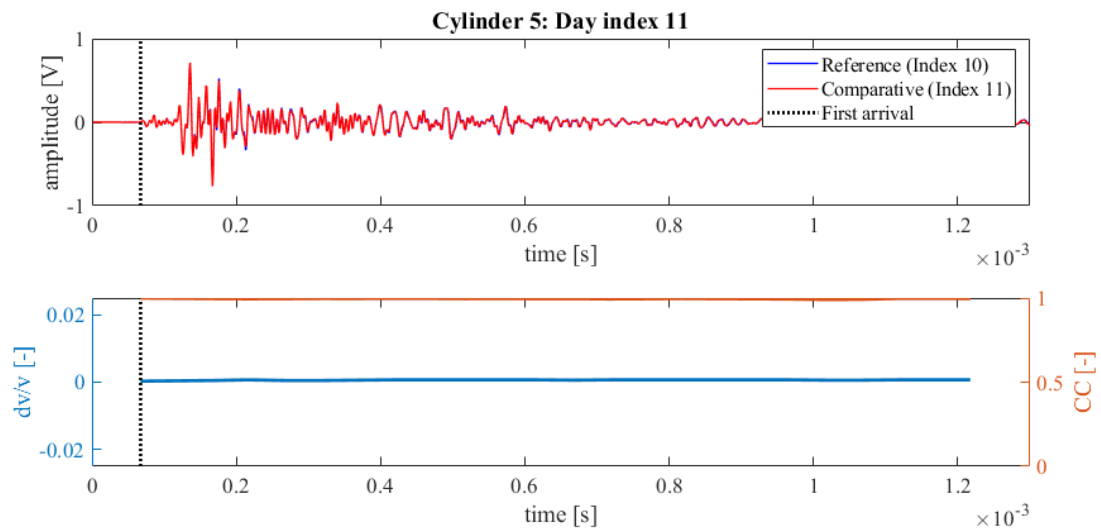


Figure 363: Wave signals of Measurement 8 (blue) and Measurement 9 (red) of concrete hydration test Cylinder 5 (top),  $dv/v$  (blue) and  $CC$  (orange) results from CWI over the signal travel time divided in stretching windows (bottom)



**Figure 364:** Wave signals of Measurement 9 (blue) and Measurement 10 (red) of concrete hydration test Cylinder 5 (top),  $dv/v$  (blue) and CC (orange) results from CWI over the signal travel time divided in stretching windows (bottom)



**Figure 365:** Wave signals of Measurement 10 (blue) and Measurement 11 (red) of concrete hydration test Cylinder 5 (top),  $dv/v$  (blue) and CC (orange) results from CWI over the signal travel time divided in stretching windows (bottom)

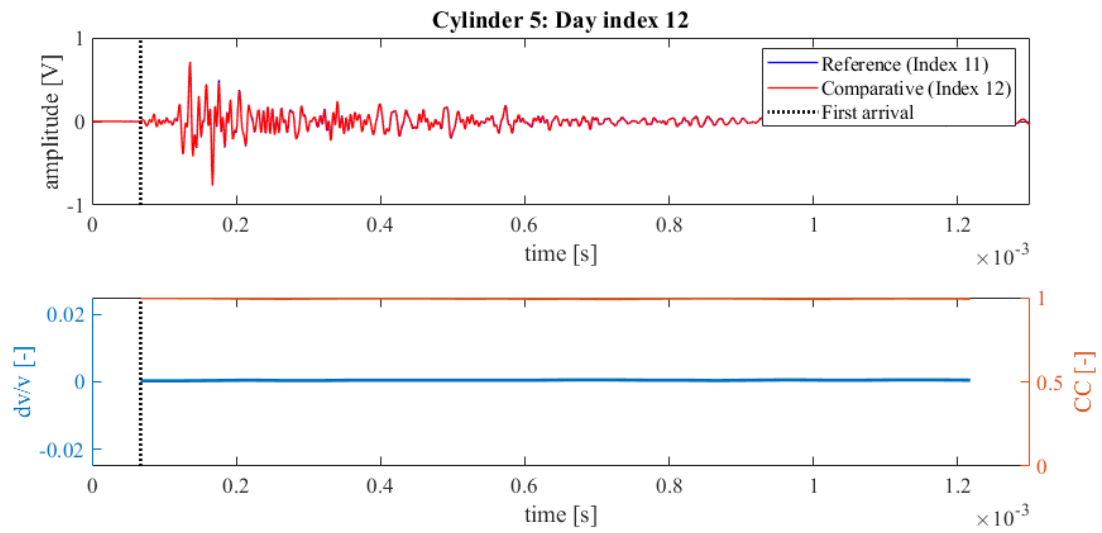


Figure 366: Wave signals of Measurement 11 (blue) and Measurement 12 (red) of concrete hydration test Cylinder 5 (top),  $dv/v$  (blue) and  $CC$  (orange) results from CWI over the signal travel time divided in stretching windows (bottom)

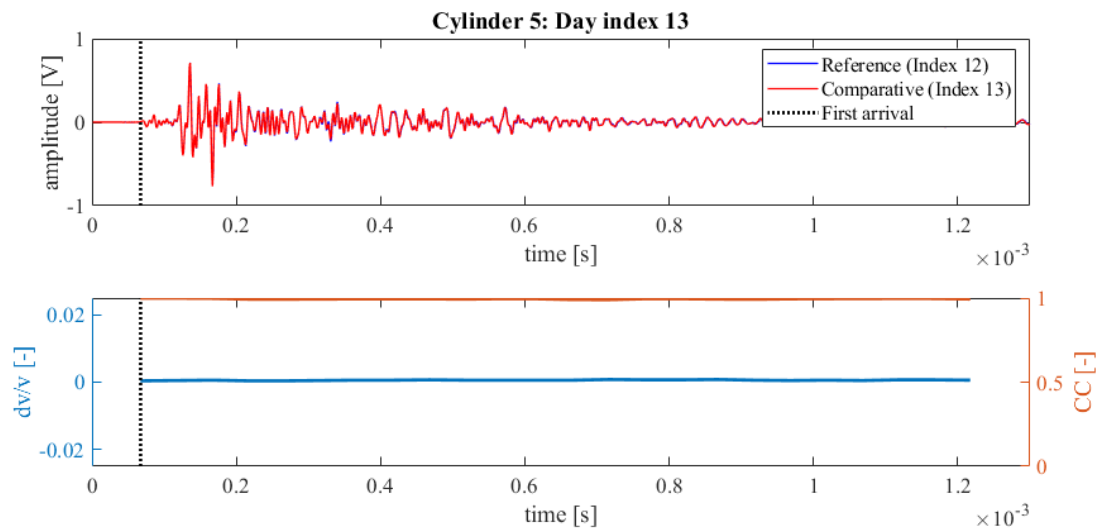


Figure 367: Wave signals of Measurement 12 (blue) and Measurement 13 (red) of concrete hydration test Cylinder 5 (top),  $dv/v$  (blue) and  $CC$  (orange) results from CWI over the signal travel time divided in stretching windows (bottom)

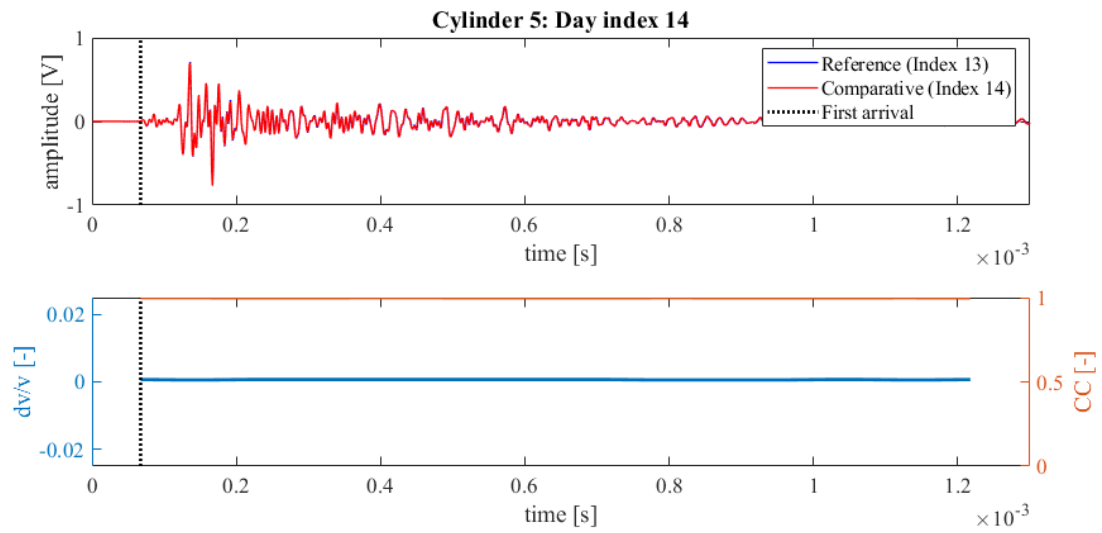


Figure 368: Wave signals of Measurement 13 (blue) and Measurement 14 (red) of concrete hydration test Cylinder 5 (top),  $dv/v$  (blue) and  $CC$  (orange) results from CWI over the signal travel time divided in stretching windows (bottom)

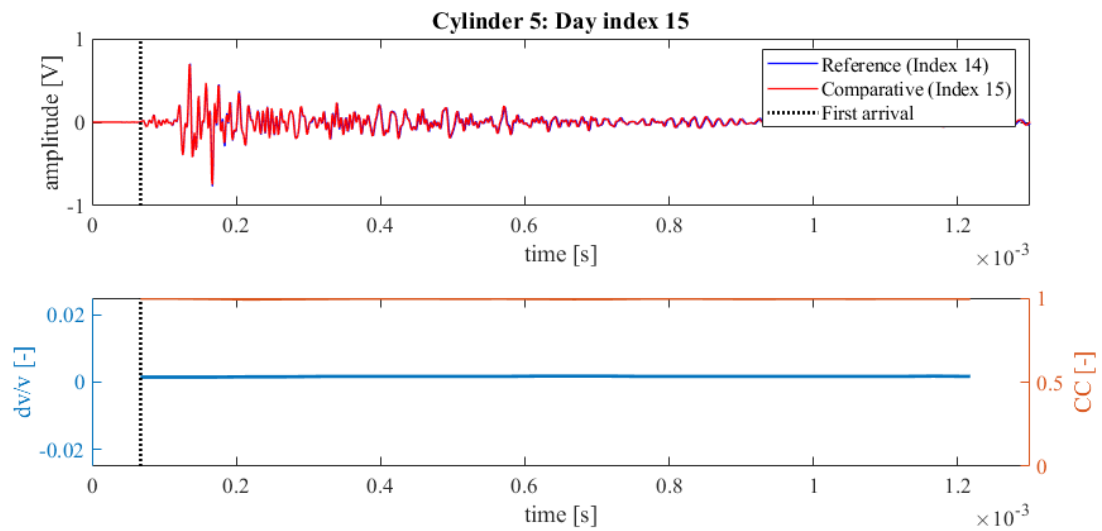


Figure 369: Wave signals of Measurement 14 (blue) and Measurement 15 (red) of concrete hydration test Cylinder 5 (top),  $dv/v$  (blue) and  $CC$  (orange) results from CWI over the signal travel time divided in stretching windows (bottom)

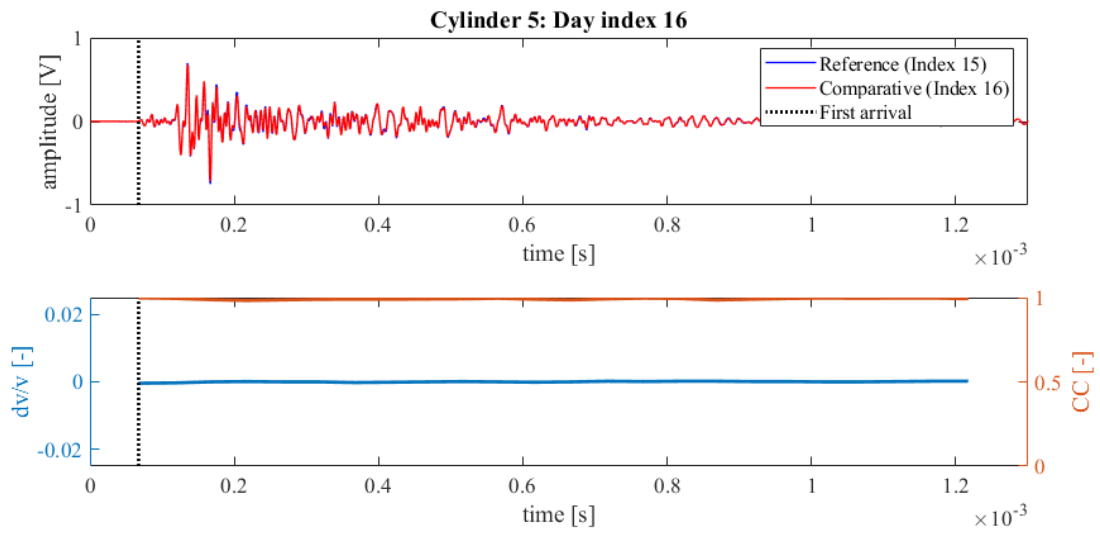


Figure 370: Wave signals of Measurement 15 (blue) and Measurement 16 (red) of concrete hydration test Cylinder 5 (top),  $dv/v$  (blue) and  $CC$  (orange) results from CWI over the signal travel time divided in stretching windows (bottom)

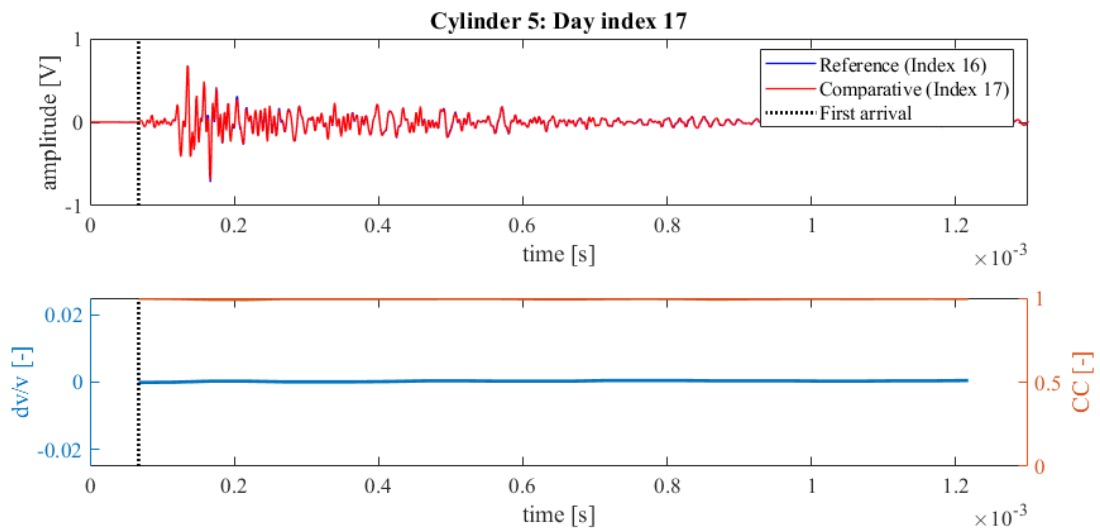


Figure 371: Wave signals of Measurement 16 (blue) and Measurement 17 (red) of concrete hydration test Cylinder 5 (top),  $dv/v$  (blue) and  $CC$  (orange) results from CWI over the signal travel time divided in stretching windows (bottom)

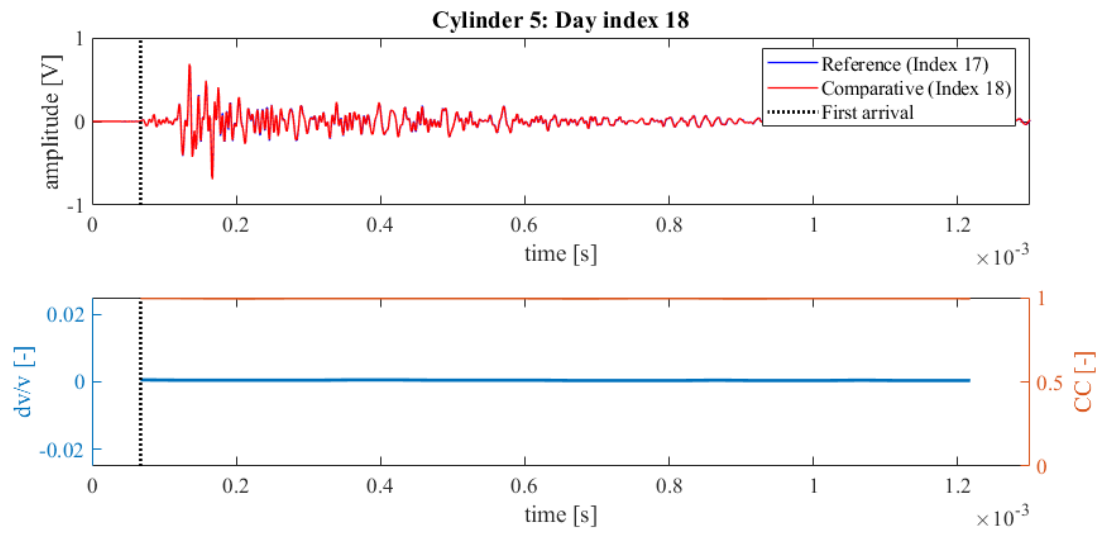


Figure 372: Wave signals of Measurement 17 (blue) and Measurement 18 (red) of concrete hydration test Cylinder 5 (top),  $dv/v$  (blue) and  $CC$  (orange) results from CWI over the signal travel time divided in stretching windows (bottom)

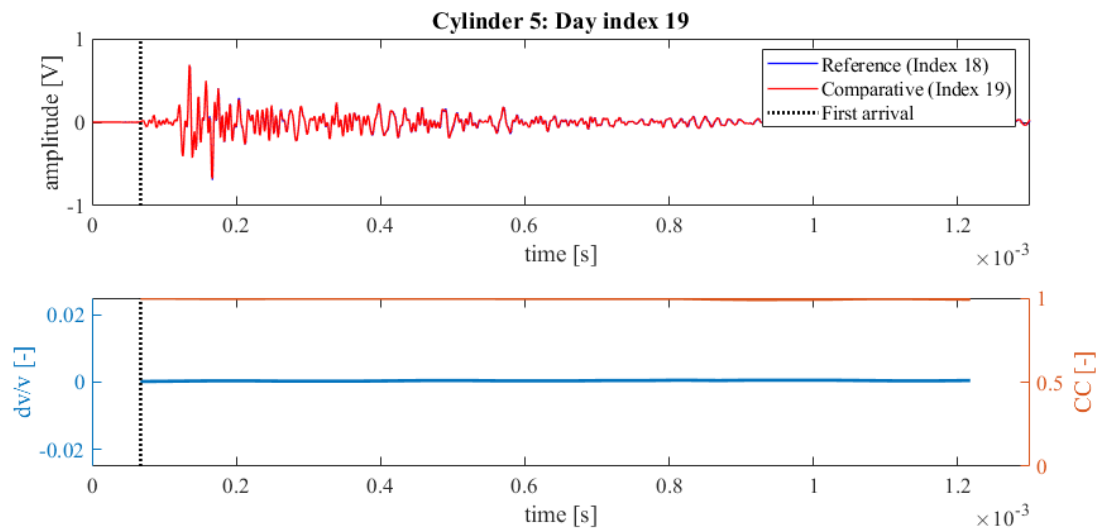


Figure 373: Wave signals of Measurement 18 (blue) and Measurement 19 (red) of concrete hydration test Cylinder 5 (top),  $dv/v$  (blue) and  $CC$  (orange) results from CWI over the signal travel time divided in stretching windows (bottom)

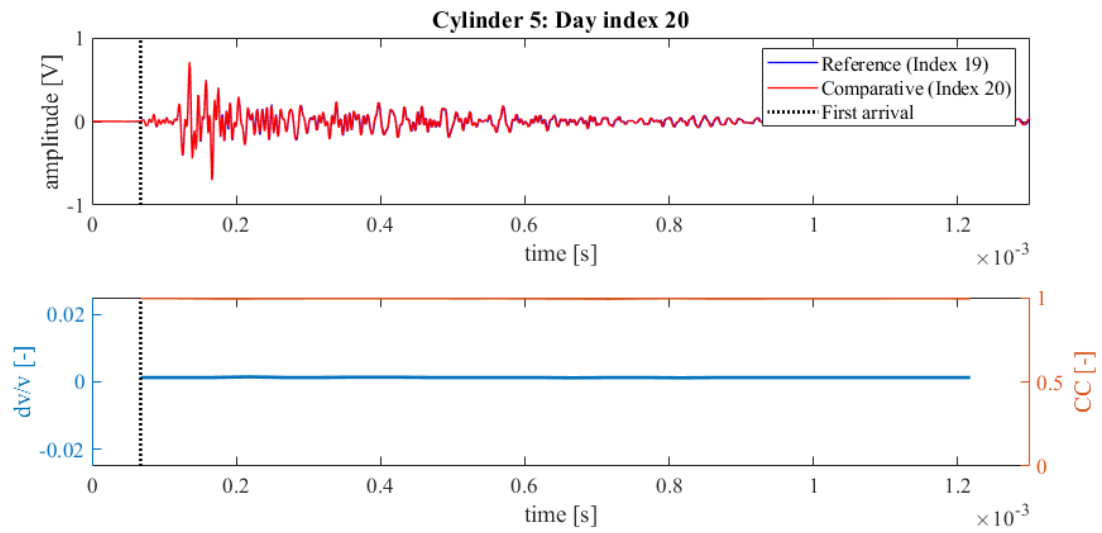


Figure 374: Wave signals of Measurement 19 (blue) and Measurement 20 (red) of concrete hydration test Cylinder 5 (top),  $dv/v$  (blue) and  $CC$  (orange) results from CWI over the signal travel time divided in stretching windows (bottom)

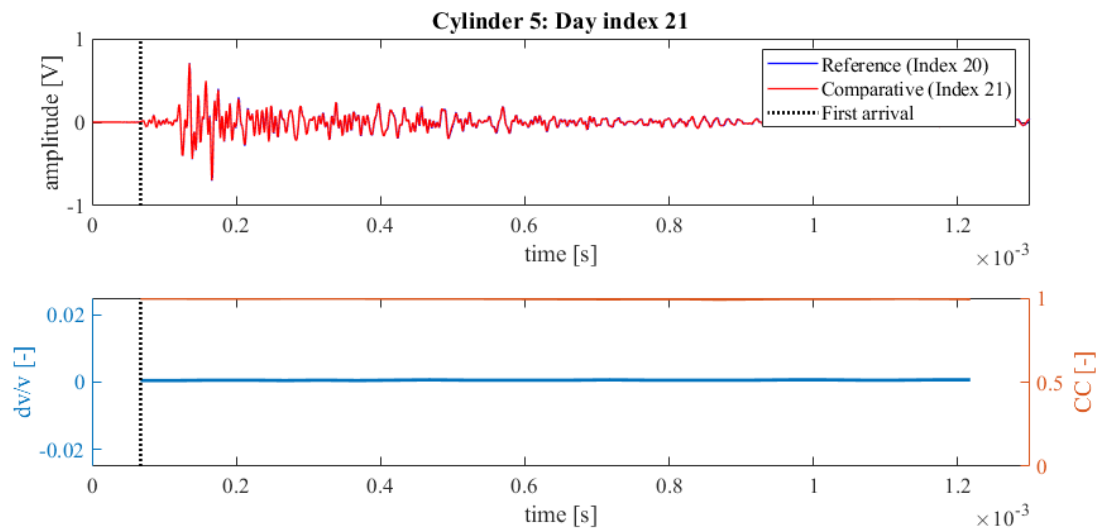


Figure 375: Wave signals of Measurement 20 (blue) and Measurement 21 (red) of concrete hydration test Cylinder 5 (top),  $dv/v$  (blue) and  $CC$  (orange) results from CWI over the signal travel time divided in stretching windows (bottom)

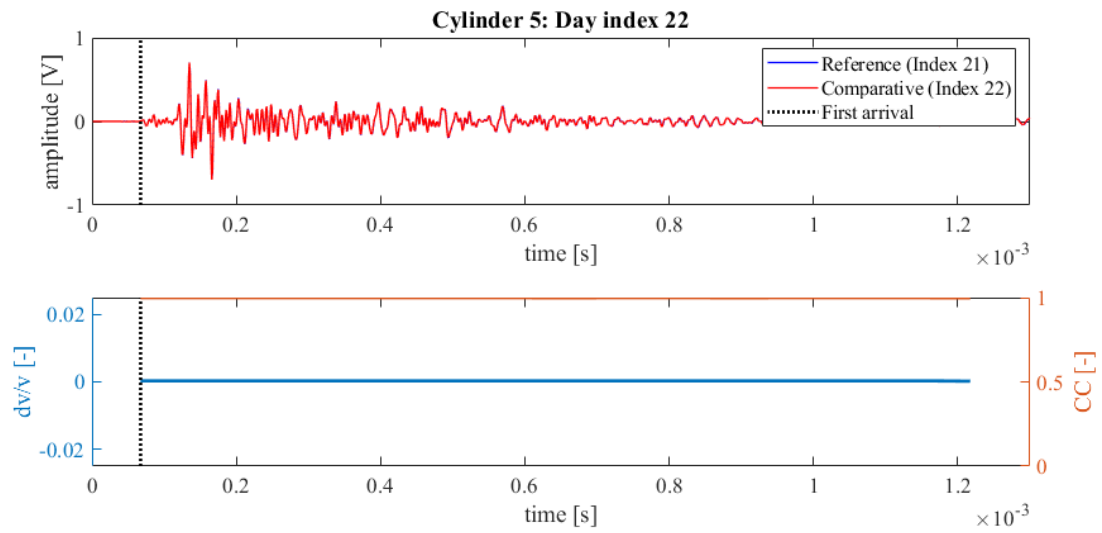


Figure 376: Wave signals of Measurement 21 (blue) and Measurement 22 (red) of concrete hydration test Cylinder 5 (top),  $dv/v$  (blue) and  $CC$  (orange) results from CWI over the signal travel time divided in stretching windows (bottom)

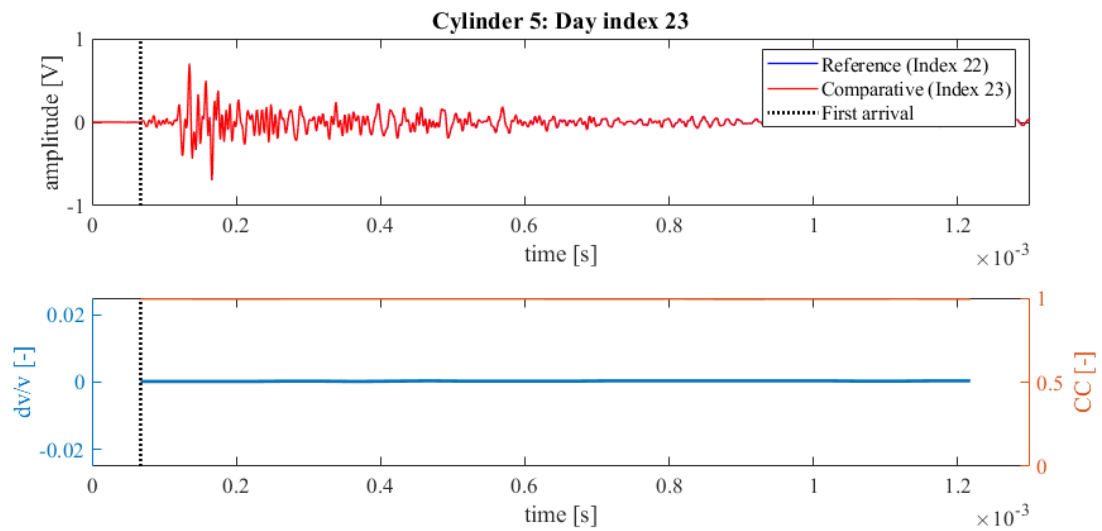
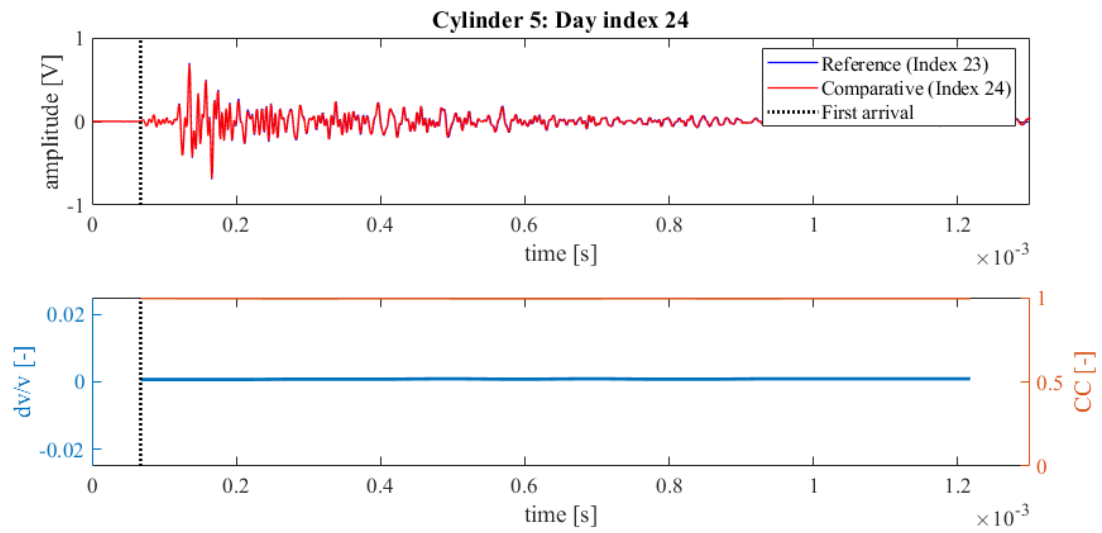
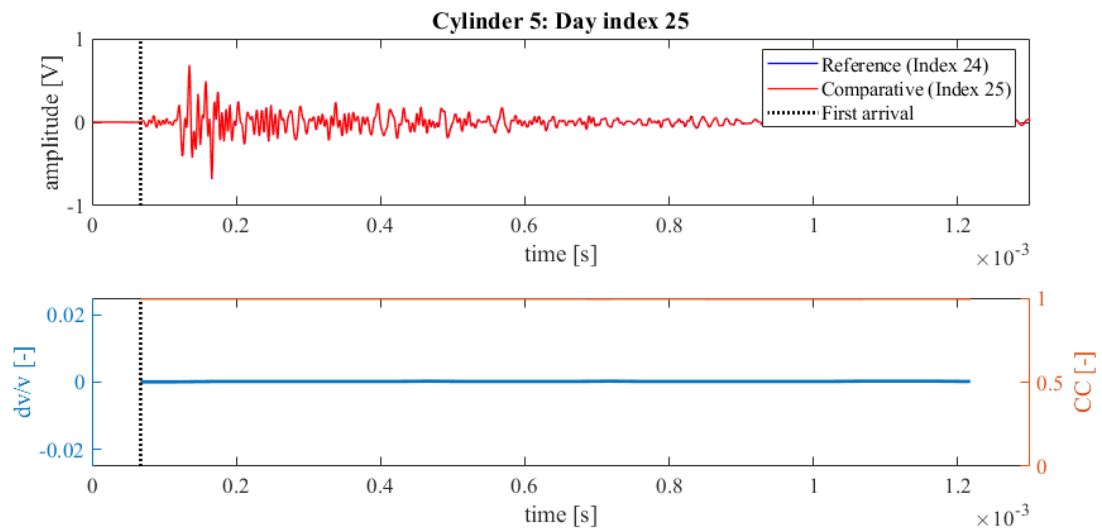


Figure 377: Wave signals of Measurement 22 (blue) and Measurement 23 (red) of concrete hydration test Cylinder 5 (top),  $dv/v$  (blue) and  $CC$  (orange) results from CWI over the signal travel time divided in stretching windows (bottom)



**Figure 378: Wave signals of Measurement 23 (blue) and Measurement 24 (red) of concrete hydration test Cylinder 5 (top),  $dv/v$  (blue) and CC (orange) results from CWI over the signal travel time divided in stretching windows (bottom)**



**Figure 379: Wave signals of Measurement 24 (blue) and Measurement 25 (red) of concrete hydration test Cylinder 5 (top),  $dv/v$  (blue) and CC (orange) results from CWI over the signal travel time divided in stretching windows (bottom)**

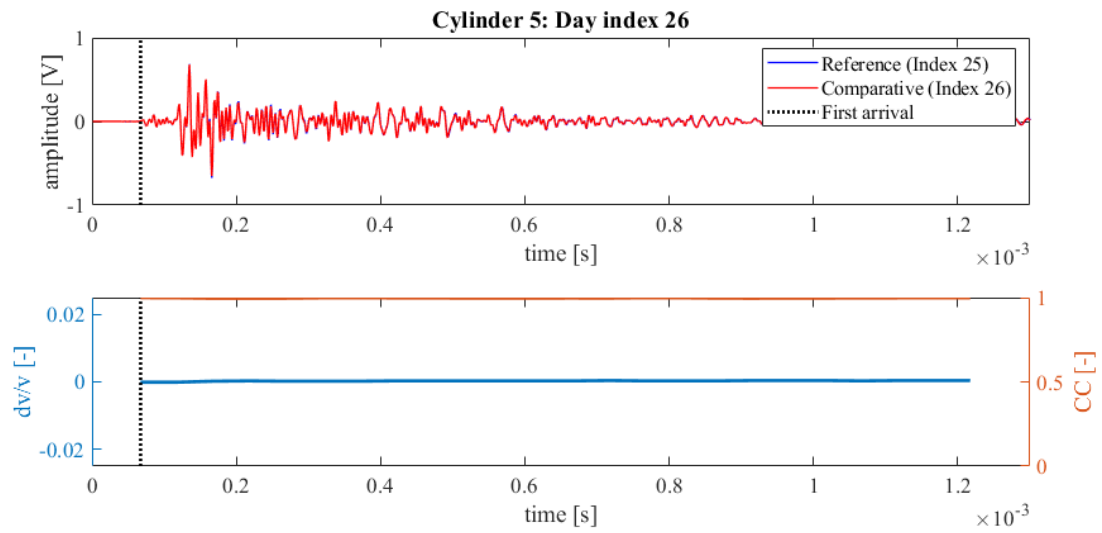


**Figure 380: Wave signals of Measurement 25 (blue) and Measurement 26 (red) of concrete hydration test Cylinder 5 (top),  $dv/v$  (blue) and CC (orange) results from CWI over the signal travel time divided in stretching windows (bottom)**

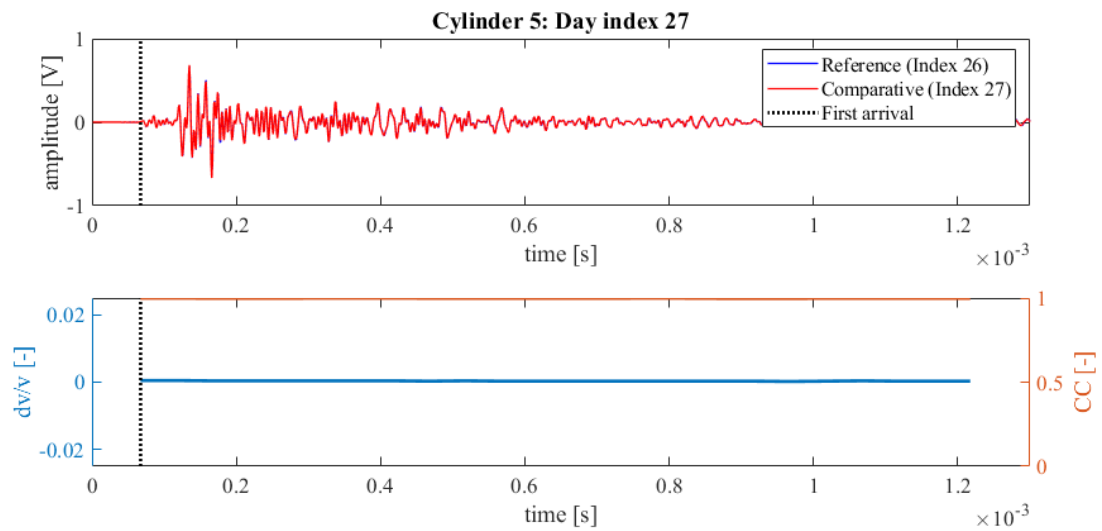


**Figure 381: Wave signals of Measurement 26 (blue) and Measurement 27 (red) of concrete hydration test Cylinder 5 (top),  $dv/v$  (blue) and CC (orange) results from CWI over the signal travel time divided in stretching windows (bottom)**

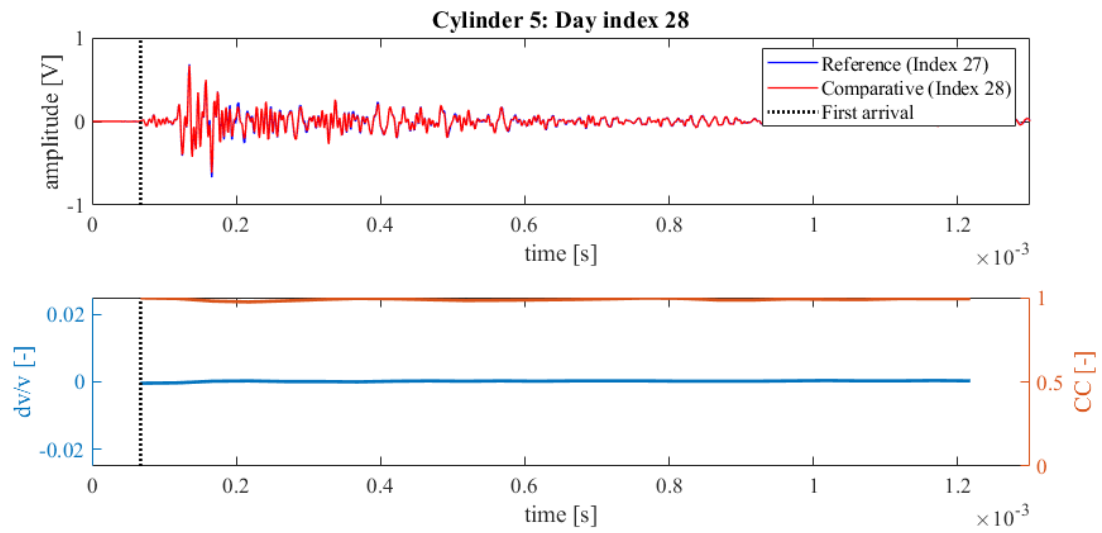


**Figure 382: Wave signals of Measurement 27 (blue) and Measurement 28 (red) of concrete hydration test Cylinder 5 (top),  $dv/v$  (blue) and  $CC$  (orange) results from CWI over the signal travel time divided in stretching windows (bottom)**

## F. CWI results of cylinder compression tests

Two concrete cylindrical concrete samples (Cylinder 1 and Cylinder 2) are tested in uniaxial compressive loading. Measurements are taken in between load steps and the loading specifics are defined in Table 21. For both cylinders, cross-correlation becomes difficult when the cylinders are initially loaded and when the cylinders are nearly fully unloaded. The difficulties stem from differences in the waveform between measurements.

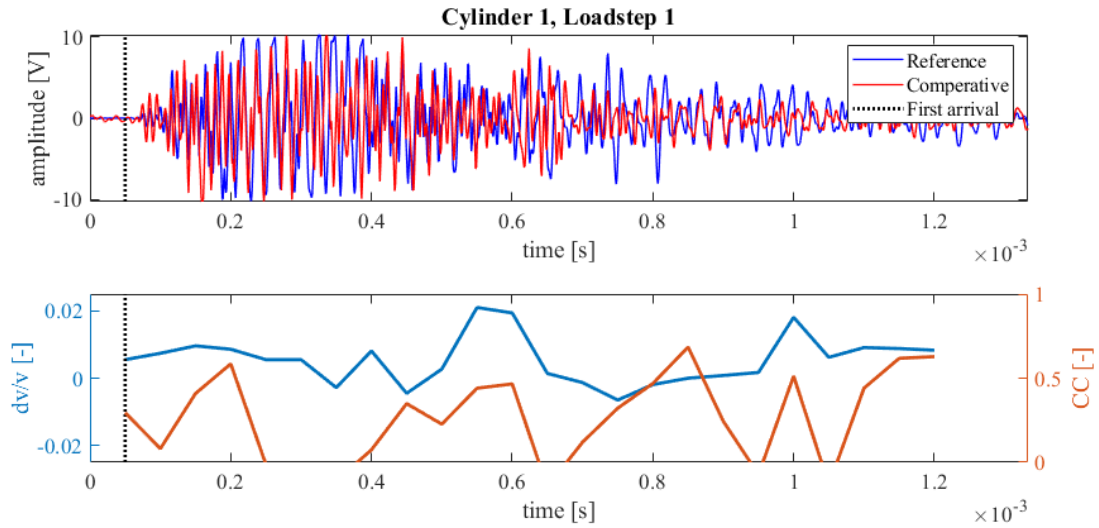


Figure 383: Wave signals of No load (blue) and Load step 1 (red) of concrete compression test Cylinder 1 (top),  $dv/v$  (blue) and CC (orange) results from CWI over the signal travel time divided in stretching windows (bottom)

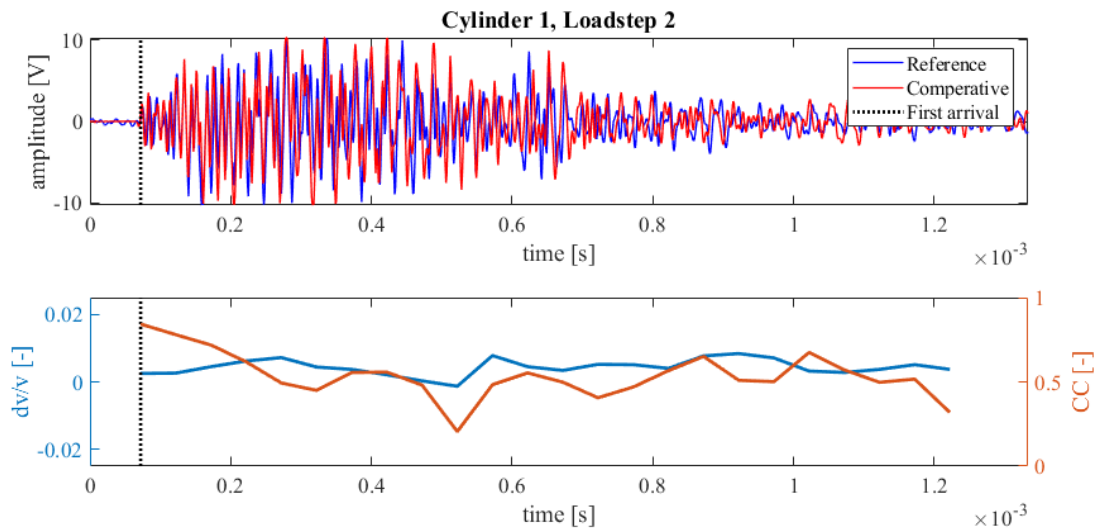


Figure 384: Wave signals of Load step 1 (blue) and Load step 2 (red) of concrete compression test Cylinder 1 (top),  $dv/v$  (blue) and CC (orange) results from CWI over the signal travel time divided in stretching windows (bottom)

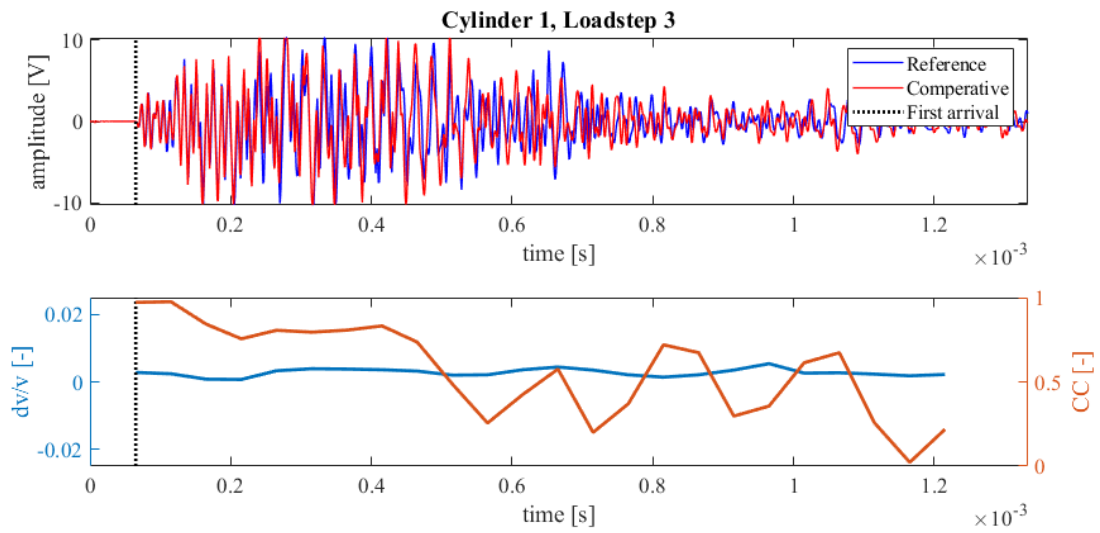


Figure 385: Wave signals of Load step 2 (blue) and Load step 3 (red) of concrete compression test Cylinder 1 (top),  $dv/v$  (blue) and CC (orange) results from CWI over the signal travel time divided in stretching windows (bottom)

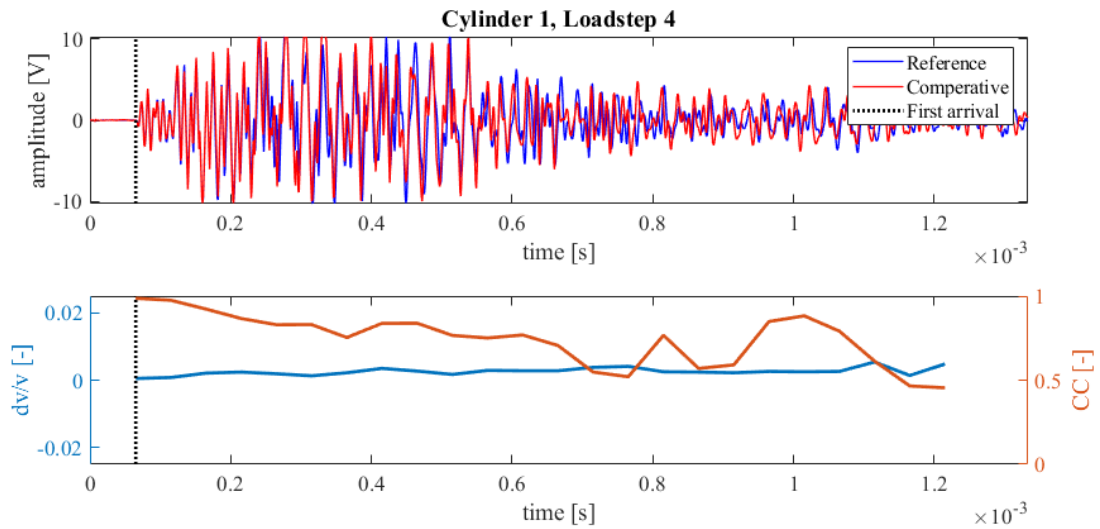


Figure 386: Wave signals of Load step 3 (blue) and Load step 4 (red) of concrete compression test Cylinder 1 (top),  $dv/v$  (blue) and CC (orange) results from CWI over the signal travel time divided in stretching windows (bottom)

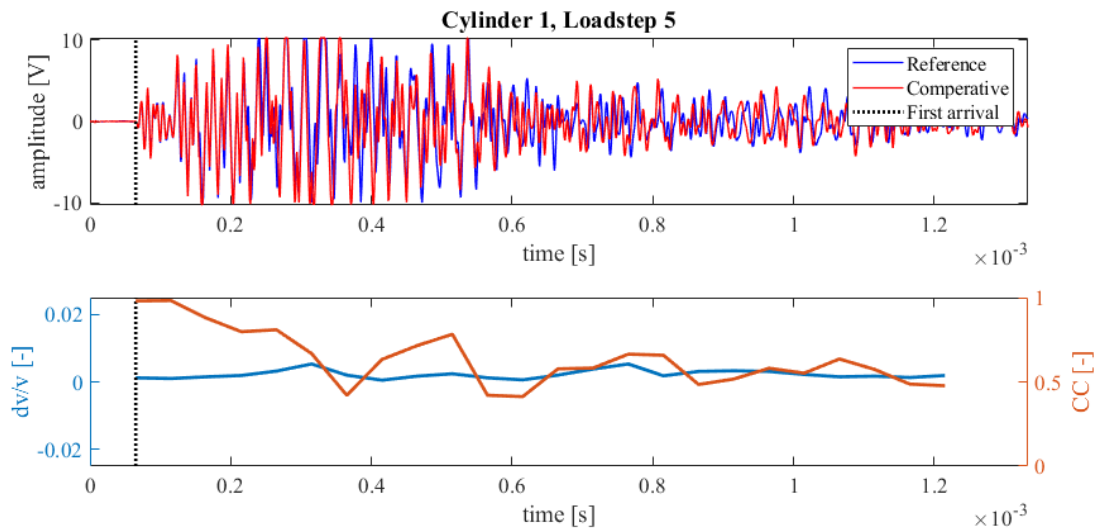


Figure 387: Wave signals of Load step 4 (blue) and Load step 5 (red) of concrete compression test Cylinder 1 (top),  $dv/v$  (blue) and CC (orange) results from CWI over the signal travel time divided in stretching windows (bottom)

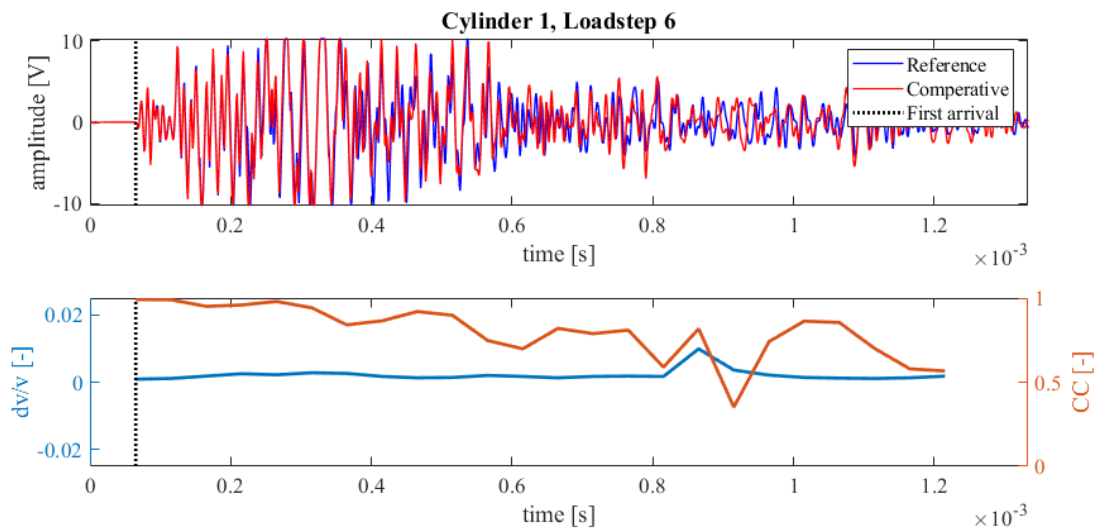


Figure 388: Wave signals of Load step 5 (blue) and Load step 6 (red) of concrete compression test Cylinder 1 (top),  $dv/v$  (blue) and CC (orange) results from CWI over the signal travel time divided in stretching windows (bottom)

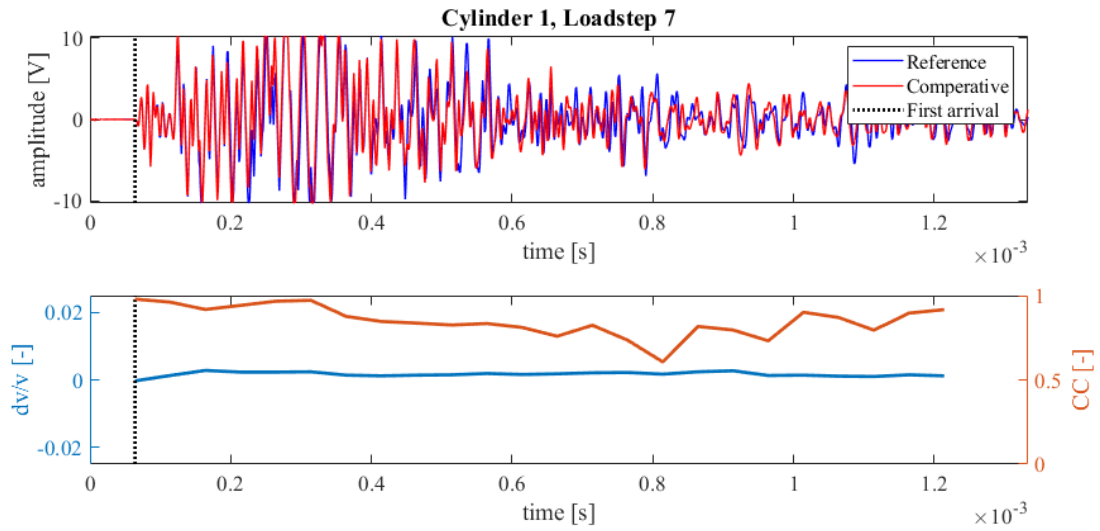


Figure 389: Wave signals of Load step 6 (blue) and Load step 7 (red) of concrete compression test Cylinder 1 (top),  $dv/v$  (blue) and CC (orange) results from CWI over the signal travel time divided in stretching windows (bottom)

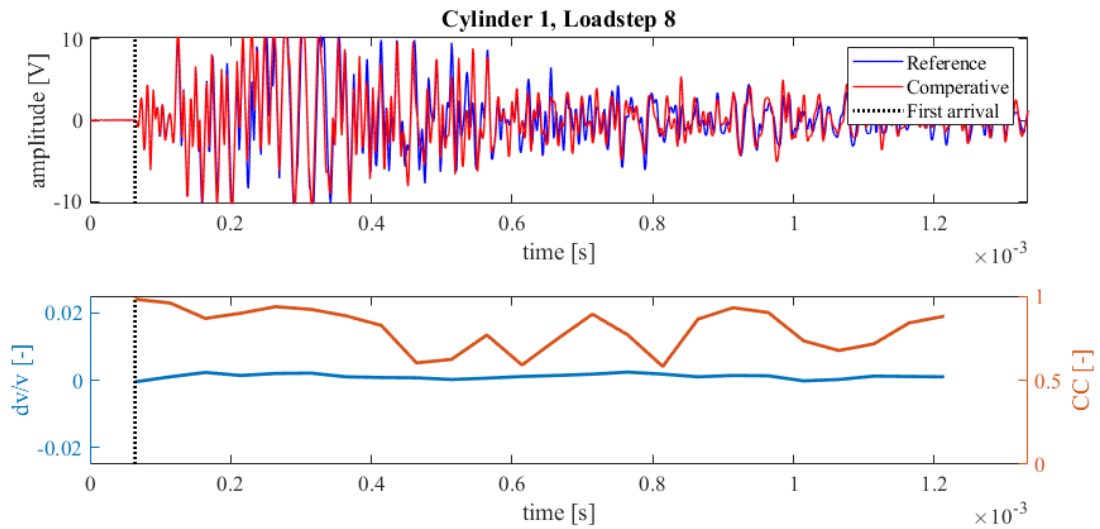


Figure 390: Wave signals of Load step 7 (blue) and Load step 8 (red) of concrete compression test Cylinder 1 (top),  $dv/v$  (blue) and CC (orange) results from CWI over the signal travel time divided in stretching windows (bottom)

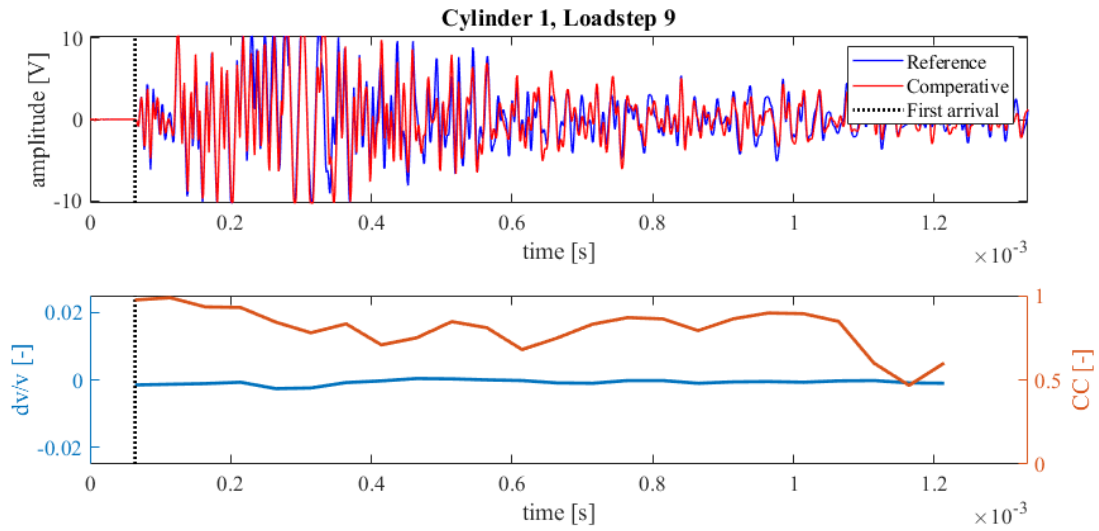


Figure 391: Wave signals of Load step 8 (blue) and Load step 9 (red) of concrete compression test Cylinder 1 (top),  $dv/v$  (blue) and CC (orange) results from CWI over the signal travel time divided in stretching windows (bottom)

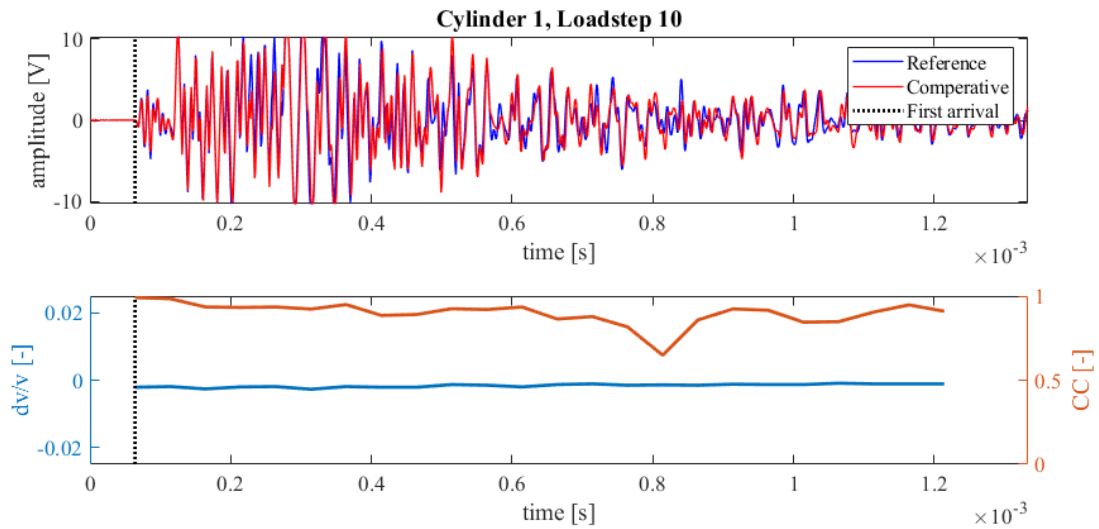


Figure 392: Wave signals of Load step 9 (blue) and Load step 10 (red) of concrete compression test Cylinder 1 (top),  $dv/v$  (blue) and CC (orange) results from CWI over the signal travel time divided in stretching windows (bottom)

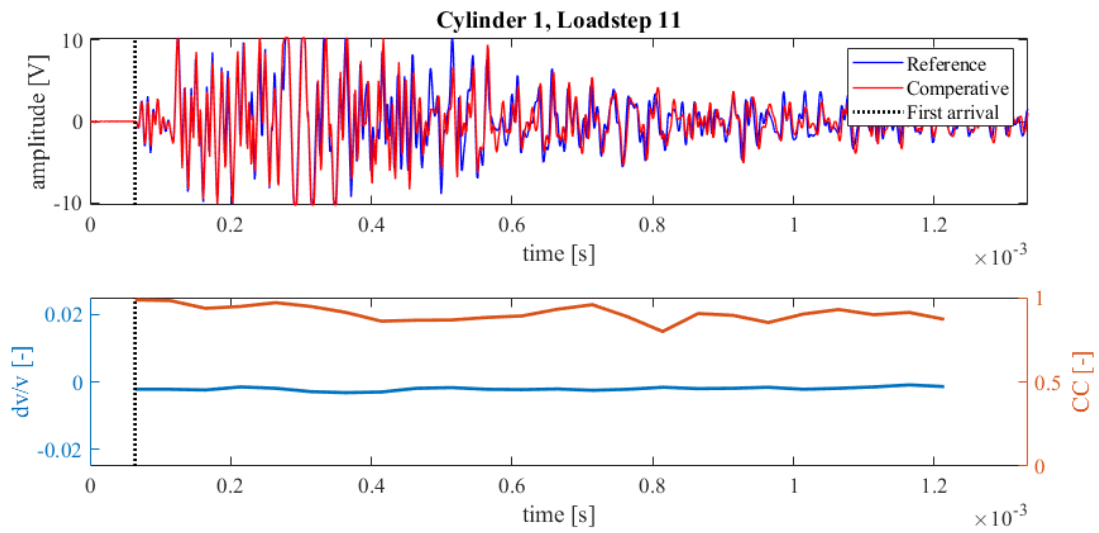


Figure 393: Wave signals of Load step 10 (blue) and Load step 11 (red) of concrete compression test Cylinder 1 (top),  $dv/v$  (blue) and CC (orange) results from CWI over the signal travel time divided in stretching windows (bottom)

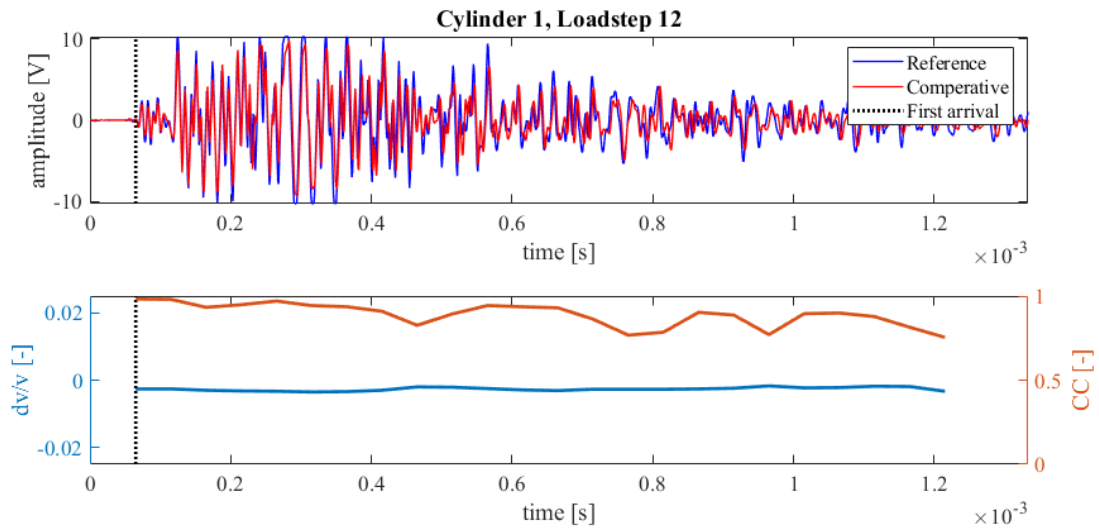


Figure 394: Wave signals of Load step 11 (blue) and Load step 12 (red) of concrete compression test Cylinder 1 (top),  $dv/v$  (blue) and CC (orange) results from CWI over the signal travel time divided in stretching windows (bottom)

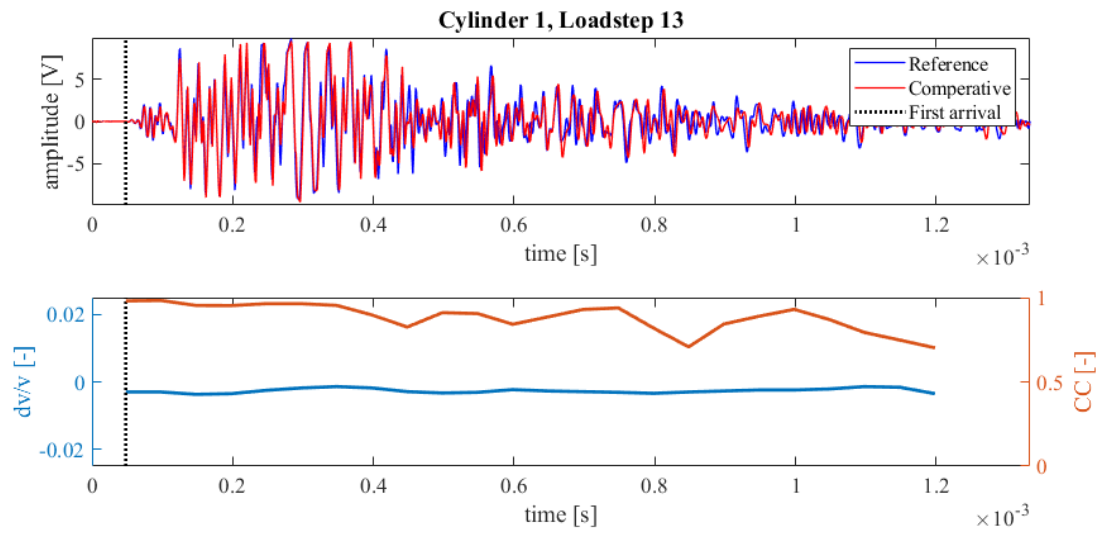


Figure 395: Wave signals of Load step 12 (blue) and Load step 13 (red) of concrete compression test Cylinder 1 (top),  $dv/v$  (blue) and CC (orange) results from CWI over the signal travel time divided in stretching windows (bottom)

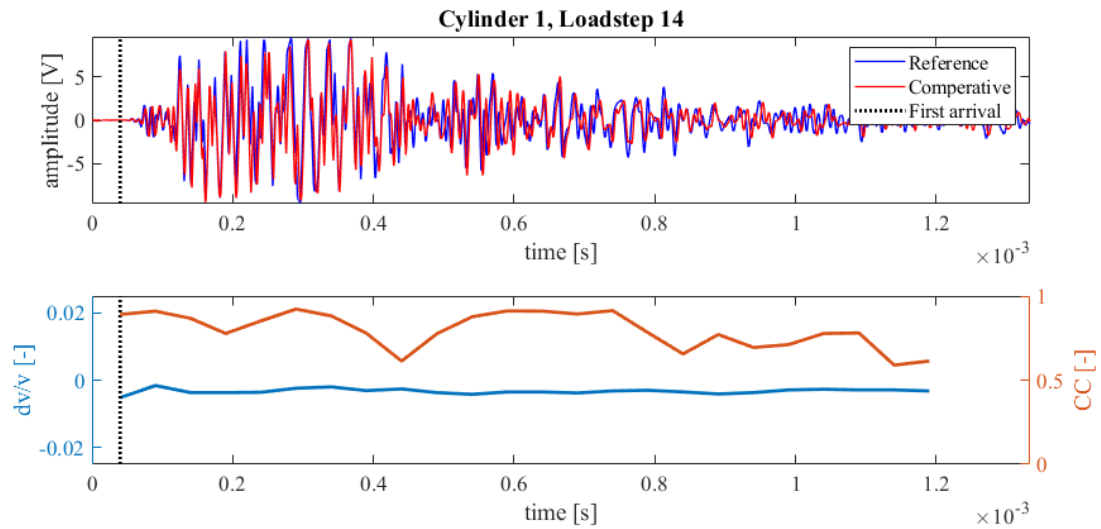


Figure 396: Wave signals of Load step 13 (blue) and Load step 14 (red) of concrete compression test Cylinder 1 (top),  $dv/v$  (blue) and CC (orange) results from CWI over the signal travel time divided in stretching windows (bottom)

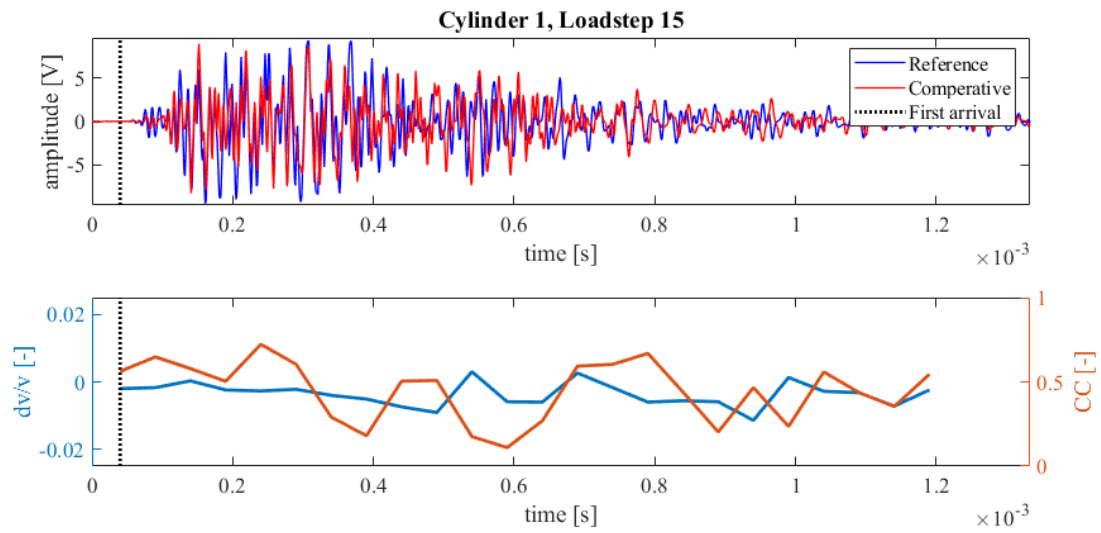


Figure 397: Wave signals of Load step 14 (blue) and Load step 15 (red) of concrete compression test Cylinder 1 (top),  $dv/v$  (blue) and CC (orange) results from CWI over the signal travel time divided in stretching windows (bottom)

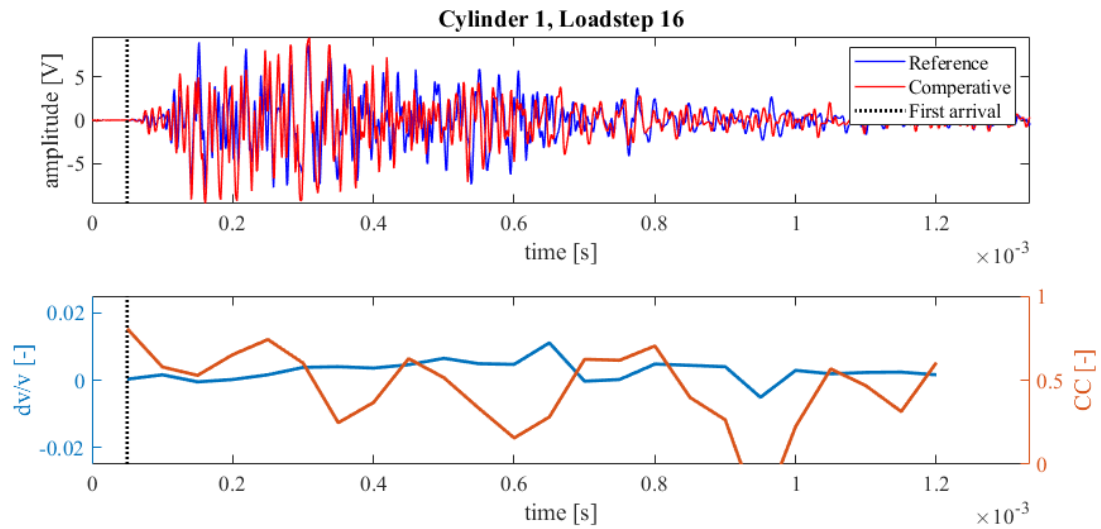
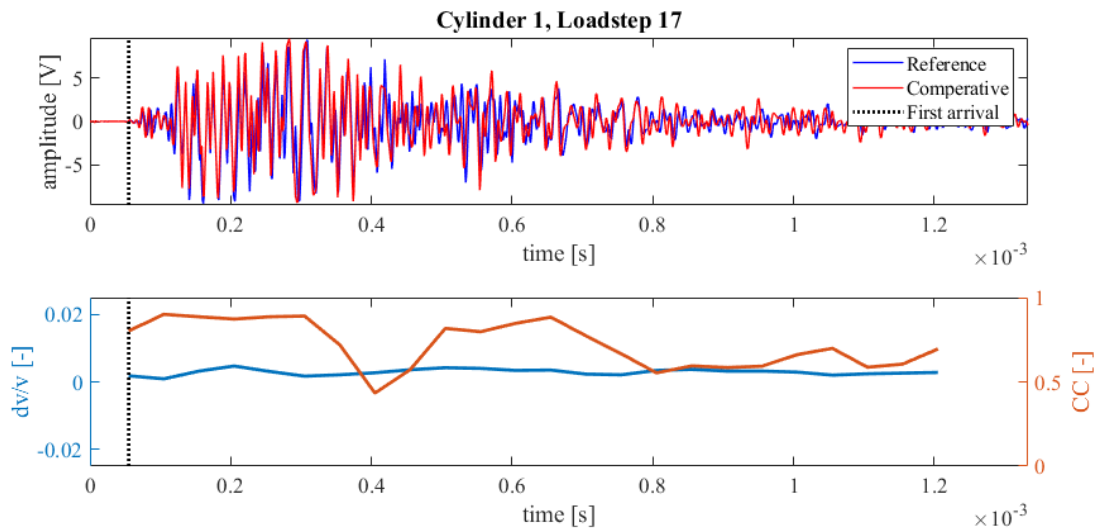
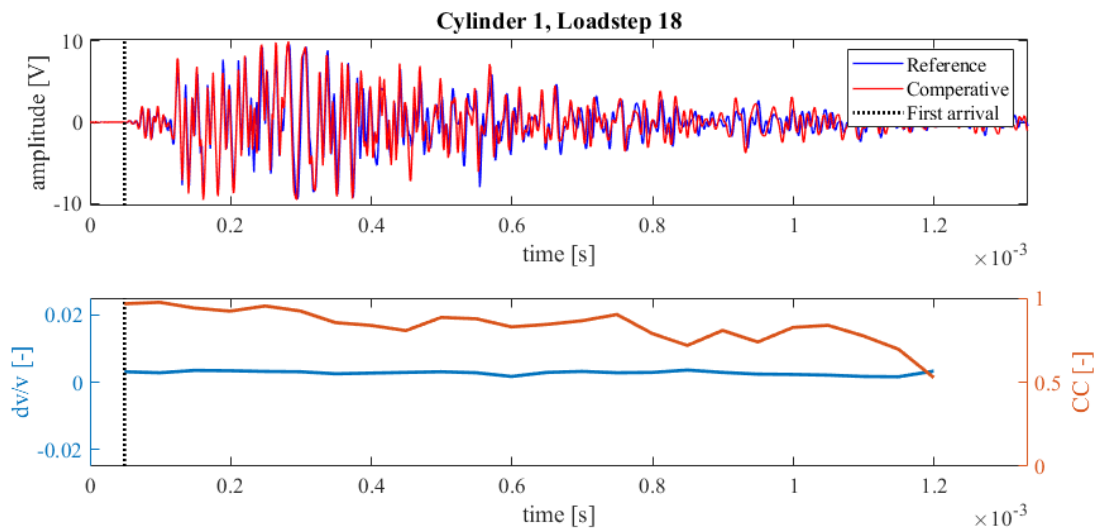


Figure 398: Wave signals of Load step 15 (blue) and Load step 16 (red) of concrete compression test Cylinder 1 (top),  $dv/v$  (blue) and CC (orange) results from CWI over the signal travel time divided in stretching windows (bottom)



**Figure 399: Wave signals of Load step 16 (blue) and Load step 17 (red) of concrete compression test Cylinder 1 (top),  $dv/v$  (blue) and CC (orange) results from CWI over the signal travel time divided in stretching windows (bottom)**



**Figure 400: Wave signals of Load step 17 (blue) and Load step 18 (red) of concrete compression test Cylinder 1 (top),  $dv/v$  (blue) and CC (orange) results from CWI over the signal travel time divided in stretching windows (bottom)**

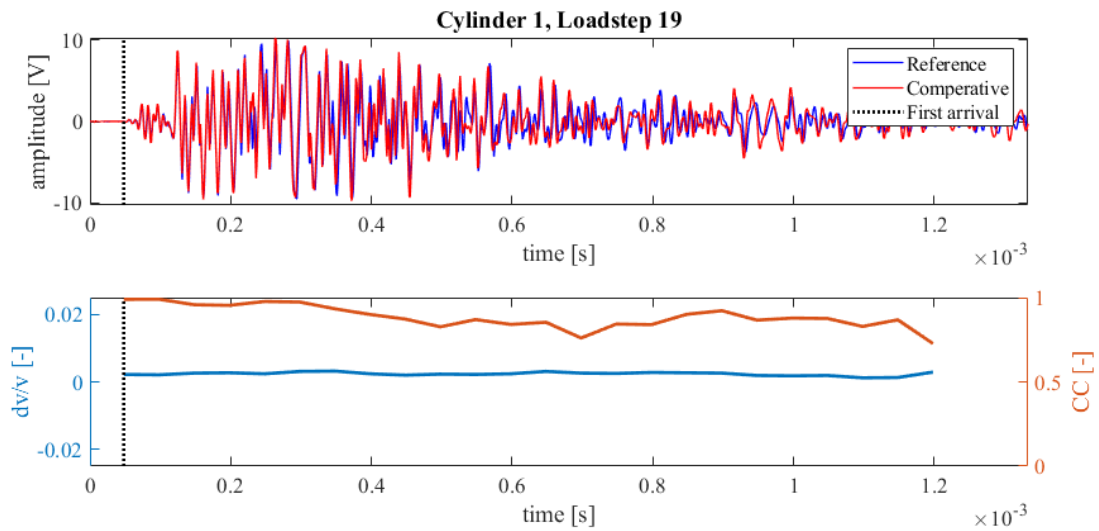


Figure 401: Wave signals of Load step 18 (blue) and Load step 19 (red) of concrete compression test Cylinder 1 (top),  $dv/v$  (blue) and CC (orange) results from CWI over the signal travel time divided in stretching windows (bottom)

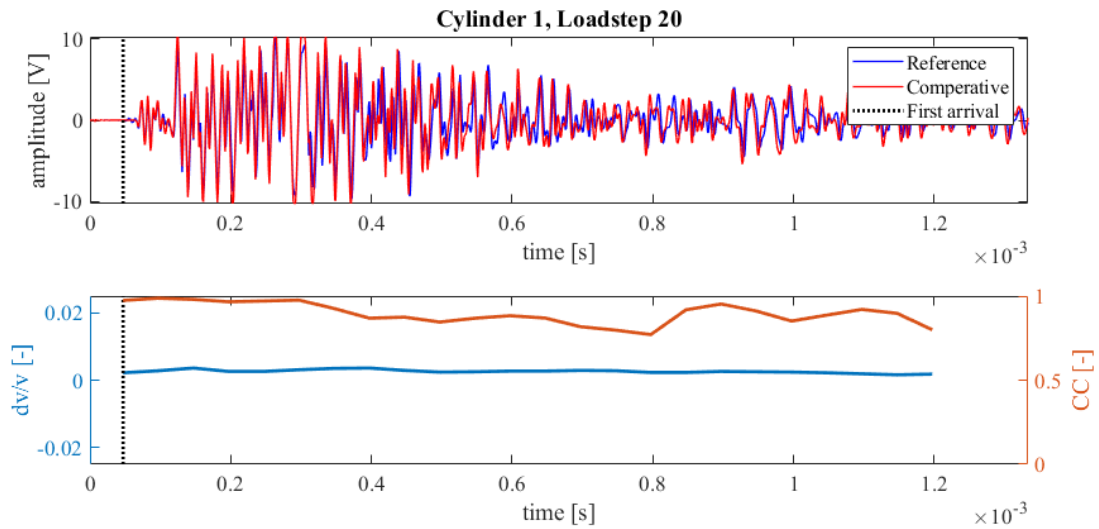


Figure 402: Wave signals of Load step 19 (blue) and Load step 20 (red) of concrete compression test Cylinder 1 (top),  $dv/v$  (blue) and CC (orange) results from CWI over the signal travel time divided in stretching windows (bottom)

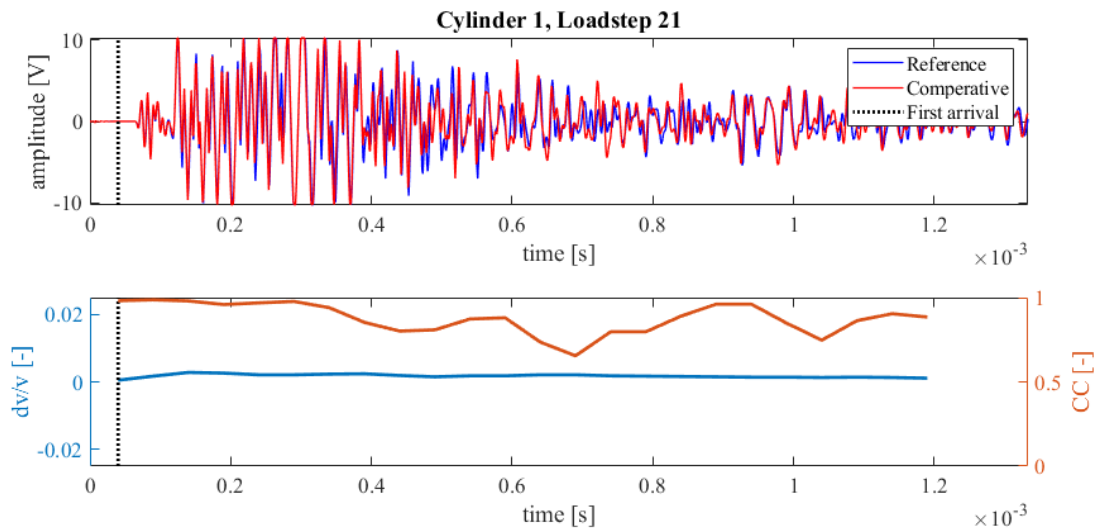


Figure 403: Wave signals of Load step 20 (blue) and Load step 21 (red) of concrete compression test Cylinder 1 (top),  $dv/v$  (blue) and CC (orange) results from CWI over the signal travel time divided in stretching windows (bottom)

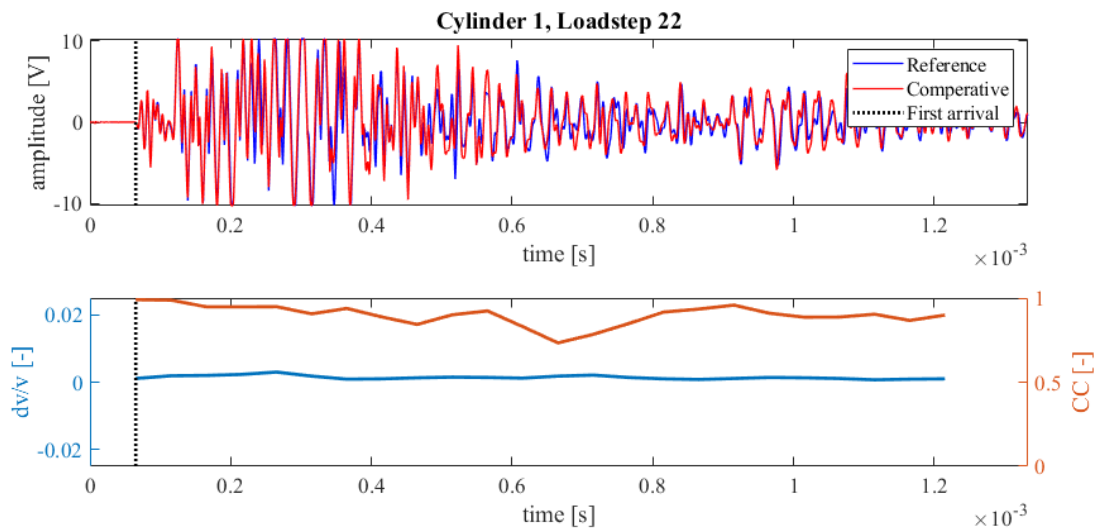


Figure 404: Wave signals of Load step 21 (blue) and Load step 22 (red) of concrete compression test Cylinder 1 (top),  $dv/v$  (blue) and CC (orange) results from CWI over the signal travel time divided in stretching windows (bottom)

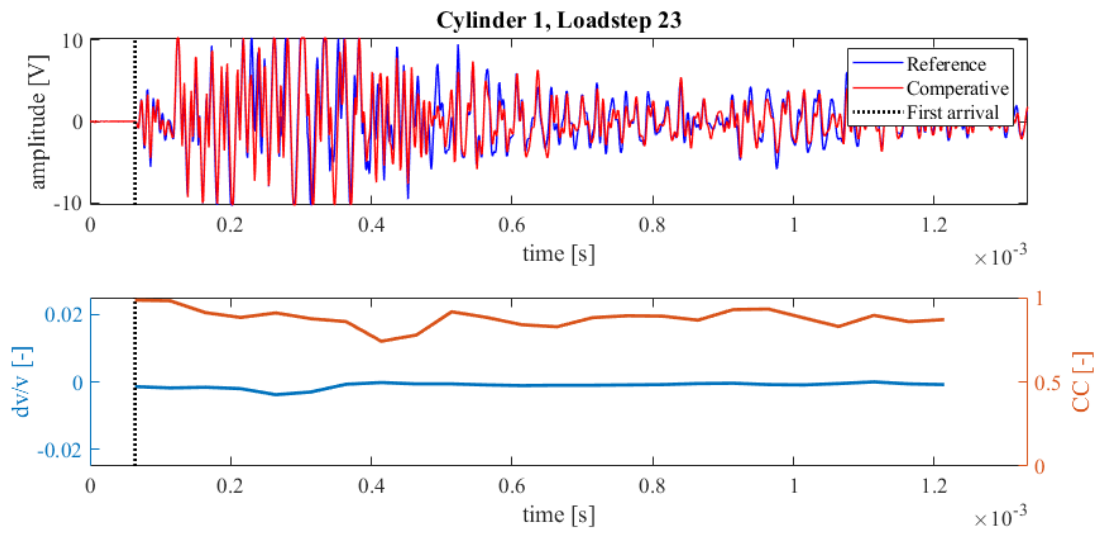


Figure 405: Wave signals of Load step 22 (blue) and Load step 23 (red) of concrete compression test Cylinder 1 (top),  $dv/v$  (blue) and CC (orange) results from CWI over the signal travel time divided in stretching windows (bottom)

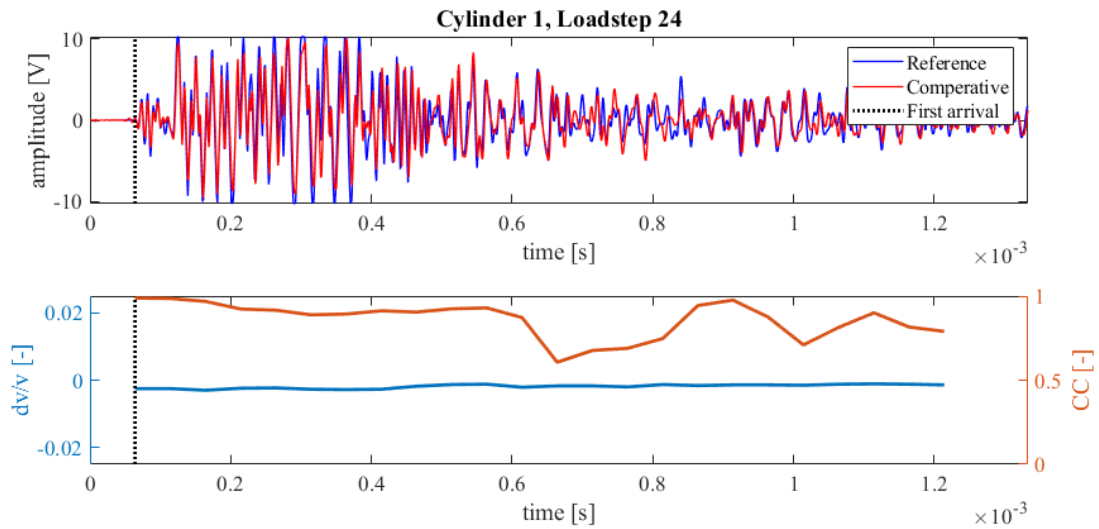


Figure 406: Wave signals of Load step 23 (blue) and Load step 24 (red) of concrete compression test Cylinder 1 (top),  $dv/v$  (blue) and CC (orange) results from CWI over the signal travel time divided in stretching windows (bottom)

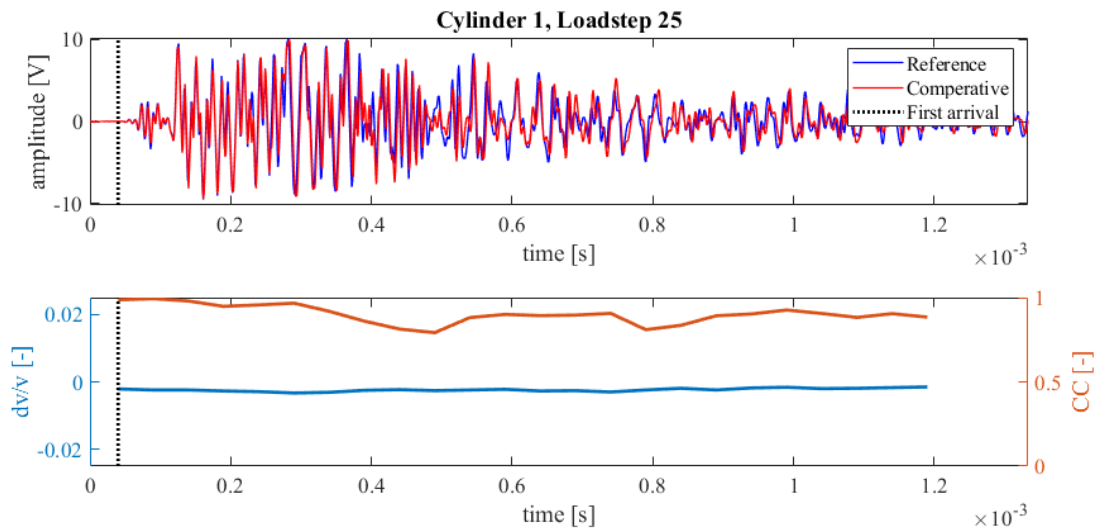


Figure 407: Wave signals of Load step 24 (blue) and Load step 25 (red) of concrete compression test Cylinder 1 (top),  $dv/v$  (blue) and CC (orange) results from CWI over the signal travel time divided in stretching windows (bottom)

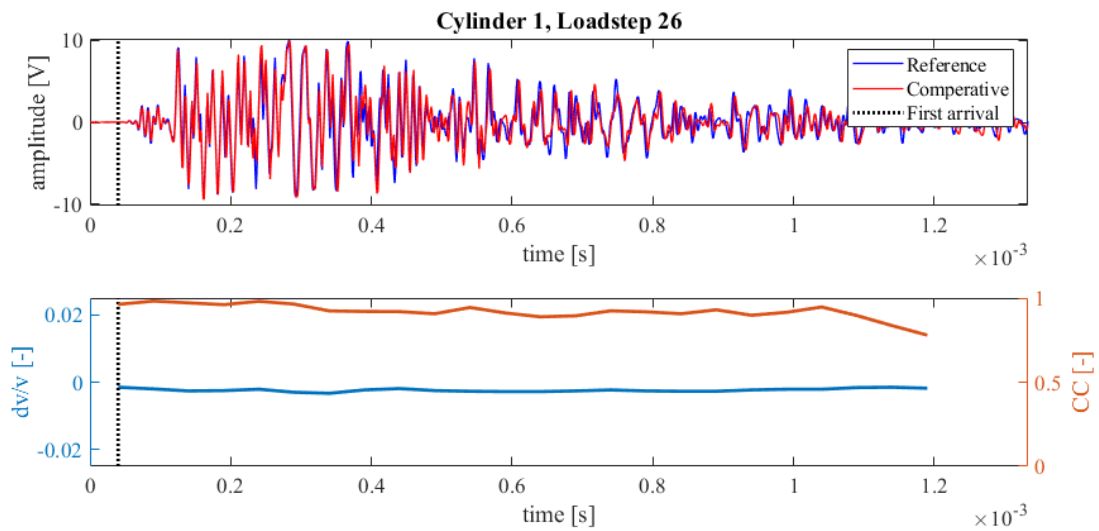


Figure 408: Wave signals of Load step 25 (blue) and Load step 26 (red) of concrete compression test Cylinder 1 (top),  $dv/v$  (blue) and CC (orange) results from CWI over the signal travel time divided in stretching windows (bottom)

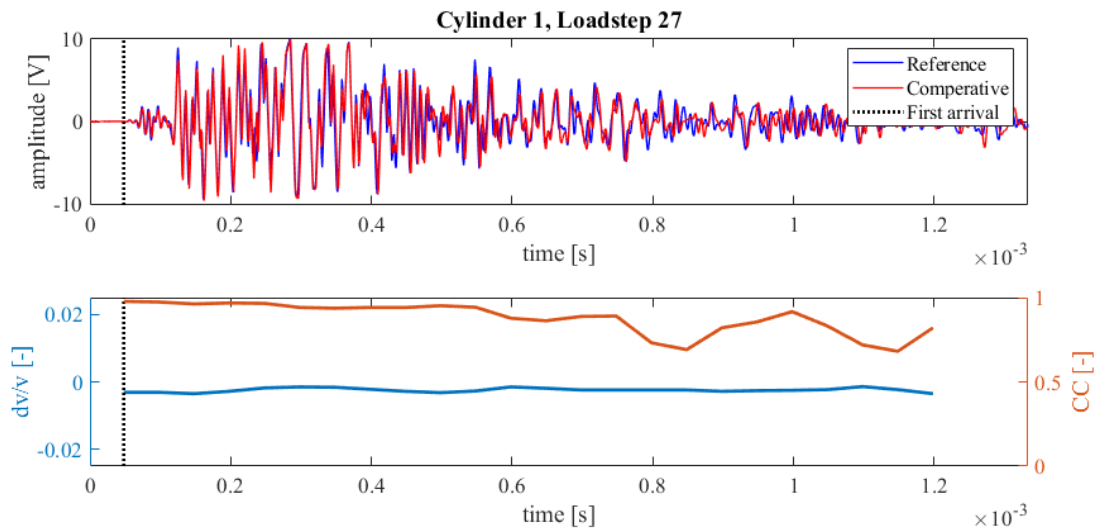


Figure 409: Wave signals of Load step 26 (blue) and Load step 27 (red) of concrete compression test Cylinder 1 (top),  $dv/v$  (blue) and CC (orange) results from CWI over the signal travel time divided in stretching windows (bottom)

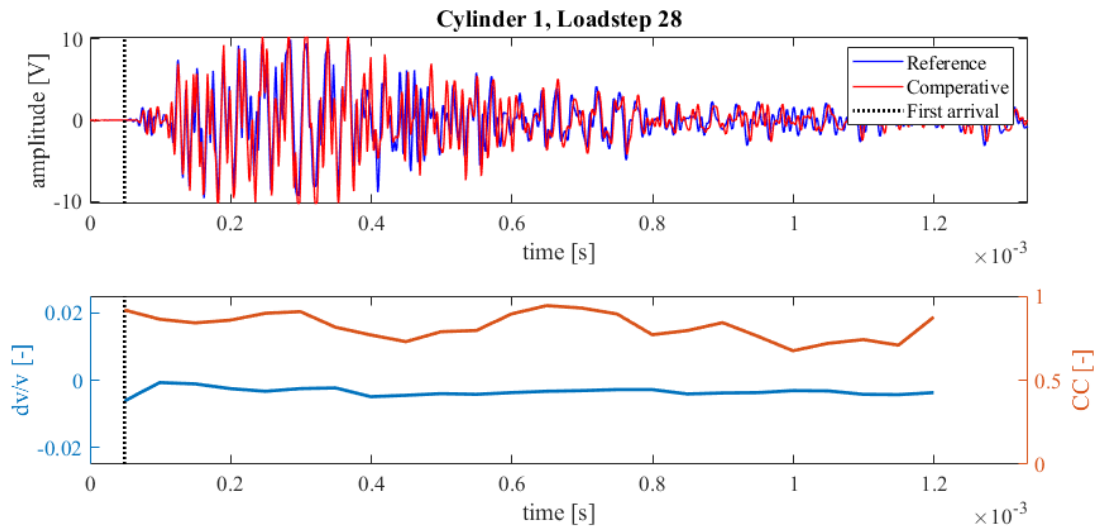


Figure 410: Wave signals of Load step 27 (blue) and Load step 28 (red) of concrete compression test Cylinder 1 (top),  $dv/v$  (blue) and CC (orange) results from CWI over the signal travel time divided in stretching windows (bottom)

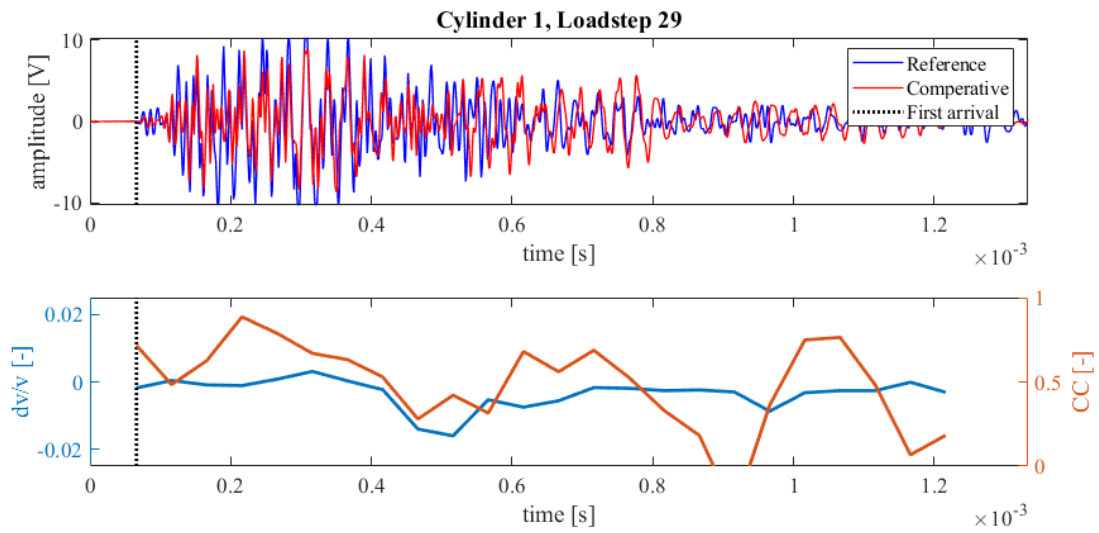


Figure 411: Wave signals of Load step 28 (blue) and Load step 29 (red) of concrete compression test Cylinder 1 (top),  $dv/v$  (blue) and CC (orange) results from CWI over the signal travel time divided in stretching windows (bottom)

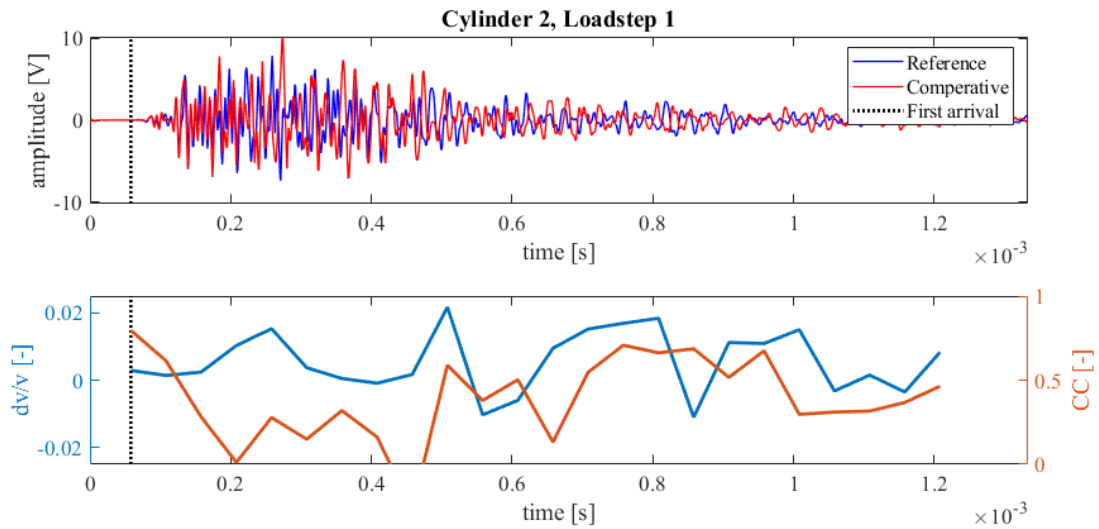


Figure 412: Wave signals of No load (blue) and Load step 1 (red) of concrete compression test Cylinder 2 (top),  $dv/v$  (blue) and CC (orange) results from CWI over the signal travel time divided in stretching windows (bottom)

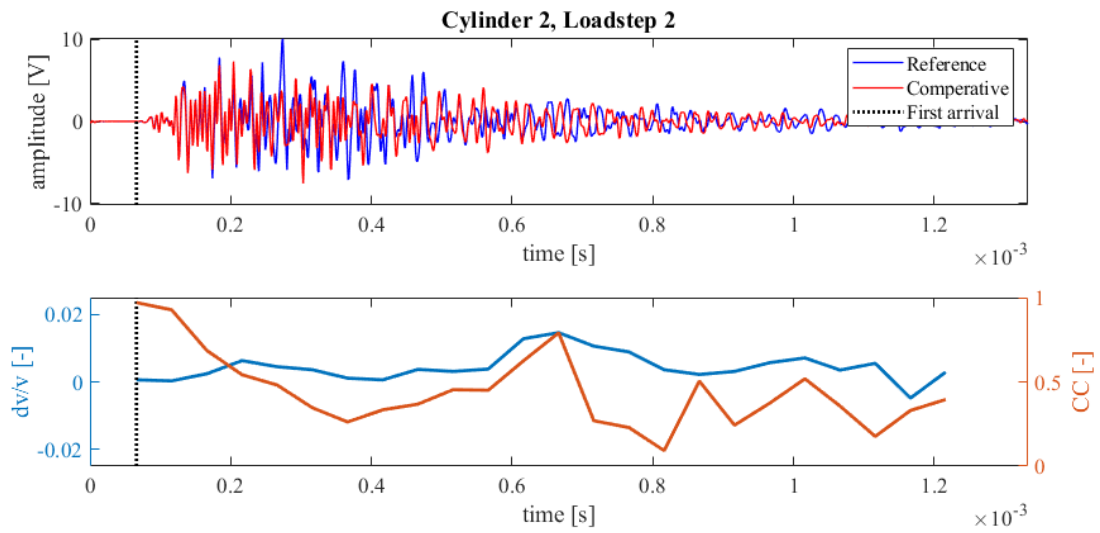


Figure 413: Wave signals of Load step 1 (blue) and Load step 2 (red) of concrete compression test Cylinder 2 (top),  $dv/v$  (blue) and CC (orange) results from CWI over the signal travel time divided in stretching windows (bottom)

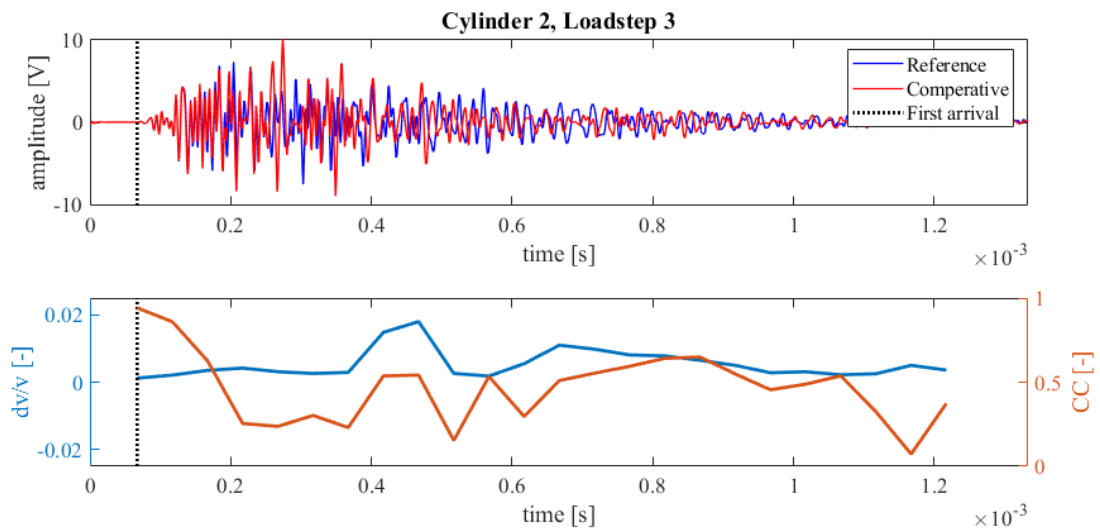


Figure 414: Wave signals of Load step 2 (blue) and Load step 3 (red) of concrete compression test Cylinder 2 (top),  $dv/v$  (blue) and CC (orange) results from CWI over the signal travel time divided in stretching windows (bottom)

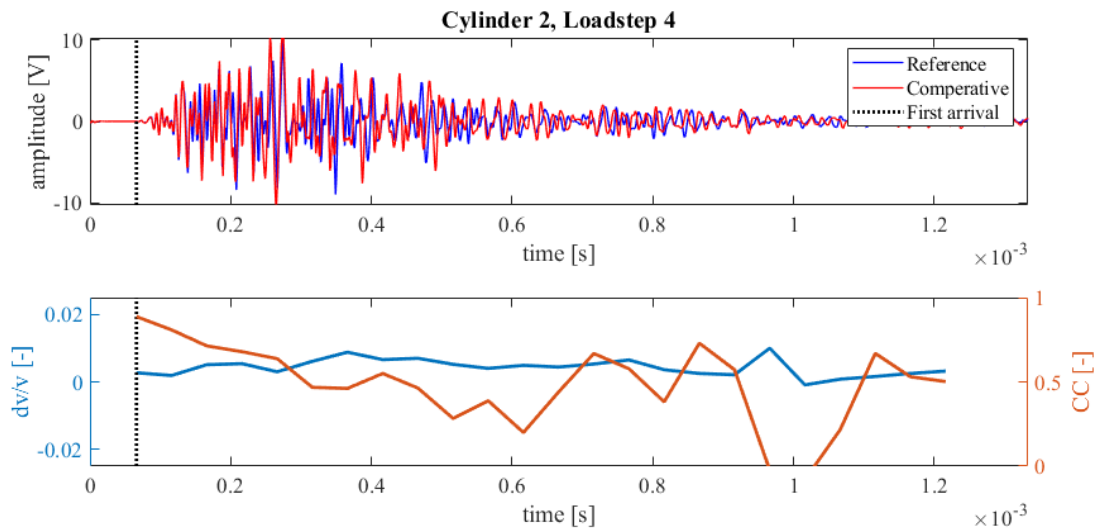


Figure 415: Wave signals of Load step 3 (blue) and Load step 4 (red) of concrete compression test Cylinder 2 (top),  $dv/v$  (blue) and CC (orange) results from CWI over the signal travel time divided in stretching windows (bottom)

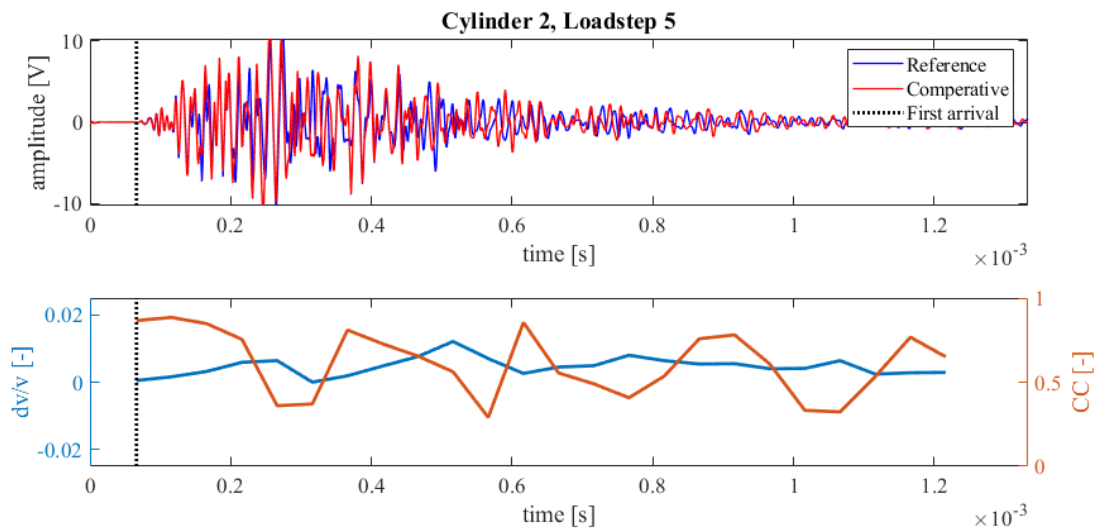
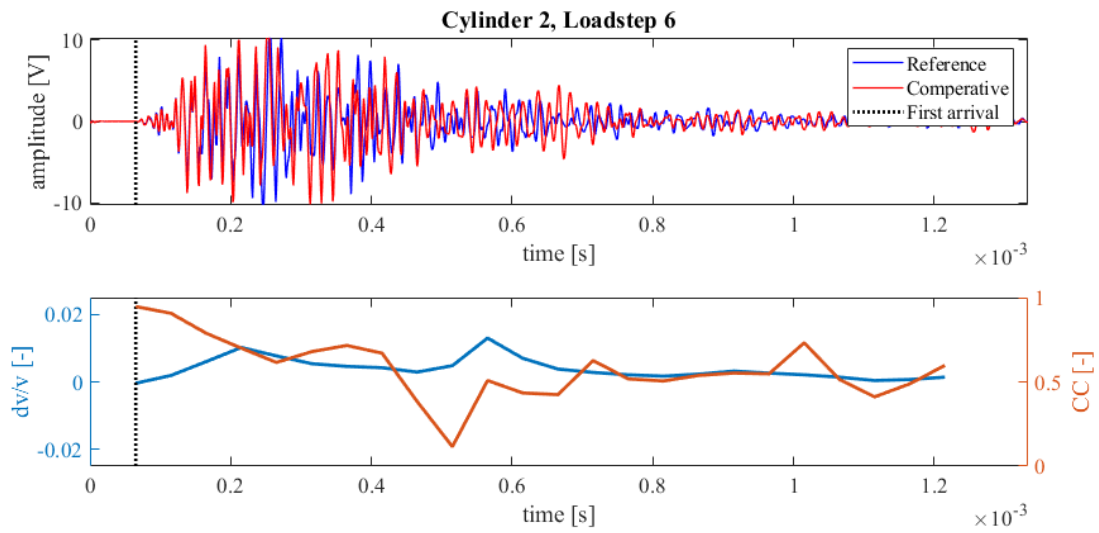
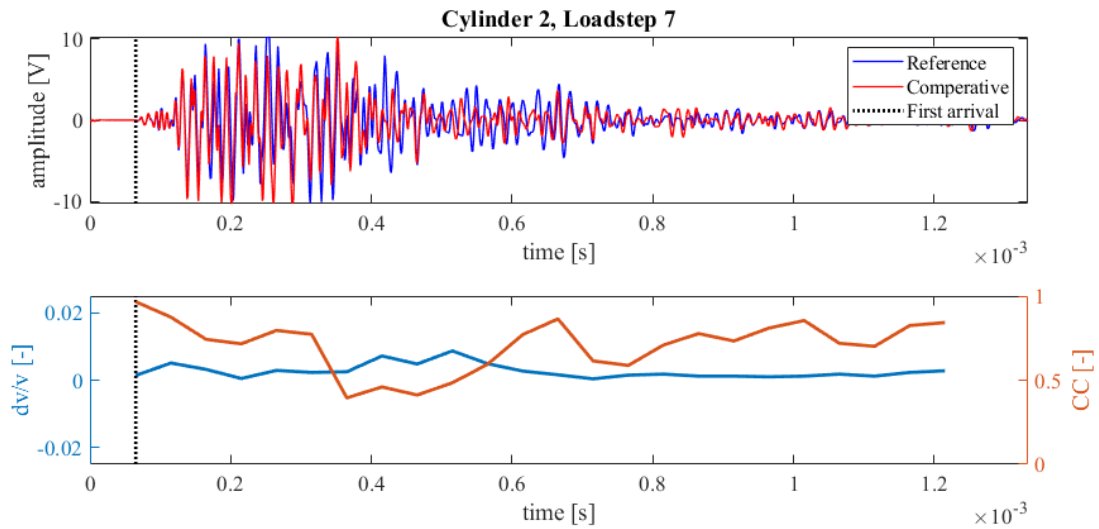


Figure 416: Wave signals of Load step 4 (blue) and Load step 5 (red) of concrete compression test Cylinder 2 (top),  $dv/v$  (blue) and CC (orange) results from CWI over the signal travel time divided in stretching windows (bottom)



**Figure 417: Wave signals of Load step 5 (blue) and Load step 6 (red) of concrete compression test Cylinder 2 (top),  $dv/v$  (blue) and CC (orange) results from CWI over the signal travel time divided in stretching windows (bottom)**



**Figure 418: Wave signals of Load step 6 (blue) and Load step 7 (red) of concrete compression test Cylinder 2 (top),  $dv/v$  (blue) and CC (orange) results from CWI over the signal travel time divided in stretching windows (bottom)**

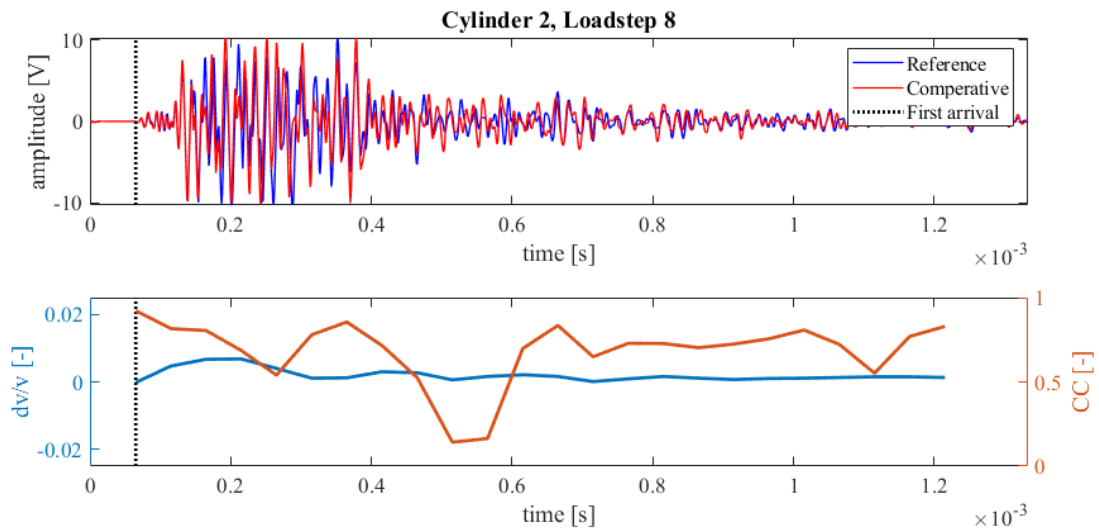


**Figure 419: Wave signals of Load step 7 (blue) and Load step 8 (red) of concrete compression test Cylinder 2 (top),  $dv/v$  (blue) and CC (orange) results from CWI over the signal travel time divided in stretching windows (bottom)**

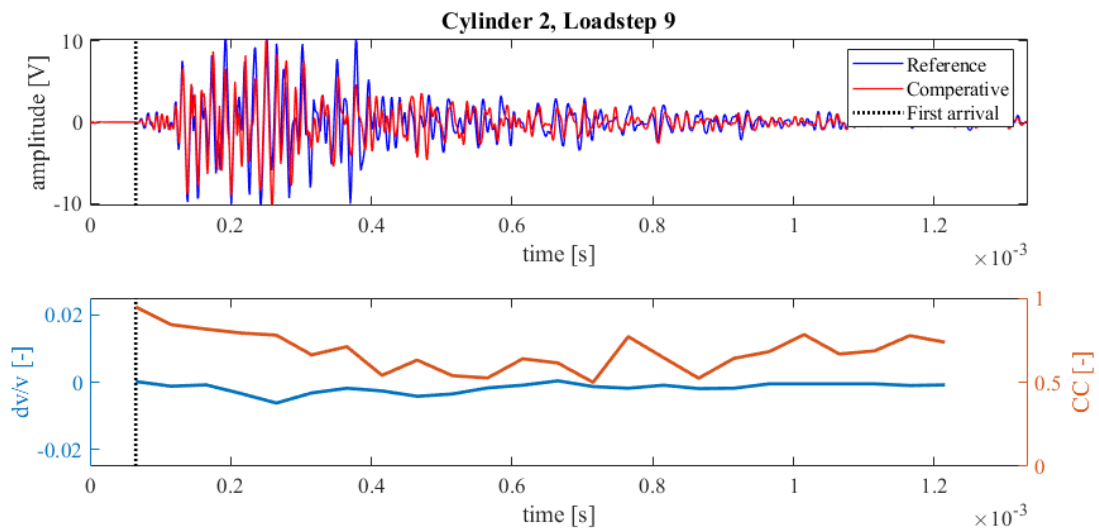


**Figure 420: Wave signals of Load step 8 (blue) and Load step 9 (red) of concrete compression test Cylinder 2 (top),  $dv/v$  (blue) and CC (orange) results from CWI over the signal travel time divided in stretching windows (bottom)**

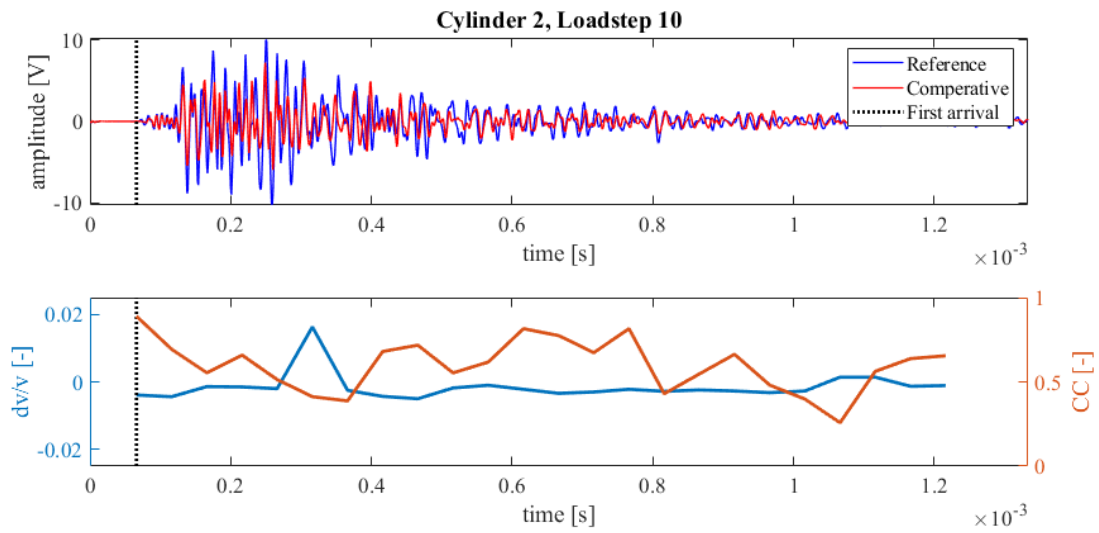


Figure 421: Wave signals of Load step 9 (blue) and Load step 10 (red) of concrete compression test Cylinder 2 (top),  $dv/v$  (blue) and CC (orange) results from CWI over the signal travel time divided in stretching windows (bottom)

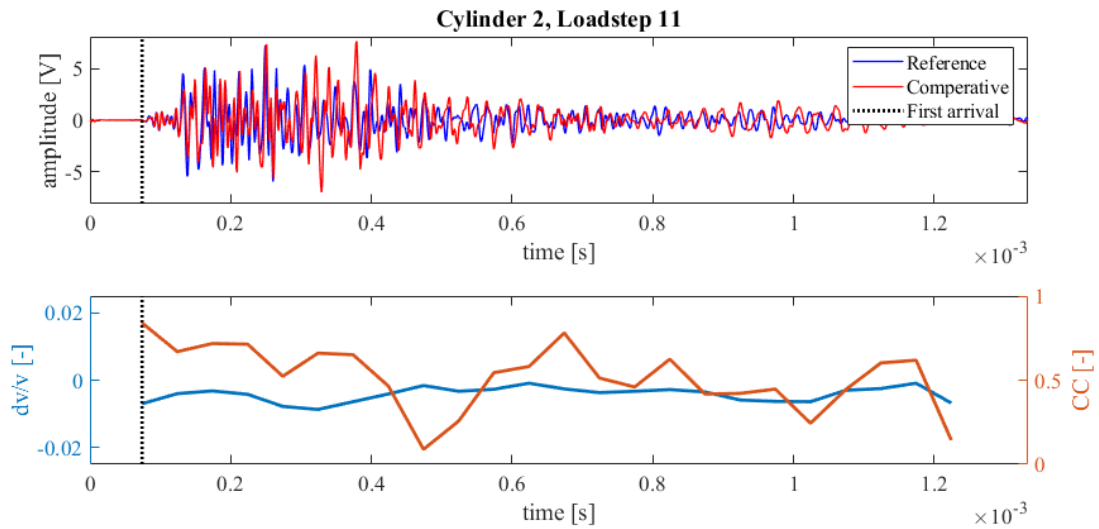


Figure 422: Wave signals of Load step 10 (blue) and Load step 11 (red) of concrete compression test Cylinder 2 (top),  $dv/v$  (blue) and CC (orange) results from CWI over the signal travel time divided in stretching windows (bottom)

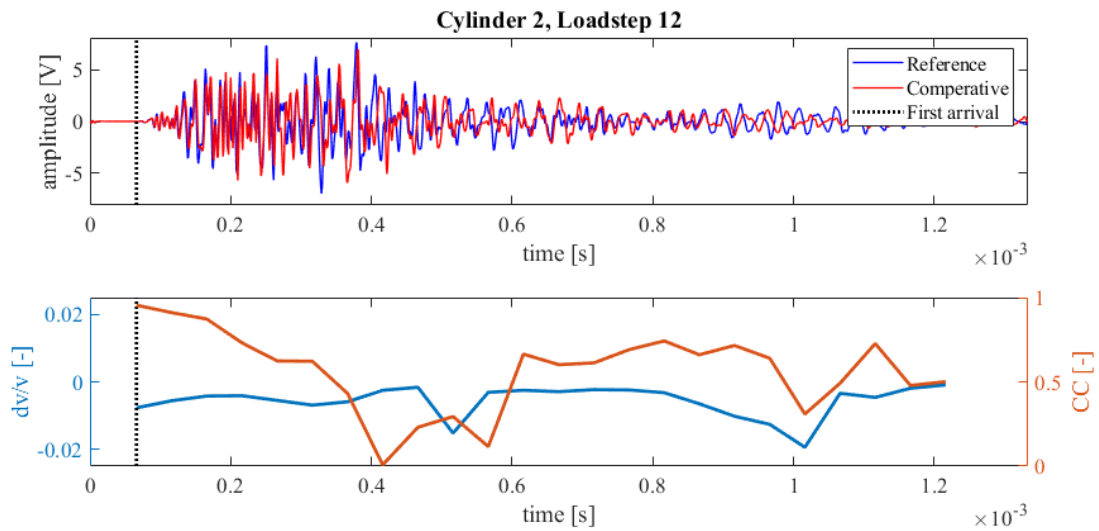


Figure 423: Wave signals of Load step 11 (blue) and Load step 12 (red) of concrete compression test Cylinder 2 (top),  $dv/v$  (blue) and CC (orange) results from CWI over the signal travel time divided in stretching windows (bottom)

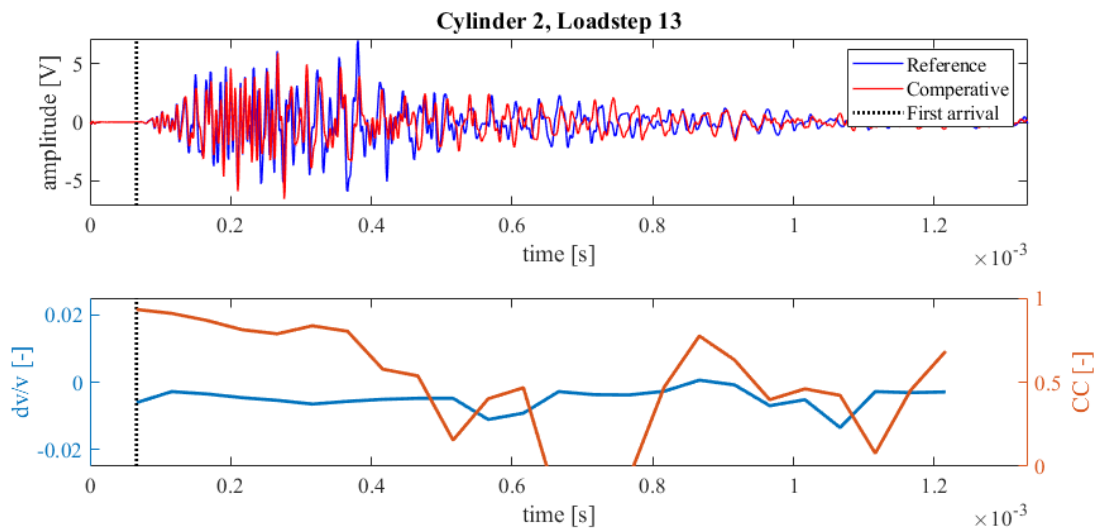


Figure 424: Wave signals of Load step 12 (blue) and Load step 13 (red) of concrete compression test Cylinder 2 (top),  $dv/v$  (blue) and CC (orange) results from CWI over the signal travel time divided in stretching windows (bottom)

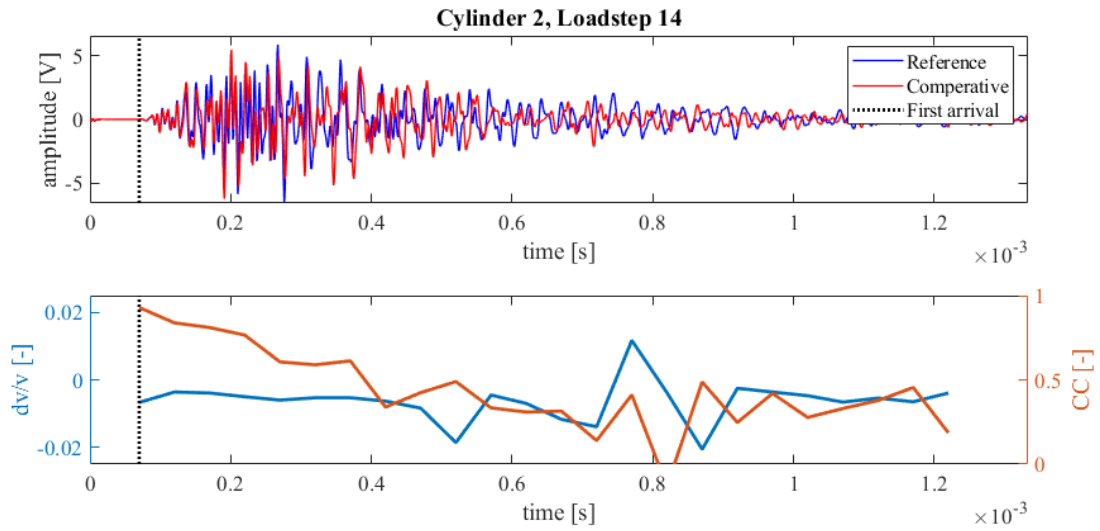


Figure 425: Wave signals of Load step 13 (blue) and Load step 14 (red) of concrete compression test Cylinder 2 (top),  $dv/v$  (blue) and CC (orange) results from CWI over the signal travel time divided in stretching windows (bottom)

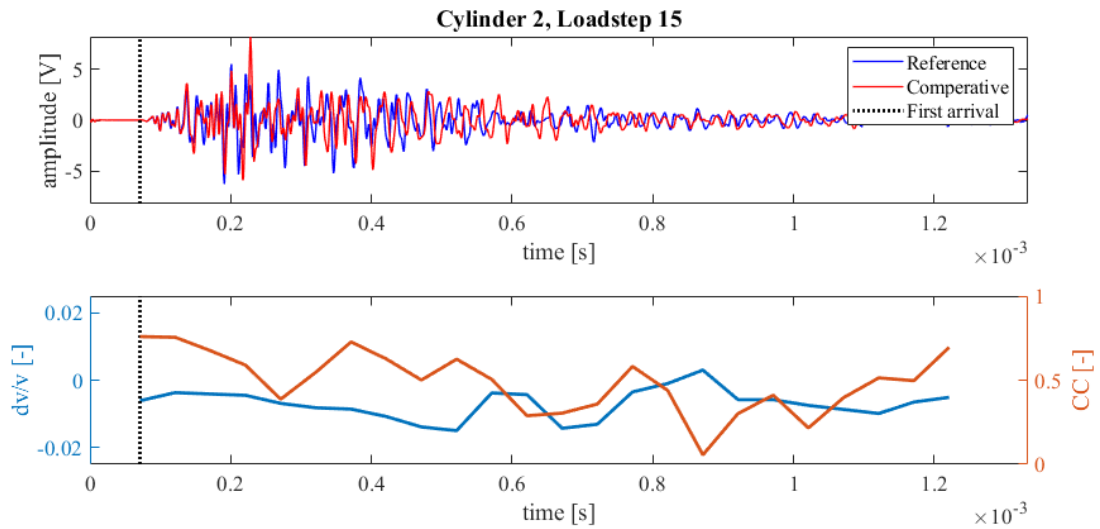


Figure 426: Wave signals of Load step 14 (blue) and Load step 15 (red) of concrete compression test Cylinder 2 (top),  $dv/v$  (blue) and CC (orange) results from CWI over the signal travel time divided in stretching windows (bottom)

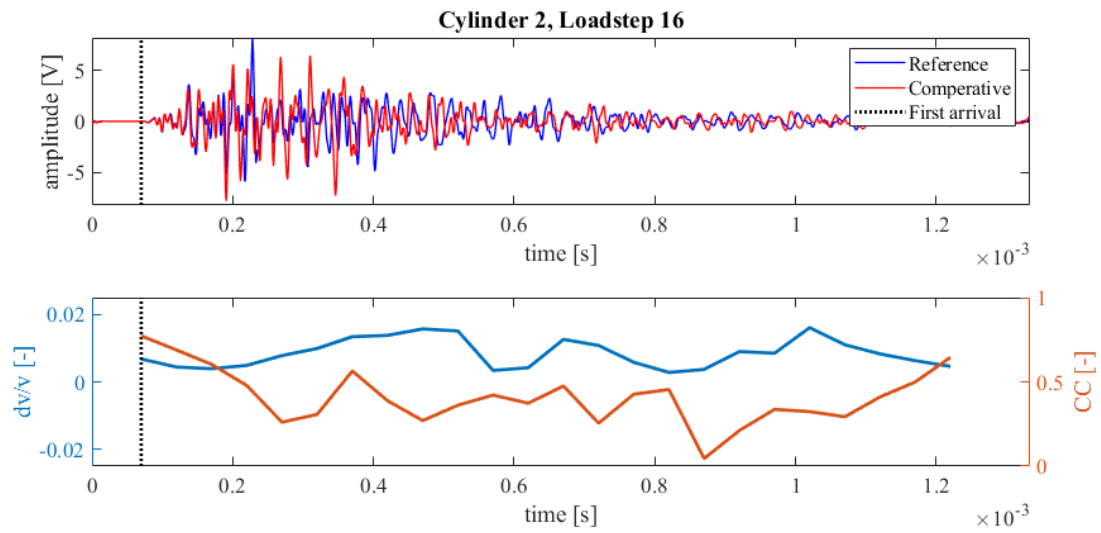


Figure 427: Wave signals of Load step 15 (blue) and Load step 16 (red) of concrete compression test Cylinder 2 (top),  $dv/v$  (blue) and CC (orange) results from CWI over the signal travel time divided in stretching windows (bottom)

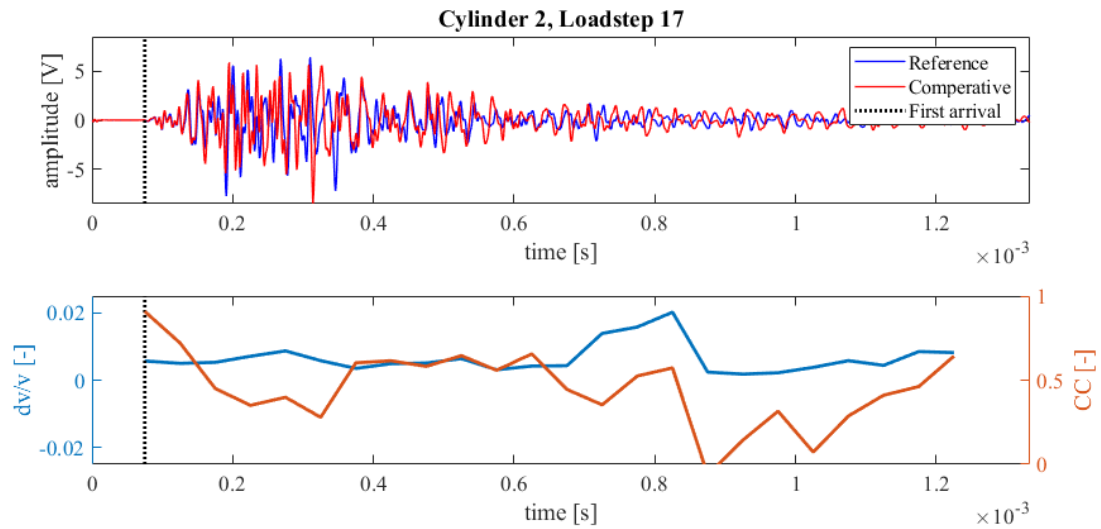


Figure 428: Wave signals of Load step 16 (blue) and Load step 17 (red) of concrete compression test Cylinder 2 (top),  $dv/v$  (blue) and CC (orange) results from CWI over the signal travel time divided in stretching windows (bottom)

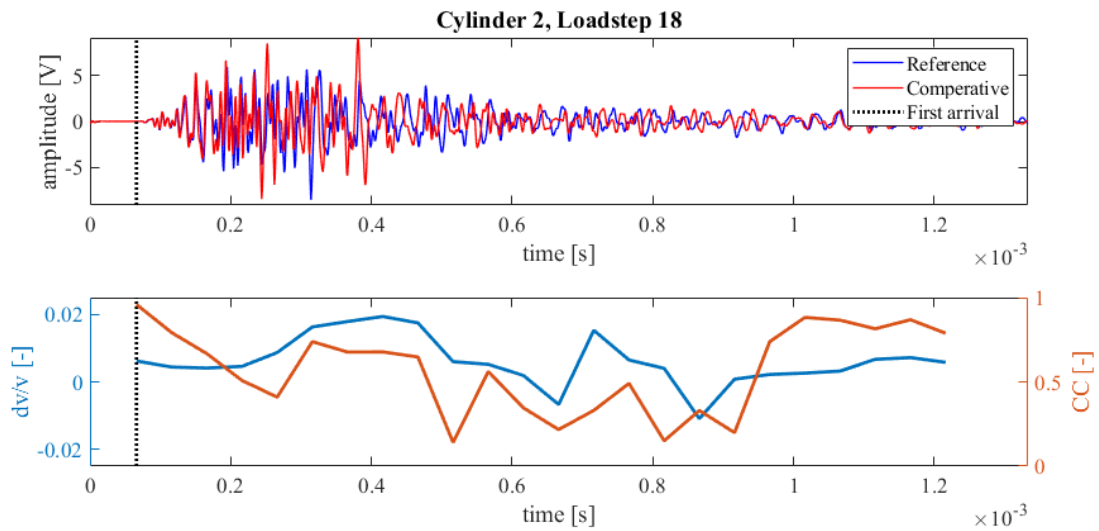


Figure 429: Wave signals of Load step 17 (blue) and Load step 18 (red) of concrete compression test Cylinder 2 (top),  $dv/v$  (blue) and CC (orange) results from CWI over the signal travel time divided in stretching windows (bottom)

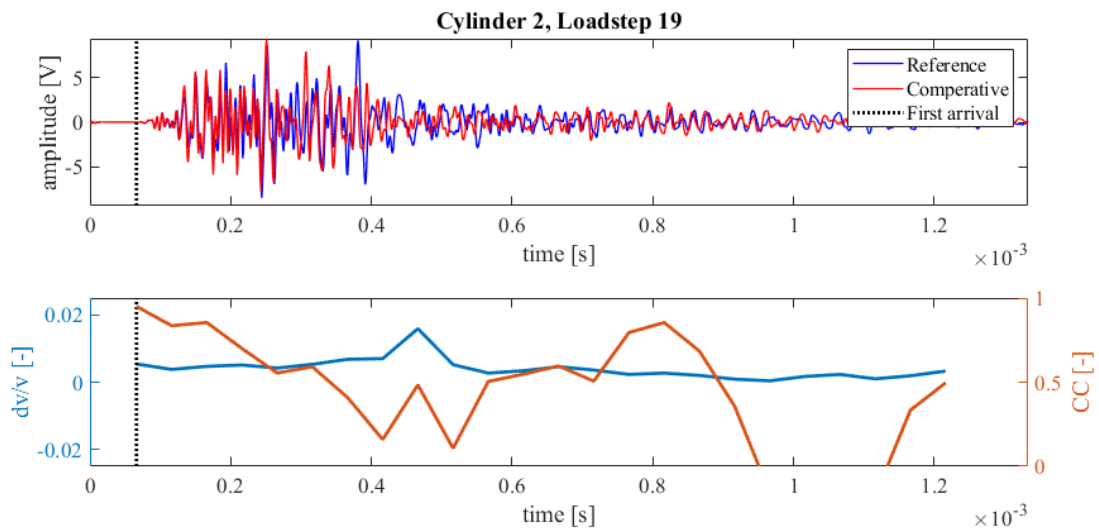


Figure 430: Wave signals of Load step 18 (blue) and Load step 19 (red) of concrete compression test Cylinder 2 (top),  $dv/v$  (blue) and CC (orange) results from CWI over the signal travel time divided in stretching windows (bottom)

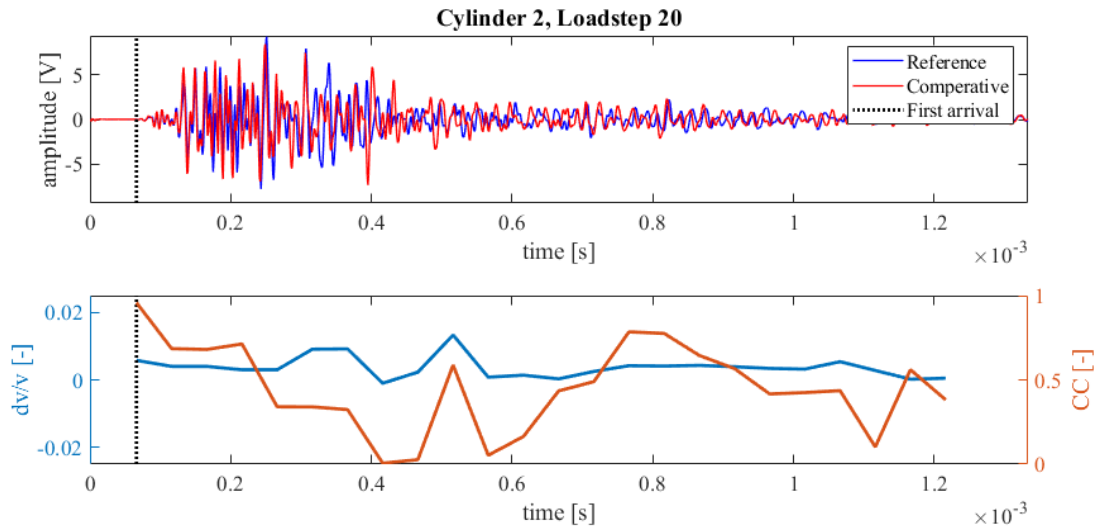


Figure 431: Wave signals of Load step 19 (blue) and Load step 20 (red) of concrete compression test Cylinder 2 (top),  $dv/v$  (blue) and CC (orange) results from CWI over the signal travel time divided in stretching windows (bottom)

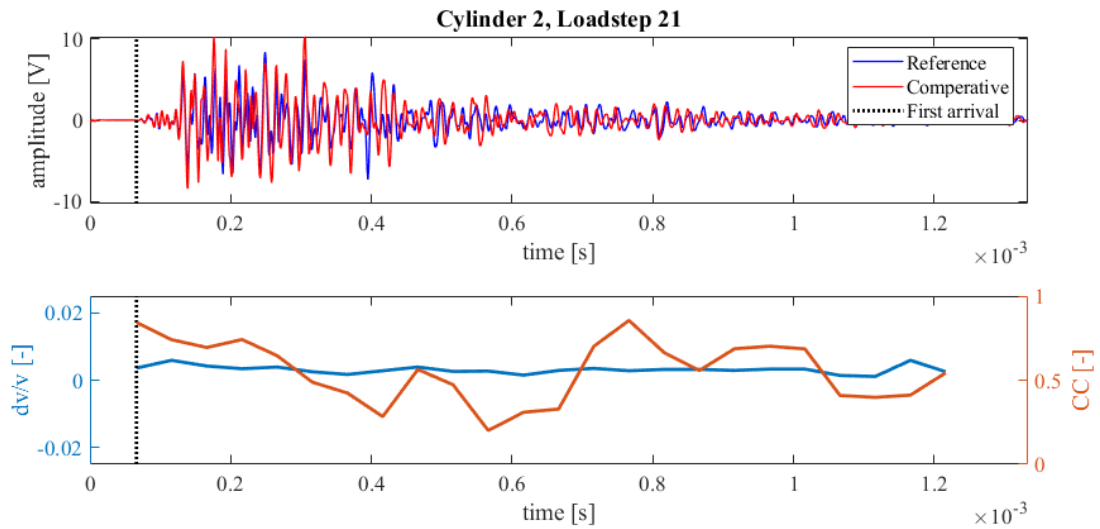


Figure 432: Wave signals of Load step 20 (blue) and Load step 21 (red) of concrete compression test Cylinder 2 (top),  $dv/v$  (blue) and CC (orange) results from CWI over the signal travel time divided in stretching windows (bottom)

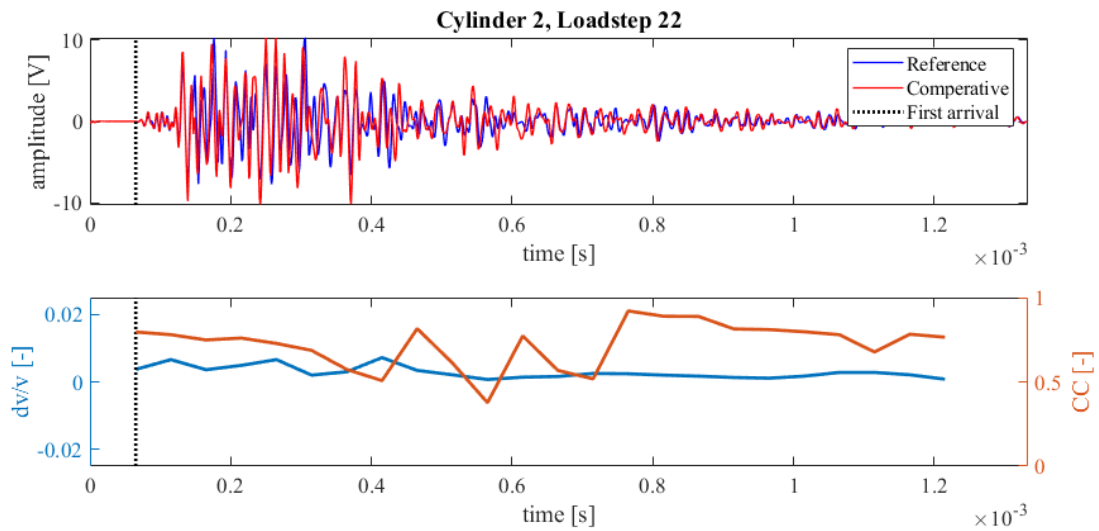


Figure 433: Wave signals of Load step 21 (blue) and Load step 22 (red) of concrete compression test Cylinder 2 (top),  $dv/v$  (blue) and CC (orange) results from CWI over the signal travel time divided in stretching windows (bottom)

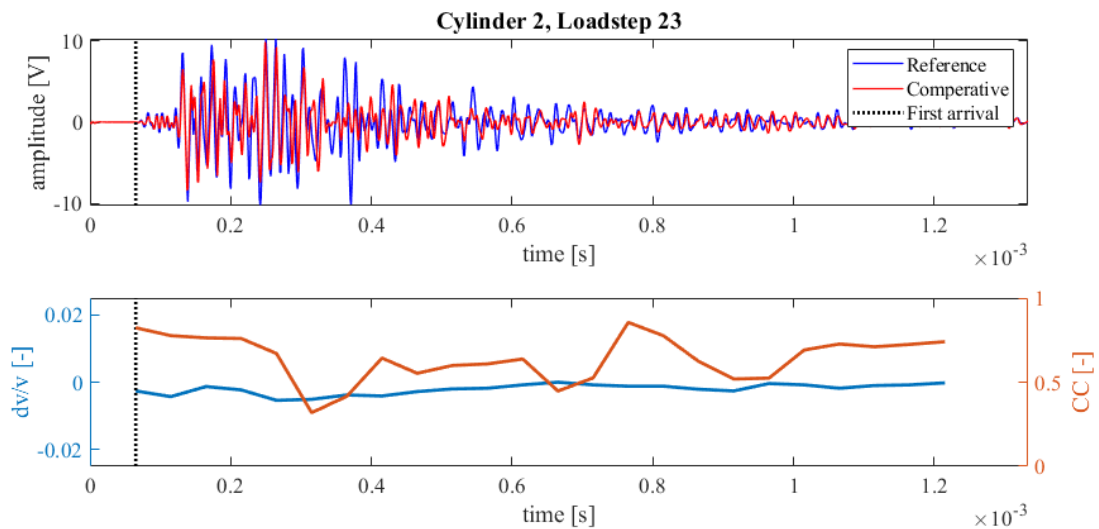


Figure 434: Wave signals of Load step 22 (blue) and Load step 23 (red) of concrete compression test Cylinder 2 (top),  $dv/v$  (blue) and CC (orange) results from CWI over the signal travel time divided in stretching windows (bottom)

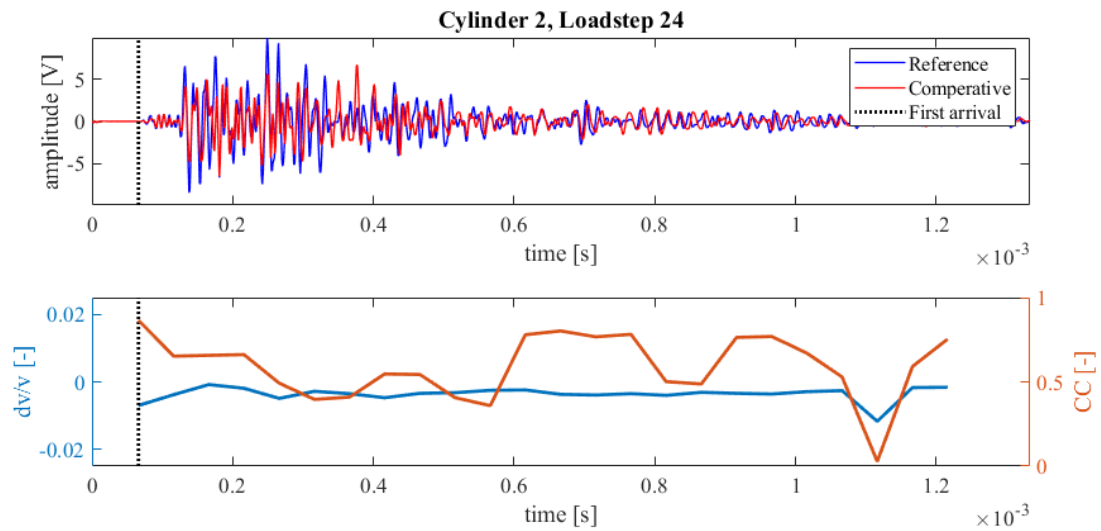


Figure 435: Wave signals of Load step 23 (blue) and Load step 24 (red) of concrete compression test Cylinder 2 (top),  $dv/v$  (blue) and CC (orange) results from CWI over the signal travel time divided in stretching windows (bottom)

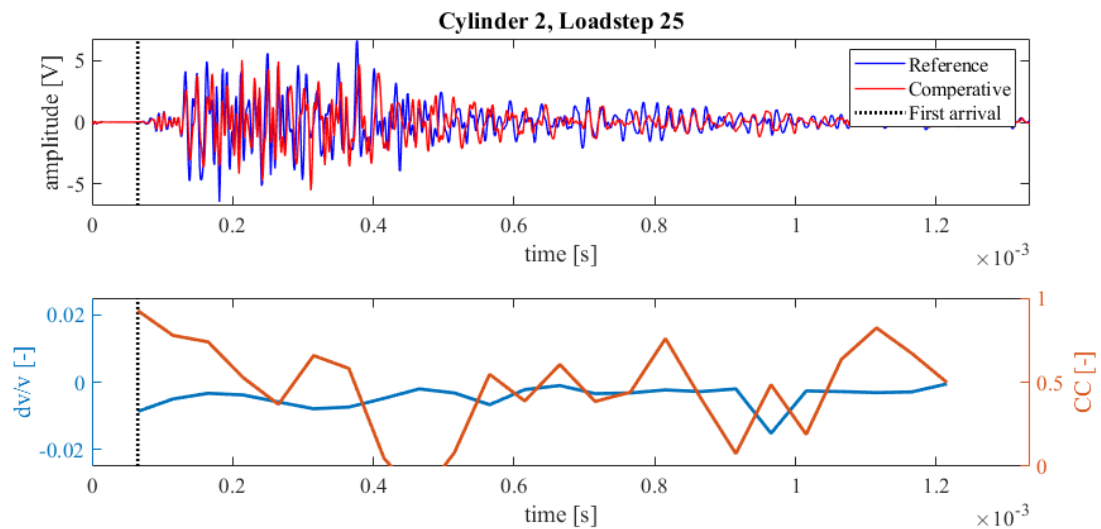


Figure 436: Wave signals of Load step 24 (blue) and Load step 25 (red) of concrete compression test Cylinder 2 (top),  $dv/v$  (blue) and CC (orange) results from CWI over the signal travel time divided in stretching windows (bottom)

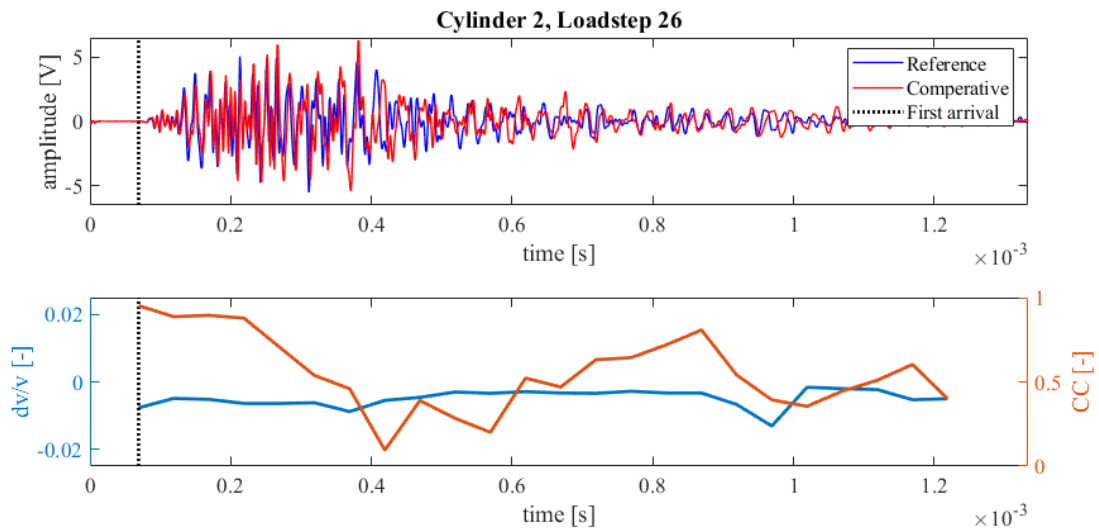


Figure 437: Wave signals of Load step 25 (blue) and Load step 26 (red) of concrete compression test Cylinder 2 (top),  $dv/v$  (blue) and CC (orange) results from CWI over the signal travel time divided in stretching windows (bottom)

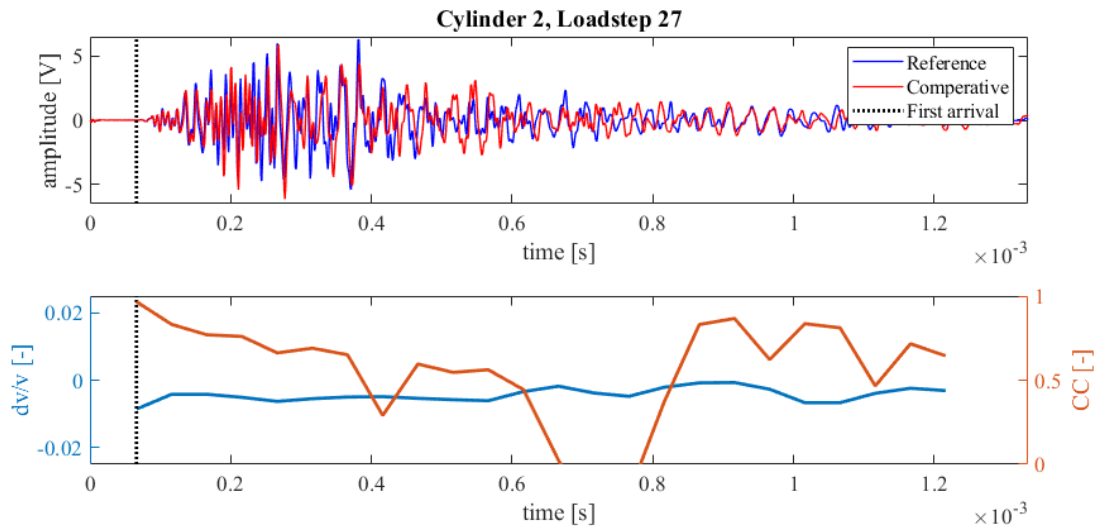


Figure 438: Wave signals of Load step 26 (blue) and Load step 27 (red) of concrete compression test Cylinder 2 (top),  $dv/v$  (blue) and CC (orange) results from CWI over the signal travel time divided in stretching windows (bottom)

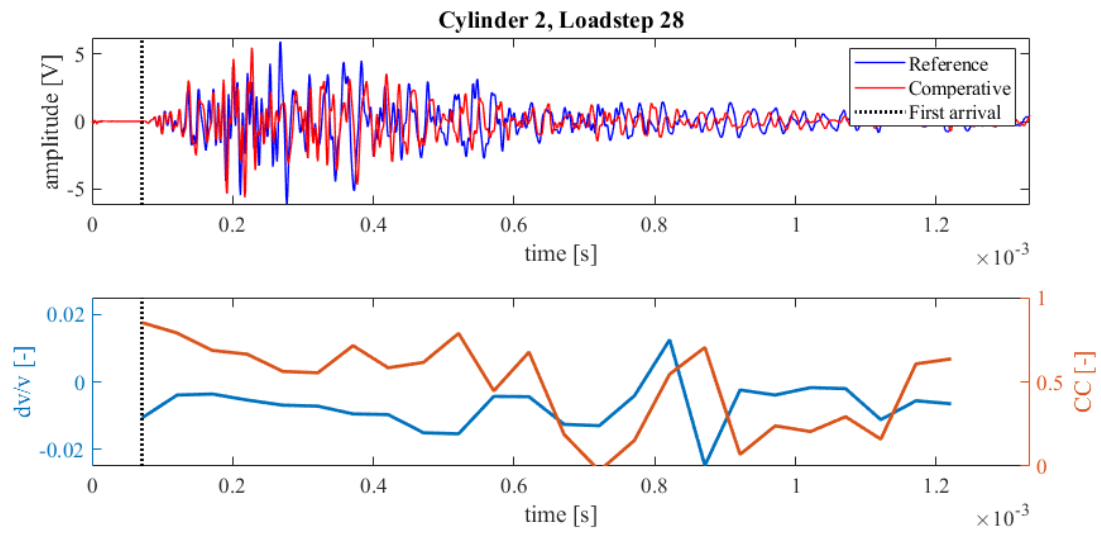


Figure 439: Wave signals of Load step 27 (blue) and Load step 28 (red) of concrete compression test Cylinder 2 (top),  $dv/v$  (blue) and CC (orange) results from CWI over the signal travel time divided in stretching windows (bottom)

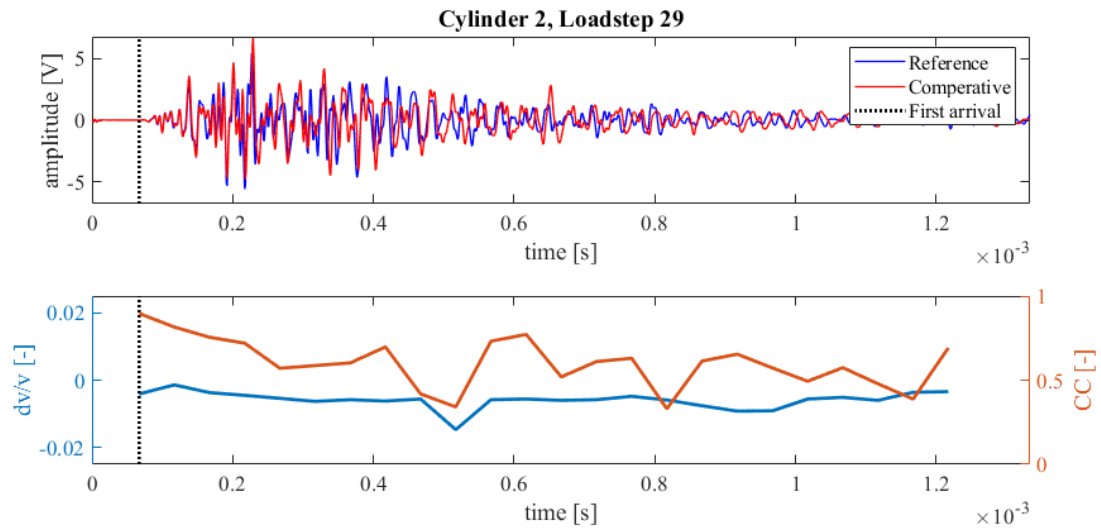


Figure 440: Wave signals of Load step 28 (blue) and Load step 29 (red) of concrete compression test Cylinder 2 (top),  $dv/v$  (blue) and CC (orange) results from CWI over the signal travel time divided in stretching windows (bottom)

## G. CWI results of geopolymer creep test

The effects of creep deformation on the signal's wave velocity are examined in rectangular geopolymer concrete samples with embedded SA. The samples are exposed to a constant load within a climate controlled room. The deformation of the samples is measured over several weeks and the wave signal between sensors is measured in intervals according to Table 22. Cross-correlation between measurements when the loading is applied, display some difficulties. The same occurs when several days pass in between measurements. In these instances, the  $CC$  is considerably lower in the late coda arrivals. This suggests the formation of cracks or rearrangement of the microstructure.

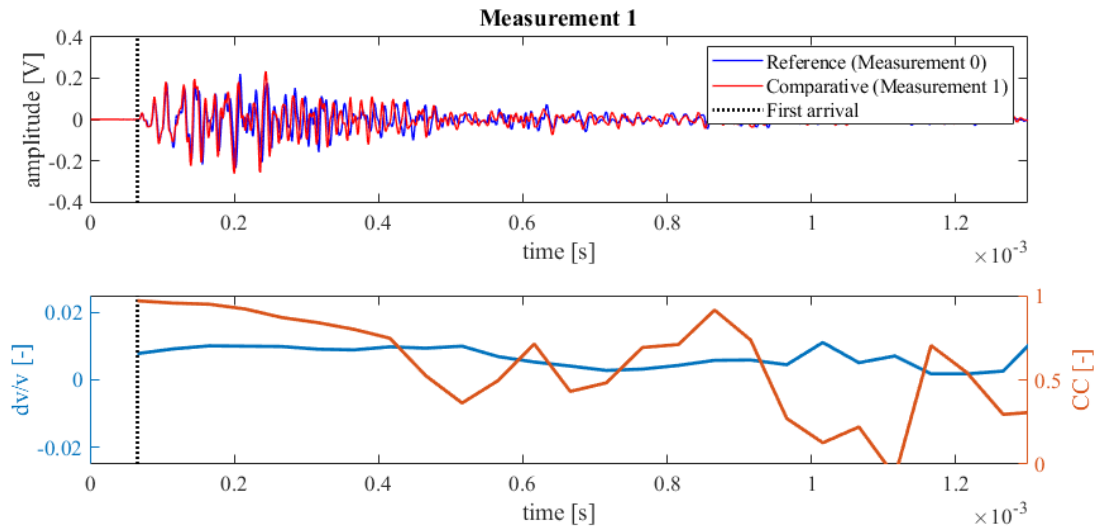


Figure 441: Wave signals of Unloaded (blue) and Measurement 1 (red) of geopolymer creep test (top),  $dv/v$  (blue) and  $CC$  (orange) results from CWI over the signal travel time divided in stretching windows (bottom)

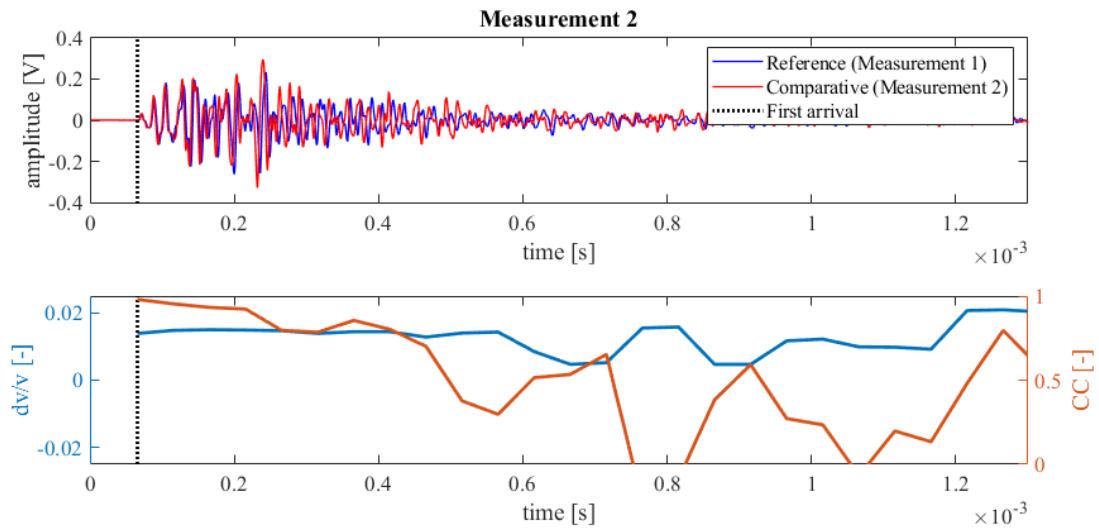


Figure 442: Wave signals of Measurement 1 (blue) and Measurement 2 (red) of geopolymer creep test (top),  $dv/v$  (blue) and  $CC$  (orange) results from CWI over the signal travel time divided in stretching windows (bottom)

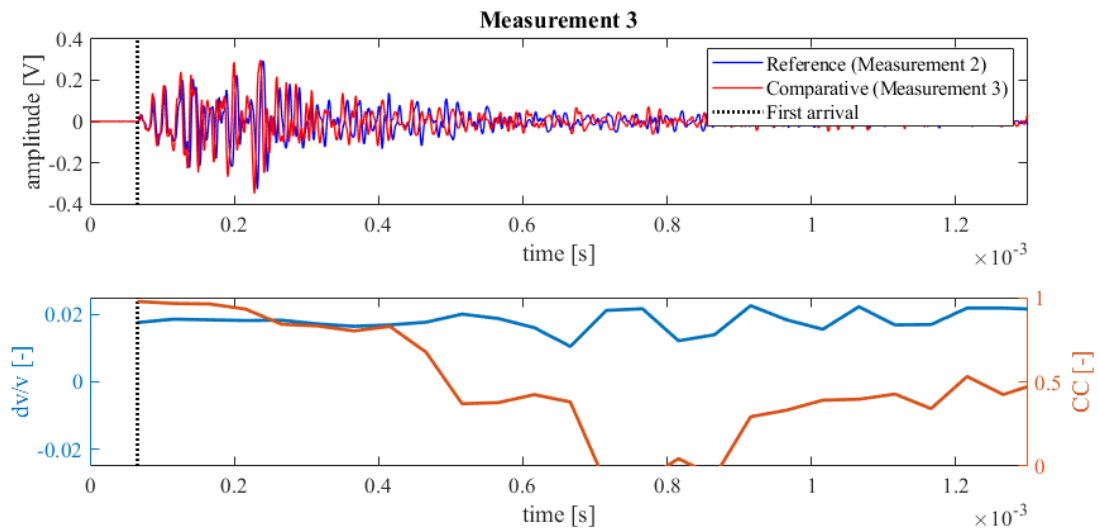


Figure 443: Wave signals of Measurement 2 (blue) and Measurement 3 (red) of geopolymer creep test (top),  $dv/v$  (blue) and CC (orange) results from CWI over the signal travel time divided in stretching windows (bottom)

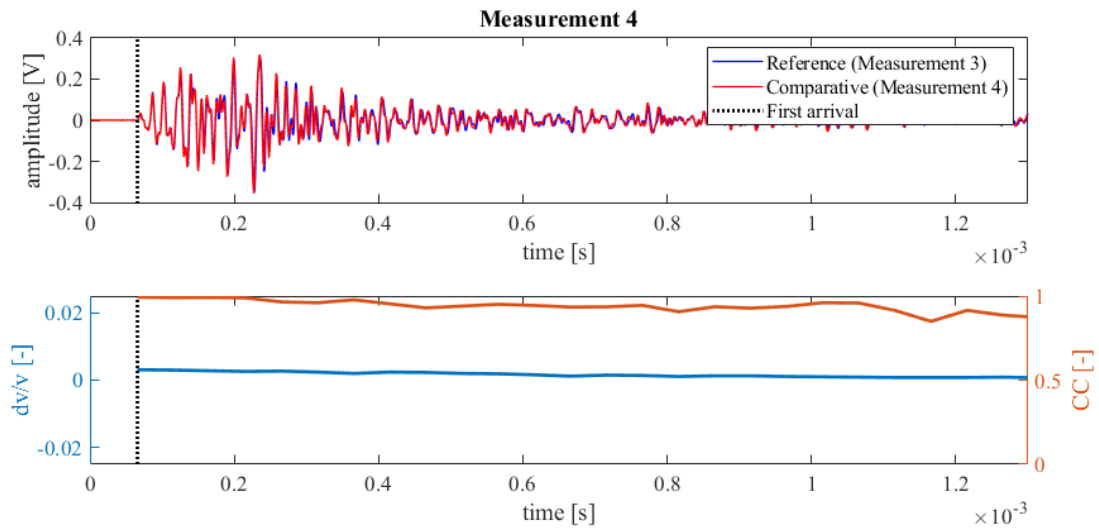


Figure 444: Wave signals of Measurement 3 (blue) and Measurement 4 (red) of geopolymer creep test (top),  $dv/v$  (blue) and CC (orange) results from CWI over the signal travel time divided in stretching windows (bottom)

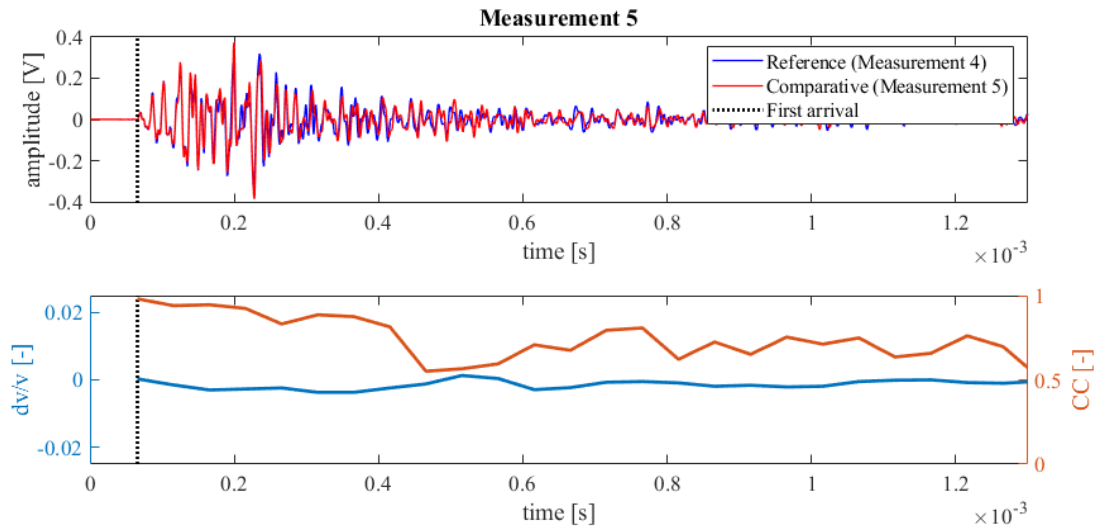


Figure 445: Wave signals of Measurement 4 (blue) and Measurement 5 (red) of geopolymer creep test (top),  $dv/v$  (blue) and  $CC$  (orange) results from CWI over the signal travel time divided in stretching windows (bottom)

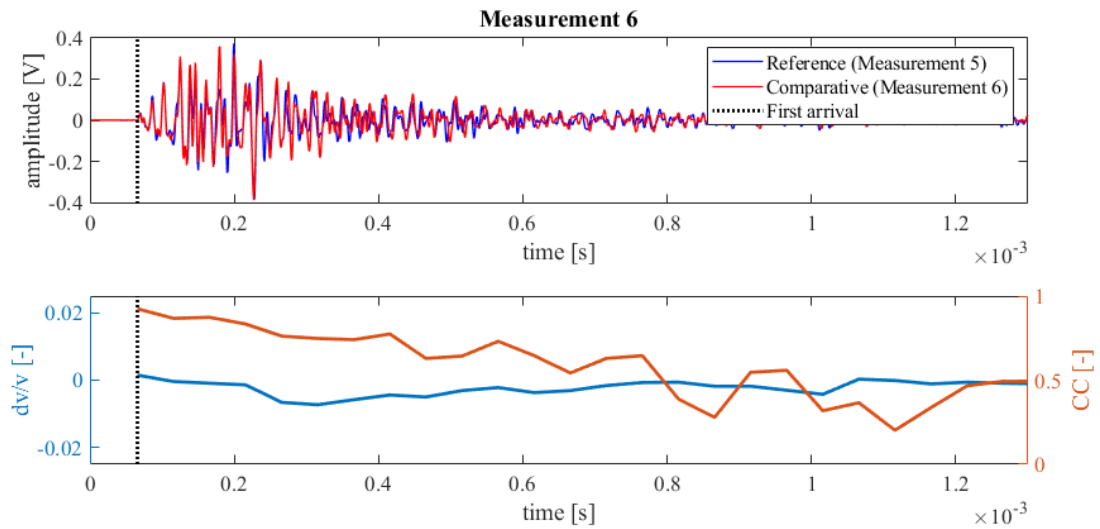


Figure 446: Wave signals of Measurement 5 (blue) and Measurement 6 (red) of geopolymer creep test (top),  $dv/v$  (blue) and  $CC$  (orange) results from CWI over the signal travel time divided in stretching windows (bottom)

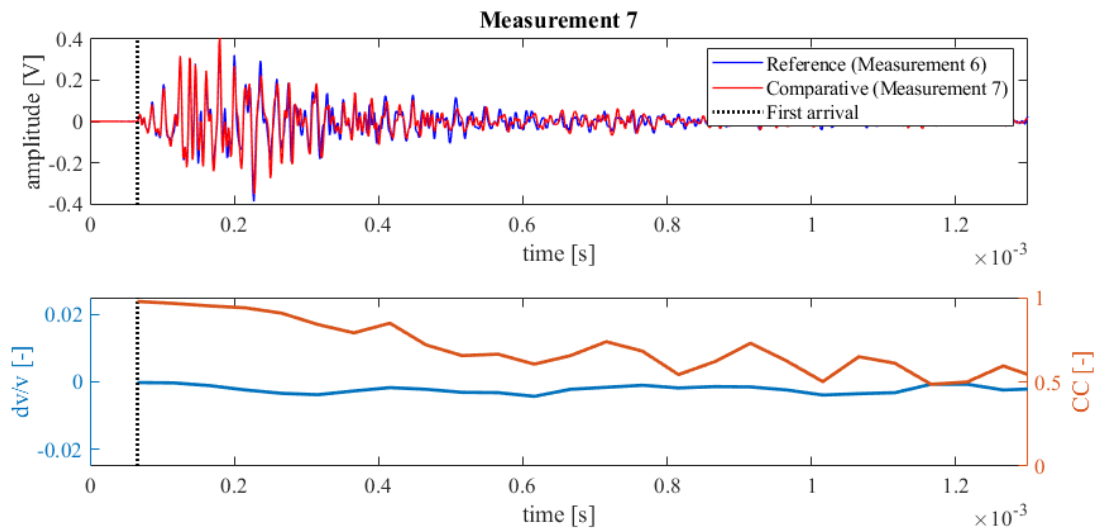


Figure 447: Wave signals of Measurement 6 (blue) and Measurement 7 (red) of geopolymer creep test (top),  $dv/v$  (blue) and  $CC$  (orange) results from CWI over the signal travel time divided in stretching windows (bottom)

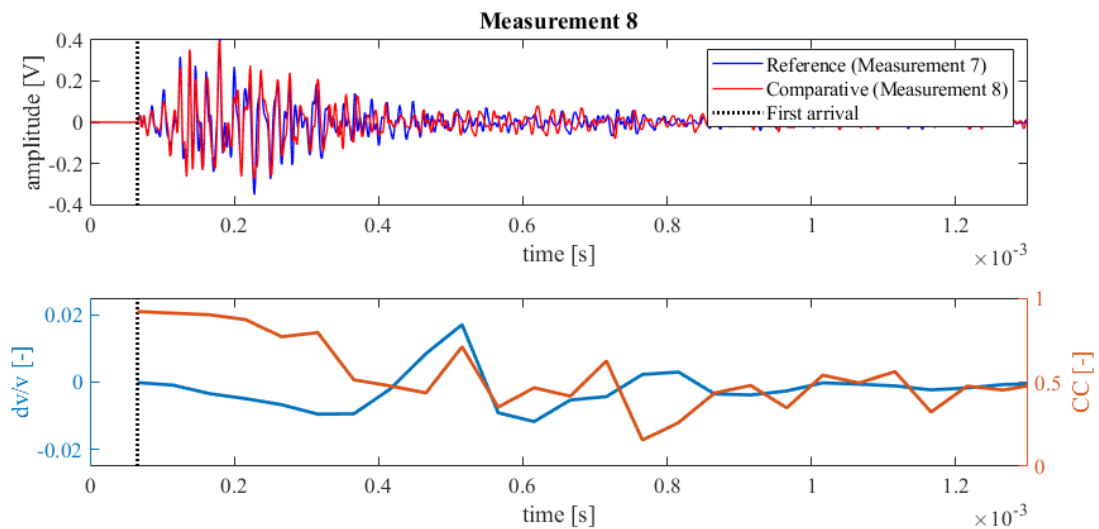


Figure 448: Wave signals of Measurement 7 (blue) and Measurement 8 (red) of geopolymer creep test (top),  $dv/v$  (blue) and  $CC$  (orange) results from CWI over the signal travel time divided in stretching windows (bottom)

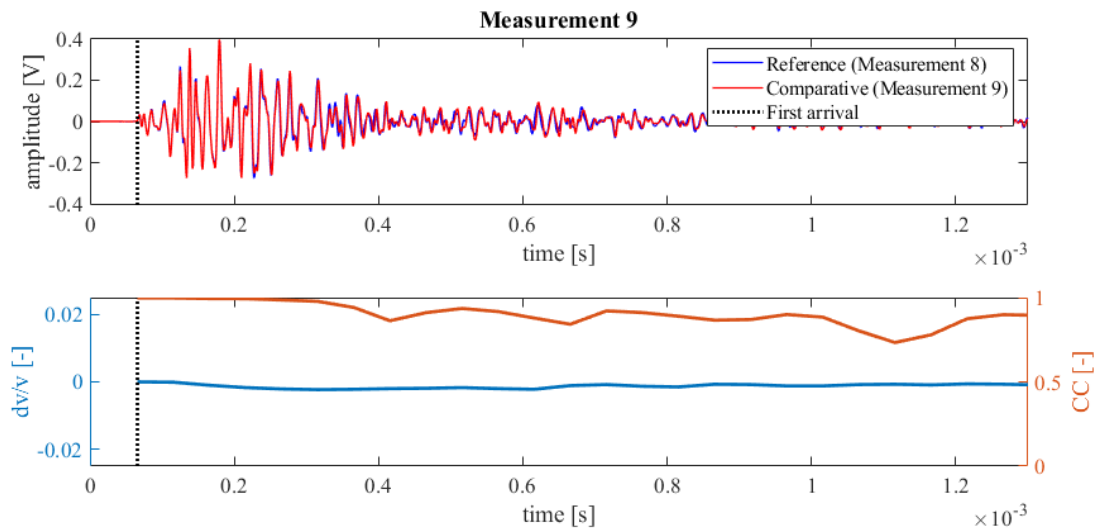


Figure 449: Wave signals of Measurement 8 (blue) and Measurement 9 (red) of geopolymer creep test (top),  $dv/v$  (blue) and CC (orange) results from CWI over the signal travel time divided in stretching windows (bottom)

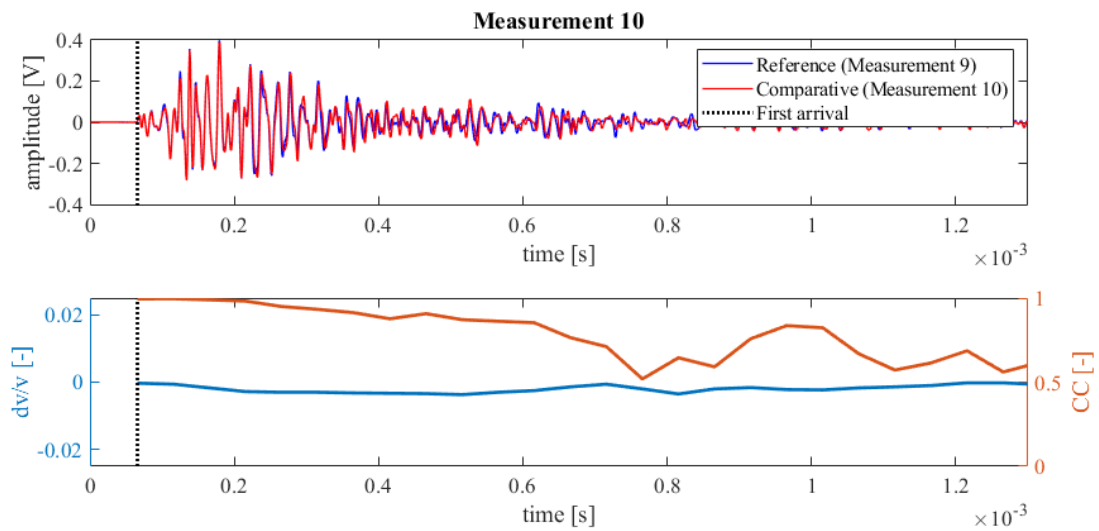


Figure 450: Wave signals of Measurement 9 (blue) and Measurement 10 (red) of geopolymer creep test (top),  $dv/v$  (blue) and CC (orange) results from CWI over the signal travel time divided in stretching windows (bottom)

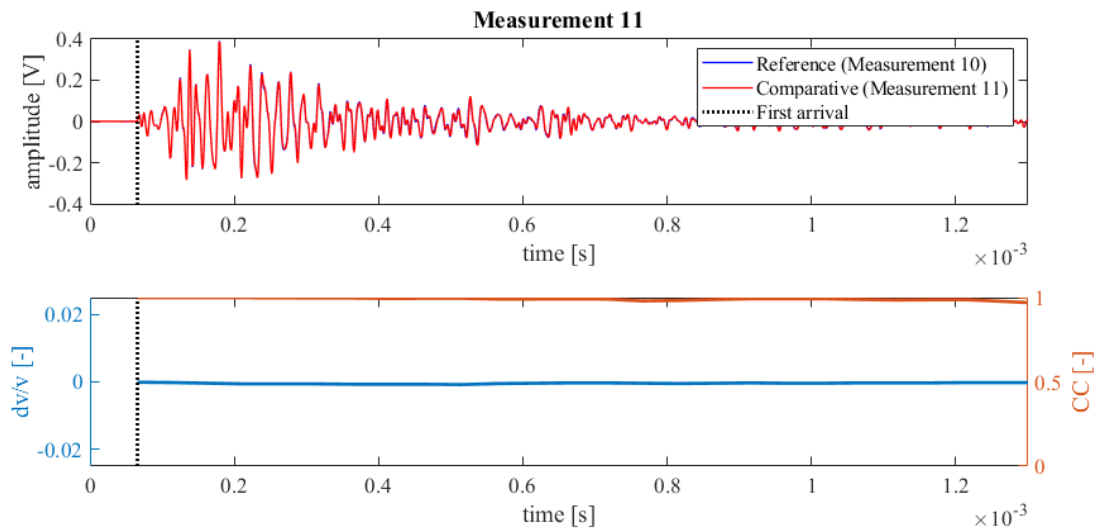


Figure 451: Wave signals of Measurement 10 (blue) and Measurement 11 (red) of geopolymer creep test (top),  $dv/v$  (blue) and CC (orange) results from CWI over the signal travel time divided in stretching windows (bottom)

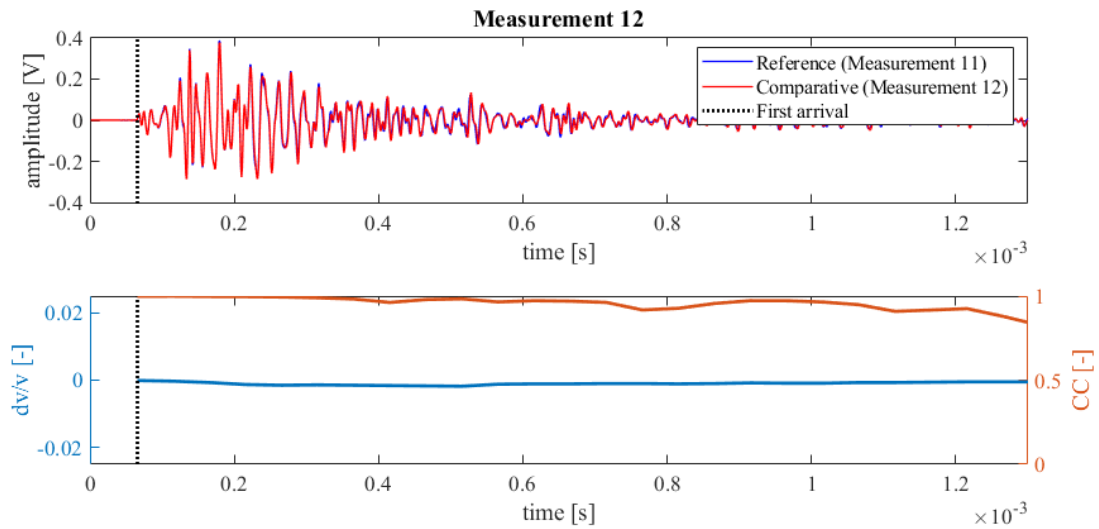


Figure 452: Wave signals of Measurement 11 (blue) and Measurement 12 (red) of geopolymer creep test (top),  $dv/v$  (blue) and CC (orange) results from CWI over the signal travel time divided in stretching windows (bottom)

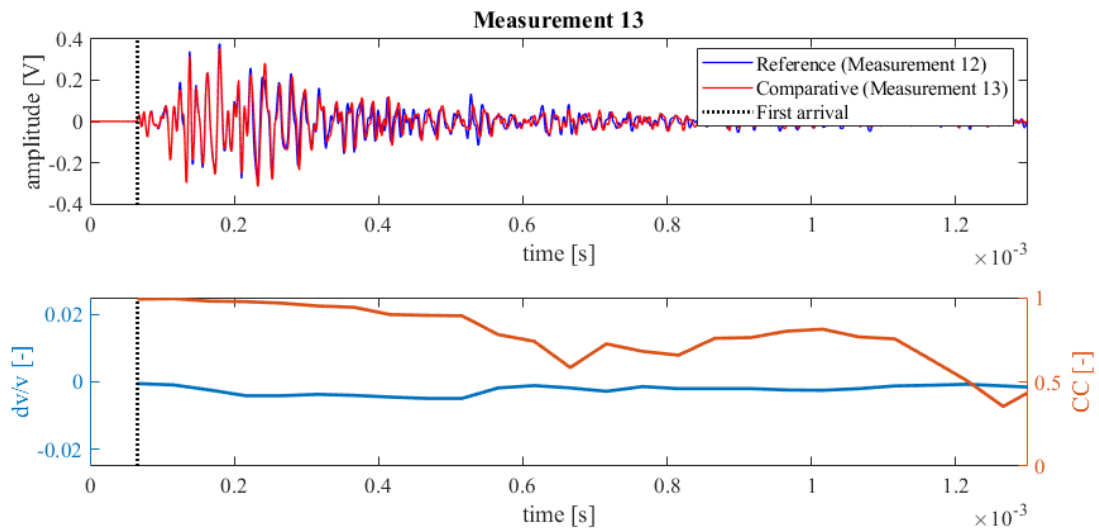


Figure 453: Wave signals of Measurement 12 (blue) and Measurement 13 (red) of geopolymer creep test (top),  $dv/v$  (blue) and CC (orange) results from CWI over the signal travel time divided in stretching windows (bottom)

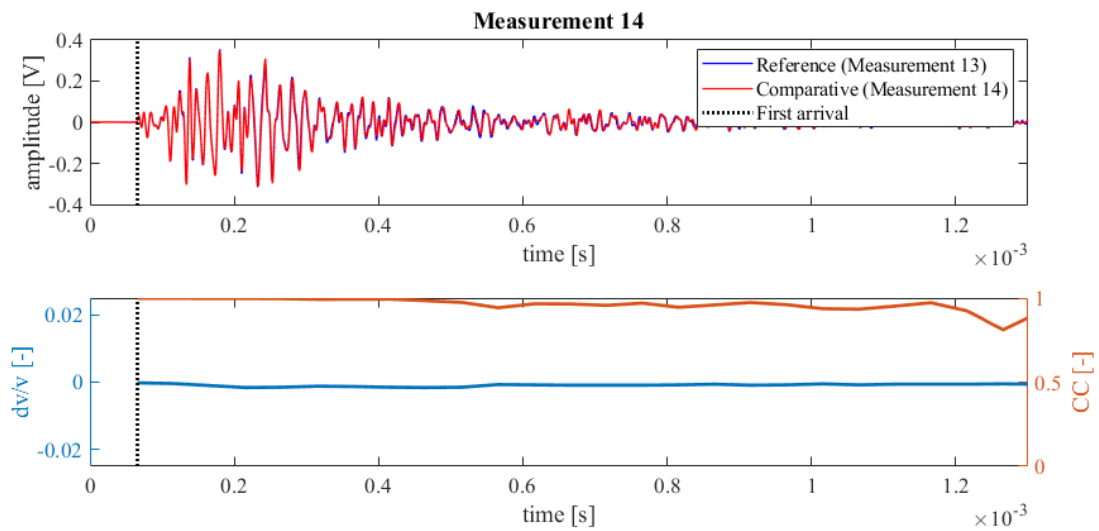


Figure 454: Wave signals of Measurement 13 (blue) and Measurement 14 (red) of geopolymer creep test (top),  $dv/v$  (blue) and CC (orange) results from CWI over the signal travel time divided in stretching windows (bottom)

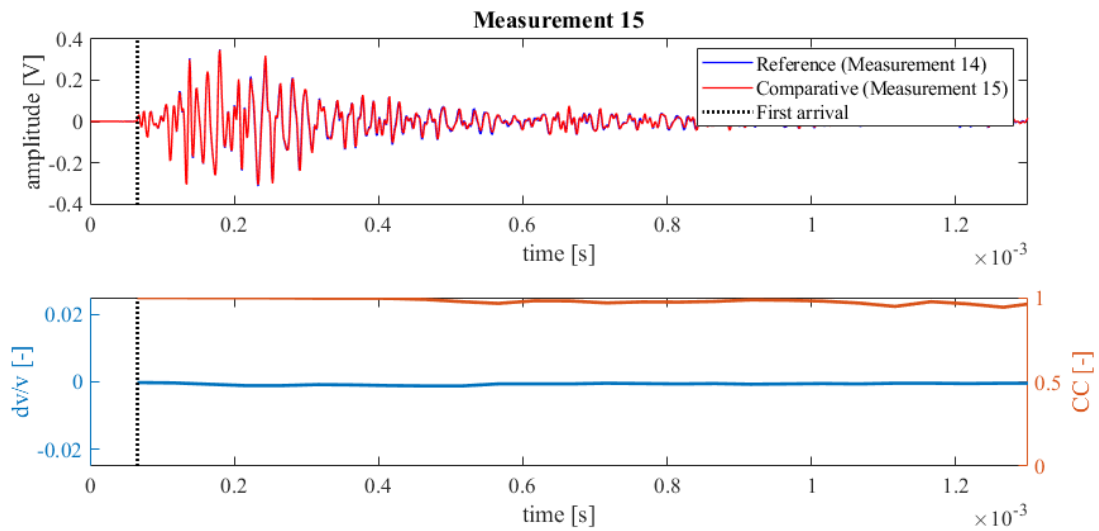


Figure 455: Wave signals of Measurement 14 (blue) and Measurement 15 (red) of geopolymer creep test (top),  $dv/v$  (blue) and CC (orange) results from CWI over the signal travel time divided in stretching windows (bottom)

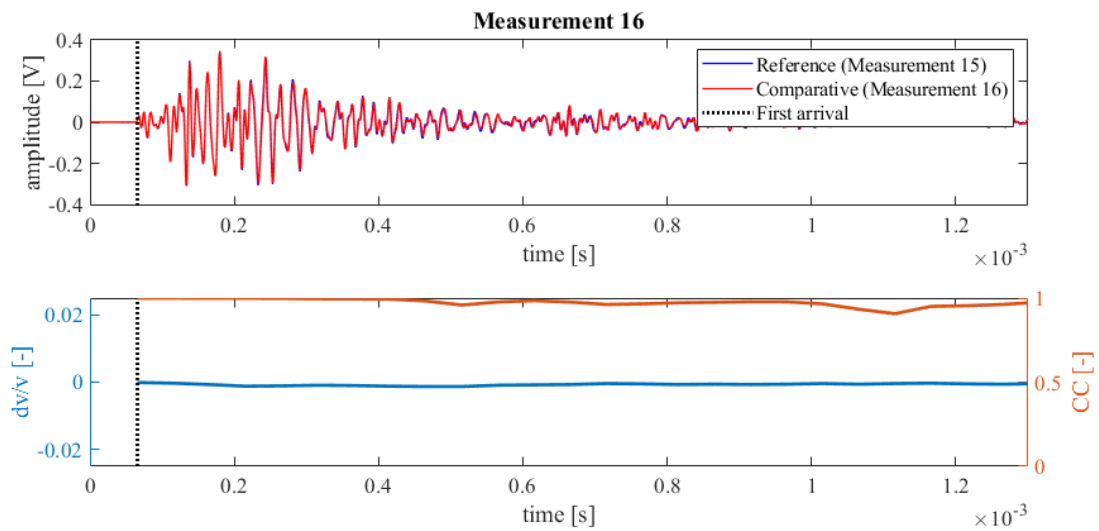


Figure 456: Wave signals of Measurement 15 (blue) and Measurement 16 (red) of geopolymer creep test (top),  $dv/v$  (blue) and CC (orange) results from CWI over the signal travel time divided in stretching windows (bottom)

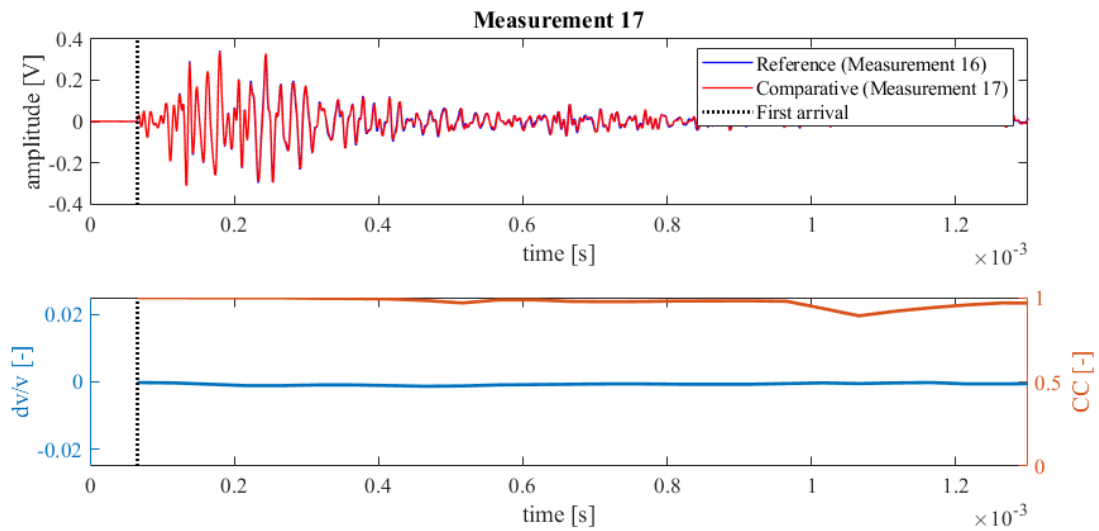


Figure 457: Wave signals of Measurement 16 (blue) and Measurement 17 (red) of geopolymer creep test (top),  $dv/v$  (blue) and CC (orange) results from CWI over the signal travel time divided in stretching windows (bottom)

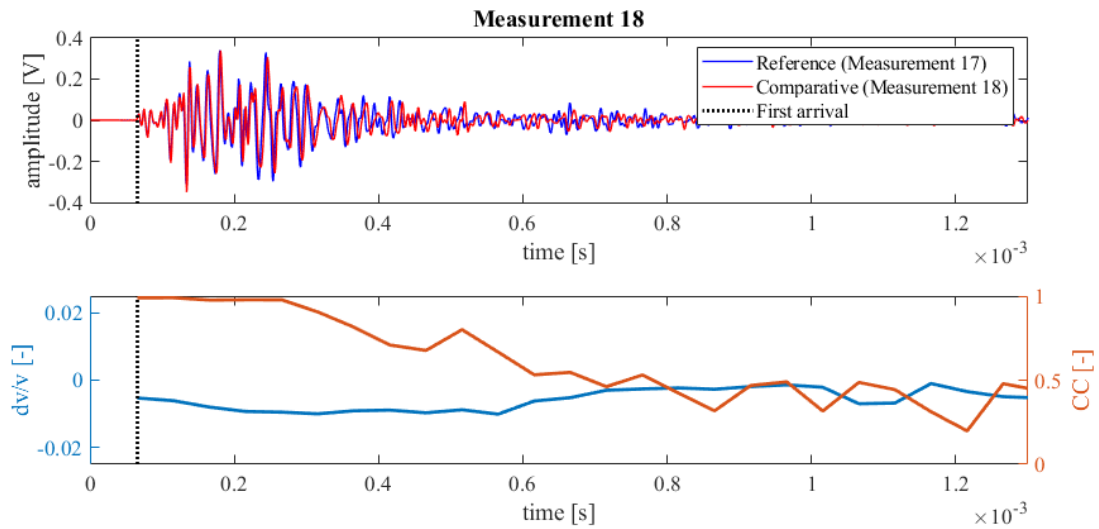


Figure 458: Wave signals of Measurement 17 (blue) and Measurement 18 (red) of geopolymer creep test (top),  $dv/v$  (blue) and CC (orange) results from CWI over the signal travel time divided in stretching windows (bottom)

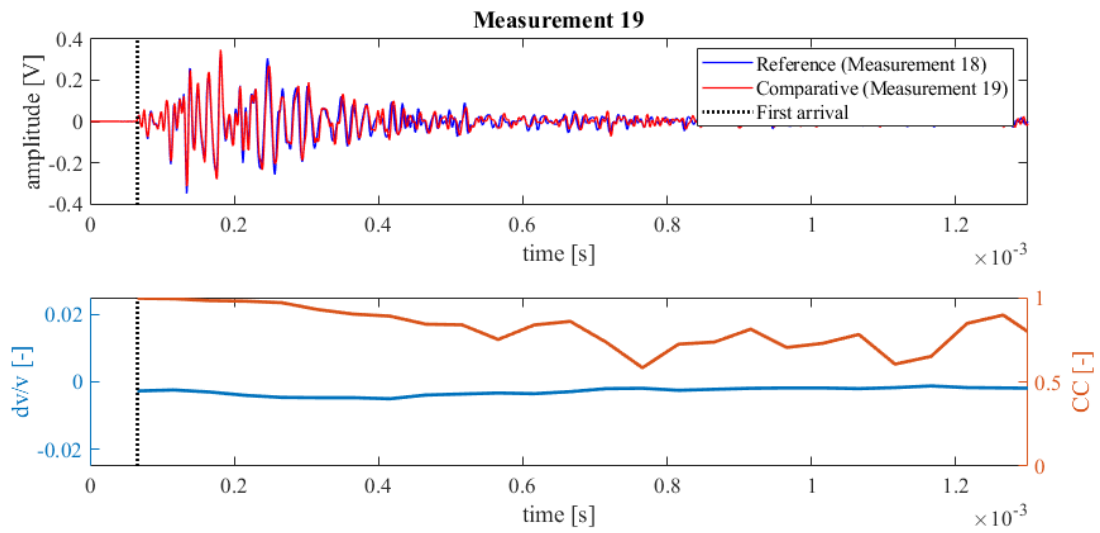


Figure 459: Wave signals of Measurement 18 (blue) and Measurement 19 (red) of geopolymer creep test (top),  $dv/v$  (blue) and CC (orange) results from CWI over the signal travel time divided in stretching windows (bottom)

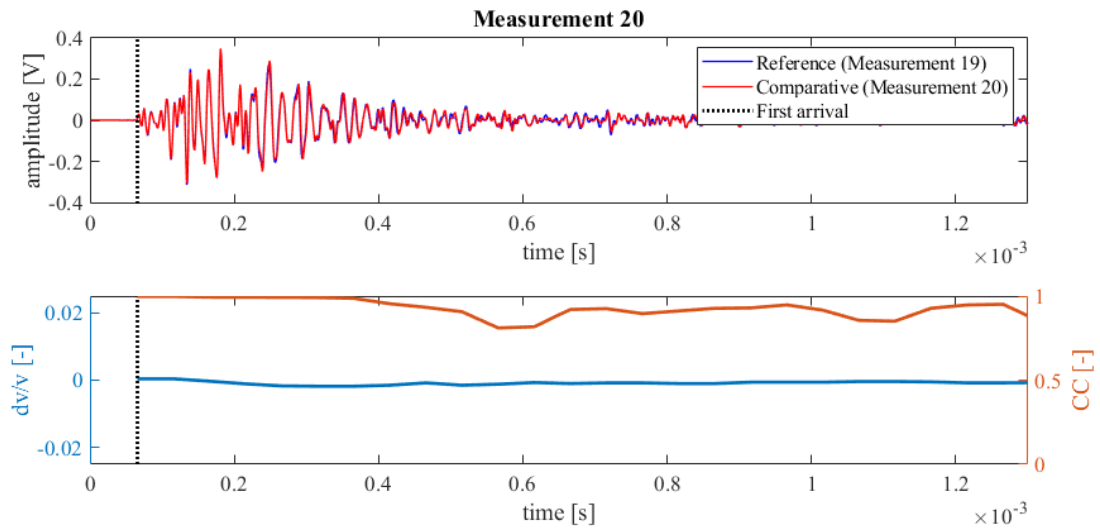


Figure 460: Wave signals of Measurement 19 (blue) and Measurement 20 (red) of geopolymer creep test (top),  $dv/v$  (blue) and CC (orange) results from CWI over the signal travel time divided in stretching windows (bottom)

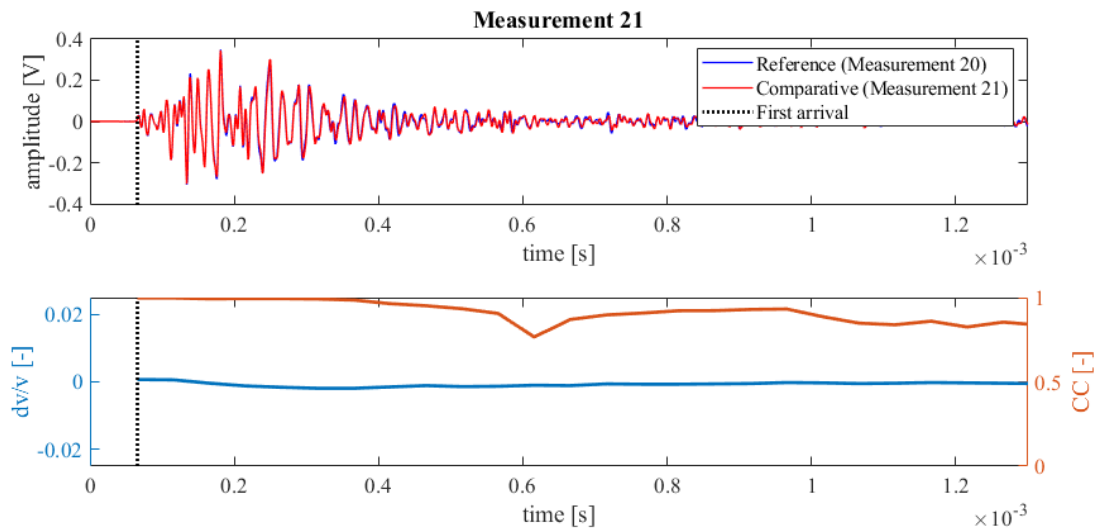


Figure 461: Wave signals of Measurement 20 (blue) and Measurement 21 (red) of geopolymer creep test (top),  $dv/v$  (blue) and CC (orange) results from CWI over the signal travel time divided in stretching windows (bottom)

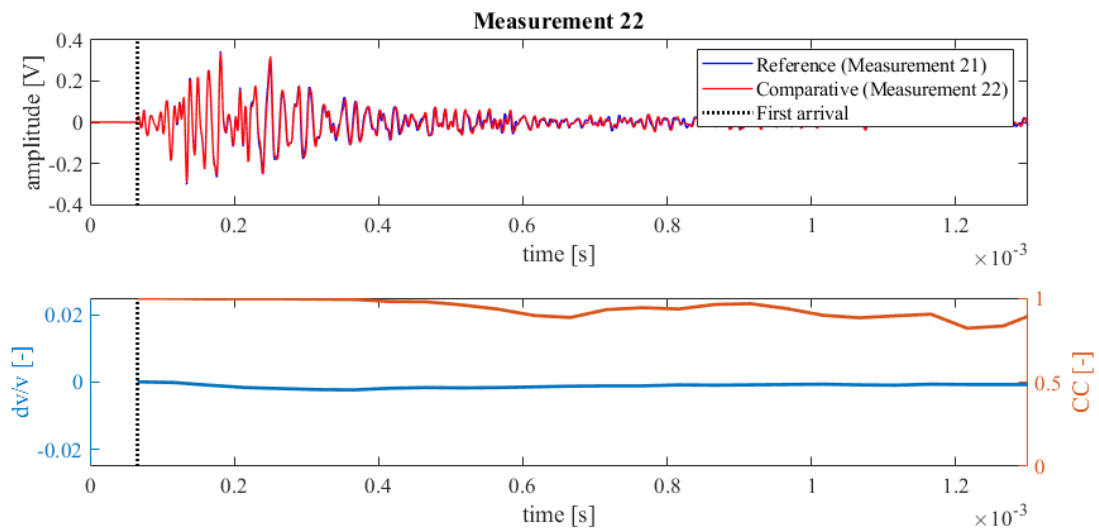


Figure 462: Wave signals of Measurement 21 (blue) and Measurement 22 (red) of geopolymer creep test (top),  $dv/v$  (blue) and CC (orange) results from CWI over the signal travel time divided in stretching windows (bottom)

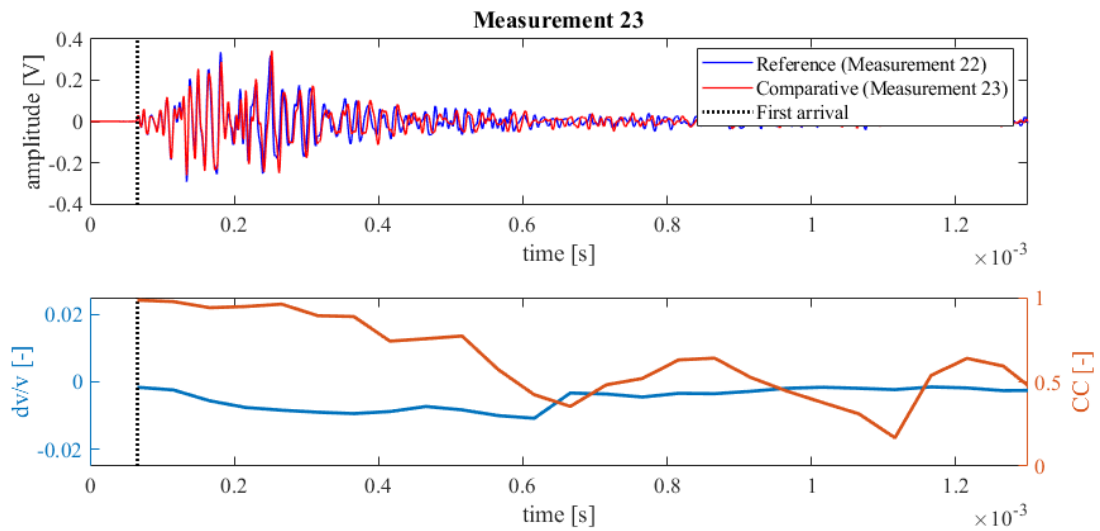


Figure 463: Wave signals of Measurement 22 (blue) and Measurement 23 (red) of geopolymer creep test (top),  $dv/v$  (blue) and CC (orange) results from CWI over the signal travel time divided in stretching windows (bottom)

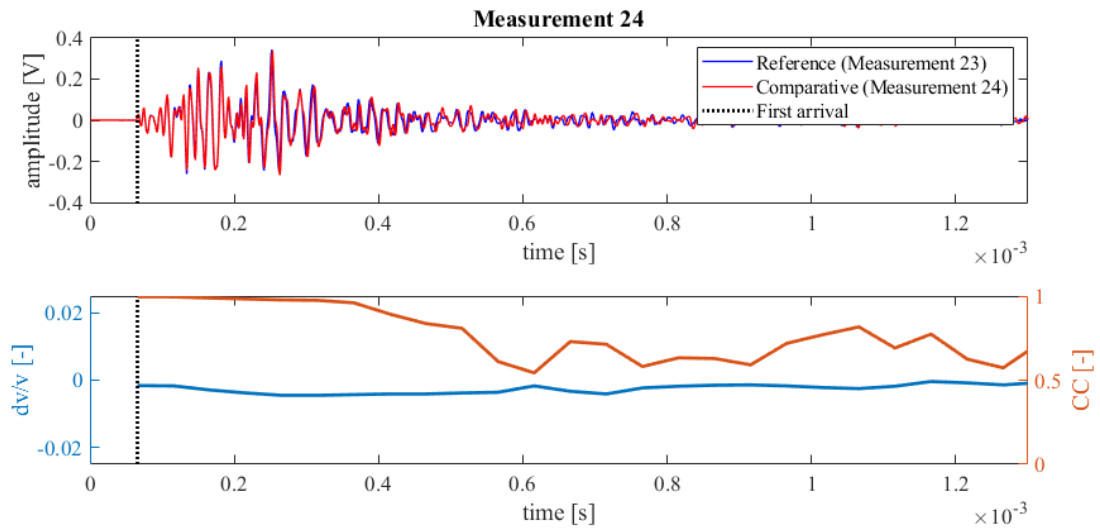


Figure 464: Wave signals of Measurement 23 (blue) and Measurement 24 (red) of geopolymer creep test (top),  $dv/v$  (blue) and CC (orange) results from CWI over the signal travel time divided in stretching windows (bottom)

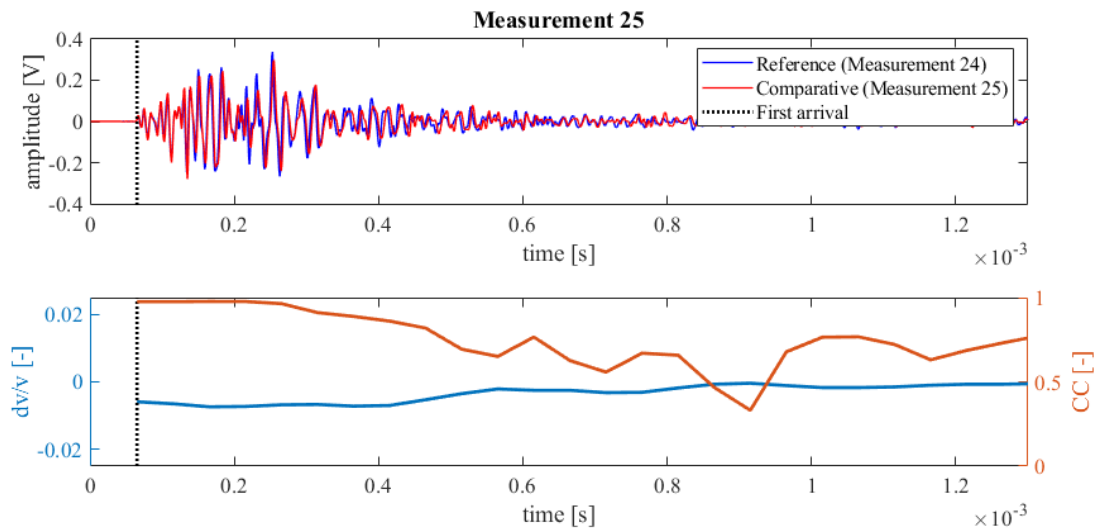


Figure 465: Wave signals of Measurement 24 (blue) and Measurement 25 (red) of geopolymer creep test (top),  $dv/v$  (blue) and CC (orange) results from CWI over the signal travel time divided in stretching windows (bottom)

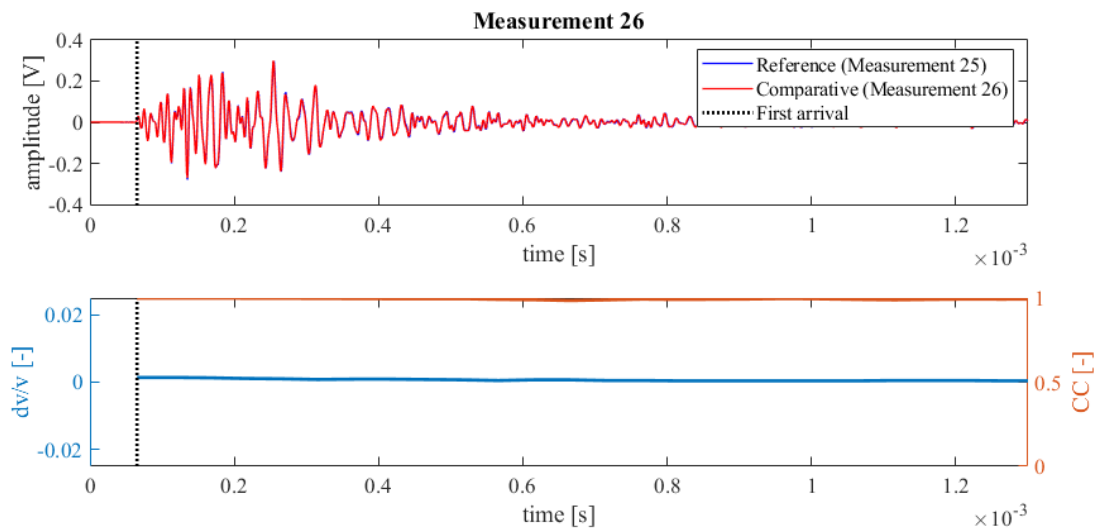


Figure 466: Wave signals of Measurement 25 (blue) and Measurement 26 (red) of geopolymer creep test (top),  $dv/v$  (blue) and CC (orange) results from CWI over the signal travel time divided in stretching windows (bottom)

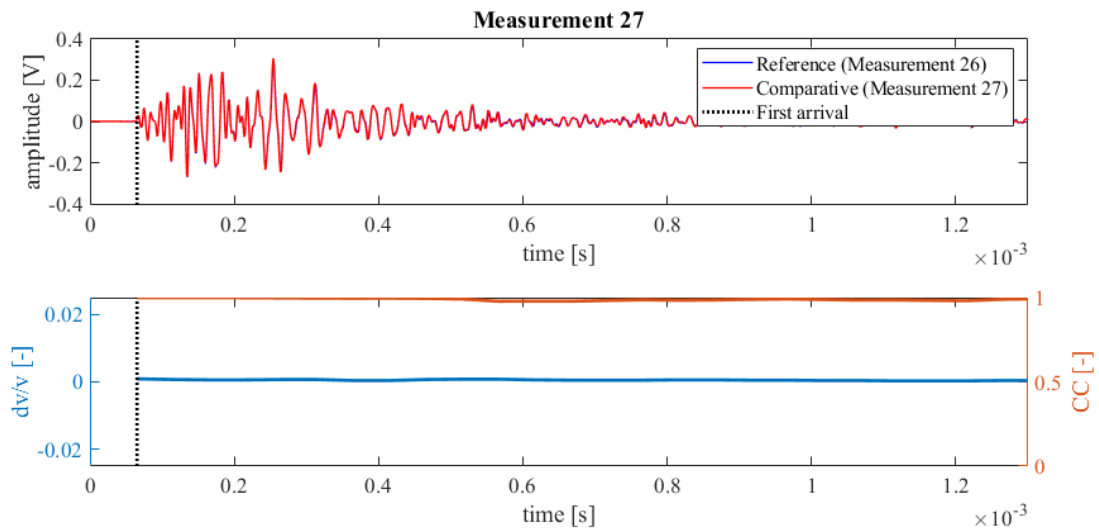


Figure 467: Wave signals of Measurement 26 (blue) and Measurement 27 (red) of geopolymer creep test (top),  $dv/v$  (blue) and CC (orange) results from CWI over the signal travel time divided in stretching windows (bottom)

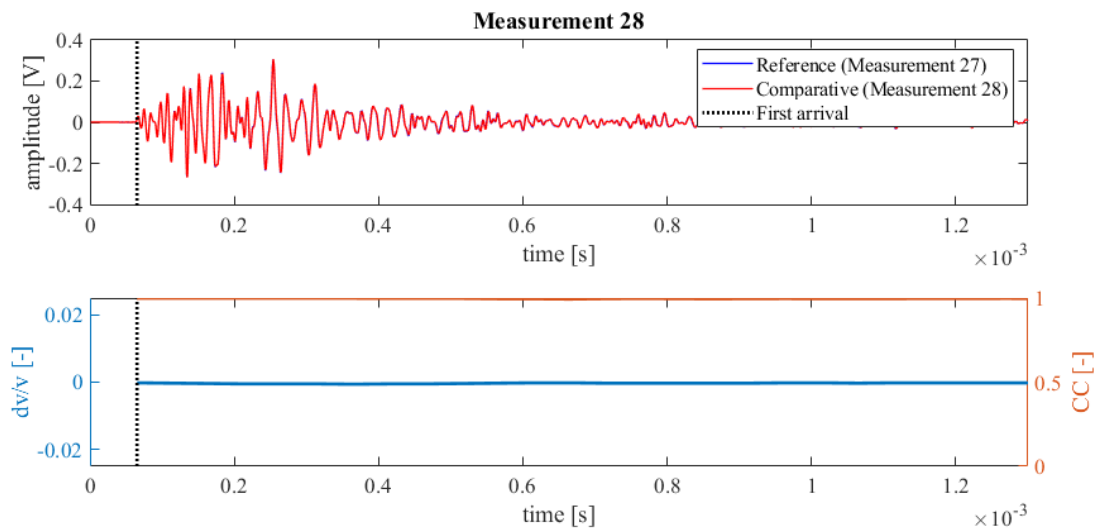


Figure 468: Wave signals of Measurement 27 (blue) and Measurement 28 (red) of geopolymer creep test (top),  $dv/v$  (blue) and CC (orange) results from CWI over the signal travel time divided in stretching windows (bottom)

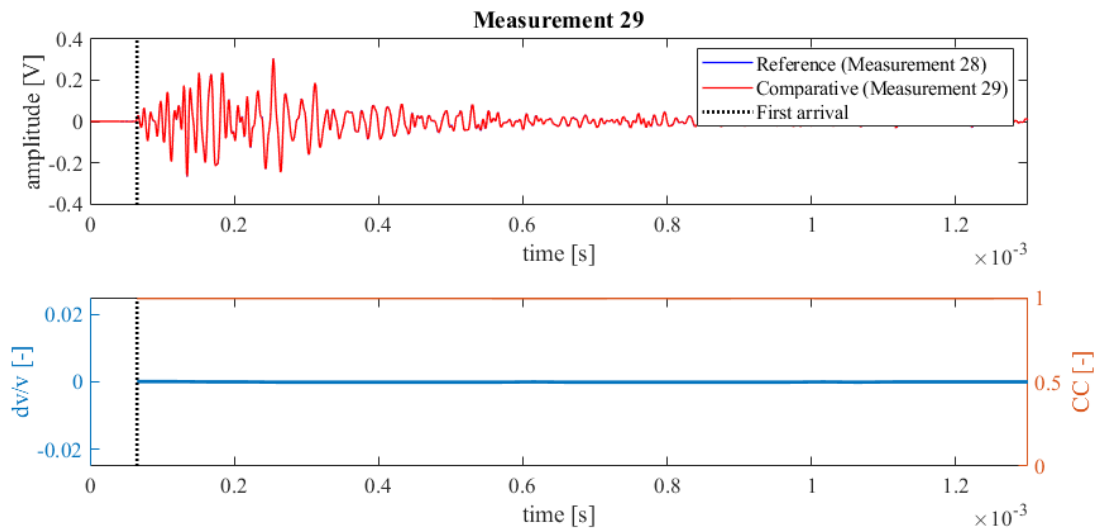


Figure 469: Wave signals of Measurement 28 (blue) and Measurement 29 (red) of geopolymer creep test (top),  $dv/v$  (blue) and CC (orange) results from CWI over the signal travel time divided in stretching windows (bottom)

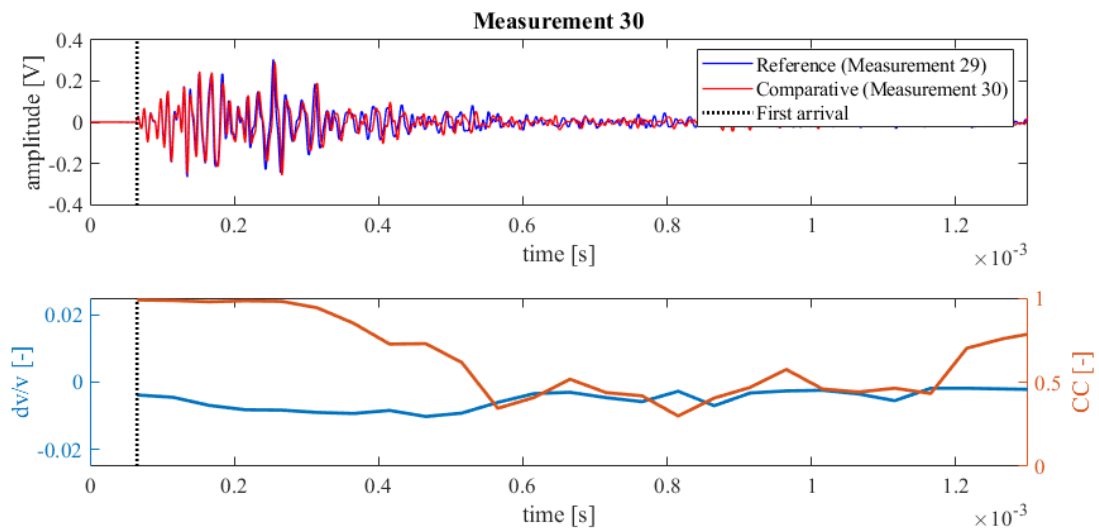


Figure 470: Wave signals of Measurement 29 (blue) and Measurement 30 (red) of geopolymer creep test (top),  $dv/v$  (blue) and CC (orange) results from CWI over the signal travel time divided in stretching windows (bottom)

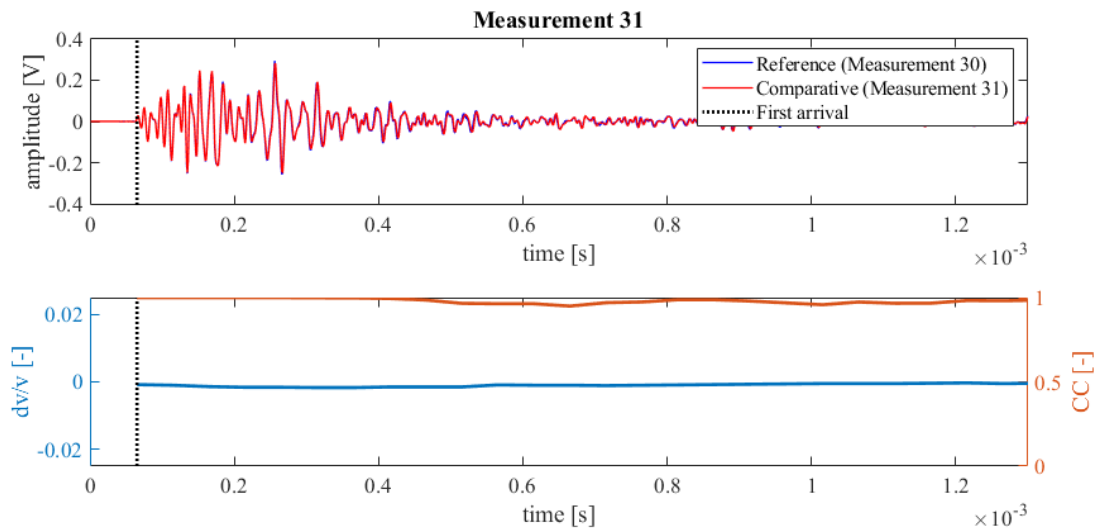


Figure 471: Wave signals of Measurement 30 (blue) and Measurement 31 (red) of geopolymer creep test (top),  $dv/v$  (blue) and CC (orange) results from CWI over the signal travel time divided in stretching windows (bottom)

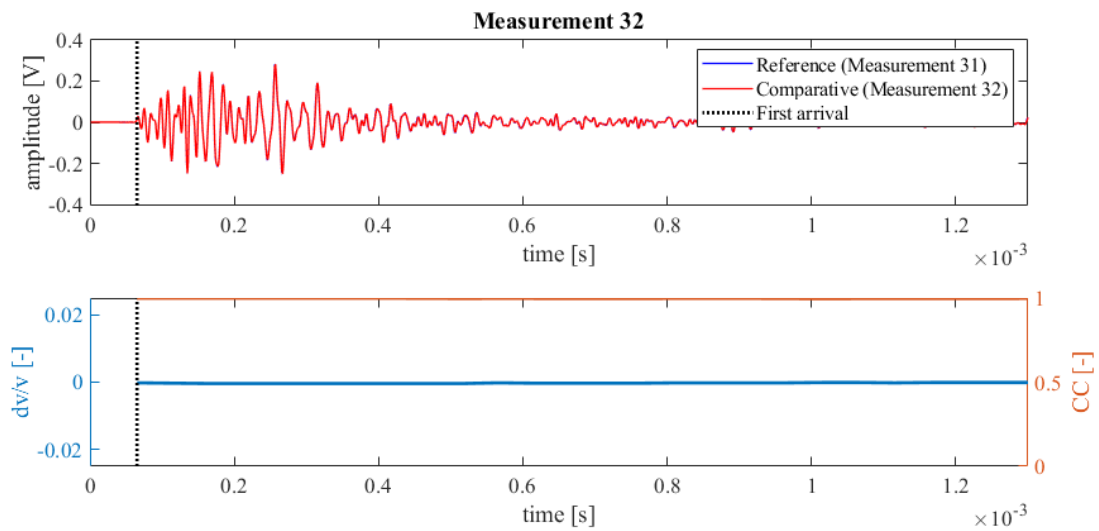


Figure 472: Wave signals of Measurement 31 (blue) and Measurement 32 (red) of geopolymer creep test (top),  $dv/v$  (blue) and CC (orange) results from CWI over the signal travel time divided in stretching windows (bottom)

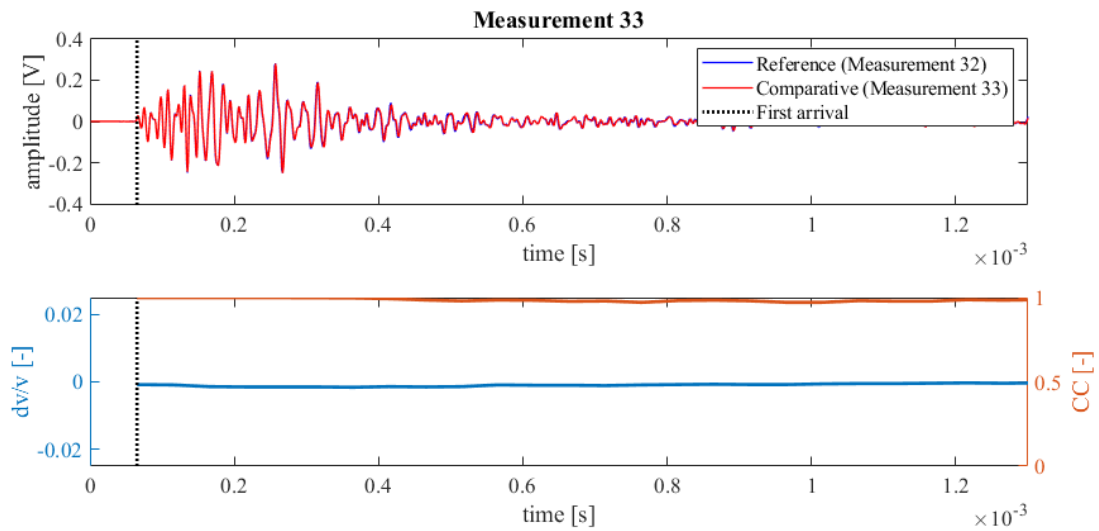


Figure 473: Wave signals of Measurement 32 (blue) and Measurement 33 (red) of geopolymer creep test (top),  $dv/v$  (blue) and CC (orange) results from CWI over the signal travel time divided in stretching windows (bottom)

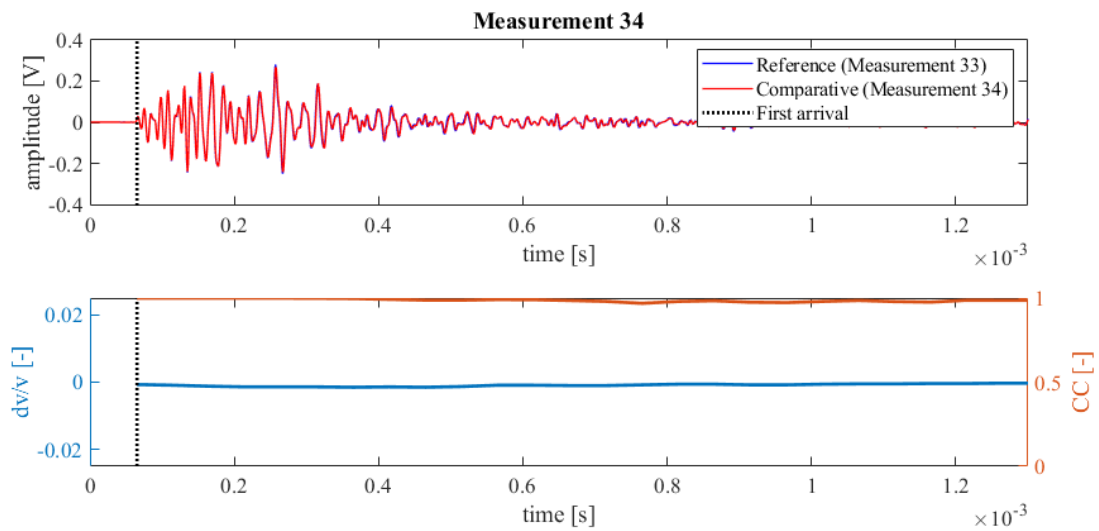


Figure 474: Wave signals of Measurement 33 (blue) and Measurement 34 (red) of geopolymer creep test (top),  $dv/v$  (blue) and CC (orange) results from CWI over the signal travel time divided in stretching windows (bottom)